

**Hydroclimate Changes to Arid regions subjected to Impact of climate change,
human activities, and Large-scale climate patterns**

by

Shereif Hassan Mahmoud

A thesis submitted in partial fulfillment of the requirements for the degree of

Doctor of Philosophy

in

Water Resources Engineering

Department of Civil and Environmental Engineering

University of Alberta

Abstract

In recent years, many regions worldwide have suffered from natural hazards related to the impact of human activities and climate change, such as floods and droughts, sea level rise, extreme weather events and an accelerated hydrological cycle. In Africa, the driest continent on Earth, climate change has led to more frequent occurrences of droughts of greater severity. Beside climate change, human activities have also incurred negative environmental impact which in turn has likely affected the climate at a wide range of temporal-spatial scales worldwide. For example, in the Middle East, floods of greater magnitude have been occurring more frequently in recent decades, which could be attributed partly to rapid urbanization or the effect of climate change, or both. In the Nile River basin (NRB), recurring droughts and increasing population have led to rising tension between competing users for water. Therefore, to develop more effective mitigation strategies against the potential impact of climate change, there is an urgent need to better understand changes to the hydrologic cycle of arid regions and linkage to regional climate change.

The objectives of this dissertation are: 1) To investigate the potential implications of urbanization and climate change to the flood risk of Egypt and Saudi Arabia of arid climate in the Middle East. 2) To develop a GIS decision support system to delineate flood susceptibility zones in the Middle East. 3) To analyze the long-term impact of rapid urbanization on urban climate in a hot and arid environment. 4) To assess how past and future anthropogenic climate change and land use change (LUC) patterns have impacted arid regions' environment, water resources, and ecosystems. 5) To develop a remote sensing-based water management model in arid regions of Middle East to help water managers devise sustainable water use planning and management. 6) To

analyze the interdecadal variability in the hydroclimate of the Nile River basin and possible linkages to large-scale climate patterns. 7) To investigate the key climatic changes that contributed to recent increasing aridity of the Nile river basin.

Chapter 1. From analyzing the implications of urbanization and climate change to the flood risk management of two governorates in Egypt, the results show that since 1970s, urbanization has led to higher flood risk despite of the decline in precipitation, because annual surface runoff and runoff anomaly show an increasing trend of 12.7 and 14.39 mm/decade, respectively. The surface runoff time series of the two governorates is also developed, which is one of such database first developed in Egypt, and it can be used to investigate the hydrologic impact of urbanization.

Chapter 2. A multi-criteria approach to map flood susceptibility zones in the Middle East was developed. An analytical hierarchy procedure was employed to derive the weight of each susceptibility factor. An analysis was done to test the sensitivity of susceptibility factors to the flood susceptibility zones of urban watersheds, and the contribution of different susceptibility factors in developing urban flood susceptibility maps. The multi-criteria methodology was applied to the Riyadh Province, the central region of Saudi Arabia, where the flood susceptibility maps developed were validated against historical flood records and re-applied in the Riyadh city of different spatial scale. The results show that the proposed methodology is useful for general urban planning and assessment of flood susceptibility. Based on results obtained from the sensitivity analysis, it is advisable to consider six or more susceptibility factors in developing urban flood susceptibility maps, especially factors related to surface runoff and flow accumulation.

Chapter 3. To study the influence of rapid urbanization on urban climate of Middle Eastern countries, the long-term impact of rapid urbanization on air temperature (T_a), relative humidity (RH), vapor pressure (VP) and human thermal comfort in the Cairo governorate of Egypt was

analyzed. Land use change (LUC) between 1973 and 2017 were derived from Landsat satellite data. Next, non-parametric change point and trend detection algorithms were applied to Ta, RH and VP over 1950-2017 to assess the impact of urbanization on the urban climate of Egypt. Three historical thermal comfort indices: temperature humidity index (THI), effective temperature index (ETI) and relative strain index (RSI) were estimated from climate data collected between 1950 and 2017 to assess the impact of urbanization on human thermal comfort. The result shows that rapid urbanization in the Cairo governorate had led to severe heat stress levels and thermal discomfort risk in urban areas with limited vegetation covers.

Chapter 4. To investigate the impact of anthropogenic climate change, human activities and land use change (LUC) on the environment and ecosystem services in arid regions, Earth observation data, Markov Chain, Cellular Automata, Pettit's and Mann-Kendall tests were used to characterize the dynamic of LUC over coastal regions of Saudi Arabia and their impacts on regional climate and environment. Future effects of LUC and climate change in the study area, were also projected. The analysis shows that human alteration from natural vegetation and forests to other land uses after 1970s had resulted in the loss, degradation, and fragmentation of forests and vegetation, all of which have significant negative effects on the biodiversity of the region.

Chapter 5. Using meteorological data, gridded climate and satellite data, a water management model was developed in arid regions of Middle East. First, the FAO Penman-Monteith method was used to model the spatial distribution of potential evapotranspiration (ET_p) on a grid-by-grid basis over the central regions of Saudi Arabia. Then, crop coefficients (K_c) were modelled as a function of 16-day time-series MODIS normalized difference vegetation index (NDVI). Actual evapotranspiration (AET) at daily, monthly and annual time scales were estimated from a soil water balance (SWB) model, K_c maps and ET_p. The analysis of NDVI-K_c relationships

at each pixel, showed strong agreement between NDVI modeled K_c and actual K_c which fits crop growth conditions in the field. The average daily AET data show a statistically significant positive trend of 1.5 mm/decade in the study area since 1990. The positive trend in AET is expected to give rise to more severe droughts in the future. Therefore, a strategic management of irrigated water is necessary to minimize unnecessary wastage.

Chapter 6. A comprehensive analysis on the interannual to interdecadal variability in the hydroclimate of the Nile River basin (NRB) and possible teleconnection to large-scale climate patterns, the spatio-temporal variability, frequency, intensity, change point and trend of monthly precipitation, precipitation anomaly, temperature, temperature anomaly, geopotential height, relative humidity, specific humidity, actual evapotranspiration (AET), and wind stresses data over the basin level was conducted. The results show significant hydroclimate changes in NRB in recent decades. Besides climate warming, statistical analysis, wavelet transform coherence (WTC) analysis, composite analysis, and detrended cross-correlation analysis (DCCA) also show that beside ENSO, IOD plays a crucial role on NRB's hydroclimate variability over inter-decadal and longer timescales.

Chapter 7. The primary driving factors that contributed to recent increased aridity of the Nile river basin (NRB) were identified. Besides climate warming, statistical and wavelet transform coherence (WTC) analysis shows that the influence of stronger ENSO and Indian Ocean dipole (IOD) in NRB has increased after 1980s, particularly the influence of IOD on NRB's hydroclimate over inter-decadal timescales. A shift in zonal winds (westward) and meridional winds (southward) associated with stronger El Niño events has contributed to the increased aridity of NRB after 1970s, given stream function, GPH and U-wind anomalies associated with El Niño show that changes in regional atmospheric circulations during more persistent and stronger El Niño has

resulted in drier NRB. After 1970s, WTC between El Niño, IOD, sc-PDSI (self-calibrating Palmer Drought Severity Index) and SPI (Standard Precipitation Index) shows significant anti-phase relationships, which again demonstrates that more frequent and severe El Niño, IOD and SST gradient over the Arabian Sea (WTIO) in recent years has led to more severe droughts in NRB. Furthermore, from WTC and strong negative correlations between SPI, sc-PDSI and WTIO, NRB's hydroclimate is shown to be more strongly influenced by WTIO than by IOD, and the Nile flow is more strongly teleconnected to IOD and WTIO than El Niño at inter-annual and inter-decadal time scales. Contrary to past finding, our results show that IOD and WTIO are better predictors of the Nile flow than El Niño. Climate projections suggest that under the combined impact of warming and stronger WTIO and El Niño events, future droughts of the NRB are expected to worsen.

Conclusions and future work are provided in Chapter 8.

Preface

This thesis is my original work and is organized in an article format. The thesis consists of eight chapters and each chapter is written as an integrated paper for journal submission. As such, each chapter contains standalone introductions, methods, results and conclusions. A general introduction section is provided at the beginning of the thesis, research conclusions and recommendations are summarized in Chapter 8, and supplementary materials are provided at the end of thesis. Chapter 1 of the thesis has been published as Mahmoud, S. H., & Gan, T. Y. (2018). Urbanization and climate change implications in flood risk management: Developing an efficient decision support system for flood susceptibility mapping. *Science of The Total Environment*, 636, 152-167. Chapter 2 has been published as Mahmoud, S. H., & Gan, T. Y. (2018). Multi-criteria approach to develop flood susceptibility maps in arid regions of Middle East. *Journal of Cleaner Production*, 196, 216-229. Chapter 3 has been published as Mahmoud, S. H., & Gan, T. Y. (2018). Long-term impact of rapid urbanization on urban climate and human thermal comfort in hot-arid environment. *Building and Environment*, 142, 83-100.

Chapter 4 has been published as Mahmoud, S. H., & Gan, T. Y. (2018). Impact of anthropogenic climate change and human activities on environment and ecosystem services in arid regions. *Science of the Total Environment*, 633, 1329-1344. Chapter 5 has been published as Mahmoud, S. H., & Gan, T. Y. (2019). Irrigation water management in arid regions of Middle East: assessing spatio-temporal variation of actual evapotranspiration through remote sensing techniques and meteorological data. *Agricultural Water Management*, 212, 35-47. The work on Chapter 6 has

been submitted to Journal of Climate Dynamics as Mahmoud, S.H., Gan, T.Y. 2020. Multidecadal variability in the Nile River Basin hydroclimate controlled by ENSO and Indian Ocean Dipole.

Chapter 7 Worsening Drought of Nile Basin by Atmospheric Circulation Shift, Stronger ENSO and Indian Niño has been written to be submitted to one of Nature journals. In addition, I am planning to reorganize the work in the supplementary section (Mahmoud, S.H & Gan, T.Y) into three other journal articles. An aggregated bibliography has been provided for the entire thesis to avoid references overlapping.

Dedication

This thesis is dedicated to Selim's family for all their support, in particular, Jasmine Selim for her endless love, support and understanding which has helped me through my entire academic journey, I love you so much. I would not be the person I am today without Jasmine's constant patience, sacrifices and encouragement throughout the years. I also wish to dedicate this thesis to my family parents, brothers, sisters, and to everyone who taught, encouraged, and inspired me along the way.

Acknowledgments

First, I would like to express my deep appreciation and sincere gratitude to my supervisor Professor Thian Yew Gan for giving me this opportunity, for his continuous support and encouragement of my PhD research, for his enthusiasm, immense knowledge, inspiration, patience, motivation and guidance over the past three years, I could not have imagined having a better supervisor and mentor. My sincere thanks also go to the rest of my thesis committee for their valuable comments and suggestions. I also would like to thank all faculty and staff of Department of Civil and Environmental Engineering, University of Alberta for their support and encouragement.

Table of Contents

Abstract	ii
Preface	vii
Dedication	ix
Acknowledgments	x
Table of Contents	xi
List of Tables	xvi
List of Figures	xviii
General Introduction	1
Chapter 1 Urbanization and climate change implications in flood risk management	1
1.1 Introduction	1
1.2 Study area	5
1.3 Research methodology	5
1.3.1 Change point analysis	5
1.3.2 Effects of Urbanization in surface runoff	8
1.3.3 Flood susceptibility mapping.....	9
1.3.4 Selection Criteria and Data Processing.....	9
1.3.5 Assessment of factors susceptibility level	10
1.3.6 Assignment of weights to watershed and climatic factors.....	12
1.4 Results and Discussions	15
1.4.1 Impact of climate change in flood risk	15
1.4.2 Effects of Urbanization on surface runoff	18
1.4.3 Development of database for factors related to floods	21
1.4.4 Flood Susceptibility Zones	29
1.5 Conclusions and recommendations	36
Chapter 2 Multi-criteria Approach to develop flood susceptibility maps in arid regions	38
2.1 Introduction	38

2.2 Study area	41
2.3 Materials and methods.....	44
2.3.1 Selection of susceptibility factors and data processing.....	44
2.3.2 Assignment of weights for susceptibility factors.....	47
2.3.3 Flood susceptibility index.....	50
2.3.4 Model sensitivity analysis.....	50
2.4 Results and discussions	51
2.4.1 Development of flood susceptibility factors database	51
2.4.2 Flood susceptibility zones in Riyadh Province (large-scale).....	58
2.4.3 Flood susceptibility map for Riyadh City (small-scale)	62
2.4.4 Models validation (large-scale and small-scale).....	64
2.4.5 Sensitivity analysis (test cases).....	65
2.5 Conclusions and recommendations	70
Chapter 3 Impact of urbanization on Urban Climate and Human thermal comfort	72
3.1 Introduction	72
3.2 Data and Research Methods.....	75
3.2.1 Study area and data sets	75
3.2.2 Historical land use dynamics	77
3.2.3 Urban climate change detection.....	78
3.2.4 Thermal comfort indices	80
3.3 Discussion of Results	82
3.3.1 Land use dynamics.....	82
3.3.2 Influence of urbanization on urban climate.....	91
3.3.3 Impact of urbanization on historical thermal comfort indices	98
3.3.4 Impacts of urbanization on temperature health-related illness	104

3.4 Conclusion and recommendations.....	106
Chapter 4 Impact of anthropogenic climate change and human activities on environment and ecosystem services in arid regions.....	108
4.1 Introduction	108
4.2 Data and Research Methods.....	111
4.2.1 Study area and data sets	111
4.2.2 Land use classification and accuracy assessment	112
4.2.3 Changes and Dynamics of Land Use/Cover	113
4.2.4 Anthropogenic climate change detection.....	117
4.3 Discussion of Results	119
4.3.1 Impact of land use dynamics on environment	119
4.3.2 Anthropogenic climate change and human activities	125
4.3.3 Land use change prediction	133
4.3.4 Impacts of land use change and climate change on Fauna and Flora	138
4.4 Conclusions and recommendations	140
Chapter 5 Irrigation Water Management in arid regions of Middle East	143
5.1 Introduction.....	143
5.2 Material and methods	146
5.2.1 Description of the study area:	146
5.2.2 Reference Evapotranspiration (ET _o)	148
5.2.3 Actual evapotranspiration estimated by a soil water balance model.....	149
5.2.4 Long-term average annual actual evapotranspiration at stations.....	153
5.3 Discussions of Results:.....	154
5.3.1 Spatial distribution of reference evapotranspiration	154
5.3.2 Monthly NDVI and Crop Coefficients Patterns for irrigated crops.....	156
5.3.3 Spatial distribution of monthly and annual actual evapotranspiration (AET)	159

5.3.4 Long-term average daily actual evapotranspiration.....	164
5.4 Conclusion.....	165
Chapter 6 Multidecadal variability in the Nile River Basin hydroclimate	168
6.1 Introduction	168
6.2 Study area and data.....	171
6.3 Methods	175
6.3.1 Spatio-temporal variability, trends and change points of NRB hydroclimate	175
6.3.2 Wavelet Analysis and wavelet coherence.....	176
6.3.3 Composite analysis and cross-correlation.....	177
6.4 Results and discussion.....	179
6.4.1 Nile River Basin hydroclimate variability and trends.....	179
6.4.2 Spatial variability of the Nile River basin hydroclimate under climate warming ..	184
6.4.3 Influence of Indian Ocean dipole (IOD) and ENSO on NRB's hydroclimate	188
6.5 Conclusion.....	194
Chapter 7 Worsening Drought of Nile River Basin by Atmospheric Circulation Shift, Stronger ENSO and Indian Ocean Dipole	197
7.1 Introduction	197
7.2 Methods	199
7.2.1 Description of datasets used in this study	199
7.2.2 Change points and trends	201
7.2.3 Spatiotemporal variability of reference and actual evapotranspiration	201
7.2.4 Meteorological drought variability and trend using standardized precipitation index	204
7.2.5 Agricultural droughts assessment	205
7.2.6 Hydrological droughts severity and drivers	206
7.2.7 Wavelet Analysis and wavelet coherence.....	207

7.2.8 Composite Analysis and Future climate change.....	208
7.2.9 Teleconnections to Indian Ocean dipole (IOD) and ENSO.....	209
7.3 Results and discussion.....	210
Chapter 8 Conclusion and recommendations	232
Bibliography	244
Appendices.....	271
Appendix A: Spatiotemporal variability of reference and actual evapotranspiration	271
Appendix B: NRB’s metrological drought under climate warming.....	276
Appendix C: NRB’s agricultural drought assessment.....	279
Appendix D: Influence of Indian Ocean dipole (IOD) and ENSO on NRB’s hydroclimate .	282
Appendix E: Flow variability and response of hydrological droughts to climate change	291
Appendix F: Response of NRB’s streamflow, soil moisture content and groundwater storage to El Niño 3.4 and IOD.....	298
Appendix G: Countries ‘drought classification system based on drought severity indexes ..	307
Appendix H: Changes to driving variables and atmospheric circulation.....	324
Appendix I: Wavelet power spectrum of drought drivers.....	328
Appendix J: Wavelet coherence between driving variables and El-Nino 3.4.....	332
Appendix K: Projected climatic changes in the NRB	337

List of Tables

Table 1.1	Susceptibility levels of various watershed and climatic factors in relation to flooding	10
Table 1.2	Analytical Hierarchy Process	14
Table 1.3	Normalized flood susceptibility factors	14
Table 1.4	Climate variables and surface runoff change detection and trend	16
Table 1.5	Weight (percent of influence)	30
Table 1.6	Classes of Flood susceptibility and number of historical flood events	31
Table 2.1	Classes of the flood susceptibility factors and their ratings	45
Table 2.2	Factors of flood susceptibility: Analytical Hierarchy Process	49
Table 2.3	Normalized flood susceptibility factors: Analytical Hierarchy Process	49
Table 2.4	Percent of influence	59
Table 2.5	Susceptibility classes and flood records	60
Table 2.6	Examples of major floods in Saudi Arabia from 1964 to 2013	64
Table 2.7	Sensitivity analysis for weights	66
Table 2.8	Number of historical flood events in the test cases	69
Table 3.1	Data used in this study: Landsat data from 1973–2017	76
Table 3.2	Accuracy assessment and validation	82
Table 3.3	Area measurements of land use within Cairo for each subperiod and the full period 1973–2017	87
Table 3.4	Detected land use gains and losses within Cairo for each subperiod and the full period 1973-2017	87
Table 3.5	Atmospheric variables and human thermal comforts indices trend	93
Table 3.6	Areal distributions of thermal discomfort risk zones	103
Table 3.7	Sample records of temperature health-related illness and deaths	106
Table 4.1	Earth observation data used in this study	112
Table 4.2	Accuracy assessment and validation of land use-land cover maps	116
Table 4.3	Land use transitions probabilities 1970–2014	117
Table 4.4	Area measurements of land-cover /use within Jizzan province for each subperiod and the full period 1970–2014	124

Table 4.5 Detected land cover/use gains and losses within Jizzan province for each subperiod and the full period 1970–2014.....	124
Table 4.6 Change point and trend detection.....	126
Table 4.7 Area measurements of land cover/use projection 2025, 2050, 2075, and 2100.....	137
Table 4.8 Expected gains and losses during projected period (2014-2100).....	137
Table 5.1 Relationship between monthly NDVI and monthly crop coefficients under irrigated crop condition.	153
Table 6.1 Change point and trend analysis of hydroclimate variables over the NRB	181
Table 7.1 SPI drought severity categories.....	205

List of Figures

Figure 1.1 Location of Beheira and Alexandria governorates in Egypt	5
Figure 1.2 Workflow chart.....	9
Figure 1.3 Warming trend in temperature anomaly in the two governorates	15
Figure 1.4 Mean annual rainfall time series and trend in the two governorates	17
Figure 1.5 Rainfall anomaly in the two governorates.....	17
Figure 1.6 Urbanization implication in monthly surface runoff time series, and trend in the two governorates.....	19
Figure 1.7 Annual surface runoff time series, and trend in the two governorates.....	20
Figure 1.8 Surface runoff anomaly time series, and trend in the two governorates	21
Figure 1.9 Conditioning factors for flood susceptibility: (a) DEM, (b) slope, (c) flow accumulation, (d) drainage density, (e) distance from the drainage network, (f) land use/cover, (h) rainfall intensity, (i) runoff, (j) geology, (k) soil type, (l) curvature.....	23
Figure 1.10 Flood susceptibility map for the districts of Beheira governorates	33
Figure 1.11 Flood susceptibility map for Districts of Alexandria governorates.....	34
Figure 2.1 (a) Location of Riyadh Province in KSA. (b) Photos of flood taken on November 16, 2013, in Riyadh Province.....	43
Figure 2.2 Susceptibility factors used in this study: (a) DEM, (b) slope, (c) flow accumulation, (d) drainage density, (e) distance from the drainage network, (f) land use/cover, (g) annual rainfall, (h) geology, (i) soil type, (j) runoff.....	52
Figure 2.3 Flood susceptibility map for Central Arabia	62
Figure 2.4 Flood susceptibility map for Riyadh's neighborhood	63
Figure 2.5 Sensitivity analysis for weights: (a) flood susceptibility if annual rainfall was eliminated, (b) if runoff is not considered as susceptibility factor, (c) if soil type and land use were eliminated, (d) if distance to drainage network is not a susceptibility factor, (e) flood susceptibility if adopting the same susceptibility used in Kazakis et al. 2015.....	68
Figure 3.1 Location of study area	77
Figure 3.2 Space distribution of land use type from 1973 to 2017 in Cairo.....	84
Figure 3.3 Space distribution of land use type from 1973 to 2017 in New Cairo City	89
Figure 3.4 Space distribution of land use type from 1973 to 2017 in Shrouk City.	90

Figure 3.5 Trend of land use change in New Cairo City (a) and Shrouk City (b).....	91
Figure 3.6 Long-term warming trend: (a) average annual air temperature, (b) air temperature anomalies	92
Figure 3.7 Long-term variability in relative humidity: (a) average monthly relative humidity, (b) average annual relative humidity, (c) relative humidity anomalies	95
Figure 3.8 Long-term variability in vapor pressure: (a) average monthly vapor pressure, (b) average annual vapor pressure, (c) vapor pressure anomalies	97
Figure 3.9 Long-term historical THI: (a) average monthly THI, (b) average annual THI, (c) THI anomalies	100
Figure 3.10 Long-term historical ETI: (a) average monthly ETI, (b) average annual ETI, (c) ETI anomalies	101
Figure 3.11 Long-term historical RSI: (a) average monthly RSI, (b) average annual RSI, (c) RSI anomalies	102
Figure 3.12 Thermal discomfort risk zones: (a) THI risk zones, (b) RSI risk zones, (c) ETI risk zones	104
Figure 3.13 Urban and built up changes against average annual THI and ETI	105
Figure 3.14 Thermal comfort above the upper limits: (a) THI-upper limits, (b) RSI-upper limits	106
Figure 4.1 Location map of Jizzan Province. Kingdom of Saudi Arabia.	111
Figure 4.2 Spatial distribution of LULCC in Jizzan Province a) 1970, b) 1980, c) 1990, d) 2000, e) 2010, and f) 2014.	123
Figure 4.3 Temperature anomaly and trend	126
Figure 4.4 Precipitation anomaly and trend	126
Figure 4.5 Carbon dioxide emissions timeseries and trend analysis.....	127
Figure 4.6 Other greenhouse gas emissions, HFC, PFC, and SF6.....	128
Figure 4.7 Total greenhouse gas emissions including all anthropogenic sources	128
Figure 4.8 Projection of temperature anomaly (a) average temperature anomaly trend (b).....	129
Figure 4.9 Average annual temperature (a) and Future projection in 2050 (b) future projection in 2075 (c).....	131
Figure 4.10 Average annual precipitation (a) and Future projection in 2050 (b) future projection in 2075 (c).....	132

Figure 4.11 Spatial distribution of projected LULC a) 2025, b) 2050, c) 2075, d) 2100	135
Figure 4.12 Annual Evapotranspiration trend and future projection	140
Figure 4.13 Annual precipitation surplus and future projection	140
Figure 5.1 Location map of the study area.....	147
Figure 5.2 (a) Land cover map; (b) Rainfall map of the study area.....	151
Figure 5.3 Spatial distribution of annual reference evapotranspiration.	156
Figure 5.4 Spatial distribution of monthly crop coefficients	158
Figure 5.5 Spatial distribution on monthly actual evapotranspiration	160
Figure 5.6 a) Average annual actual evapotranspiration based on soil water balance model; b) Average annual actual evapotranspiration based on Schreiber equation.....	163
Figure 5.7 Average daily actual evapotranspiration in the study area	164
Figure 5.8 Daily measured and modelled actual evapotranspiration for alfalfa crop	165
Figure 6.1 Location map of the study area.....	173
Figure 6.2 Spatial distribution of long-term average precipitation and surface temperature between 1948 and 2017 (b), and 2017 land cover map for the Nile River basin (c)	173
Figure 6.3 Temporal variability and trend of (a) temperature anomaly, (b) precipitation anomaly, (c) wind speed, (d) relative humidity, (e) specific humidity, (f) geopotential height, and (g) AET	182
Figure 6.4 Composite maps of (a) Precipitation, (b) Specific humidity, (c) Scalar wind, (d) Meridional wind, (e) Zonal wind, (f) GPH for 1985 to 2017 minus 1948 to 1984	186
Figure 6.5 Composite maps of (a) air temperature ($^{\circ}\text{C}$), (b) relative humidity (%), (c) soil moisture (kg/m^2), (d) surface runoff (mm), and (e) potential evaporation (mm).	187
Figure 6.6 Wavelet coherence between El Nino 3.4 and (a) precipitation, (b) temperature, (c) relative humidity, (d) geopotential height, (e) meridional wind stress, (f) zonal wind stresses, (g) AET.....	190
Figure 6.7 Wavelet coherence between IOD and (a) surface temperature, (b) GPH, (c) precipitation, (d) relative humidity, (e) meridional wind stress, (f) zonal wind stresses, (g) AET	192
Figure 6.8 ENSO and IOD Teleconnections on NRB hydroclimate. IOD and El Niño 3.4 amplitudes cross- correlations with NRB surface temperature (a), GPH (b), precipitation anomaly (c), relative humidity (d), AET (e). Surface temperature anomaly, precipitation anomaly, relative	

humidity, and AET are computed over 30-year running periods from 1920 to 2017, El Niño 3.4 and IOD amplitude are the SD of El Niño 3.4 and IOD indexes over 30-year windows from 1920 to 2017 using the ERSST data sets. The numbers in the top right are the cross-correlation coefficient between hydrologic variables and IOD amplitude (brown colour) and El Niño 3.4 amplitude (red colour) at the 5% level. In a and c, black and yellow points represent neutral ENSO conditions and strong positive IOD in 1961, green point is the response on surface temperature “increase” and decrease in precipitation anomalies “decrease” in the same year. 194

Figure 7.1 El Niño 3.4 index time series, where Mb is the long-term average before the change point, and Ma the long-term average after the change point 212

Figure 7.2 Observed ENSO and Indian Ocean dipole (IOD) amplitude, and zonal and meridional winds stresses over the NRB: ENSO and IOD amplitude (°C), defined as the standard deviation (s.d.) of the Niño3.4 and IOD index over 20-, 30-, 40- and 50-year windows from 1950 to 2017 (a,b), and IOD characteristics over the NRB (c) using the ERSST data sets. Zonal and meridional wind stresses amplitude (10^{-1} N m^{-2}) are defined as the s.d. of zonal and meridional winds stresses over 20-, 30-, 40- and 50-year windows from 1950 to 2017, using NCEP/NCAR data sets from 1950–2017 (d, e). An increasing meridional wind amplitude (e) associated with a prominent anticyclonic circulation in southern NRB have contributed to the observed increasing intensity of recent El Niño events (a). There is also a statistically significant in-phase, inter-annual relationship between meridional wind stress and El Niño over 1960-2017, and an in-phase, inter-annual relationship between zonal wind stress and El Niño over 1988-2017, while IOD, meridional and zonal wind stresses showed in-phase coherence after 2000s (supplementary Figure D3(a-b)). Warm spell duration (WSD), defined as the annual number of days contributing to events where 6 or more consecutive days experience a daily maximum temperature $\text{TX} > 90\text{th}$ percentile, averaged over the NRB using the HadEX2 observational data set given in Figure 7.2(f) shows a linear increasing trend that is significant at 0.001 significant level (p-value). 213

Figure 7.3 The influence of El Niño and La Niña on drought conditions of NRB: (a) 1-month SPI, (b) 48-month SPI vs El Niño 3.4, (c) wavelet coherence between El Niño 3.4 and SPI, (d) self-calibrated PDSI (sc-PDSI) vs. El Niño 3.4, (e) wavelet coherence between the El Niño 3.4 and sc-PDSI, (f) wind stress vs. actual evapotranspiration, and (g) wavelet coherence between wind stress and actual evapotranspiration. The 1-month SPI values ranged from -1.5 to 1.62 with a standard deviation of 0.514. The sc-PDSI shows a statistically significant change point in 1988, where the

long-term average PDSI decreased from 0.125 between 1960 and 1988 to -0.185 between 1988 and 2014 with a statistically significant declining trend of 0.58/decade and a strong correlation with El Niño events. Solid contours in the wavelet coherence plot and the phase difference between El Niño 3.4 and SPI, PDSI enclose periods of statistically significant coherence at 5% level against the red noise process. Right-pointing arrows represent in-phase signals, while left-pointing arrows represent anti-phase signals. After 1970s, the WTC between El Niño, IOD, sc-PDSI and SPI shows significant anti-phase relationships, which demonstrates that more frequent and severe El Niño, IOD and SST gradient over the Arabian Sea (WTIO) in recent years, has led to more severe droughts in NRB. From WTC and strong negative correlations between SPI, sc-PDSI and WTIO, NRB's hydroclimate is shown to be more strongly influenced by WTIO than by IOD. 216

Figure 7.4 Observed annual flows and wavelet coherence with El Niño 3.4: (a) Blue Nile flow, (b) wavelet coherence between El Niño 3.4 and Blue Nile flow, (c) Dongola station flow, (d) wavelet coherence between the El Niño 3.4 and Dongola flow, (e) Aswan station flow, and (f) wavelet coherence between El Niño 3.4 and Aswan station flow. In Figure 7.4, the annual flow of the Blue Nile river decreased from 1645 CBM/s over 1912-1964 to 1478 CBM/s over 1964-2010, with a decreasing trend of about 13.7 CBM/decade after 1964 due to higher AET losses, warmer WTIO and IOD, and more intensive El Niño events. 223

Figure 7.5 Responses of NRB flow variability to El Niño events, IOD amplitude and the IOD two pole amplitudes i.e. western pole amplitude (WTIO) over the Arabian Sea and eastern pole amplitude (SEIO) based on the correlation between NRB flow at Blue Nile and Dongala stations and El Niño 3.4, IOD amplitudes (a, b), SEIO, and WTIO amplitudes (c, d), respectively. The NRB flow are computed over 30-year running periods from 1913 to 2012 for the Blue Nile station, and from 1913 to 1984 for Dongala station. El Niño 3.4, IOD, SEIO, WTIO amplitudes are computed as the s.d. of the El Niño 3.4, IOD, SEIO, WTIO over 30-year windows from 1913 to 2017, using the ERSST data sets. The peak correlation between IOD and the Nile flow occurred one year earlier than that between El Niño and the Blue Nile flow, which agrees with the WTC between IOD and El Niño (i.e. one lead the other as shown in supplementary Figure D1(a, b)). From the WTC and strong negative correlations between Nile flow, SEIO, WTIO and IOD, the Nile flow is more strongly teleconnected to IOD, SEIO and WTIO than to El Niño at inter-annual and inter-decadal time scales. 225

Figure 7.6 The effect of ENSO to the atmospheric circulation over NRB shown by the 750-mb stream function anomaly associated with El Nino (a) and La Nina (b) episodes, 300-mb geopotential height anomaly associated with El Nino (c) and La Nina (d) episodes, zonal and meridional wind anomaly patterns associated with El Nino (e, g) and La Nina (f, h) episodes, respectively. The signals between ENSO and GPH, stream functions, and meridional/zonal wind in the troposphere demonstrates the teleconnection between El Niño and the atmospheric circulation over of NRB. The warming over the Arabian sea and stronger El Niño, the southward shift of the lower atmospheric stream functions and meridional winds, and the westward shift of zonal winds have together contributed to worsening droughts observed in NRB in recent years.
..... 228

General Introduction

In recent decades, many regions worldwide have suffered from the significant impact of human activities, urbanization, climate change, hydrologic extremes such as floods and droughts, rising sea level, extreme weather events and an accelerated hydrological cycle. In Africa, the driest continent on Earth, has been linked to more frequent occurrences of severe droughts, rising temperature and altered precipitation patterns (Ramanathan et al., 2001; Shanahan et al., 2009; Williams and Funk, 2011). Besides climate change, human activities have also incurred negative environmental impact which in turn will affect the climate at a wide range of scales worldwide. For example, in the Middle East, floods of greater magnitude have been occurring more frequently in recent decades, which could be attributed partly to rapid urbanization or the effect of climate change or both. There is a lack of flood susceptibility studies in arid regions of Africa and information related to the influence of climate change and urbanization in surface hydrology of these regions. An analysis of long-term surface runoff data of urban areas can generally reveal the effects of urbanization. However, most studies have not considered the effects of both urbanization and climate change impact to urban surface runoff and the development of flood susceptibility maps, e.g., (Cherqui et al., 2015; Chen et al., 2015; Xiao et al., 2017; Hong et al., 2017; Termeh et al., 2018; Zhao et al., 2018).

The frequent occurrences of extreme weather have caused flooding to be one of the most destructive natural hazards in arid regions. In arid regions of Africa, surface runoff from high latitude regions tend to pose a threat to its urban residents, facilities, and infrastructure. Recent flooding events that occurred in countries such as Egypt and others in Africa show that arid/semi-arid regions in the Middle East region are susceptible to floods. Therefore, it is critical to control

floods through proper land use management. Owing to their magnitude and sudden arrival often with minimal warning, floods usually lead to serious disasters locally. Since the 1970s, population growth in Africa has increased dramatically and therefore urbanization has become a major issue socially and politically. Rapid urbanization has also led to an imbalance between demand and supply, the available infrastructure is under stress, and the urban climate is altered. Therefore, more efforts are needed to better understand the influence of rapid urbanization on urban climate in many if not all Middle Eastern countries of arid climate. There also a need for how land use change (LUC) and climate change have affected the ecosystems and the environment at various spatiotemporal scales. Under the impact of global warming, many hydroclimate variables of arid regions have changed, therefore there is an essential need for a strategic management of water resources, which are limited in many Middle Eastern countries. The development of models to estimate irrigation water requirement based on remotely sensed data applicable over large areas in arid regions of Middle East can be challenging because irrigation water requirements are essential but available water resources are limited.

In a larger scale, recurring droughts and increasing population have led to rising tension between competing users for water in the Nile River basin (NRB). Therefore, there is a need for better understanding of the hydrological cycle of arid regions and linkage to regional climate change to better develop mitigation strategies against the potential impact of future climate change. Most of the published research on the NRB climatology and climate change impact studies has been concentrated in the upper BNB stream countries (Cheung et.al., 2008; Zhang et al., 2012; Muhire and Ahmed, 2015; Ongoma et.al., 2018). Other studies analyzed the effects of climate change on a specific hydroclimate variable such as precipitation, temperature and streamflows at sub-basin level (Phillips and McIntyre, 2000; Nyeko-Ogiramoi et al., 2013; Taye and Willems,

2012; Tierney et al., 2013; Onyutha, 2016; Onyutha and Willems, 2015). However, impact of climate change on the hydroclimate of the NRB in a lumped manner is still unclear. Therefore, it is necessary to improve our understanding of the hydrological cycle and variability in hydroclimate variables of the Nile River basin, giving there is generally a lack of similar studies at the basin level. The results from such studies would help us to better develop mitigation strategies for these riparian countries against the potential impact of climate change.

In this thesis, the potential implications of urbanization and climate change to the flood risk of Egypt and Saudi Arabia of arid climate in the Middle East are examined in Chapters 1. Then, in Chapters 2, a GIS decision support system was developed to delineate flood susceptibility zones in the Middle East to develop more effective mitigation strategies against the potential impact of climate change and urbanization. The long-term impact of rapid urbanization on urban climate in arid environment is presented in Chapter 3. Important information on how past and future anthropogenic climate change and land use change (LUC) patterns have impacted arid regions' environment, water resources, and ecosystems in Chapter 4. In Chapter 5, a remote sensing-based water management model is developed to help water managers devise sustainable water use planning and management in arid regions of Middle East. After devoting the first five chapters on the regional impacts of climate change, human activities and urbanization in arid regions' climate, water resources and ecosystem services, the last two chapters (Chapter 6 and 7) expands to inter-annual to interdecadal variability in the hydroclimate of the Nile River basin and possible linkages to large-scale climate patterns (Chapter 6). Then, the primary driving factors that contributed to recent increased aridity of the Nile river basin (NRB) were identified and is presented in Chapter 7. An overall summary and recommendations of all conclusions from Chapters 1-7 is presented in Chapter 8.

Chapter 1 has been published in the Journal of Science of The Total Environment with the following citation: Mahmoud, S. H., & Gan, T. Y. (2018). Urbanization and climate change implications in flood risk management: Developing an efficient decision support system for flood susceptibility mapping. *Science of The Total Environment*, 636, 152-167.

The effects of urbanization and climate change impact to the flood risk of two governorates in Egypt were analyzed. Non-parametric change point and trend detection algorithms were applied to the annual rainfall, rainfall anomaly, and temperature anomaly of both study sites. Next, change points and trends of the annual and monthly surface runoff data generated by the Curve Number method over 1948-2014 were also analyzed to detect the effects of urbanization on the surface runoff. Lastly, a GIS decision support system was developed to delineate flood susceptibility zones for the two governorates. The significant decline in annual rainfall and rainfall anomaly after 1994 at 8.96 and 15.3 mm/decade respectively was likely due to climate change impact, especially significant warming trend since 1976 at 0.16 °C/decade, though that could partly be attributed to rapid urbanization.

Since 1970, effects of urbanization to flood risk are clear, because despite a decline in rainfall, the annual surface runoff and runoff anomaly show positive trends of 12.7 and of 14.39 mm/decade, respectively. Eleven flood contributing factors have been identified and used in mapping flood susceptibility zones of both sites. In the El-Beheira Governorate, 9.2%, 17.9%, 32.3%, 28.3% and 12.3% of its area are categorized as very high, high, moderate, low and very low susceptibility to flooding, respectively. Similarly, in Alexandria Governorate, 15.9%, 33.5%, 41%, 8.8% and 0.8% of its area are categorized as very high, high, moderate, low and very low susceptibility to flooding, respectively. Very high and high susceptible zones are located in the northern, northwestern and northeastern parts of the Beheira Governorates, and in the northeastern

and northwestern parts of Alexandria. The flood related information obtained in this study will be useful to assist mitigating potential flood damages and future land use planning of both governorates of Egypt.

Chapter 2 has been published in the Journal of Cleaner Production with the following citation: Mahmoud, S. H., & Gan, T. Y. (2018). Multi-criteria approach to develop flood susceptibility maps in arid regions of Middle East. Journal of Cleaner Production, 196, 216-229.

The research study introduced a methodology for identifying flood susceptibility zones using a multi-criteria analysis. The methodology was applied in the Riyadh Province, the central region of Saudi Arabia, validated using historical flood records and re-applied in the Riyadh city to assess the effect of scale on the results. The methodology incorporates 10 susceptibility factors: flow accumulation, annual rainfall, slope, runoff, land use/cover, elevation, geology, soil type, distance from the drainage network, and drainage density. An analytical hierarchy process was employed to derive the weight of each susceptibility factor, and sensitivity analysis was done to test how sensitive are the results to changes in the weights of susceptibility factors, and to evaluate the contribution of different susceptibility factors in developing the flood susceptibility maps. These maps were found to be in good agreement with historical flood events in the Riyadh province and Riyadh city and so they should be useful to assist flood mitigation and for future land use planning in both Riyadh province and Riyadh city. The proposed methodology is useful for general planning and assessment purposes, since it has been shown to be independent of scale, given similar flood susceptibility zones for the Riyadh region were obtained from both large-scale and small-scale models. The highest flood susceptibility areas are found in northern, northeastern, and northwestern parts of the Riyadh Province. Key contributing factors to flood susceptibility are

surface runoff, flow accumulation, soil type, elevation, distance to drainage network, drainage density, land use, slope, and geology. Based on results obtained from the sensitivity analysis, it is advisable to consider six or more susceptibility factors in developing flood susceptibility maps, especially factors related to surface runoff and flow accumulation.

Chapter 3 has been published in the Journal of Building and Environment with the following citation: Mahmoud, S. H., & Gan, T. Y. (2018). Long-term impact of rapid urbanization on urban climate and human thermal comfort in hot-arid environment. *Building and Environment*, 142, 83-100.

The long-term impact of rapid urbanization on air temperature (T_a), relative humidity (RH), vapor pressure (VP) and human thermal comfort in the Cairo governorate of Egypt was analyzed. Land use change (LUC) between 1973 and 2017 were derived from Landsat satellite data. Next, non-parametric change point and trend detection algorithms were applied to T_a , RH and VP over 1950-2017 to estimate the impacts of urbanization on urban climate. Three historical thermal comfort indices: temperature humidity index (THI), effective temperature index (ETI) and relative strain index (RSI) were estimated from climate data collected between 1950 and 2017 to assess the impact of urbanization on human thermal comfort. The results reveal substantial LUC, rapid increasing impervious surface areas in low-lying areas of Cairo at $75.2 \text{ km}^2 / \text{decade}$ since the 1990s. Rapid urbanization had resulted in a statistically significant change point in T_a after 1995 with a warming trend of $0.19 \text{ }^\circ\text{C} / \text{decade}$, a negative trend in RH of $0.55\% / \text{decade}$ and a rising trend in VP of $0.24 \text{ hPa} / \text{decade}$. Severe heat stress levels emerged and persisted every July-September since 1994. THI, ETI, and RSI show statistically significant change points at 1994 and a rising trend of $0.33 \text{ }^\circ\text{C} / \text{decade}$, $0.29 \text{ }^\circ\text{C} / \text{decade}$, and $0.06 / \text{decade}$, respectively. The highest thermal discomfort risk was found in urban areas of the old Cairo, but the risk is marginally smaller

at new cities where there are vegetation covers. This study clearly demonstrates the impacts of rapid urbanization on the urban climate of hot-arid environment.

Chapter 4 has been published in the Journal of Science of The Total Environment with the following citation: Mahmoud, S. H., & Gan, T. Y. (2018). Impact of anthropogenic climate change and human activities on environment and ecosystem services in arid regions. *Science of the Total Environment*, 633, 1329-1344.

The implications of anthropogenic climate change, human activities and land use change (LUC) on the environment and ecosystem services in the coastal regions of Saudi Arabia were analyzed. Earth observations data was used to drive land use categories between 1970-2014. Next, a Markov-CA model was developed to characterize the dynamic of LUC between 2014-2100 and their impacts on regions' climate and environment. Non-parametric change point and trend detection algorithms were applied to temperature, precipitation and greenhouse gases data to investigate the presence of anthropogenic climate change. Lastly, climate models were used to project future climate change between 2014-2100. The analysis of LUC revealed that between 1970 and 2014, built up areas experienced the greatest growth during the study period, leading to a significant monotonic trend. Urban areas increased by 2349.61 km² between 1970 and 2014, an average increase of more than 53.4 km² /yr. The projected LUC between 2014- 2100 indicate a continued increase in urban areas and irrigated cropland.

Human alteration of land use from natural vegetation and forests to other uses after 1970, resulted in a loss, degradation, and fragmentation, all of which usually have devastating effects on the biodiversity of the region. Resulting in a statistically significant change point in temperature anomaly after 1968 with a warming trend of 0.24 °C/decade and a downward trend in precipitation anomaly of 12.2 mm/decade. Total greenhouse gas emissions including all anthropogenic sources

showed a statistically significant positive trend of 78090 Kt/decade after 1991. This is reflected in the future projection of temperature anomaly between 1900-2100 with a future warming trend of 0.19 °C/decade. In conclusion, human activities, industrial revelation, deforestation, land use transformation and increase in greenhouse gases had significant implications on the environment and ecosystem services of the study area.

Chapter 5 has been published in the Journal of Agricultural Water Management with the following citation: Mahmoud, S. H., & Gan, T. Y. (2019). Irrigation water management in arid regions of Middle East: assessing spatio-temporal variation of actual evapotranspiration through remote sensing techniques and meteorological data. *Agricultural Water Management*, 212, 35-47.

Spatial and temporal distribution of reference (ET_o) and actual evapotranspiration (AET) over the central region of Saudi Arabia during 1950–2013 are estimated using remote sensing and GIS techniques. Firstly, the FAO Penman-Monteith method was used to model the spatial distribution of ET_o on a grid-by-grid basis using data collected from meteorological stations and GIS techniques. Then, crop coefficients (K_c) were modeled as a function of 16-day time-series MODIS normalized difference vegetation index (NDVI). Next, using K_c maps and ET_o as input, daily AET was simulated by the soil water balance (SWB) model and aggregated to monthly and annual AET. From empirical NDVI-K_c relationships developed and applicable at pixel level, K_c derived from the NDVI-K_c relationships agree well with K_c recommended by FAO over various crop growth stages in the field. The monthly AET maps for 1950-2013 show a gradual increase in AET during the crop-growing season in January to May but a subsequent decline as the season progresses from June to December. The AET estimated for January to June are arranged in descending order, which are May (3.67-44.7 mm/day), April (5.99-36.8 mm/day), March (2.96-32.7 mm/day), February (0.68-20 mm/day), June (2.42-17.7 mm/day) and January (1-11 mm/day), respectively. Statistical

analysis shows that statistically significant change point in daily AET generally occurred in 1990, such that the long-term average daily AET of 1950-1990 at 3.6 mm/day increased to about 5.3 mm/day between 1990 and 2016 with a positive trend of 1.5 mm/decade. The annual AET estimated for irrigated cropland in northern and central regions of Riyadh, Al-Qassim province and Hail province range from 1200 to 2900 mm/year. In these regions, low AET values are found in shrubland, grassland, and other natural vegetation. The annual AET estimated by the SWB model are about 9-11% higher than modeled AET in the study area, where the long-term average daily AET estimated for 1950-2013 range from 2 mm/day to 30 mm/day. Representative AET maps derived from applying the NDVI-Kc relationships to the SWB model will be useful to achieve the planning and management of sustainable water use in arid regions of Middle East.

Chapter 6. Our analysis of the Nile River basin (NRB) hydroclimate shows significant climate change impact in recent decades: a decreasing trend in precipitation at 16.2 mm/decade since 1970s, increasing trend in wind speed and zonal wind stress at 0.02 m/decade and 1.51 $\text{m}^2/\text{s}^2/\text{decade}$ respectively since 1975, increasing trend in geopotential height (GPH) at 3.1 m/decade since 1976, warming trend at 0.19°C/decade, decreasing trend in relative humidity (RH) since 1977, and increasing trend in actual evapotranspiration (AET) at 1.2 mm/decade since 1995, mainly from water bodies of many riparian countries of NRB between 1985 and 2017. Higher AET in recent decades can be partly attributed to stronger El Niño amplitudes. Composite analysis of NRB's hydroclimate data between 1948 and 2017 also shows significant changes across the entire NRB: a drop in daily precipitation in the NRB except for Uganda. RH has decreased by 1-5%/decade after 1985. The decrease in RH, soil moisture, had been the most significant in Uganda, Sudan, and northwestern Ethiopia where the increase in temperature, GPH, AET and wind stresses had also been the highest. Specific humidity decreased in Sudan, northwestern regions of Ethiopia

(in lowland) except Uganda. The increase in scalar, zonal, meridional wind was maximum in Uganda, Sudan, and northwestern regions of Ethiopia between 1985 and 2017.

The composite analysis also showed that GPH become thicker in the last few decades as the temperature increases. Besides climate warming, statistical analysis, wavelet transform coherence (WTC) analysis, composite analysis, and detrended cross-correlation analysis (DCCA) also show that beside ENSO, IOD plays a crucial role on NRB's hydroclimate variability over inter-decadal and longer timescales. This is particularly evident in the strong correlation between El Niño 3.4, surface temperature T_s ($\rho = 0.97$), GPH ($\rho = 0.81$), relative humidity ($\rho = -0.97$), precipitation ($\rho = -0.7$). There is also a significant positive correlation between AET and El Niño 3.4 ($\rho = 0.93$) in contrast to negative correlation between AET and IOD ($\rho = -0.47$), which shows that El Niño affect the AET of NRB. The correlation of these hydroclimate variables with IOD are generally high but lower than with El Niño's. However, WTC showed that IOD plays a more important role on the hydroclimate variability in the NRB at longer timescales than El Niño. There is also a strong negative correlation between IOD and the NRB precipitation. The results from this study improve our understanding of the NRB hydroclimate and help us to better develop mitigation strategies for these riparian countries against the potential impact of climate change.

Chapter 7. Low precipitation and warming have been attributed as key drivers to droughts of Africa. From the analysis of hydroclimate data, we identify key driving forces behind the recent increasing aridity of the Nile river basin (NRB). Our results show that the increased influence of stronger ENSO and Indian Ocean dipole (IOD) in NRB after 1980s, particularly the influence of IOD and SST gradient over the Arabian Sea (WTIO), have significantly contributed to NRB's drought severity over inter-annual to inter-decadal timescales. Further, shift in zonal winds (westward) and meridional winds (southward) associated with stronger El Niño events, and

southward shift of atmospheric stream functions have contributed to the increased aridity of NRB after 1970s. Recent changes in atmospheric circulations represented by stream function, geopotential height and zonal/meridional wind anomalies associated with El Niño, which has become more persistent and stronger, has resulted in drier NRB, where its streamflow at gauging stations have decreased from 13.7 to 114.1 CBM/decade. Contrary to past findings, we also show that IOD and WTIO are better predictors of the Nile streamflow than El Niño. Furthermore, climate projections suggest that under the combined impact of warming and stronger WTIO and El Niño events, future droughts of the NRB will worsen.

Chapter 1 Urbanization and climate change implications in flood risk management

1.1 Introduction

In recent years, because of urbanization, there is an increase in flood risk even in arid regions with a limited amount of annual rainfall. Various flood risk studies reported the effect of urbanization in surface runoff (Satterthwaite, 2008, Zhang et al., 2008a; Fernández et al., 2010). These studies reported that increase in urban areas and impervious surfaces have led to an increase in surface runoff because less water is lost by soil infiltration. On the other hand, there are studies that attributed the rising frequency of flood occurrences to the impact of climate change (Gizaw and Gan, 2015; Jiang et al., 2015). Precipitation in arid regions tends to be more variable in time than in humid regions (Pilgrim, 1988), and so are more vulnerable to hydrologic extremes such as flood and droughts. In the driest continent of Africa, climate change has been linked to more frequent occurrences of severe droughts, rising temperature and altered precipitation patterns (Ramanathan et al., 2001; Shanahan et al., 2009; Williams and Funk, 2011). In countries such as Egypt, floods have been occurring more frequently and in greater severity in recent decades. A hypothesis is herein investigated whether increasing flood events in Egypt are due to rapid urbanization or the effect of climate change.

Therefore, we will investigate the implications of urbanization and climate change in the flood risk of Egypt, which is representative of the climate of other arid regions in the Middle East. The recurrent occurrences of flooding in Egypt, especially in its coastal regions has led to catastrophic and costly damage to properties and threat to human life, which may be because of rapid urbanization along the Nile River. In northern, coastal regions of Egypt's Nile Delta and coastal areas along the Mediterranean Sea, flood discharge from wadi basins can be a threat to

coastal cities, towns, and villages. Since 1990, more than seven hundred people in Egypt had lost their life because of flash floods, and about 250,000 people were affected (Guha-Sapir et al., 2014). Therefore, flood-susceptible areas should be identified so that responses to flooding emergencies can be executed quickly and effectively. Historically, Egypt's most affected regions are El-Beheira, Alexandria, Sinai, Matruh, Cairo, and Giza, which are vulnerable to the potential threat of increased surface runoff, particularly in arid regions where people tend to be ill-prepared against flood hazards.

An analysis of long-term surface runoff data of urban areas can generally reveal the effects of urbanization. A limited number of studies have used the runoff curve number method to compute surface runoff and its effects to urban communities (Lim et al., 2006; Shi et al., 2007; Banasik et al., 2014). However, most studies have not considered the effects of both urbanization and climate change impact to urban surface runoff and the development of flood susceptibility maps, e.g., (Cherqui et al., 2015; Chen et al., 2015; Xiao et al., 2017; Hong et al., 2017; Termeh et al., 2018; Zhao et al., 2018). Methods such as Multi-criteria decision support system and analytic hierarchy process have proven to be effective tools in developing flood susceptibility maps (Ouma and Tateishi, 2014; Kazakis et al., 2015; Melesse and Abtew, 2016). Researchers have used various hydrologic and climatic data that contribute to floodings, such as precipitation, runoff, digital elevation model (DEM), curvature, geology, land use/cover (urbanization), soil type, topographic wetness index and slope (Şen, 2004; Nouh, 2006). However, because of a lack of data, only a limited number of studies have used comprehensive datasets in delineating flood-prone areas of river basins. For instance, Fernandez and Lutz (2010) used five flood contributing factors to analyze flood-prone areas in the Tucumán Province of Argentina: distance to the drainage channels, topography, groundwater table depths, and land use. Kazakis et.al (2015) mapped flood

hazard areas of the Rhodope–Evros region of Greece based on seven factors, namely, flow accumulation, distance from the drainage network, elevation, land use, rainfall intensity and geology. Tehrany et.al (2015) did that for Malaysia using ten factors: altitude, slope, curvature, stream power index (SPI), topographic wetness index (TWI), distance from the river, geology, land use/cover (LULC), soil, and annual surface runoff, but they used a different set of factors in an earlier study (Tehrany et al., 2013).

We expect that a systematic analysis of a comprehensive dataset will lead to a representative delineation of flood susceptibility areas, which can later be validated against ground observations of past flood events. Elkharchy (2015) used an AHP approach to map flood hazards zones in Najran city of Saudi Arabia. Among the conditions considered, annual surface runoff, soil type, surface slope, surface roughness, drainage density, distance to the main channel and land use, Elkharchy (2015) assigned a weighting factor of 35.5% to the annual surface runoff, making it one of the most important factors in flood susceptibility mapping. Many past studies derived the relative contribution of each factor to floods based on authors' experience, literature review and weighting methods and validate final flood susceptibility maps developed against historical flood records. Flash floods occur periodically in El-Beheira and Alexandria governorates due to a lack of proper drainage systems and rapid urbanization. In 2013, surface runoff destroyed about 121 km² of agricultural land in El-Beheira governorate. Alexandria governorate also suffered from increased surface runoff that badly flooded streets of the coastal city and damaged many private properties. Residents of Alexandria expressed their outrage at the former government of Alexandria that failed to efficiently flood-proof the city against foreseeable events. In recent years, floods in El-Beheira had caused twenty-five deaths, forced hundreds of schools to shut down, dozens of people were forced to evacuate from their homes, and large swathes of buildings in the

region were destroyed. Therefore, the objective of this study was to investigate the effects of urbanization and climate change in the flood risk management of arid regions, in addition, to developing flood susceptibility maps to support decision making in the rescue operation.

To achieve our objectives, we first analyzed the variability and trends of the annual precipitation and temperature of the two governorates to estimate the possible impact of climate change. Next, to estimate the effects of urbanization to the flood risk of the two governorates, we applied the runoff curve number method to develop the time series of surface runoff for the two governorates between 1948-2014. Change point detections and trend analysis techniques were then applied to the surface runoff data to find the change points and trend. Surface runoff anomalies were also analyzed to assess the influence of urbanization in surface runoff. Finally, we developed a GIS decision support system to delineate flood susceptibility zones in the Beheira and Alexandria Governorates of Egypt. The accuracy of the flood susceptibility maps developed was verified with historical flood records.

This study is necessary given there is generally a lack of flood susceptibility maps in Egypt and information related to the influence of climate change and urbanization in the surface runoff of Egypt. Similar situations are found in many if not all Middle Eastern countries of arid climate. Other than useful for flood risk management, flood susceptibility maps we have developed will also benefit planners and governments in choosing suitable locations for future developments and in mitigating potential flood damages and future land use planning in Beheira and Alexandria governorates. Furthermore, the surface runoff time series developed could be used in other hydrological studies in the two governorates of Egypt.

1.2 Study area

This study was conducted in two governorates of Egypt. The first is the El-Beheira governorate (Figure 1.1) is located in the north coastal region of Egypt's Nile Delta (30.61°N, 30.43°E) with an area of about 10,130 km². El-Beheira's annual rainfall ranges from 29 mm/year in the south to 190 mm/yr in the north. The second is the Alexandria governorate (31.20° N, 29.92° E) which lies along the Mediterranean coast, at about 70 km northwest of the Nile Delta (Figure 1.1) occupying an area of 2818 km² and an average annual rainfall of about 169 mm/yr. Alexandria's rainfall predominantly occurs along the north coastal area, which is heavily urbanized, and it decreases quickly southwards.

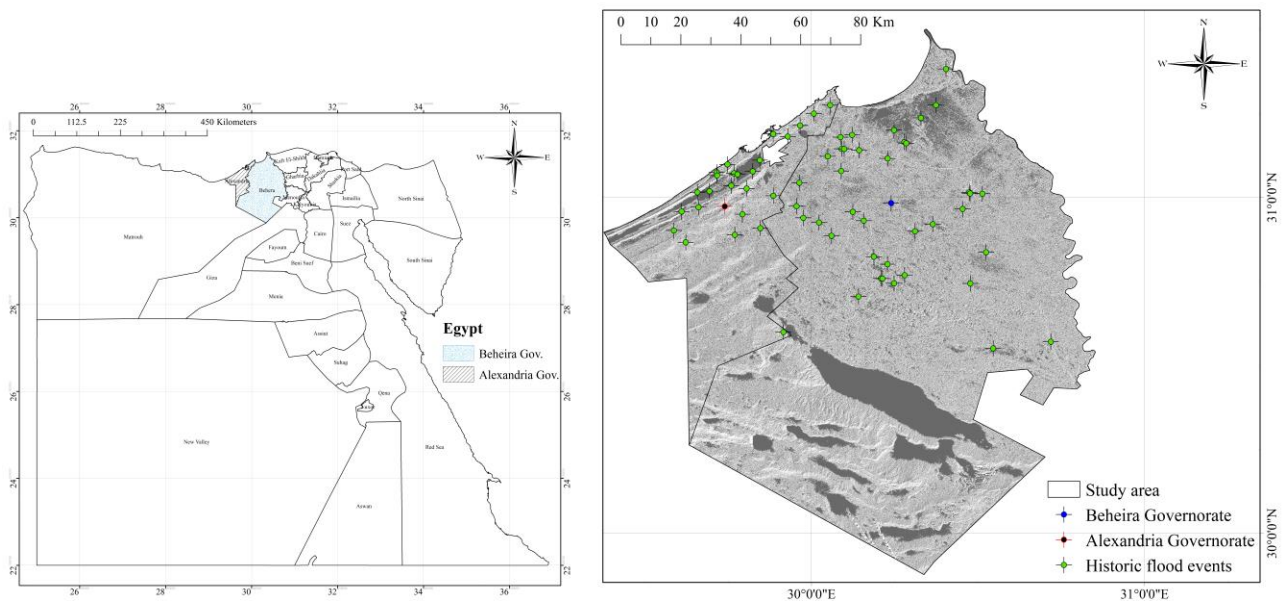


Figure 1.1 Location of Beheira and Alexandria governorates in Egypt

1.3 Research methodology

1.3.1 Change point analysis

Long-term monthly rainfall and temperature data between 1948-2014 were obtained from the University of Delaware and processed to derive mean annual temperature and rainfall, rainfall and temperature anomalies between 1948 and 2014. We applied two nonparametric, change point

detection methods, SNHT and Buishand's methods to mean monthly rainfall, annual rainfall, and rainfall anomaly data. We also conducted trend analysis on temperature data to detect warming trends which has been attributed to rising concentration of greenhouse gases caused by anthropogenic activities (Ren et al., 2008; Yan et al., 2010; Banasik et al., 2014). The SNHT test has been commonly used to detect a shift in the mean value of climate time-series (Wijngaard et al., 2003; Wang et al., 2007; Zhang et al., 2008b). The test check for a null hypothesis (no change point or trend) and an alternative hypothesis, where the time series tested may have a change point or a trend, or both:

$$M_x = x\bar{Z}_1 + (n - x)\bar{Z}_2 \quad \text{where } x = 1, 2, 3, \dots, n. \quad (1-1)$$

M_x is a statistic to compute the mean temperature/rainfall value at year x with the mean value at year $n-x$.

$$\text{Where } \bar{Z}_1 = \frac{1}{x} \sum_{i=1}^n \frac{(x_i - \bar{x})}{s} \text{ and } \bar{Z}_2 = \frac{1}{n-x} \sum_{i=x+1}^n \frac{(x_i - \bar{x})}{s}$$

Where s is the number of positive minus the number of negative differences between x_{i+1} and x_i , $(x_{i+1} - x_i)$, $i = 1, 2, \dots, n-1$. If s is positive, $x_{i+1} > x_i$, and if s is negative, then $x_{i+1} < x_i$. The year x is considered as a change point if the value of M_x is maximum. To reject the null hypothesis the following statistic should be achieved; The value of T_0 should be greater than the critical value of the test.

$$T_0 = \max_{1 \leq x \leq n} M_x \quad (1-2)$$

Buishand's method works in a similar manner but instead on comparing the mean at each year to the critical value, the test uses the adjusted partial sum defined as:

$$Sum_0 = 0 \quad (1-3)$$

$$Sum_x = \sum_{i=1}^x (x_i - \bar{x}) \quad (1-4)$$

If $Sum_0 = 0$, the time series is homogeneous, and we accept the null hypothesis. However, if Sum_x is maximum or minimum which means there is a change point at year x. The magnitude of Sum_x indicates the type of shift in the time series such that a maximum value indicates a downward shift and a minimum value indicates upward shift. The adjusted range, A is as follow:

$$A = \frac{(\max_{0 \leq x \leq n} Sum_x - \min_{0 \leq x \leq n} Sum_x)}{S} \quad (1-5)$$

Where A/\sqrt{n} is then compared with the critical values of the test according to Buishand (1982), to check if the change point is statistically significant. Then, the non-parametric Mann–Kendall was used to detect trend in temperature anomalies and monthly, annual and anomaly rainfall time series between 1948 and 2014:

$$S = \sum_{i=1}^{n-1} \sum_{j=i+1}^n sgn(x_j - x_i) \quad (1-6)$$

Each data point x_i is considered as a reference and compared with the remaining data points x_j :

$$sgn(x_j - x_i) = \begin{cases} +1 & \text{if } (x_j - x_i) > 0 \\ 0 & \text{if } (x_j - x_i) = 0 \\ -1 & \text{if } (x_j - x_i) < 0 \end{cases} \quad (1-7)$$

The variance statistic is calculated as follow:

$$Var(S) = \frac{n(n-1)(2n+5) - \sum_{j=1}^p t_j(t_j-1)(2t_j+5)}{18} \quad (1-8)$$

Where p is the number of groups in which each group consists of data points of equal values, and t_j is the number of data points in the j^{th} group. Using the following Z-transformation, the statistic S is approximately normally distributed:

$$Z = \begin{cases} \frac{S-1}{(Var(S))^{0.5}} & \text{if } S > 0 \\ 0 & \text{if } S = 0 \\ \frac{S+1}{(Var(S))^{0.5}} & \text{if } S < 0 \end{cases} \quad (1-9)$$

The slope (T_j) is computed according to Sen (1968) as follow:

$$T_j = \frac{x_j - x_i}{j-1} \quad (1-10)$$

The sign of the slope indicates if the trend of the time series is positive or negative.

1.3.2 Effects of Urbanization in surface runoff

In general, there is a lack of surface runoff data in Egypt and Middle East Countries. Therefore, surface runoff data was estimated from the popular curve number method to transform to surface runoff and soil infiltration loss (Zhan and Huang, 2004; Bo et al., 2011). In the absence of detailed watershed information, this method is practical for it only requires general information such as landuse, treatment or practice, soil hydrologic condition, hydrologic soil group, and antecedent moisture condition to determine the curve number (CN) needed to estimate the storage at saturation and then the surface runoff. A composite or a really weighted CN is often for a river basin with several sub-regions (Zhan and Huang, 2004). The curve number method was applied to the two governorates based on their respective hydrological soil groups, land use, and slope.

A series of Landsat images of 1972-2014 were obtained from the U.S. Department of the Interior U.S. Geological Survey and classified into land use maps to track changes in urbanization over the years. The urban areas remained more or less unchanged over 1948-1970, but starting in 1970, urban areas gradually increased. Based on the hydrological soil groups, land use maps of different years, we calculated the CN for the two governorates, and update them every four years. From applying monthly rainfall data of 1948-2014 to the CN calculated, we derived the monthly and annual surface runoff data between 1948 and 2014. Next, two nonparametric change point tests, SNHT and Buishand's were applied on monthly, annual surface runoff, and surface runoff anomaly to detect possible change points in the surface runoff. The trends of these surface runoff data were estimated using the Mann–Kendall trend test. The magnitude of change in the surface runoff was estimated using Sen's slope method. There is no historical runoff data exist for the two study areas.

So, our results were validated against annual surface runoff data of 2006-2014 and was found to agree well with recorded annual surface runoff.

1.3.3 Flood susceptibility mapping

After investigating effects of rapid urbanization and climate change in surface runoff, we developed the following flood susceptibility maps by an approach shown in Figure 1.2 for the flood risk management of the two governorates of Egypt.

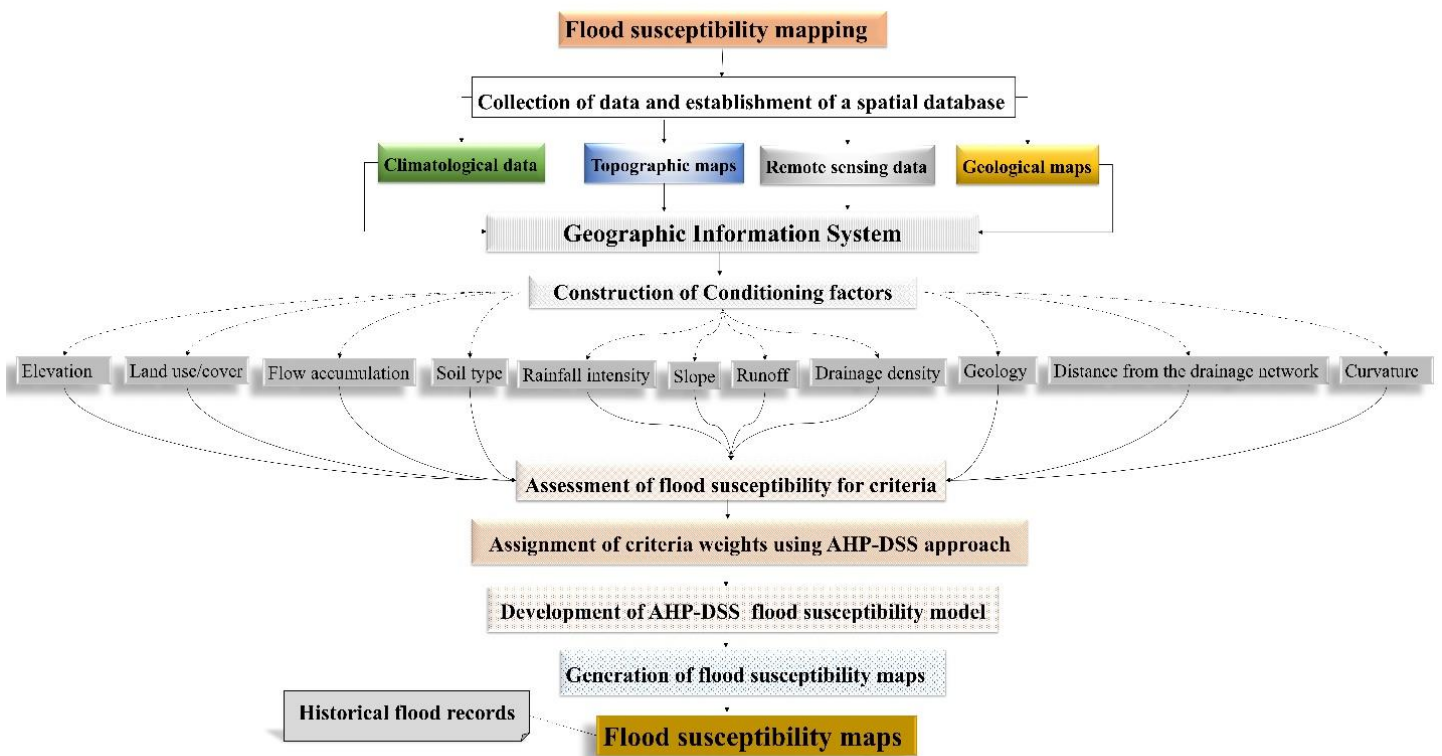


Figure 1.2 Workflow chart

1.3.4 Selection Criteria and Data Processing

Compared with past flood susceptibility studies, we have used a field survey and historical flood records of Egypt to identify eleven factors based on their relations to flooding in Egypt, to map flood susceptibility zones of the two governorates: land use/cover, rainfall intensity, runoff,

flow accumulation, drainage density, distance from the drainage network, elevation, slope, soil type, geology, and curvature.

1.3.5 Assessment of factors susceptibility level

From the literature review, and the ranking method of Saaty (1980), we ranked the above eleven factors with respect to their respective level of susceptibility and relevance to flood hazards as shown in Table 1.1. The susceptibility to flood in the two governorates is strongly related to the level of urbanization since surface runoff increases with urbanization. In contrast, permeable soils or areas with forest covers and shrubland tend to have lower surface runoff (Jacinto et al., 2014). In other words, soil types affect the water holding capacity and infiltration characteristics of an area which consequently affects its susceptibility to flood (Nyarko, 2002). According to Hill et al. (2010), even under dry moisture conditions, flooding can occur in clayey soil subjected to intensive rainfall. Rainfall intensity also plays an important role in flood susceptibility, for more intensive rainfall events lead to more surface runoff and vice versa. A denser drainage network and steeper slope can also lead to significant increase in surface runoff, and so more likely to result in flooding, especially in areas located close to flow accumulation path. Each flood susceptibility factor in Table 1.1 is classified under five classes, ranging from very high to very low flood susceptibility as follows: 5 “very high flood susceptibility”, 4 “high flood susceptibility”, 3 “moderate flood susceptibility”, 2 “low flood susceptibility” and 1 “very low flood susceptibility”.

Table 1.1 Susceptibility levels of various watershed and climatic factors in relation to flooding

Thematic layers	Classes	Rating
Flow accumulation (pixels)	0-850	1
	850-1250	2
	1250-3415	3
	3415-17525	4

	17525-10885000	5
	<150	5
	150-350	4
Distance to drainage network (m)	350-750	3
	750-1250	2
	>1250	1
	-26-18'	5
	18-70	4
Elevation (m)	70-121	3
	121-172	2
	172-221	1
	Irrigated cropland	3
	Grassland	2
	Shrubland	4
LULC	Sparse vegetation	3
	Built up areas	5
	Vegetation regularly flooded	4
	Bare soil	2
	Water bodies	5
	0-42	1
	42-75	2
Rainfall intensity units MFI	75-105	3
	105-150	4
	150-191	5
	0-2	5
	2-5.	4
Slope (%)	5-15.	3
	15-35	2
	35-90	1
	Holocene	3
	Pleistocene	2
Geology	Quaternary	3
	Sea	5
	Cenozoic	2
	Water	4
	0-25	1
Runoff (mm/yr)	25-50	2

	50-75	3	
	75-150	4	
	150-184	5	
Soil type	Dunes or shifting sands	1	
	Calcaric Fluvisols	2	
	Calcaric Regosols	4	
	Eutric Gleysols	4	
	Inland water	4	
	Calcisols and gypsisols	3	
	Calcic Yermosols	4	
	Gleyic Solonchaks	5	
	0-0.37	1	
	0.37-0.65	2	
	Drainage density (km/km ²)	0.65-1	3
1-2.9		4	
2.9-5.3		5	
Curvature		Concave	1
		Flat	1
	Convex	3	

1.3.6 Assignment of weights to watershed and climatic factors

Under an analytical hierarchy process, watershed and climatic factors were assigned with weights using the pairwise ranking and rank sum methods. The TerrSet Geospatial Monitoring and Modeling System was used to obtain optimal weights from the principal eigenvector of the pairwise comparison matrix (Janssen and Van Herwijnen, 1994). The rank sum method of Eq (11) was used to validate weights derived for each flood related factor based on the pairwise comparison between each two factors.

$$W_k^{rs} = \frac{n+1-k}{\sum_{i=1}^n (n+1-i)} \quad (1-11)$$

Where W is the weighting factor while k of number 1 to 11 represents one of the flood related factors. The accuracy of each pairwise comparison was assessed by the consistency index of Saaty

(1977, 1980, 1990), which is a measure of departure from the consistency or inconsistency of pairwise judgments in the comparison matrices. The analytical hierarchy process for rating each cell in the matrix is shown in Table 1.2. This rating was systematically calculated in a pairwise comparison approach via a matrix operation by multiplying factors of a row with other factors of a corresponding column. Because the matrix is symmetrical, it is only necessary to compute the ratings for half of the matrix.

The consistency ratio of the matrix obtained was 0.06 which means an acceptable consistency (Saaty, 1977). The final consistency ratios obtained for each flood related factor are shown in Table 1.3.

Table 1.2 Analytical Hierarchy Process.

Factors	Flow accumulation	Distance	Elevation	Land use/cover	Rainfall intensity	Slope	Geology	Runoff	Soil type	Drainage density	Curvature
Flow accumulation	1	2	2	3	3	5	7	1	2	2	7
Distance drainage network	1/2	1	1	2	2	3	4	1/2	1/4	1	4
Elevation	1/2	1	1	2	2	2	5	1/3	1/2	1	5
Land use/cover	1/3	1/2	1/2	1	2	5	5	1/2	1/5	1/2	3
Rainfall intensity	1/3	1/2	1/2	1/2	1	3	4	1/2	1/2	1/3	4
Slope	1/5	1/3	1/2	1/5	1/3	1	3	1/4	1/2	2	3
Geology	1/7	1/4	1/5	1/5	1/4	1/3	1	1/6	1/3	1/3	2
Runoff	1	2	3	4	2	4	6	1	2	4	6
Soil type	1/2	4	2	5	2	2	3	1/2	1	2	3
Drainage density	1/2	1	1	2	3	1/2	3	1/4	1/2	1	3
Curvature	1/7	1/4	1/5	1/3	1/5	1/3	1/2	1/6	1/3	1/3	1

Table 1.3 Normalized flood susceptibility factors

	Flow accumulation	Distance	Elevation	Land use/cover	Rainfall intensity	Slope	Geology	Runoff	Soil type	Drainage density	Curvature
Flow accumulation	0.19	0.16	0.17	0.15	0.17	0.19	0.17	0.20	0.25	0.14	0.17
Distance drainage network	0.10	0.08	0.08	0.10	0.11	0.11	0.10	0.10	0.03	0.07	0.10
Elevation	0.10	0.08	0.08	0.10	0.11	0.08	0.12	0.07	0.06	0.07	0.12
Land use/cover	0.06	0.04	0.04	0.05	0.11	0.19	0.12	0.05	0.02	0.03	0.07
Rainfall intensity	0.06	0.04	0.04	0.02	0.06	0.11	0.10	0.10	0.06	0.02	0.10
Slope	0.04	0.03	0.04	0.01	0.02	0.04	0.07	0.05	0.06	0.14	0.07
Geology	0.03	0.02	0.02	0.01	0.01	0.01	0.02	0.03	0.04	0.02	0.05
Runoff	0.19	0.16	0.25	0.20	0.11	0.15	0.15	0.20	0.25	0.28	0.15
Soil type	0.10	0.31	0.17	0.25	0.11	0.08	0.07	0.10	0.12	0.14	0.07
Drainage density	0.10	0.08	0.08	0.10	0.17	0.02	0.07	0.05	0.06	0.07	0.07
Curvature	0.03	0.02	0.02	0.02	0.01	0.01	0.01	0.03	0.04	0.02	0.02

1.4 Results and Discussions

1.4.1 Impact of climate change in flood risk

From applying SNHT and Buishand's change point detection techniques to temperature anomalies between 1948 and 2014, a statistically significant change point in temperature anomaly was detected in 1976 (Figure 1.3), because the mean temperature anomaly of -0.333 °C/yr between 1948-1976 increased to 0.242 °C/yr between 1976-2014. This increase in temperature anomaly is attributed to climate change caused by rising concentration of greenhouse gases, rapid urbanization, and deforestation (Grimmond, 2007; Ren et al., 2008; Yan et al., 2010; Banasik et al., 2014). A statistically significant warming trend of 0.16 °C/decade in the two governorates was detected by the Mann–Kendall trend test (Table 1.4). Similar studies show that urbanization or more impervious surfaces have led to rising temperature in urban areas and higher surface runoff than in non-urban areas of the same governorates (Bounoua et al., 2015).

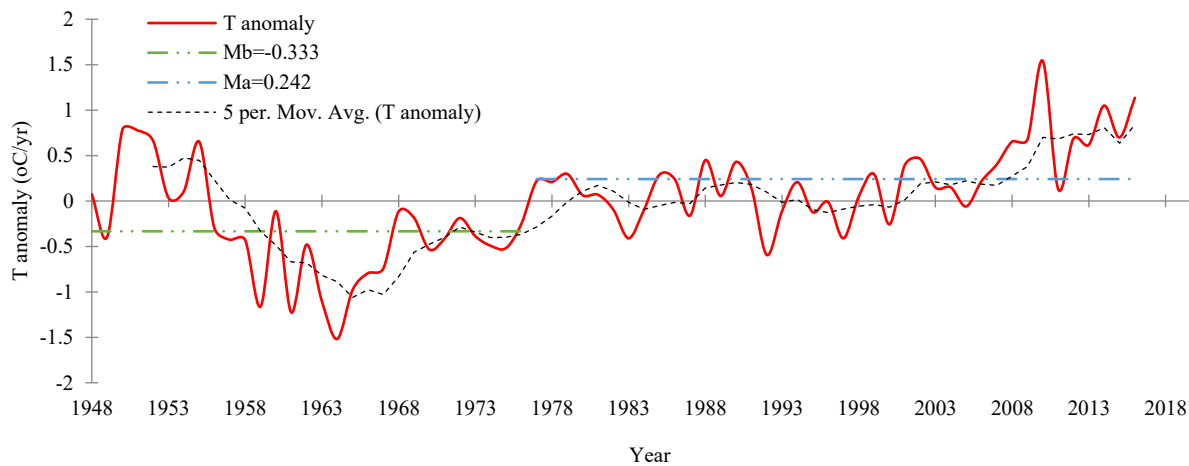


Figure 1.3 Warming trend in temperature anomaly in the two governorates

Table 1.4 Climate variables and surface runoff change detection and trend

Variable	Year	SNHT		Buishand's test			Mann-Kendall trend test				
		T	trend	T	p-value	trend	Mb	Ma	p-value	trend	Sen's slope
Annual rainfall	1948-2014	1994	Ha	1994	0.0232	Ha	139.7	98.82	0.0009	-	0.896
Rainfall anomaly	1948-2014	1994	Ha	1994	0.0236	Ha	12.21	-28.7	0.0089	-	1.530
Temperature anomaly	1948-2014	1976	Ha	1976	< 0.0001	Ha	-0.333	0.242	< 0.0001	+	0.016
Monthly runoff	1948-2014	1984	Ha	1984	< 0.0001	Ha	2.47	7.23	0.0003	+	0.015
Annual runoff	1948-2014	1970	Ha	1970	< 0.0001	Ha	21.15	76.55	< 0.0001	+	1.27
Runoff anomaly	1948-2014	1970	Ha	1970	< 0.0001	Ha	-36.38	19.02	< 0.0002	+	1.439

To investigate if climate change impact has contributed to recent flooding in the two governorates, we conducted trend analysis and change point detection in annual rainfall and rainfall anomalies. Both SNHT and Buishand's tests detected statistically significant change points in annual rainfall and rainfall anomalies in 1994, because the average annual rainfall decreased from 139.73 mm/yr between 1948 and 1994 to 98.82 mm/yr between 1994 and 2014 (Figure 1.4). Trend analysis also reveals statistically significant declining trends in annual rainfall since 1994 at the rate of 8.96 mm/decade. To further confirm the declining trend in annual rainfall we checked rainfall anomalies. Similarly, statistically significant declining trends were detected in rainfall anomaly at 15.3 mm/decade (Figure 1.5).

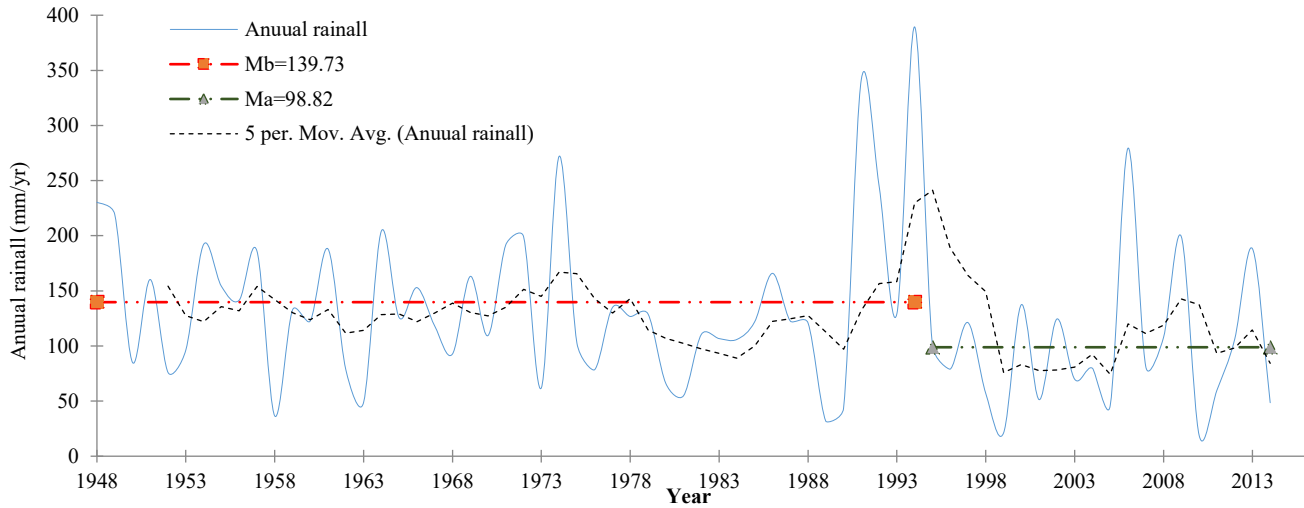


Figure 1.4 Mean annual rainfall time series and trend in the two governorates

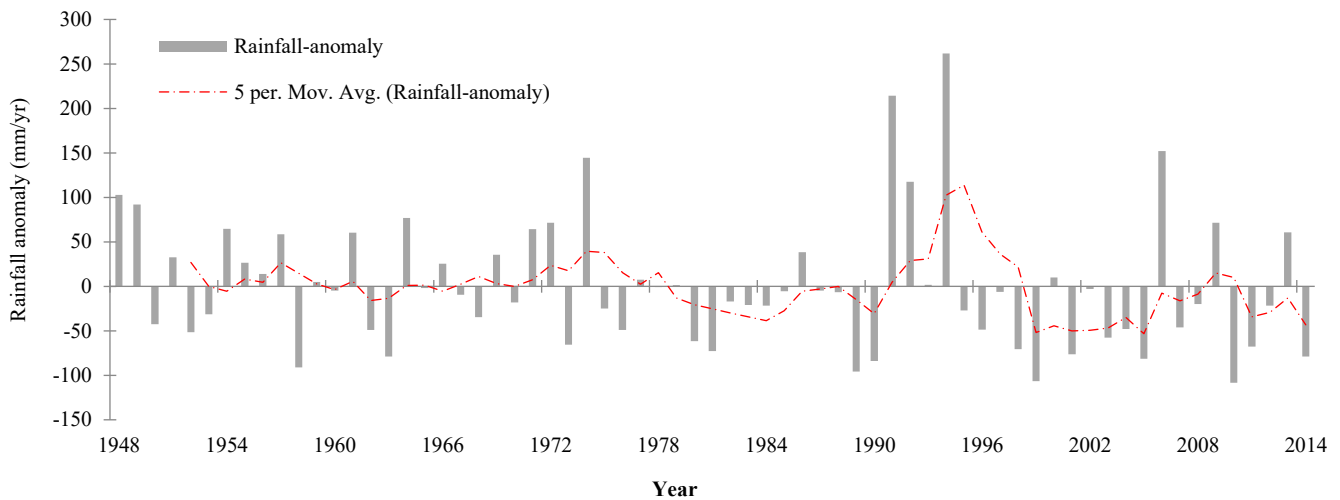


Figure 1.5 Rainfall anomaly in the two governorates

Under a warming trend since 1976 of $0.16\text{ }^{\circ}\text{C}/\text{decade}$, it seems that climate change has resulted in a significant decline in rainfall anomalies and annual rainfall in the two governorates. According to some past studies, urbanization has a major effect on the surface energy budget of the atmosphere (Kerschgens and Drauschke, 1986), resulted in the heat island effect in addition to climate warming caused by greenhouse effects (Changnon and Huff, 1986). Cao et al. (2018) studied the impact of rapid urbanization on the summer temperature in eastern China where they projected extensive warming trends up to $5\text{ }^{\circ}\text{C}$, $3\text{ }^{\circ}\text{C}$, and $2\text{ }^{\circ}\text{C}$ under three different urban growth

scenarios. According to Arsiso et al. (2018), land use change is the second most important anthropogenic influence on climate beside the emission of greenhouse gases, e.g., they reported that urbanization has caused climate warming. In addition, urbanization has also contributed to increased flood risk in many regions globally (Gu et al., 2011; Birhanu et al., 2016). In China, Gu et al. (2011) reported an increase in flood susceptibility because of rapid urbanization. Similarly, Birhanu et al. (2016) found that rapid urbanization has resulted in an increase in flood susceptibility of Addis Ababa of Ethiopia. Some studies even found a causal relationship between urbanization and carbon emissions. For example, Xu et al. (2018) reported that urbanization had the most obvious impact on carbon emissions of the Pearl River Delta of China; Fu et al. (2016) found that urbanization has resulted in a significant increasing trend of about 1.8 °K per decade in the metropolitan area of Atlanta, Georgia, USA.

1.4.2 Effects of Urbanization on surface runoff

The monthly surface runoff estimated by the CN method show high temporal variability between 1948 and 2014. Statistically significant change points were at 1984, after which monthly surface runoff increased from 2.47 mm/m between 1948 and 1984 to 7.23 mm/m between 1984 and 2014. Despite of a decline annual precipitation, a statistically significant positive trend in monthly surface runoff at 0.015 mm/m (18 mm/decade) was also detected after 1984 (Figure 1.6) because of rapid urbanization, as reflected in higher curve number in the two governorates. Long-term monthly surface runoff ranges from 0 to 99 mm/month, with the highest surface runoff since 1984 occurring in January, February, November, and December, which have been the months with recurrent flooding every year, where 50 to 99 mm of surface runoff could be generated in a few hours. In the last few decades, because of noticeable increase in impervious surfaces in Alexandria

and El-Beheira, more surface runoff has been generated, which shows the effects of urbanization on the flood risk of arid regions of Egypt.

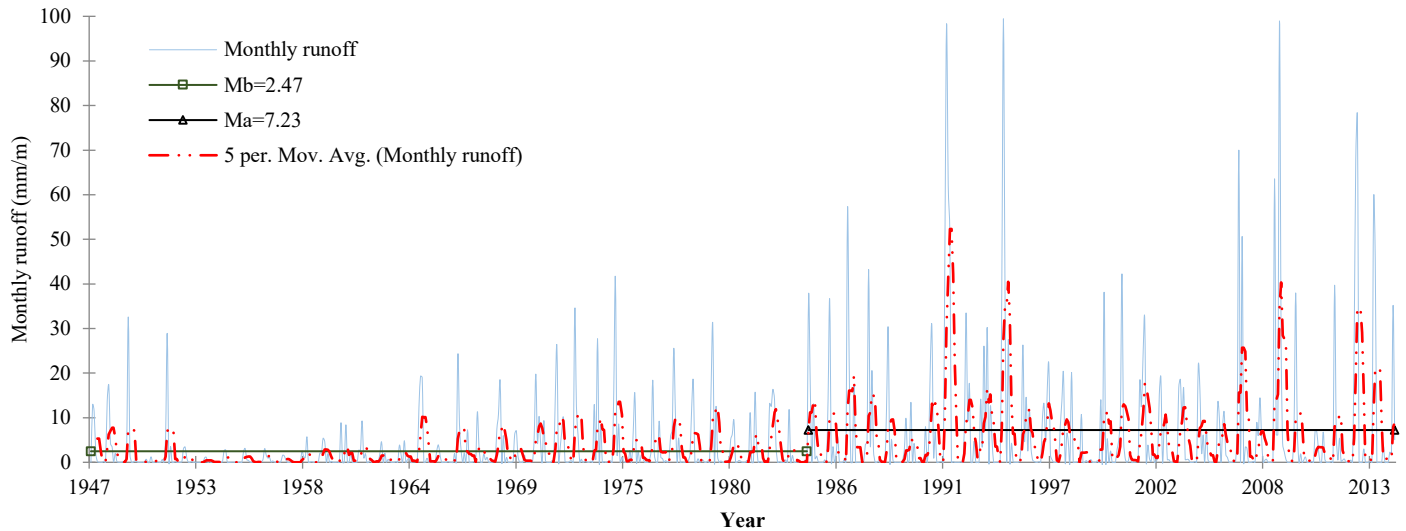


Figure 1.6 Urbanization implication in monthly surface runoff time series, and trend in the two governorates

Because of urbanization, annual surface runoff in the two governorates has been relatively high with respect to the annual precipitation. Annual surface runoff range widely, from 2.29 mm/yr to 242.86 mm/yr, with a long-term annual mean of 57.5 mm/yr and a standard deviation of 53.2 mm/yr. According to the surface runoff data estimated using the CN method, the two governorates generated more than 150 mm/yr of surface runoff in 1991, 1992, 1994, 2000, 2002, 2006, 2009, 2012 and 2013. The last four years of high surface runoff estimated agree with historical flooding records of the two governorates in 2006, 2009, 2012 and 2013. The effects of urbanization in surface runoff become clearer by increasing the time scale of the analysis (Figure 1.7). Other studies also found that rapid urbanization has led to increased surface runoff (Guan et al., 2016; Chen et al., 2017; Bian et al., 2017). From the statistically significant change point in surface runoff detected in 1970, the mean annual surface runoff had increased from 21.15 mm/yr between 1948 and 1970 to 76.55 mm/yr between 1970 and 2014. In other words, the annual runoff had been

increasing at a statistically significant positive trend of 12.7 mm/decade since 1970s, which agrees with rapid urban expansion after 1970. This was partly because between 1970 to 2014, Egypt had experienced a significant increase in population from 35 million in 1970 to more than 100 million in 2014.

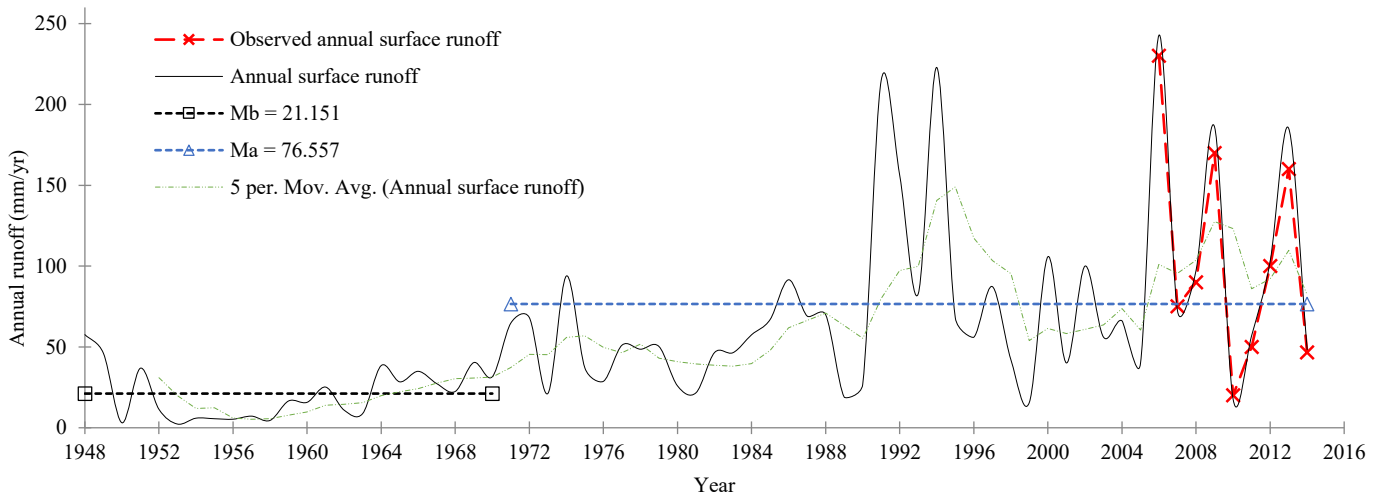


Figure 1.7 Annual surface runoff time series, and trend in the two governorates

Similarly, the analysis of surface runoff anomalies (Figure 1.8) shows significant temporal variations with a change point detected in 1970, such that the mean surface runoff anomaly increased from -36.38 mm/yr between 1948-1970 to 19.02 mm/yr between 1970 and 2014. This means a statistically significant positive trend of 14.39 mm/decade after 1970. Again, years with relatively high surface runoff anomalies are 1991, 1992, 1994, 2000, 2002, 2003, 2006, 2009, 2012 and 2013 since surface runoff increased with rapid urbanization. The estimated surface runoff anomalies also agree with historical flood records in 2006, 2009, 2012 and 2013 in both governorates, respectively. Similarly, surface runoff anomalies with reference to the long-term, mean annual surface runoff has an increasing trend at 14.39 mm/decade. It seems that the curve number (CN) method applied to the two governorates has realistically accounted for the effects of urbanization on the surface runoff values.

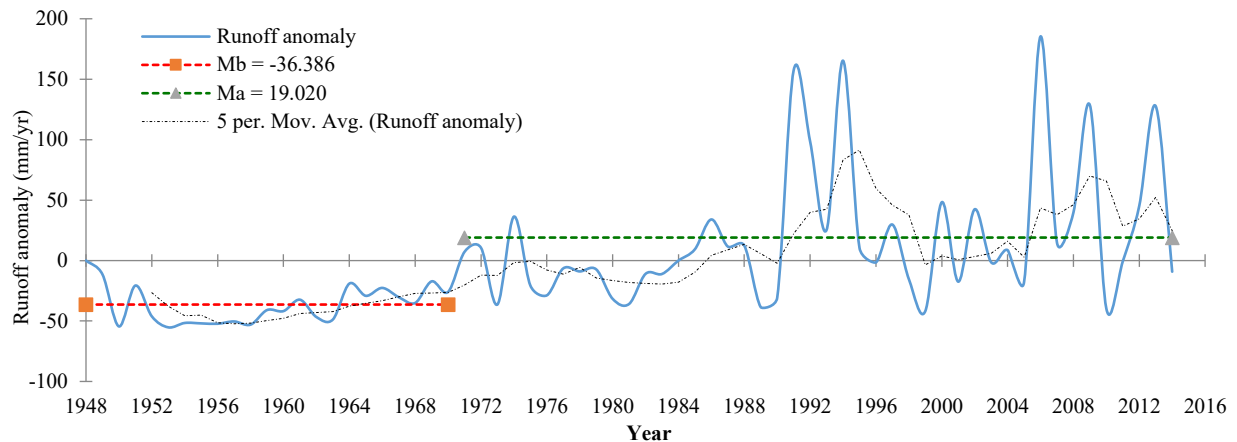


Figure 1.8 Surface runoff anomaly time series, and trend in the two governorates

After investigated the effect of climate change and urbanization on the surface runoff, we further developed the flood susceptibility model of the two governorates to identify their flood-prone areas useful for flood risk management.

1.4.3 Development of database for factors related to floods

- **Elevation, slope and flow accumulation**

Digital elevation model (DEM) and its derivatives are very useful to develop flood susceptibility model in any region (Pradhan, 2009). DEM data of 30m resolution (Figure 1.9(a)) was obtained from the U.S. Department of the Interior U.S. Geological Survey to generate a map representing the slope (%) of the study area (Figure 1.9(b)). As expected, flood prone areas are detected in low lying and flat areas. In relating elevation/slope to flood susceptibility, the two governorates were divided into five elevations and five slope zones. On the basis of historical flood records, low lying areas (elevations between -26 and +18 m) with mild slopes (0 to 2%) are prone to flooding and so are assigned with very high flood ratings, and vice versa. In contrast, steep slopes tend to have rapid flows and so are less prone to flooding. Next, areas with 2–5% slope are also relatively susceptible to flooding, areas with 5–15% slope are moderately susceptible to

flooding, while areas with 15–35% slope or higher have low to very low susceptibility to flooding. Figure 1.9(c) shows accumulation paths that contribute flow to a specific cell (group of pixels). Flow paths or drainage networks in a flow accumulation map identify cells where water will potentially accumulate, or where surface runoff will converge. Therefore, flow accumulation is crucial in flood studies for an increase in the accumulation of flow to an area or cell means an increase in the flood susceptibility of that area/cell (Lehner et al., 2006).

In an area represented by a set of pixels joined together spatially, the numbers of surrounding pixels that contribute flow to a particular pixel vary widely, ranging from small to very high numbers. In general, pixels that represent buildings or municipal infrastructure tend to have a larger number of pixels that contribute to flow. In Figure 1.9c, red and blue-green pixels are those with high flow accumulation, green and yellow pixels have lower, while grey pixels have very low flow accumulation. Pixels with high flow accumulation are where surface runoff tends to converge (concentrated flow) and consequently are vulnerable to flood hazards, and vice versa. In this study, the total number of pixels in the flow accumulation map is 10885000. These pixels are divided into five zones, pixels with very low (0-850) to very large (17525-10885000) number of pixels contributing to flow accumulation.

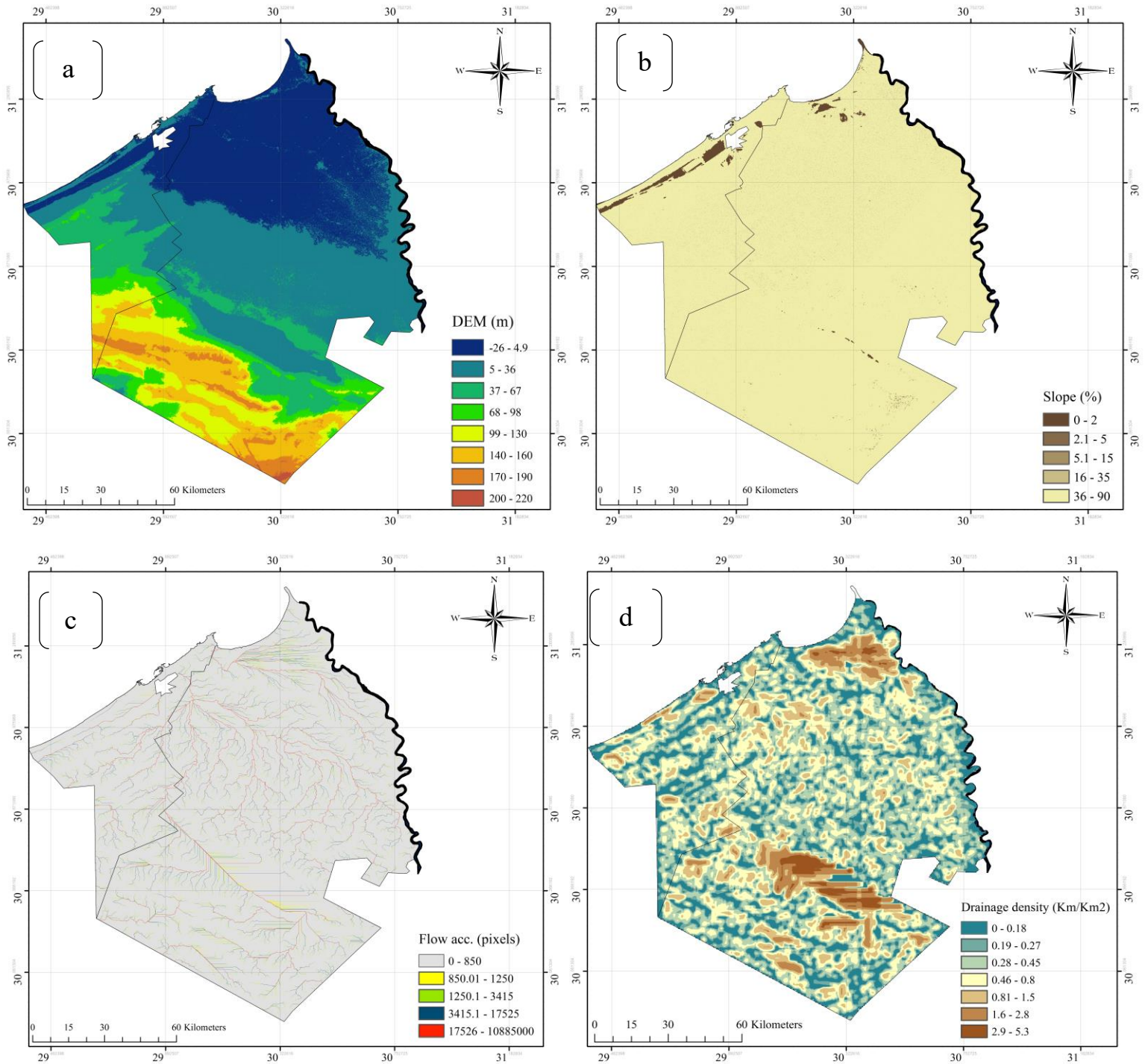


Figure 1.9 Conditioning factors for flood susceptibility: (a) DEM, (b) slope, (c) flow accumulation, (d) drainage density, (e) distance from the drainage network, (f) land use/cover, (h) rainfall intensity, (i) runoff, (j) geology, (k) soil type, (l) curvature

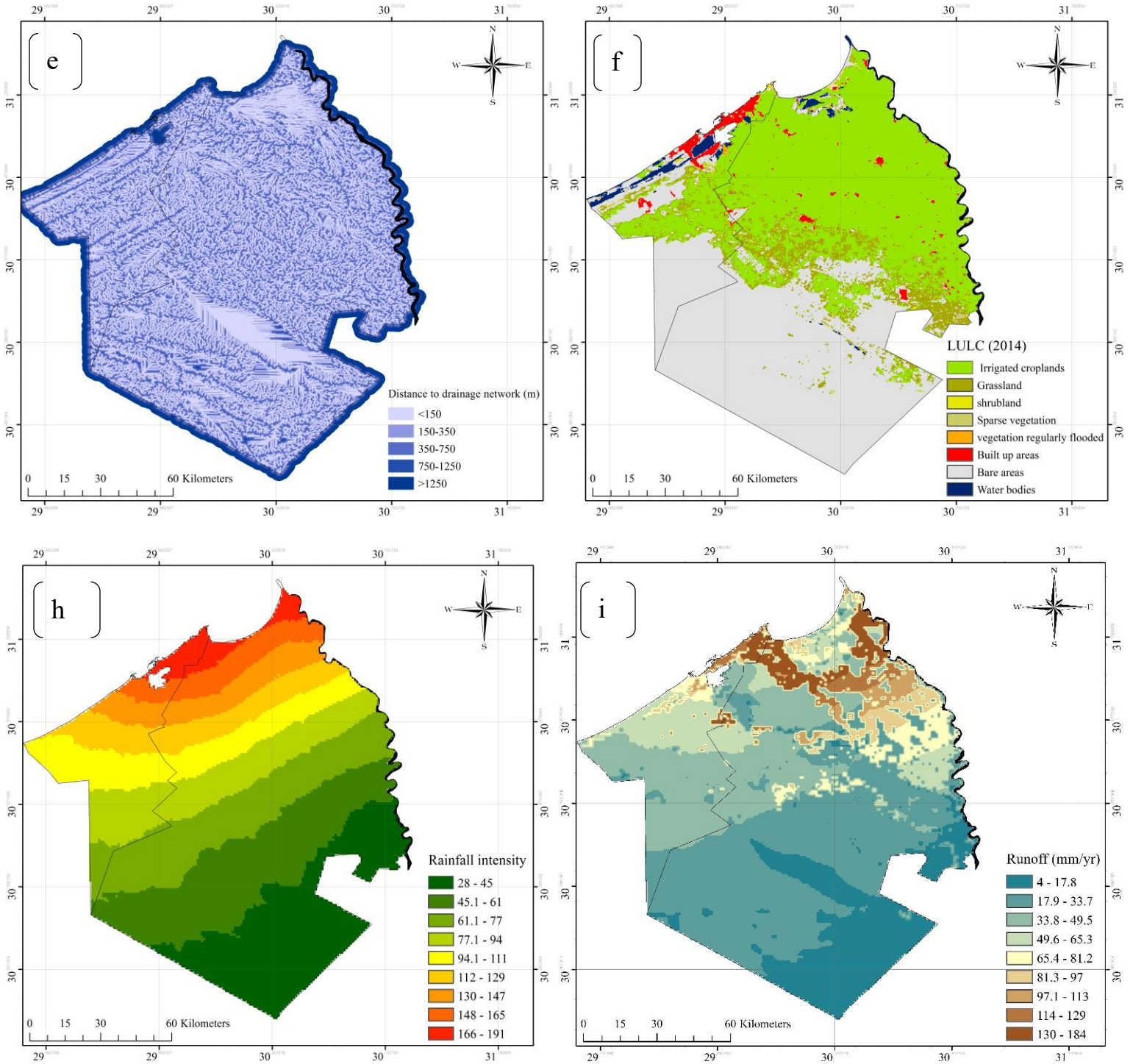


Figure 1.9 (continued)

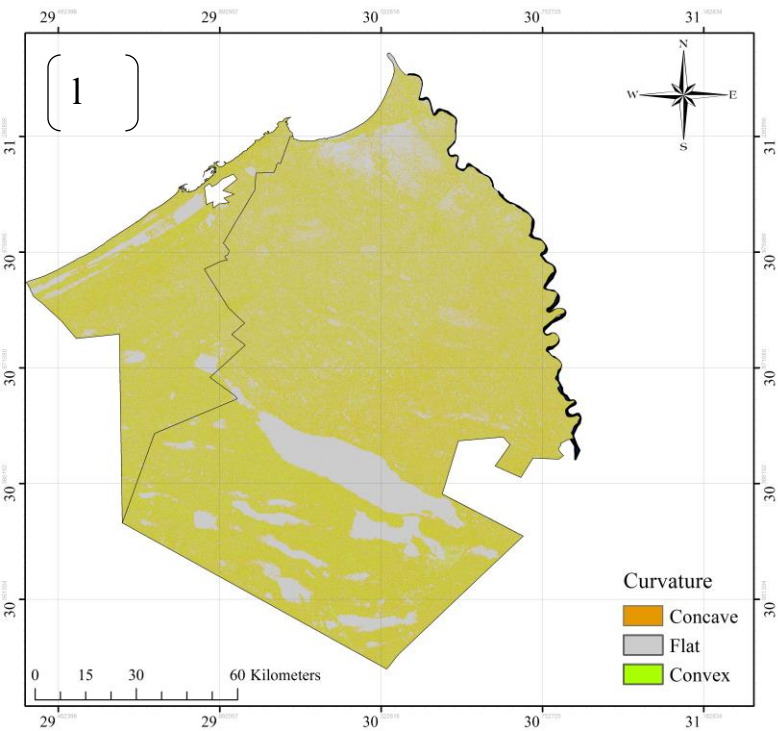
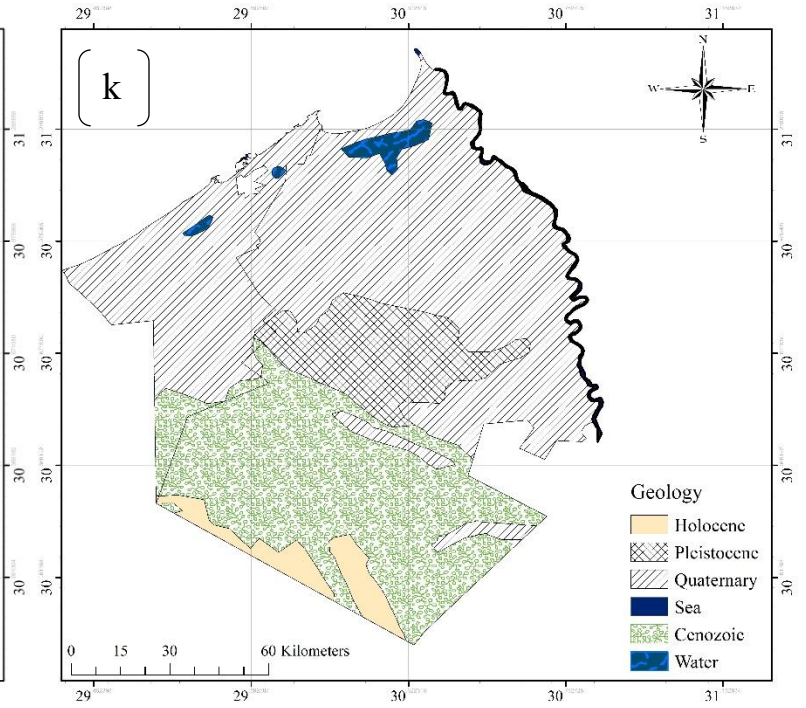
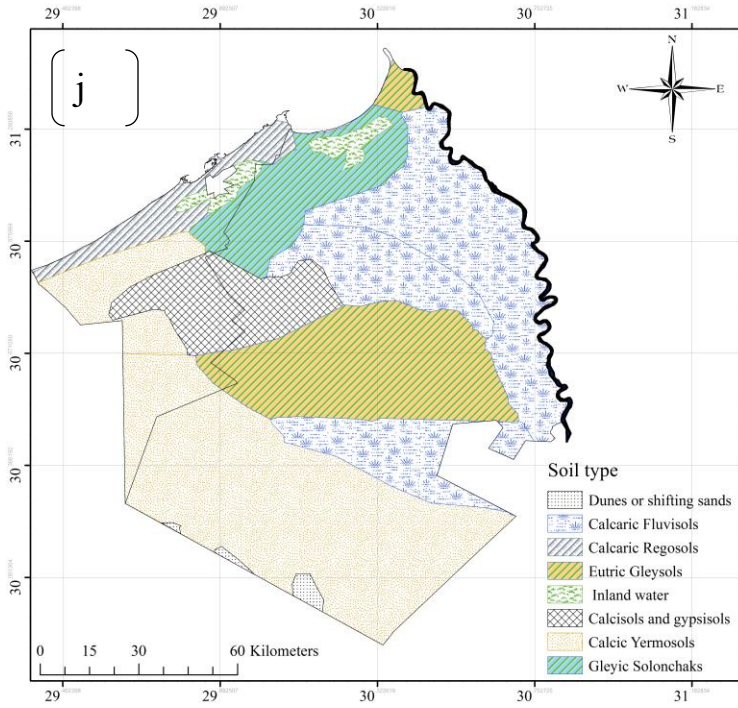


Figure 1.9 (continued)

- **Drainage density and distance to drainage network**

The drainage density maps of the two governorates, defined as the total length of all streams in a drainage basin divided by the total area of the drainage basin, (Figure 1.9(d)) was prepared using the density analysis tool of ArcGIS. In these maps, the drainage density is classified into five classes, such that a dense drainage network means a high flow accumulation path and more likely to get flooded. These five classes are categorized as ‘very high’ (2.9-5.3 Km/Km²), ‘high’ (1-2.9 Km/Km²), ‘moderate’ (0.65-1 Km/Km²), ‘low’ (0.37-0.65 Km/Km²), and ‘very low’ (0-0.37 Km/Km²) drainage density, respectively. Furthermore, areas located close to the drainage network and flow accumulation path tend to have a higher susceptibility to flooding (Islam and Sado, 2000). To delineate flood susceptible zones based on the proximity to the flow path defined as the buffer distance, the two governorates were delineated into five classes with very high, high, moderate, low and very low susceptibility to flooding (Figure 1.9(e)), which are validated against records of areas subjected to historical floods. Based on the historical flood record, areas located within 150m from the drainage network were classified as areas highly susceptible to flood hazard. Next, areas that are at a distance of 350, 750, 1250 and >1250 m from the drainage network are classified as areas of high, moderate, low and very low, susceptibility to flooding hazards, respectively. As expected, areas near the drainage network (within 150m) are highly susceptible to flood hazard, which decreases as the distance away from the river network increases, as found in other studies, e.g., Kazakis et al (2015).

- **Land use/cover, rainfall intensity and surface runoff**

To track how urbanization has contributed to increase in the surface runoff of Egypt, we also categorized a Landsat image every four years between 1970 and 2014 into classes of landuse for the two governorates by supervised classification, e.g., training samples of various land use types

were collected in field surveys and matched with spectral signatures of corresponding pixels of Landsat images (Figure 1.9(f) shows the land use map of 2014). Landsat images are remotely sensed data widely used to monitor the environment, e.g., Hossain et al. (2013), Biftu and Gan (2004). Eight landuse classes were identified: irrigated cropland, grassland, shrubland, sparse vegetation, built-up areas, vegetation regularly flooded, bare soil and water bodies. The classified images were validated using the Kappa Agreement Index (KIA) where a KIA value exceeding 0.8 represents good classification performance (Jensen, 2005). The overall KIA statistic obtained was 0.938 which demonstrates that the classified land use maps are accurate. Under moderate storms, our analysis shows that flooding is more likely to occur in an urban than a rural environment.

Rainfall intensity (Figure 1.9(h)) is expressed by a modified Fournier index (MFI) which is the sum of mean monthly rainfall intensity estimated from 66 years of monthly rainfall data. As high surface runoff corresponds to months and years of the high rainfall intensity, high rainfall intensity means more susceptibility to flash flooding and vice versa. Despite of low annual rainfall, a major cause of flooding in the study area are infrequent occurrences of extremely heavy, short-duration rain storms over soils of low water absorptive capacity, resulting in excessive overland flow which, enhanced by urbanized land of steep relief converges to the channel network as a flash flood. Therefore, despite generally low annual rainfall in Egypt, the occurrences of very intensive storms still result in flooding problems. For the study area, MFI values that range between 28 and 191 mm/yr are classified into five classes according to the potential for flood occurrences (Table 1.1). From the 1948-2014 surface runoff data for the two governorates, surface runoff varies from as low as 4 to a max of 184 mm/year (see the latest surface runoff of Figure 1.9(i)). The runoff depth tends to increase in urban areas due to compacted soils and the presence of impervious areas

because of urbanization, which leads to periodic occurrences of flash floods in Alexandria and Beheira.

The highest runoff depth was recorded within northern and northeastern parts of the Beheira governorates, which contain following regions: Edko, El Mahmoudiyah, Abu Hummus, Rosetta, Shubrakhit, Damanhur, Rahmaniya, Kafr el-Dawwar, and Wadi El Natrun, with surface runoff depth ranging from 65 to 184 mm/year. High runoff depths (81-184 mm/yr) have also occurred in northeastern and northwestern parts of Alexandria that consists of following cities: Montazah, El-Raml, Sidi Gaber, Bab Sharq, Al Attareen, Moharrem Beik, El-Dekheila, El-Agamy, and El-Ameriah. Towards south and western parts of Alexandria (Karamouz and Mina El-Bassal) and southwestern region of Beheira, the runoff depth tends to be slightly lower because these regions are dominated by agriculture land. However, these areas recently suffered unexpected flash floods which incurred huge damages. Given major historical floods had occurred for surface runoff higher than 150 mm/yr, e.g., the likelihood of a flood risk increases as the amount of surface runoff increase, the runoff depth map was classified as follows: ‘very high susceptibility’ (150-184 mm/yr), ‘high susceptibility’ (75-150 mm/yr), ‘moderate susceptibility’ (50-75 mm/yr), ‘low susceptibility’ (25-50 mm/yr), and ‘very low susceptibility’ (0-25), respectively.

- **Soil type, geology and curvature**

The soil map of the two governorates was prepared from the soil data published by the Egyptian government (Figure 1.9(j)), with following main soil types identified according to the FAO (1974) soil classification procedure: Calcaric Fluvisols; Calcaric Regosols; Calcic Yermosols; Gleyic Solonchaks; Eutric Gleysols; Calcisols; Gypsisols and shifting sands. Calcaric Fluvisols soils have the potential to become croplands because of their high infiltration rate which reduces the soil erosion problems and the susceptibility to flooding. Calcaric Regosols soil can be found in highly

urbanized, coastal lowlands of Alexandria where flooding is usually a major concern. Calcic Yermosols soils consist of clay accumulation and therefore of high susceptibility to flooding. Gleyic Solonchaks and Yermosols soils have moderate to low infiltration rate due to high clay content. Eutric Gleysols soils also tend to be easily saturated, and so are highly susceptible to flooding. Calcisols and gypsisols soils have poor water-holding capacity, and of low susceptibility to flooding due to the low clay content.

Figure 1.9(k) shows six geological groups in the two governorates assigned with various susceptibility levels to flooding: Holocene, Pleistocene, Quaternary, Cenozoic, and rocks undersea and rocks with groundwater. Cenozoic rocks and Pleistocene sand and gravel rocks (Itoh et al., 2001) are assigned low susceptibility to flood occurrences because of high hydraulic permeability; while both Quaternary rocks and Holocene clay deposits are assigned moderate susceptibility to flooding because of high porosity, and moderate to high permeability, respectively. We used ArcGIS 10.1 to produce the curvature map (Figure 1.9(l)) of which a positive curvature is convex, a zero curvature is flat, and a negative curvature is concave, respectively. Curvature highly influences the surface flow, for concave and flat shapes tend to retain more water and for a longer period than convex shapes (Moghaddam et al. 2015; Lee and Pradhan 2006). Therefore, concave/flat shapes are considered as low flood susceptibility zones while convex shapes as high flood susceptibility zones because a convex slope could generate higher surface runoff than a concave slope during heavy rainfall.

1.4.4 Flood Susceptibility Zones

Finally, after developing the flood susceptibility model, physical factors related to flooding, we used the model and the information to generate flood susceptibility maps by combining the eleven-factor maps using a weighted approach from weighting factors developed in Table 1.5 and

the weight module of TerrSet Geospatial Monitoring and Modeling System. The susceptibility model generated flood susceptibility maps for both governorates, each with five vulnerability classes ranging from Very high, High, Moderate, Low, to Very low. For the Beheira Governorate area (Table 1.6), 9.2% (930.1 Km²) and 17.9% (1815.2 Km²), 32.3% (3269.7 Km²), 28.3% (2869.2 Km²) and 12.3% (1245.8 Km²) are assigned very high and high susceptibility, moderate, low and very low susceptibility, respectively. For the Alexandria Governorate area, 15.9% (400.1 Km²), 33.5% (841.9 Km²), 41% (1028.3 Km²), 8.8% (220.6 Km²) and 0.8% (19.7 Km²) are assigned very high and high susceptibility, moderate, low and very low susceptibility, respectively (Table 1.6).

Table 1.5 Weight (percent of influence)

SL.NO.	Thematic layers	Weight	Weight %
1	Flow accumulation	0.178	17.8
2	Distance drainage network	0.089	8.9
3	Elevation	0.090	9.0
4	Land use/cover	0.073	7.3
5	Rainfall intensity	0.066	6.6
6	Slope	0.052	5.2
7	Geology	0.025	2.5
8	Runoff	0.189	18.9
9	Soil type	0.138	13.8
10	Drainage density	0.079	7.9
11	Curvature	0.022	2.2

Table 1.6 Classes of Flood susceptibility and number of historical flood events.

Flood susceptibility	Beheira Governorate			Alexandria Governorate		
	Area (Km ²)	Area (%)	# of events	Area (Km ²)	Area (%)	# of events
Very low	1245.8	12.3	-	19.7	0.8	-
Low	2869.2	28.3	1	220.6	8.8	-
Medium	3269.7	32.3	4	1028.3	41	1
High	1815.2	17.9	17	841.9	33.5	9
Very high	930.1	9.2	21	400.1	15.9	14

Figure 1.10 shows the spatial distribution of flood susceptibility zones in Beheira Governorate where most of very high and high susceptible zones are located in northern, northwestern and northeastern parts, which consist of the following areas: Edko, El Mahmoudiyah, Aboul Matamir, Abu Hummus, Rosetta, Shubrakhit, Damanhur, Rahmaniya, Kafr el-Dawwar, and Wadi El Natrun. In the last few decades, there had been an increasing trend in the occurrence of flood events due to rapid urbanization. Flooding in these areas has been occurring every winter, causing heavy damage to roads, agricultural lands, and cities. In November 2015, the low-lying areas in Wadi al-Natrun, al-Rahmaniya, Aboul Matamir, Kafr al-Dawar and Edko areas were flooded by heavy rainfall event, as was also confirmed from the surface runoff estimated for El-Beheira. By a collaboration between Egyptian armed forces and Beheira' local authorities, many lives were rescued from flooded homes during flood events. However, still twenty-five people were killed in the Beheira governorate, either from drowning or electrocution caused by heavy rain occurring in villages such as Wadi Al-Natroun Valley, El Mahmoudiyah, Abu Hummus, Rosetta, Shubrakhit, Damanhur, Rahmaniya, and Kafr el-Dawwar. Hundreds of schools were shut down due to floods. Large swathes of homeland in the region had been devastated as well.

The level of damage to areas affected by the flooding in Beheira governorate, which included cities such as Damanhour, Edkou, and Kafr El Dawar and in the Mediterranean city of Alexandria, had caused public outrage and provoked criticism of the government's negligence and cities' poor infrastructure. Therefore, the Egyptian government allocated two billion Egyptian pounds to help solving problems of flooding, such as upgrading the sewage and drainage systems of the coastal city of Alexandria and Beheira governorate, under the supervision of the military. There are also zones with high to moderate susceptibility to floods in El Delengat, Etay El Barud, Hosh Issa, Kom Hamada, Nubariyah, and Badr (see Figure 1.10).

A good match between records of historical flood events and the developed flood susceptibility map for districts of Alexandria governorates (Figure 1.11, Table 1.6) demonstrate the accuracy and credibility of the map since many recorded flood events fall within areas with high flood susceptibility, such as Montazah, El-Raml, Sidi Gaber, Bab Sharq, Al Attareen, Moharrem Beik, El-Dekheila, El-Agamy, and Borg El Arab. For example, in November 2015, Alexandria was paralyzed when a severe rainstorm amounted to five times the mean November rainfall occurred over the city within a few days, which left many streets flooded, slowed down the traffic, and the Burj Al Arab Stadium was inundated with flood water partly due to a lack of proper drainage systems. Seven people died from electric shock when a power cable of the tram line in Moharrem Beik fell into the flood water.

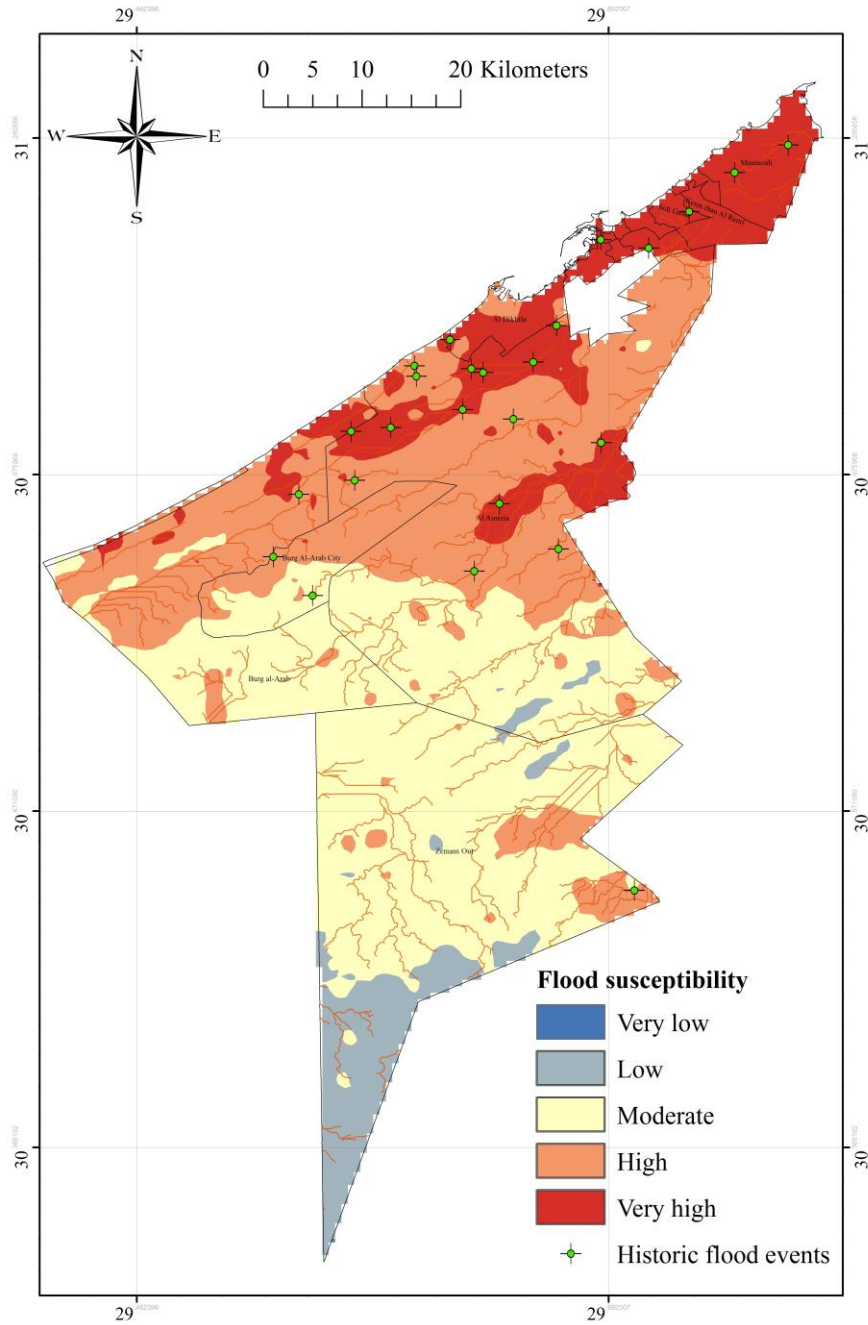


Figure 1.11 Flood susceptibility map for Districts of Alexandria governorates

Furthermore, rising sea levels attributed to melting of Arctic sea ice, Greenland and glaciers worldwide because of climate change would also contribute to flooding in Alexandria, for seawater had flooded streets of Alexandria on multiple occasions. Despite a decrease in annual precipitation, unpredictable intensive rain events of short durations exacerbate chances of flooding, compounded

by poor drainage systems and rapid urbanization. Alexander the Great constructed the ancient Alexandria city on shores of the Mediterranean Sea in 332 B.C. A part of that ancient city lies 6 to 8 m under seawater because of sea level rise in modern times (La Riche, 1996). The areas submerged in seawater and surrounding coastal regions of Alexandria are evidence of the impact of changing climate. Since 1989, more than 58 meters of coastlines have vanished every year in Rasheed, also known as Rosetta. Flooding in these areas could displace entire communities in Alexandria and in the low-lying Nile Delta, where Winter storms have flooded Alexandria's streets with seawater annually.

Therefore, flood susceptibility maps will be useful to the Egyptian Civil Defence authority for conducting rescue operations during flash flood events; for municipal planners and engineers in choosing suitable locations to implement developments in the two governorates; for land use planning and flood mitigation in municipalities. For example, according to these maps, northern and northeastern parts of Beheira governorates, and northeastern and northwestern parts of Alexandria will likely be inundated during flood events, partly because of their poor, under-developed drainage systems.

We considered eleven contributing factors in developing flood susceptibility maps, such as surface runoff, flow accumulation, soil type, rainfall intensity, drainage density, land use, slope, and others, which are generally more than factors considered in other studies. For instance, probably due to a lack of available information, Kazakis et al. (2015) who used seven flood contributing factors: flow accumulation, distance from the drainage network, elevation, land use, rainfall intensity and geology to map flood susceptibility zones in Rhodope–Evros region of Greece, considered flow accumulation as the most important contributing factor to flood, instead of surface runoff. In another study by Elkhachy (2015), even though he also ranked surface runoff

as the most important contributing factor, the weighting factor assigned for surface runoff of 35.5% may be too high (compared to 18.9% in our study) partly because he only used six factors in his study.

1.5 Conclusions and recommendations

In this study, we investigated the effects of urbanization and climate change to the flood risk of Beheira and Alexandria governorates of Egypt, developed a flood susceptibility model, and their flood susceptibility maps useful for rescue operations during flood hazards. We investigated changes to annual rainfall and temperature, and effects of urbanization to flood risk by using the runoff curve number method to estimate surface runoff time series for the two governorates over 1948-2014. Anomalies in surface runoff were computed to examine the effect of urbanization on the surface runoff time series generated. Finally, we developed a GIS decision support system to delineate flood susceptibility zones in the two governorates of Egypt. Likely related climate change impact, the annual rainfall of the two governorates had declined since 1994 at about 8.96 mm/decade, while rainfall anomalies had declined at about 15.3 mm/decade which is statistically significant. Since 1976, the climate has been warming at about 0.16 °C/decade partly due to effects of rising concentrations of greenhouse gases and partly due to rapid urbanization with a noticeable increase in impervious surfaces in Alexandria and El-Beheira in recent decades. Because of urbanization, the flood risk of both arid regions has increased, despite of a decline in the annual rainfall, for the annual surface runoff show a significant increasing trend of 12.7 mm/decade after 1970 because of rapid urbanization in both two governorates. With reference to the long-term annual surface runoff, the surface runoff anomalies of both governorates show upward trend of 14.39 mm/decade after 1970.

The flood susceptibility model delineated flood susceptibility zones in the Beheira Governorate to 9.2% (930.1 Km²), 17.9% (1815.2 Km²), 32.3% (3269.7 Km²), 28.3% (2869.2 Km²) and 12.3% (1245.8 Km²) of its area as very high, high moderate, low and very low susceptibility to flooding, respectively. In contrast, for Alexandria Governorate, the flood susceptibility model delineated 15.9% (400.1 Km²), 33.5% (841.9 Km²), 41% (1028.3 Km²), 8.8% (220.6 Km²) and 0.8% (19.7 Km²) of its area as very high, high, moderate, low and very low susceptibility to flooding, respectively. The very high and high susceptible zones were located in the northern, northwestern and northeastern parts of the Beheira governorates, which include Edko, El Mahmoudiyah, Aboul Matamir, Abu Hummus, Rosetta, Shubrakhit, Damanhur, Rahmaniya, Kafr el-Dawwar, and Wadi El Natrun, where for the past decade flooding had occurred every winter, causing heavy damages to roads, agricultural lands and cities. Floods had also occurred in some high to moderate susceptible zones such as El Delengat, Etay El Barud, Hosh Issa, Kom Hamada, Nubariyah, and Badr. For the Alexandria governorates, areas classified as high and very high susceptible zones are Montazah, El-Raml, Sidi Gaber, Bab Sharq, Al Attareen, Moharrem Beik, El-Dekheila, El-Agamy, Borg El Arab, and El-Ameriah areas where many flood events had occurred. From checking historical flood events against flood susceptibility zones of these maps, the results show that they are in good agreement, which demonstrates the accuracy of these maps.

Similar surface runoff data developed for Beheira and Alexandria governorates can be replicated for other governorates of Egypt. Such data and flood susceptibility maps developed will be beneficial to planners and governments for choosing suitable locations for future developments to minimize potential flood damages in Beheira and Alexandria governorates. To develop representative flood susceptibility maps, as many flood contributing factors as possible should be considered unless appropriate data are not available.

Chapter 2 Multi-criteria Approach to develop flood susceptibility maps in arid regions

2.1 Introduction

Millions of people are affected by flooding every year worldwide. Therefore, it is critical to control floods through proper land use management. Owing to their magnitude and sudden arrival often with minimal warning, floods usually lead to serious disasters locally. In other words, effective flood prevention has been a significant challenge in many countries. The frequent occurrences of extreme weather have caused flooding to be one of the most destructive natural hazards in arid regions. Many studies show that the rising number of major flood events is mainly due to the rapid increase in artificial surfaces, extensive urbanization and deforestation (Bronstert, 2003; Christensen and Christensen, 2003). Therefore, representative maps of flood-prone areas should be developed to prepare a fast and effective response under flooding circumstances. In the Arabian Peninsula, surface runoff from high latitude regions tend to pose a threat to its urban residents, facilities, and infrastructure. Recent flooding events that occurred in Mecca, Jizan, Al-Baha, Riyadh, Jeddah, and Abha regions among others in the Kingdom of Saudi Arabia (KSA) show that arid/semi-arid regions in the Middle East region are susceptible to floods. Therefore, developing flood warning systems in any of these regions could be one of the most effective ways to reduce the loss of life and property damage due to flooding (Negri et al., 2005).

Conjunctive applications of GIS (Geographic Information System), and multiple criteria decision support system (MCDSS) helps researchers to manage large amounts of data in solving complex problems. The Analytic Hierarchy Process (AHP) developed by Saaty (1980) is one of the most popular methods in applying a multi-criteria decision support system to optimize decision making under a set of qualitative, quantitative, and sometimes conflicting factors. Saaty (2008) proposed a procedure that involves arranging variables in a hierarchy from which the best possible

solution is determined via a pairwise comparison. The application of AHP and GIS in an integrated manner has been successful in various studies such as flood susceptibility mapping (Kazakis et al., 2015), landfall delineation, natural hazard (Fernandez and Lutz, 2010; Ahn and Merwade, 2015; Singh et al., 2017) and geo-environmental studies (Ju et al., 2012; Mahmoud and Tang, 2015; Singh et al., 2017; Patra et al., 2018). For example, Mahmoud and Tang (2015) applied AHP for managing the stormwater of the United Kingdom using five factors: rainfall excess, slope, curve number, land cover/use, and soil texture. To control flooding in UK, they developed a stormwater management map for UK that shows areas ranging from very high to low stormwater harvesting potential. They also identified locations for constructing flood control facilities based on a weighted combination of such factors, in which soil type and runoff depth contributed about 70% in developing maps for stormwater management, which is expected surface runoff is closely linked to flood occurrences (Nouh, 2006).

Other factors used in flood susceptibility mapping are such as flow accumulation, annual rainfall, elevation, distance from the drainage network, geology, slope, runoff, land use/cover, soil type, and drainage density. Fernandez and Lutz (2010) attempted to map urban flood susceptibility zones in the Tucumán Province, Argentina, using AHP. Due to a lack of spatial data, he only used five factors which are the distance to the drainage channels, topography, groundwater table depths, and urban land use. There is a lack of test on the effect of scale in flood susceptibility mapping, say from large to small scales, or vice versa, e.g. (Fernandez and Lutz, 2010; Kazakis et al., 2015). To improve our understanding of the effect of scale, testing the effect can be achieved by comparing results obtained from flood susceptibility maps for large-scale to small-scale areas located in the same region.

In the past few decades, AHP has been applied to many diverse applications of Decision Support Systems (DSS), such as applying an AHP-DSS in flood susceptibility mapping. For example, Chen et al. (2011) integrated AHP and GIS to delineate flood susceptibility zones in two cities of Taiwan. Tehrany et al. (2013) identified flood susceptibility areas in the Kelantan River basin using an advanced rule-based decision tree and ensemble statistical method and 10 susceptibility factors: DEM, curvature, geology, river, SPI, rainfall, land use/cover, soil type, TWI, and slope. Kazakis et al. (2015) delineated flood susceptibility zones in the Rhodope–Evros region of Greece using seven factors which were weighted according to their contribution to flood occurrences based on AHP. The factors with the highest weights of influence identified were elevation, slope, and distance from the drainage network. The flood susceptibility map developed was validated against observed flood records. Elkhachy (2015) also used AHP to generate flood susceptibility map for the Najran city, KSA. AHP was used to determine relative weights of flood susceptibility factors, of which runoff and soil type were the dominant factors that contributed 35.5% to surface runoff in the flood susceptibility map, while less important factors were surface slope, surface roughness, drainage density, and land use.

Hsu et al. (2017) employed AHP and GIS to map flood susceptibility zones in the Fangshan District, China, using nine susceptibility factors such as rainstorm intensity and frequency, elevation, slope, river network density, and others. The flood susceptibility maps they developed agree well with historical flood records. In another study, Trail et al., (2017) integrated five factors into an AHP to map flood susceptibility zones in coastal lowland areas of central Vietnam, of which they showed that elevation and distance to drainage network play a major role in the development of flood susceptibility zones. It seems common for many studies to miss factors such as surface runoff and drainage density in flood susceptibility mapping, in which important factors

to be considered are such as surface runoff, drainage density, annual rainfall, distance to drainage network, soil type, and land use. Using a limited number of factors in flood susceptibility mapping will increase the possibility of getting some over-rated factors.

It is important to develop flood susceptibility maps in Riyadh province, the central region of Saudi Arabia (18 % of KSA total area) where recurring flood events have occurred, for possible rescue operations and for including migration procedures in future land use planning in both the Riyadh province and Riyadh city. A multi-criteria approach is introduced to identify flood susceptibility zones and then a sensitivity analysis was done to examine how sensitive are the results to changes in weights applied to susceptibility factors and the relative importance of these susceptibility factors. The methodology was applied in Riyadh Province, and the result was validated against historical flood records. To test the effect of scale in the proposed methodology, it was applied again in the Riyadh City which is only 4.85 % in area of the Riyadh Province, and 0.89 % of the total area of KSA.

2.2 Study area

The Riyadh Province (24°38" N and longitude 46°43' E) (Figure 2.1(a)), located in central Arabia, was selected as the study site because the entire study area has no flood susceptibility maps. Similar to most arid regions in the Middle East, where rainfall is scarce, there is a general lack of proper drainage system which tends to cause catastrophic flooding when extreme weather occurs. In the last 30 years, KSA constructed many rainwater harvesting dams in the mountainous region for agriculture development (Mahmoud and Alazba, 2015). Furthermore, floods could occur because of rugged topography and geological structures. Figure 2.1(b) shows that a flood event in the northern Riyadh province had caused severe damages to infrastructure and private properties.

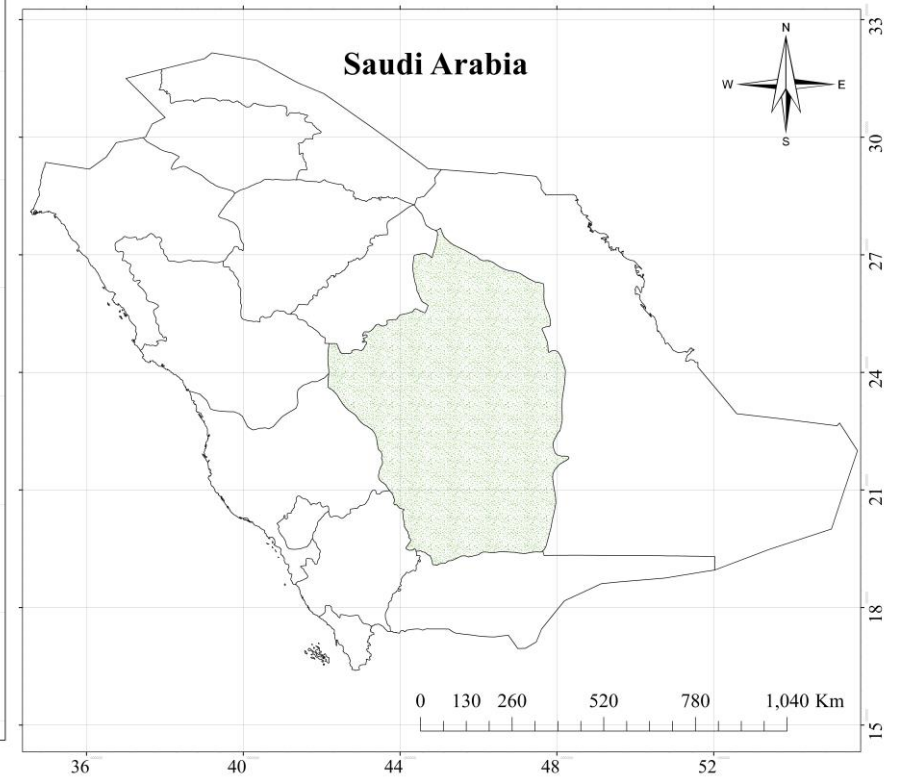
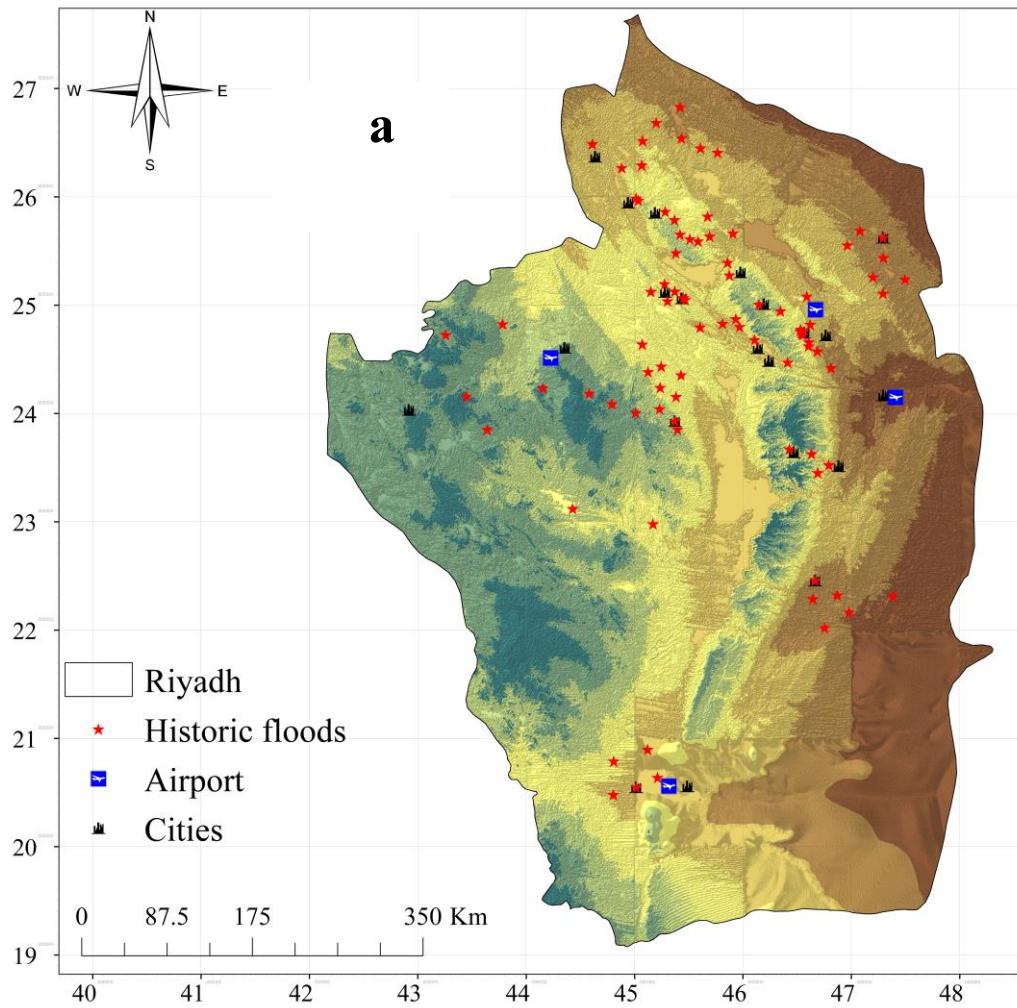




Figure 2.1 (a) Location of Riyadh Province in KSA. (b) Photos of flood taken on November 16, 2013, in Riyadh Province.

2.3 Materials and methods

2.3.1 Selection of susceptibility factors and data processing

Information from different data sources was collected and a database was developed in a geospatial environment. Ten susceptibility factors were selected based on literature reviews, which are flow accumulation, distance from the drainage network, elevation, LULC, annual rainfall, geology, slope, runoff, soil type, and drainage density. These factors were then characterized based on field survey and long-term flood records in KSA. Based on earlier studies (Fernandez and Lutz, 2010; Elkharchy, 2015; Bathrellos et al., 2016; Hong et al., 2018), the importance of each flood susceptibility class such as flow accumulation, annual rainfall, geology, distance from the drainage network, slope, runoff, soil type, elevation, LULC, and drainage density. Because the susceptibility factors were measured on different scales, certain reclassifications were necessary to convert susceptibility factors to five comparable units or susceptibility classes: 5 (very high susceptibility), 4 (high susceptibility), 3 (medium susceptibility), 2 (low susceptibility), and 1 (very low susceptibility) as shown in Table 2.1, based on their contributions to flooding probability. For instance, based on historical flood records, the elevation of the study area was divided into five categories. An area with low elevation (0–250 m) falls under very high susceptibility category, while an area at a high elevation falls under a very low susceptibility category (Jacinto et al., 2014).

Similarly, the raster slope map was classified into five classes. Areas with 0–2 % slope was assigned a very high susceptibility to flooding; areas with 2–5 % slope has high susceptibility to flooding; areas of 5–15 % slope has moderate susceptibility to flooding; areas of 15–35 % slope has low susceptibility to flooding; while areas of slope higher than 35 % has very low susceptibility to flooding. Moreover, clay soils may result in greater surface runoff than sandy soils; higher annual rainfall can lead to more surface runoff; high soil moisture content can increase the risk of

flooding more than dry soil; and land cover and land use are other factors that influence the occurrence of flood (Alexakis et al., 2014). Topographic elements are also important, e.g. surface slope is also an important flood susceptibility indicator because when the slope increases, the flow velocity will also increase; a denser drainage network means more flow accumulation and so a higher possibility of flood occurrences. On the other hand, dense vegetation cover and farmland reduces the probability of flooding because they restrict flow path, but built-up areas or urbanization generate more surface runoff.

Table 2.1 Classes of the flood susceptibility factors and their ratings

Number	Thematic layers	Classes	Rating
1	Flow accumulation (pixels)	0-250	1
		731-2195	2
		2195-3415	3
		3415-15125	4
		15125-151000	5
2	Distance to drainage network (m)	<200	5
		200-500	4
		500-1000	3
		1000-2000	2
3	Elevation (m)	>2000	1
		0-286	5
		286-485	4
		485-697	3
		697-899	2
4	LULC	899-1523	1
		Irrigated cropland	3
		Forest	1
		Shrubland	4
		Sparse vegetation	2
		Built up areas	5
		Bare soil	2
		Water bodies	5

		0-45	1
		45-79	2
5	Annual rainfall mm/yr	79-120	3
		120-170	4
		170-230	5
		0-2	5
		2-5.	4
6	Slope (%)	5-15.	3
		15-35	2
		35-90	1
		Cenozoic	2
		Mesozoic - Jurassic and Cretaceous	3
		Mesozoic – Triassic	2
7	Geology	Plutonic rocks	5
		Precambrian (Archean+Proterozoic)	4
		Quaternary	3
		Upper paleozoic (Dev,Car,Per)	1
		0-25	1
		25-47	2
8	Runoff (mm/yr)	47-74	3
		74-144	4
		144-179	5
		Arenosols	1
		Lithosols	2
9	Soil type	Miscellaneous land units	4
		Regosols	2
		Solonchaks	3
		Yermosols	5
		0-0.25	1
		0.25-0.35	2
10	Drainage density (km/km2)	0.35-0.72	3
		0.72-0.9	4
		0.9-1.85	5

2.3.2 Assignment of weights for susceptibility factors

Analytical hierarchy process (AHP) was applied to create a pairwise matrix of conditional factors. AHP is a well-known approach for analyzing complex problems. In flood susceptibility studies, various researchers have used the pairwise rating techniques to capture the importance and contributions of each conditional factors in flood mapping (Sinha et al., 2008; Zou et al., 2013; Hu et al., 2017). In this approach, all flood susceptibility factors were arranged in a hierarchical manner to facilitate pairwise comparison (Table 2.2). In this study, we evaluated the relative importance of susceptibility factors based on a comparative scale proposed by Saaty (1980) that consists of integer numbers of 1 to 9, where 1 means that the factors are equally important, while 9 is much more important than others. Table 2.2 illustrates a 10×10 pairwise comparison matrix, where diagonal elements are equal to 1 because it compares the importance of each factor to itself. The remaining values in each row reflect the relative importance of other factors, e.g., the first row in Table 2.2 illustrates the relative importance of flow accumulation compared to other factors (in columns). For instance, the importance of flow accumulation is 3 times that of land use, 5 times that of the slope, and 7 times that of geology. Similarly, comparison of rows values is inverse of the pairwise comparison (e.g., land use, slope, and geology are $1/3$, $1/5$, $1/7$ the importance of flow accumulation, respectively).

To estimate the respective contribution of key factors to flood susceptibility, weights associated with the key factors were calculated using the rank sum method. Principal eigenvectors of the pairwise matrix were calculated and then used to optimize the weight calculation procedures. The multi-criteria AHP weighting is based on the approach proposed by Janssen and Van Herwijnen (1994) as:

$$W_j = \frac{m+1-j}{\sum_{i=1}^m (m+1-i)} \quad (2-1)$$

where W_j is the weight for each factor, and j is the factor number and range from 1-10

The consistency index was calculated and validated with acceptable value to ensure a representative pairwise comparison matrix. This index is calculated as follows:

$$\text{consistency index} = \frac{\mu - m}{m - 1} \quad (2-2)$$

where, μ is the average of the consistency vector and m is the number of susceptibility factors used to create the pairwise comparison according to Saaty (1990). The consistency ratio was then calculated as follows:

$$\text{consistency ratio} = \frac{CI}{RI} \quad (2-3)$$

where, CI is the consistency index, and RI is the random index which is dependent on the number of factors used in the pairwise matrix (Saaty 1980, 1990). The model so developed produced an acceptable consistency ratio which was less than the recommended ratio of Saaty (1980). The normalized susceptibility factors are presented in Table 2.3,

Table 2.2 Factors of flood susceptibility: Analytical Hierarchy Process.

Factors	Flow accumulation	Dist. to drainage net	Elevation	Land use/cover	Rainfall intensity	Slope	Geology	Runoff	Soil type	Drainage density
Flow accumulation	1	2	2	3	3	5	7	1	2	2
Dist. to drainage net	1/2	1	1	3	3	4	6	1/3	1/5	1
Elevation	1/2	1	1	3	3	4	6	1/2	1/3	1
Land use/cover	1/3	1/3	1/3	1	2	4	5	1/7	1/6	1/2
Annual rainfall	1/3	1/3	1/3	1/2	1	4	5	1/2	2	1/3
Slope	1/5	1/4	1/4	1/4	1/4	1	3	1/3	1/2	3
Geology	1/7	1/6	1/6	1/5	1/5	1/3	1	1/6	1/3	1/3
Runoff	1	3	2	7	2	3	6	1	2	5
Soil type	1/2	5	3	6	1/2	2	3	1/2	1	4
Drainage density	1/2	1	1	2	3	1/3	3	1/5	1/4	1

Table 2.3 Normalized flood susceptibility factors: Analytical Hierarchy Process.

Factors	Flow accumulation	Dist. to drainage net	Elevation	Land use/cover	Rainfall intensity	Slope	Geology	Runoff	Soil type	Drainage density
Flow accumulation	0.20	0.14	0.18	0.12	0.17	0.18	0.16	0.21	0.23	0.11
Dist. to drainage net.	0.10	0.07	0.09	0.12	0.17	0.14	0.13	0.07	0.02	0.06
Elevation	0.10	0.07	0.09	0.12	0.17	0.14	0.13	0.11	0.04	0.06
Land use/cover	0.07	0.02	0.03	0.04	0.11	0.14	0.11	0.03	0.02	0.03
Annual rainfall	0.07	0.02	0.03	0.02	0.06	0.14	0.11	0.11	0.23	0.02
Slope	0.04	0.02	0.02	0.01	0.01	0.04	0.07	0.07	0.06	0.17
Geology	0.03	0.01	0.01	0.01	0.01	0.01	0.02	0.04	0.04	0.02
Runoff	0.20	0.21	0.18	0.27	0.11	0.11	0.13	0.21	0.23	0.28
Soil type	0.10	0.35	0.27	0.23	0.03	0.07	0.07	0.11	0.11	0.22
Drainage density	0.10	0.07	0.09	0.08	0.17	0.01	0.07	0.04	0.03	0.06

2.3.3 Flood susceptibility index

After calculating the weights, a flood susceptibility index (FSI) was defined based on conditional factors and their percentage of influence as follows

$$FSI = \sum(W_j * X_j) \quad (2-4)$$

Where, W is the weight of factors j and X is the susceptibility classes to flooding provided in Table 2.1. Furthermore, the FSI derived are classified into five flood susceptibility classes according to the probability of flood occurrence. Finally, flood susceptibility classes were derived from this index (FSI) and the total area of each class was estimated and validated against historical flood records in the study area. The same approach was applied to the small-scale study area (Riyadh city) to identify scale effects on the developed FSI.

2.3.4 Model sensitivity analysis

Developing a flood susceptibility model involves a set of factors related to flood susceptibility. In previous studies, various flood susceptibility factors were employed, and some of these factors are strongly inter-related, such as i) rainfall and surface runoff (Saharia et al., 2017; Tang et al., 2018); ii) surface runoff, soil type, and land use (Elkhrachy, 2015; Mojaddadi et al., 2017; Shehata and Mizunaga, 2018); iii) flow accumulation and distance from the drainage network (Kazakis et al. 2015; Zehra and Afsar, 2016; Dou et al., 2018). A sensitivity analysis of these inter-relationships was conducted to check how sensitive the results are to changes in the list of susceptibility factors considered in the analysis. The following test cases were conducted: (a) Case 1: annual rainfall is removed from the model, (b) Case 2: runoff is removed from the model, (c) Case 3: soil type and land use were eliminated from the model, (d) Case 4: distance to drainage network was eliminated from the model, (e) Case 5: test the approach of Kazakis et al. (2015) based on seven susceptibility factors: flow accumulation, elevation, land use, slope, distance from

the drainage network, annual rainfall, and geology. The results of Case 5 were compared with the results of Kazakis et al. (2015). The flood susceptibility map obtained for each case was compared with historical flood records to check the accuracy of the flood susceptibility maps developed from these test cases.

2.4 Results and discussions

2.4.1 Development of flood susceptibility factors database

By conjunctively applying AHP with a multicriteria decision analysis to the study site involving 10 susceptibility factors, the extent of each flood susceptibility zone was identified. Thematic maps in Figure 2.2 shows the spatial distributions of these factors.

Elevation and slope.

To obtain the slope map (Fig. 2(b)), a DEM dataset of 30m resolution (Figure 2.2(a)) was processed using ArcGIS 10.1 such as filling sinks and removing continuous flat regions to maintain flow continuity. Elevation and slope are two key factors that influence the susceptibility of any area to flooding (Pradhan, 2009). Mostly, flood-prone areas tend to have low surface slopes, and located in low-elevation zones, e.g., elevation classification is often employed in flood mapping studies (Fernandez and Lutz 2010; Dahri and Habib, 2017). On the other hand, how high the elevation of any region is relative to elevations of surrounding regions, and it should be categorized on the basis of historical flood events. Furthermore, given slope defined as the percentage of an area elevation model does not vary much between regions, similar ratings have been assigned to slope percentages in different studies, such that a high rating was given to areas with a low slope and vice versa (Mahmoud and Tang, 2015; Dahri and Habib, 2017).

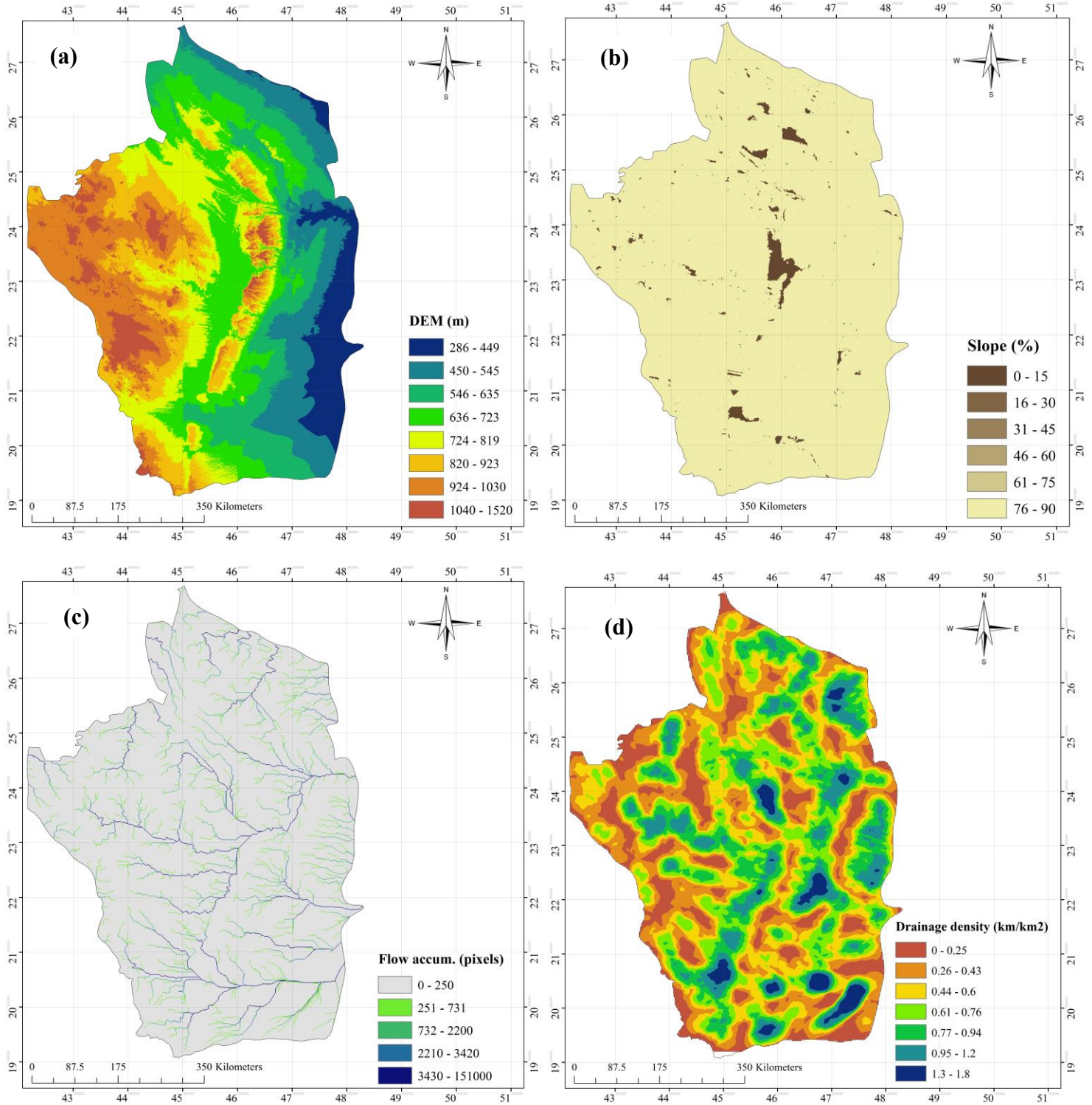


Figure 2.2 Susceptibility factors used in this study: (a) DEM, (b) slope, (c) flow accumulation, (d) drainage density, (e) distance from the drainage network, (f) land use/cover, (g) annual rainfall, (h) geology, (i) soil type, (j) runoff

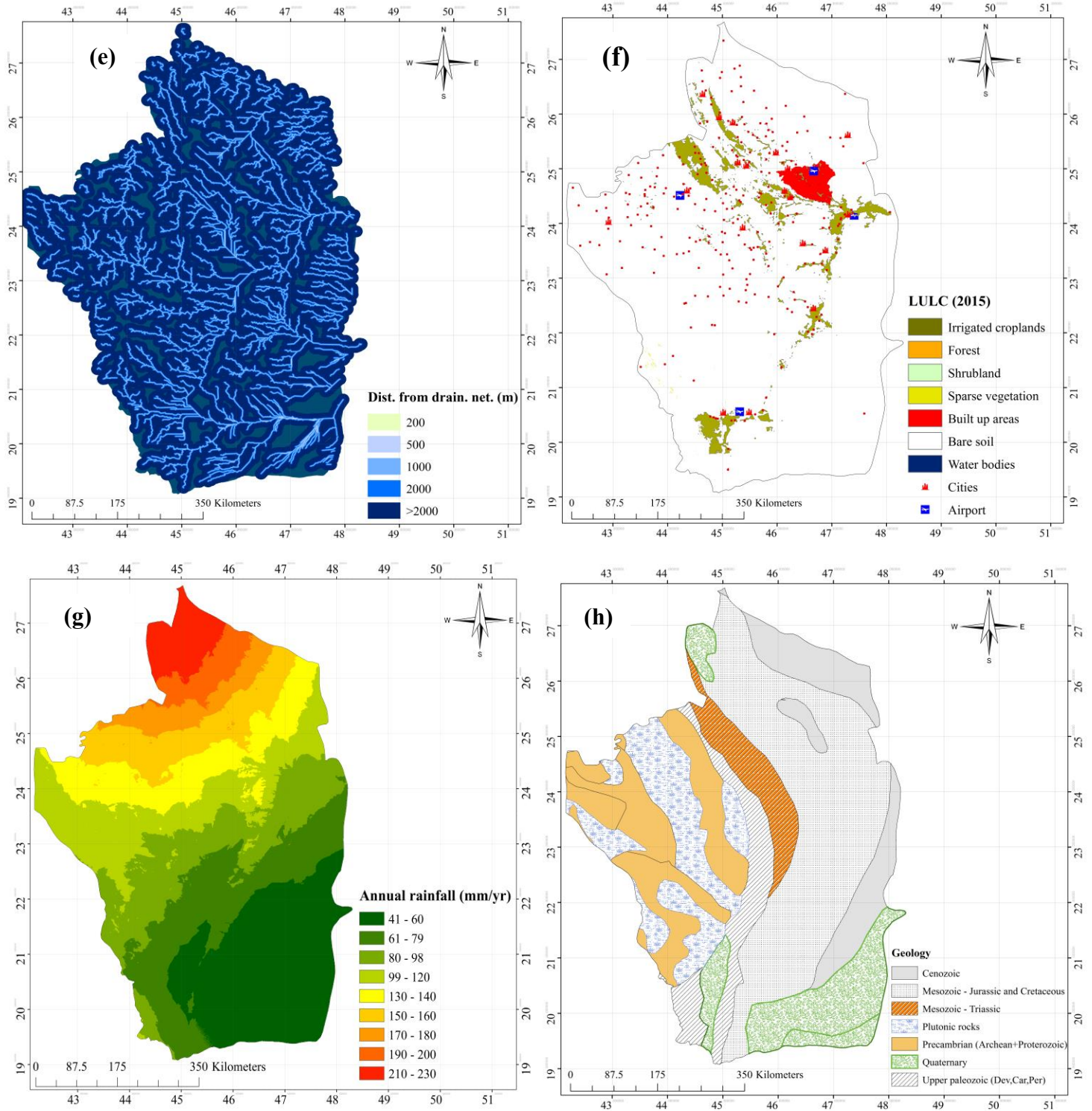


Figure 2.2 (continued)

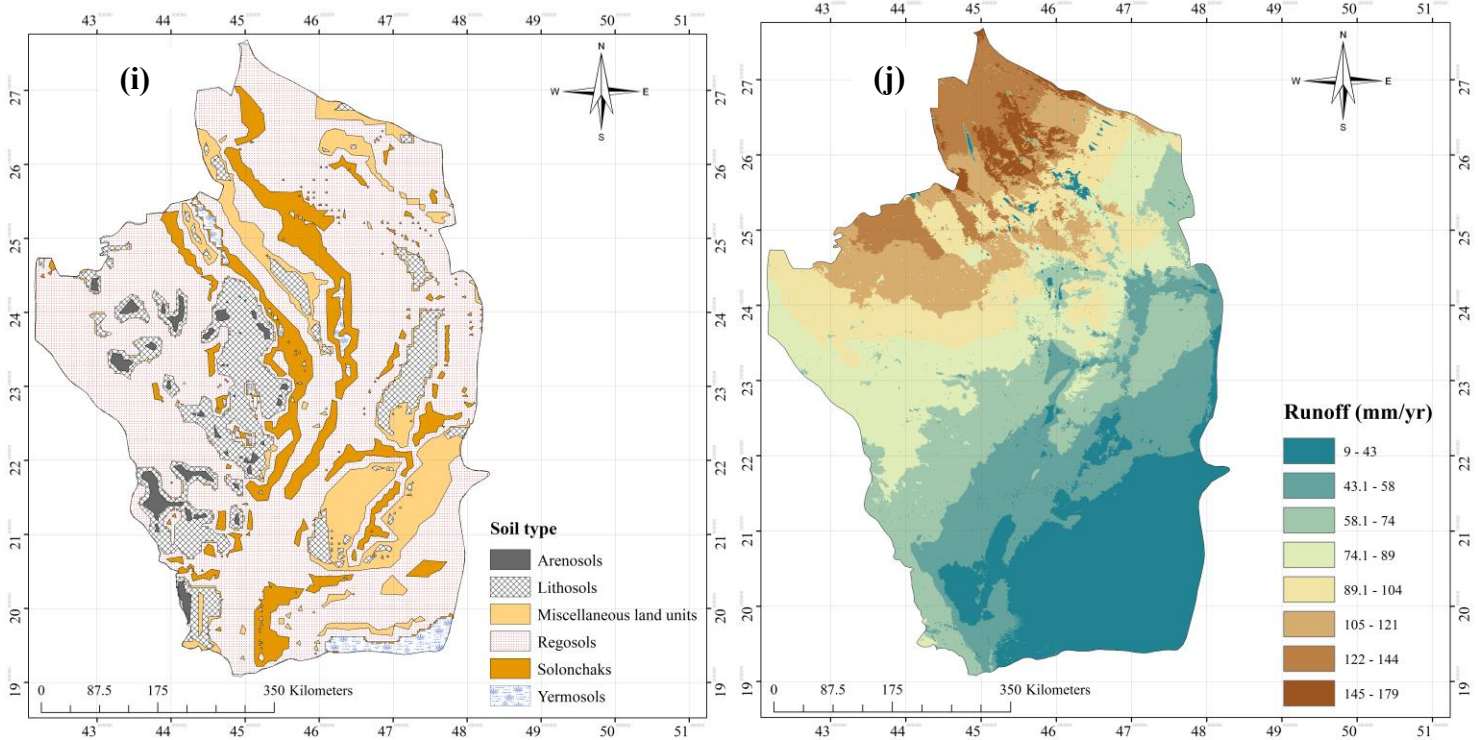


Figure 2.2 Continued

Flow accumulation.

Flow accumulation is likely the most important parameter in delineating flood susceptibility zones (Kazakis et al. 2015). In other words, high flow accumulation means high susceptibility to flooding (Lehner et al., 2006). Buildings and other municipal infrastructure located in high flow accumulation areas are naturally more vulnerable to flooding. Flow accumulation in a study area (Figure 2.2(c)) means the accumulation of flow from surrounding cells and paths, leading to increased flow in a specific cell, and which helps to map out the convergence zone of surface runoff. In Figure 2.2(c), blue and green pixels represent high flow accumulation while the back-surrounding (black pixels) low flow accumulation. Areas with more flow accumulations tend to be more vulnerable to flooding for such areas act as convergent points for surface runoff. In this study, flow accumulation values are classified into five classes, ranging from very low (0–250 pixels) to very high (3430–151000 pixels) flow accumulation.

Drainage density.

Higher drainage density generally means greater surface runoff and therefore higher probability of flooding, and vice versa. Figure 2.2(d) shows the drainage density map of the study area calculated from the drainage network classified into five classes ranging from very high to low drainage densities. As expected, the susceptibility to flooding decreases from very high drainage density (0.9–1.85 km/km²), which means very high susceptibility to flooding: to high (0.72–0.9 km/km²), moderate (0.35–0.72 km/km²), low (0.25–0.35 km/km²), and very low (0–0.25 km/km²) drainage densities. Kumar et al (2007) reported that areas with high drainage density mean high flood susceptibility because a higher drainage density means more surface runoff generation than areas with low drainage density (Srivastava and Bhattacharya, 2006). Therefore, flood risk will increase with an expansion in the drainage network, which is a critical factor in surface runoff generation (Ogden et. Al, 2011). This drainage density classification has also been used in other studies (Elkhrachy, 2015).

Distance from the drainage Network.

Areas located far away from the drainage network are generally less likely to suffer flooding than areas that are nearby because the latter are within the flow path of surface runoff. Relating flood susceptibility to the distance from the drainage network can be subjective even though ideally it should be based on historical records. For example, Samanta et al (2016) considered areas at a distance <100m from the drainage network have high flood susceptibility while areas at distance >2000 m have very low flood susceptibility. Pradhan (2009) considered areas located within 90m from the drainage network have high flood susceptibility. Similar to studies that follow the paradigm, areas within shorter distances from the drainage network are more likely to suffer from flooding (Islam and Sado, 2000), flood-prone zones of the study site are delineated accordingly. Based on historical flood data, areas that are within 200 m from the drainage network are classified as very highly susceptible to flooding, while areas within a

distance of 500, 1000, 2000, and >2000 m from the drainage network are considered to have high, moderate, low, and very low susceptibility to flooding, respectively (Figure 2.2(e)).

Land use classification.

By supervised classification using multiple ground control points collected from google earth images and a field survey, a 2015 Landsat image of 30 m spatial resolution was used to generate for the study site (Figure 2.2(f)) a land use map categorized into seven classes: irrigated cropland, forest, shrubland, sparse vegetation, built-up areas, bare soil, and water bodies. The Kappa index of agreement (KIA) was used to evaluate the classified land use map based on a random number of ground control points such that $KIA > 0.8$ implies high accuracy (Jensen, 2005). Given the KIA obtained is 0.946, the land use map developed is representative. Because urbanization can generate more surface runoff than bare soil and vegetation cover, in this study built-up areas are assigned with relatively large weights (Samanta et al., 2016; Kourgialas and Karatzas, 2011).

Annual rainfall.

Figure 2.2(g) presents the mean annual rainfall for the study area. As expected, the susceptibility to flooding increases with higher rainfall depth. Even in an arid region such as Riyadh, it can experience extreme rain events leading to very high surface runoff and flooding (Mahmoud and Alazba, 2015), which could get worse with urbanization. Surface runoff is controlled by topography, slope and the drainage network. Almost everywhere in KSA is prone to flooding, especially in central Saudi Arabia, where very intensive rainfall could occur in extensively urbanized areas, leading to flooding. The annual rainfall at Riyadh, ranging from 41 to 230 mm/year is classified into five classes in relation to their contribution to flood occurrences (Table 2.1). For example, annual rainfall ranging from 170 to 230 mm/year is considered high because it means high flood susceptibility.

Geology.

The geology of Riyadh Province is very complex, varies from region to region, which affects its hydrologic processes. Figure 2.2(h) shows the geology of the Riyadh Province divided into seven geological classes, which range from Precambrian, to Quaternary rocks and to Paleozoic rocks. At 33.6%, Mesozoic–Jurassic and Cretaceous rocks, considered to have moderate susceptibility zones for flooding, occupy the largest area in the study site. The 2nd most prevalent is the Precambrian rocks that occupy 15.6% of the study area. These rocks are extremely rich in clay, have low permeability and therefore are classified to be of high susceptibility to flooding. Next is the Plutonic rocks which occupy 13.8% of the study area, has very low porosity and therefore are also of high flood susceptibility. Quaternary rocks that occupy 12.6 % of the total area are classified as of moderate susceptibility to flooding due to its medium infiltration rate. Cenozoic rocks that occupy 10.8% of the study area are characterized by high infiltration rate and therefore have low flood susceptibility. Lastly, Upper Paleozoic and Mesozoic–Triassic rocks that occupy only 8% and 5.7% of the study area have low and very low susceptibility, respectively.

Soil type.

The soil map of the Riyadh Province presented in Figure 2.2(i) shows six soil types identified. Arenosols which only constitutes 1.4 % of the study area is a sandy soil characterized with high permeability, and so it is classified to be of very low susceptibility to flooding because of its high rate of infiltration. Lithosols soil that occupies 12.6 % of the study area has a low clay content, very high infiltration rate and so of low flood susceptibility (Mahmoud and Alazba, 2015). Miscellaneous soil that occupies 10.3% of the study area has a low sand content and therefore of high susceptibility zones. Regosols, which constitute 62.6 % of the total area, is mainly characterized by rocky surface, coarse texture, high infiltration rate, and therefore of low flood susceptibility. Solonchaks soils that occupy 11.2 % of the study area has a moderate infiltration rate, and so has moderate flood susceptibility. Lastly, Yermosols

soil that occupies only 1.9% of the study area has low infiltration rate due to its clay content and so it constitutes very high susceptibility zones.

Surface runoff.

The curve number (CN) for Riyadh Province was developed using the CN of NRCS (Natural Resources Conservation Service) method. A CN is based on the area's hydrologic soil group, land use, treatment and hydrologic condition estimated using a GIS. Next, the monthly runoff depth is estimated based on the monthly rainfall depth and the CN of Riyadh. Lastly, the spatial distribution of annual surface runoff (Figure 2.2(j)) is developed as a runoff depth map classified into five classes, categorized as “very high susceptibility” (144–179 mm/year), “high susceptibility” (74–144 mm/year), “moderate susceptibility” (47–74 mm/year), “low susceptibility” (25–47 mm/year), and “very low susceptibility” (0–25 mm/year). Similarly, Elkharchy (2015) included surface runoff in their study commonly found in urbanized areas with extensive impervious surfaces, and which had improved the results of Samanta et al. (2016), and this study. However, surface runoff was not considered in some studies, e.g., Tehrany et al., (2013); Kazakis et al. (2015); and Samanta et al. (2016).

2.4.2 Flood susceptibility zones in Riyadh Province (large-scale)

A model has been developed to generate a flood susceptibility map from integrating thematic maps of 10 factors. Table 2.4 shows the final weight for each factor, which reflects its estimated contribution to flood occurrences in the Riyadh Province: surface runoff (19.3%), flow accumulation (16.9%), soil type (15.7%), elevation (10.2%), distance to drainage network (9.7%), annual rainfall (8%), drainage density (7.1%), land use (6%), slope (5%), and geology (2%). Figure 2.3 shows that the final flood susceptibility map developed for the Riyadh province was classified into five susceptibility classes: very high, high, moderate, low, and very low susceptibility. Table 2.5 shows the estimated area of each susceptibility class: 3.4% (13033.6 km²), 14.4% (54658.6 km²), 27.9% (106277.7 km²), 36.5% (138784.3 km²), and

17.8% (67743.7 km²) of the study area are classified as very high, high, moderate, low, and very low susceptibility zones, respectively. This means that 45.7% of the study area is characterized by very high to moderate flood susceptibility zones which explains reasons behind the recurrent flood events in the Riyadh province. These zones have slope ranging from 0-5 %, annual rainfall ranging from 120 to 230 mm/year, and consist mainly of built-up areas, shrublands, and irrigated croplands. Miscellaneous land units and Yermosols are the main soil types in the very high to high susceptibility zones. The primary geological structures include plutonic and Precambrian rocks. These zones have a drainage density ranging from 0.72 to 1.85 km/km², and with an accumulative path of 200–500 m. Areas that fall within 200 m buffer zones of the drainage network are found to be highly prone to flooding, but areas far away have a lower susceptibility to flooding, as also found by Kazakis et al. (2015).

The flood susceptibility map shows that most of the very high and high susceptibility zones are located within northern, northeastern, and northwestern regions of the Riyadh Province. Historically, several neighborhoods in these regions had suffered very high flooding caused by high surface runoff, which ranged from 110 to 179 mm/year, such as Wadi Hanifa, Wadi Nisah, Wadi Ghilannah, and Wadi Nimar. These wadis witnessed many flooding events in recent years. Urban and built-up areas within these wadis are prone to flooding because during heavy rain runoff from surrounding areas will flow to these wadis, which will suddenly filled with water. The very low and low susceptibility zones are located in western parts of the Riyadh Province. There are also some high to moderate susceptibility zones located in central Riyadh Province, some moderate flood susceptibility zones in Wadi Nisah and Wadi Hanifah, and high susceptibility zones are restricted to northeastern part of the Riyadh Province.

Table 2.4 Percent of influence

SL.NO.	Thematic layers	Weight	Weight %
1	Flow accumulation	0.169	16.9

2	Distance to drainage network	0.097	9.7
3	Elevation	0.102	10.2
4	Land use/cover	0.06	6
5	Annual rainfall	0.08	8
6	Slope	0.05	5
7	Geology	0.02	2
8	Runoff	0.193	19.3
9	Soil type	0.157	15.7
10	Drainage density	0.071	7.1

Table 2.5 Susceptibility classes and flood records

Flood susceptibility	Riyadh Province			Riyadh region neighborhoods		
	Area (Km ²)	Area (%)	# of events	Area (Km ²)	Area (%)	# of events
Very low	67743.7	17.8	0	-	-	-
Low	138784.3	36.5	9	-	-	-
Medium	106277.7	27.9	28	9037.5	40.9	8
High	54658.6	14.4	68	4704.3	29.5	4
Very high	13033.6	3.4	33	4718.5	29.6	13

When an intense rain event occurs, the highest surface runoff is observed in urban and built-up areas of Riyadh due to the increase in impervious surface which decreases the soil infiltration loss, and factors that contribute to increase in surface runoff such as topography, rainfall of high intensity, slope and geology of the area. The impact of increased urbanization is evident in recurrent flood events observed in some parts of Riyadh. While moderate and low flood susceptibility zones can be seen in the southeastern portions of Riyadh. In summary, factors that contribute to flood susceptibility in Riyadh include soil types, annual rainfall and low elevation. The southeastern regions of Riyadh province have the largest CN, ranging over 40–100. These areas are mainly urban areas and government buildings, universities and schools. Under large CN, most of the rainfall in these areas is transformed to surface

runoff, resulting in loss of lives and properties. Because the surface runoff of the Riyadh province is generally high, it is included as a key factor in this study. Sometimes even areas with low surface runoff could suffer major floods that caused huge damages to the infrastructure. Southwestern Riyadh belong to very low and low susceptibility zones partly because they have high elevation. Figure 2.3 shows Riyadh City and its surroundings have moderate, high and very high flood susceptibility risk.

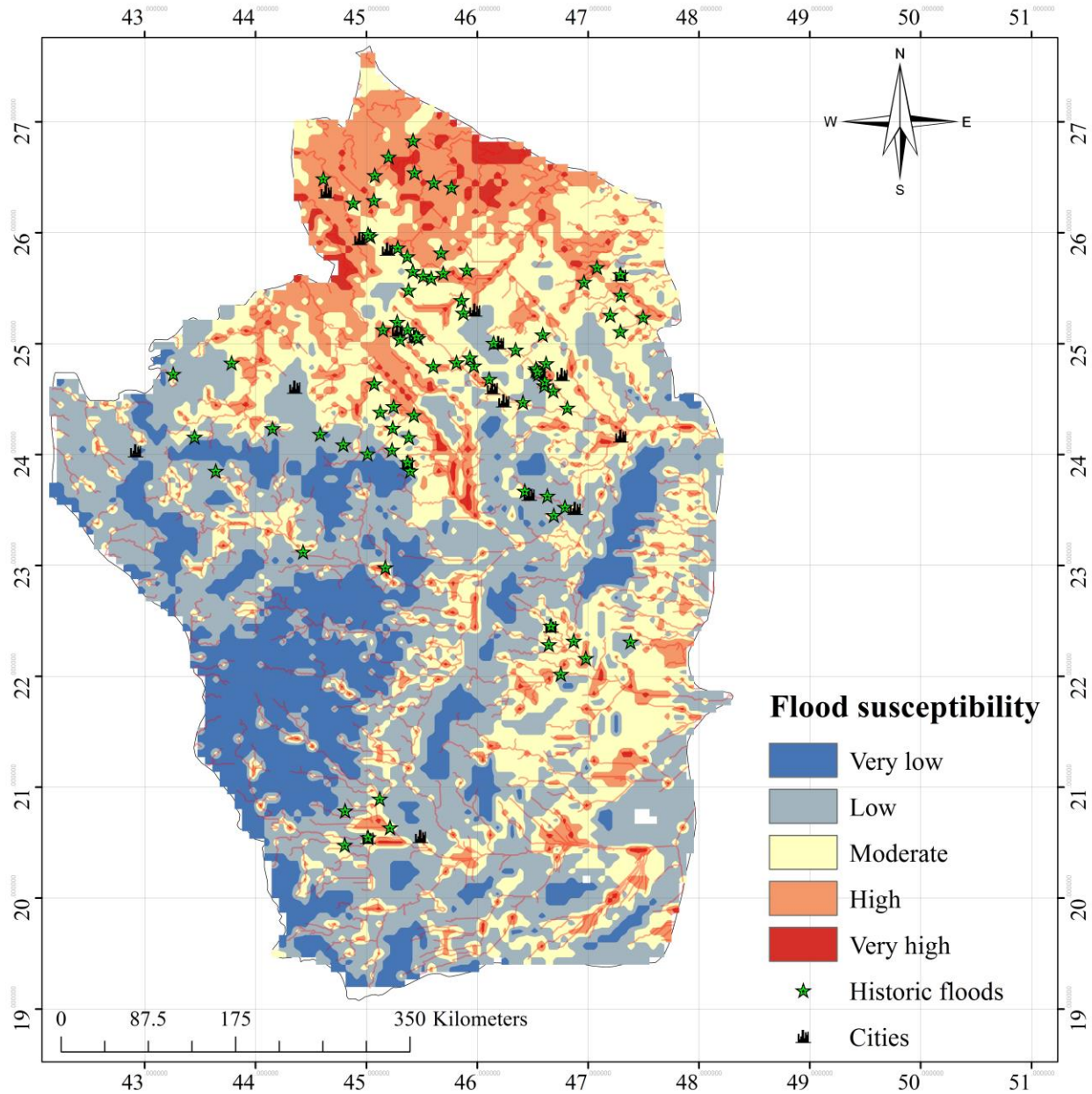


Figure 2.3 Flood susceptibility map for Central Arabia

2.4.3 Flood susceptibility map for Riyadh City (small-scale)

The flood susceptibility map for the Riyadh City, which is part of the Riyadh Province, was similarly developed based on 10 thematic maps. However, the flood susceptibility map developed (Figure 2.4) has three vulnerability classes: very high, high, and moderate. As shown in Table 2.5, 29.6 % (4718.5 km²) and 29.5 % (4704.3 km²) of the Riyadh City belong to very high and high flood susceptibility

zones dominated by urban and built-up areas, respectively, while 40.9 % (9037.5 km²) belong to moderate susceptibility zones.

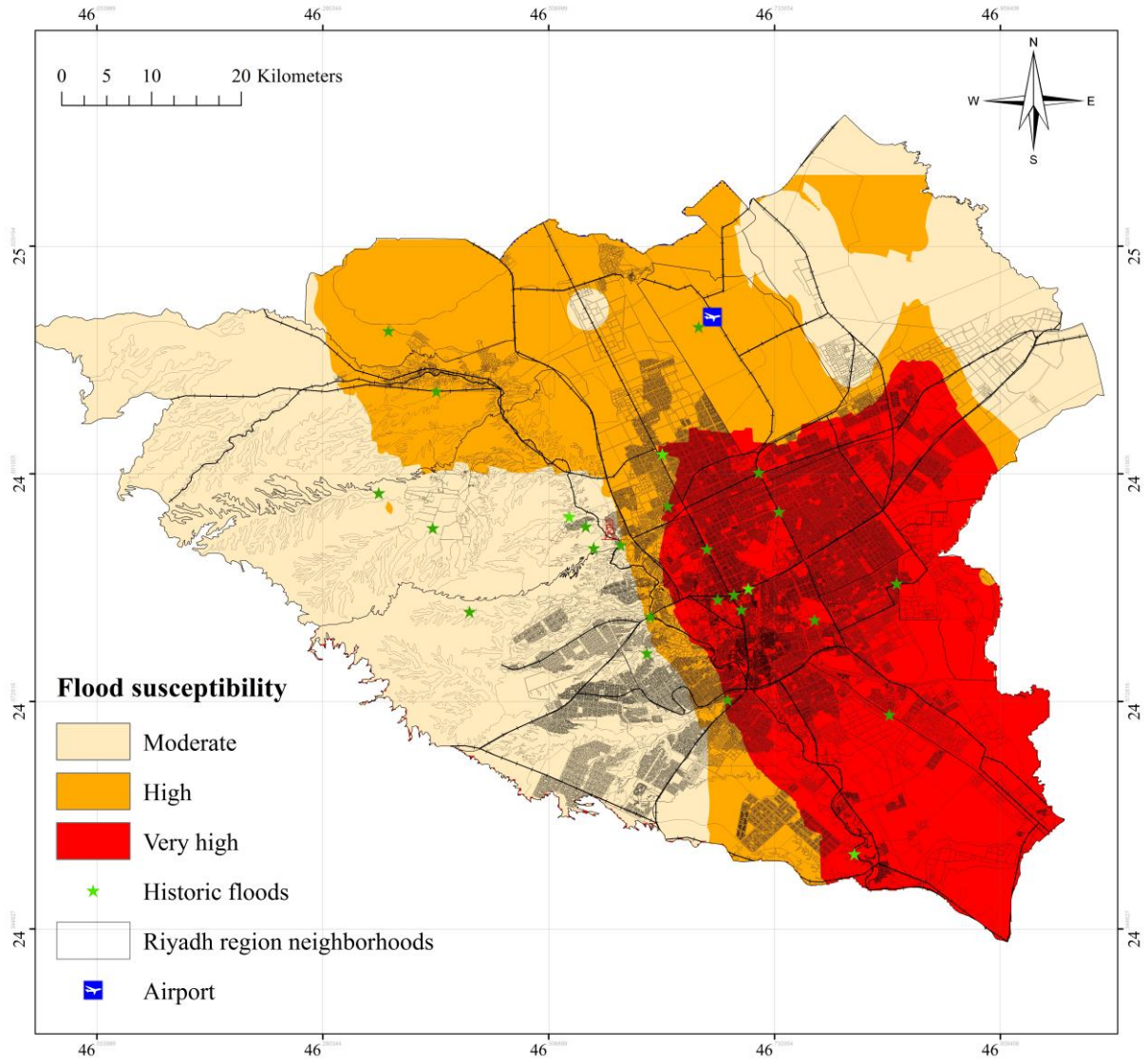


Figure 2.4 Flood susceptibility map for Riyadh’s neighborhood

Unfortunately, southeastern and southwestern parts of the city, with important infrastructure and administrative offices, are in the middle of very high flood susceptibility zones. However, to the west of Riyadh City, high and medium flood susceptibility zones are common, which include low lying areas such as Wadi Nisah and Wadi Hanifah. These two wadis act like a lake collecting surface runoff coming from surrounding areas, making them the most prone to flooding zones in the city (Figure 2.4). Wadi

Hanifah of 4 km² in area and highly populated, lies in very high to moderate flood susceptibility zones. This wadi, with buildings and heavy constructions, is flooded almost yearly even though its storage capacity exceeds 0.7 million m³ of rainwater. However, the impact of future floods could be mitigated if flood susceptibility studies are carried out and applied for any further development. According to historical records, 319 people had lost their lives due to flooding in Saudi Arabia since 1964 (Table 2.6), which is a relatively large number in this arid country. This shows that flooding could impact arid regions with severe consequences especially if no flood proofing efforts are implemented in such regions. For example, the 2005 Riyadh flood due to severe rainfall claimed the life of seven people. Another recent flood was the 2010 Al-Riyadh flood that resulted in severe damages to infrastructure.

Table 2.6 Examples of major floods in Saudi Arabia from 1964 to 2013

# of Event	Event	Date	Totals deaths	Total affected
2	Flood	4/4/1964	20	1000
3	Flood	24-12-1985	32	5000
2	Flood	8/8/2003	-	13000
2	Flood	14-04-2004	-	430
1	Flood	22-01-2005	29	-
3	Flood	28-04-2005	34	-
1	Flood	24-11-2009	161	10000
2	Flood	10/7/2010	-	85
3	Flood	14-04-2012	19	1021
2	Flood	2/5/2013	24	-

2.4.4 Models validation (large-scale and small-scale)

To verify the two susceptibility models, the flood susceptibility maps developed are compared against actual historical flood records. The results reveal quite good agreement between the susceptibility maps with historical records. It seems that the proposed method can develop representative flood susceptibility mapping in other study areas for it does not depend on the scale of the study site. Figure 4 shows that historical flood records occurred in areas designated by the susceptibility map as

very high to high flood susceptibility. For example, in the flood event of November 16, 2013 in Riyadh City, streets and major facilities were flooded after heavy rainfall storm hit the city, leading to traffic jams, and death of more than 20 people. Out of 138 historical flooding events of the Riyadh province, 101 flooding records occurred within the very high and high flood susceptibility zones. In addition, there were only 28 flood events recorded in moderate flood susceptibility zones and only 9 events in low flood susceptibility areas. In another word, the flood susceptibility zones developed out of the factors and their weights to yield accurate results in both the Riyadh Province and the city. This shows that the adopted flood susceptibility method can predict the likelihood an area will be flooded quite accurately. Further, the results obtained from both models compare well with historical flood events which demonstrate that the performance of the adopted flood susceptibility model is likely not scale dependent.

2.4.5 Sensitivity analysis (test cases)

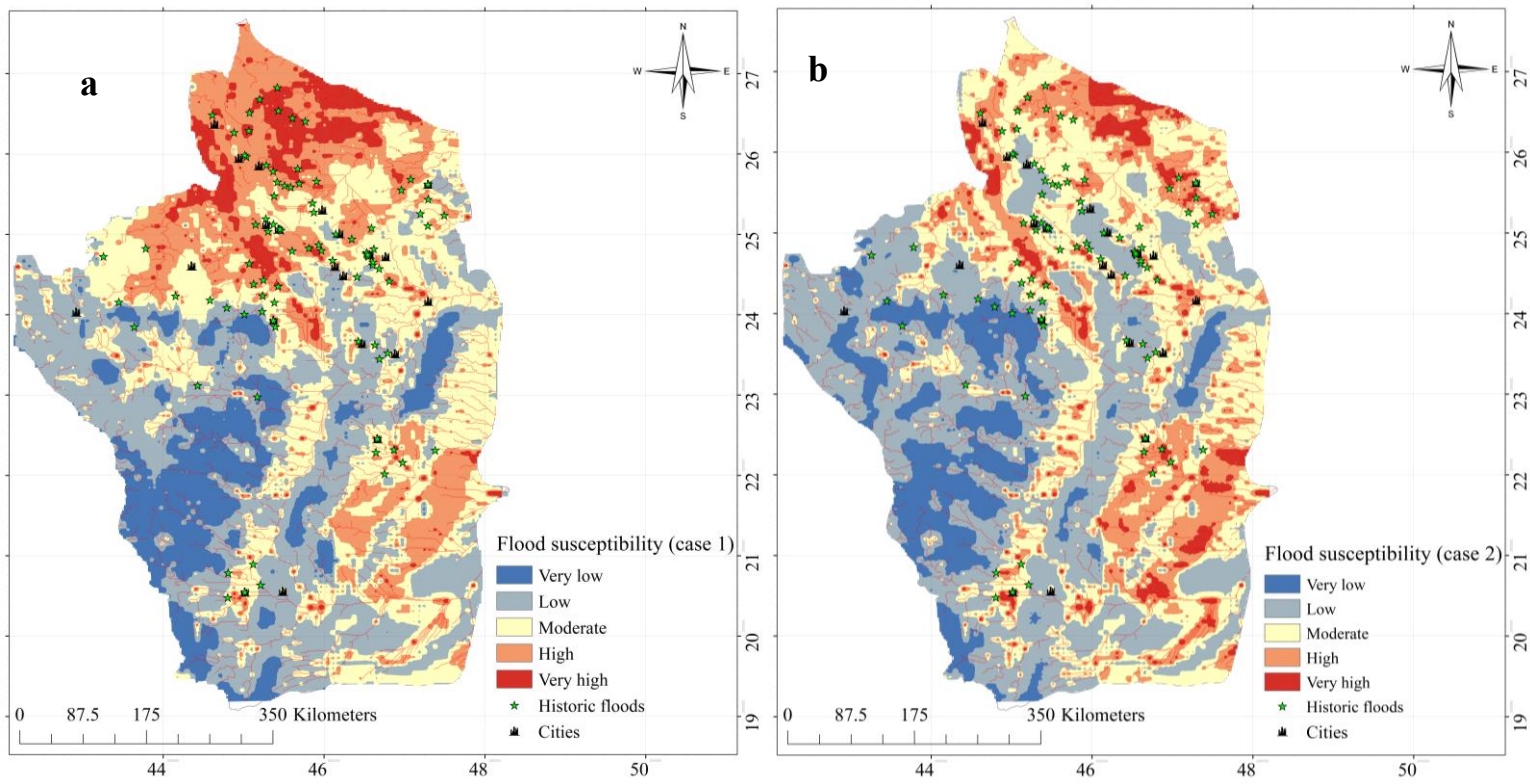
A sensitivity analysis shows that eliminating certain susceptibility factors from the model will result in different weights as shown in Table 2.7. For instance, in Case 1, if rainfall was eliminated as a susceptibility factor from the model, the weights of other key factors such as runoff increased from 19.3% to 22.1%, soil type and flow accumulations increased from 15.7% and 16.9% to 18.2% and 18.8%, respectively. If runoff is eliminated, key factors will be flow accumulation, soil type, distant to drainage network and elevation. Similar weights were obtained from the AHP, if land use and soil type were not considered as susceptibility factors. In Case 5, if the same susceptibility factors are used as in Kazakis et al. (2015), the weights obtained for this study are the same as the previous study. Some susceptibility factors have a larger influence than others on the final weights (Table 2.7).

Table 2.7 Sensitivity analysis for weights.

Thematic layers	Case 1		Case 2		Case 3		Case 4		Case 5	
	Weight	Weight %								
Flow accumulation	0.19	18.8	0.203	20.3	0.217	21.7	0.191	19.1	0.3	30
Distance to drainage network	0.1	9.7	0.121	12.1	0.132	13.2			0.21	21
Elevation	0.1	10.4	0.123	12.3	0.138	13.8	0.119	11.9	0.21	21
Land use/cover	0.06	6.1	0.076	7.6			0.074	7.4	0.12	12
Annual rainfall			0.094	9.4	0.087	8.7	0.096	9.6	0.1	10
Slope	0.06	5.9	0.061	6.1	0.069	6.9	0.058	5.8	0.05	5
Geology	0.02	2.4	0.023	2.3	0.024	2.4	0.023	2.3	0.03	3
Runoff	0.22	22.1			0.236	23.6	0.211	21.1		
Soil type	0.18	18.2	0.207	20.7			0.148	14.8		
Drainage density	0.06	6.5	0.091	9.1	0.097	9.7	0.08	8		

Figure 2.5 shows the final flood susceptibility map for the Riyadh Province for cases presented earlier. If rainfall is eliminated as a susceptibility factor, the very high and high susceptibility zones will be mainly located within northern, northeastern, and northwestern regions of the Riyadh Province (Figure 2.5(a)) because by eliminating rainfall, the weight of runoff will increase. On the other hand, if runoff is not considered as a susceptibility factor, the very high and high susceptibility zones will be found all over the study area, even in rural areas (Figure 2.5(b)). This shows the crucial role of runoff as a susceptibility factor. Figure 2.5(c) shows that by eliminating soil type and land use from the model, the very high and high susceptibility zones will mainly locate within the northern, northeastern, and northwestern parts of the Riyadh Province. Despite surface runoff, soil type, and land use are very inter-related, eliminating the last two factors will lead to low flood susceptibility in cities and urban areas. Therefore, researchers tend to include highly inter-related factors in the same model (Elkhrachy, 2015; Mojaddadi et al., 2017; Shehata and Mizunaga, 2018). Even though some factors are highly inter-related, each factor considered will add more information to the model and make the results more realistic. For instance, if the flood susceptibility map is developed without the rainfall as a susceptibility factor, 74 flood historical records are found to have occurred within the very high and high flood susceptibility

zones, 48 historical records in moderate flood susceptibility zones and only 16 events in low flood susceptibility zones. This means that removing this factor from the model, somewhat decreases the accuracy of the flood susceptibility map developed even though the results are still acceptable. However, if runoff is not included as a susceptibility factor, the model will fail to successfully predict locations of historical flood records. In that case (see Table 2.8), only 35 flood records fall within the very high and high flood susceptibility zones and 24 flood events in the very low and low flood susceptibility zones. Therefore, it is important to consider this factor in the model. If soil type and land use are not considered as susceptibility factors, 89 flood records fall within the very high and high flood susceptibility and 30 flood events in the very low and low flood susceptibility zones (Table 2.8), which again shows the importance of these two factors.



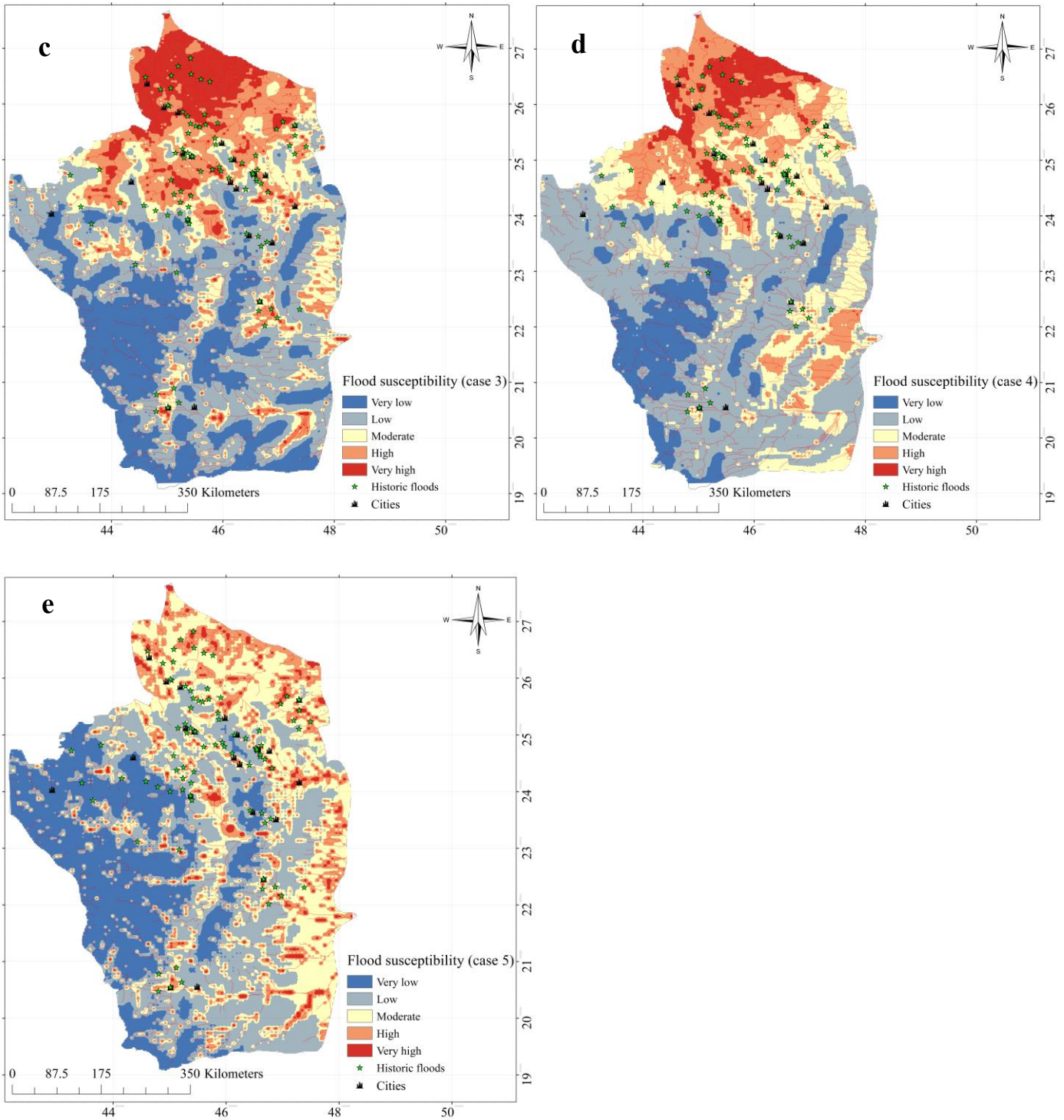


Figure 2.5 Sensitivity analysis for weights: (a) flood susceptibility if annual rainfall was eliminated, (b) if runoff is not considered as susceptibility factor, (c) if soil type and land use were eliminated, (d) if distance to drainage network is not a susceptibility factor, (e) flood susceptibility if adopting the same susceptibility used in Kazakis et al. 2015.

Table 2.8 Number of historical flood events in the test cases.

Flood susceptibility	Case 1	Case 2	Case 3	Case 4	Case 5
	# of events				
Very low	0	5	1	1	17
Low	16	37	29	31	35
Medium	48	61	19	35	20
High	61	27	77	40	57
Very high	13	8	12	11	9

On the other hand, if distance to drainage network is not a susceptibility factor, most of the study area falling within the low and very low susceptibility zones, including major cities and urban areas (Figure 2.5(d)). In that case, 31 flood events fall within the very low and low susceptibility zones and only 51 flood records fall within the very high and high susceptibility zones (Table 2.8), which demonstrates that this factor should be included in this study and in previous studies such as Kazakis et al. (2015); Zehra and Afsar (2016); and Dou et al. (2018). To compare this study with previous studies, another model was developed using the same factors as Kazakis et al. (2015) and the results are shown in Figure 2.5(e). The elimination of runoff, drainage density and soil type have a critical impact on the final weights and the final outcomes, resulting in three susceptibility factors dominating the final weights; flow accumulation (30%), distance to drainage network (21%) and elevation (21%). In that case, the performance of the model deteriorated significantly, with only 66 flood records fall within the very high and high flood susceptibility zones and 52 flood records fall within the very low and low flood susceptibility zones. This again shows the importance of including runoff, drainage density and soil type as key susceptibility factors. In general, flow accumulation has been shown to be a key contributor to flood susceptibility. The contribution of flow accumulation to flood susceptibility could be more important than geology, slope, annual rainfall and land use. The geology of the study area was found to play a relatively minor role compared to other factors listed above. On the other hand, soil types generally play a major role in the flood susceptibility of a region for more soil infiltration loss means

less surface runoff and vice versa. Soil types classified under hydrological soil groups is one of several key information required by the CN method. Therefore, to avoid any susceptibility factor to be unduly dominating, it is generally advisable to consider six to ten factors in delineating flood susceptibility zones, of which factors surface runoff and flow accumulation tend to have larger weights than other factors such as soil type, elevation and distance to drainage network, and drainage density.

2.5 Conclusions and recommendations

In this study, the spatial distribution of flood susceptibility zones of the Riyadh province and the Riyadh City of Saudi Arabia were mapped using the Analytic Hierarchy Process (AHP) method. According to our findings, very high and high flood susceptibility zones are mainly identified in the northern, northeastern, and northwestern parts of the Riyadh Province typically in areas with slopes $< 5\%$, dense flow accumulation, high annual rainfall, extensive built-up areas, and high runoff depth, where according to historical records, a large number of flood events had occurred in recent years. According to the flood susceptibility map, Riyadh City and its surrounding areas are prone to flooding. In contrast, western parts of Riyadh province are classified in zones of very low to low flood susceptibility. Using historical flood records, the methodology chosen is shown to develop reliable flood susceptibility maps which should be used to assist flood mitigation and in future land use planning in both the province and the city of Riyadh. Further, reliable results obtained for both the Province and the City of Riyadh show that this methodology is useful for planning and flood assessment purposes, and its reliability is independent of the scale of the study site.

The proposed methodology in developing flood susceptibility maps should be more extensively tested in other regions of different climate regimes and basin characteristics. The importance of each contributing factor to floods and the optimal number factors to include in the model should also be further tested against historical flood records of the region. This study shows that key contributing

factors in developing flood susceptibility maps are: surface runoff, flow accumulation, soil type, elevation, distance to drainage network, drainage density, land use, slope, and geology. The optimized weights obtained for the factors are sensitive to the number of factors included in the model. Typically, if less than six factors or if key important factors are not included, it could produce unrepresentative weights dominated by a single weight which increase the possibility of over-rating some contributing factors. It is generally advisable to include more than six factors, from which based on AHP larger weights tend to be for factors related to flow such as surface runoff and flow accumulation, followed by factors related to soil type, elevation and distance to drainage density. Sensitivity analysis is useful to examine the influence of each susceptibility factor in developing mapping flood susceptibility maps.

Chapter 3 Impact of urbanization on Urban Climate and Human thermal comfort

3.1 Introduction

Since the 1970s, population growth in Egypt has increased dramatically from 35 million (1970) to about 100 million (2017) and therefore urbanization has become a major issue socially and politically. The Cairo governate, the capital of Egypt, is likely one of the most densely populated regions in the world with a population of over 10 million concentrated in an area of 2886 km² (Goldschmidt, 2008). Rapid urbanization has led to an imbalance between demand and supply, the available infrastructure is under stress, and the urban climate in Egypt is altered. A rapid expansion of urban areas within Cairo governates has resulted in serious environmental and social problems, such as the rise of urban slum communities. Many studies have showed the usefulness of remotely sensed (RS) data in monitoring landuse information and the earth surface obtained from an integration of RS data and geographic information systems (GIS) (Eastman and Fulk, 1993; Jensen and Cowen, 1999; Lu et al., 2004; Longley et al., 2005). Various change detections techniques were used in past studies such as band differencing, principal component analysis and band ratioing, to detect the change and to monitor historical land use changes (Lu et al., 2004, Srivastava et al., 2012; Petrosillo et al., 2013). In addition, neural network models such as the support vector machine (SVM) have been successfully applied in land use classifications of small cities, and small-scale studies (Ustuner et al., 2015; Martins et al., 2016). There are studies that used ensemble learning techniques to detect long-term land use and land cover changes (Giacinto and Roli, 2001; Han and Liu, 2015; Chakraborty et al., 2016).

In the last few decades, several studies have investigated the impact of rapid urbanization on urban climate [Unkasevic et al., 2001; Liu et al., 2009; Myint et al., 2013; Mahmoud and Gan, 2018a,b). According to these studies, urban growth has caused increased air temperature (Liu et al., 2009; Lee, 1991; Streutker, 2003; Fu and Weng, 2016), but decreased relative humidity (Liu et al., 2009; Wolkoff

and Kjaergaard, 2007). Relative humidity, a ratio of actual to saturation water vapor of air, and is closely dependent on the air temperature, has a significant impact on the local climate (Wypych, 2010). In addition, relative humidity and air temperature are important climate variables because of their impact on human physiological comfort (Wolkoff and Kjaergaard, 2007; Wypych, 2010). Wolkoff and Kjaergaard (2007) stated that variability in temperature and relative humidity have a great impact on human health and energy requirements. Adebayo (1991) found that urbanization has a significant effect on relative humidity and vapor pressure. Similar observations were found in other countries e.g. Lee (1991) found a strong relationship between the urban heat island and urban vapor pressure in London, UK. In a different study, Liu et al. (2009) analyzed urban-rural humidity and temperature differences in the Beijing area, China. Their study showed that urbanization has led to a significant increase in air temperature and a decrease in relative humidity.

Most of earlier studies that investigated the impact of urbanization on urban heat island have assessed the relation between urbanization and human thermal comfort in cities e.g. (Mahmoud, 2011; Shaharuddin et al., 2014; Eludoyin et al., 2014; Ghaffarianhoseini et al., 2015; Morris et al., 2017; Yahia et al., 2018; Li et al., 2018). These studies have shown that increased air temperature in cities will increase heat stress, energy consumption that causes an increase in the emissions of greenhouse gases. Furthermore, several studies reported that urbanization has a significant impact on human thermal comfort. For instance, Shaharuddin et al. (2014) reported that land use change caused an increase in air surface temperature and led to the Urban Heat Island effect (UHI). In a different study, Mahmoud (2011) who investigated users' thermal comfort in an urban park in Cairo, Egypt found the human comfort to depend on landscape zones because human thermal comfort varies widely in a hot and arid environment. Li et al. (2018) shows that under both reanalysis data and simulations of CMIP5 global climate models,

apparent temperature, the human-perceived equivalent temperature, has increased faster than air temperature over land.

Various studies reported positive improvement in urban climate by increasing areas occupied by vegetation cover, which help to decrease air temperature and increase the air humidity or water vapor (Mahmoud, 2011; Emmanuel, 2005). Emmanuel (2005) analyzed the implications of land cover change on human thermal comfort based on two indices; the temperature humidity index (THI) and relative strain index (RSI) in the Colombo Metropolitan Region, Sri Lanka. He found a strong correlation between thermal discomfort and land cover change, with an increasing trend in thermal discomfort in urban areas compared to rural areas. Similarly, in Malaysia, Morris et al. (2007) found that the level of urbanization had a significant effect on urban climatology and human thermal comfort, resulting in a significant increase in THI, RSI and the effective temperature index (ETI). In eastern China, Cao et al. (2018) found that future urban expansion will lead to an increase in air temperatures and sensible heat flux, and urban expansion (increase in impervious surfaces) will greatly reduce relative humidity, which will increase the thermal discomfort of urban residents.

This study will provide important information to the influence of rapid urbanization on long-term air temperature, relative humidity, vapor pressure and human thermal comfort in Egypt. Similar impacts are found in many if not all Middle Eastern countries of arid climate. The main objectives of our study are (1) to detect land use change at different spatial and temporal scales in Cairo, Egypt; (2) to estimate the effects of historical land use change on the urban climate of Egypt; and (3) to assess impacts of land use change on human thermal comfort. To achieve these objectives, earth observation data was employed to measure land use change in Cairo governorate between 1973-2017. Buishand's non-parametric change point detection and Mann-Kendall tests were applied on monthly air temperature, relative humidity, and vapor pressure data over 1950-2017, to estimate the impacts of urbanization on

urban climate in the region. Then, the non-parametric Mann–Kendall was used to detect trends in annual air temperature, relative humidity, vapor pressure, and their anomalies between 1950 and 2017. To detect the impact of urbanization on human thermal comfort, three historical thermal comfort indices series were developed between 1950 and 2017: Temperature Humidity Index-THI, Relative Strain Index-RSI, and Effective Temperature Index (ETI). Change point detections and trend analysis techniques were applied to monthly, annual THI, RSI, and ETI and their anomalies to assess the influence of urbanization on human thermal comfort. The results will be useful to urban planners for regions of other arid environments.

3.2 Data and Research Methods

3.2.1 Study area and data sets

Cairo governate of Egypt (Figure 3.1), located at 30°02'N and 31°21'E, in the middle of the Delta Region in Egypt. Cairo is one of the densest urban areas on Earth, where there has been extensive land use changes but no official studies have been conducted on how urban expansion has affected the urban climate. The rapid urban expansion that is not well planned has resulted in an imbalance between demand and supply and has resulted in the stress of available infrastructure. Any data on when and how urban changes have affected the climate and human thermal comfort could be of great help in city planning and management. Two new cities within Cairo; Shrouk city (67 Km²) and New Cairo (275 Km²) are considered in this study to track their urban growth in the last 45 years over the desert of old Cairo. Landsat images were obtained from the U.S. Department of the Interior U.S. Geological Survey (Table 3.1). Digital elevation model, population, road network, land price, in addition to ground control points obtained from Visual interpretations of Google Earth images and field survey were used to support the land use classification process. Monthly air temperature, relative humidity data between 1950-2017 were derived from the 20th Century Reanalysis V2 Dataset, and monthly vapor pressure data

from the CRU TS4.01 vapor pressure dataset. Natural disaster events for Egypt between 1954 and 2016 were obtained from the Emergency Events Database of Universite Catholique de Louvain (2018) which consists of meteorological, hydrological, and climatological disasters data such as flooding, extreme temperature, dry mass movement and convective storm and their impacts on human health issues in Egypt. The number of heat-related deaths and people affected by extreme temperature in Cairo and Egypt between 1954 and 2016 were extracted from this database and checked against historical thermal comfort indices.

Table 3.1 Data used in this study: Landsat data from 1973–2017

Images Used for the study	Resolution (m)	Date of acquisition	Format	Product Type (Cloud Cover %)
Landsat 1 -5 MSS	30	29/01/1973	GEOTIFF	L1T (0%)
Landsat 1 -5 MSS	30	20./09/1984	GEOTIFF	L1T (0%)
Landsat 5 TM “Band 1 -7”	30	16/02/1990	GEOTIFF	L1T (0%)
Landsat 7 ETM+ “Band 1 -8”	30	30/09/1998	GEOTIFF	L1T (0%)
Landsat 7 ETM+	30	24/08/2006	GEOTIFF	L1T (0%)
Landsat 8	30	01/10/2017	GEOTIFF	L1T (0%)

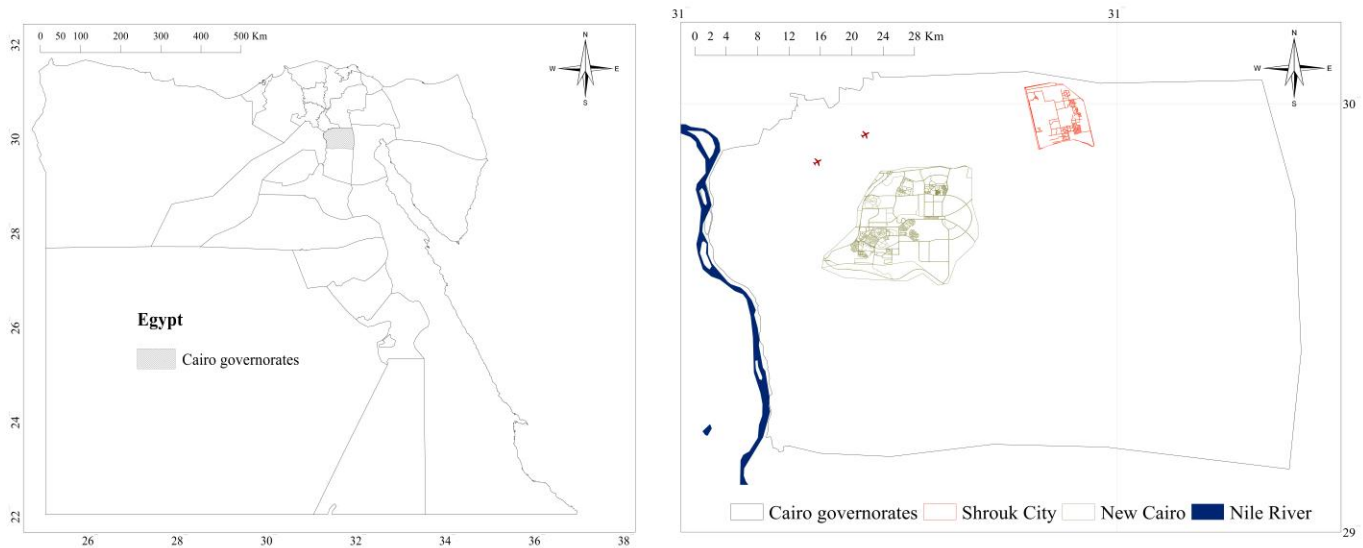


Figure 3.1 Location of study area

3.2.2 Historical land use dynamics

Cloud-free Landsat images of 30m spatial resolution were resampled using the nearest neighbour algorithm, keeping the original brightness and pixel values. The resultant root mean squared error of each image was less than 0.64 pixel. Furthermore, the images have been radiometrically corrected to a base image (SPOT-5 “2.5 m”) using manually identified pseudo-invariant features (PIFs). After identifying 14 PIFs, a linear regression was used to transform the data of each band onto the same radiometric reference. Finally, prior to land use classifications, these images were preprocessed and corrected for atmospheric absorption using the cost function of IDRISI Selva. Two field surveys were conducted to collect data to support land use classification, which include ground control points, visual interpretations of Google Earth images together with satellite night images that highlight locations of urban areas. More than 700 ground control points were collected. A database for each land use class was developed using ArcGIS. The Maximum Likelihood Supervised Classification (MLC) and the ISO Cluster Unsupervised Classification methods were performed on Landsat images to produce land use

maps. The Iso Cluster Unsupervised Classification was used to collect more training data and to check the results obtained from the two supervised classification methods.

Based on the collected ground control points, a supervised signature extraction using the MLC to classify the Landsat images into different land use maps. These two methods are widely used in land use classification (Srivastava et al., 2012; Kolios and Stylios, 2013, Silva et al., 2018). 70% of data collected in the two field surveys was used for landuse classification and 30% of the data for validating the classified land use maps. Four main land use categories have been identified in Cairo: Water bodies, Urban and built-up areas, Cropland or Vegetation, and Bare soil. Finally, each land use map developed was checked against the validation dataset with respect to some simple random patterns. Then, a change detection technique was applied between two land use maps to evaluate the dynamics and patterns of land use change in Cairo. The area percentages of each land use category over time were calculated to detect the trends in land use change. To estimate land use dynamics, a net change between earlier and newer land use maps was derived for each land use category. Historical change or urban expansion in new cities in Cairo was also derived to provide essential information about the state of land uses or urbanization in Cairo.

3.2.3 Urban climate change detection

Effects of urbanization on urban climate have long been documented (Liu et al., 2009; Fu and Weng, 2016; Cao, 2018), which include an increase in air temperature, a decrease in relative humidity, and an increase in vapor pressure, which are also investigated in this study. Buishand's nonparametric test has been used to detect change points in climate time series (Jarušková, 1996; Buishand, 2013; Minaei and Irannezhad, 2018). However, the non-parametric Mann–Kendall has been more widely applied to detect the trend and variability in regional climate (Yue et al., 2002; Gocic and Trajkovic, 2013; Abahous et al., 2007; Worku et al., 2018). Long-term monthly air temperature, relative humidity, and vapor pressure

data were processed to derive mean annual and anomalies of air temperature, relative humidity and vapor pressure between 1950 and 2017. Buishand's nonparametric detection method was applied on monthly, annual and anomalies of air temperature, relative humidity, and vapor pressure data to detect change points of urban climate of the region. This test check for a null hypothesis (no change point) and an alternative hypothesis, where change point is detected. Next, the non-parametric Mann–Kendall was also adopted to investigate the long-term trend in monthly, annual and anomalies of air temperature, relative humidity and vapor pressure between 1950 and 2017. The Buishand test (Buishand, 1982) utilizes the adjusted partial sums or cumulative deviations from the mean given by

$$S_0^* = 0 \quad (3-1)$$

$$S_k^* = \sum_{i=1}^k (x_i - x_{mean}) \quad k=1, 2, \dots, n \quad (3-2)$$

If S_k^* , the cumulative deviations from the mean fluctuates around zero, the null hypothesis is accepted.

On the other hand, if there is an increase or decrease in the cumulative deviations from the mean at a particular year k , the alternative hypothesis is accepted. The test of significance is based on the rescaled, adjusted partial sums obtained by dividing the cumulative deviations from the mean by the standard deviation:

$$S_k^{**} = S_k^* / \sigma \quad (3-3)$$

$$\sigma^2 = \sum_{i=1}^n (x_i - x_{mean})^2 / n \quad (3-4)$$

Q statistic, sensitive to departures in the series from the variable mean, is estimated as follow:

$$Q = \text{Max}|S_k^{**}| - \text{Min}|S_k^{**}| \quad (3-5)$$

$$0 \leq k \leq n$$

where a high Q indicates a large departure level. If $Q / \sqrt{n} >$ tabulated critical value obtained from a table of the Kolmogorow-Smirnov goodness-of-fit statistic (Buishand, 1982), the null hypothesis is rejected and therefore at year k , a change point is detected. To detect the trend of a climate data, the Mann–Kendall test was applied as follows:

$$S = \sum_{i=1}^{n-1} \sum_{j=i+1}^n \text{sgn}(x_j - x_i) \quad (3-6)$$

To estimate trend for a time series $x_i, i = 1, 2, \dots, n-1$ and $x_j, j = i+1, i+2, \dots, n$. Each x_i is a reference and compared with remaining data points x_j (see 7):

$$Sgn(x_j - x_i) = \begin{cases} +1 & \text{if } (x_j - x_i) > 0 \\ 0 & \text{if } (x_j - x_i) = 0 \\ -1 & \text{if } (x_j - x_i) < 0 \end{cases} \quad (3-7)$$

The variance statistic for each climate variable is then calculated as follow:

$$Var(S) = \frac{1}{18} (n(n-1)(2n+5) - \sum_{j=1}^p t_j(t_j-1)(2t_j+5)) \quad (3-8)$$

Where p is the number of groups in which each group consists of data points of equal values, and t_j is the number of data points in the j_{th} group. Using the following Z-transformation, S is approximately normally distributed:

$$Z = \begin{cases} (S-1)/\sqrt{Var(S)} & \text{if } S > 0 \\ 0 & \text{if } S = 0 \\ (S+1)/\sqrt{Var(S)} & \text{if } S < 0 \end{cases} \quad (3-9)$$

The slope (T_j) is computed according to Sen (1968) as follow:

$$T_j = (x_j - x_i)/(j - 1) \quad (3-10)$$

The trend magnitude is obtained from the slope estimator method (Sen, 1968). The sign of the slope indicates if the trend of the time series is positive or negative.

3.2.4 Thermal comfort indices

To detect the impact of urbanization on human thermal comfort, three historical thermal comfort indices series were estimated from data collected between 1950 and 2017, the Temperature Humidity Index-THI, Relative Strain Index-RSI, and Effective Temperature Index (ETI), which were developed to evaluate the thermal comfort in hot, humid and tropical countries (Emmanuel, 2005; Hwang et al., 2011; Eludoyin et al., 2014; Fang et al., 2018; Johansson et al., 2018). The climate of Egypt can be divided into two seasons, a mild winter from November to April and a hot and dry summer from May to October. In this study, historical human thermal comfort indices were estimated only for summer seasons. THI, also known as the Discomfort Index, was first developed by Thom (1959) to estimate an approximate

thermal stress level in a city over time. This index is also highly utilized in urban cities design. Thom (1959) classified THI as $21 \leq \text{THI} \leq 23$ uncomfortable, $23.8 \leq \text{THI} \leq 26.1$ very uncomfortable, and $\text{THI} \geq 26.67$ serious discomforts. Other studies found that THI values of 22-25 °C are thermally comfortable (Emmanuel, 2005; Eludoyin et al., 2014; Morris et al., 2017). THI was calculated as follow:

$$\text{THI} = 0.8T_a + 0.002T_a \times \text{RH} \quad (3-11)$$

Where T_a is air temperature “°C”, and RH is relative humidity in %.

Matzarakis (2001) reported that increase in urbanization in Greece had caused an increase in temperature-related diseases. Similar studies reported a strong connection between ETI and human health issues in different countries (Williams and Boren, 2008; Coêlho and Gonçalves, 2008; Ostro et al., 2011). For instance, Ostro et al. (2011) conducted a study in California, USA to study the effect of ETI on human health. The study showed that an increase in ETI had increased mortality and hospital admissions, which are also found by Coêlho and Gonçalves (2010) in another similar study. Different studies (Emmanuel, 2005; Eludoyin et al., 2014; Morris et al., 2017) found that the thermally comfortable ETI that ranges between 22.5 to 25.5 °C, is based on air temperature and relative humidity as follow:

$$\text{ETI} = T_a - 0.4(T_a - 10) (1 - 0.002\text{RH}) \quad (3-12)$$

The third thermal comfort index is the RSI, which is closely related to human mortality rate. Different studies reported the thermally comfortable range for this index are 0.14-0.2 (Emmanuel, 2005; Eludoyin et al., 2014; Morris et al., 2017). This index was calculated as follow:

$$\text{RSI} = (T_a - 21)/(58 - \text{VP}) \quad (3-13)$$

Where T_a is air temperature “°C” and VP is vapor pressure “hPa”.

The above change point detection and trend analysis techniques were applied to monthly, annual and anomalies THI, RSI, and ETI to assess the influence of urbanization on human thermal comfort.

3.3 Discussion of Results

3.3.1 Land use dynamics

The Landsat images are classified into four primary classes: water bodies, urban and built-up areas, and cropland/ vegetation. An assessment of the accuracy of the classified images was determined by both simple random patterns. The results showed an overall good accuracy, as the accuracy of the land use maps for 1973, 1984, 1990, 1998, 2006, and 2017 was estimated to be 80.13%, 85.6%, 88.16%, 86.80%, 87.31%, and 94.56%, respectively (Table 3.2). Given the Egyptian population has drastically increased from 35 million in 1970 to 100 million in 2017 has led to a drastic change and rapid urbanization, which occurred after 1973 (Figure 3.2). The land use classes identified show that bare soil was the largest class throughout the study period, but it was shrinking with time, leading to less available land for development. LUC in Cairo had followed a dynamic pattern. People tend to invest in new houses rather than occupying them, resulting in the lower population density in newer cities, as has been the case in New Cairo and Shrouk City. The greatest increase was observed in urban and built-up areas at the expense of bare soil, from 142.5 Km² in 1973 to 473.7 Km² in 2017.

Table 3.2 Accuracy assessment and validation

Land use class	1973		1984		1990		1998		2006		2017	
	UA (%)	Kappa										
Water bodies	80.20	0.72	78.12	0.71	86.80	0.69	89.10	0.82	79.61	0.88	93.21	0.86
Urban and built up areas	79.90	0.81	92.62	0.82	90.35	0.77	90.20	0.86	94.58	0.98	96.85	0.92
Bare soil	84.20	0.62	88.22	0.71	88.12	0.67	79.60	0.83	88.50	0.78	95.47	0.79
Cropland/Vegetation	76.20	0.86	83.44	0.76	87.35	0.73	88.29	0.78	86.55	0.85	92.69	0.89
OA	80.13	0.75	85.60	0.75	88.16	0.71	86.80	0.82	87.31	0.87	94.56	0.87

UA, user's accuracy; Kappa, index of agreement; OA, overall accuracy

In the past, little was known about the spatial and temporal changes of LUC that have shaped the urban expansion of Cairo. Such data are also lacking in other provinces of Egypt where extensive LUC has also taken place without much official statistics on LUC patterns. The extent of land use distributions

throughout the study period (1973-2017) is presented in Table 3.3. An analysis of LUC change in the region shows a dramatic increase in urban and built-up areas, as shown in Table 3.3. Urbanized areas had rapidly increased from 142.5 km² (4.9 % of total area) in 1973 to 194.4 km² (6.7%) in 1984, a 34.6% increase in just 11 years. In this period vegetated land had marginally increased from 36.6 km² (1.3%) in 1973 to 52.2 km² (1.8%) in 1984 (Table 3.4).

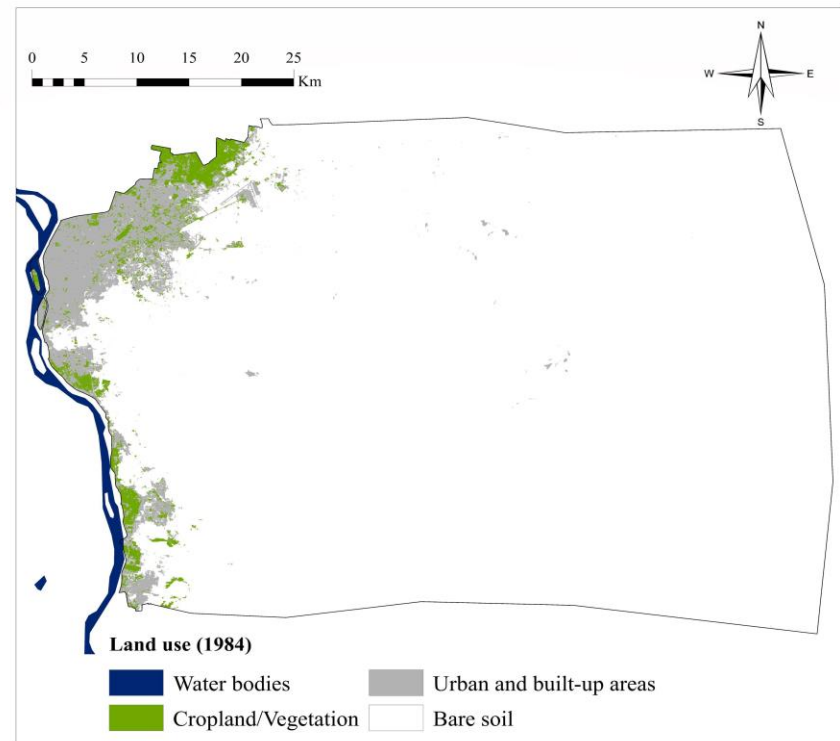
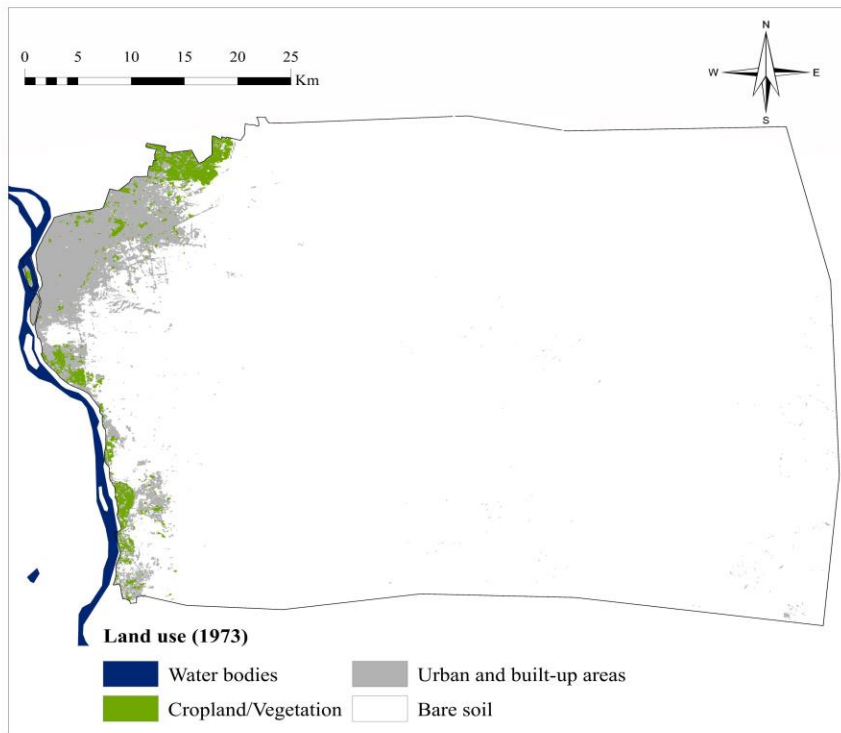


Figure 3.2 Space distribution of land use type from 1973 to 2017 in Cairo.

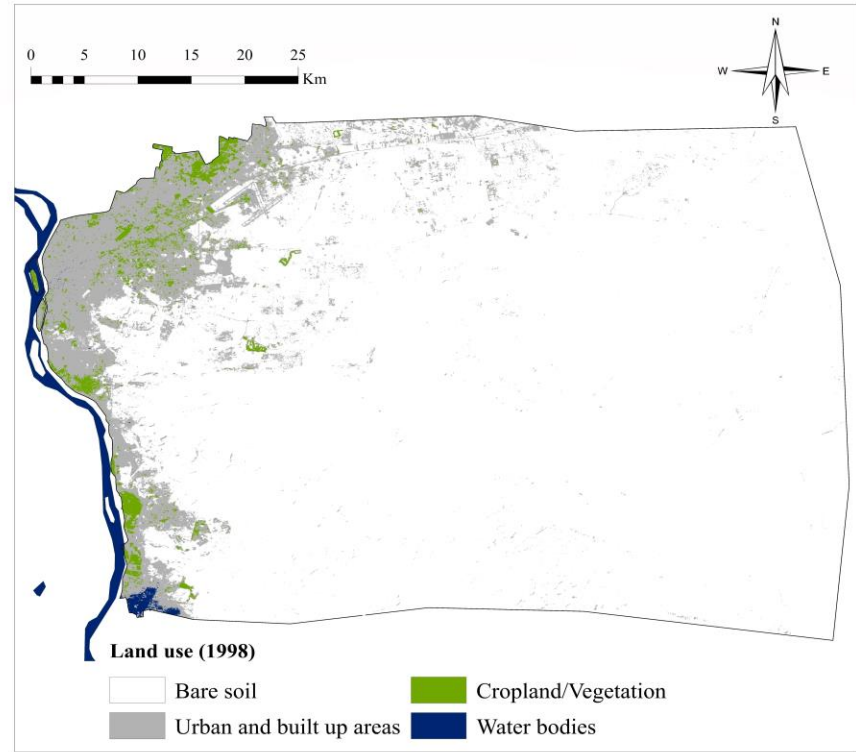
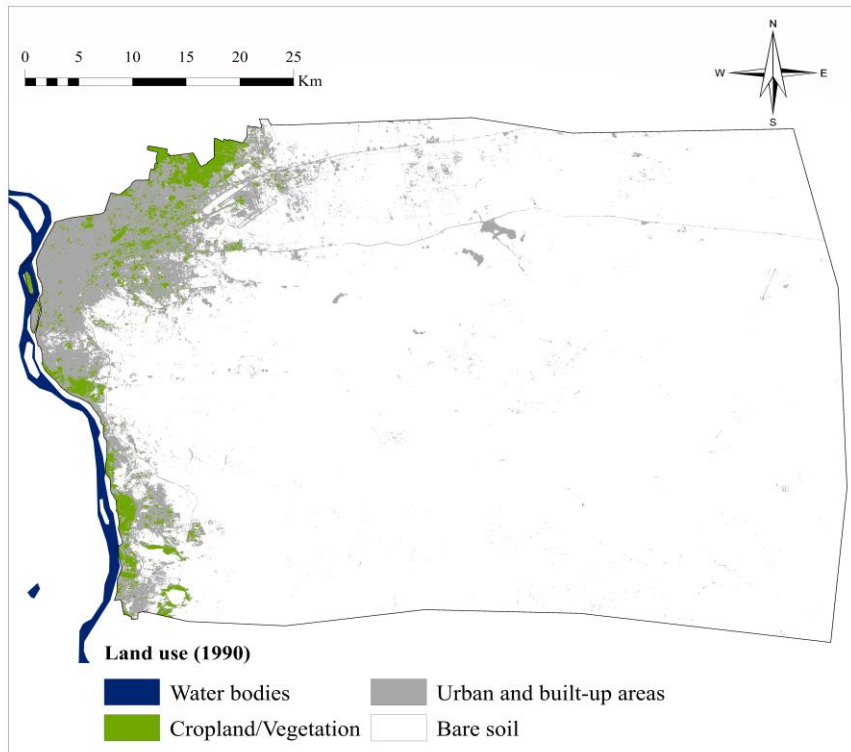


Figure 3.2 (continued)

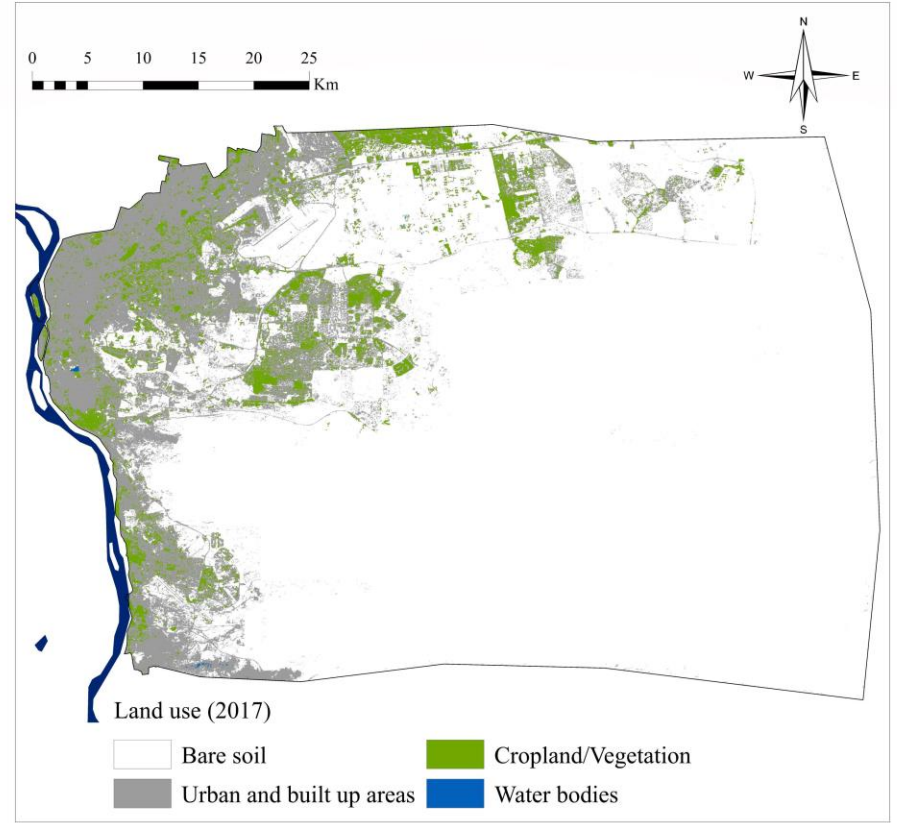
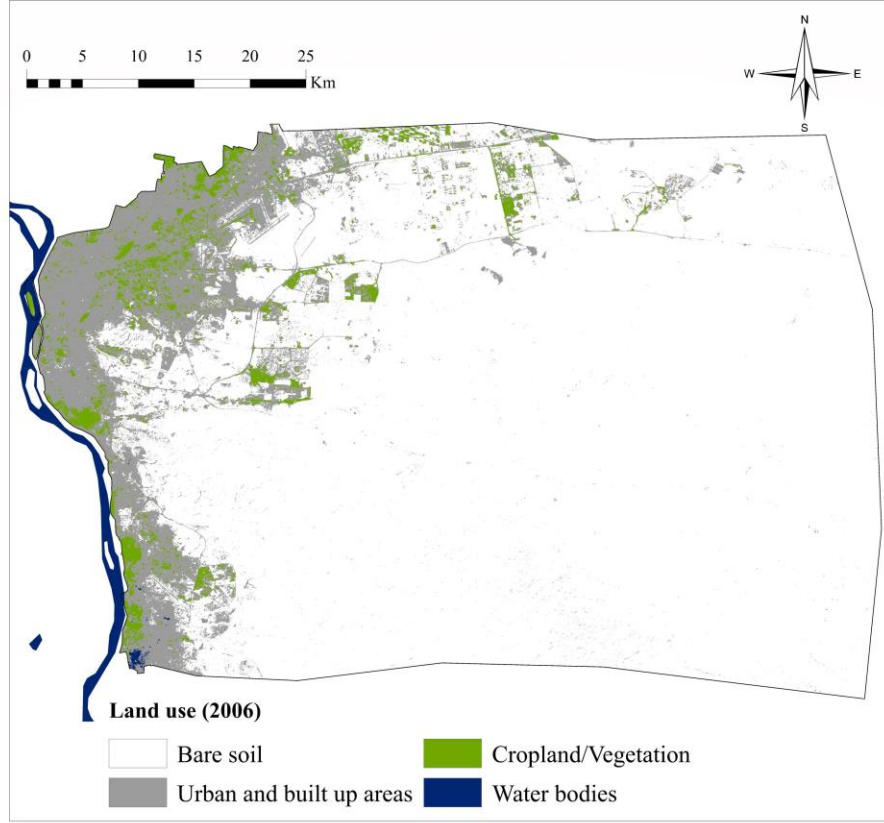


Figure 3.2 (continued)

Table 3.3 Area measurements of land use within Cairo for each subperiod and the full period 1973–2017

Land use class	1973		1984		1990		1998		2006		2017	
	Area (km ²)	%										
Urban and built up areas	142.5	4.9	194.4	6.7	250.7	8.7	298.4	10.3	378.5	13.1	473.7	16.4
Cropland /Vegetation	36.2	1.3	52.2	1.8	58.0	2.0	47.5	1.6	79.1	2.7	128.7	4.5
Bare soil	2708.0	93.8	2640.5	91.5	2578.1	89.3	2535.7	87.8	2427.6	84.1	2283.3	79.1
Water bodies	0.0	0.0	0.0	0.0	0.1	0.0	5.3	0.2	1.6	0.1	1.1	0.0

Table 3.4 Detected land use gains and losses within Cairo for each subperiod and the full period 1973-2017

Land use class	1984-1973		1990-1984		1998-1990		2006-1998		2017-2006	
	Km ²	%	Km ²	%	Km ²	%	Km ²	%	Km ²	%
Urban and built up areas	51.9	36.41	56.30	28.96	47.66	19.01	80.10	26.84	95.23	25.16
Cropland /Vegetation	16.0	44.26	5.73	10.96	-10.41	-17.96	31.58	66.41	49.60	62.69
Bare soil	-67.5	-2.49	-62.41	-2.36	-42.45	-1.65	-108.03	-4.26	-144.35	-5.95
Water bodies	0.0	250.00	0.03	114.29	5.20	9626.67	-3.64	-69.38	-0.47	-29.43

Between 1984 and 1990, urban areas grew from 194.4 km² (6.7%) in 1984 to 250.7 km² (8.6%) in 1990. Relative to 1984, there was a significant increase in urban areas between 1990-2017. In general, the spatial patterns of LUC changes in Cairo for 1973, 1984, 1990, 1998, 2006, and 2017 (Figure 3.2 and Table 3.3) show that urban areas and vegetated land dominated the direction of urbanization in Cairo. In other words, over 1990-2017, urbanized areas replaced most of the bare soil, extending into the low-lying areas of Cairo along the direction of roads. According to previous studies, population density plays a major role on the locations of urbanization, even though elevations and road network are also main drivers of land use change in Cairo. The trend of urbanization in developing countries such as Egypt is also dictated by the cost of development, and services and roads are easier to implement in low-lying areas. Another reason behind the expansion of urban areas in new cities is the attitude of people, instead of just population density, e.g., most residents of old Cairo tend to invest in new homes in new cities which led to this large urban expansion, giving rise to the emergence of what's called ghost cities, which become moderately populated only 40 to 50 years after their constructions. Urban areas in Cairo had

considerably increased by 331.2 km² between 1973 and 2017, an average increase of more than 7.52 km² per year. Overall, the trend in land use change is dominated by urban growth in new cities. Factors such as land price, socioeconomic and distance to nearest roads contributed to shifting most of the urban growth toward New Cairo (Figure 3.3) and Shrouk City (Figure 3.4).

Area occupied by each land use class in new cities are shown in Figure 3.5. In New Cairo, a city that did not exist before 1973 started growing after 1990. Urban areas in New Cairo City (see Figure 3.3 and Figure 3.5(a)) occupied 90 Km² in 2017 compared to 4 Km² in 1990 (Figure 3.5(a)). Similarly, the Shrouk City (Figure 3.4 and Figure 3.5(b)) also grew after 1990. The Cramer's V test was used to relate driving factors for land use change and the level of urbanization, a "statistic measuring the strength of association or dependency between two (nominal) categorical variables" (Woo and Chi, 2003). Variables that had Cramer's V of 0.4 or higher are good indicators of the major drivers of land use change (Eastman and Fulk, 1993). The overall Cramer's V for the six classes ranged from 0.6 to 0.72, with highest values observed for distance to nearest road, land price, built-up areas, bare soil as the main drivers for LUC. The trend of LUC in the Shrouk City is lower than that in the New Cairo city (Figure 3.5). Since early 1990s there was a significant shift in the concept of new cities leading to an increase in land price because of demand attributed to investment opportunities. Geographic elements to infrastructure such as distance to roads, distance from cities, and infrastructure availability had influenced the direction of land use change in different cities globally in the past. In contrast, the direction of urban expansion in new cities of Cairo has been towards low-lying areas of Cairo, as confirmed from the Cramer's V test for autocorrelation between urbanization and the direction of urban growth.

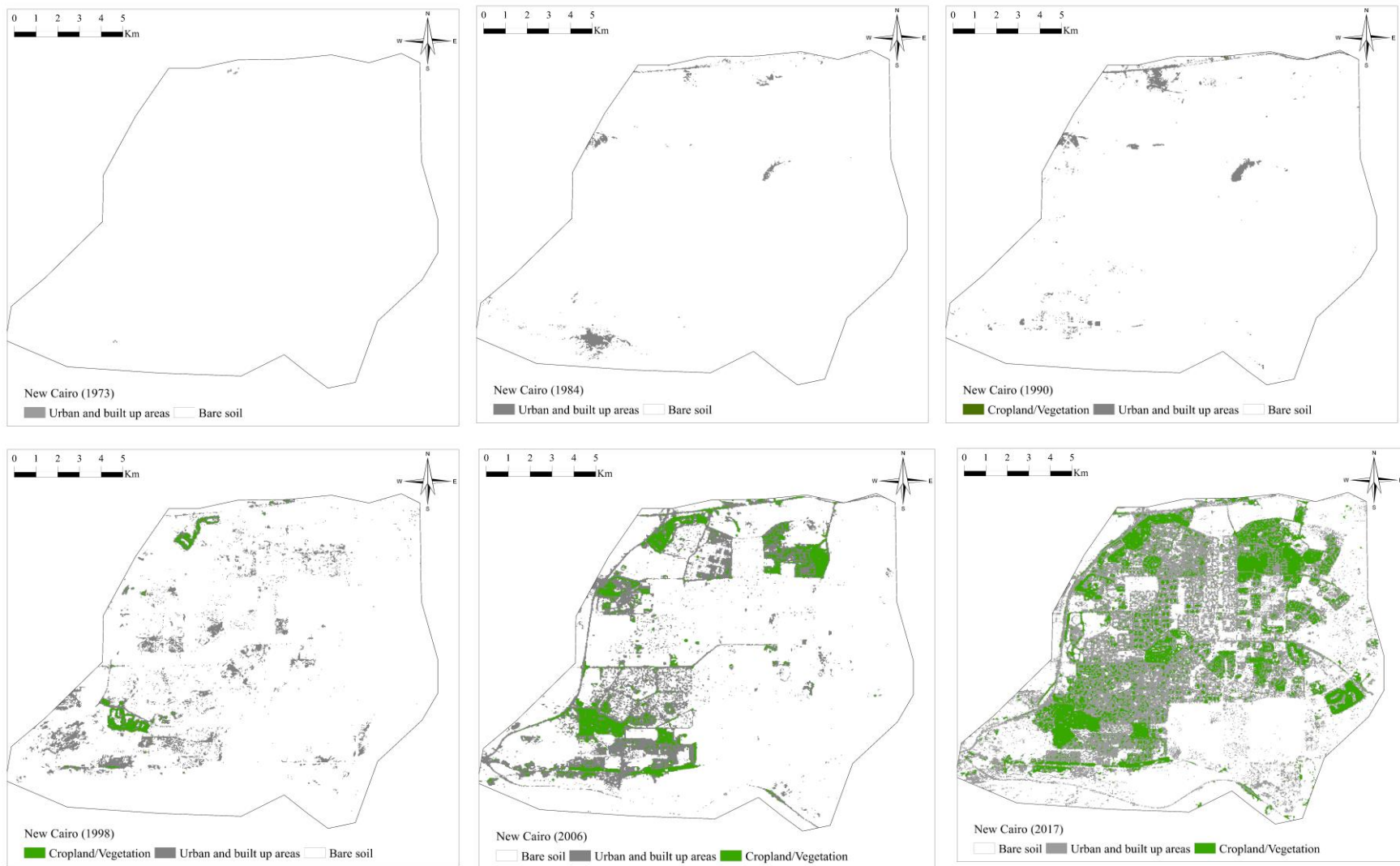


Figure 3.3 Space distribution of land use type from 1973 to 2017 in New Cairo City

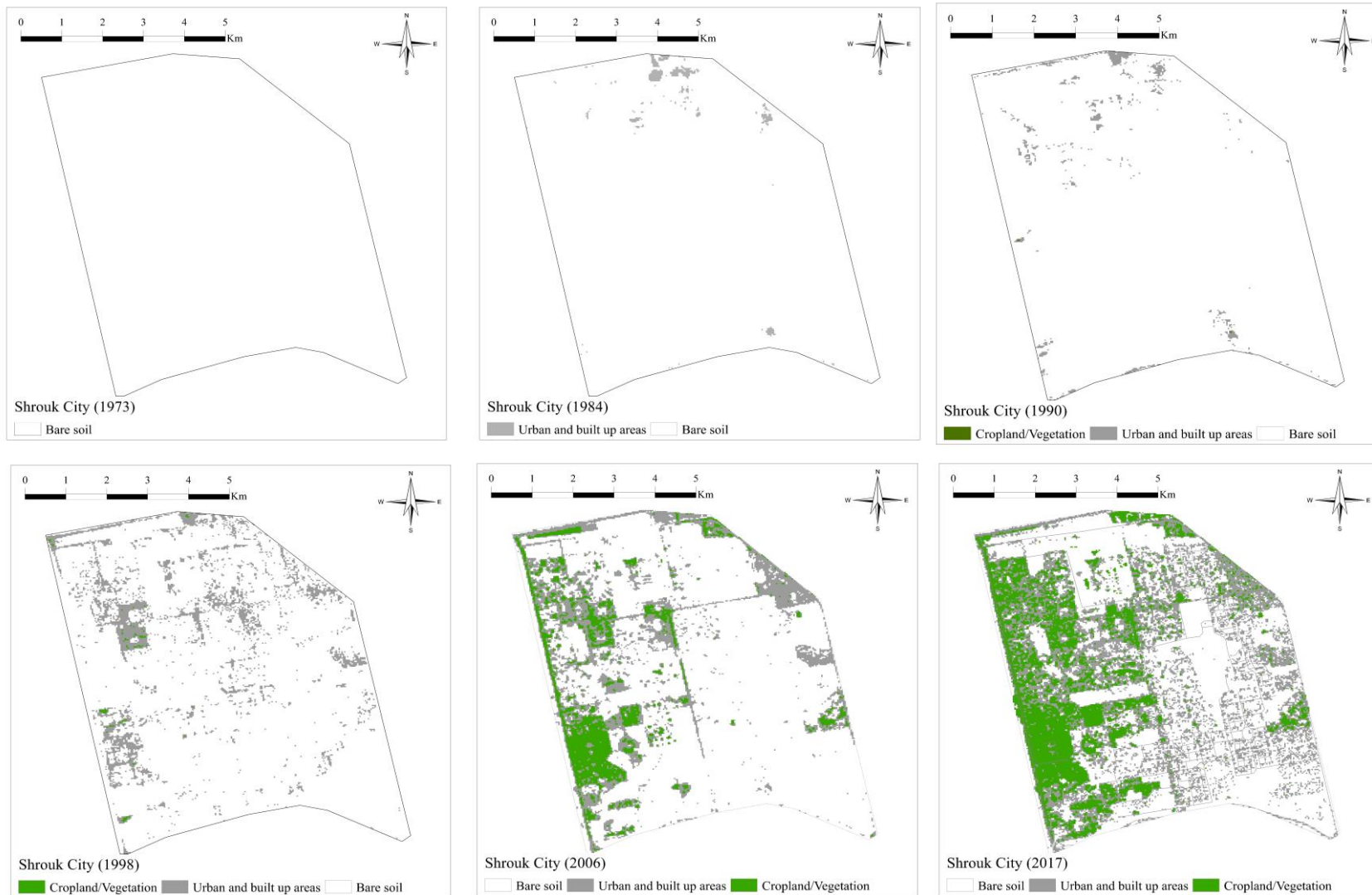


Figure 3.4 Space distribution of land use type from 1973 to 2017 in Shrouk City.

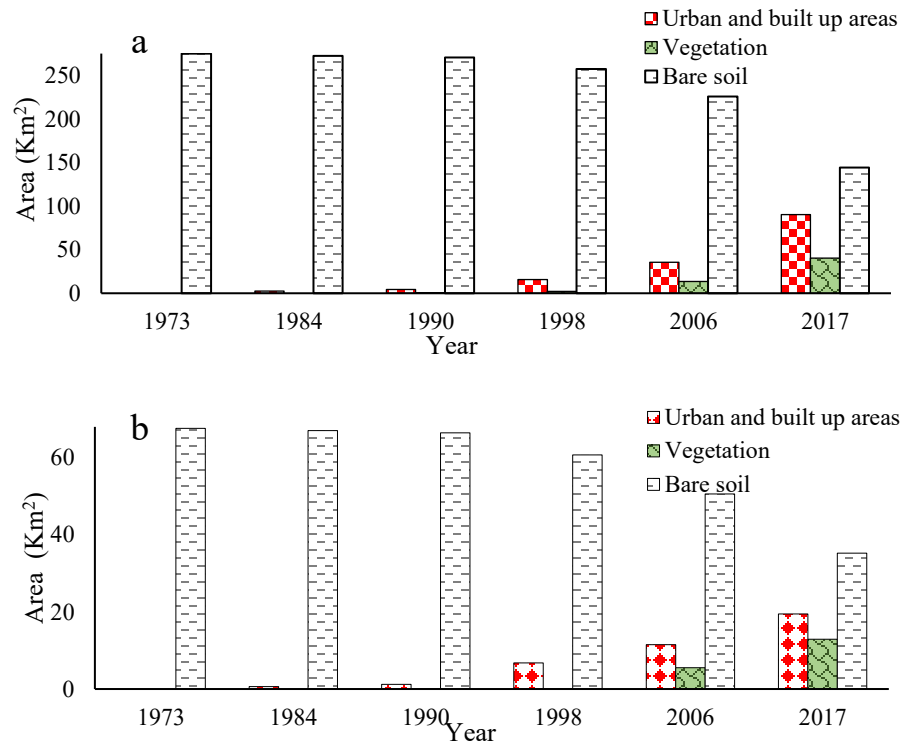


Figure 3.5 Trend of land use change in New Cairo City (a) and Shrouk City (b)

3.3.2 Influence of urbanization on urban climate

Studies showing how rapid urbanization had affected air temperature are well documented, e.g. (Shojaei et al., 1993; Mushore et al., 2017; Tong et al., 2008; Silva et al., 2018). For instance, Mushore et al. (2017) projected a continuous increase in urban surface temperatures through to 2045 due to rapid urbanization. In the present study, from applying the Buishand's change detection test to average annual air temperature and air temperature anomalies between 1950 and 2017, a statistically significant change points in annual air temperature and air temperature anomaly were both detected in 1995 (Figure 3.6). The mean annual air temperature of 21.68 °C and air temperature anomalies of 0.287 °C between 1950-1995 had increased to 22.57 °C and 0.6 °C between 1995-2017, respectively. This increase in air temperature is attributed to a significant increase in urban areas between 1990-2017.

The Mann–Kendall trend test detected a statistically significant warming trend of 0.19 °C /decade in the mean annual air temperature and air temperature anomalies (Table 3.5). Similar studies show that urbanization or more impervious surfaces have led to rising temperature in urban areas. For example, Silva et al. (2018) found that rapid urbanization in Paço do Lumiar County, Brazil had a remarkable impact on its surface temperature, resulting in 5.3 °C increase in urban surface temperature between 1988 and 2014 (a warming trend of 2.03 °C /decade), because of the increase in the areas of impervious surfaces. Xiong et al. (2012) who studied the impact of urbanization in the urban climate of Guangzhou, South China stated that the highest increase in temperature anomalies was strongly associated with built-up areas.

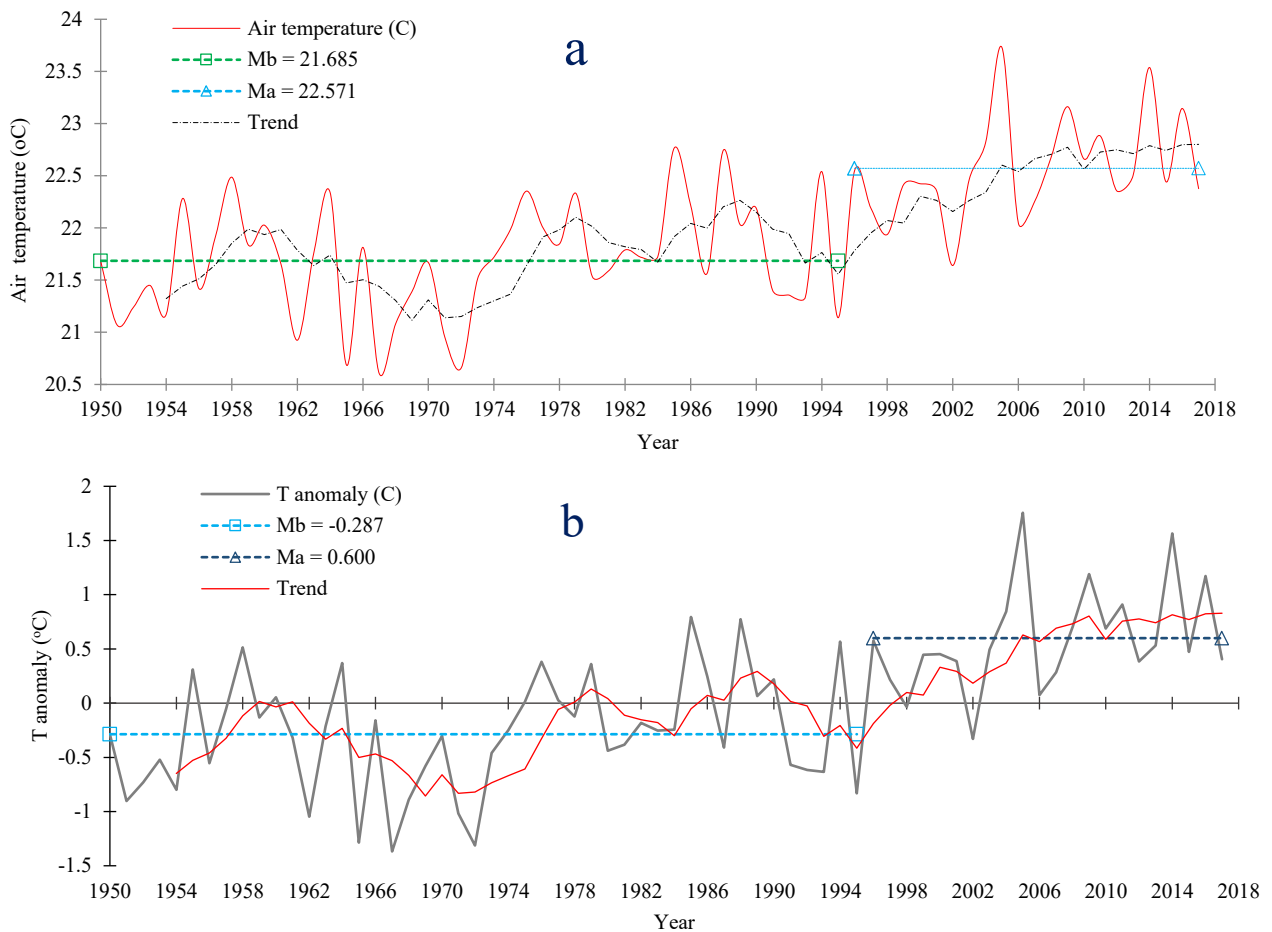


Figure 3.6 Long-term warming trend: (a) average annual air temperature, (b) air temperature anomalies

Table 3.5 Atmospheric variables and human thermal comforts indices trend

Atmospheric variables	Bushland's test				Mann-Kendall trend test					
	Q	T	p-value	trend	Mb	Ma	Kendall's tau	p-value	trend	Sen's slope
Air Temperature	19.98	1995	<0.0001	Ha	21.68	22.57	0.438	<0.0001	+	0.019
Temperature anomaly	19.98	1995	<0.0001	Ha	0.287	0.6	0.438	<0.0001	+	0.019
Monthly relative humidity	70.45	1967	0.0001	Ha	63.61	60.53	0.092	0.0001	-	0.055
Avg. annual relative humidity	13.54	1966	0.0001	Ha	63.48	60.53	0.156	<0.0001	-	0.048
Relative humidity anomaly	13.54	1966	<0.0001	Ha	0.543	-2.84	0.156	<0.0001	-	0.048
Monthly vapor pressure	55.85	1993	<0.0001	Ha	14.55	15.58	0.085	<0.0001	+	0.024
Avg.annual vapor pressure	27.85	1993	<0.0001	Ha	14.59	15.76	0.532	<0.0001	+	0.029
Vapor pressure anomaly	247	1993	<0.0001	Ha	0.162	1.052	0.375	<0.0001	+	0.029
Human thermal comfort indices										
Temperature-humidity index (THI)	24.07	1994	0.005	Ha	25.57	26.31	0.09	0.001	+	0.033
Avg. annual THI	17.30	1984	<0.0001	Ha	25.53	26.11	0.468	<0.0001	+	0.019
THI anomaly	17.08	1984	<0.0001	Ha	-0.246	0.331	0.468	<0.0001	+	0.019
Effective temperature index (ETI)	22.4	1994	0.001	Ha	24.32	25.71	0.078	0.002	+	0.029
Avg. annual ETI	15.86	1984	<0.0001	Ha	24.26	24.9	0.428	<0.0001	+	0.016
ETI anomaly	16.69	1984	<0.0001	Ha	-0.178	0.252	0.428	<0.0001	+	0.016
Relative strain index (RSI)	25.04	1994	0.004	Ha	0.175	0.205	0.086	0.0014	+	0.006
Avg.annual RSI	16.97	1984	<0.0001	Ha	0.173	0.197	0.46	<0.0001	+	0.006
RSI anomaly	18.25	1984	<0.0001	Ha	-0.003	0.021	0.460	<0.0001	+	0.008

Studies on how rapid urban growth influences the relative humidity of urban areas (Emmanuel, 2005; Um et al., 2007; Zhang et al., 2016) reported a considerable decrease in the relative humidity of urban areas due to rapid urbanization. To investigate the impact of rapid urban growth in Cairo on its relative humidity, change point detections and trend analysis techniques were applied on monthly, annual and anomaly of relative humidity. Buishand's tests detected statistically significant change points in mean monthly relative humidity in 1967, when the monthly relative humidity decreased from 63.61% in 1950-1967 to 60.53 % in 1967-2017 (Figure 3.7(a)). Statistically significant declining trends are also detected in the mean monthly relative humidity since 1967 at the rate of 0.55 % /decade.

Statistically significant change point is detected in both annual relative humidity and relative humidity anomalies in 1966 (Figure 3.7(b)). The results also show a very high variability in relative humidity due to a significant increase in impervious surfaces of Cairo. Figure 3.7(c) shows a continuous decline in relative humidity after 1966. The increase in impervious surfaces and built up areas has led to a decrease in long-term average relative humidity anomaly from 0.543% in 1950-1966 to -2.84% in 1966-2017 (Table 3.5). Furthermore, mean annual relative humidity and relative humidity anomalies were also analysed, where statistically significant declining trends were also detected at 0.48 %/decade (Table 3.5). This finding agrees with previous studies (Adebayo, 1991; Omoto et al., 1994; Zhang et al., 2016).

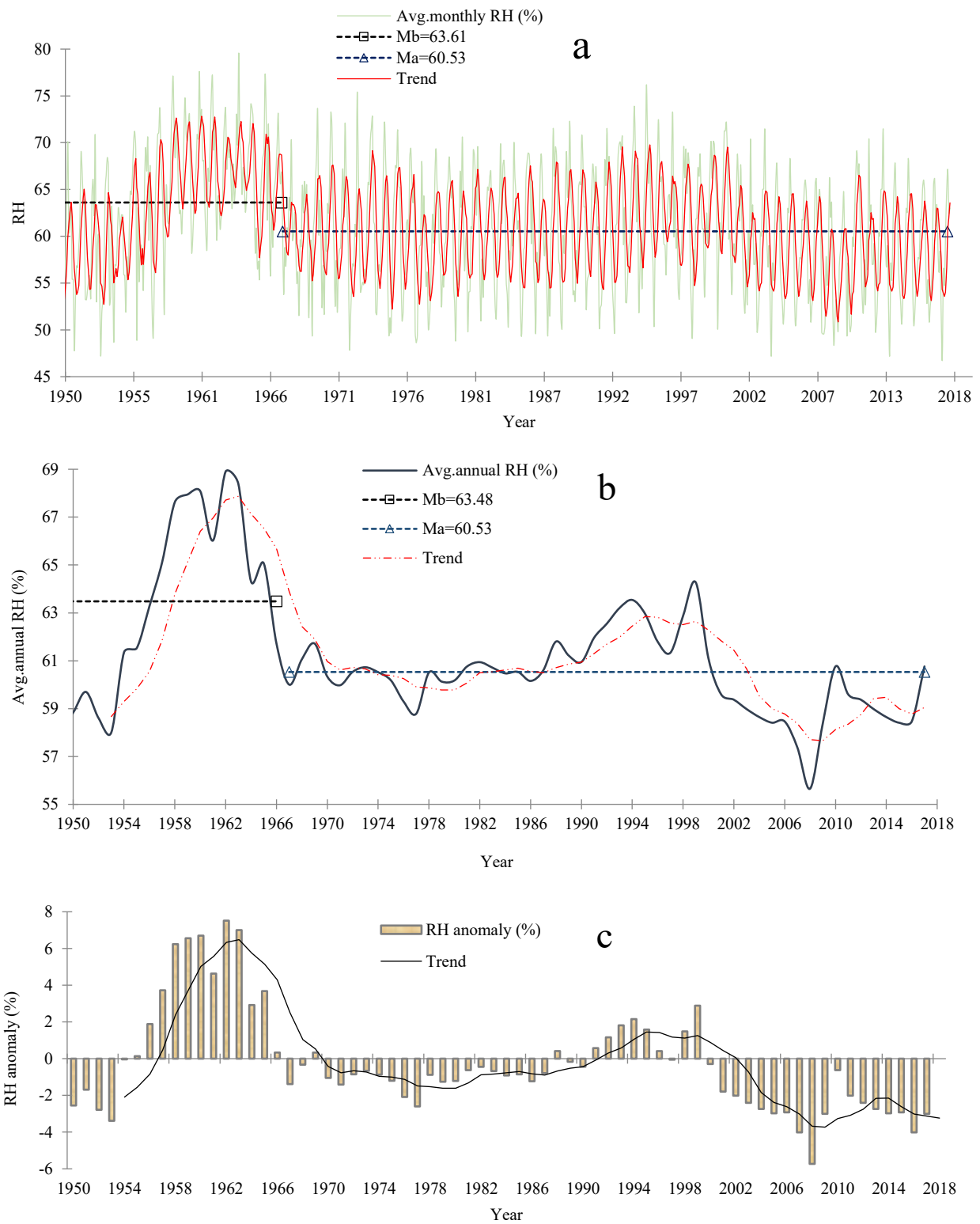


Figure 3.7 Long-term variability in relative humidity: (a) average monthly relative humidity, (b) average annual relative humidity, (c) relative humidity anomalies

Vapor pressure data between 1950 and 2017 also showed a statistically significant change point in the average monthly and annual vapor pressure and vapor pressure anomalies in 1993, as monthly vapor pressure series increased significantly after 1993, from 14.55 hPa in 1950-1993 to 15.58 hPa in 1993-2017 (Figure 3.8(a)). This again was the impact of rapid urbanization on urban climate, as the urbanization increases both air temperatures and vapor pressure, but it reduces the relative humidity. The mean annual vapor pressure also increased from 14.59 hPa in 1950-1993 to 15.57 hPa in 1993-2017 (Figure 3.8(b)), while long-term average vapor pressure anomalies increased significantly from 0.162 hPa in 1993 to 1.052 hPa in 1993-2017. Between 1950 and 1993, vapor pressure anomalies only had minimal changes, but after 1993 the vapor pressure anomalies increased significantly (Figure 3.8(c)).

This increase can be attributed a significant increase in impervious surfaces in Cairo, as urban growth in new cities tends to have little vegetation cover, as also shown by Argüeso et al. (2015). To detect the magnitude of change in vapor pressure due to urbanization, trend detection techniques were applied to monthly vapor pressure, average annual and anomalies vapor pressure between 1950 and 2017. A statistically significant increasing trend was detected in monthly vapor pressure at 0.24 hPa /decade (Table 3.5). Similarly, a statistically significant rising trend was detected in the annual vapor pressure and vapor pressure anomalies at 0.29 hPa /decade (Table 3.5).

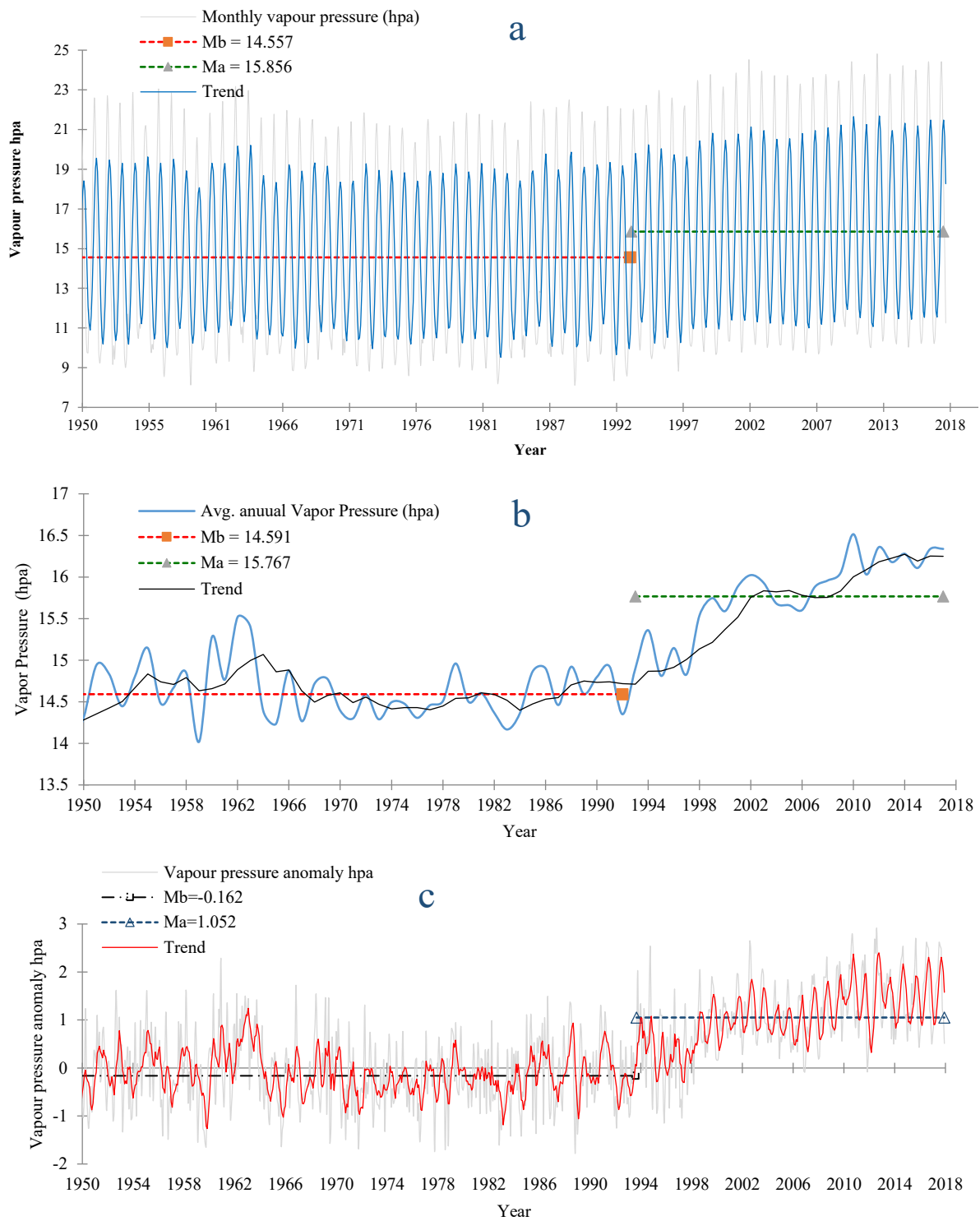


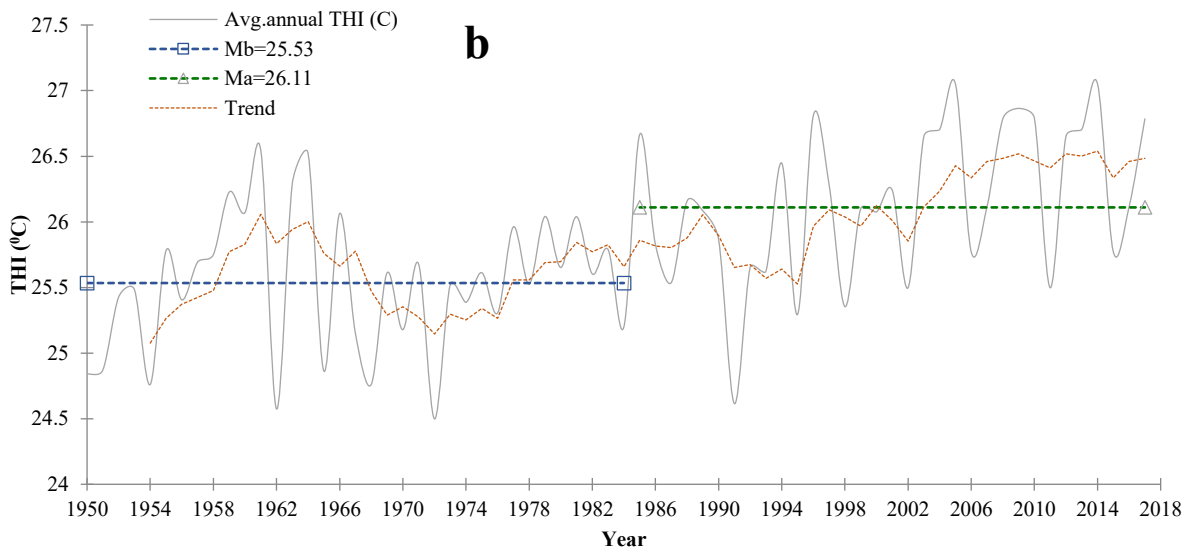
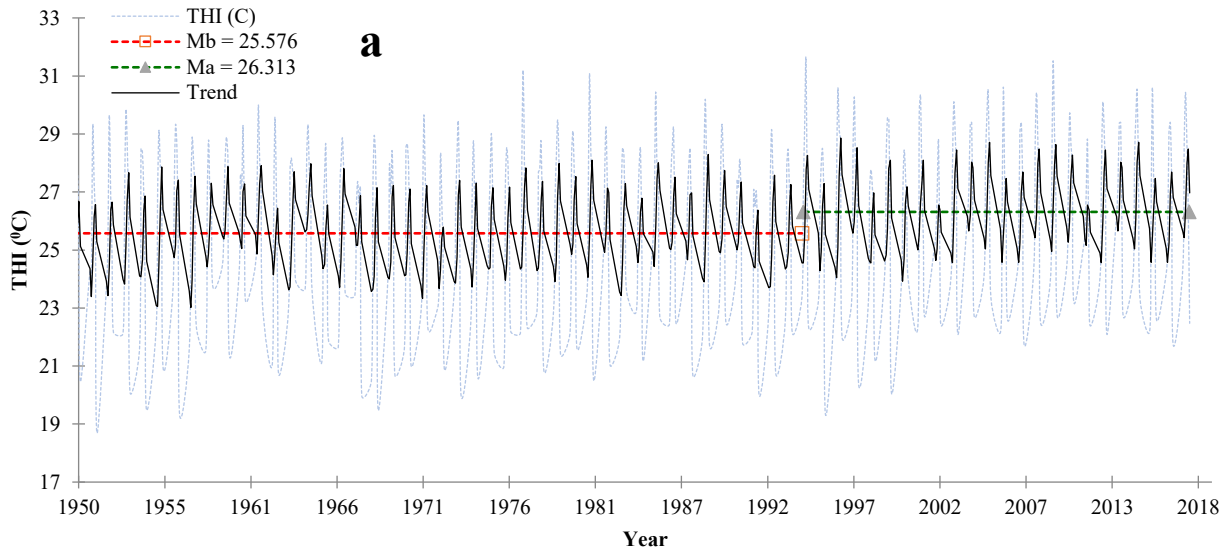
Figure 3.8 Long-term variability in vapor pressure: (a) average monthly vapor pressure, (b) average annual vapor pressure, (c) vapor pressure anomalies

3.3.3 Impact of urbanization on historical thermal comfort indices

The analysis of the historical thermal comfort indices showed a limited number of cold distress levels in the last 67 years in Cairo. On the other hand, there has been a very high variability in summer historical thermal comfort indices. The effect of urban growth on summer climate and heat-related human health issues in Cairo was investigated on three summer historical thermal comfort indices. From applying change detection techniques to monthly summer Temperature–humidity index (THI) between 1950 and 2017, a statistically significant change point was detected in 1994 (Figure 3.9(a)), where the mean monthly THI increased from 25.57 °C in 1950-1994 to 26.31 °C in 1994-2017. The monthly THI index over Cairo were strongly correlated with air temperature. Between 1950 and 1994, Cairo had a moderate thermal comfort conditions, with a long-term mean monthly THI (25.57 °C) is within the critical conditions, and no hot distress levels were observed during this period. However, between 1994 and 2017, the influence of urbanization on human thermal comfort had increased. After 1994, the THI past the upper limits of the comfort zones (25.5 °C) due to rapid urbanization. The worst hot distress levels (26.5-33.52 °C of THI) were observed in 169 months out of 252 months between 1994 and 2017, compared to no hot distress observed prior to 1994.

The highest recorded thermal discomfort levels (> 30 °C of THI) were observed in July, August and September between 1994 and 2017. To relate changes in THI due to urban growth, trend detection techniques were applied to monthly THI records between 1950 and 2017, from which a statistically significant positive trend was detected at 0.33 °C /decade after 1994 (Table 3.5). This was attributed to a significant increase in urban and built-up areas in Cairo from 250.7 km² in 1990 to 473.7 km² in 2017. Figure 3.9(b) shows the annual THI between 1950-2017 attributed to rapid urban growth in Cairo. Statistically significant change points were detected in annual THI and THI anomalies at 1984, where the mean annual THI and THI anomalies increased from 25.53 °C and -

0.246 °C over 1950-1984 to 26.11°C and 0.331°C over 1984-2017, respectively. Figure 3.9(c) shows the intensity of thermal discomfort level after 1984, as THI anomalies increased dramatically with time, leading to continuous hot distress between 1984 and 2017, except for 1991. A statistically significant increasing trend in annual THI and THI anomalies since 1984 was estimated at 0.19 °C /decade.



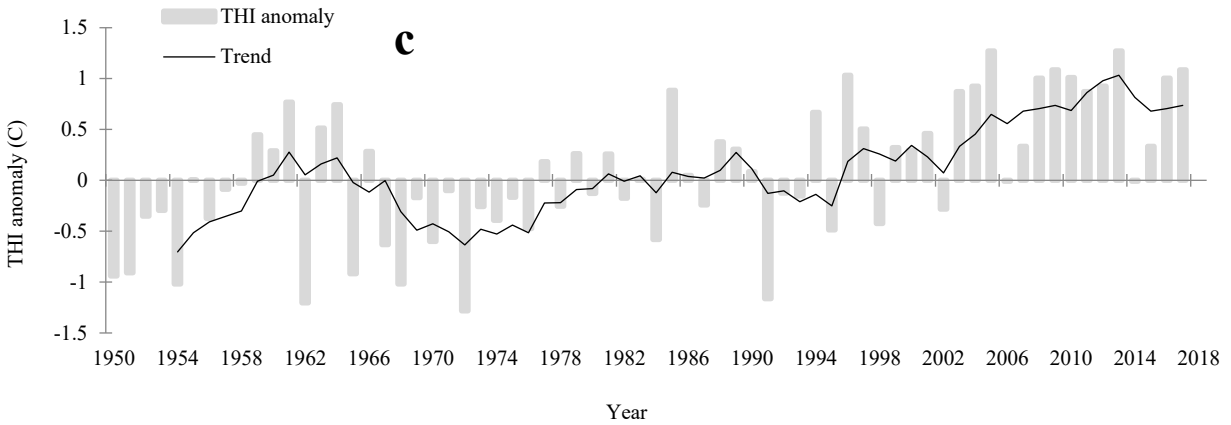
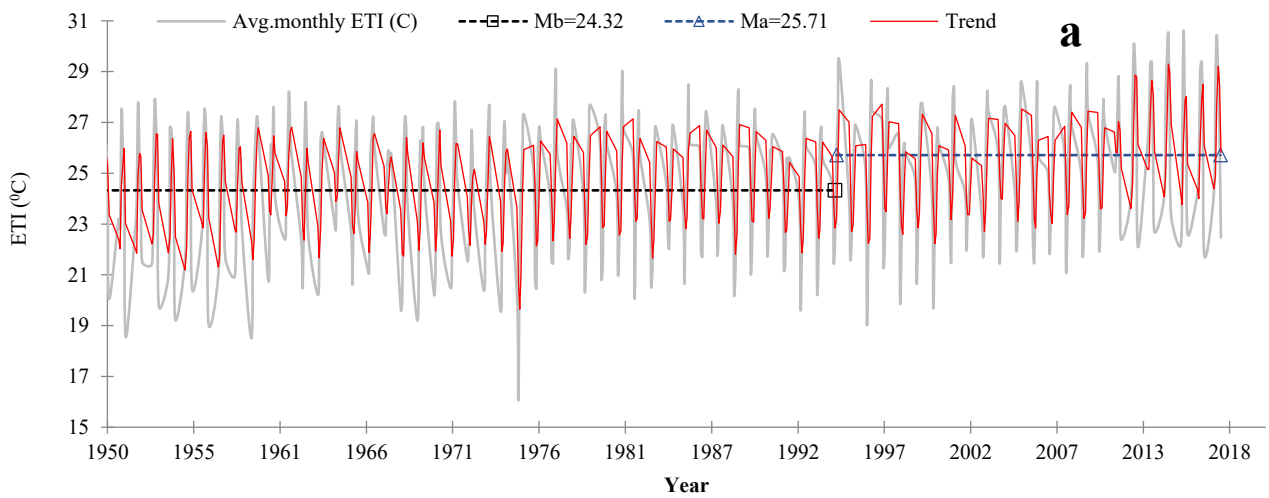


Figure 3.9 Long-term historical THI: (a) average monthly THI, (b) average annual THI, (c) THI anomalies

The historical ETI between 1950 and 2017 also showed a similar pattern with THI, that a statistically significant change point was detected at 1994 and a positive trend of $0.29\text{ }^{\circ}\text{C}/\text{decade}$, for the mean monthly temperature increased from $24.32\text{ }^{\circ}\text{C}$ over 1950-1994 to $25.71\text{ }^{\circ}\text{C}$ over 1994-2017 (Figure 3.10(a)). Similarly, the mean annual and anomalies of ETI shows statistically significant change points at 1984, with a rising trend at $0.16\text{ }^{\circ}\text{C}/\text{decade}$ after 1984 (Figure 3.10(b, c)). This reflects the effect of rapid urban growth on both thermal comfort indices and the observed increasing trends.



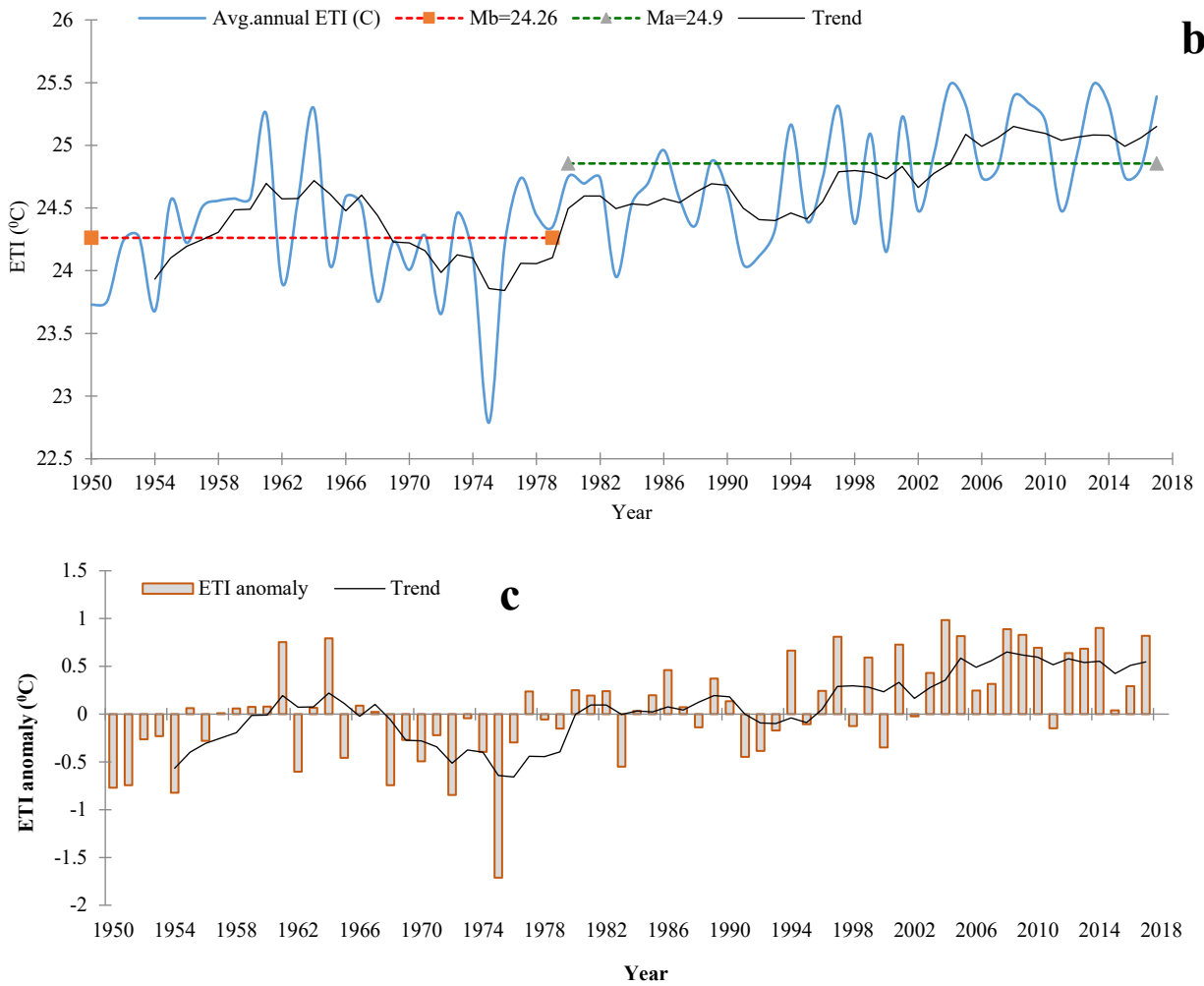


Figure 3.10 Long-term historical ETI: (a) average monthly ETI, (b) average annual ETI, (c) ETI anomalies

The increasing trend in the thermal discomfort in Cairo after 1994 is further confirmed by the analysis on monthly RSI which also shows a statistically significant change point at 1994 (Figure 3.11(a)) and an increasing trend of 0.06 /decade (Table 3.5). According to this index, the highest observed thermal discomfort (0.25-0.409 of RSI) was observed between 1994 and 2017. The annual RSI shows statistically significant change points at 1984 and a positive trend of 0.06 /decade after 1984 (Figure 3.11(b)). RSI anomalies (Figure 3.11(c)) show an even higher increasing trend than the annual RSI at 0.08 /decade. The relative humidity is negatively correlated

with both air temperature and vapor pressure and is negatively correlated with human comfort indices. This shows that as relative humidity decreases, hot distress will increase in Cairo.

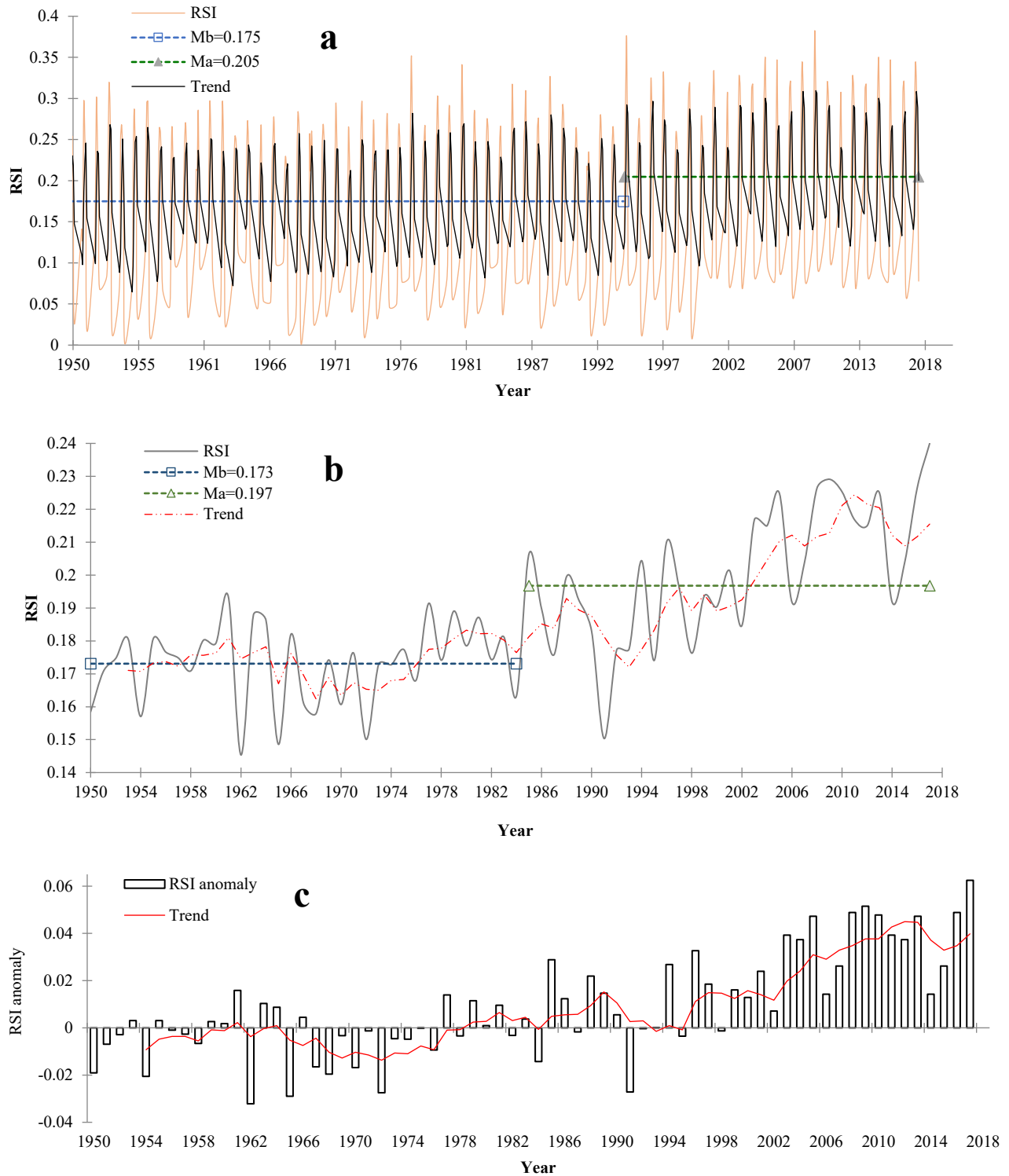


Figure 3.11 Long-term historical RSI: (a) average monthly RSI, (b) average annual RSI, (c) RSI anomalies

To further illustrate the relative importance of each index for the study area, the spatial distribution of thermal discomfort risk zones in the Cairo Governate was developed for each index. Figure 3.12 shows the majority of urban and built-up areas fall within the very high and high-risk zones. Based on the THI index, 35.67% of the study area falls within the very high to high-risk thermal discomfort zones (Figure 3.12(a)), which agrees with results obtained from the RSI index (Table 3.6). These two indices showed similar thermal discomfort zones in the study area (Figure 3.12(a, b)). On the other hand, the spatial distribution of discomfort risk zones based on the ETI index only agree partially with previous findings. The majority of New Cairo city falls within the moderate risk zone with ETI values at the upper thermal comfort limits. The highest thermal discomfort risk was found in urban areas located in northwestern parts of the old Cairo, but the risk is marginally smaller at new cities where there are vegetation covers. In addition, located in higher latitudes, the temperature of new cities as expected is lower than the old Cairo. According to the spatial distribution of discomfort zones and the extent of urban and built-up areas in the study area, the THI and the RSI indices are likely indices that best represent the discomfort zones of the study area.

Table 3.6 Areal distributions of thermal discomfort risk zones.

Thermal discomfort risk zones	THI	RSI	ETI
	Area (%)		
Very high	17.63	17.74	9.57
High	17.16	17.93	22.1
Moderate	13.12	18.43	34.37
Low	30	31.9	28.66
Very low	21	13.98	5.2

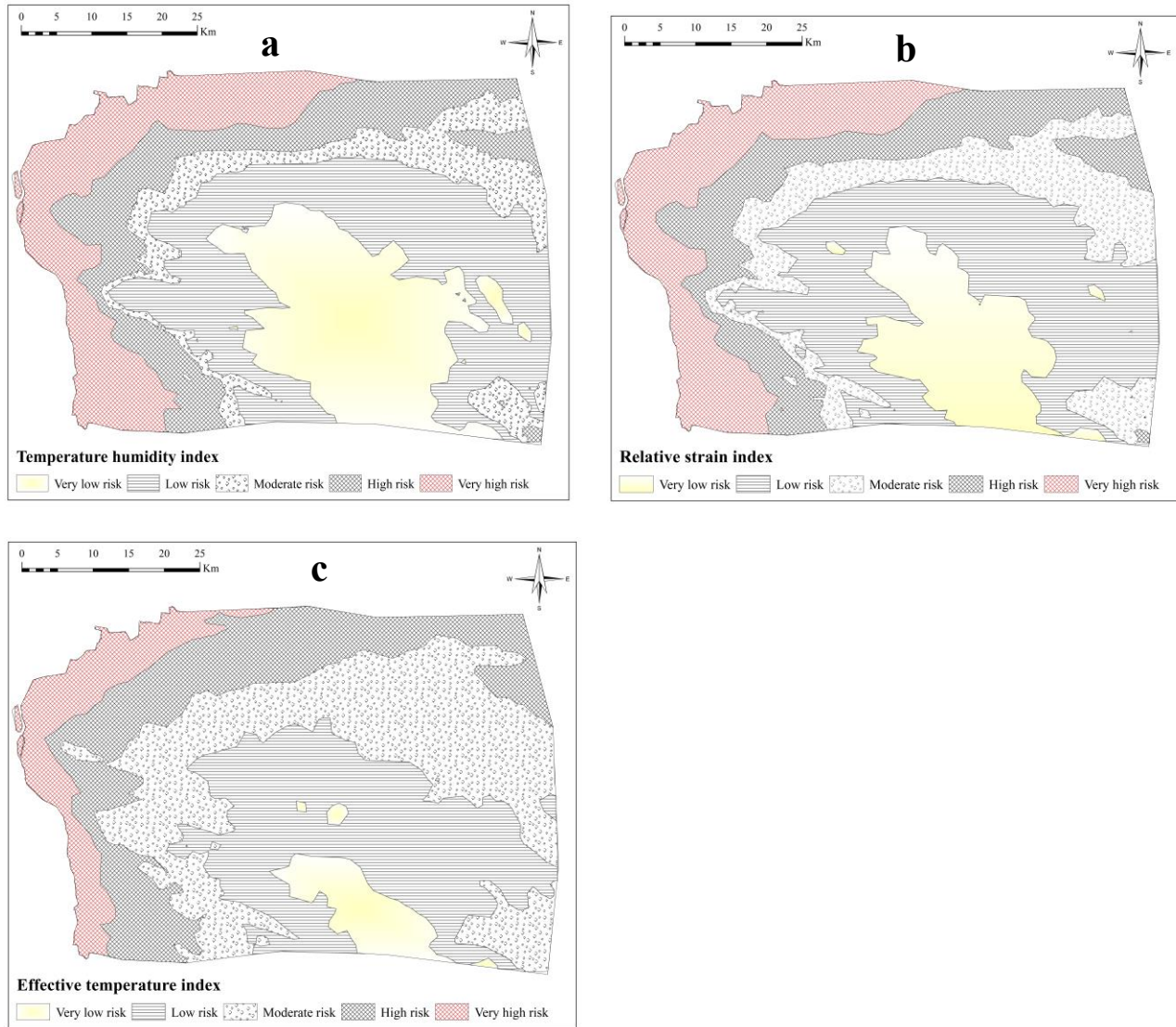


Figure 3.12 Thermal discomfort risk zones: (a) THI risk zones, (b) RSI risk zones, (c) ETI risk zones

3.3.4 Impacts of urbanization on temperature health-related illness

Regarding impacts of urbanization on human thermal comfort in Cairo, Figure 3.13 shows that serious thermal discomfort began after 1994, when all thermal comfort indices exceeded the upper limits (Figure 3.14). Results also show that rapid urban growth caused air temperature to increase, relative humidity to decrease and vapor pressure to increase which leads to human discomfort.

This thermal discomfort had affected human health in Cairo. Data obtained from the Emergency Events Database - Universite Catholique de Louvain shows a number of deaths and sickness due to hot distress in Cairo and Egypt that occurred between 1954 and 2016. Despite of limited records available, the effect of rising trends in thermal discomfort indices on health-related illness and deaths in Cairo is obvious. For example; in July 1995, the severe thermal discomfort in Cairo (30.54 °C of THI, 27.5 °C of ETI, 0.32 of RSI) had resulted in 32 deaths. Another example was the hot distress in July 1996 (28.42 °C of THI, 26.8 °C of ETI, 0.28 of RSI), causing 22 deaths. More recently, in August 2015, the thermal discomfort level had led to 110 deaths and 66 affected cases in one day (Table 3.7), because thermal comfort indices were way above upper critical limits (33.52 °C of THI, 28.5 °C of ETI, 0.409 of RSI). Findings from this study demonstrated the severe impacts of urban growth on the microclimate, human thermal discomfort and heat stress in Cairo. Results from this study should be useful in urban planning and development, and applicable to other governorates in Egypt and arid regions.

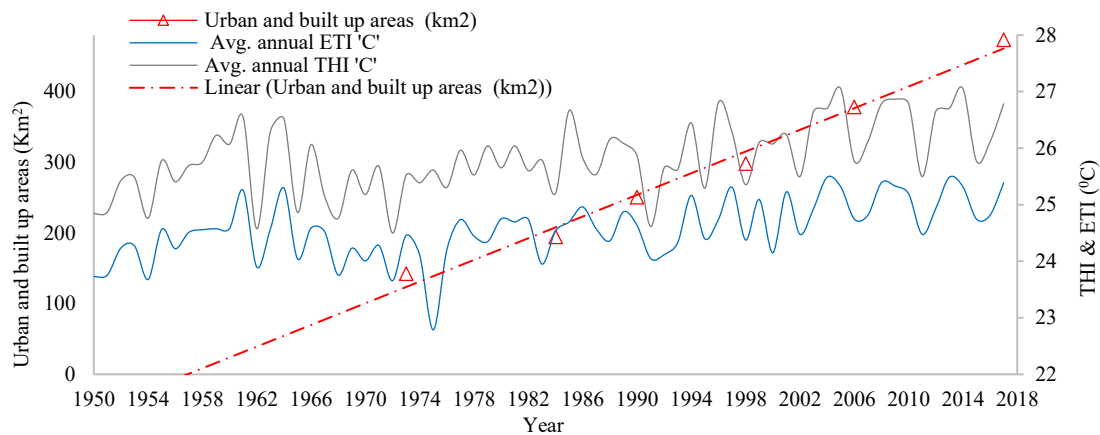


Figure 3.13 Urban and built up changes against average annual THI and ETI

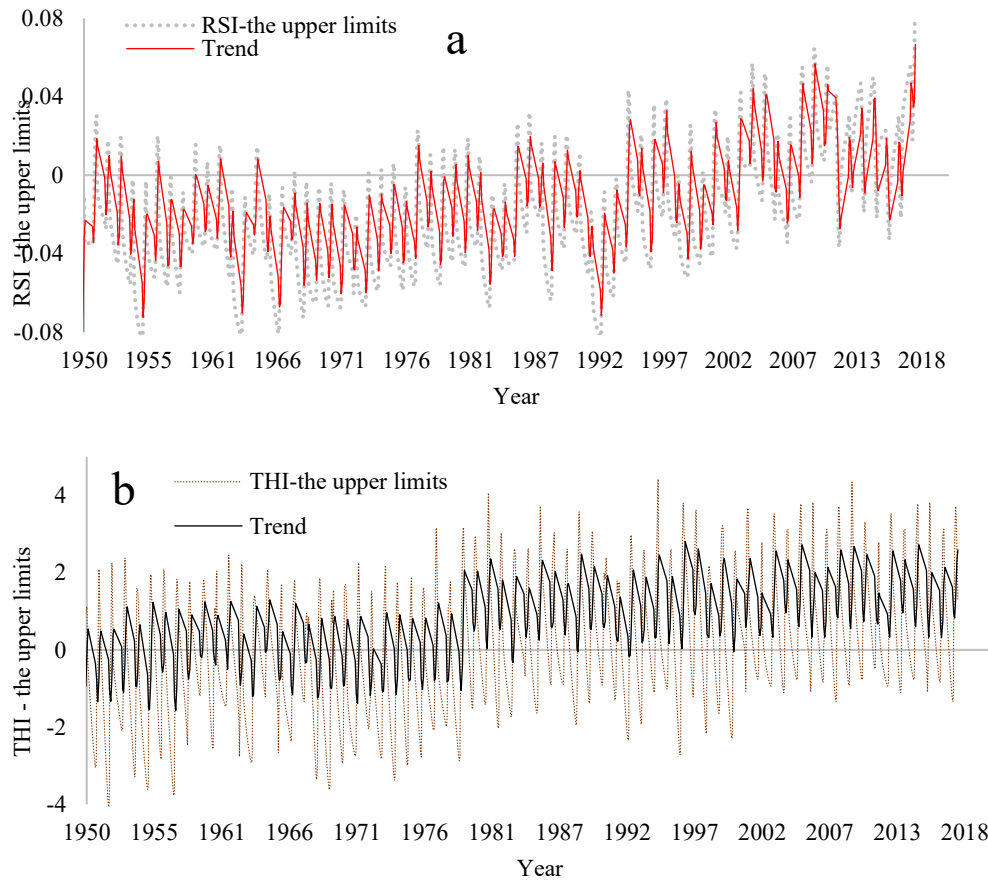


Figure 3.14 Thermal comfort above the upper limits: (a) THI-upper limits, (b) RSI-upper limits

Table 3.7 Sample records of temperature health-related illness and deaths

Start date	End date	Disaster type	Total deaths	Total affected	THI	RSI	ETI
12/6/1995	12/6/1995	Extreme temperature	32	0	30.54	0.32	27.5
7/7/1996	7/7/1996	Extreme temperature	22	0	28.42	0.28	26.8
9/8/2015	9/8/2015	Extreme temperature	110	66	33.52	0.409	28.5

3.4 Conclusion and recommendations

In this study, the long-term impact of rapid urbanization on air temperature, relative humidity, vapor pressure and human thermal comfort in Egypt was analyzed. Three thermal comfort indices; temperature humidity index (THI), effective temperature index (ETI) and relative strain index

(RSI) were estimated from climate time series collected between 1950 and 2017. Over this study period, LUC in Cairo was dominated by the growth of new cities, with urban expansion at 75.2 km²/decade, extending into low-lying areas of Cairo and along the direction of roads to lower the cost of development. This trend contributed to shifting most of the urban growth toward New Cairo and Shrouk City after 1990. The significant increase in urban and built-up areas between 1990 and 2017 resulted in rising air temperature after 1995 at 0.19 °C /decade, relative humidity decreasing at 0.55 % /decade, and vapour pressure increasing at 0.24 hPa /decade. These observed changes in the urban climate of Cairo are likely associated with significant LUC, such as growing impervious areas due to rapid urbanization since the 1990s. Heat stress problems and thermal discomfort began to emerge and persisted every July-September after 1994. The THI series computed between 1950 and 2017 showed a statistically significant change point at 1994 and thereafter a rising trend of 0.33 °C /decade. After 1994, the THI index exceeded the upper limits of the comfort zones because of rapid urbanization. Similarly, the ETI index computed for the 1950-2017 data also show a statistically significant change point at 1994, and thereafter a rising trend of 0.29 °C /decade. The RSI index also show a rising trend of 0.06 /decade.

In conclusion, the rising level of thermal discomfort based on the positive trends of the three indices is primarily attributed to the significant LUC or rapid urbanization in Cairo and the new cities. The relative humidity is negatively correlated with both air temperature and vapor pressure, and negatively correlated with human comfort indices. This shows that as relative humidity decreases, hot distress will increase. Findings from this study demonstrate the significant impact of urban growth on the microclimate, heat stress or human thermal discomfort in Cairo. Findings of this study will benefit urban planners in the urban planning and development of Cairo and other regions of arid environments.

Chapter 4 Impact of anthropogenic climate change and human activities on environment and ecosystem services in arid regions

4.1 Introduction

Some countries have suffered from significant impact of climate change, such as rising sea level, extreme weather events and changing hydrological cycle. However, human activities could also incur severe negative effects on our environment which in turn affect our livelihood worldwide. There have been studies on how land use change (LUC) and climate change have affected the ecosystems and the environment at various spatiotemporal scales (Perrings et al., 2011; Tong et al., 2012; Reeves et al., 2018). In this study, we assess how have LUC patterns and climate change impacted the environment and ecosystem services of coastal regions of Arabia. In recent years, studies show that human activities, including LUC and deforestation, have resulted in major global environmental change and impacts (Verburg et al., 2011; Sirami et al., 2017; Prestele et al., 2017). In Saudi Arabia, for instance, the impact of human exploitation of water resources are obvious in the Layla Aflaj lakes and deep waterholes of the Al-Kharj region. Since 1980s, excessive water consumption due to agriculture activities and domestic purposes have significantly depleted these resources (Schleusener et al., 2013). Sadly, valuable water sources from limited number of natural lakes in Arabia formed by groundwater aquifers over many centuries are now the region' history. In the past, the region was characterized by heavy rainfall and were large occupied by shrubland and forests (Thouless et al., 1991). However, human activities and land use change had further decreased the already scarce water resources of this region, and similarly in other parts of the Arabian Peninsula. To mitigate the impact of severe droughts, growing population, and food security, multiple rainwater harvesting dams were constructed in high mountains to collect

rainwater for all purposes, forestlands were replaced by agriculture fields and wild animals were hunted for food.

Human and climate change impacts on the arid environment are generally not well documented, even though such information will help us to better understand how these human activities will affect natural resources in the arid environment, and what conservation plans would be helpful. In recent decades, many LUC studies have been conducted (Shalaby et al., 2007; Wang et al., 2009; Woldesenbet et al., 2017), of which some have considered extensive LUC as the main drivers to biodiversity loss, fragmentation, habitat reduction, and food security (Wilson and Weng, 2011; Nasta et al., 2017; Liang et al., 2017; Fu et al., 2017). It seems uncurbed human exploitation of natural resources could irreversibly impact the future of mankind in centuries to come. From remotely sensed data acquired by earth observation satellites, it is now possible to use a geographic information system to derive various LUC patterns, trends and magnitude of high temporal and spatial resolutions (Lu et al., 2004; Long et al., 2007; Shalaby et al., 2007).

Various change detection methods have been employed in LUC studies, such as the principal component analysis (PCA), band differencing, band ratioing, neural network, support vector machine, and post-classification techniques (Ridd and Liu, 1998; Lu et al., 2004; Petrosillo et al., 2013). However, the Markov Chains method has dominated many LUC studies (Pontius and Malanson, 2005). Researchers often combine this method with Cellular Automata (CA) to control the decision-making process and to enhance the ability to change/add or even modify factors that drives LUC in form of transition rules (Longley and Batty, 1996; Clarke and Gaydos, 1998; Zhang et al., 2009). Cellular Automata has been successfully utilized to project future LUC (Myint and Wang, 2006; Marshall and Randhir, 2008; Guan et al., 2011; Huishi et al., 2012; Huang et al., 2014). By combining these two methods to a LUC study conducted in Norman, Oklahoma, USA, Myint and Wang (2006) achieved an accuracy of 86% which is of acceptable accuracy (Anderson et al., 1976; Townshend, 1981). Similar accuracy was obtained by Marshall and Randhir (2008)

to assess future land cover based on transition rules of Markov-CA. More recently, Guan et al. (2011) and Huishi et al. (2012) found that a combination of Markov-CA is more accurate than other LUC models.

Past studies suggest that LUC patterns would affect local temperature and precipitation (e.g., Pielke et al., 2007). Weng (2001) concluded that rapid urbanization led to climate warming because of increasing CO₂ emissions. Moreover, Pielke (2005) showed that rising concentration of greenhouse gases in the atmosphere is the best-known impact of human activities on climate change and LUC. Pettit's test and Mann-Kendall test have been widely used to detect changes in climate data. Pettit's test (Pettit, 1979) is a popular non-parametric approach for detecting change points in the time series of climate variables (Ma et al., 2008; Mahé and Paturel, 2009; Martínez et al., 2010). The non-parametric Mann-Kendall (Sneyers, 1992) test is widely used to estimate trends in climate data and whether the trend is statistically significant (Zhang, et al., 2000; Yue et al., 2002; Dawood, 2017).

We investigated the impacts of anthropogenic climate change and LUC caused by human activities on the environment and ecosystem services of the study sites. To achieve our objectives, we used earth observations data (EO) of satellites to derive land use categories at different spatial and temporal scales in the Jizzan Province-Arabia for 1970-2014. Then, using the Markov-CA approach, the temporal/spatial dynamics of LUC patterns in the study area for 2014-2100 were derived and their impacts on the climate, environment, and water resources were analyzed. Pettit's and Mann-Kendall tests were applied on temperature data over 1900-2010, and precipitation data over 1948-2014 to detect change points and to estimate trends in the region. The impact of global warming due to increasing greenhouse gases were also analyzed between 1960 and 2015. Lastly, future effects of LUC and climate change in the study area, were analyzed using RCP4.5, RCP6.0 and RCP8.5 climate change scenarios projected by climate models of CMIP5 and IPSL-CM5A-LR between 2014-2100. Without any major river, the water resources of Saudi Arabia depend

heavily on precipitation and groundwater sources. Given evapotranspiration (ET) plays a major role in its climate and the fauna and flora of its desert environment, we have also estimated the potential ET of the study area over 1950-2016 and projected possible changes over 2016-2100.

4.2 Data and Research Methods

4.2.1 Study area and data sets

As the Jizzan Province (Figure 4.1) lies on the coastal regions of Arabia ($16^{\circ}53'21''\text{N}$ $42^{\circ}33'40''\text{E}$), it has a different climate than the rest of Arabia. In the past Jizzan was dominated by forest, shrubland and different species of wild animals. The province also includes more than 100 islands in the Red Sea that in the past were rich in animals and biodiversity. Landsat cloud-free images for Jizzan in 1970, 1980, 1990, 2000, 2010, and 2014 were obtained from the King Abdulaziz City for Science and Technology (KACST) (Table 4.1). Monthly precipitation data between 1948-2014 and temperature data between 1900-2010 were derived from the 20th Century Reanalysis V2 Dataset. CO₂ and other greenhouse gas emissions data were obtained from the Carbon Dioxide Analysis Center of Environmental Sciences Division, USA.

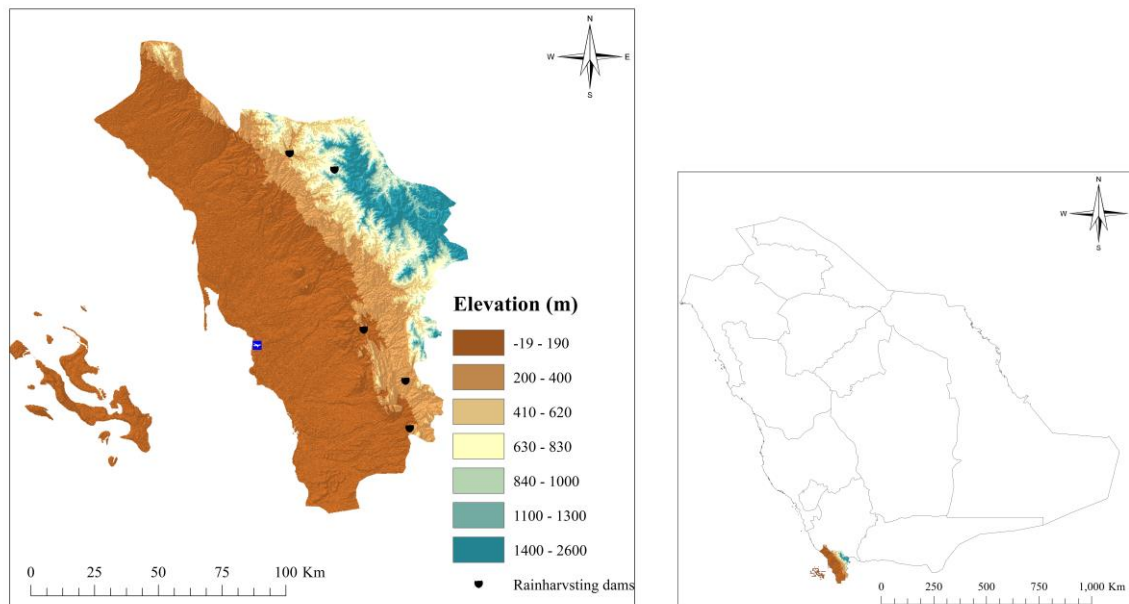


Figure 4.1 Location map of Jizzan Province, Kingdom of Saudi Arabia.

Table 4.1 Earth observation data used in this study

Images Used for the study	Resolution (m)	Date of acquisition	Format	Product Type (Cloud Cover %)
Landsat 1 -5 MSS	30	06/03/1970	GEOTIFF	L1T (0%)
Landsat 1 -5 MSS	30	01./09/1980	GEOTIFF	L1T (0%)
Landsat 5 TM “Band 1 -7”	30	24/02/1990	GEOTIFF	L1T (0%)
Landsat 7 ETM+ “Band 1 -8 ”	30	04/01/2000	GEOTIFF	L1T (0%)
SPOT-5 “PSM”	2.5	06/03/2000	GEOTIFF	L1T (0%)
Landsat 7 ETM+	30	05/01/2010	GEOTIFF	L1T (0%)
Landsat 8	30	03/04/2014	GEOTIFF	L1T (0%)

4.2.2 Land use classification and accuracy assessment

Landsat images were preprocessed, made as mosaic, and geometrically corrected based on a rectified SPOT-5 “2.5m PSM” satellite image for the Jizzan province. This image also served as the reference image for land use classification and accuracy assessment. Then, these images were also atmospherically corrected by normalizing these images to the SPOT-5 image. Lastly, the Landsat images have been radiometrically normalized to the reference image based on manually identified 16 pseudo-invariant features (PIFs). Two field surveys were set up, the first was before land use classification to collect ground control points (GCP). Five hundred GCP were collected in the first trip for land use classification, which was performed using these GCP and visual interpretations of Google Earth images. In the second trip, we collected 100 points for validating the classified images.

The popular, Iso Cluster Unsupervised and Maximum Likelihood Classification was applied to the Landsat images, to classify the land use/cover (Baker et al., 2006; Panda et al., 2009; Mukherjee et al., 2010; Jiménez-Bello et al., 2012). Six land use/cover classes were identified in each land use map: water bodies, built-up areas, bare soil, sparse vegetation, irrigated cropland, forest and shrubland. The accuracy of these maps was assessed using both simple random and

stratified random patterns. Further, a questionnaire consists of two types of questions was prepared to ask residents about anthropogenic effects on the region. The first type consists of preliminary questions such as areas of cultivated lands, and number of groundwater wells used to irrigate crops. The second type of questions consist of three tables, which include affirmative statements about social and environmental impacts of oil discovery, climate change and human activities in the study area. The questionnaire was set up under a five-point scale (strongly agree, agree, not sure, disagree, strongly disagree) to allow farmers to choose the extent of their agreement or disagreement to each statement.

4.2.3 Changes and Dynamics of Land Use/Cover

The areal distribution of each land use class was estimated for all time periods to determine the dynamics and patterns of land use/cover change (LUC). LUC and trends were estimated in terms of gain, loss and net change for each temporal period by class. LUC drivers were then identified based on the Markov Chains transition probabilities. A coupled Markov–CA model was used to project changes and the future spatial distribution of LUC. From the results, we derive the transition probability matrix which represents the probability of each land use class to change to another class or to remain unchanged in the next time period. Next, transition area matrices were developed to estimate the total area expected to change at each period. Finally, based on the historical LUC in the area, conditional probability images, one for each land use/cover class was developed to show the likelihood of each class will change to other classes or not. Five historical transition matrices were constructed from the cross-tabulation of the land use/cover maps between 1970, 1980, 1990, 2000, 2010, and 2014. The time interval between the transition matrices was 10 years. The approach of Pastor et al. (1993) was adopted to transform transition probabilities to annual time steps to consider the differences in the lengths of the last period (2010-2014) (Table 4.3). Major drivers of land use dynamics in the study area for each study period were identified.

As expected, urbanization and agriculture activities at the expenses of forestland and shrubland were the major drivers for LUC.

To project future LUC in the study area, we first tested the model's ability to simulate historical LUC based on the annualized transition matrices. Transition probabilities for future LUC are developed from trends observed in the past, e.g., the land use in 2010 was simulated on the basis of the 1990 and 2000 transition matrices. Various studies have adopted this approach (Araya and Cabral, 2010; Yang et al., 2014; Singh et al. 2015; Keshtkar and Voigt, 2016; Han and Jia, 2017). For instance, Araya and Cabral (2010) compared the actual land use map in 2010 derived from EO data with that simulated for 2010 based on LUC between 1990 and 2000. Similarly, Singh et al. (2015) used actual transition probabilities between 2000 and 2010 to project LUC in 2020. In this study, we used the transition probability between 1970 and 1980 to simulate LUC in 1990. Similarly, the 2000 land use map was simulated from the 1980-1990 transition matrix. Finally, the land use map of 2010 and 2014 were simulated based on transition probability matrices of 1990-2000 and 2000-2010, respectively.

The main limitation of the Markov-CA model is that it assumes factors of past changes remain the same in the future. However, using multiple actual land use maps as an accuracy assessment, high accuracies of projection could be obtained (Yagoub and Al Bizreh, 2014; Guan, 2011). Guan et al. (2011) used the transition probability matrix of 1997–2006 to project LUC for 2024, which then was set as the starting year to project LUC for 2033, but again based on the transition probability matrix of 1997–2006, and 2033 as the starting year to project the 2042 LUC. In our study, we followed this approach and applied the Kappa Index of Agreement (KIA) to validate the model performance by comparing the simulated land use map at each year against the actual land maps. KIA was also used to test for spatial and quantitative agreement between every two maps. Table 4.2 shows how well the land use maps were classified. The overall accuracy of the land use maps for 1970, 1980, 1990, 2000, 2010, and 2014 was assessed to be 80.52%, 84.33%, 85.17%,

84.9%, 87.2%, and 94.8% respectively. KAPPA indices for these maps estimated at 0.76, 0.755, 0.717, 0.82, 0.85, and 0.89, respectively are all of acceptable accuracy. Next, the Markov-CA model was used to project the future LUC and land use map at 2025 based on the transition probability of 2010-2014, taking 2014 as the starting point. Then land use map at 2050 was simulated based on the same transition probability matrix but taking 2025 as the starting point. Finally, land use map at 2075 and 2100 was simulated taking 2050 and 2075 as the starting point respectively.

Table 4.2 Accuracy assessment and validation of land use-land cover maps

	1970			1980			1990			2000			2010			2014		
	UA (%)	PA (%)	Kappa															
LULC																		
Water bodies	80.2	79	0.72	78.12	76.5	0.71	86.8	77.6	0.69	89.1	90.9	0.82	79.61	70.4	0.88	93.21	94.6	0.86
Built up areas	79.9	82.2	0.81	92.62	90.4	0.82	90.35	89.8	0.77	90.2	85.62	0.86	94.58	92.8	0.98	96.85	94.36	1
Bare soil	84.2	84.8	0.62	88.22	78.2	0.71	88.12	85	0.67	79.6	75.43	0.83	88.5	84.64	0.78	95.47	93.85	0.79
Sparsely vegetated	81.5	77.51	0.7	79.32	80.3	0.68	75.41	80.2	0.735	81.3	91.5	0.9	91.7	79.3	0.76	94.65	96.92	0.84
Irrigated cropland	76.2	78.52	0.86	83.44	84.35	0.76	87.35	90.24	0.725	88.29	89	0.78	86.55	90.4	0.845	92.69	94.54	0.89
Forest & shrubland	78.9	83.3	0.87	91.1	89.4	0.85	84.9	86.23	0.71	79.5	78.41	0.75	93.32	94.6	0.86	93.74	96.77	0.94
OA	80.519		0.76	84.33		0.755	85.17		0.717	84.90		0.82	87.20		0.85	94.80		0.89

Table 4.3 Land use transitions probabilities 1970–2014

1970–1980 Markov matrix ^a							
Code	Land cover/use class	Water bodies	Built up areas	Bare soil	Sparsely vegetated	Irrigated cropland	Forest and shrubland
1	Water bodies	0	0.0491	0.0844	0.0055	0.0009	0.0005
2	Built up areas	0.8597	0.1496	0.7078	0.0213	0.0014	0.0005
3	Bare soil	0.1194	0.0177	0.8893	0.082	0.0044	0.0027
4	Sparsely vegetated	0.004	0.0032	0.7375	0.2412	0.0124	0.0049
5	Irrigated cropland	0.0007	0.0007	0.203	0.6457	0.1185	0.0318
6	Forest and shrubland	0.0005	0.0003	0.0672	0.4327	0.267	0.2328
1980–1990 Markov matrix ^a							
Code	Land cover/use class	Water bodies	Built up areas	Bare soil	Sparsely vegetated	Irrigated cropland	Forest and shrubland
1	Water bodies	0.9231	0.0461	0.0285	0.0013	0.0006	0.0003
2	Built up areas	0.1102	0.2392	0.6506	0	0	0
3	Bare soil	0.0012	0.0167	0.9072	0.07	0.003	0.002
4	Sparsely vegetated	0	0	0.6487	0.3317	0.0147	0.0049
5	Irrigated cropland	0.0005	0	0	0.7752	0.1881	0.0362
6	Forest and shrubland	0.0002	0.0004	0	0.3282	0.3078	0.3633
1990–2000 Markov matrix ^a							
Code	Land cover/use class	Water bodies	Built up areas	Bare soil	Sparsely vegetated	Irrigated cropland	Forest and shrubland
1	Water bodies	0.7992	0.0527	0.137	0.0093	0.0012	0.0006
2	Built up areas	0.1278	0.053	0.7584	0.0562	0.0029	0.0017
3	Bare soil	0.0067	0.0188	0.871	0.0944	0.0058	0.0033
4	Sparsely vegetated	0.0018	0.0118	0.8261	0.1452	0.0101	0.005
5	Irrigated cropland	0.0005	0.0001	0.5817	0.3526	0.0449	0.0203
6	Forest and shrubland	0.0002	0	0.2593	0.4946	0.1474	0.0986
2000–2010 Markov matrix ^a							
Code	Land cover/use class	Water bodies	Built up areas	Bare soil	Sparsely vegetated	Irrigated cropland	Forest and shrubland
1	Water bodies	0.6152	0.0766	0.248	0.0271	0.0238	0.0093
2	Built up areas	0.0399	0.5438	0.3791	0.0169	0.0164	0.0039
3	Bare soil	0	0.1069	0.798	0.0577	0.0281	0.0083
4	Sparsely vegetated	0.0001	0.0087	0.5982	0.2039	0.1613	0.0277
5	Irrigated cropland	0	0.0032	0.3339	0.2021	0.3278	0.1329
6	Forest and shrubland	0	0.0017	0.0807	0.0817	0.3756	0.4604
2010–2014 Markov matrix ^a							
Code	Land cover/use class	Water bodies	Built up areas	Bare soil	Sparsely vegetated	Irrigated cropland	Forest and shrubland
1	Water bodies	0.4735	0.1019	0.342	0.0369	0.0325	0.0132
2	Built up areas	0.0477	0.4051	0.4871	0.0303	0.0231	0.0068
3	Bare soil	0.0031	0.1354	0.7455	0.0644	0.04	0.0125
4	Sparsely vegetated	0	0.0446	0.6555	0.1279	0.1282	0.0438
5	Irrigated cropland	0	0.0177	0.4592	0.1584	0.2358	0.1289
6	Forest and shrubland	0.002	0.0005	0.1767	0.1347	0.3598	0.3283

4.2.4 Anthropogenic climate change detection

Land-use change is a major player to climate change since it contributes to atmospheric CO₂ emission (Dale et al., 2011). Therefore, we also analyzed CO₂ and other greenhouse gases emissions and their by-product: hydrofluorocarbons (HFC), perfluorocarbons (PFC), sulfur

hexafluoride (SF₆), all anthropogenic CH₄ and N₂O sources in thousand metric tons (Kt) of CO₂ equivalent. Change point and trend detections were applied to these data to detect climate change in the study area which might be attributed to LUC and increased global warming as suggested by Dale et al., (2011) and Searchinger et al. (2008). For the Jizzan province, we analyzed the variability of long-term monthly precipitation and temperature anomalies from the long-term mean precipitation of 1948 to 2016, and long-term mean temperature of 1900-2010, respectively. To detect trends and change points, we used nonparametric, Pettitt (Pettitt, 1979) and Mann–Kendall tests (MK) on the time series of temperature, temperature anomaly, precipitation, precipitation anomaly, respectively. The magnitude of the trend is obtained from the slope estimator method (Sen, 1968). The sign of the slope indicates if the trend of the time series is positive or negative.

Climate change scenarios of RCP4.5, RCP6.0 and RCP8.5 projected by climate models of CMIP5 and IPSL-CM5A-LR between 2014-2100 were used to project future warming in the study area. Future climate projections of these climate models were analyzed separately and then averaged for the study area. Statistical downscaling techniques of Frias et al. (2006) and Guo et al., (2014) based on empirical relationships between climate models' output and local weather information were used to downscale climate models' projections to local scale. Again, the Pettitt's test and Mann-Kendall approach were used to detect change points and trends of climate projections that have been downscaled statistically. Given evapotranspiration (ET) plays a major role in the climate of a desert environment, the increase in ET has been linked to rising atmospheric CO₂ concentration and climate warming (Kang et al.,1999; Abteu and Melesse, 2013).

We estimated the potential ET of the study area over 1950-2016 and projected possible changes over 2016-2100 of the study area using Penman Monteith's method (Allen et al., 1998). Precipitation surplus (precipitation - PET), which represents the hydrologic impact of climate change in the region, was also estimated.

4.3 Discussion of Results

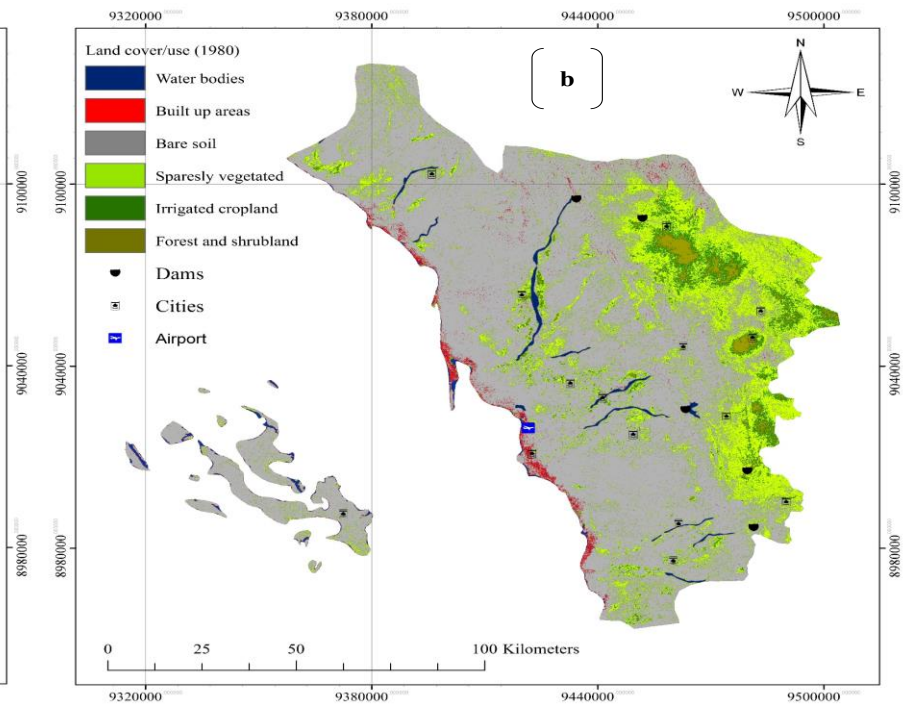
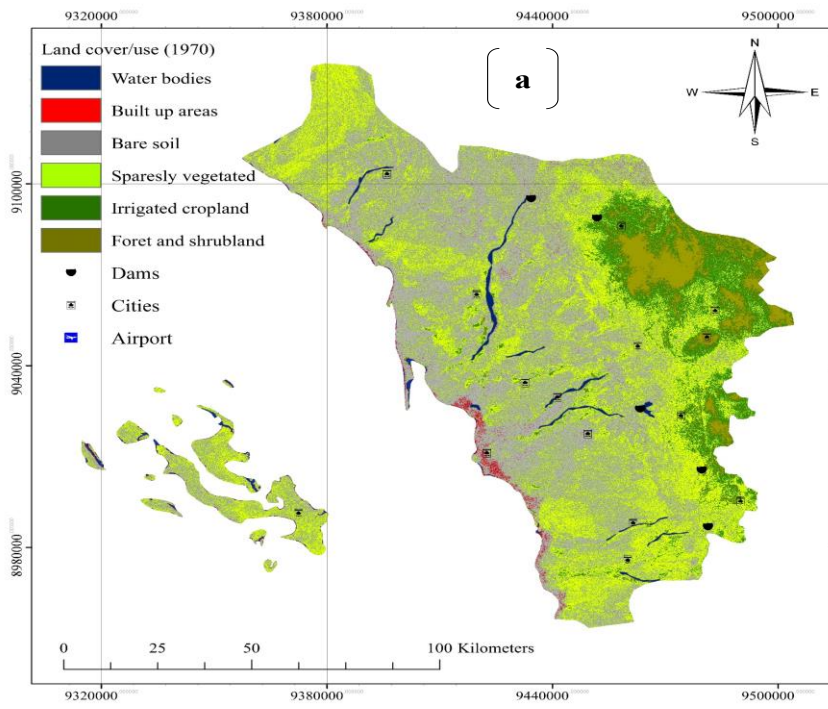
4.3.1 Impact of land use dynamics on environment

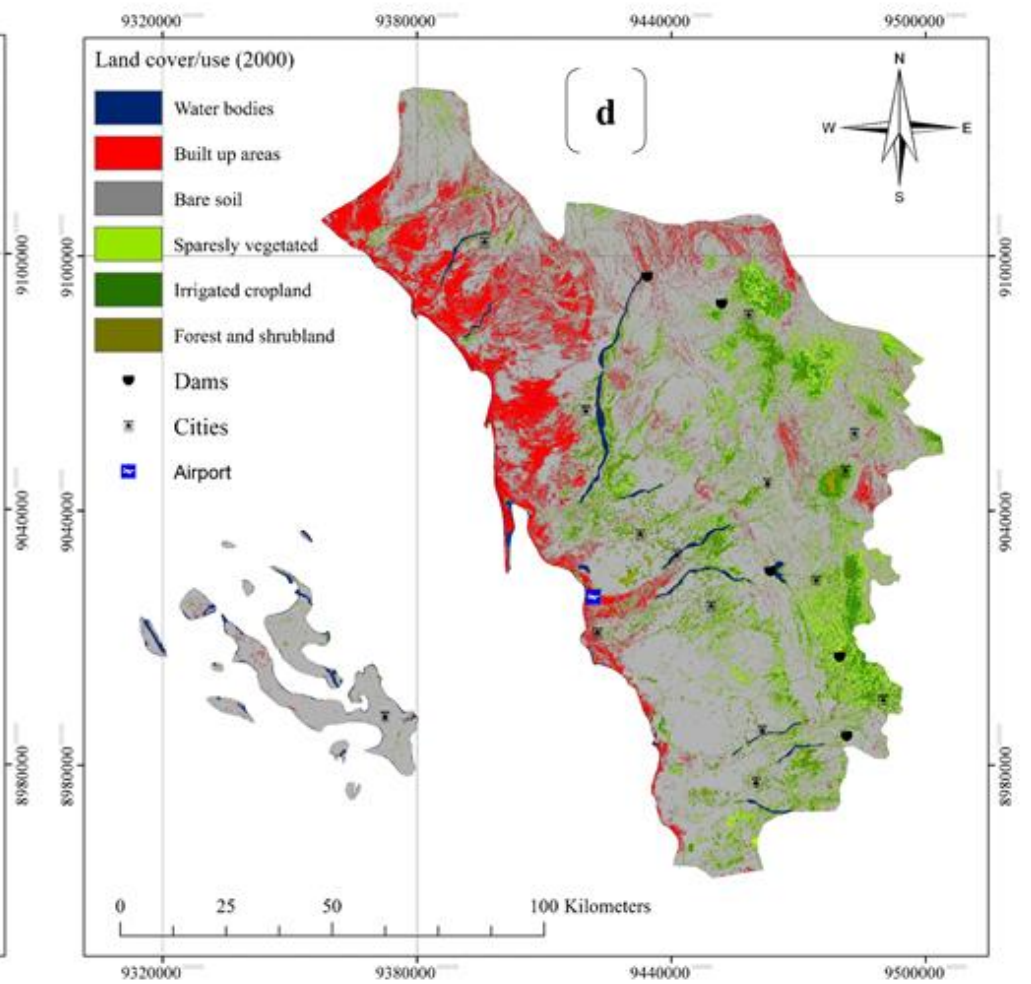
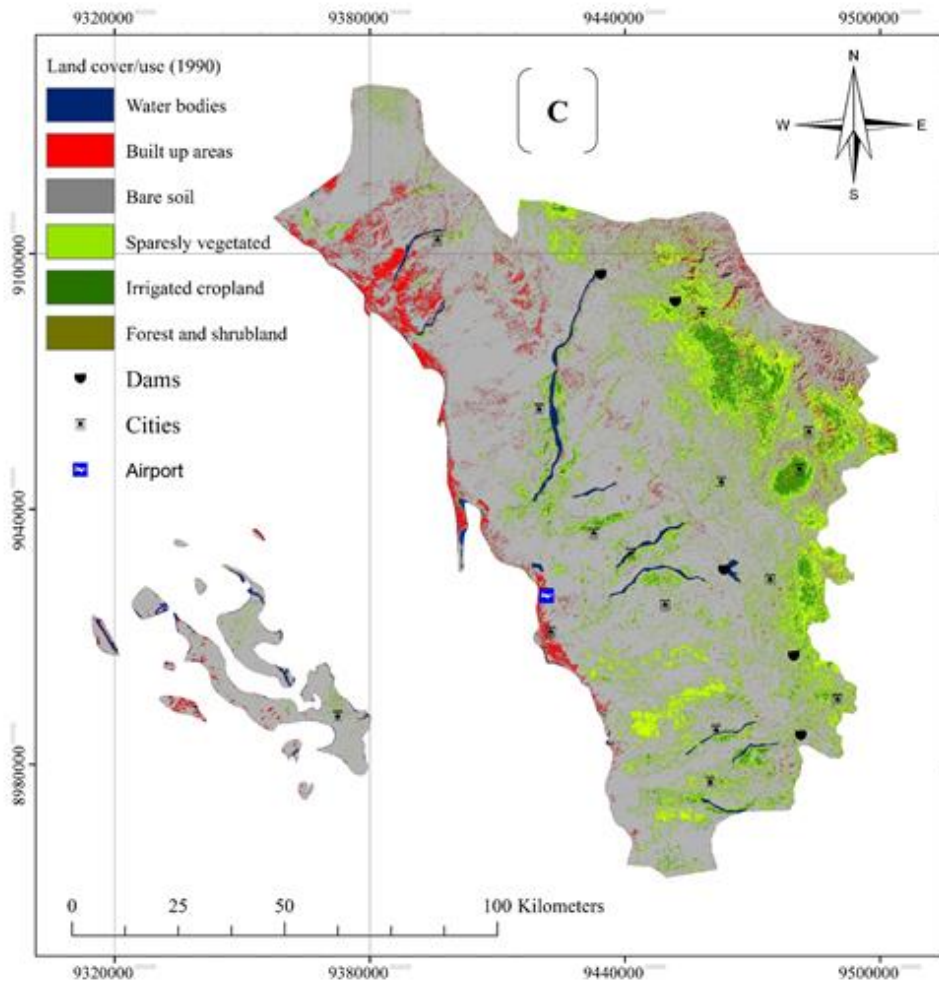
Impacts of climate change and human activities to the study area have not been documented even though environmental changes such as plant distributions have been going on for years. We have analyzed results of a survey based on questionnaire we developed with local farmers about possible environmental and social impacts of climate change and LUC on the study area. The local residence's responses strongly advocated the high social and environmental costs associated with human activities such as mining of oil, LUC, and dams in the region are: loss of biodiversity and fertile soil, air and water pollution, degradation of farmland, damage to aquatic ecosystem, increased desertification and a decline in vegetative cover. Results of the analysis presented in

Figures 4.2(a) and 4.2(b) reveal a large expansion in urban areas after 1970s, and a decline in irrigated cropland, forest, shrubland, and sparse vegetation cover during 1970s and 1980s, respectively. During this period, many farmers left their agricultural land and migrated to cities for jobs, which led to a decline in vegetative cover and lumbering for industrial uses. The construction of five dams in 1970, 1998 and 2000 to store rainwater for agriculture activities and domestic purposes affected the biodiversity of the region, and significantly increased the LUC. The extent of LUC distribution over the study period (1970-2014) is presented in Table 4.4. Urbanized areas increased from 106.82 km² (0.81% of total area) in 1970 to 139.39 km² (1%) in 1980, a 25% increase in 10 years, while sparsely vegetated land declined dramatically from 5290.94 km² (40%) in 1970 to 2817.407 km² (21%) in 1980.

There was an increase in areas of water bodies from 70.47 km² (0.5% of the total area) in 1970 to 100.90 km² (0.8%) in 1980 due to the construction of rainwater retention facilities, which helped farmers to recover loss of agricultural land in later years. From 1980 to 1990, areas of bare soil increased from 9395.7 km² to 10147.2 km², urbanized areas increased from 1.057% to

4% of the total area, but areas of forest and shrubland significantly decreased from 278.3 km² to 23.4 km², which fortunately was restored to 221.7 km² due to conservation efforts implemented in 2000. Sparse vegetative cover continued to decline, losing more than 975.0 km² of its 1980 area to 1842.2 km² in 1990 and to 1085.4 km² in 2000, which marginally increased between 2010 and 2014 to 1120.0 km² in 2014. Relative to 1980, irrigated cropland increased significantly from 450.4 km² in 1980 to 1963.7 km² over the 1990-2014 period. Table 4.5 shows LULCC (%) in the study area for each subperiod and the 1970–2014 period. Spatial patterns of LUCs in the Jizzan Province for 1970, 1980, 1990, 2000, 2010, and 2014 given in Figure 4.2 show that bare soil and sparse vegetative cover were dominant, but over the years urbanization expanded in the coastal regions. From 1990 to 2014, urbanized areas replaced most of the water bodies and extended into coastal areas, and consequently areas of bare soil and water bodies declined markedly. The rate of urban expansion since 1970s was more than 53.4 km² yr⁻¹.





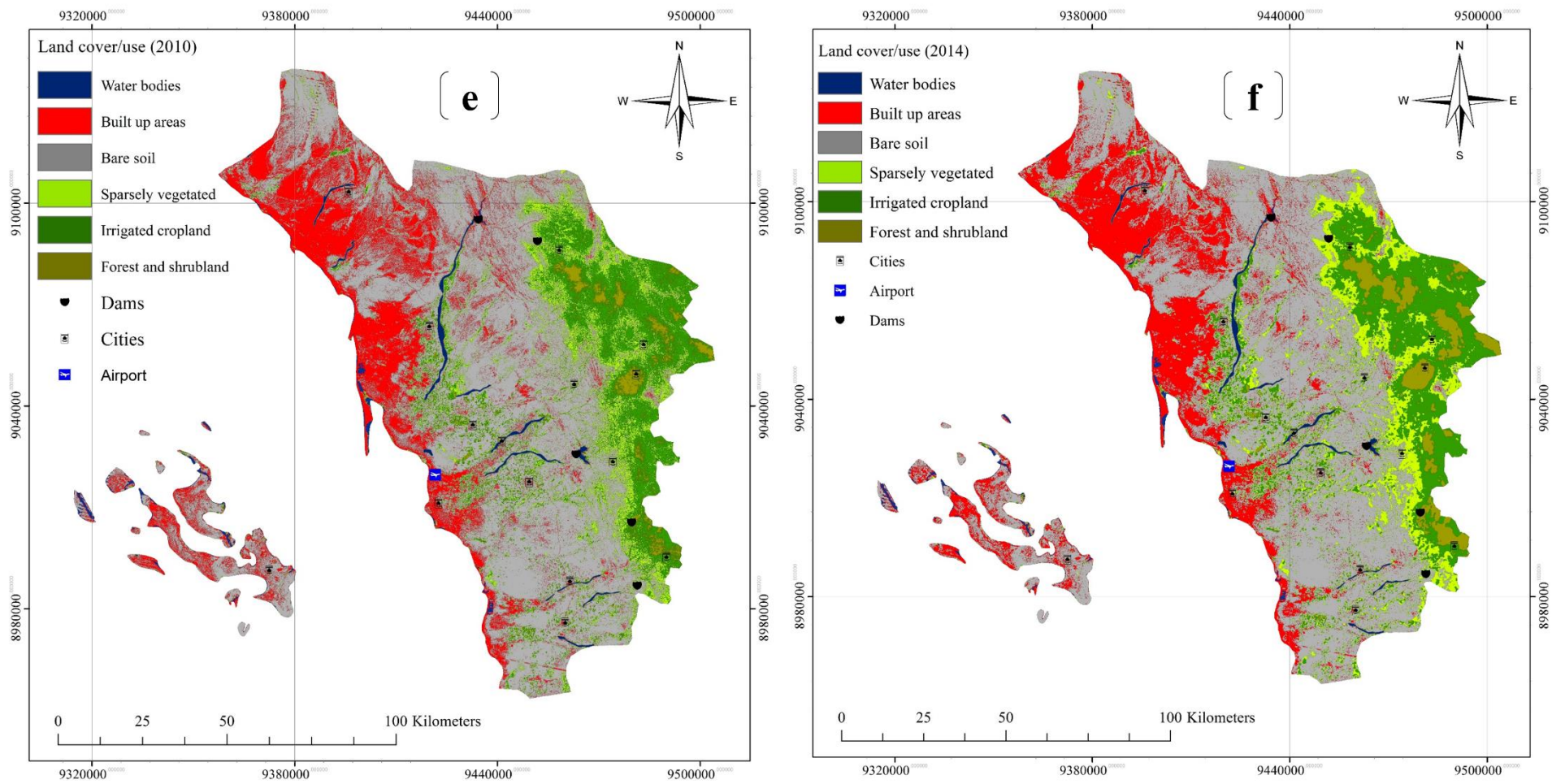


Figure 4.2 Spatial distribution of LULCC in Jizzan Province a) 1970, b) 1980, c) 1990, d) 2000, e) 2010, and f) 2014.

Table 4.4 Area measurements of land-cover /use within Jizzan province for each subperiod and the full period 1970–2014

Code	Land cover/use class	1970		1980		1990		2000		2010		2014	
		Area (Km2)	Area (%)										
1	Water bodies	70.470	0.535	100.918	0.766	86.573	0.657	84.677	0.642	78.027	0.592	73.362	0.557
2	Built up areas	106.820	0.810	139.392	1.057	532.915	4.043	1399.518	10.617	2223.766	16.870	2456.430	18.635
3	Bare soil	5776.400	43.820	9395.668	71.276	10147.186	76.981	9608.147	72.891	7593.928	57.611	7020.124	53.256
4	Sparsely vegetated	5290.940	40.137	2817.407	21.373	1842.248	13.976	1085.457	8.235	1129.829	8.571	1120.279	8.499
5	Irrigated cropland	1065.295	8.081	450.4329	3.417	549.1719	4.166	781.9578	5.932	1792.368	13.598	1963.683	14.897
6	Forest and shrubland	872.1918	6.616	278.3241	2.111	23.4	0.178	221.7375	1.682	363.5766	2.758	548.0865	4.158

Table 4.5 Detected land cover/use gains and losses within Jizzan province for each subperiod and the full period 1970–2014

Code	Land cover/use class	1970-1980		1980-1990		1990-2000		2000-2010		2010-2014	
		Change (Km ²)	Change (%)								
1	Water bodies	-30.45	-0.23	14.35	0.11	1.90	0.01	6.65	0.05	4.67	5.98
2	Built up areas	-32.57	-0.25	-393.52	-2.99	-866.60	-6.57	-824.25	-6.25	-232.66	-10.46
3	Bare soil	-3619.27	-27.46	-751.52	-5.70	539.04	4.09	2014.22	15.28	573.80	7.56
4	Sparsely vegetated	2473.53	18.76	975.16	7.40	756.79	5.74	-44.37	-0.34	9.55	0.85
5	Irrigated cropland	614.86	4.66	-98.74	-0.75	-232.79	-1.77	-1010.41	-7.67	-171.32	-9.56
6	Forest and shrubland	593.87	4.51	254.92	1.93	-198.34	-1.50	-141.84	-1.08	-184.51	-50.75

Where (-) gain, (+) loss

LUC had significantly affected forest, shrubland and vegetation covers, which in turn might have affected ecosystems, natural habitat and biodiversity of the region. Human alteration of land use from natural vegetation and forests to other land uses typically results in a loss, degradation, and fragmentation of ecosystems, which tend to have negative effects on the biodiversity of the region, as also reported by local residents impacts over the years. Because of depleted groundwater resources, rainwater harvesting dams were constructed which substantially captured the surface water. The regional change in hydrology due to human activities resulted in the loss of forest covers, altered landscape patterns and ecosystem of the region.

4.3.2 Anthropogenic climate change and human activities

We applied Pettit's test to detect anthropogenic change points of the region, which reveals statistically significant change points in monthly temperature and temperature anomaly in 1968. The mean temperature anomaly increased significantly from $-0.206\text{ }^{\circ}\text{C}$ between 1900 and 1968 (Mb: average before the change point) to $0.326\text{ }^{\circ}\text{C}$ (Ma: average after the change point) between 1968 and 2010 (Table 4.6). The Mann–Kendall trend test also show a statistically significant warming trend of $0.24\text{ }^{\circ}\text{C}$ per decade since 1968, which reflects the impact of anthropogenic climate change and LUC such as decline in forest, shrubland, and sparsely vegetated land since 1970 (Figure 4.3) due to agricultural development which reached its zenith in 2000s. Similarly, from Pettitt's test applied to monthly precipitation anomaly data for 1948-2014, a statistically significant change point was detected in 1967, as the mean precipitation anomaly declined from 7.9 mm/yr (Mb= 7.9 mm/yr) between 1948-1967 to -3.12 mm/yr (Ma= -3.12 mm/yr) between 1967-2010 (Figure 4.4). Trend analysis shows a statistically significant negative trend in precipitation anomaly of 12.2 mm/decade (Table 4.6).

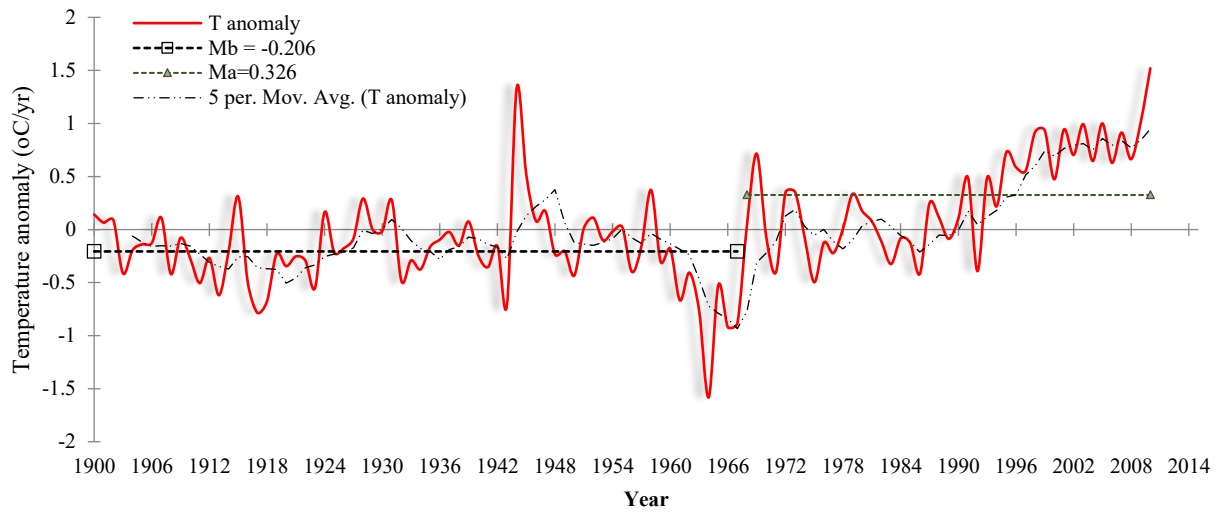


Figure 4.3 Temperature anomaly and trend

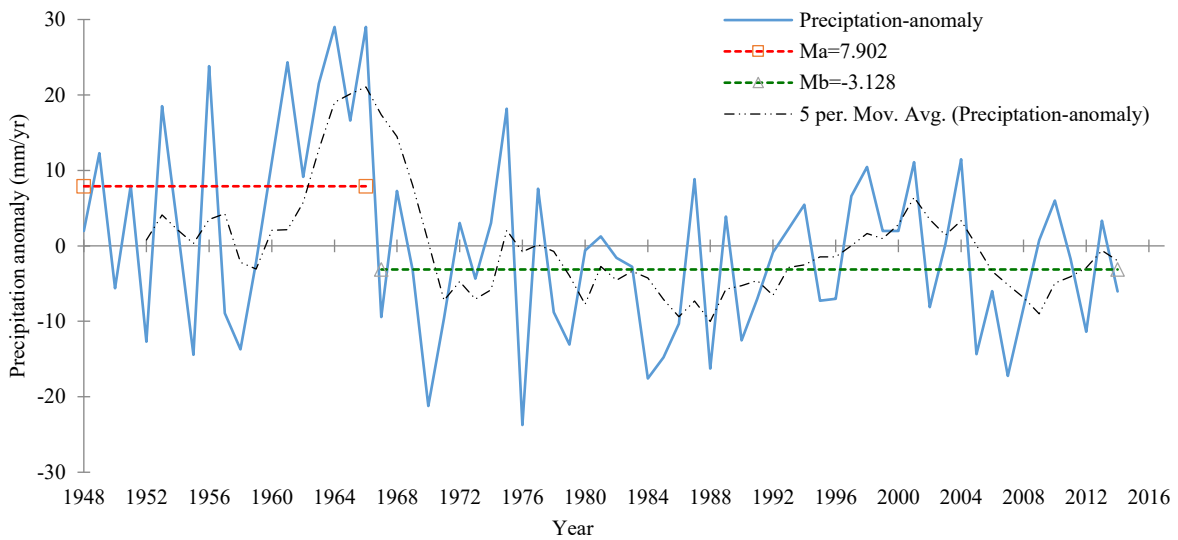


Figure 4.4 Precipitation anomaly and trend

Table 4.6 Change point and trend detection

	Pettitt test				Mann-Kendall test				Mb	Ma
	Years	t	P	trend	Tau	Sen's slope	P	trend		
T anomaly	1900-2010	1968	< 0.0001	Ha	0.434	0.024	< 0.0001	+	-0.206	0.326
Precipitation anomaly	1948-2014	1967	0.0001	Ha	0.133	-1.22	< 0.0001	-	7.9	-3.12
CO ² emissions (Kt)	1960-2015	1985	< 0.0001	Ha	1	9434	< 0.0001	+	78660	337701
Other greenhouse gas emissions HFC, PFC and SF6 (Kt)	1971-2012	1984	< 0.0001	Ha	0.6	48.85	< 0.0001	+	884.4	2025
Total greenhouse gas emissions (Kt of CO ² equivalent)	1971-2012	1991	< 0.0001	Ha	0.94	7809	< 0.0001	+	196902	348896

Given rising temperature anomalies are mainly attributed to increasing concentrations of greenhouse gases due to burning of fossil fuels and the manufacture of cement (IPCC, 2013), we have analyzed changes to greenhouse gas emissions data between 1960 and 2015. We detected a statistically significant change point in CO₂ emission data in 1985, such that CO₂ emissions increased from 78660 Kt/yr between 1960 and 1985 to 337701 Kt/yr between 1985 and 2015 (Figure 4.5), because of increasing consumption of solid, liquid, and gas fuels and flaring after 1985. A trend analysis shows a statistically significant positive trend in CO₂ emissions of 94340 Kt/decade (Table 4.6).

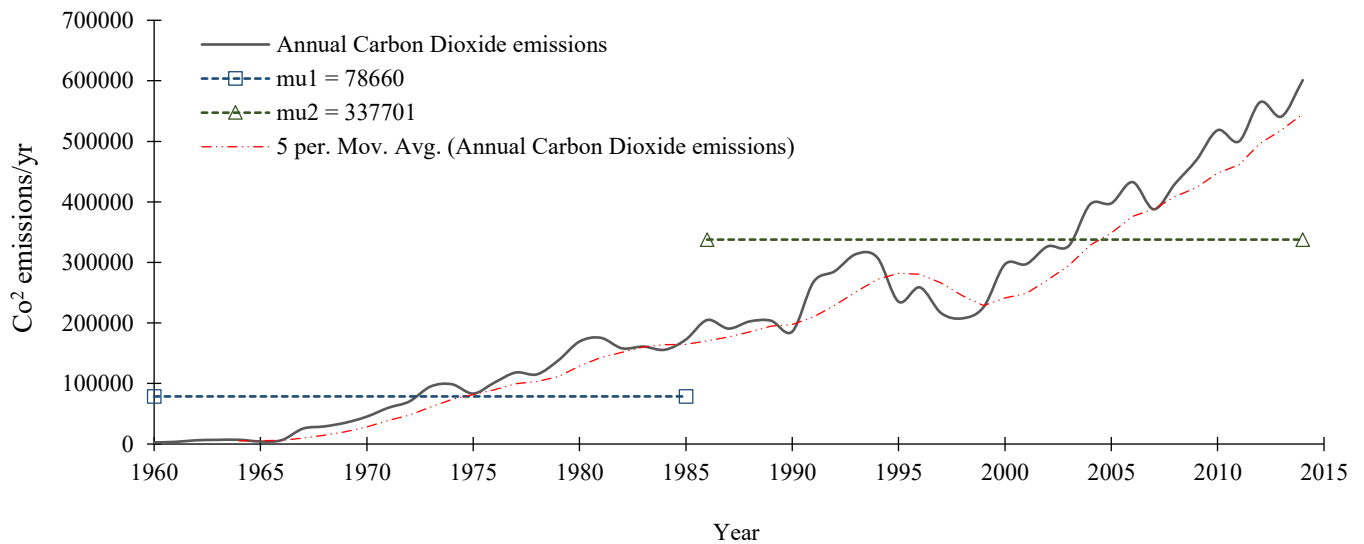


Figure 4.5 Carbon dioxide emissions timeseries and trend analysis

Other greenhouse gases produced by industrial processes are such as hydrofluorocarbons (HFC), perfluorocarbons (PFC), and sulfur hexafluoride (SF₆), as presented in Figure 4.6. These greenhouse gases also show statistically significant change point in 1984, where the mean annual HFC, PFC, and SF₆ emissions increased dramatically from 884.4 Kt/yr between 1971 and 1984 to 2025 Kt/yr between 1984 and 2012, and an overall statistically significant positive trend of 488.5 Kt/decade. The warming effects of these greenhouse gases and LUC such as urbanization,

deforestation and construction of dams in the study area had resulted in the consistent, observed positive temperature trend since the mid-Twentieth Century. Figure 4.7 shows the time series of total greenhouse gas emissions that include all anthropogenic sources, which show a statistically significant change point in 1991, with positive trend of 78090 Kt/decade (Table 4.6).

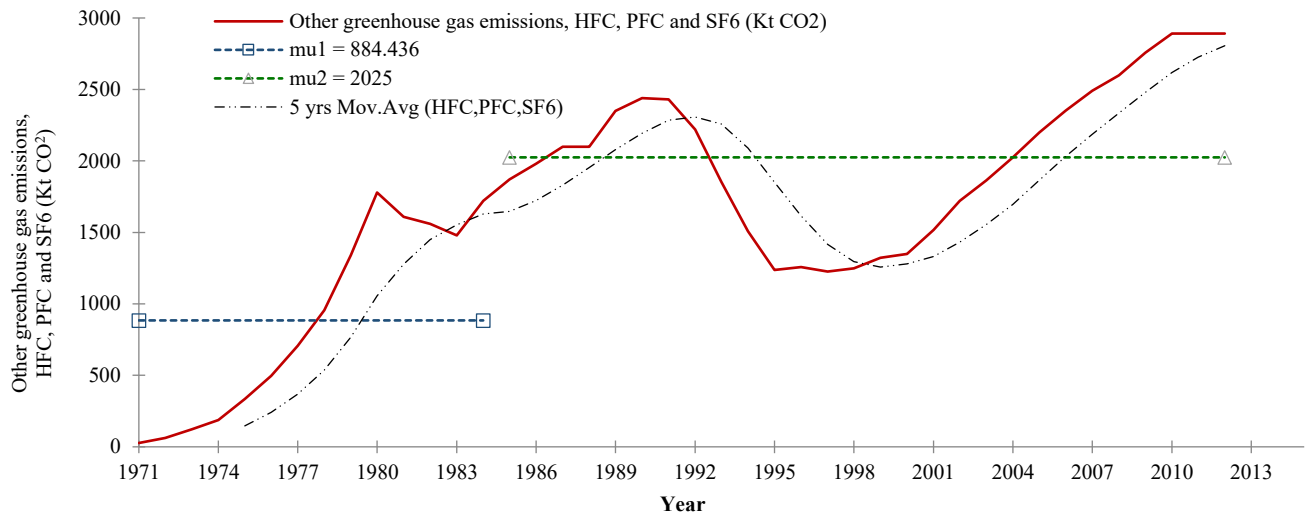


Figure 4.6 Other greenhouse gas emissions, HFC, PFC, and SF6

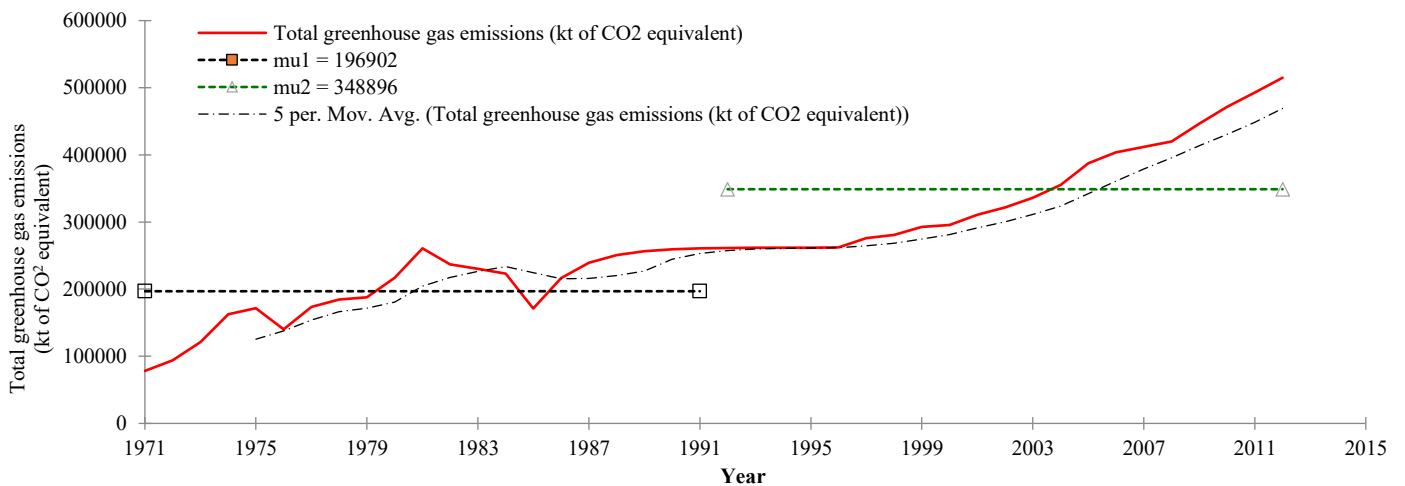


Figure 4.7 Total greenhouse gas emissions including all anthropogenic sources

From Figure 4.8(a) that shows the historical and projected change in temperature anomalies between 1900 and 2100, it can be seen that significant warming trend started to occur in 1970s attributed to human activities such as industrial boom, deforestation, rapid urbanization and increase in greenhouse gas emissions. Future temperature anomalies in the study area simulated

by global climate models of CMIP5 and IPSL-CM5A-LR under three climate scenarios (RCP4.5, RCP6.0 and RCP8.5) project a continuous warming trend between 2014-2100. Figure 4.8(b) shows the time series of the average temperature anomaly simulated by all climate models between 1900 and 2100 with a statistically significant change point that occurred in 1999 and a projected warming trend of $0.19\text{ }^{\circ}\text{C}/\text{decade}$.

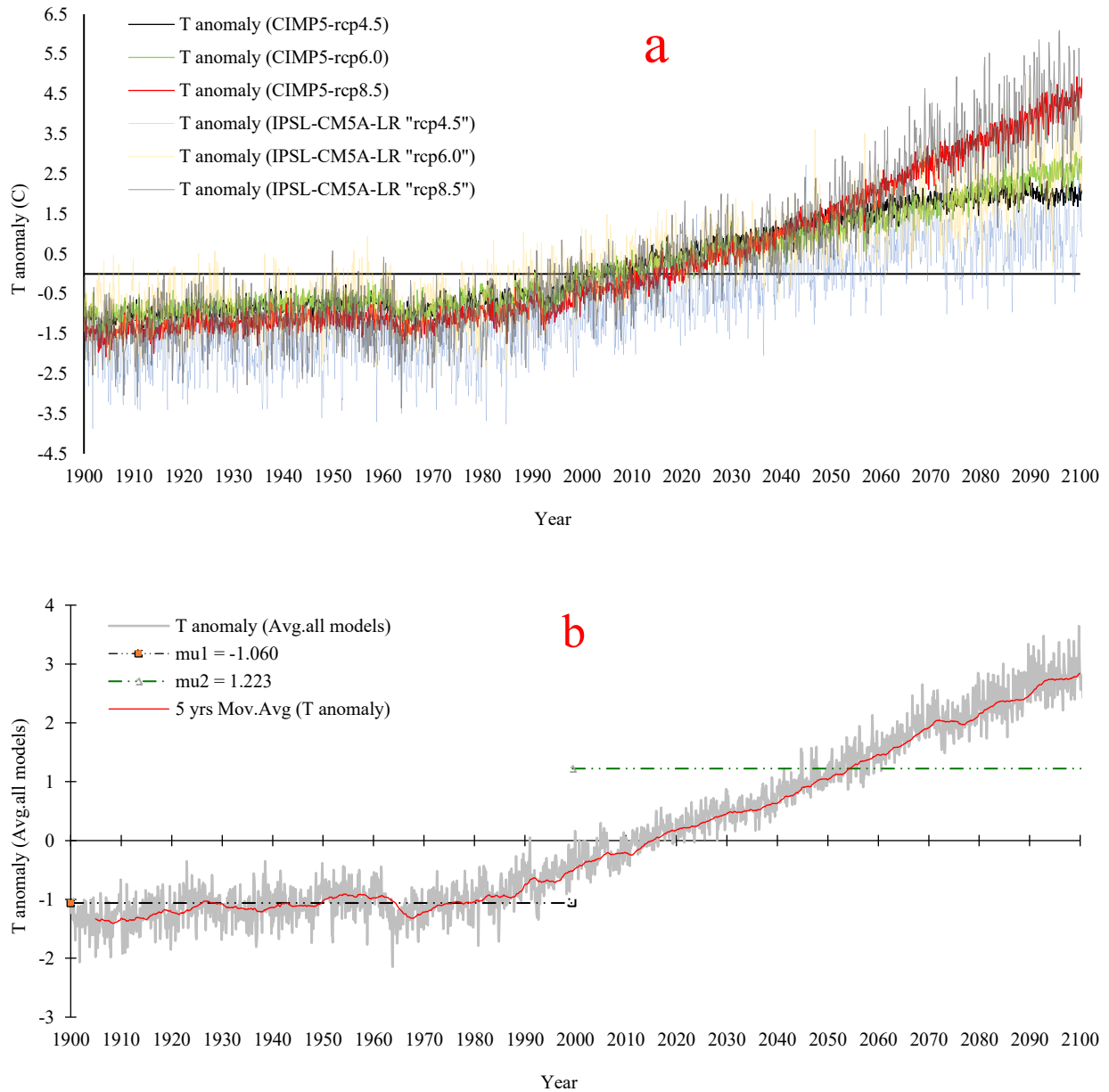


Figure 4.8 Projection of temperature anomaly (a) average temperature anomaly trend (b)

The warming trend in the study area varies spatially with the nature of land use. We compare the projected change with the projected LUC patterns over the study area. As a warming trend is expected to continue, especially in the mountains areas where the warming trend is projected at 0.55 -0.83 °C/decade between 2014 and 2050. In south and eastern parts of the Jizzan Province, warming is projected at 0.55 °C/decade (Figure 4.9(b)), where Ragab and Prudhomme (2002) projected that the temperature may increase by 1.5–2.5°C (0.41-0.7 °C/decade) in 2050. By 2075, mountains areas and its surroundings are projected to experience an increase in the mean annual temperature by 4.2-5 °C, a warming trend of 1.25-1.38 °C/decade between 2050 and 2070, while the temperature of south and western parts of Jizzan province is projected to increase by 2.3 to 3.3 °C, a warming trend of 0.63-0.92 °C/decade between 2050 and 2075 (Figure 4.9(c)).

The mean annual precipitation of Jizzan ranges spatially from 77 to 272 mm/year (Figure 4.10(a)) with mountainous regions receiving the highest amount of 179-272 mm/year, followed by northeastern and northwestern regions with an annual rainfall ranging from 140 to 272 mm/year. As expected, high spatial variability of rainfall in Jizzan also means that Jizzan has high hydrologic variability (e.g., Jiang et al., 2014; Mwale et al., 2009). However, the annual rainfall of Jizzan projected to 2050 (Figure 4.10(b)) is expected to decline by 6% in southeastern regions of Jizzan, and by 3% in northwestern, eastern, and southwestern regions which are occupied by built-up areas, crops, forest, and bare soil. The negative trend is projected to worsen from 2050 to 2075 (Figure 4.10(c)), by as much as 8% in the mean annual rainfall in northwestern, eastern, and southwestern regions. However, the negative trend is projected to be only 2% in both the southeastern and central regions.

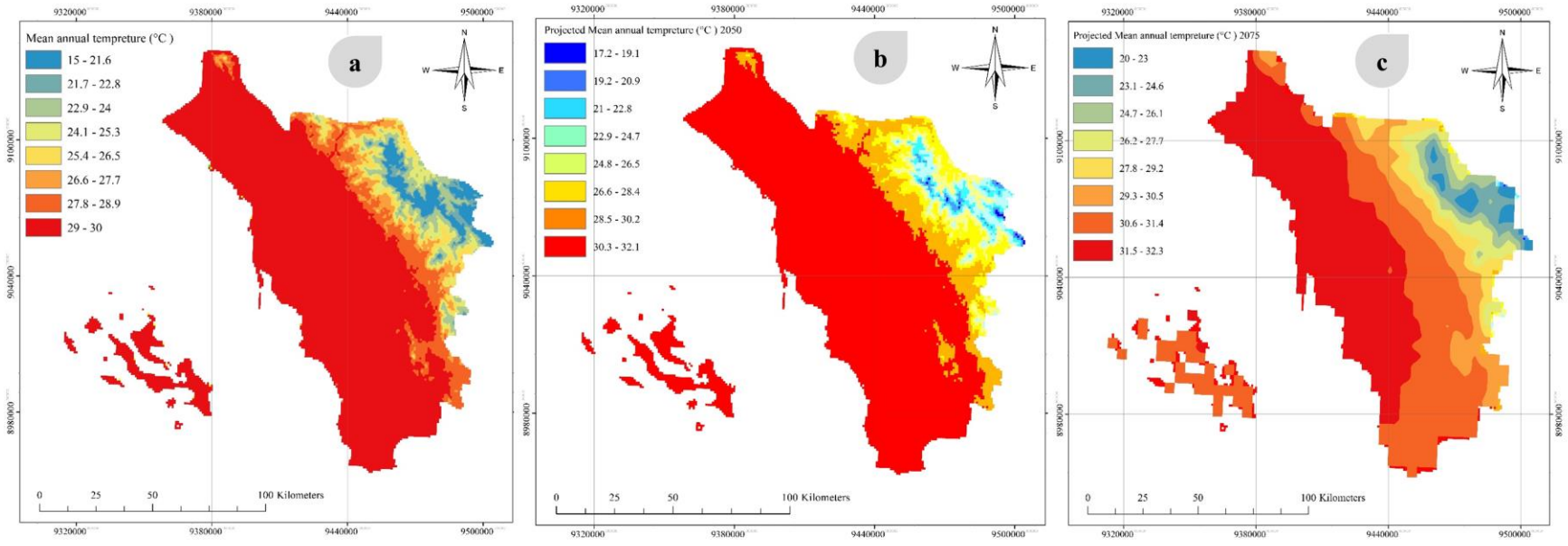


Figure 4.9 Average annual temperature (a) and Future projection in 2050 (b) future projection in 2075 (c)

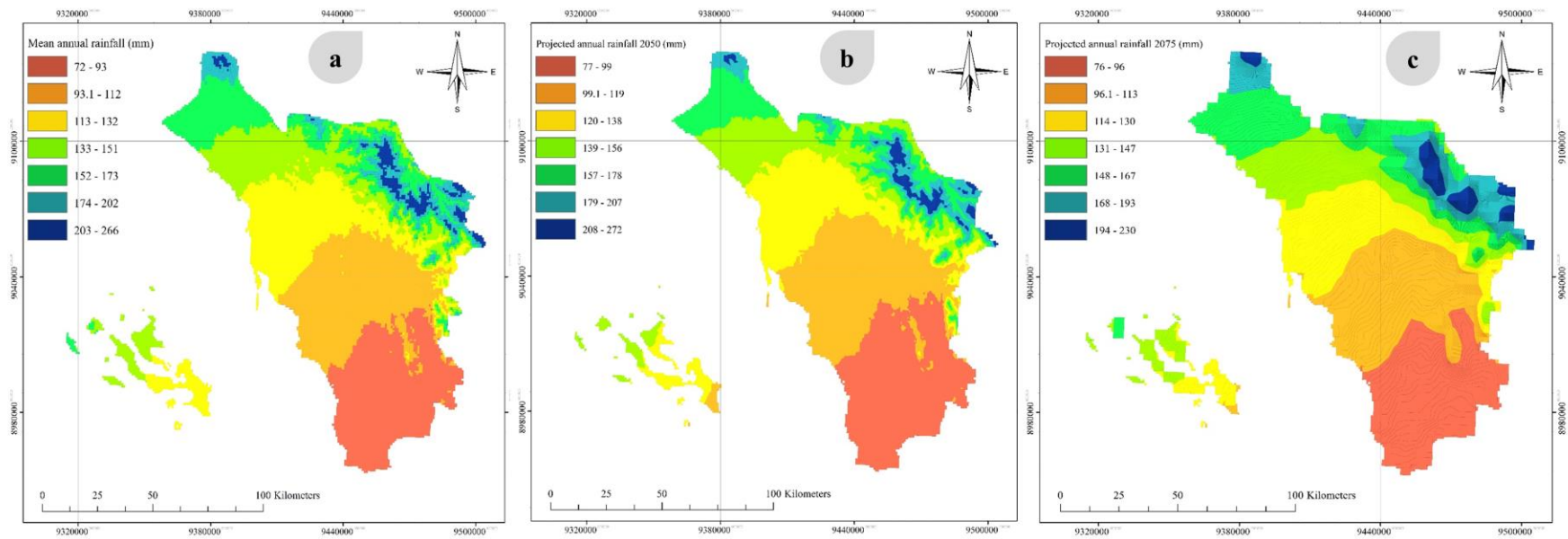
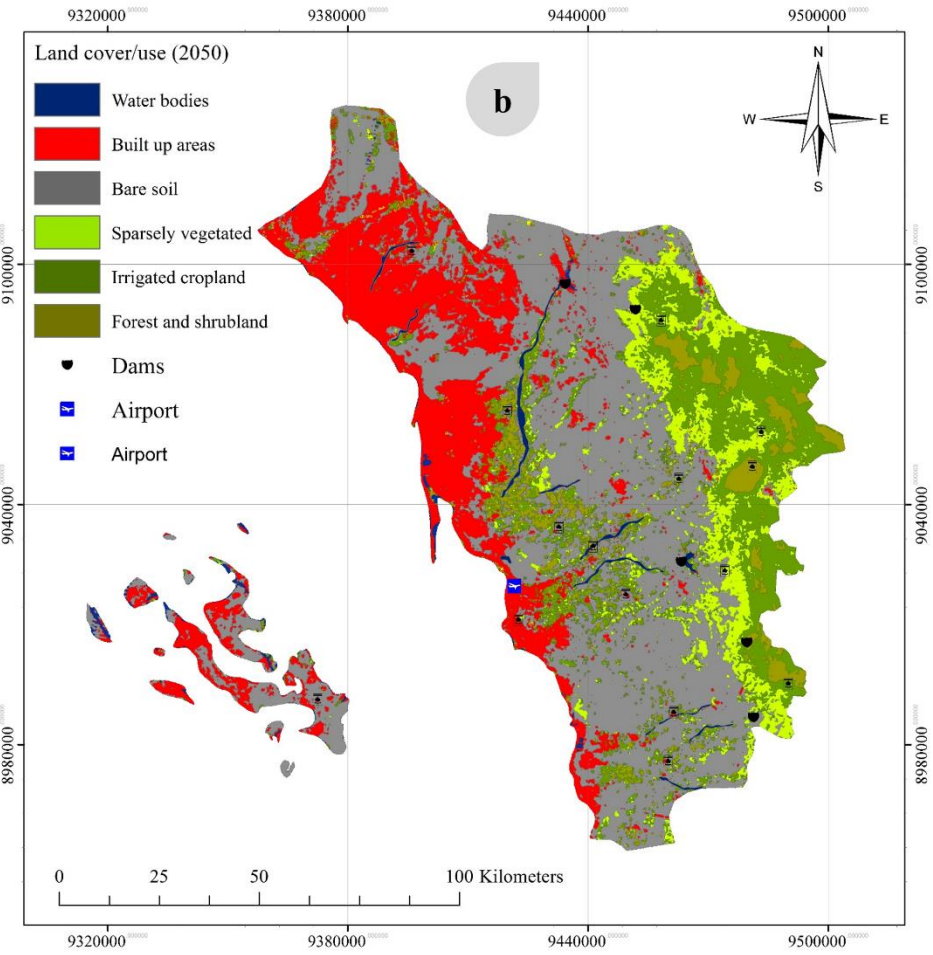
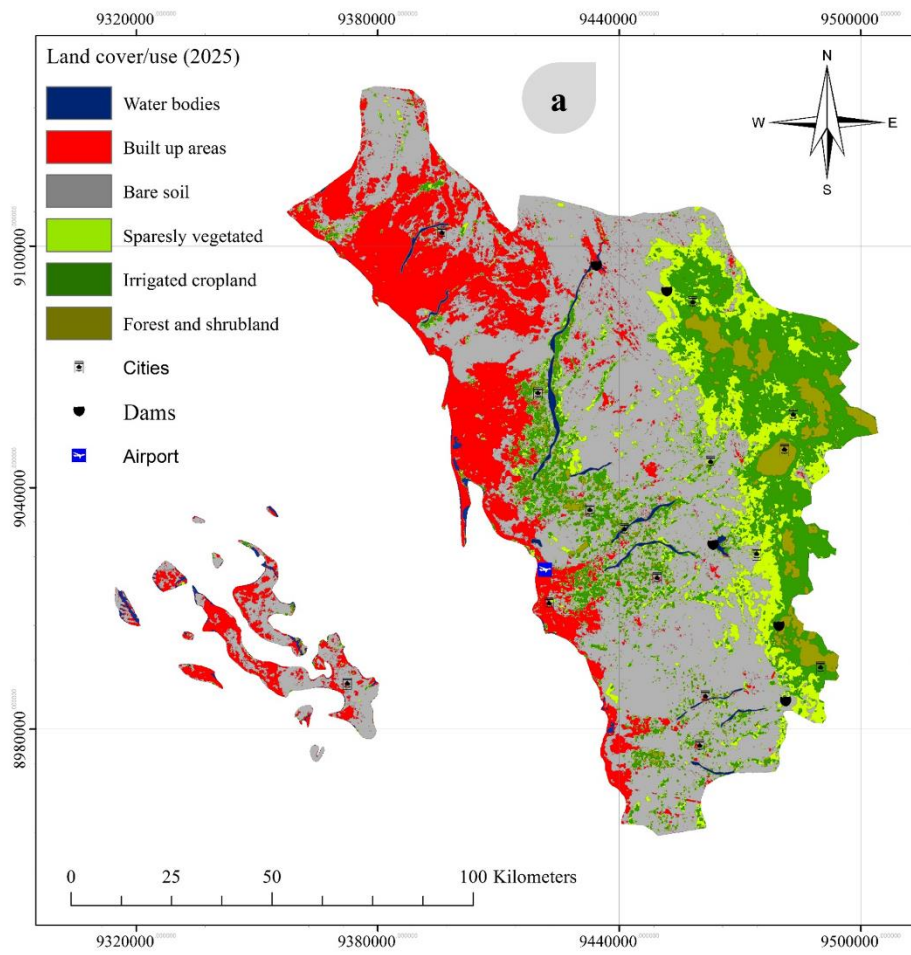


Figure 4.10 Average annual precipitation (a) and Future projection in 2050 (b) future projection in 2075 (c)

4.3.3 Land use change prediction

The land use of Jizzan is projected to increase in urbanization and irrigated cropland in 2025, 2050, 2075, and 2100 as presented in Table 4.7 and Figure 4.11. The bare soil area is projected to decrease from 7020.1 km² in 2014 to 6498.4 km² in 2025, while water bodies areas are projected to decrease from 73.4 km² in 2014 to 63.8 km² in 2025. In contrast, urban areas are projected to increase from 2456.4 km² in 2014 to 2640.6 km² in 2025, and then to 2732.9 km² in 2050. Similarly, sparse vegetation, and forest and shrubland are projected to increase from 1120.3 km² and 548.1 km² in 2014 to 1169.3 km² and 648.5 km² in 2025, respectively. In addition, irrigated cropland is projected to substantially increase from 1963.6 km² in 2014 to 2161.2 km² in 2025.

By 2050, irrigated cropland is also projected to expand from an area of 2161 km² in 2025 to 2279.0 km² in 2050, or a projected increase of 5% (Table 4.8). In contrast, bare soil is projected to decrease by 5%, sparse vegetative cover to decrease by 1%, but water bodies are projected to decrease significantly by almost 8% due to continued urbanization. For forest and shrubland, the model projected a 17% increase between 2025 and 2050. By 2075, the model projected urban areas, irrigated cropland, forest, and shrubland to increase by 0.8%, 1.5%, and 3%, respectively, but water bodies, bare soil, and sparsely vegetated land are projected to decline by 15%, 1%, and 0.2%, respectively. However, between 2075 and 2100, urban areas, irrigated cropland, forest and shrubland, and sparsely vegetated areas are projected to increase by 1%, 4%, 0.5%, and 1% respectively. In contrast, water bodies are projected to decrease by 13% of its area in 2075, a slight decrease is also projected in bare soil by 2% of its area in 2075 (Table 4.8).



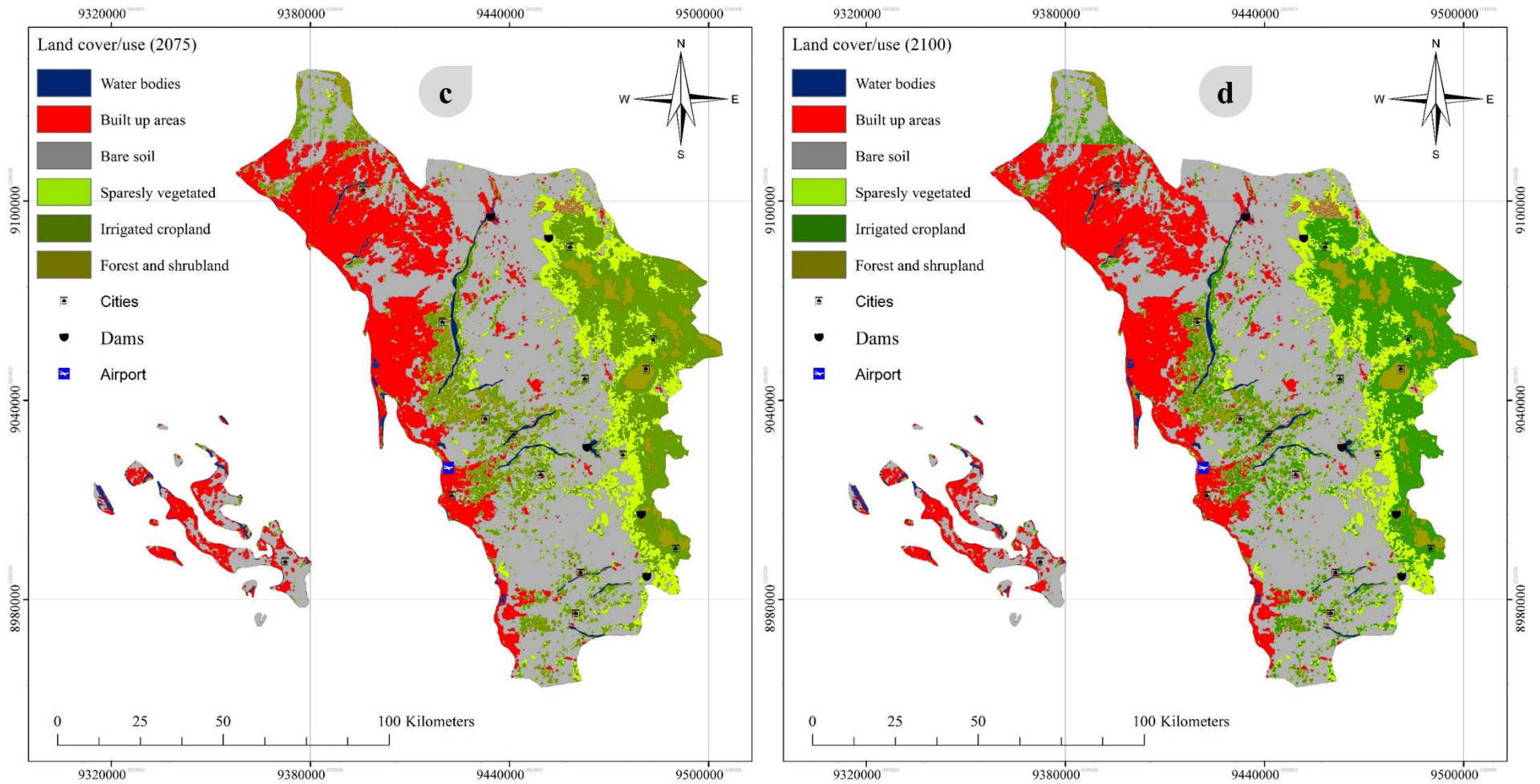


Figure 4.11 Spatial distribution of projected LULC a) 2025, b) 2050, c) 2075, d) 2100

Urbanization further exacerbated the climate change impact of rising greenhouse gases in the province, as warming trend became statistically significant after 1970, which happened to be the year urbanization began to exhibit increasing trend. Spatially, the annual temperature is projected to increase most significantly within urban areas and mountainous regions by 2050 and 2075. Mountainous areas are projected to be much warmer because the cooling effect of evapotranspiration is significantly reduced by deforestation, which were previously occupied by shrubland and forest reflects the impacts of deforestation in the warming trend.

Table 4.7 Area measurements of land cover/use projection 2025, 2050, 2075, and 2100

Code	Land cover/use class	2025		2050		2075		2100	
		Area (Km2)	Area (%)						
1	Water bodies	63.800	0.484	58.900	0.447	50.102	0.380	43.669	0.331
2	Built up areas	2640.653	20.032	2732.886	20.732	2753.937	20.892	2790.300	21.168
3	Bare soil	6498.476	49.298	6164.481	46.765	6100.740	46.281	5970.401	45.292
4	Sparsely vegetated	1169.357	8.871	1182.924	8.974	1180.068	8.952	1189.728	9.025
5	Irrigated cropland	2161.152	16.395	2279.9475	17.296	2313.637	17.552	2400.4565	18.210
6	Forest and shrubland	648.5265	4.920	762.8256	5.787	783.4806	5.944	787.4091	5.973

Table 4.8 Expected gains and losses during projected period (2014-2100)

Code	Land cover/use class	2014-2025		2025-2050		2050-2075		2075-2100	
		Change (Km2)	Change (%)						
1	Water bodies	9.562	13.034	4.900	7.680	8.798	14.937	6.433	12.840
2	Built up areas	-184.223	-7.500	-92.233	-3.493	-21.050	-0.770	-36.363	-1.320
3	Bare soil	521.648	7.431	333.995	5.140	63.741	1.034	130.339	2.136
4	Sparsely vegetated	-49.078	-4.381	-13.567	-1.160	2.856	0.241	-9.660	-0.819
5	Irrigated cropland	-197.469	-10.056	-118.7955	-5.497	-33.6895	-1.478	-86.8195	-3.753
6	Forest and shrubland	-100.44	-18.326	-114.2991	-17.624	-20.655	-2.708	-3.9285	-0.501

Where (-) gain, (+) loss

4.3.4 Impacts of land use change and climate change on Fauna and Flora

Results collected from the field survey and from the questionnaire reveal a strong agreement between our study and local residents, that increasing emissions of greenhouse gases and human activities have led to climate warming in the study area and a significant decline in its ecosystem services. For their survival, in the past 50 years, many wild animals had migrated to cities and villages in search of water, which may jeopardize human health and life. LUC due to urbanization of rural and mountainous areas have likely contributed to the decline in annual rainfall at about 12.2 mm/decade and the biodiversity of these areas. For example, the Arabian Baboon (*Papio hamadryas*) populations were partially controlled by their natural predators, leopards (*Panthera pardus*) and striped hyenas (*Hyaena hyaena*) but these predators have been hunted to extinction in these regions which have the habitats needed by the predators. On the other hand, these areas are facing serious threats of loosing of their habitats due to major agricultural expansion and irrigation projects (Biquand et al., 1992 and Winney et al., 2004). In other words, aforementioned human activities have led to significant degradation of the environment, impacts on the Afrotropical biodiversity of the region, coastal marine ecosystems, fragmentation and destruction of habitats.

The draining of coastal areas for tourism and ornamental projects have caused marked declines of many species of mammals and birds that rely on this habitat for food, either being eliminated or have migrated to other areas. Wading shorebirds, for example, have lost their niche due to the urbanization of most coastal areas in the Jizzan Province. The Farasan Islands, the first conservation protected area in Saudi Arabia, is home to the endangered Arabian gazelle, *Gazella arabica* (Lichtenstein), and serves as a rest area for many migratory bird in their migration route between Europe, northern Asia, and Africa. Farasan Ghazal is a distinctive subspecies of well-known Arabic gazelle, native to the islands. For the last fifty years, this island supported large

populations of Farasan Ghazal because of low human impacts and consistent high annual rainfall (Thouless, 1991; Thouless and Al Bassri, 1991). Unfortunately, overhunting and a gradual decrease in the annual rainfall has led to a major collapse of this animal's population.

LUC has probably been a stronger driver of twentieth-century changes in wild plants and animals than climate change (Parmesan and Yohe, 2003). LUC pattern showed a large decline in flora and natural vegetation cover in the study area partly because rainwater, the only source of water that supports fauna and flora, has been decreasing in recent years. Moreover, significant deforestation, rapid urbanization, increased greenhouse gases have direct effects in plant distributions, as discussed before. Another impact of climate change is more ET loss, which in turn decrease the soil moisture and affecting plant growth (Narasimhan and Srinivasan, 2005).

The annual ET time series estimated from local climatic factors for the study area over 1950-2014 (Figure 4.12) has a statistically significant change point in 1975 with positive trend of 5.5 mm/decade. The rising trend in ET would increase plant stress and enhance drought conditions. The annual ET is also projected to increase significantly from 1500 mm/yr in 2014 to about 1850 mm/yr in 2100. If precipitation surplus, the net flux of water from the atmosphere to the soil surface is positive, it means wet soil; if it is negative, we will expect dry soil (Swenson and Wahr, 2006). Figure 4.13 shows a significant increase in water losses from the soil profile over time which means dry soil and it is expected to continue according to our future projection. Therefore, under diminishing soil moisture, warming trend and rapid urbanization, we expect the flora and natural vegetation cover in the study area to continue to decline in the 21st Century.

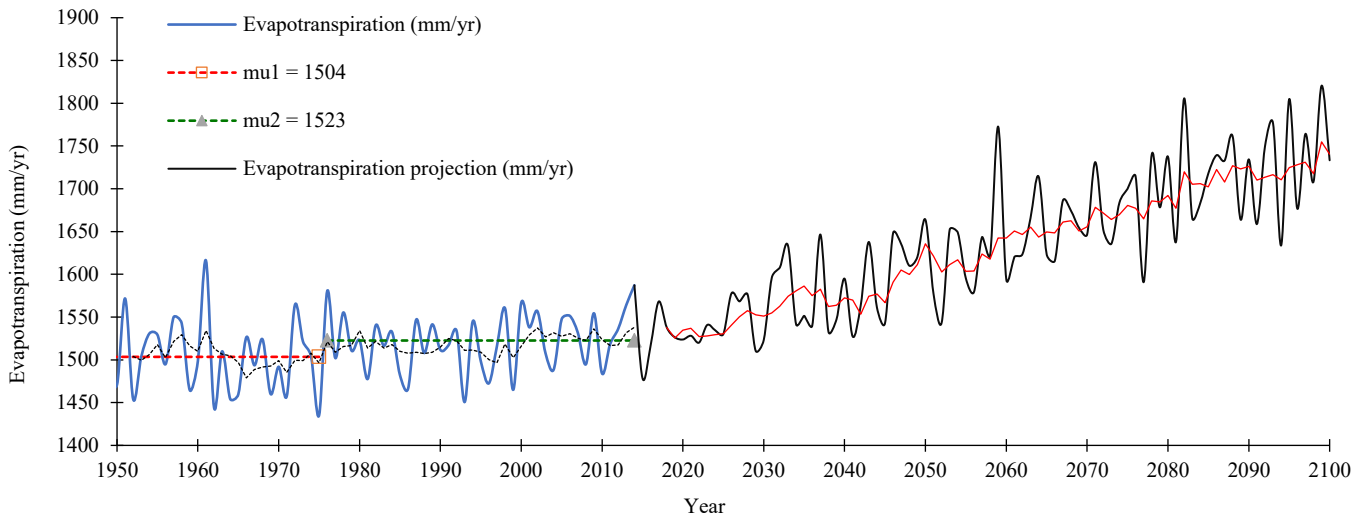


Figure 4.12 Annual Evapotranspiration trend and future projection

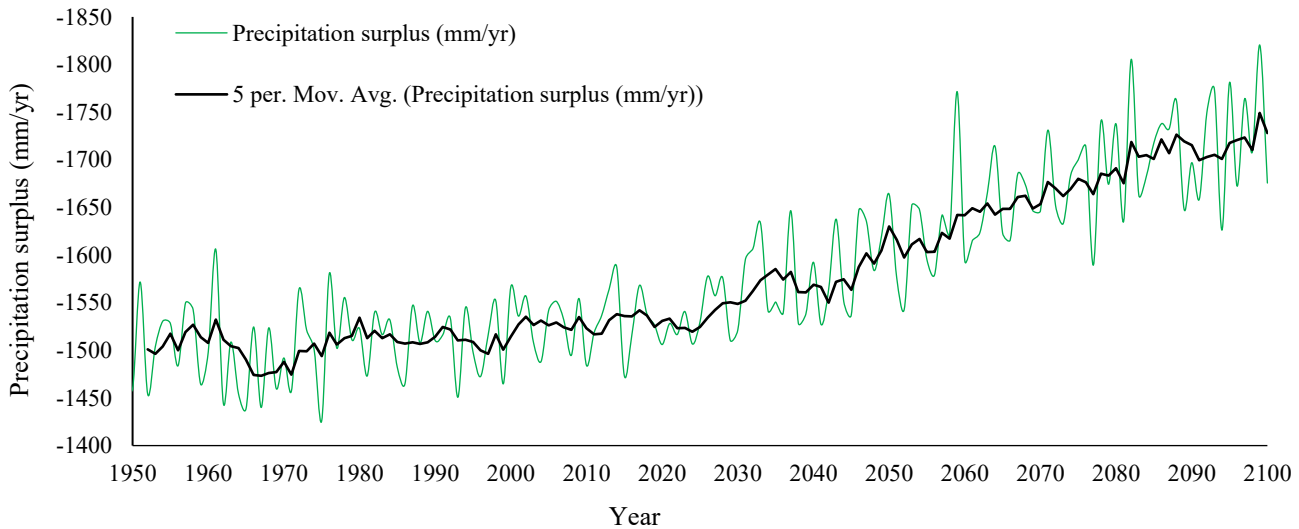


Figure 4.13 Annual precipitation surplus and future projection

4.4 Conclusions and recommendations

We investigated the impact of anthropogenic climate change and human activities such as LUC on the environment and ecosystem services in the Jizzan Province, Arabia. First, we used earth observation data of the Landsat satellite to derive historical, 1970-2014, land use maps of Jizzan. Next, we used a Markov-CA model to project the dynamics of its LUC pattern over 2014-2100 in response to human activities and their impacts on the study area's climate, environment, and water

resources. We applied Pettit's and Mann-Kendall tests to detect change points and to estimate trends of temperature data of 1900-2010 and precipitation data of 1948-2014 and their anomalies, respectively. We have also detected change points and estimated trends of data of CO₂ and several rare gases emitted between 1960 and 2015. Climate scenarios (RCP4.5, RCP6.0 and RCP8.5) of the study area projected by climate models of CMIP5 were used to project future warming in the study area between 2014-2100.

Urbanization and LUC has significant impact the ecosystems, biodiversity and natural habitats of the Jizzan province. In 1970s, human impacts were minimal. However, following the construction of rain-harvesting dams which capture most surface runoff, and with urban expansion at about 53.4 km² yr⁻¹ which extended into coastal regions, areas of forest, shrubland, sparse vegetative cover, bare soil and water bodies declined markedly over 1990–2014. Likely due to climate change impact and urbanization, a statistically significant change point was detected in the monthly temperature data of Jizzan in 1968 and a warming trend of 0.24 °C per decade after 1970. The precipitation data also had a statistically significant change point in 1967, but a negative trend of 12.2 mm/decade. Observed changes in the hydro-climatology of Jizzan are likely associated with significant LUC, such as urbanization and agricultural development (irrigated croplands) at the expense of vegetative cover, forest, shrubland, and sparse vegetative cover since 1970s.

A statistically significant change point was detected in CO₂ emissions data in 1985 and statistically significant positive trend of 94,340 Kt/decade. Other anthropogenic greenhouse gases mainly due to industrial processes also have a statistically significant positive trend of 488.5 Kt/decade. On a whole, total greenhouse gas emissions including all anthropogenic sources have been increasing at a statistically significant trend of 78,090 Kt/decade after 1991. Therefore, it is very likely that long-term increasing emission of greenhouse gases, and aforementioned

human activities have resulted in warming trends observed in the study area and globally. Future projection of temperature anomaly between 1900-2100 showed a statistically significant future warming trend of $0.19\text{ }^{\circ}\text{C}/\text{decade}$ after 1999.

The spatial distribution of the projected annual temperature in 2050 and 2075, also shows that the highest increase in temperature is within urban areas and the mountains regions. The increase in the warming trend in the mountains areas which were previously occupied by shrubland and forest reflects the impacts of deforestation in the warming trend. The warming trend in mountains regions is estimated at $0.55\text{ }^{\circ}\text{C}/\text{decade}$ between 2014 and 2050, and at $0.55\text{ }^{\circ}\text{C}/\text{decade}$ in south and eastern parts of Jizzan Province. Precipitation is projected to continue declining while LUC such as urbanization and irrigated cropland are projected to continue towards the end of the 21st Century.

In conclusion, to reduce the impacts of climate change and LUC, conservation plans for the Jizzan Province are essential to mitigate the significant impact human activities and global warming on the environment and ecosystem services of the study area in the 21st Century.

Chapter 5 Irrigation Water Management in arid regions of Middle East

5.1 Introduction

The Kingdom of Saudi Arabia (KSA) (24° N, 45° E) is the largest Arab country located in Western Asia. The kingdom has an area of 2.15 million square kilometers, but its mean annual rainfall is only about 112 mm/year (Mahmoud 2014 and Mahmoud et al., 2014). The agricultural sector of KSA equipped with modern irrigation technology has more than 1.1 million hectares of irrigated land (Department of Statistics and Information, 2008). Because of its arid climate, almost all agricultural lands are dependent on groundwater as the main source of water supply, which, however, is costly to withdraw (Mahmoud 2014 and Mahmoud et al., 2014). Major crops grown in Saudi Arabia include cereals (wheat, sorghum, barley, and millet), vegetables (tomato, watermelon, eggplant, potato, cucumber, and onions), fruits (dates, citrus, and grapes), and the forage crop of alfalfa. Agricultural water demand in KSA is very high, ranging between 83–90% of the total water demands during 1990–2009 (Chowdhury and Al-Zahrani, 2015). Therefore, evapotranspiration (ET) loss from irrigated lands is a key factor to consider for water supply to the agriculture sector (for example, as part of an early warning system). As large amount of irrigated water are lost through ET partly dependent on irrigation methods employed (Mahmoud and Alazba, 2016), accurate regional estimation of ET will be helpful for effective management of irrigation water.

Actual evapotranspiration (AET) reflects the crop's water need which consists of transpiration and evaporation (Alberto et al. 2014; Senay et al. 2017; Olivera-Guerra et al., 2018). AET can be estimated by: (i) in situ measurements using lysimeters or flux towers, (ii) crop coefficients approach (Allen et al. 1998), and (iii) remotely sensed data (Kalma et al. 2008) and models, which are either based on empirical / statistical or energy balance approaches. Using a spline model and

a linear sub-model dependent on elevation, McVicar et al. (2007) interpolated maximum (T_{max}) and minimum (T_{min}) air temperatures, wind speed (u) and vapor pressure (e_a) to estimate the radiative energy affected by the topography (i.e., elevation, slope and aspect), to calculate ET_o for each grid-cell of the Yellow River basin of China. The crop evapotranspiration (ET_c), defined as $K_c \times ET_o$, is commonly used to estimate crop water requirements (Doorenbos and Pruitt, 1977; Allen et al. 1998). Tables of K_c have been developed for crops of various growth stages, soil, and climate characteristics (Doorenbos and Pruitt, 1977; Allen et al., 1998). From the strengths and weaknesses of some potential evapotranspiration (PET) models developed for land covers commonly found in southwestern United States, Douglas et al. (2009) selected a PET model for Florida.

Recent studies that applied remotely sensed (RS) data to estimate spatio-temporally estimated AET and crop-water consumption are such as Duchemin et al. 2006; Er-Raki et al. 2007; González-Dugo and Mateos 2008; Er-Raki et al. 2010; Sánchez et al. 2010; Cruz-Blanco et al. 2014; Senay et al. 2017; and Parka et al. 2017. Similar seasonal patterns of vegetation indices and evapotranspiration have been found over annual crops (Bausch, 1995; Duchemin et al., 2006; Er-Raki et al., 2007). Agrometeorological monitoring of crop production is often done on a large spatial scale and small temporal resolutions using RS vegetation indices of visible and near-infrared wavelengths, such as normalized difference vegetation index (NDVI) to assess the leaf area index, LAI, biomass, or the absorbed photosynthetically active radiation/ soil-adjusted vegetation index. NDVI can be used to estimate real-time K_c given the high correlation between NDVI and K_c (Ray and Dadhwal, 2001; Er-Raki et al. 2007; González-Dugo et al. 2013; Mateos et al. 2013; Kullberg et al. 2017; Campos et al. 2017). Because of this close relationship between NDVI and K_c , NDVI has been widely used for vegetation monitoring, crop yield assessment and drought detection (Justice and Townshen, 2002). High NDVI values generally indicate more

photosynthetic activity. On the other hand, higher K_c due to higher temperature results in less soil water and therefore a decline in NDVI, while denser vegetation indices mean more ET losses which lower the land surface temperature (Boegh et al, 1999).

Integrating remote sensing data into soil water balance models are one of the most commonly used methods for estimating crop water requirements (Bodner et al., 2007). For instance, Campos et al. (2016a) estimated the total soil moisture in soil layers of southwestern Spain based on AET and time series of multispectral imageries of (vegetation cover). They developed a simple linear relationship between the NDVI and K_c . Such a relationship has been shown to be effective in mapping AET of crops (Campos et al., 2016a, b; Toureiro et al. 2017). Senay et al. (2017) developed historical ET maps for major irrigation districts in California, USA using Landsat images. Parka et al. (2017) estimated AET in northeast Asia using K_c , E_{To} , and surface soil moisture data from satellite images. They found that K_c estimated from NDVI data correspond well with observed K_c . Consoli and Vanella, (2014) mapped crop ET in southern Italy using a soil-water balance model driven with vegetation indices and climate data. The authors reported that this method has the potential to estimate crop water requirements and water management over large agricultural areas. Many earlier studies tend to estimate field scale crop coefficient and crop water requirements only for a specific crop, such as maize, soybean, cotton, and wheat (Duchemin et al., 2006; Irmak et al., 2013; Campos et al. 2017; Drerup et al. 2017; Rozenstein et al. 2018).

The development of models to estimate AET based on remotely sensed data applicable over large areas in arid regions of Middle East can be challenging because irrigation water requirements are essential but available water resources are limited. The objectives of the present study are: (1) To estimate Reference Evapotranspiration using data collected from meteorological stations and Geographic information system techniques on a grid-by-grid basis (2) Modeling K_c as a function

of 16-day time-series of MODIS-NDVI, (3) To estimate AET based on soil water balance, K_c , and ETo , and (4) To detect change points and trends in long-term average daily AET.

5.2 Material and methods

5.2.1 Description of the study area:

The study area is in three provinces of central Saudi Arabia: (1) Al-Riyadh, (2) Al-Qassim and (3) Hail Province (Figure 5.1). The Al-Riyadh Province has an area of 380497.8 km² and a population of 6,777,146 (2010), making it the second largest province of Saudi Arabia in terms of both area and population. It is located at the center of the Arabian Peninsula (24 ° 38' N and 46 ° 43' E) on a large plateau, with an arid climate and an annual rainfall ranging from 41 to 230 mm/year. The Al-Qassim Province is one of the largest agricultural areas of central Saudi Arabia at 647 m above sea-level (26.31° E and 43.77° N). The Hail Province in north-central Saudi Arabia borders provinces of Madinah, Tabouk, Northern Border, Riyadh and Qassim. Hail is largely agricultural with a significant production of grains, date, and fruits. A large percentage of the kingdom's wheat production comes from Ha'il Provinces. Hail has a continental desert climate with hot summers and cool winters. With an arid to extremely arid climate pattern, Hail's annual precipitation of about 110 mm comes from two peaks rainfall in March and November.

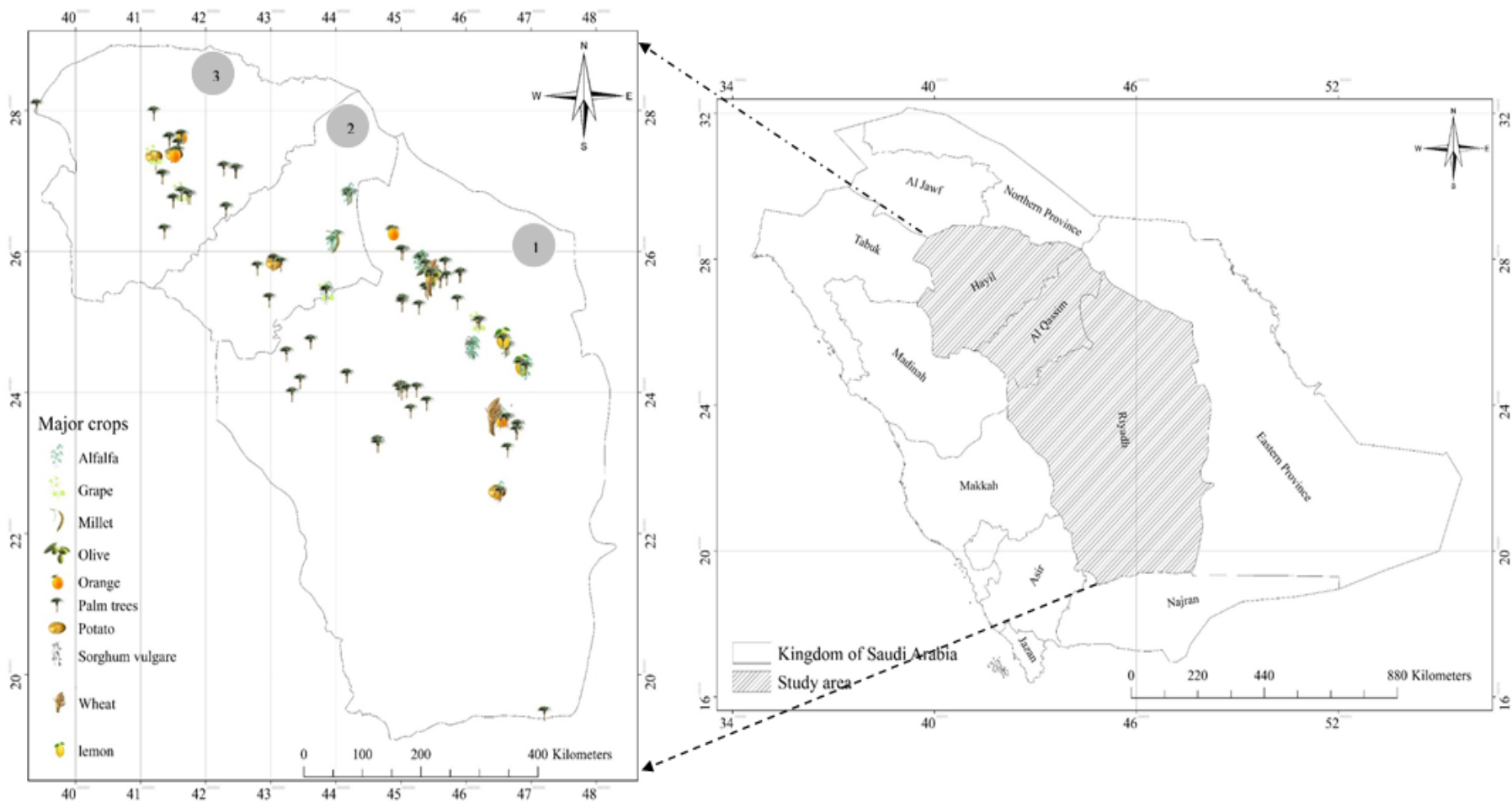


Figure 5.1 Location map of the study area

5.2.2 Reference Evapotranspiration (ET_o)

Daily climate data between 1950 and 2013 was collected from weather stations located across the study area. In this study, ET_o is the evapotranspiration from a hypothetical surface that consists of grass as the reference crop at 0.12-m height, actively growing, adequately watered, and with a surface roughness of 70 (s m⁻¹) and an albedo of 0.23. The ET_o of this reference surface is estimated according to the following Penman– Monteith equation (Allen et al., 1998) on a grid-by-grid basis.

$$ET_o = \frac{0.408\Delta(Rn - G) + \gamma \frac{900}{T + 273} u_2 (e_s - e_a)}{\Delta + \gamma(1 + 0.34u_2)} \quad (5-1)$$

Where

ET_o = reference evapotranspiration (mm/day)

R_n = net radiation at the crop surface (MJ/m²/day),

G = soil heat flux density (MJ/m²/day),

T = mean daily air temperature at 2 m height (°C),

u₂ = wind speed at 2 m height (m/s),

e_s = saturation vapour pressure (kPa),

e_a = actual vapor pressure (kPa),

Δ = slope vapor pressure curve (kPa/°C),

γ = psychrometric constant (kPa/°C).

e_s - e_a = saturation vapor pressure deficit (kPa)

The data used in this study include elevation, latitude and longitude of selected climate stations, total monthly rain, maximum and minimum air temperature, relative humidity, wind speed at 2 m height, and daily sunshine hours. The Inverse Distance Weighted (IDW) interpolation function was utilized to interpolate the input daily climate data. Daily ET_o was estimated from the Penman-Montieth approach implemented within the main program of GIS to produce twelve maps of mean daily reference evapotranspiration for each month (mm/day).

5.2.3 Actual evapotranspiration estimated by a soil water balance model

The model uses soil water balance equations proposed by the Food and Agriculture Organization (FAO) (Allen et al., 1998). Inputs to the water balance model consist of observed climatic data and gridded soil property characteristics (two soil parameters) obtained from the IGBP-DIS Global Gridded Surfaces of Selected Soil Characteristics database (Global Soil Data Task Group, 2000). This soil database was derived from the soil physical attributes of the 1995 digital 1:5 million-scale FAO Soil Map of the World and the Global Pedon Database. More details about this dataset are given in Tempel et al. (1996), Global Soil Data Task Group (2000), and Batjes (2002a, b). The study area's soil parameters were extracted using a 5x5 arc-minutes gridded format with ArcGIS 10.1. The gridded water-holding capacity at 0.25° grid resolution was calculated using hydrologic soil properties linked to soil texture, and the wilting point (WP), field capacity (FC), and *saturated* water content (SAT) for each grid (Saxton and Rawls, 2006). The monthly soil water balance in mm of water is:

$$\Delta\text{SWC}_m = \text{EP}_m - \text{AET}_m - \text{R}_m \quad \text{mm/month} \quad (5-2)$$

Where: ΔSWC_m is the change in soil water content, EP_m the effective precipitation, AET_m the actual evapotranspiration, and R_m is the runoff for month m , which includes both surface runoff and subsurface drainage. SWC is less than or at most equal to SWC_{max} , which is the total maximum SWC available in the soil for evapotranspiration. If the monthly water input exceeds SWC_{max} , the excess becomes the runoff (R_m). Realistic initial SWC values are obtained via a trial and error search approach.

Effective precipitation (EP), the portion of total precipitation used for crop production, is estimated according to the method of the USDA Soil Conservation Service (Dastane, 1974). The

method assumes that crops can use almost 60 to 80 percent of the precipitation, up to 250 mm/month. Beyond 250 mm/month, crops would only be able to use about 10 percent of that amount. Rainfall interception is that intercepted by plant canopy and litter and becomes evaporation loss. Interception loss plays an important role in the water budget because it reduces the amount of precipitation available for SWC. EP is the gross precipitation (GP) minus the precipitation intercepted by canopy cover and litter, and interception loss is a function of the storage space of canopy structure. The amount of rainfall intercepted is proportional to the interception coefficients K_{int} . For each month, the Effective Precipitation is:

$$EP_m = \text{Gross P} - (\text{Gross P} * K_{int}) = \text{Gross P} * (1 - K_{int}) \quad \text{mm/month} \quad (5-3)$$

Actual evapotranspiration (AET) is calculated as a function of meteorological, phenological and soil moisture conditions:

$$AET_m = ET_{o_m} * K_{veg} * K_{soil} \quad \text{mm/month} \quad (5-4)$$

K_{veg} = vegetation coefficients dependent on vegetation characteristics

K_{soil} = the soil stress coefficients dependent on the volumetric soil water content (0-1).

K_{soil} represents a reduction factor resulted from the limit imposed by the monthly soil water content (SWC_m). At monthly time step, the model uses a simple algorithm to estimate K_{soil} as a ratio of SWC_m to the maximum SWC (Zomer et al., 2006):

$$K_{soil} = SWC_m / SWC_{max} \quad (5-5)$$

The maximum amount of soil water available for ET processes within the plant rooting depth zone is equal to the SWC at field capacity (SWC_{fc}) minus the SWC at wilting point (SWC_{wp}) times the rooting depth (RD).

$$SWC_{max} = RD * (SWC_{fc} - SWC_{wp}) \quad \text{mm} \quad (6-6)$$

To estimate K_c , a land cover map that represents the extent of irrigated crops in the study area is developed for 2013 (Figure 5.2(a)). Phenological information for this map is based on NDVI estimated from remotely sensed spectral pixel values in the red and near-infrared spectra.

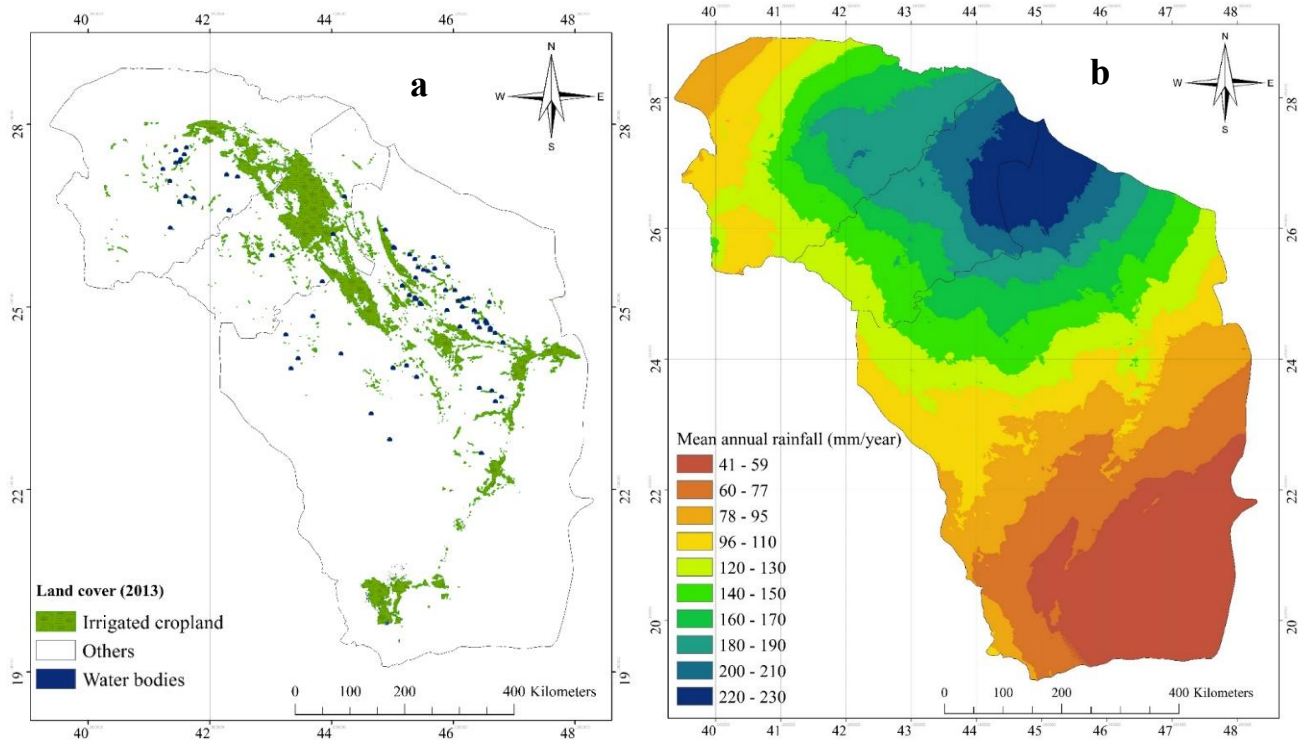


Fig 2: (a) Land cover map; (b) Rainfall map of the study area

Figure 5.2 (a) Land cover map; (b) Rainfall map of the study area

K_c is estimated from NDVI data averaged between 2000 and 2013 available from the 16-day NDVI (MOD13A2). To validate NDVI derived from MODIS images, 258 sampling sites representing different climatology and vegetation covers were selected. A database of default K_c to be used in the ArcGIS ET calculation tool was also developed. The database contains 10 crop types (palm trees, grape, lemon, wheat, alfalfa, orange, olive, potato, sorghum vulgare, and millet), and land covers such as evergreen forest and scrublands. For actual crops, K_c values are obtained from FAO's Water Development and Management Unit database, which also contains growing season dates. K_c is estimated from NDVI time series data.

$$K_c = k * NDVI + n \quad (5-7)$$

$$R^2 = \left[\frac{\sum_{i=1}^n (K_c - \overline{K_c}) * (NDVI - \overline{NDVI})}{\sum_{i=1}^n [(K_c - \overline{K_c})^2 * (NDVI - \overline{NDVI})^2]^{1/2}} \right]^2 \quad (5-8)$$

K_c varies significantly across the growth phase of crops, even though inter-annual variations are relatively small. The k and n coefficients in Equation (5-7) were determined from 10 different agriculture land use datasets throughout the season, so that the above equation is applicable to a wide range of agriculture land use over the whole growing season. The coefficients of determination (R^2) is a statistic used to assess the goodness-of-fit ranging from 0 to 1 (perfect fit) for 12 linear models shown in Table 5.1, along with the mean square errors (MSE) and the root mean square of the errors (RMSE). These models were developed for each crop considered in this study and for the average monthly K_c and NDVI for the study area. These regression coefficients were calculated at 0.05 significance level. Since a high R^2 itself may be insufficient to establish a strong relationship between K_c and NDVI, the F-test of equality of variances was also applied to test the statistical significance of the relationship between K_c and NDVI, assuming both are of normal populations.

Table 5.1 Relationship between monthly NDVI and monthly crop coefficients under irrigated crop condition.

Vegetation type	Linear equation	R ²	MSE	RMSE
palm tree	Kc= 0.26 x NDVI+0.74	0.89	0.001	0.031
grape	Kc = -0.12 x NDVI+0.55	0.90	0.0001	0.01
lemon	Kc = -0.41 x NDVI+1.1	0.86	0.006	0.077
wheat	Kc = -0.32 x NDVI+1.026	0.714	0.150	0.387
alfalfa	Kc = 2.11 x NDVI-0.49	0.971	0.108	0.328
orange	Kc = 0.1 x NDVI + 0.77	0.76	0.002	0.044
olive	Kc=-0.04 x NDVI +0.73	0.77	0.008	0.089
potato	Kc = 0.21 x NDVI + 0.64	0.82	0.052	0.228
sorghum vulgare	Kc = 0.19 x NDVI + 0.74	0.915	0.02	0.141
millet	Kc = -0.32 x NDVI + 1.23	0.87	0.005	0.071
Study area monthly Kc vs. NDVI				
Month	Linear equation	R ²	MSE	RMSE
January	Kc = 0.803 x NDVI + 0.398	0.72	0.007	0.083
February	Kc = 1.076 x NDVI + 0.224	0.74	0.017	0.130
March	Kc = 0.863 x NDVI + 0.314	0.90	0.008	0.090
April	Kc =1.081 x NDVI + 0.117	0.78	0.005	0.007
May	Kc = 1.061 x NDVI + 0.146	0.93	0.004	0.094
June	Kc = 1.117 x NDVI + 0.137	0.85	0.008	0.092
July	Kc =0.834 x NDVI + 0.368	0.82	0.011	0.106
August	Kc = 1.23 x NDVI + 0.028	0.95	0.004	0.066
September	Kc = 0.984 x NDVI + 0.221	0.72	0.015	0.124
October	Kc = 1.05 x NDVI + 0.162	0.87	0.009	0.095
November	Kc = 1.126 x NDVI + 0.085	0.90	0.004	0.064
December	Kc =0.639 x NDVI + 0.492	0.76	0.006	0.074

5.2.4 Long-term average annual actual evapotranspiration at stations

Three popular relationships between AET / PET and P/ PET, attributed to Schreiber (1904), Ol'dekop (1911) and Pike (1964), respectively, were used to estimate long-term average annual AET for the study area, as

$$\frac{AET}{PET} = \frac{P}{PET} \left(1 - \exp\left(-\frac{PET}{P}\right) \right) \quad (5-9)$$

$$\frac{AET}{PET} = \tanh\left(\frac{P}{PET}\right) \quad (5-10)$$

$$\frac{AET}{PET} = \frac{P}{PET} / \sqrt{\left(1 + \frac{P}{PET}\right)^2} \quad (5-11)$$

Where AET and P are the actual evapotranspiration and long-term average annual precipitation, and PET is the long-term average annual potential evapotranspiration estimated by the Penman–Monteith equation, respectively. To select the most representative method from these three methods for the study area, long-term average values estimated from the three methods are compared with values obtained from the water balance method. The Buishand's nonparametric detection method was applied to detect change points in the daily AET of the study area. This is a test for a null hypothesis (no change point) and an alternative hypothesis, where change point is detected. Next, the nonparametric Mann-Kendall test was applied to estimate the long-term trend in daily AET between 1950 and 2016.

5.3 Discussions of Results:

5.3.1 Spatial distribution of reference evapotranspiration

The mean annual precipitation in the study area over the 63-year period was less than 140 mm/year (Figure 5.2(b)), which is very low compared with the global mean annual rainfall of about 1000 mm. Under such an arid climate, the lack of available water will be very severe during drought periods. Therefore, the variability of annual precipitation plays a very important role in the water resources management, development and conservation plans of the study area. The southeastern and southwestern parts of the Al-Riyadh province, and the northwestern parts of Hail province have the lowest mean annual rainfall of 41–110 mm/year. The Al-Qassim province, northern regions of the Al-Riyadh and Hail provinces, except its northwestern parts, received the highest mean annual precipitation of 120–230 mm/year.

The spatial distributions of gridded ETo computed at 15 m resolution helps us to better understanding the spatial and temporal variability of the crop water demand for each month. The ETo of January is the lowest, ranging from 2.5 mm/day to 4.4 mm/day in the study area, while the highest

ETo are in July, ranging from 8.2 to 11.4 mm/day (Mahmoud and Gan, 2019). Between all twelve months, summer (April-September) evapotranspiration will be the highest as expected. Therefore, in the summer (April-September), ETo is the maximum in Al-Qassim Province, Hail Province, and in the northern portion of Al-Riyadh Province. From January to March and November to December, the maximum ETo will shift towards southeastern parts of Al-Qassim Province, Hail Province and Al-Riyadh Province probably due to the seasonal variation in the relative humidity and wind speed in the study area (see supplementary materials in Mahmoud and Gan, 2019).

From spatial distributions of annual ETo shown in Figure 5.3, it is obvious that there are a large spatial and seasonal variations in ETo in different regions of the study area. The mean annual ETo ranges from 2127 to 2460 mm/yr, with the lowest annual ETo located in central and southwestern parts of Al-Riyadh province, and the northwestern parts of Hail province. The maximum ETo are found mainly over the Al-Qassim province. The results appear to provide comparable or better estimates of ETo than currently available PET methodologies using ground-based observations. Topography and climatic factors contribute to variations in annual ETo values, which are also related to latitudes, which seem to play a bigger role than the temporal fluctuations of ET. The results and ETo maps can be used for agroclimatic design. The results also show that geostatistics (IDW) is useful to represent the spatial variability of ETo over large geographical areas.

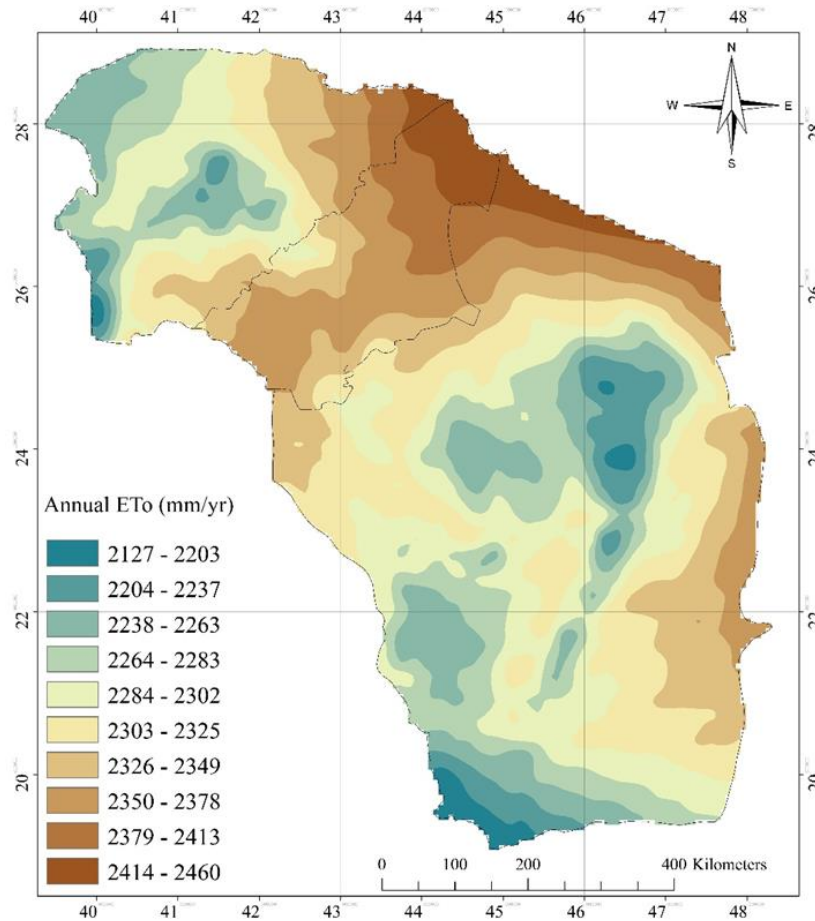


Figure 5.3 Spatial distribution of annual reference evapotranspiration.

5.3.2 Monthly NDVI and Crop Coefficients Patterns for irrigated crops

Monthly Kc values for crops were developed according to planting dates of actual crop database, which and Kc for other types of landcover were used to derive the relationships with 16-day MODIS NDVI (MOD13A2) data in the study area. Twelve simple linear regression models were developed to establish a general relationship between NDVI and the daily Kc values measured from 258 sampling sites of varying climatology, crops, and cropping practices. The monthly linear regression models developed out of monthly NDVI-Kc estimated and modeled have an R^2 of 0.72, 0.74, 0.9, 0.78, 0.93, 0.85, 0.82, 0.95, 0.72, 0.87, 0.9, and 0.76, respectively (Table 5.1). These results are

comparable to Kc-NDVI relationships developed in previous studies (Mutiibwa and Irmak, 2013; Er-Raki et al., 2013; Parka et al., 2017). For instance, Mutiibwa and Irmak (2013) derived Kc from NDVI data in the U.S. High Plains based on a regression model with R^2 of 0.72 and RMSE of 0.12, which according to the authors represent a good model performance. In another study, Er-Raki et al. (2013) regarded R^2 of 0.63 to be acceptable in deriving Kc for grapes of Northwestern Mexico. In our study, the results also show a strong correlation between monthly Kc and NDVI with low MSE and RMSE (Table 5.1). Kc obtained from NDVI data of MODIS images are also comparable to Kc provided in FAO-56 (Allen et al., 1998). As expected, simple regression models of NDVI and Kc developed for the 10 selected crops individually show higher goodness-of-fit statistics (higher R^2) to field data collected in 258 sampling sites than similar monthly regression models developed for all irrigated crops of each month (Table 5.1).

The number of days of an average year (DOY) with a maximum NDVI of 0.8 for palm trees (DOY 241), $NDVI_{max}$ of 0.64 for grape (DOY 193), $NDVI_{max}$ of 0.79 for wheat (DOY 129), $NDVI_{max}$ of 0.65 for lemon (DOY 289), $NDVI_{max}$ of 0.65 for potato (DOY 113), $NDVI_{max}$ of 0.64 for orange (DOY 241), $NDVI_{max}$ of 0.77 for olive (DOY 49), $NDVI_{max}$ of 0.9 for sorghum vulgare (DOY 161), and $NDVI_{max}$ of 0.82 for millet (DOY 161), respectively. It is clear that the NDVI of irrigated alfalfa during the growing season is greater than that of other crops. Alfalfa seeds are usually planted on 8 March and it is harvested every 30-40 days throughout the year. Kc derived from the NDVI of each pixel using the NDVI-Kc regression model developed generally shows strong agreement with actual Kc measured in the field over the growing stage of crops. Twelve monthly Kc maps developed from NDVI data of MODIS images show spatial variability of Kc in the study area, and also temporal variations over the growing season (Figure 5.4). Figure 5.4 shows that the maximum Kc of crops for all irrigated lands range from < 0.5 to 1.2 for different months, such that high Kc values are generally

observed in January, February, March, May, August, and November, respectively. Spatial variations in K_c are partly attributed to different crop types and partly to different growth stages of crops because of different planting dates.

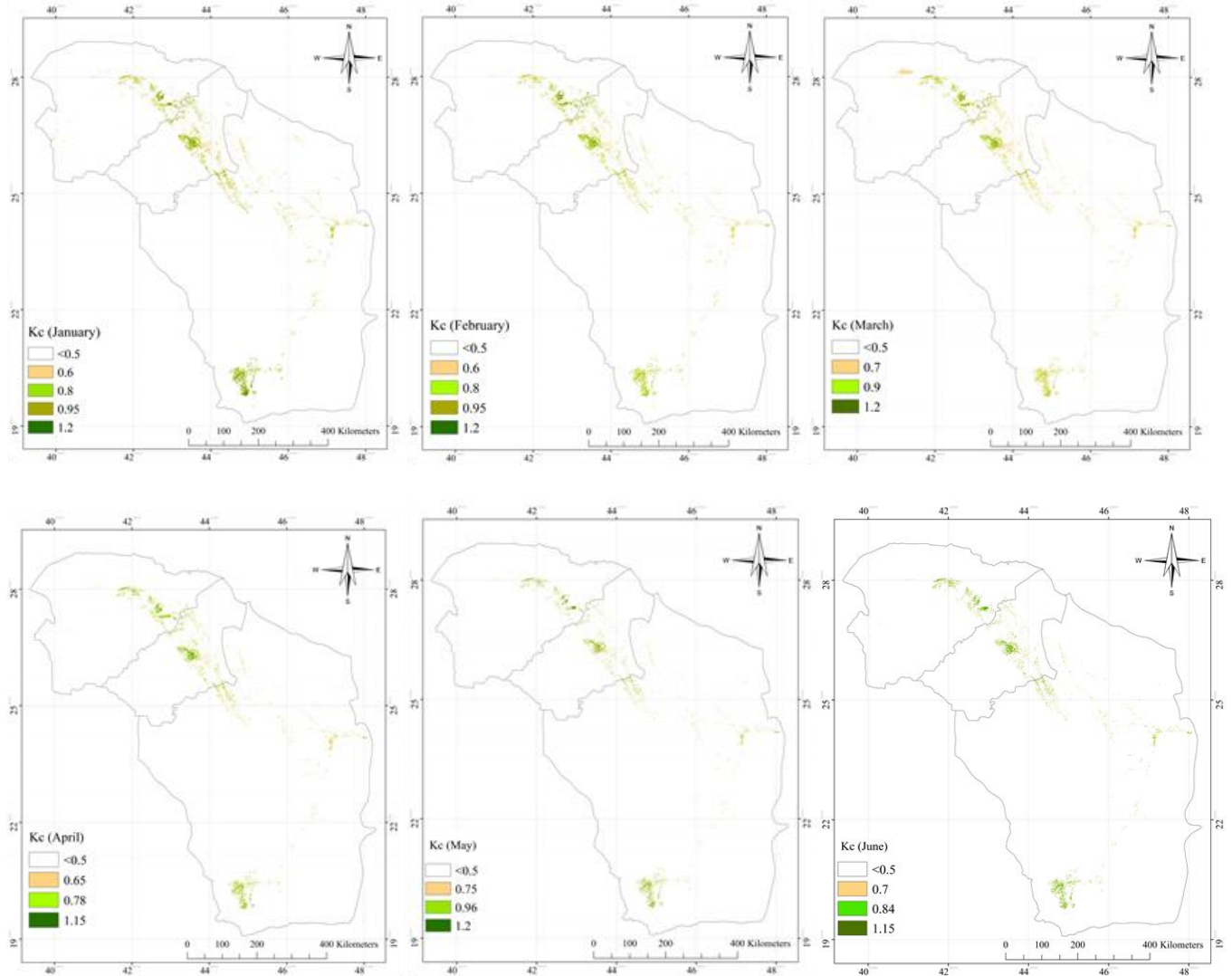


Figure 5.4 Spatial distribution of monthly crop coefficients

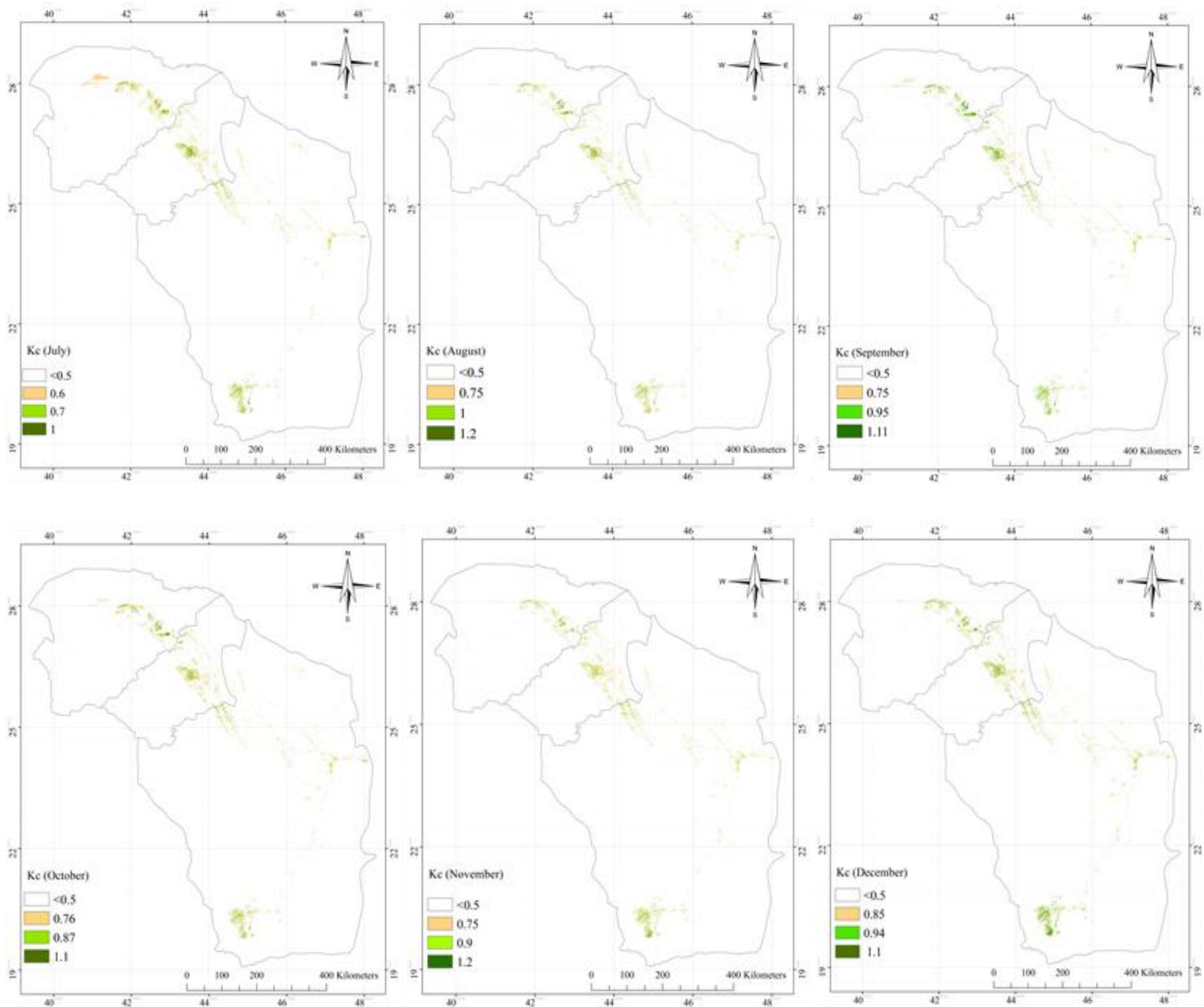


Figure 5.4 (continued)

5.3.3 Spatial distribution of monthly and annual actual evapotranspiration (AET)

Monthly AET was estimated using the aforementioned soil water balance model driven with soil stress coefficients, monthly Kc and monthly ETo estimated from Equation 5.4. The AET output represents the average monthly evapotranspiration (mm) of irrigated cropland for the 1950-2013 period. It is observed that Kc fluctuates between inter-monthly low-and high values throughout the year. With high water consumption by crops due to high irrigation water supply in February, March,

April and May, Kc in these months also increase dramatically. Monthly AET maps derived for the study area from the soil water balance model are shown in Figure 5.5. It should be noted that monthly Kc map derived from the twelve regression equations were based on NDVI extrapolated from NDVI data of 312 MODIS images of 16-day time step.

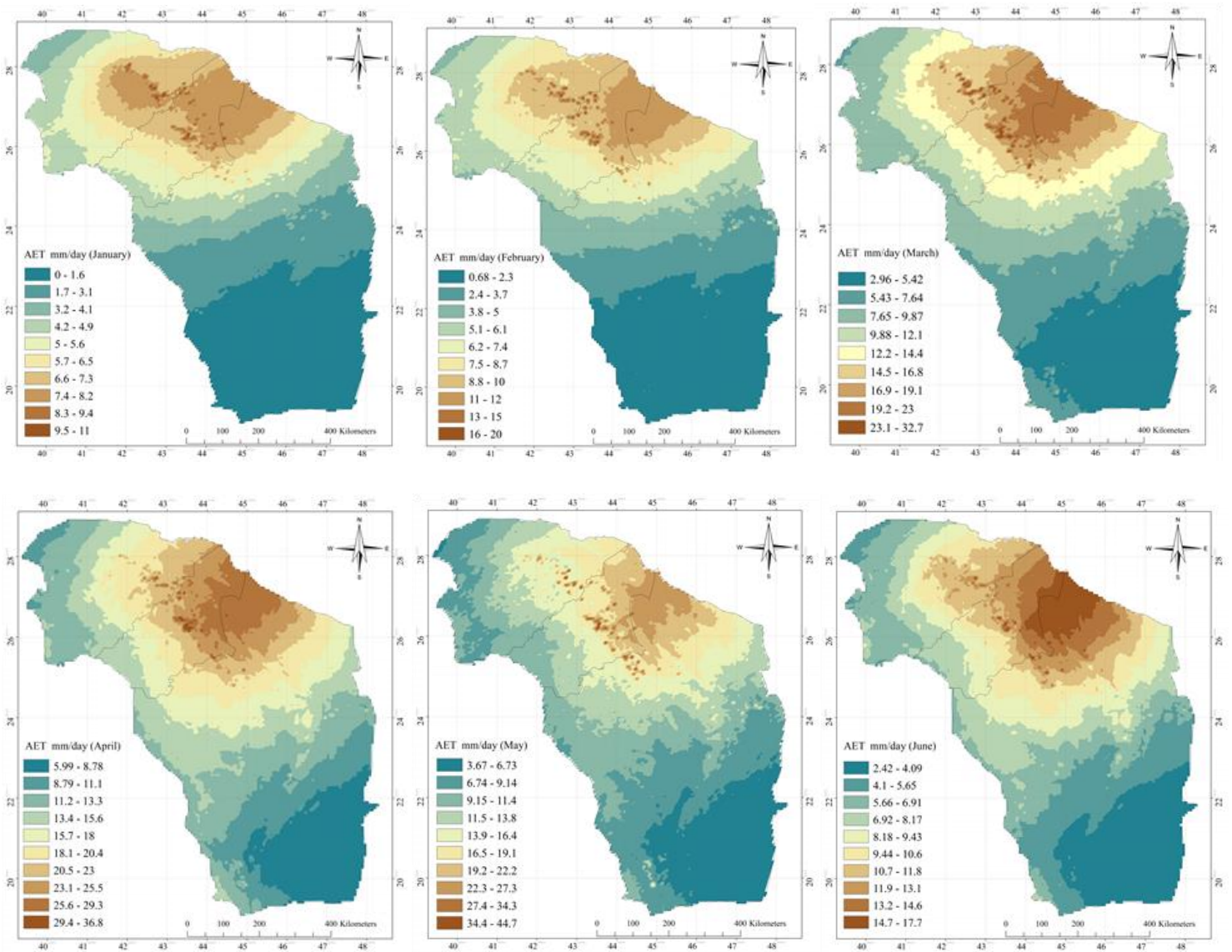


Figure 5.5 Spatial distribution on monthly actual evapotranspiration

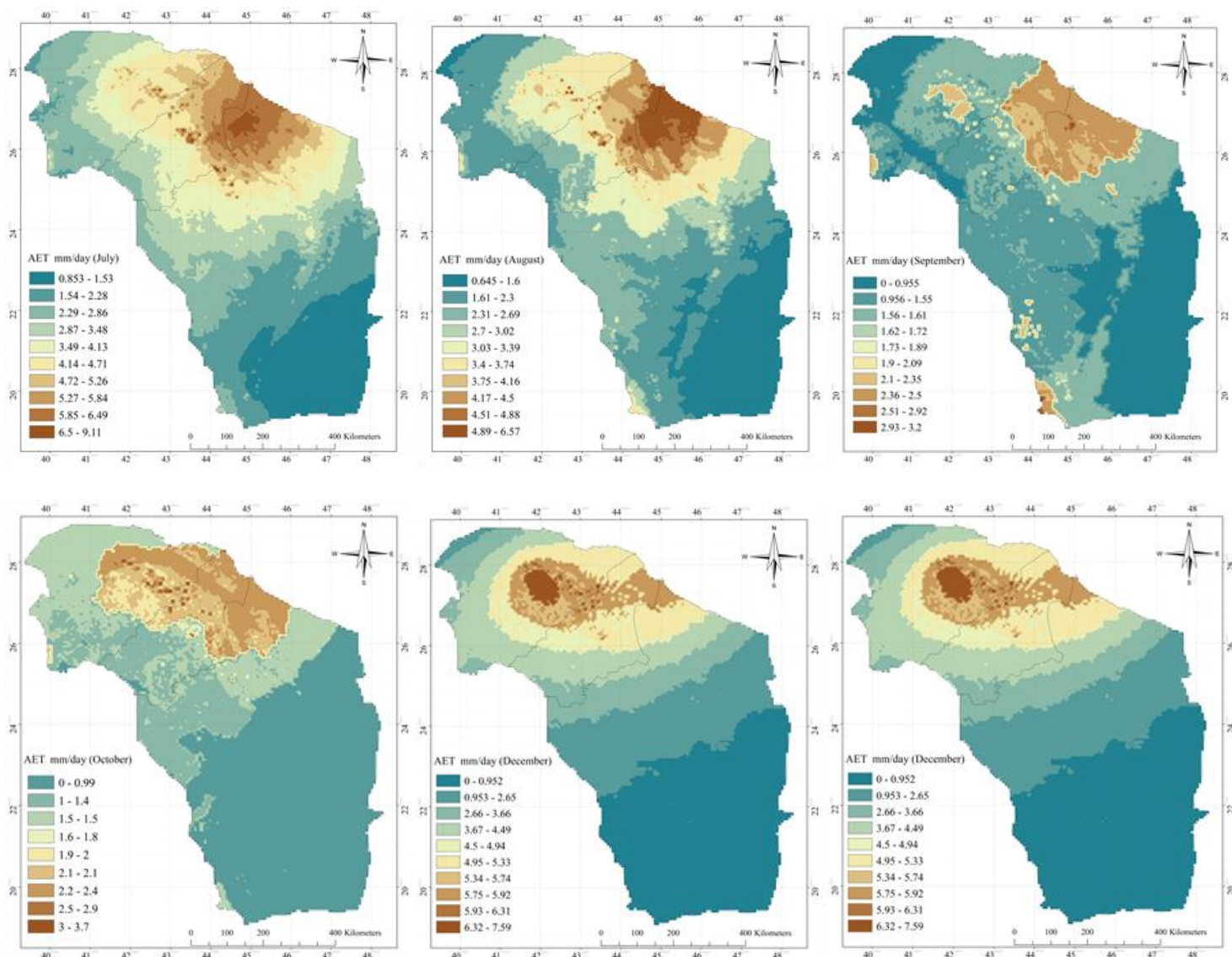


Figure 5.5 (continued)

The monthly AET maps for 1950-2013 show a gradual increase in AET during the crop-growing season from January to May but a subsequent decline from June to December as the season progresses from summer to winter, and as plant transpiration decreases drastically in June, the month when most crops are harvested. The AET estimated for January to June arranged in descending order are May (3.67-44.7 mm/day), April (5.99-36.8 mm/day), March (2.96-32.7 mm/day), February (0.68-20 mm/day), June (2.42-17.7 mm/day) and January (1-11 mm/day), respectively. High AET losses in these months are of major concern because crops are irrigated from groundwater sources where the

rate of withdrawal far exceeds the rate of replenishment. The AET losses estimated are similar to AET of other regions of KSA (Mahmoud and Alazba, 2016; Madugundu et al., 2018). For instance, Madugundu et al., (2018) found that crop water requirements for carrot in the Riyadh region of Saudi Arabia in the summer were about 3243 mm (about 36 mm/day), and 620 mm in winter. Crop water requirements for silage maize was 1622 mm in the summer, and 1359 mm in spring. Using a surface energy balance algorithm, Mahmoud and Alazba (2016) estimated the average daily AET in the southern and western regions of KSA varies widely, from 4.97 to 49 mm/day in April, and from 3.43 to 48.9 mm/day in May. In the study area, high AET losses found in some small spots in AET maps are mainly due to evaporation from water bodies such as lakes impounded behind rain harvesting dams and water storage facilities. Such high AET values in an arid region such as Saudi Arabia are examples of mismanagement of irrigation water, which could cause soil salinity to increase. To address rising soil salinity problems, farmers resort to apply excessive amount of irrigation water; higher than the crop water requirement for leaching of soil salinity, which is a common issue in irrigated land in Saudi Arabia due to high evaporation loss of irrigated water.

Figure 5.5 shows the spatial variations of AET over the study area, where maximum AET values are found in Al-Qassim Province, Hail Province, and in the northern portion of Al-Riyadh Province. The results also show that irrigated cropland has access to moisture because of irrigation and groundwater. So monthly AET of irrigated cropland depend on moisture availability and the atmospheric water demand. From June to December, there were a gradual decrease in AET values. Where AET estimate ranged from 2.42 -17.7 mm/day in June, 0.85-9.1 mm/day in July, 0.64-6.57 mm/day in August. The lowest observed values for AET were in September and October where its value ranged from 0-3.7 mm/day. The average annual AET estimated by the soil water balance model given in Figure 5.6(a) shows moderate AET in non-irrigated areas in the southern parts of Riyadh

(351-993 mm/year), in contrast to very high annual AET ranging from 1200 to 2900 mm/year in irrigated cropland in the northern and central region of Riyadh, Al-Qassim province and Hail province. The average annual AET losses estimated using the Pike and Ol'dekop methods are unrealistically low even in irrigated crop field and the results are not presented. On the other hand, AET estimated by the Schreiber model, ranging from 492 to 2710 mm/year, agrees well with that estimated by the soil water balance model ranging from 351 to 2900 mm/year, and so it is shown in Figure 5.6(b). The annual AET estimated by the soil water balance model are about 9-11% greater than that estimate by the Schreiber model.

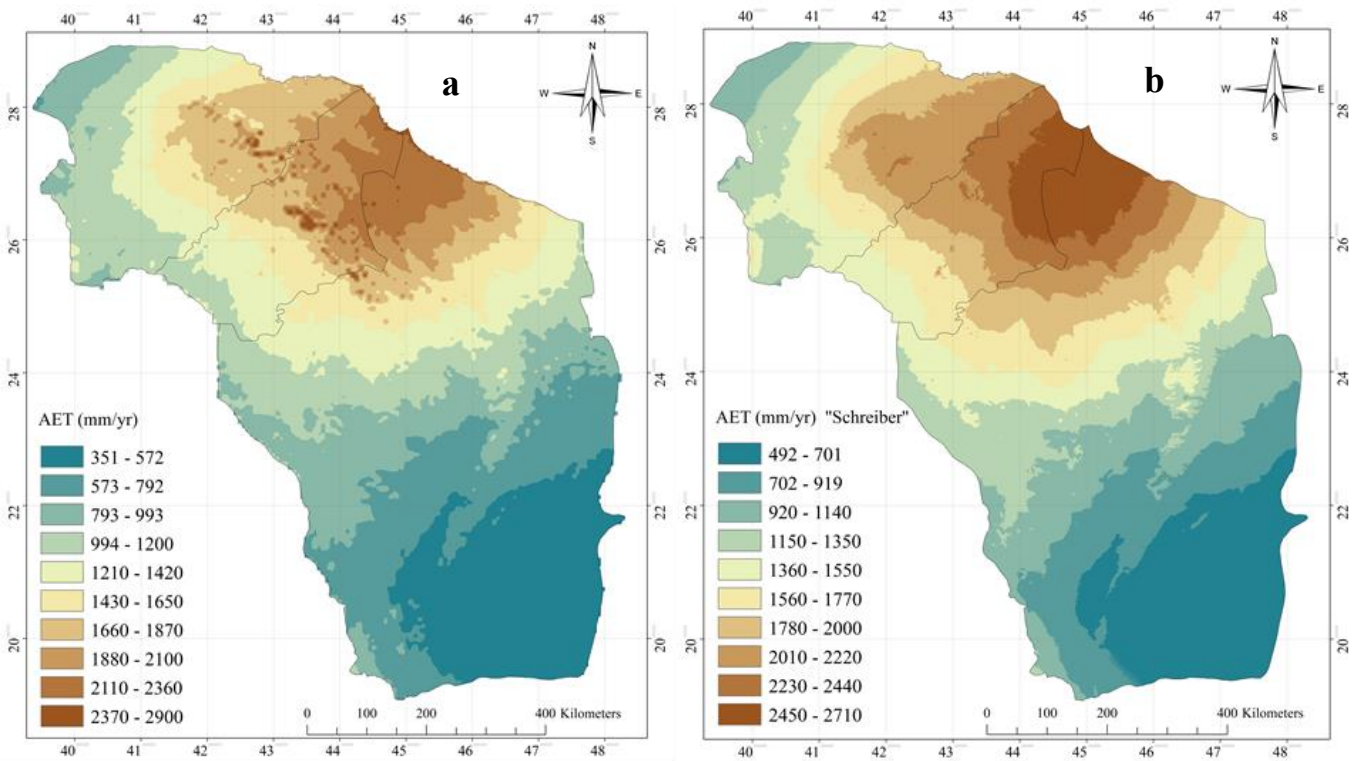


Figure 5.6 a) Average annual actual evapotranspiration based on soil water balance model; b) Average annual actual evapotranspiration based on Schreiber equation.

5.3.4 Long-term average daily actual evapotranspiration

Long-term average daily AET estimated by the soil water balance model for 1950-2016 (Figure 5.7 generally agree with those obtained from field measurements as shown in Figure 5.8). The long-term average daily AET ranges from 2 mm/day to 30 mm/day in some areas. In general, uniform daily irrigation is applied to crops, from 0 to 2 mm/day for alfalfa during the initial crop growth stage, and from 1.0 to 5.0 mm/day for other crops, with the highest values for grapes under the driest conditions. From Buishand's change detection test applied to average daily AET between 1950 and 2016, statistically significant change points in daily AET were detected in 1990 because the average daily AET of 3.6 mm/day over 1950-1990 had increased to 5.3 mm/day over 1990-2016. Furthermore, the Mann-Kendall trend test also detected a statistically significant positive trend of 1.5 mm/decade in the average daily AET over 1990-2016, likely caused by climate warming in the last three decades. The recent rising trend in AET detected is expected to cause stress to crops and to enhance drought conditions (Mahmoud and Gan, 2018).

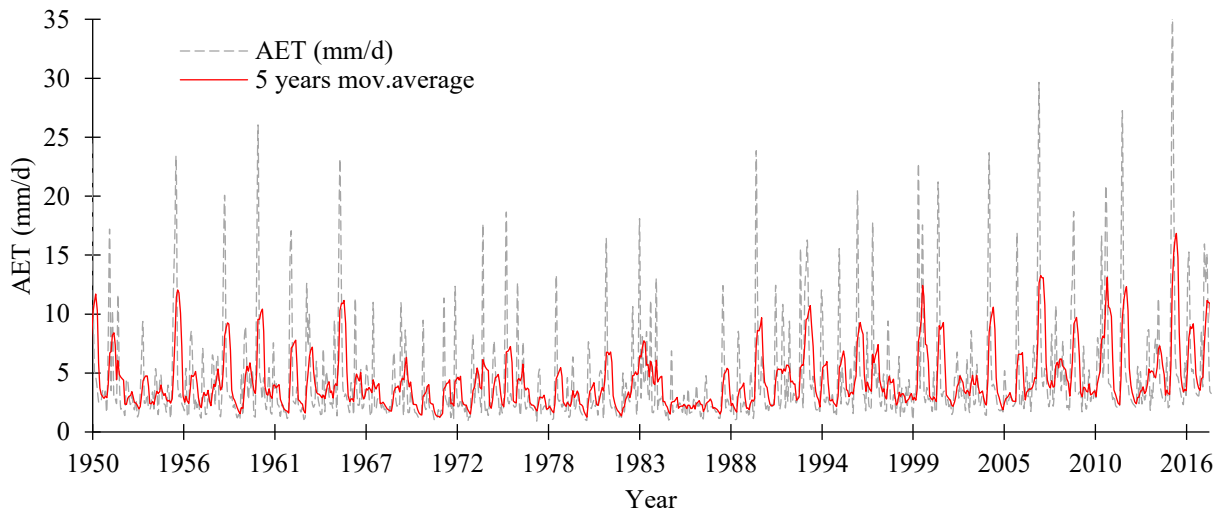


Figure 5.7 Average daily actual evapotranspiration in the study area

To validate the soil water balance model developed in this study, both models estimated, and field observed daily AET via a water balance analysis for alfalfa crop are compared. Overall, Figure 5.8 shows good agreements between model estimated and observed daily AET for alfalfa, even though the model estimated daily AET are about 4-5% higher than the observed AET for January to April, the period with the best agreement between both datasets. Between the end of April and the middle of June, estimated AET is about 2% lower than the observed AET, and even lower from July to August because of lower atmospheric demand of evaporation loss. The successful application of the soil water balance model developed in this study in deriving representative AET maps will be useful to achieve the planning and management of sustainable water use in arid regions of Middle East, such as the Kingdom of Saudi Arabia.

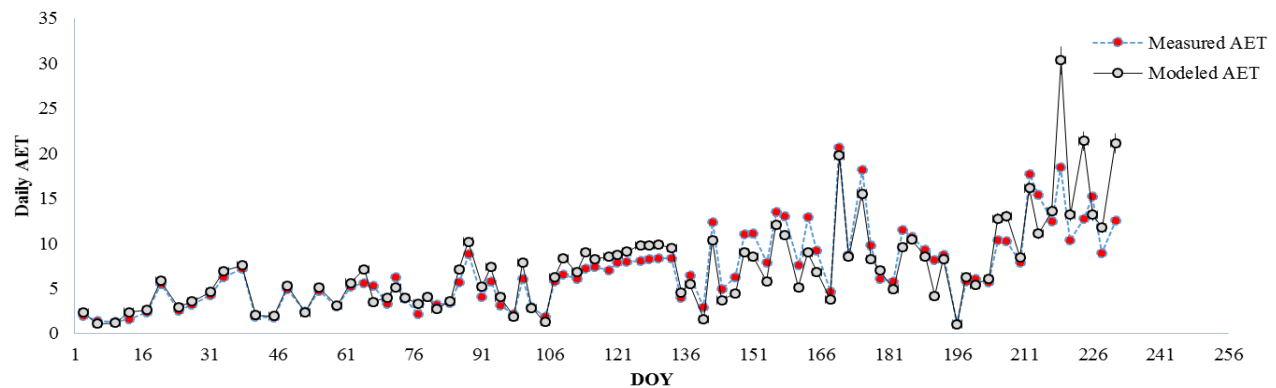


Figure 5.8 Daily measured and modelled actual evapotranspiration for alfalfa crop

5.4 Conclusion

This study was designed to estimate average reference and AET over Al-Riyadh, Al-Qassim and Hail Province in the central region of Saudi Arabia during 1950–2013 using soil water balance model on daily, monthly and annual basis. Firstly, the FAO Penman-Monteith method was used to model the spatial distribution of ETo on a grid-by-grid basis using data collected from meteorological stations and GIS techniques. Then, crop coefficients (K_c) were modeled as a function of 16-day time-

series MODIS normalized difference vegetation index (NDVI). Next, using Kc maps and ETo as input, daily AET was simulated by the soil water balance (SWB) model and aggregated to monthly and annual AET. ETo is found to be the highest and of the most concern in Al-Qassim Province, Hail Province, and in the northern portion of Al-Riyadh Province. From January to March and from November - December there is a shift of maximum ETo towards southeastern parts of Al-Qassim Province, Hail Province and Al-Riyadh Province except in its northern portion. The annual ETo shows very high values in the entire study area as it ranged from 2127 to 2460 mm/year. From empirical NDVI-Kc relationships developed and applicable at pixel level, Kc derived from the NDVI-Kc relationships agree well with Kc recommended by FAO over various crop growth stages in the field.

The monthly AET maps for 1950-2013 show a gradual increase in AET during the crop-growing season in January to May but a subsequent decline as the season progresses from June to December. The AET estimated for January to June are arranged in descending order, which are May (3.67-44.7 mm/day), April (5.99-36.8 mm/day), March (2.96-32.7 mm/day), February (0.68-20 mm/day), June (2.42-17.7 mm/day) and January (1-11 mm/day), respectively. Statistical analysis shows that statistically significant change point in daily AET generally occurred in 1990, such that the long-term average daily AET of 1950-1990 at 3.6 mm/day increased to about 5.3 mm/day between 1990 and 2016 with a positive trend of 1.5 mm/decade. The annual AET estimated for irrigated cropland in northern and central regions of Riyadh, Al-Qassim province and Hail province range from 1200 to 2900 mm/year. In these regions, low AET values are found in shrubland, grassland, and other natural vegetation. The annual AET estimated by the SWB model are about 9-11% higher than modeled AET in the study area, where the long-term average daily AET estimated for 1950-2013 range from 2 mm/day to 30 mm/day. The lowest long-term average daily AET is observed from the start of August

to the end of September. The measured daily AET for alfalfa crop used to test and validate the SWB model. good agreement between SWB-based daily AET and the measured daily AET for alfalfa. Overall, there was very good agreements between model estimated and observed daily AET for alfalfa, even though the model estimated daily AET are about 4-5% higher than the observed AET for January to April, the period with the best agreement between both datasets. Between the end of April and the middle of June, estimated AET is about 2% lower than the observed AET, and even lower from July to August because of lower atmospheric demand of evaporation loss. Representative AET maps derived from applying the NDVI-Kc relationships to the SWB model will be useful to achieve the planning and management of sustainable water use in arid regions of Middle East.

Chapter 6 Multidecadal variability in the Nile River Basin hydroclimate

6.1 Introduction

Most of the published research on the Nile River basin (NRB) climatology and climate change impact studies have been concentrated in the upper BNB stream countries. However, in recent years, recurring droughts and increasing population have led to rising tension between competing users for water. There is a need for better understanding of the hydrological cycle of the entire Nile River basin (NRB) and linkage to regional climate change. Several previous studies have explored hydroclimate variability in the Nile River basin mostly at sub-basin level (Cheung et.al., 2008; Zhang et al., 2012; Muhire and Ahmed, 2015; Ongoma et.al., 2018). In Ethiopia, Cheung et.al., (2008) investigated the variability and trends in Ethiopian ‘precipitation between 1960 and 2002 using precipitation observation data from 134 stations and found a significant decline in Kiremt precipitation over the Baro-Akobo, Omo-Ghibe, Rift Valley, and the southwestern and central regions of Ethiopia. In another study, Zhang et al., (2012) analyzed the spatio-temporal variations of precipitation in Sudan during 1948–2005 and reported a significant decreasing trend in annual precipitation over the central regions of Sudan after 1960s. Similarly, Muhire and Ahmed (2015) observed a decrease in the frequency of precipitation over the northern, eastern and central plateau of Rwanda, the authors also reported an increase in total precipitation during the short rainy seasons mainly over the highlands, Kivu Lake. Ongoma et.al., (2018) examined changes and trends in Kenyan’ surface temperature between 1951–2012 and reported a warming of + 0.15 °C/decade since 1970s, where its highland exhibited a more significant warming than its lowland.

Other studies analyzed the effects of climate change on specific hydroclimate variables such as precipitation, temperature and streamflows at sub-basin level (Phillips and McIntyre, 2000;

Nyeko-Ogiramoi et al., 2013; Taye and Willems, 2012; Tierney et al., 2013; Onyutha, 2016; Onyutha and Willems, 2015). For example, Phillips and McIntyre (2000), Taye and Willems (2012), Nyeko-Ogiramoi et al. (2013), and Tierney et al., (2013) analyzed trend and variability in observed precipitation extremes of Uganda, the BNB, Lake Victoria basin, and East Africa respectively. These authors reported strong connection between inter-annual precipitation variability and climate indices such as El Niño and IOD. More recently, studies have shown that rapid urbanization and climate change are causing extreme weather conditions at a given location in the Nile River basin (e.g. Mahmoud and Gan, 2018 a,b; Seyoum, 2018), however, impact of climate change on the hydroclimate of the Nile River basin in a lumped manner is still unclear. For instance, downstream in Egypt, rapid urbanization and climate change had resulted in frequent deadly heat wave, warming trend of 0.19 °C/decade, a negative trend in relative humidity (0.55%/decade), and a rising trend in vapour pressure (0.24 hPa/decade) (Mahmoud and Gan, 2018a). In another study, Mahmoud and Gan, (2018b) reported a downward trend of 8.96 mm/decade in Egypt annual precipitation since 1994 (Mahmoud and Gan, 2018b). Upstream in Ethiopia, Seyoum, (2018) reported that the Upper BNB' precipitation is strongly linked to El Niño-Southern Oscillation (ENSO), specifically during the Kiremt season(June-September), this was evident from the strong negative correlation between El Niño (positive ENSO) and Upper BNB' precipitation ($\rho = -0.62$).

Statistical analysis techniques such as the least squares method, quantile perturbation method (QPM), Mann-Kendall (MK), Sen's slope and Pettitt tests have been widely employed in the Upper BNB to assess trends in hydrological variables (Seleshi and Zanke, 2004; Cheung et al., 2008; Tesemma et al., 2010; Bitew et al., 2010; Tekleab et al. 2013; Mengistu et al., 2014; Tabari et al., 2015; Seyoum, 2018). Most of these studies employed the non-parametric trends detection techniques to detect trends of meteorological variables (Gocic and Trajkovic, 2013; Tabari et al.,

2015; Gebremedhin et al., 2016; Mahmoud and Gan, 2018a). For example, Tekleab et al. (2013) applied MK and Pettitt tests to assess trends of the Upper BNB' streamflow, temperature, and precipitation. This study showed a statistically significant increasing trend in surface temperature but no significant trends in mean seasonal precipitation or streamflow, this can be attributed to the limited number of meteorological gauges in the Upper BNB, which fail to capture accurate spatial distribution. Earlier studies also show that precipitation in the Ethiopian highlands, the Upper BNB and other regions significantly varies in space and that meteorological gauges are not enough (Bitew et al., 2010). In another study, Mengistu et al., (2014) used the least squares method to analyze the spatio-temporal variability and trends of the Upper BNB' precipitation and surface temperature. Their study found an increasing trend in the Upper Blue Nile 'precipitation and a statistically significant warming trend in the southwestern parts of the basin, whereas other studies reported a non-significant decreasing trends in annual precipitation in the Upper BNB based on MK and the Sen's slope tests (Seleshi and Zanke, 2004; Cheung et al., 2008; Tesemma et al., 2010; Gebremicael et al., 2013; Tabari et al., 2015).

On the other hand, a few studies have investigated the long-term trends of hydroclimate variables at the basin level (Onyutha and Willems, 2015; Onyutha, 2016a, b; Nashwan and Shahid). Onyutha (2016a) used nonparametric detection methods to drive the long-term variability of precipitation over the Nile River Riparian countries. This study concluded that the northern Riparian countries of the Nile River basin are significantly linked to Indian and Atlantic Oceans and El Niño. In a similar study, Onyutha and Willems, (2015) analyzed the spatio-temporal variability of annual precipitation at 37 station over the Nile River basin and reported significant linkages between station-based observed precipitation and El Niño, Indian and Atlantic Oceans. In another study, Onyutha (2016b) analyzed the changes in potential evapotranspiration (PET) between 1930 and 2012 in all the Nile River Riparian Countries. The author reported that seasonal

and annual PET in most of the Nile River Riparian Countries was generally above the long-term average after 1980s. In a more recent study, Nashwan and Shahid (2019) analyzed changes and trends in precipitation and temperature over the Nile River basin. The authors reported an increasing trend of 0.26–26.4 mm/decade in annual precipitation at Atbara sub-basins and other few locations in the Nile River basin and a decreasing of about – 76.6 mm/decade in Sobat sub-basin. Moreover, a warming trend of 0.09–0.48 °C/decade in maximum temperatures over the Nile River basin and 0.17–0.50 °C/decade in minimum temperatures over majority of the Nile River basin.

This study is necessary to improve our understanding of the hydrological cycle and variability in hydroclimate variables of the Nile River basin, giving there is generally a lack of similar studies at the basin level. Therefore, the objective of this study was to analyze the multidecadal variability in the Nile River basin hydroclimate and possible linkages to the large-scale climate patterns. To achieve our objectives, we analyzed the spatio-temporal variability, frequency, intensity, change point and trend of monthly precipitation, precipitation anomaly, temperature, temperature anomaly, geopotential height, relative humidity, specific humidity, actual evapotranspiration (AET), and wind stress data at the basin level. Given IOD has been shown to play a primary role on the precipitation of East Africa over inter-decadal timescales, therefore we have also investigated the IOD and El Niño role on NRB's hydroclimate variability over inter-decadal and longer timescales. The results from this study would help us to better develop mitigation strategies for these riparian countries against the potential impact of climate change.

6.2 Study area and data

This study cover the entire area of the NRB (Figure 6.1), the NRB is situated in (31°N to 4°S, 24°- 40°E), has a total catchment area of 3.4 million km², and is shared by 11 countries (Burundi, Rwanda, Uganda, Kenya, Tanzania, South Sudan, Democratic Republic of Congo, Sudan, Eritrea,

Ethiopia, and Egypt). About 86% of NRB total area lies in Sudan, Ethiopia and Egypt. The northern parts of the basin including countries such as Egypt and Sudan exhibit an arid condition (Camberlin, 2009). The lowest average annual precipitation in the NRB is in Egypt which is almost 15 mm/yr, while the highest amount of annual precipitation is in Ethiopia with 2292 mm/yr (Figure 6.2(a)). There are two wet seasons in the NRB, rainy season upstream registering 400 mm/m from March to May and a wet season downstream with just 60 mm/m between July-September. Temperature also varies spatially and temporally, large portions of Egypt and the White Nile region in Sudan have the highest annual mean surface temperatures (T_m) in the basin (27-31°C). On the other hand, the Ethiopian highlands and the equatorial lakes region (17- 28°C) with relatively lower temperature in areas near the coastal land (Figure 6.2(b)). Majority of irrigated cropland. Savana forest lies upstream in countries such as Ethiopia, Uganda, Burundi, Congo, Kenya, Rwanda, and Tanzania (Figure 6.2(c)). In these countries, rainfed agriculture is common, where most of the farmers depend on the rainy season to irrigate their crops. In Egypt and northern regions of Sudan, irrigated croplands are mainly in the Nile delta and floodplains of the main Nile River respectively.

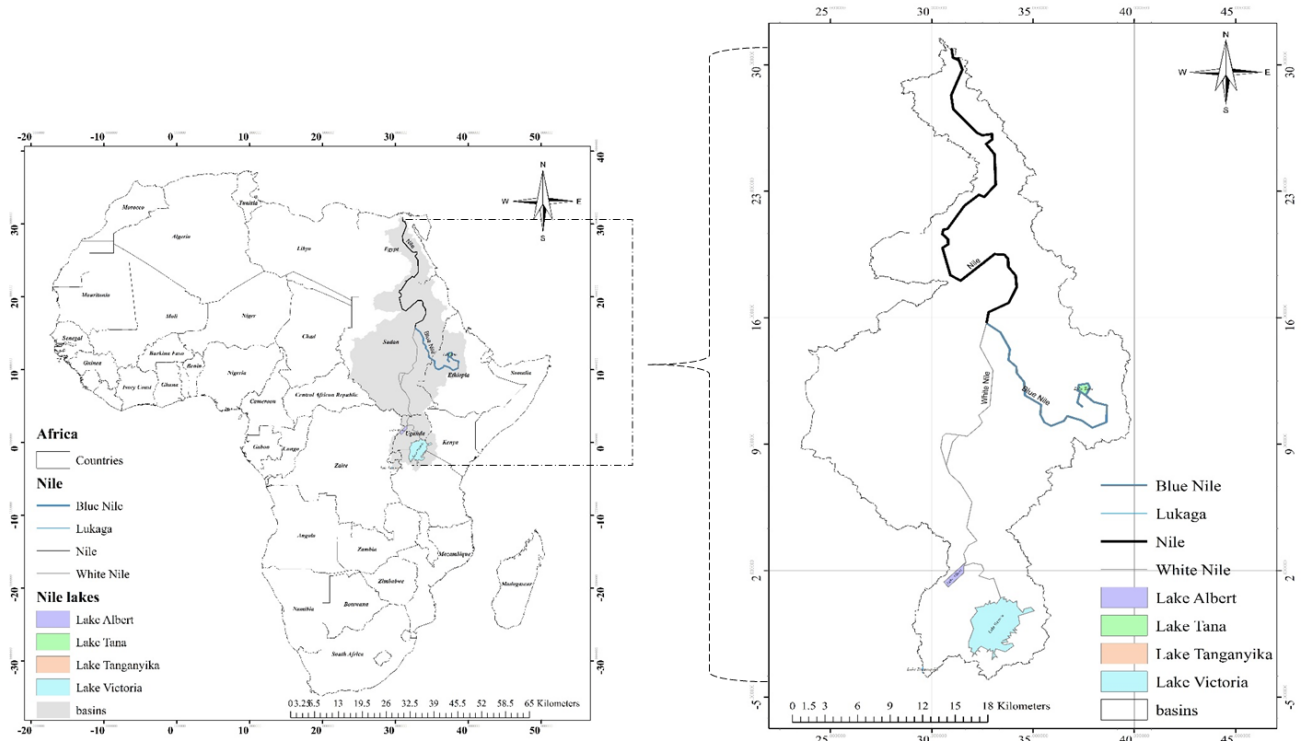


Figure 6.1 Location map of the study area

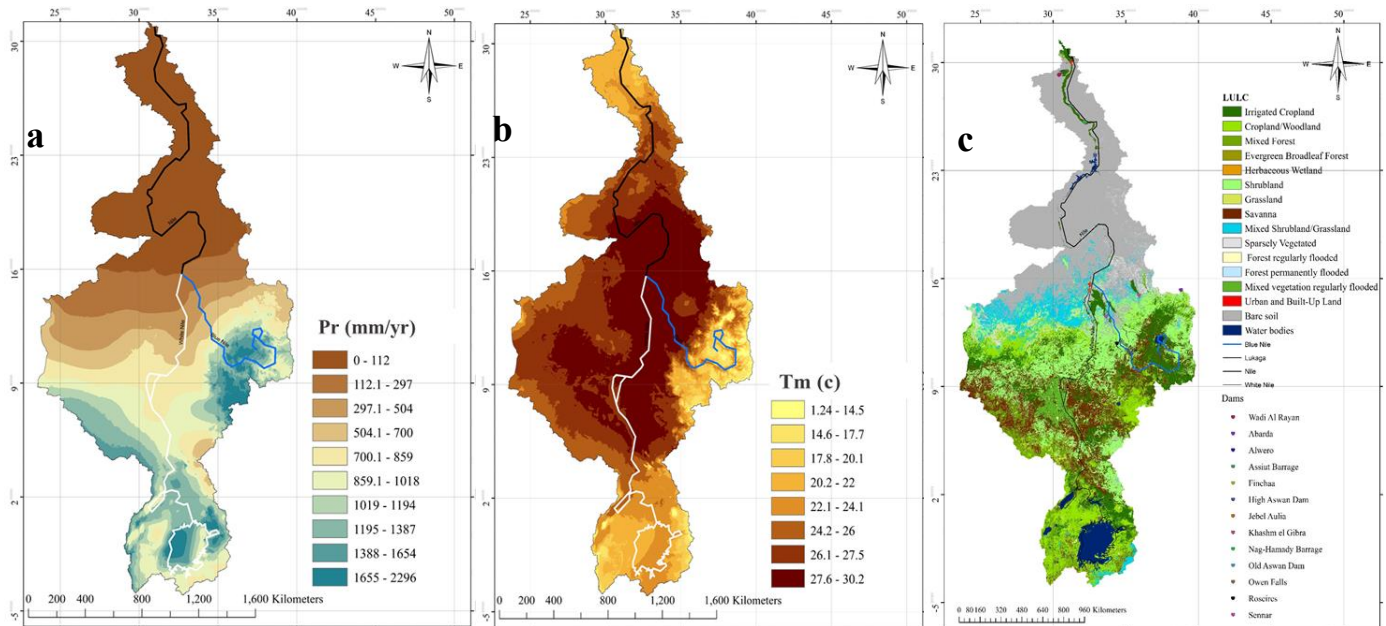


Figure 6.2 Spatial distribution of long-term average precipitation and surface temperature between 1948 and 2017 (b), and 2017 land cover map for the Nile River basin (c)

Historical monthly temperature, relative humidity, and specific humidity data from the year 1900-2017 were extracted from the 20th Century Reanalysis V2 Dataset, the 20th Century

Reanalysis V2 data provided by the NOAA/OAR/ESRL (<https://www.esrl.noaa.gov/psd/>). This data was filtered and developed in form of timeseries dataset. Temperature anomalies data from 1910-2017 was derived from HadCRUT4 global temperature dataset, these datasets have been developed by the Climatic Research Unit (University of East Anglia) in conjunction with the Hadley Centre (UK Met Office). Historical observed monthly precipitation data from 1948- 2017 was derived from University of Delaware precipitation datasets, this dataset is created from a large number of climate stations from the Global Historical Climate Network. Monthly Geopotential height and zonal wind flow from 1900-2017 were derived from the NCEP Reanalysis Dataset. Digital elevation model (DEM) of 30 m resolution was obtained from the Global Elevation Model (GDEM) version 2 databases ([http:// aster.usgs.gov](http://aster.usgs.gov)).

Monthly precipitation and temperature data in gridded form ($0.5^{\circ} \times 0.5^{\circ}$) from 1948 -2017 was obtained from the Global monthly precipitation / temperature data of the Princeton global forcings (Sheffield et al., 2006). These datasets are of the observational-reanalysis hybrid type (Sheffield et al., 2006), they are derived from a combinations of datasets which include the NCEP–NCAR reanalysis dataset (Kalnay et al., 1996), the TRMM dataset, the CRU TS2.0, the GPCP, and the NASA Langley Research Center SRB products (Sheffield et al., 2006). These datasets are widely used in climatology studies due to their robustness for variability analyses (Hoell et al., 2015; Zeng and Cai, 2016; Onyutha and Willems, 2017). Total atmospheric water vapor content was extracted from MODIS atmosphere profiles product (MOD07), and emissivity values were derived by averaging MODIS-bands 31 and 32. Land cover map was derived from the global land cover of Africa archive of the year 2008 and was updated using available Landsat images.

6.3 Methods

6.3.1 Spatio-temporal variability, trends and change points of NRB hydroclimate

To monitor changes in NRB hydroclimate, precipitation, surface temperature, geopotential height, wind speed, meridional and zonal wind stresses, relative humidity (%), specific humidity, and AET were derived from remote sensing data and weather stations over the Nile river basin, as well as for each riparian countries of the Nile basin. We used a surface energy balance algorithm to model the spatio-temporal distribution of reference (ET_o) and actual AET in the NRB (see Mahmoud and Alazba, 2016 for a detailed methods). Spatio-temporal distribution of monthly precipitation, temperature, wind speed, relative humidity, geopotential height, AET and specific humidity were analyzed to identify departure from long-term average, variability was derived in terms of anomalies precipitation, surface temperature, geopotential height, wind speed, meridional and zonal wind stresses, relative humidity (%), specific humidity, and AET. For example, precipitation anomalies have been calculated to find the dry and wet years in the record and used to assess frequency and severity of droughts (Zhai et al., 2005; Woldeamlak and Conway, 2007; Eiste et al., 2012; Mueller and Seneviratne, 2012). In the present study, precipitation anomalies were calculated from total annual precipitation compared with the long-term average precipitation from 1948 to 2017.

To detect trends and change points in hydroclimate variables, we applied two non-parametric tests; Pettitt test and Mann–Kendall test (MK) on time-series data of precipitation, surface temperature, geopotential height, wind speed, meridional and zonal wind stresses, relative humidity (%), specific humidity, and AET. Pettitt's test is commonly used to test the degree of homogeneity of the hydrological data (Bitew et al., 2010; Tekleab et al. 2013; Mengistu et al., 2014; Tabari et al., 2015; Mahmoud and Gan, 2018). While, MK non-parametric test is generally used to detect the trend and if a change point is detected. The Theil-Sen estimator was applied to

estimate the trend magnitudes of all hydroclimate variables. Data quality and length of hydroclimate records play an important role in trend analysis. Although, due to variability and the nature of climate in the NRB, full-time series trend may be non-significant as shown in previous studies (Seleshi and Zanke, 2004; Cheung et al., 2008; Tesemma et al., 2010; Gebremicael et al., 2013; Tabari et al., 2015). Therefore, time-series of monthly precipitation, surface temperature, geopotential height, wind speed, meridional and zonal wind stresses, relative humidity (%), specific humidity, and AET were divided into short time periods to reveal any significant sub-trends and short-durational climate fluctuations in the Nile basin.

One of the main advantages of using MK trend test is its ability to detect monotonic trends in hydrological data and whether the trend is statistically significant or not. Trend is detected in form of + or – sign (increase or decrease), and therefore, the trend is less affected by the outliers (Birsan et al., 2005). The null hypothesis, H_0 , is that precipitation, surface temperature, geopotential height, wind speed, meridional and zonal wind stresses, relative humidity (%), specific humidity, and AET data come from a population with independent realizations and are identically distributed.

6.3.2 Wavelet Analysis and wavelet coherence

Wavelet analysis is a time-frequency analysis widely used to transform a time series of climate data into time and frequency domains, highlighting dominant modes of variability and frequency changes of the dominant oscillations of the time series. Compared to the traditional Fourier transform, this method is more powerful tool to analyze nonstationary series such as climate data (Jevrejeva et al., 2003; Maraun and Kurths, 2004). Another advantage of wavelet transformation over Fourier transform is its ability to search for periodicities in a series and analyzes the temporal behavior of the cycles present. The Morlet wavelet analysis was used to investigate the temporal variability, periodicities, and the cyclic behavior of precipitation, surface temperature, geopotential height, wind speed, meridional and zonal wind stresses, relative humidity (%), specific humidity,

and AET of the NRB. To evaluate the possible impacts of El Niño and IOD on the hydroclimate of the NRB, wavelet coherence was used to estimate the spatio-temporal correlation field between these hydroclimate variables and El Niño and IOD. The wavelet power spectra of each time series were calculated as follow:

$$W_{x,\Psi}(s, t) = (X(t) * \Psi_s(t)) \quad (6-1)$$

Where t is the time series, Ψ_s is the Morlet mother wavelet at the scale s. The Morlet mother wavelet can be defined as follow:

$$\Psi_s(\eta) = \pi^{-1/4} e^{i\omega_s \eta} e^{-\eta^2/2} \quad (6-2)$$

where, η and ω_s are time and frequency.

In addition, wavelet coherence (WTC) was applied to measure the intensity of the common power between two time series, which is defined as the square of their cross-spectrum normalized by smoothed spectra of the two-time series. This method also calculates the cross-correlation between each two-time series (between 0 and 1) as a function of frequency. To evaluate the possible impacts of El Niño and IOD on hydroclimate variables, cross-wavelet power and wavelet coherence, were used to detect the relationship between El Niño and IOD and precipitation, surface temperature, geopotential height, wind speed, meridional and zonal wind stresses, relative humidity (%), specific humidity, and AET. The WTC is presented as:

$$R^2(s, t) = \frac{|S(s^{-1}W_{xy}(s,t))|^2}{S(s^{-1}|W_x(s,t)|^2) * S(s^{-1}|W_y(s,t)|^2)} \quad (6-3)$$

where S is a smoothing operator, x is the hydroclimate variable been analyzed and y is El Niño or IOD.

6.3.3 Composite analysis and cross-correlation

To investigate the hydroclimate variability and the spatio-temporal changes in the NRB riparian countries 'climate, composite maps of precipitation, surface air temperature ($^{\circ}$ C), geopotential height (GPH), relative humidity (%), specific humidity, scalar wind, meridional wind,

zonal wind, soil moisture (kg/m²), surface runoff (mm), and potential evaporation (mm) were derived from data of 1985-2017 minus data of 1948-1984. The observed ENSO and Indian Ocean dipole (IOD) amplitude over the NRB were derived and analyzed. The Indian Ocean dipole (IOD), also known as the Indian “Niño”, was computed as the difference between the western pole over the Arabian Sea (50°E - 70°E, 10°S - 10°N) and the southeast Indian Ocean (90°E to 110°E, 10°S to 0°N). ENSO and IOD amplitude were estimated as the standard deviation (SD) of the Niño3.4 and IOD index over 30-year windows from 1920 to 2017 using the ERSST data sets. Then, detrended cross-correlation analysis (DCCA) was used to investigate the role of ENSO and IOD on the NRB’s hydroclimate variability over inter-decadal and longer timescales. Cross correlations between IOD and El Niño 3.4 amplitudes and NRB surface temperature, GPH, precipitation anomaly, relative humidity, and AET were used to analyze the ENSO and IOD Teleconnections on NRB hydroclimate. NRB’s hydroclimate data were computed over 30-year running periods from 1920 to 2017. In recent years, several studies have employed DCCA to investigate the long-range cross-correlations between two climate variables (nonstationary time series) (Hajian and Movahed, 2010; Baranowski et al., 2015; Dobrica et al., 2018; Liu et al., 2018). The DCCA coefficients of hydroclimate variable $x(i)$ and El Niño or IOD $y(i)$ were calculated as follow:

$$X_k = \sum_{i=1}^k x_i \text{ and } Y_k = \sum_{i=1}^k y_i, \text{ where } k = 1, \dots, N. \quad (6-4)$$

First, the hydroclimate variables, El Niño, and IOD were divided into equal length segments (N_n). Then, using regression models, we have defined the local trend in each segment $\check{X}_{n,s}(k)$ and $\check{Y}_{n,s}(k)$, where $s = 1, \dots, N_n$. The time series data X_k and Y_k are detrended by subtracting the local trends $\check{X}_{n,s}(k)$ and $\check{Y}_{n,s}(k)$ from original time-series in each segment. Next, we calculated the detrended covariance and variance function in each segment as follow:

$$F_{DCCA}^2(n) = \frac{1}{nN_n} \sum_{s=1}^{N_n} \sum_{k=n(s-1)+1}^{ns} [X(k) - \check{X}_{n,s}(k)][Y(k) - \check{Y}_{n,s}(k)] \quad (6-5)$$

Then, the detrended variance of the two-time series, f_{DF} , is calculated as follow:

$$f_{DFA,X}(n) = \sqrt{\frac{1}{N-n} \sum_{i=1}^{N-n} \left[\frac{1}{(n-1)} \sum_k^{i+n} (X_k - \tilde{X}_{k,i}) \right]} \quad (6-6)$$

$$f_{DFA,Y}(n) = \sqrt{\frac{1}{N-n} \sum_{i=1}^{N-n} \left[\frac{1}{(n-1)} \sum_k^{i+n} (Y_k - \tilde{Y}_{k,i}) \right]} \quad (6-7)$$

This calculation is repeated for all segment, if the series are power-law cross-correlated, then $V_{DCCA} \sim n^{2\tau}$. The τ exponent is the long-range power-law cross correlation between two-time series, and is calculated through linear regression of $\log[V_{DCCA}(n)]$ and $\log n$. Finally, the DCCA cross correlation coefficient (ρ) was calculated according to:

$$\rho = \frac{F_{DCCA}^2(n)}{f_{DFA,X}(n)f_{DFA,Y}(n)} \quad (6-8)$$

The value of ρ ranges from -1 to 1, a value of $\rho = 0$ means there is no cross-correlation between the two-time series being analyzed.

6.4 Results and discussion

6.4.1 Nile River Basin hydroclimate variability and trends

The NRB has experienced significant climate change impact in recent decades, as shown in the detected change point of 1976, and a statistically significant warming trend of 0.19 °C/decade over 1910-2017 (Figure 6.3(a)). The results also show a significant increase in the long-term average surface temperature anomaly from -0.1°C between 1910 and 1976 to 0.523 °C between 1976 and 2017 (Table 6.1, Figure 6.3(a)). Mean monthly surface temperature also showed a statistically significant change point in 1987, and a warming trend of 0.14 °C/decade. Because mean monthly surface temperature increased from 28.65 °C between 1900-1987 to 29.11 °C between 1978 and 2017 (Table 6.1). The NRB also experienced a significant increase in daily maximum temperature of about 0.35 °C/decade since 1975. In case of monthly precipitation data, summary statistics revealed that the maximum, minimum, standard deviation, were 279.9, 27, and 55.915 respectively. A statistically significant change point was detected in 1970 in the monthly

precipitation anomaly data with an overall decreasing trend of 16.2 mm/decade (Figure 6.3(b), Table 6.1), because monthly precipitation anomaly decreased from 55.7 mm/m between 1948 and 1970 to -29.14 mm/m between 1970 and 2017. Summary statistics also revealed that mean monthly precipitation dropped from 138.68 between 1948-1970 mm/m to 130.04 mm/m between 1970-2017 over the NRB. Overall it is concluded that temporal variability in temperature and precipitation worsened drying of the NRB. Warming trend also reflects higher availability of energy for evapotranspiration; as, evapotranspiration rate is directly proportional to surface temperature.

Moreover, a statistically significant change point was detected in wind speed in 1975, and the mean wind speed increased from 2.7 m/s over 1948-1975 to 2.9 m/s over 1975-2017 (Figure 6.3(c), Table 6.1), which means a statistically significant increasing trend of 0.02 m/decade. This is critical as high wind speed tends to replace the saturated air from earth surface with dry air. For the 1948-2017 relative humidity data, there was a statistically significant change point in 1977, but a significant decreasing trend of 0.35% /decade after 1977 (Figure 6.3(d)). The monthly specific humidity data of 1948-2016 had a statistically significant change point in 1966, and an overall statistically significant decreasing trend of 0.15 gm/kg per decade, with the mean specific humidity declined from 13.34 gm/kg in 1948-1966 to 12.42 gm/kg in 1966-2017 (Figure 6.3(e)). This is critical as high wind speed tends to replace the saturated air from earth surface with dry air which cause more evapotranspiration. Similarly, monthly 1000-mb geopotential height (GPH) data had a statistically significant change point in 1976, with a mean GPH increasing from 88.79 m over 1948-1976 to 105.36 m over 1976-2016 (Figure 6.3(f)), an overall statistically significant increasing trend of 3.1 m/decade. As expected, higher surface temperature had resulted in higher GPH (Gong et al., 2007), which, as a measure of the atmospheric pressure level, means the lower atmosphere had become warmer.

In addition, from the 1950-2017 reference and actual evapotranspiration (AET) estimated for NRB using a surface energy balance algorithm (Figure 6.3(g)), the AET of NRB has increased significantly, which is also shown by other studies, that higher AET is related to higher wind speed and wind stress, warming and lower RH (Eslamian et al., 2011; Fischer and Knutti, 2013; Zaroug et al., 2014). In the present study, AET anomaly showed a statistically significant change point in 1995 with an upward trend of 1.2 mm/decade (Figure 6.3(g), Table 6.1). Figure 6.3(g) also shows a significant increase in AET anomaly after 1995, the long-term average AET anomaly increased from -2.7 mm between 1948 and 1995 to 4.7 mm between 1995 and 2017.

Table 6.1 Change point and trend analysis of hydroclimate variables over the NRB

Nile river basin	Pettitt test					Mann–Kendall test					
	Years	K	t	P	trend	Tau	Sen's slope	P	trend	Mb	Ma
Monthly Tm	1900-2017	44607	1987	0.011	Ha	0.05	0.014	< 0.0001	+	28.65	29.11
Daily Tmax	1900-2017	589200	1975	0.002	Ha	0.45	0.035	< 0.0001	+	36.7	37.7
T anomaly	1910-2017	2442	1976	< 0.0001	Ha	0.56	0.019	< 0.0001	+	-0.10	0.523
Monthly precipitation	1948-2017	11873	1970	0.0362	H0	0.069	-0.12	0.006	-	138.67	130.03
Precipitation anomaly	1948-2017	586	1970	0.0001	Ha	0.25	-1.622	0.003	-	55.75	-29.14
Geopotential height	1948-2017	86077	1976	< 0.0001	Ha	0.394	0.31	< 0.0001	+	88.79	105.37
Relative humidity	1948-2017	24125	1977	0.0004	Ha	0.144	-0.035	< 0.0001	-	44.3	42.13
Specific humidity	1900-2017	47200	1966	< 0.0001	Ha	0.254	-0.015	< 0.0001	-	13.34	12.42
Wind speed	1948-2017	56785	1975	< 0.0001	Ha	0.60	0.002	< 0.0001	+	2.7	2.9
AET	1948-2017	1522	1995	< 0.0001	Ha	0.34	0.12	< 0.0001	+	-2.72	4.8

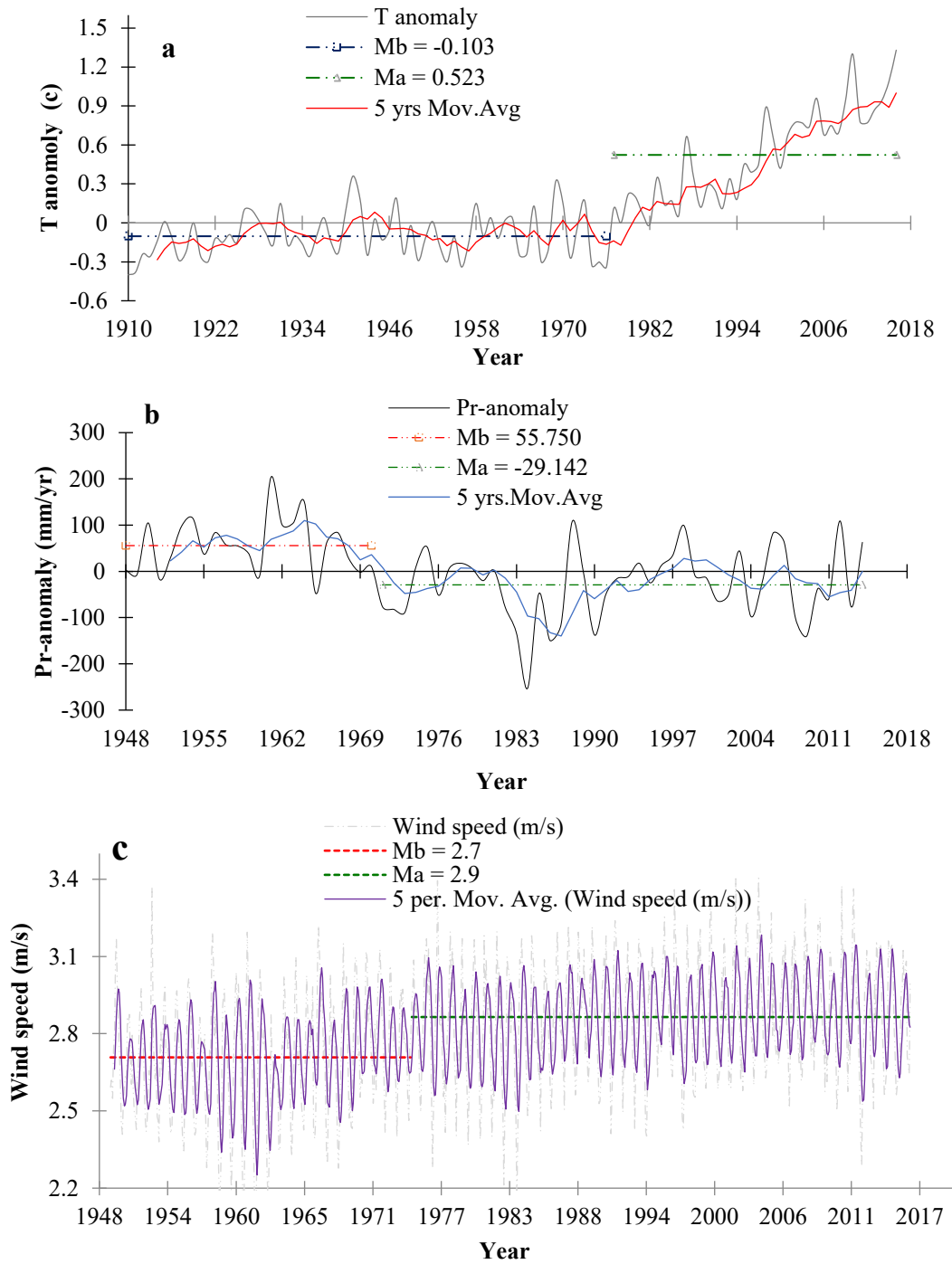
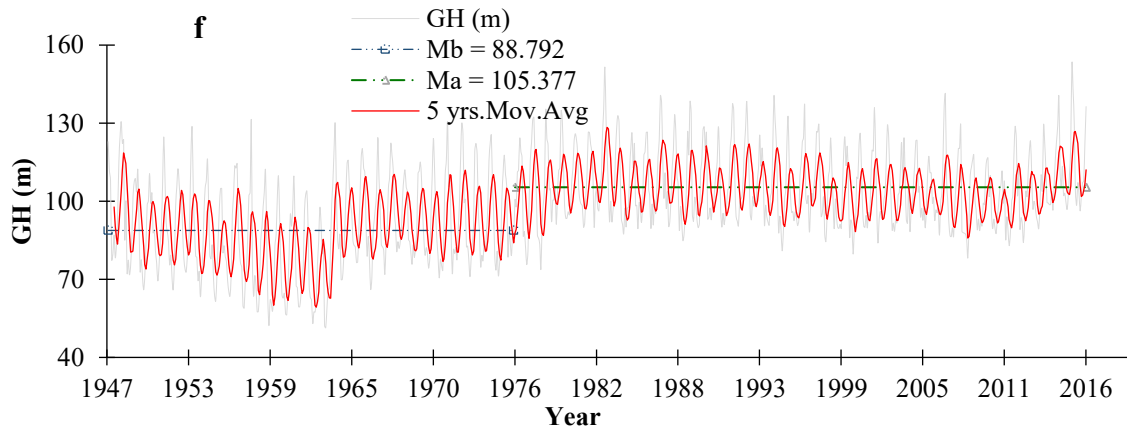
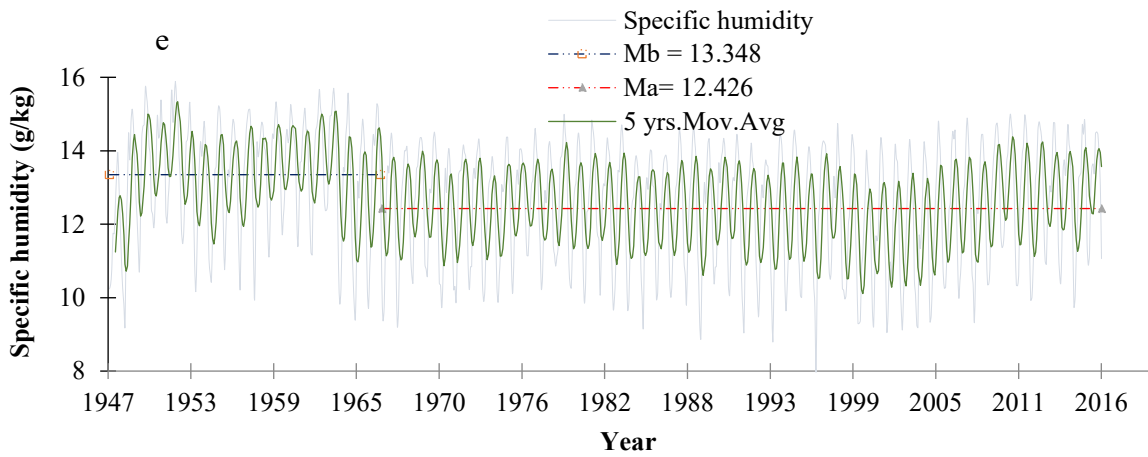
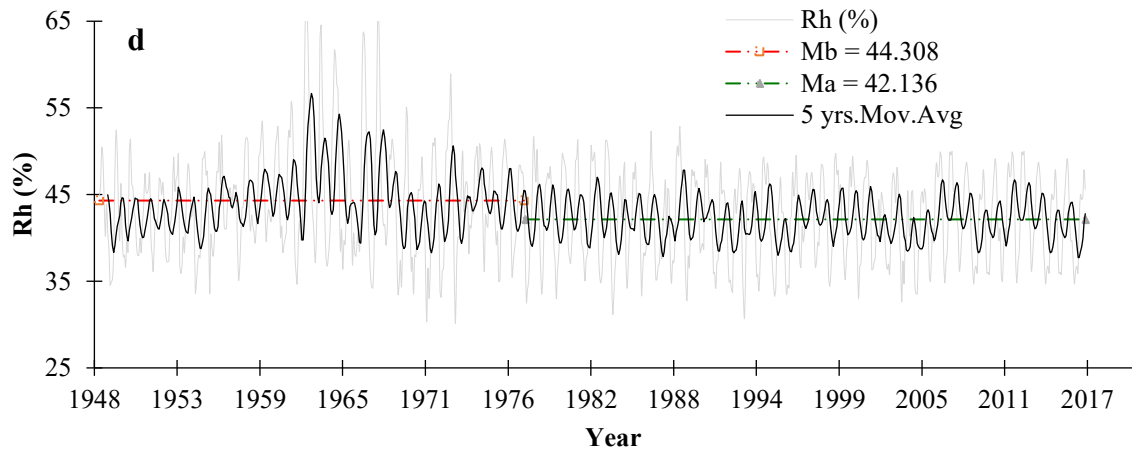


Figure 6.3 Temporal variability and trend of (a) temperature anomaly, (b) precipitation anomaly, (c) wind speed, (d) relative humidity, (e) specific humidity, (f) geopotential height, and (g) AET



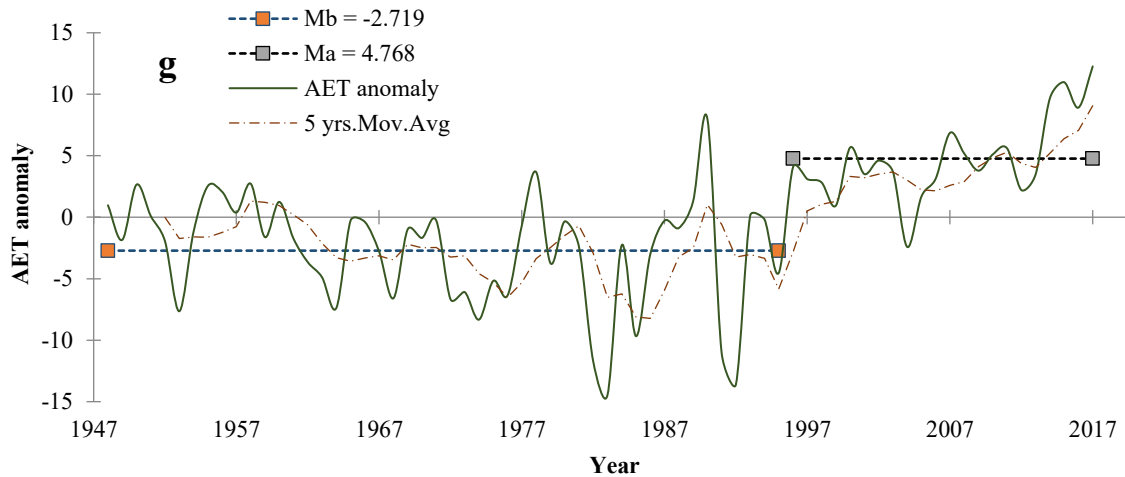


Figure 6.3 (continued)

6.4.2 Spatial variability of the Nile River basin hydroclimate under climate warming

The analysis of spatial distribution of precipitation in the NRB revealed a high variability of precipitation amounts between the riparian of the NRB. On average, annual precipitation in the NRB is approximately 700 mm. However, this amount differs significantly from one country to another, with the lowest precipitation being in Egypt and very high in Ethiopia and medium to high in the equatorial lake’s region “Burundi, Congo, Kenya, Rwanda, Tanzania and Uganda”. Spatially, there is a gradual decrease and high variability of precipitation from upstream “Ethiopia” which have an annual average of 803-1581 mm/yr in the rainy season from mid-June to September to downstream “Egypt” with an annual precipitation range from 0-112 mm/yr (Figure 6.2(a)). Some downstream countries like Egypt and Sudan is mostly desert where drought is common. Despite high precipitation in central area of Sudan, recurrent droughts events were recorded in recent years.

Composite analysis of NRB’s hydroclimate data between 1948 and 2017 also shows significant changes across the entire NRB (Figures 6.4 and 6.5). For instance, the composite mean map of precipitation shows a drop in daily precipitation in the NRB except for Uganda which had an increase of 1.5-3.5 mm/day between 1985 and 2017 (Figures 6.4(a)). On the other hand, specific

humidity decreased in Sudan, northwestern regions of Ethiopia (in lowland). Uganda had a different pattern where specific humidity increased by 2-3 g/kg between 1985 and 2017 (Figures 6.4(b)). The increase in scalar wind was maximum in Uganda, Sudan, and northwestern regions of Ethiopia with an average increase of 0.2-0.8 m²/sec² between 1985 and 2017 (Figures 6.4(c)). Meridional and Zonal wind also showed similar increase in these regions (Figures 6.4(d-e)).

The composite mean of geopotential height shows 5-15 m increase in the NRB between 1985 and 2017 compared to the mean between 1948 and 1984 (Figures 6.4(f)). The highest increase was in Egypt and Sudan (downstream) with an average increase of 3-5 m/decade. Upstream riparian of the basin such as Ethiopia had an increase of 1.5-3.75 m/decade. These results revealed that geopotential height become thicker in the last few decades as the temperature increases. The composite mean of surface temperature also shows an increase of 0.16-0.4 C°/decade over the NRB, with highest increase observed in Sudan and Egypt (Figures 6.5(a)). This finding agrees well with the earlier results from trend analysis. Because of climate warming, relative humidity has decreased by 1-5%/decade after 1985, with the largest decrease in Ethiopia, Uganda, and Sudan where warming has also been the worst (Figures 6.5(b)). The surface soil moisture shows high spatial variabilities in NRB but a decreasing trend of 16-45 mm/decade between 1985 and 2017 (Figures 6.5(c)). A slight decrease in surface runoff can also be seen in Ethiopia, Uganda, and Sudan, while there is no change over Egypt (Figures 6.5(d)). Significant evaporation losses recently observed in water bodies of many riparian countries of NRB between 1985 and 2017 (Figures 6.5(e)). The aforementioned changes related to warming had resulted in decreased daily precipitation, lower specific humidity in Sudan, northwestern regions of Ethiopia (in lowland), lower annual surface runoff over Ethiopia, Uganda, and Sudan, and higher potential evapotranspiration over Ethiopia, Uganda, and Sudan (Figures 6.5(e)).

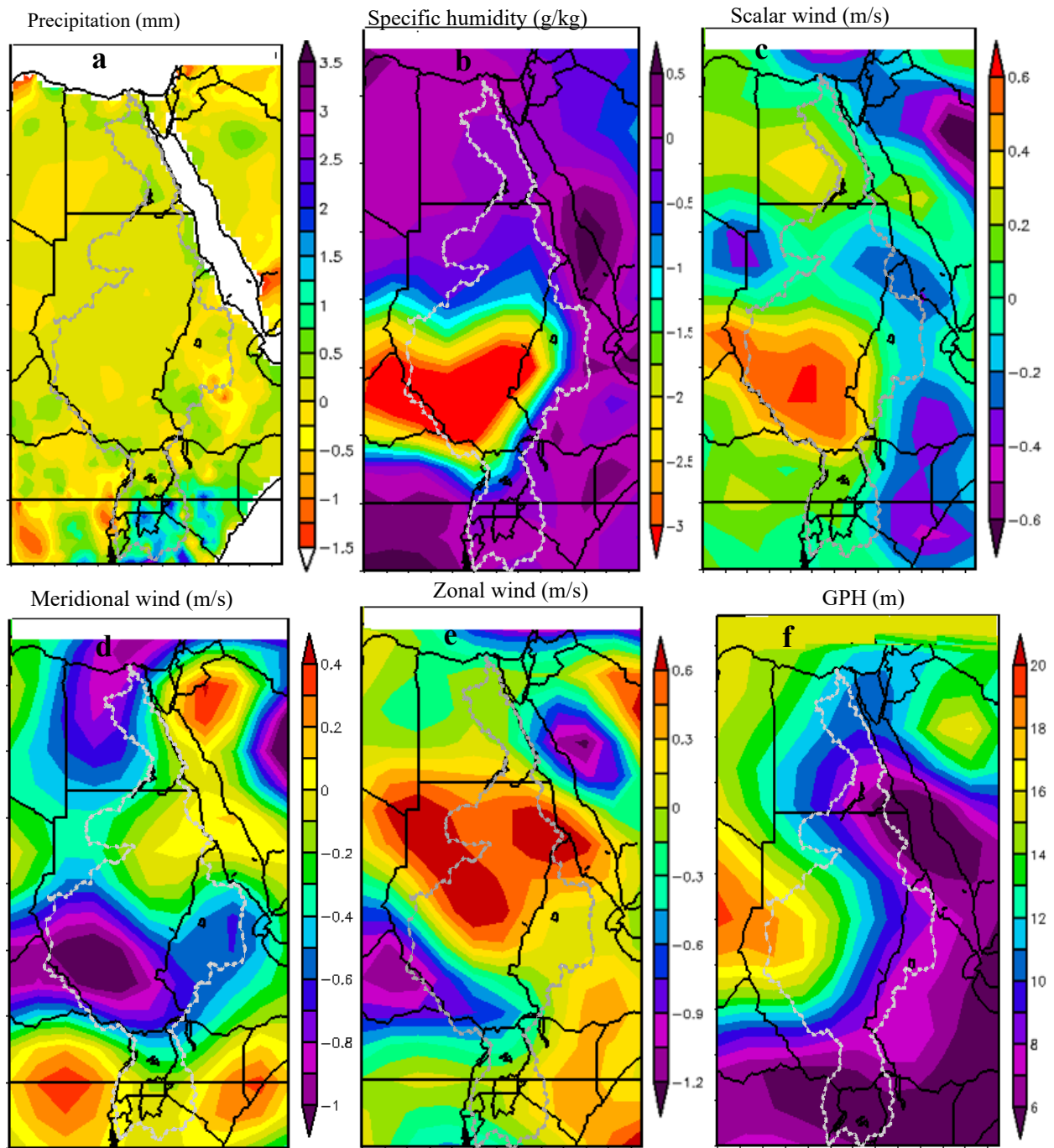


Figure 6.4 Composite maps of (a) Precipitation, (b) Specific humidity, (c) Scalar wind, (d) Meridional wind, (e) Zonal wind, (f) GPH for 1985 to 2017 minus 1948 to 1984

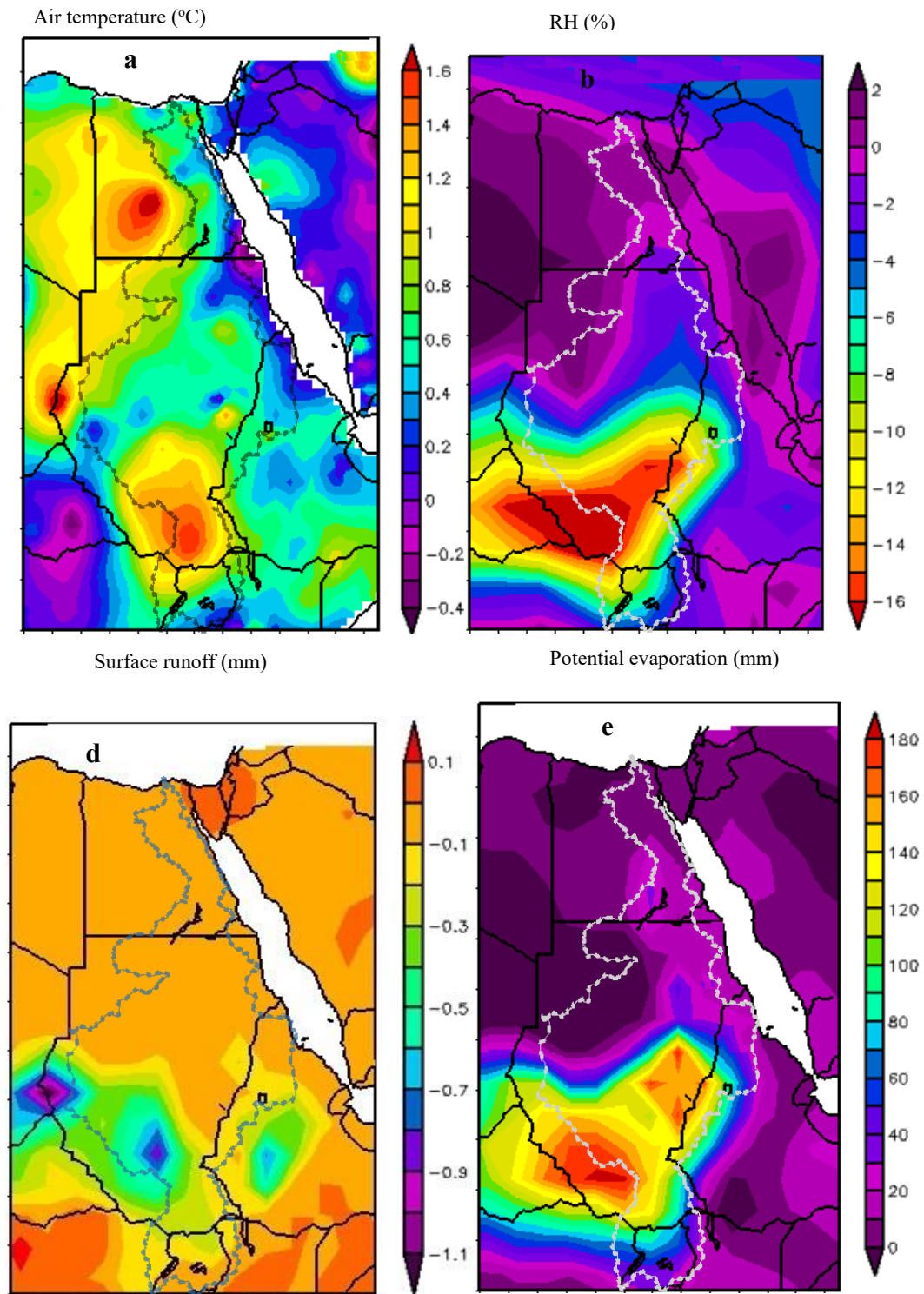


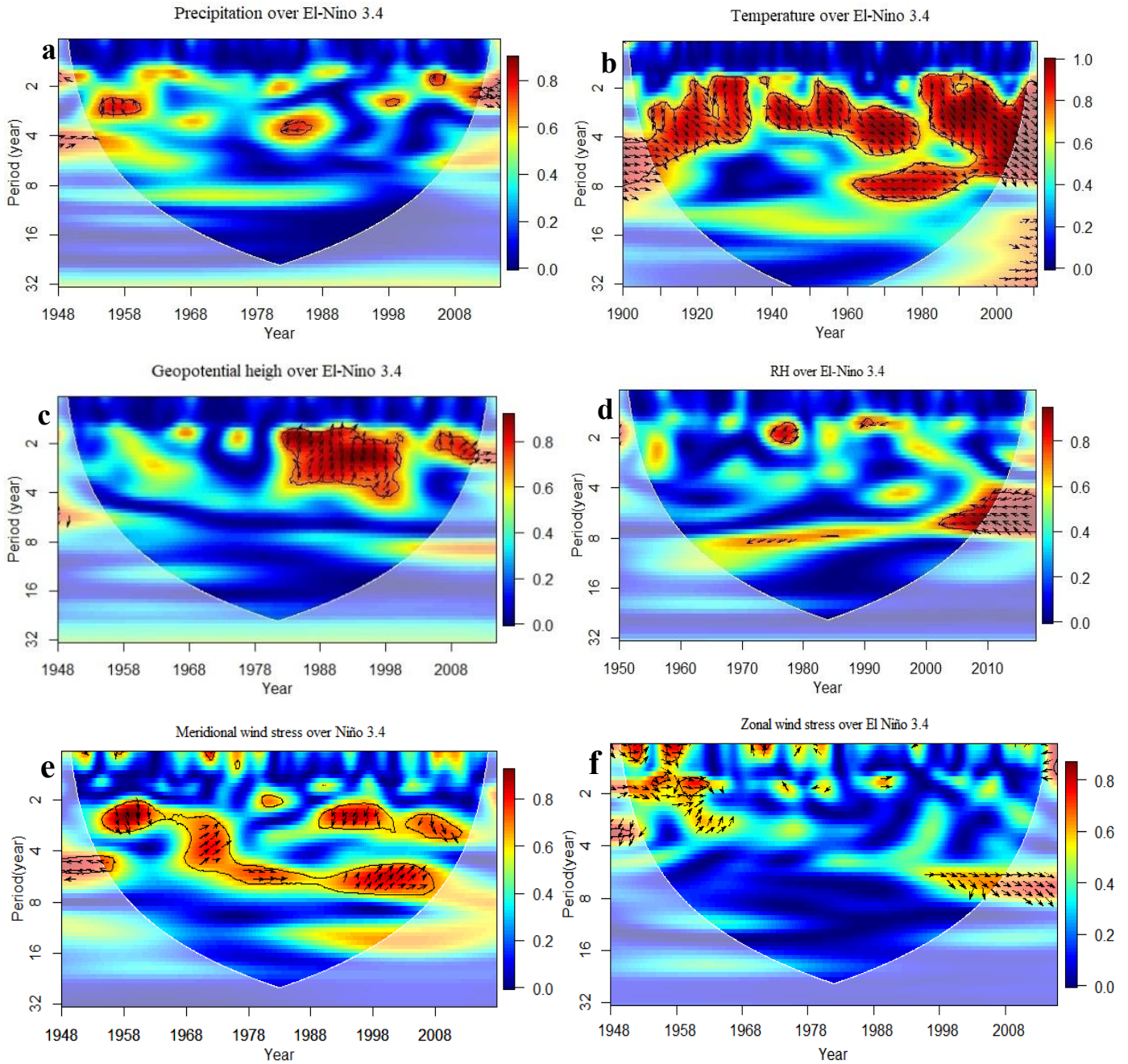
Figure 6.5 Composite maps of (a) air temperature ($^{\circ}\text{C}$), (b) relative humidity (%), (c) soil moisture (kg/m^2), (d) surface runoff (mm), and (e) potential evaporation (mm).

6.4.3 Influence of Indian Ocean dipole (IOD) and ENSO on NRB's hydroclimate

To evaluate the possible impacts of El Niño 3.4 on hydroclimate variables in the NRB, wavelet coherence and detrended cross-correlation function, was used to detect the relationship between hydroclimate variables and El Niño 3.4 and IOD. The wavelet coherence plots (WTC) between El Niño 3.4, IOD, and precipitation, surface temperature, geopotential height, wind speed, meridional and zonal wind stresses, relative humidity (%), specific humidity, and AET of the NRB are shown in Figures 6.6 and 6.7. The arrows show the phase difference: right-pointing arrows indicates that the two-time series are in phase signals, while left-pointing arrows represents anti-phase signals and mean that one time series leads (lags) the other by 90° . Wavelet coherence analysis showed that the hydroclimate of NRB is strongly correlated with El Niño (based on Niño3.4) (Figure 6.6). The influence of El Niño 3.4 on precipitation can be seen in wavelet coherence plot (Figure 6.6(a)). Precipitation exhibits coherent spatial patterns with respect to El Niño, as the wavelet coherence spectra revealed a statistically significant coherency at 2-4 yr band in 1960s and 1970s and indicates anti-phase relationships between precipitation and El Niño 3.4 after 1970s.

The coherence spectrum plots between El Niño 3.4 and surface temperature show statistically significant power at 2–4-yr bands in 1920 to 1940, 1950 to 1970, and 1975 to 2012 over NRB (Figure 6.6(b)). After 1970s, there was a consistently strong coherence at 4–8-yr bands between El Niño 3.4 and surface temperature. This observed strong in-phase relationship between El Niño 3.4 and surface temperature after 1970 indicates that El Niño 3.4 leads the warming trend in the NRB. Similarly, the power of the wavelet coherence between El Niño 3.4 and geopotential height (Figure 6.6(c)) was consistently strong at 4–8-yr band between 1975 and 2012, which is expected because of the close relationship between geopotential height and air temperature. In addition, there was a strong 1–2-yr wavelet coherence in the 1980s and the 1990s between El Niño 3.4 and

relative humidity (anti-phase) (Figure 6.6(d)), and a stronger 4–8yr wavelet coherence after the 2000s.



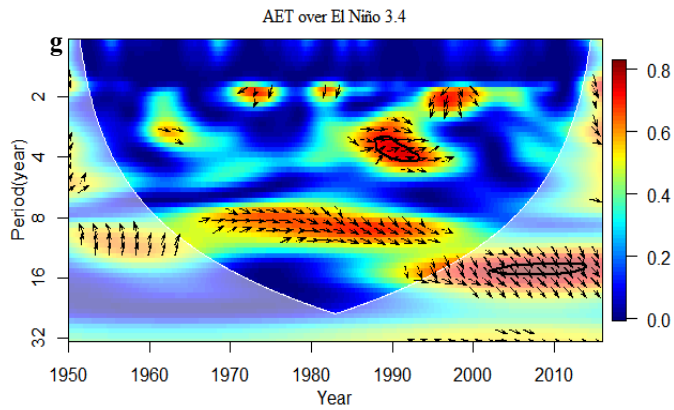


Figure 6.6 Wavelet coherence between El Niño 3.4 and (a) precipitation, (b) temperature, (c) relative humidity, (d) geopotential height, (e) meridional wind stress, (f) zonal wind stresses, (g) AET

Given IOD has been shown to play a primary role on the precipitation of East Africa over inter-decadal timescales (Tierney et al., 2013), we have also investigated the teleconnection of the dipole mode to NRB's climate, to ENSO and to the Indian Ocean, over a wide range of time scales. Beside ENSO, our results also show that IOD plays a crucial role on NRB's hydroclimate variability over inter-decadal and longer timescales. The wavelet coherence spectrum plots between AET and El Niño and IOD show in-phase, statistically significant coherent relationship at 2-4 and 8-14-years band after 1970s (Figures 6.6(g), 7.7(g)), which peaked at the 14–16-year time scale after 2000s. On the other hand, the wavelet coherence between IOD and AET show that IOD mainly lead AET after 2000s. The higher AET after 1970s can be partly attributed to stronger El Niño amplitudes, as shown by strong wavelet coherence between zonal and meridional wind stresses and AET at 1-2 years bands (Figure 6.6(e, f)). Their recurrent in-phase and anti-phase relationships at 1-2 years bands demonstrate the effect of positive (negative) wind stress anomalies when El Niño was active. while IOD, meridional and zonal wind stresses showed in-phase coherence after 2000s (Figure 6.7(e, f)). It seems both increasing meridional wind stress anomalies and stronger El Niño episodes have contributed to changes in the heat content of NRB.

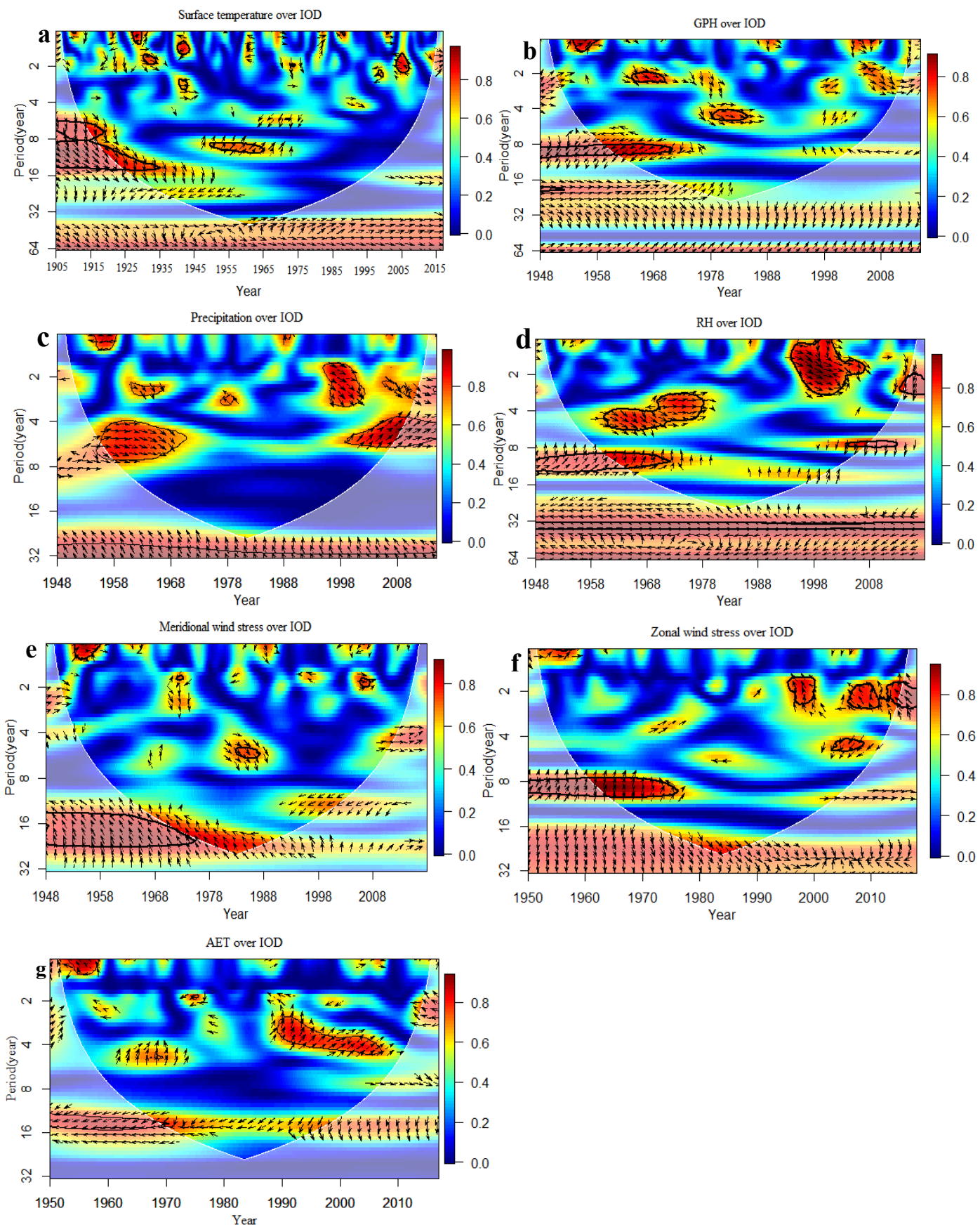


Figure 6.7 Wavelet coherence between IOD and (a) surface temperature, (b) GPH, (c) precipitation, (d) relative humidity, (e) meridional wind stress, (f) zonal wind stresses, (g) AET

The wavelet coherence plot between IOD and surface temperature (T_s) shows statistically significant, interannual (1-4yr) in-phase and anti-phase relationships over 1905 and 2018, revealing the interannual response of T_s and GPH to the variability of IOD in the last 100 years. At inter-decadal time scale, IOD and T_s show only significant, in-phase coherence at 8–16, 16-32, 32-64-year bands over 1975-2018 (Figure 6.7(a)). On the other hand, IOD and GPH were continuously in phase with significant coherent spatial pattern at 2-4- and 4-8-years band after 1970s (Figure 6.7(b)). The wavelet coherence spectrum plot between precipitation and IOD shows in phase relationship with significant coherent spatial pattern at 2-4- and 4-8-year band after 1990, and an anti-phase relationship at 32-year band between 1948 and 2018 (Figure 6.7(c)). This strong anti-phase relationship shows that IOD primarily influenced NRB's precipitation at inter-decadal timescales. There is a strong in-phase relationship between IOD and relative humidity at 2-4 yr band over 1998-2008, and at 4-8 and 8-16-year bands over 1960-1980, and an anti-phase relationship in the 32-64-year band (Figure 6.7(d)).

Figure 6.8(a-e) shows that the hydroclimate of NRB is strongly teleconnected to El Niño and IOD, especially to El Niño, with high positive or negative correlations between El Niño 3.4, surface temperature T_s ($\rho = 0.97$), GPH ($\rho = 0.81$), relative humidity ($\rho = -0.97$), precipitation ($\rho = -0.7$). There is also a significant positive correlation between AET and El Niño 3.4 ($\rho = 0.93$) in contrast to negative correlation between AET and IOD ($\rho = -0.47$) (Fig 8e), which shows that El Niño affect the AET of NRB. The correlation of these hydroclimate variables with IOD are generally lower than with El Niño's (Figure 6.8(a-e)). However, IOD still plays an important role on the hydroclimate variability in the NRB, such as its effect on NRB's surface temperature and precipitation anomalies under neutral ENSO conditions. The strong negative correlation of IOD

with precipitation ($\rho = -0.37$) suggest that besides El Niño, IOD has also impacted the precipitation of the NRB, as shown by Tierney et al. (2013) the mechanism that teleconnects East African precipitation to ENSO and IOD.

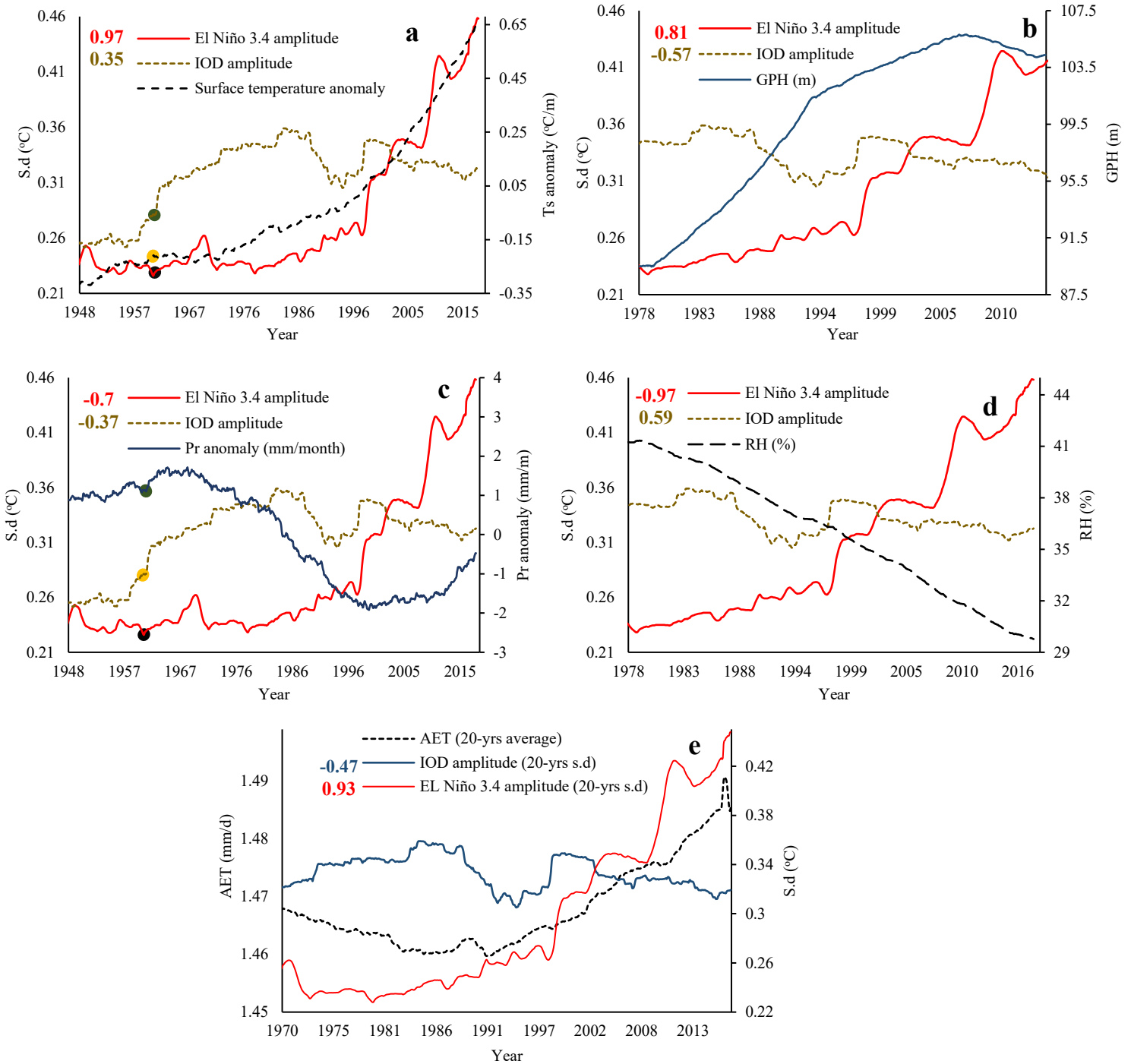


Figure 6.8 ENSO and IOD Teleconnections on NRB hydroclimate. IOD and El Niño 3.4 amplitudes cross-correlations with NRB surface temperature (a), GPH (b), precipitation anomaly (c), relative humidity (d), AET (e). Surface temperature anomaly, precipitation anomaly, relative humidity, and AET are computed over 30-year running periods from 1920 to 2017, El Niño 3.4 and IOD amplitude are the SD of El Niño 3.4 and IOD indexes over 30-year windows from 1920 to 2017 using the ERSST data sets. The numbers in the top right are the cross-correlation coefficient between hydrologic variables and IOD amplitude (brown colour) and El Niño 3.4 amplitude (red colour) at the 5% level. In a and c, black and yellow points represent neutral ENSO conditions and strong positive IOD in 1961, green point is the response on surface temperature “increase” and decrease in precipitation anomalies “decrease” in the same year.

6.5 Conclusion

The present study aimed at improving our understanding of the hydrological cycle and variability in hydroclimate variables of the Nile River basin. Change point detection, trend analysis, wavelet coherence and detrended cross-correlation function were used to analyze the variability in the Nile River basin hydroclimate at a wide range of time scales and possible linkages to the large-scale climate patterns. First, we analyzed the spatio-temporal variability, frequency, intensity, change point and trend of monthly precipitation, precipitation anomaly, temperature, temperature anomaly, geopotential height, relative humidity, specific humidity, actual evapotranspiration (AET), and wind stress data at the basin level. Next, we also investigated the IOD and El Niño role on NRB’s hydroclimate variability over inter-decadal and longer timescales. Our analysis shows that the NRB has experienced significant climate change impact in recent decades, as shown in the detected change point of 1976, and a statistically significant warming trend of 0.19 °C/decade over 1910-2017. A statistically significant change point was detected in 1970 in the monthly precipitation anomaly data with an overall decreasing trend of 16.2 mm/decade. Moreover, a statistically significant change point was detected in wind speed in 1975,

with a statistically significant increasing trend of 0.02 m/decade. This is critical as high wind speed tends to replace the saturated air from earth surface with dry air.

For the 1948-2017 relative humidity data, there was a statistically significant change point in 1977, and a significant decreasing trend of 0.35% /decade after 1977. Similarly, monthly 1000-mb geopotential height (GPH) data had a statistically significant change point in 1976, with an overall statistically significant increasing trend of 3.1 m/decade, which, as a measure of the atmospheric pressure level, means the lower atmosphere had become warmer. The monthly specific humidity data of 1948-2016 had a statistically significant change point in 1966, and an overall statistically significant decreasing trend of 0.15 gm/kg per decade. The AET anomaly of the NRB has increased significantly, with a statistically significant change point in 1995 with an upward trend of 1.2 mm/decade. This can be attributed to a higher wind speed and wind stress, warming and lower RH.

Composite analysis of NRB's hydroclimate data between 1948 and 2017 also shows significant changes across the entire NRB. Beside ENSO, our results also show that IOD plays a crucial role on NRB's hydroclimate variability over inter-decadal and longer timescales. The wavelet coherence spectrum plots between AET and El Niño and IOD show in-phase, statistically significant coherent relationship at 2-4 and 8-14-years band after 1970s (Figs 6g, 7g), which peaked at the 14–16-year time scale after 2000s. On the other hand, the wavelet coherence between IOD and AET show that IOD mainly lead AET after 2000s. The higher AET after 1970s can be partly attributed to stronger El Niño amplitudes, as shown by strong wavelet coherence between zonal and meridional wind stresses and AET at 1-2 years bands. Their recurrent in-phase and anti-phase relationships at 1-2 years bands demonstrate the effect of positive (negative) wind stress anomalies when El Niño was active. while IOD, meridional and zonal wind stresses showed in-phase coherence after 2000s. It seems both increasing meridional wind stress anomalies and

stronger El Niño episodes have contributed to changes in the heat content of NRB. A detailed cross correlation (ρ) analysis shows that the hydroclimate of NRB is strongly teleconnected to El Niño and IOD, especially to El Niño, with positive or negative correlations between El Niño 3.4, surface temperature (T_s) ($\rho = 0.97$), GPH ($\rho = 0.81$), relative humidity ($\rho = -0.97$) and precipitation ($\rho = -0.7$). The correlation of these climate variables with IOD are generally lower than with El Niño. However, IOD still plays an important role on the hydroclimate variability in the NRB, such as its effect on NRB's surface temperature and precipitation anomalies under neutral ENSO conditions, The results from this study would help us to better develop mitigation strategies for these riparian countries against the potential impact of climate change.

Chapter 7 Worsening Drought of Nile River Basin by Atmospheric Circulation Shift, Stronger ENSO and Indian Ocean Dipole

7.1 Introduction

Since the beginning of ancient civilizations in Africa, the Nile River has been the major source of water supply to its eleven riparian countries. However, in recent years, recurring droughts and increasing population have led to rising tension between competing users for water. There is a need to better understand changes in the hydrological cycle of the Nile River Basin (NRB). Among various causes of droughts identified in Africa (Giannini et al., 2003; Zeng, 2003; Shanahan et al., 2009; Williams and Funk, 2011) are the decline in precipitation related to warming caused by rising concentration of greenhouse gases (Ramanathan et al., 2001; Williams and Funk, 2011).

Intervals of severe droughts in NRB lasting for periods ranging from decades to centuries are linked to variations in Atlantic temperatures (Shanahan et al., 2009). Studies show that precipitation in the Blue Nile basin (BNB) (Ramanathan et al., 2001; Seleshi et al., 2006; Nyeko-Ogiramoi et al., 2013; Onyutha et al., 2016) with high spatial and temporal variabilities is affected by El Niño Southern Oscillation (ENSO) such that positive anomalies (wet years) tend to occur during the negative phase of ENSO (Gissila et al., 2004; Segele et al., 2009; Abteu et al., 2009), while negative anomalies (dry years) during the positive phase of ENSO, and the timing of ENSO events. Conversely, BNB's precipitation and flow tend to be high during La Nina years but low during El Niño years (Cai et al., 2015; Kim et al., 2014), and extreme droughts correspond to strong El Niño events. Long-term variations of the precipitation of NRB is also strongly controlled by the African monsoon (Zhao et al., 2012). Subsequently, a relevant question to the observed drought variability of NRB is whether droughts of NRB are primarily caused by precipitation

anomalies attributed to ENSO, or has other factors also contributed to its drought severity, such as the warming trend of Africa (Serdeczny et al., 2016), increasing frequency of extreme El Niño events under climate warming (Cai et al., 2014; Kim et al., 2014), and changes in atmospheric circulations (Siam et al., 2013).

The flow of NRB comes from two sources, the Blue Nile and the White Nile which join at Khartoum -the capital city of Sudan. The BNB occupies about 11% of the NRB but it contributes about 60% of the Nile River flow (Serdeczny et al., 2016). With a total catchment area of 3.1 million km², the NRB is shared by eleven countries, namely, Burundi, Rwanda, Uganda, Kenya, Tanzania, South Sudan, Democratic Republic of Congo, Sudan, Eritrea, Ethiopia, and Egypt. About 86% of NRB's area lies in Sudan, Ethiopia and Egypt. Despite of its recurrent occurrences, we have yet to explain droughts of NRB satisfactorily because most past drought studies mainly focus on precipitation anomalies, soil moisture, and vegetation indices of the BNB (Gissila et al., 2004; Seleshi et al., 2006; Nyeko-Ogiramoi et al., 2013; Tabari et al., 2015). To gain a comprehensive perspective on the potential impact of climate change to droughts of NRB, we conducted detailed analysis, sensitivities of its meteorological, agricultural, and hydrological droughts, and factors contributing to such droughts. We have also investigated the variability of the Nile flow data over 1900-2012 in three gaging stations, and implications of flow variability to the severity and intensity of hydrological droughts in each riparian country of the NRB. The results from this study would help us to develop mitigation strategies for these riparian countries against the potential impact of future droughts.

7.2 Methods

7.2.1 Description of datasets used in this study

- Monthly mean temperature (tm), relative humidity, and specific humidity data from the year 1900-2016 were extracted from the 20th Century Reanalysis V2 Dataset, the 20th Century Reanalysis V2 data provided by the NOAA/OAR/ESRL (<https://www.esrl.noaa.gov/psd/>). This data was filtered and developed in form of timeseries dataset.
- Temperature anomalies data from 1910-2017 was derived from HadCRUT4 global temperature dataset, these datasets have been developed by the Climatic Research Unit (University of East Anglia) in conjunction with the Hadley Centre (UK Met Office).
- Monthly Precipitation time series data from 1948- 2016 was derived from University of Delaware precipitation datasets, this dataset is created from a large number of climate stations from the Global Historical Climate Network.
- Monthly Geopotential height, monthly zonal, and meridional wind speed and zonal wind flow from 1948-2017 were drawn from the National Centers for Environmental Prediction– National Center for Atmospheric Research (NCEP– NCAR) reanalysis 1 (NCEP-R1) and the 40-yr European Center for Medium-Range Weather Forecasts (ECMWF) Re-Analysis (ERA-40).
- Land cover map was derived from the global land cover of Africa archive of the year 2008 and was updated using available Landsat images. (<http://www.africover.org./index.htm>)
- Digital elevation model (DEM) of 30 m resolution was obtained from the Global Elevation Model (GDEM) version 2 databases ([http:// aster.usgs.gov](http://aster.usgs.gov)).
- Long term observed monthly Nile River flow data were collected from three stations, the monthly flows at Dongola station-Sudan, Aswan dam station (1900-1984), and the Blue Nile station in Khartoum from 1900 to 1984 were extracted from the Global River Discharge Database (RivDIS

v1.1), in addition we obtained the monthly flows at the Blue Nile station from recorded measurements between 1984-2010.

- Monthly precipitation and temperature data in gridded form ($0.5^\circ \times 0.5^\circ$) from 1948 -2010 was obtained from the Global monthly precipitation / temperature data of the Princeton global forcings from the link

<http://hydrology.princeton.edu/login.ezproxy.library.ualberta.ca/data/pgf/0.5deg/monthly/>.

These datasets are of the observational-reanalysis hybrid type, they are derived from a combinations of datasets which include the NCEP–NCAR reanalysis dataset (Kalnay et al., 1996), the TRMM dataset, the CRU TS2.0, the GPCP, and the NASA Langley Research Center SRB products (Sheffield et al., 2006). These datasets are widely used in climatology studies due to their robustness for variability analyses (Hoell et al., 2015; Zeng and Cai, 2016; Onyutha and Willems, 2017).

- Total atmospheric water vapor content was extracted from MODIS atmosphere profiles product (MOD07) (Borbas et al., 2016), and emissivity values were derived by averaging MODIS-bands 31 and 32.
- Area-Averaged of Ground water storage daily 0.25 deg data [GLDAS Model GLDAS_CLSM025_D v2.0] were derived from GLADS-CLSM025 between 1948-2014 and the Gravity Recovery and Climate Experiment (GRACE) between 2003 and 2017. NRB’s soil moisture data were derived from ERA-Interim, FLDAS and GLADS dataset datasets.
- Warm spell duration (WSD), the annual number of days contributing to events where 6 or more consecutive days experience a daily maximum temperature $T_X > 90$ th percentile were extracted from the HadEX2 observational data set.
- CMIP5 models. We analysed the historical runs over the period 1905-2017 and RCP2.6, RCP4.5, and RCP8.5 experiments over the period 2017-2100 from 34 global climate models (GCMs) of CMIP5. The models included ACCESS1-0, ACCESS1-3, CCSM4, CNRM-CM5, CSIRO-MK3-6-0, FGOALS-g2, GFDL-CM3, GFDL-ESM2G, GFDL-ESM2M, GISS-E2-R, HadGEM2-CC,

HadGEM2-ES, IPSL-CM5A-LR, IPSL-CM5A-MR, IPSL-CM5B-LR, MIROC5, MIROC-ESM, MPI-ESM-LR, MPI-ESM-MR, MRI-CGCM3, NorESM1-M and NorESM1-ME.

7.2.2 Change points and trends

To identify main drivers to meteorological droughts of NRB, we first did a detailed analysis of monthly precipitation, precipitation anomaly, temperature, temperature anomaly, geopotential height, relative humidity, specific humidity, actual evapotranspiration, and zonal and meridional wind stresses data of the NRB; and flow, soil moisture content (SMC), and groundwater storage (GWS) data in relation to its agricultural and hydrological droughts. Change detection techniques and trend analysis were employed to detect abrupt changes and trends in these meteorological variables

7.2.3 Spatiotemporal variability of reference and actual evapotranspiration

We used surface energy balance algorithm to model the spatiotemporal distribution of reference (ET_o) and actual evapotranspiration (AET) in the NRB, variability in AET was measured in form of anomalies in annual AET. Food and Agriculture Organization (FAO) method (Monteith, 1965) was used to model reference evapotranspiration on a grid-by-grid basis using Eq. (7.1). The data included elevation, total monthly precipitation, maximum and minimum air temperature, relative humidity, wind speed at 2m height.

$$ET_o = \frac{0.408\Delta(Rn - G) + \gamma \frac{900}{T + 273} u_2 (e_s - e_a)}{\Delta + \gamma(1 + 0.34u_2)} \quad (7-1)$$

Where,

Rn= net radiation at the crop surface (MJ/m²/day), G = soil heat flux density (MJ/m²/day), T = mean daily air temperature at 2 m height (°C), u₂ = wind speed at 2 m height (m/s), e_s = saturation vapor pressure (kPa), e_a = actual vapor pressure (kPa), Δ = slope vapor pressure curve (kPa/°C), γ = psychrometric constant (kPa/°C), e_s - e_a = saturation vapor pressure deficit (kPa)

Modelling AET was based on surface energy balance algorithm (SEBAL). First, using the input data, the net solar radiation (R_n), NDVI, albedo, roughness length, and soil heat flux (G) were calculated in ArcGIS 10.1. ESRI's ArcGIS Solar Analyst tool according to Fu and Rich (1999).

Latent heat flux λET_{ins} ($W m^{-2}$) which represents the energy amount used for the surface evaporation and plant transpiration processes was then estimated based on equation 7.2.

$$\lambda ET_{ins} = R_n - G - H \quad (7-2)$$

Where R_n ($W m^{-2}$) is the net radiation, G ($W m^{-2}$) is the soil heat flux at the surface, H ($W m^{-2}$) is the sensible heat. R_n is computed from downward and upward shortwave and long-wave radiation based on eq 3.

$$R_n = (1 - \alpha)Rs_{\downarrow} - Rl_{\downarrow} - Rl_{\uparrow} - (1 - \varepsilon_o)Rl_{\downarrow} \quad (7-3)$$

Where α is the surface albedo obtained from MODIS albedos products, these products were developed based on atmospherically corrected, cloud-cleared reflectance observations from the MODIS sensors on NASA's Aqua and Terra satellites.

Rs_{\downarrow} is the incoming shortwave radiation calculated by the elevation-based method (Ruiz-Arias et al., 2009) as follow using the following formula $Rs_{\downarrow} = 1367 \times \cos\theta \times d \times \tau_{sw}$

where, $\cos\theta$ is the cosine of the solar incidence angle, d is the inverse squared relative earth-sun distance, and τ_{sw} is the atmospheric transmissivity. The atmospheric transmissivity values were

determined based on clear sky and relatively dry conditions obtained using the following elevation-based relationship, $\tau_{sw} = 0.75 + 2Z \times 10^{-5}$ where Z is the elevation above sea level (m). While,

the incoming longwave radiance Rl_{\downarrow} and the outgoing longwave radiation Rl_{\uparrow} were calculated

based on the Stefan-Boltzmann equation and MODIS-based surface temperature (T_s) and (T_a) as input, i.e.

$$RL_{\uparrow} = \varepsilon_o \times \sigma \times T_s^4 \quad (7-4)$$

$$RL_{\downarrow} = 0.85 \times (-\ln \tau_{sw})^{0.09} \times \sigma \times T_a^4 \quad (7-5)$$

where σ is the Stefan Boltzmann constant ($5.67 \times 10^{-8} \text{ W m}^{-2} \text{ K}^{-2}$), ε_o is the broad-band surface emissivity computed using an empirical equation from NDVI and the leaf area index (LAI) assuming that $\text{NDVI} > 0$ as described in the SEBAL manual. Soil heat flux were then modeled based on the relationship developed by Bastiaanssen (1995):

$$\text{Soil heat flux } (G) = \left[\frac{T_s - 273.16}{\alpha} (0.0038\alpha + 0.007\alpha^2)(1 - 0.98\text{NDVI}^4) \right] \times Rn \quad (7-6)$$

The last component of the energy balance model was to calculate the sensible heat flux from the equation of heat transport:

$$H = \frac{\rho \times c_p \times \Delta T}{r_{ah}} \quad (7-7)$$

$$\Delta T = \left(\frac{dT_{dry} - \Delta T_{wet}}{T_{sdry} - T_{swet}} \right) \times T_s - \left(\frac{dT_{dry} - dT_{wet}}{T_{sdry} - T_{swet}} \right) \times T_{swet} \quad (7-8)$$

$$r_{ah} = \frac{\ln\left(\frac{z_2}{z_1}\right)}{u^* k} \quad (7-9)$$

$$u^* = \frac{u(z)k}{\ln\left(\frac{z-d}{z_m}\right)} \quad (7-10)$$

Where ρ is the air density (kg m^{-3}), c_p is the specific heat of air ($1004 \text{ J kg}^{-1} \text{ K}^{-1}$), ΔT is the near surface temperature difference (K), and r_{ah} is the aerodynamic resistance to heat transport (s/m), z_1 is a height just above the zero displacement distance height of the plant canopy set to 0.1 m for each pixel, and z_2 is the reference height just above the plant canopy set to 2 m for each pixel. u^* is the friction velocity (m/s), and k is the von Karman constant (0.4).

Based on known values of the land surface friction (Z_m) and NDVI we calculated Z_m for each pixel by a regression equation according to the pixel NDVI value following the procedure of Wang et al. (2005) Finally, we computed the instantaneous ET_{ins} for each pixel by applying Eq. (10). Then, the evaporative fraction (EF) which is the ratio of instantaneous ET_{ins} to the reference ET from Penman—Monteith method.

$$EF = \frac{ET_{inst}}{ET_o} \quad (7-11)$$

$$ET_{sebal} = EF \times ET_o \quad (7-12)$$

We then calculated monthly and annual AET after determining the cumulative ET_o and the ratio, (K_m), of the cumulative reference evapotranspiration ET to the average potential ET over the period. The monthly ET, (AET_m), was then computed as follows:

$$AET_m = \sum_{i=1}^{i=n} (ET_{sebal})_i (K_m)_i \quad (1-13)$$

AET anomalies were calculated from total annual AET compared with the long-term average AET from 2003 to 2016 to find the departure in AET and the impact of climate change in AET variability.

7.2.4 Meteorological drought variability and trend using standardized precipitation index

The Standardized Precipitation Index (SPI) is a widely used index to characterize meteorological drought due to its capability of detecting drought at multiple time scales (Chen et al., 2009; Méndez and Magaña, 2010). Therefore, we used SPI to identify meteorological drought frequency and intensity between 1950-2016, trend and change-point were also considered based on Pettit's test and Mann kernel test. SPI computation was made based on the method proposed by McKee et al. (1993) and Edwards and McKee (1997). This computation was made to drive SPI at different scale from 1-month SPI, 3-month SPI, 6-month SPI and 12-month SPI. Information's

obtained from SPI is widely used for real time monitoring or retrospective analysis of droughts in different studies and is considered as direct effect of climate change in our world (Sheffield et al., 2006). For instance, the 1-month SPI reflects short-term drought and is closely related to soil moisture; the 3-month SPI provide conditions of seasonal drought due to variability in precipitation; 6- 9-month SPI reflects medium to long term trends in precipitation. Table 7.1 shows the category of drought severity according to the U.S. Drought Monitor (USDM), with their corresponding SPI values.

Table 7.1 SPI drought severity categories

SPI	Category
2 or more	Extremely wet
1.5 to 1.99	Severely wet
1 to 1.49	Moderately wet
0.99 to 0	Mild wet
0 to -0.99	Mild drought
-1 to -1.49	Moderate drought
-1.5 to -1.99	Severe drought
-2 or less	Extreme drought

7.2.5 Agricultural droughts assessment

To identify droughts at seasonal/shorter time scales, which is the case in agricultural drought. We applied vegetation detection technique based on NDVI over the NRB, variability was measured based on the change detection to measure the response of precipitation variability and warming in vegetation cover. Varies agricultural drought studies in the literature are NDVI base (Rojas et al., 2011; Rhee et al., 2010). In this study, NDVI data for the year 2002 to 2016 was extracted from the U.S. Geological Survey (USGS) Earth Resources Observation and Science (EROS) Center "eMODIS" products. These products are acquired by the National Aeronautics and Space Administration's (NASA) Earth Observing System (EOS) at 250-meter spatial resolution.

The theory behind the popularity of NDVI in agricultural drought studies comes from its dependency on the near infrared reflectance (NIR) from vegetation cover and the visible-red reflectance (RED). These two reflectance components measure the density of chlorophyll contained in vegetative cover. Where, high density of chlorophyll represents enough soil moisture and suitable weather conditions to grow healthy vegetation cover “green” and therefore the leaf pigments reflect nearer-more infrared and that give high NDVI values. On the other hand, absence/poor vegetation cover due to less soil moisture or extreme change on suitable weather conditions reflects less near-infrared and led to a low NDVI values. Calculation procedures is as follow: $NDVI = (NIR - RED) / (NIR + RED)$. Detection model was developed in ArcGIS model builder to capture the change in NDVI through time and identify areas with agricultural droughts. Results were later related to temperature and precipitation at the same period.

7.2.6 Hydrological droughts severity and drivers

The 1912-2012 Nile flow data of three gaging stations (upstream-downstream) was analyzed to estimate the variability of flow anomaly and departure from the long-term mean, the trend and change points over the past 100 years. To further understand the implications of flow variability and the hydrological response to meteorological drought in the NRB, we considered the Palmer hydrological drought index (PDSI), soil moisture content and groundwater storage. The Nile River flow and the main drivers for recurrent drought events in the NRB vary from one country to another, so we divided the NRB into sub-basins based on the riparian countries and investigated hydrological droughts severity and intensity in each sub-basin. The Self-calibrated PDSI with Penman-Monteith evapotranspiration for the year of 1951–2013 was obtained from Climate Analysis Section of the National Center for Atmospheric Research and was used for trend and change point analysis. The self-calibrated PDSI (scPDSI) is recommended over the original PDSI

(Dai, 2011) based on historical data. PDSI is widely used to characterize drought severity in various studies and to assess soil moisture status (Alley, 1984; Briffa et al., 1994).

The computation of PDSI is based on temperature and precipitation timeseries to calculate water supply and demand, correlated with observed soil moisture, water storage variations, and is able to successfully reflect long-term drought status. Pettitt test was applied in each sub-basin to find the departure and change points in precipitation timeseries and temperature and the response in hydrological drought in form of PDSI index, soil moisture and groundwater storage. Mann–Kendall test was also used to find long term trend in hydrological droughts and warming effect on surface aridity and changes on seasonal to longer time scales in each sub-basin to confirm the obtained results from the main basin (NRB) and find drought drivers in the region. As each sub-basin represents different climate conditions and have different characteristics, with Ethiopia being the richest in water budget despite recurrent drought in most of its land. Egypt in the other hand is the worst case where most of its water comes from the Nile River which is completely dependent on the what is released from Ethiopia, so precipitation variability in Ethiopia affect all the riparian countries in the NRB. That mean harmful effects of climate change in our world does not affect a single region but spread to surroundings and so on. So, drought drivers and weather pattern in one sub-basin become the drivers in other sub-basins.

7.2.7 Wavelet Analysis and wavelet coherence

The Morlet wavelet analysis was used to investigate the temporal variability, periodicities, and the cyclic behavior of precipitation, temperature, relative humidity, geopotential height, specific humidity, wind stresses, AET, SMC, GWS, El Niño, IOD, SPI, NDVI, sc-PDSI, Blue Nile flow, Dongola station flow, and Aswan station flow of the NRB. To evaluate the possible impacts of El Niño and IOD on droughts of NRB, wavelet coherence was used to estimate the

spatio-temporal correlation field between climate variables, drought indexes, Niño3.4, IOD, and the effect of wind stresses on the actual evapotranspiration.

7.2.8 Composite Analysis and Future climate change

Composite analysis of the NRB's hydroclimate data between 1948 and 2017 and sc-PDSI, monthly temperature, temperature anomaly, monthly precipitation and precipitation anomaly were analyzed for each riparian country of NRB, to relate climate warming to trend and change points in hydrologic droughts of these countries. Furthermore, composite analysis on geopotential height, stream function and wind speed were done to investigate changes in regional atmospheric circulation under El Niño and La Niña episodes. Lastly, based on RCP scenarios of 34 GCMs of CMIP528, future changes to the annual precipitation, temperature, PET, SMC, relative humidity, El Niño 3.4 index, and IOD of NRB until 2100, and their impact to hydrological droughts of NRB were projected.

For the March–April–May (MAM), June–July–August (JJA), September–October–November (SON) and December–January–February (DJF) seasons of 1950–2017, geopotential height and wind speed composites were computed as the ratio of mean seasonal geopotential height and wind speed in anomalous (El Niño) years relative to the long term mean seasonal geopotential height and wind speed. To emphasize the effect of El Niño on seasonal geopotential height and wind speed, years with strong El Niño activity (1958, 1982, 1983, 1987, 1992 and 1997, 2005) were only considered in the composite analysis. Finally, we aimed to predict future warming trend, precipitation, potential evapotranspiration, soil moisture content, relative humidity, sc-PDSI and El Niño 3.4 index under three climate change scenarios in addition to their effect on hydrological droughts of the basin.

Information obtained from such projection will be very helpful for drought analysis in the NRB as future climate change in the NRB will shape the life of millions of people and could

lead to war and conflicts for resources. Finally, change detection techniques were applied in predicted warming trend, precipitation, potential evapotranspiration, soil moisture content, relative humidity, sc-PDSI and El Niño 3.4 index, to find future severity of hydrological drought in the NRB. For instance, difference between current annual precipitation and predicted annual precipitation in 2050 and 2070 could provide strong indication of continuous variability in precipitation.

7.2.9 Teleconnections to Indian Ocean dipole (IOD) and ENSO

The observed ENSO and Indian Ocean dipole (IOD) amplitude, and zonal and meridional winds stresses over the NRB were derived and analyzed. ENSO and IOD amplitude were estimated as the standard deviation (SD) of the Niño3.4 and IOD index over 20-, 30-, 40- and 50-year windows from 1950 to 2017 using the ERSST data sets. Zonal and meridional wind stresses amplitude (10^{-1} N m^{-2}) were calculated as the SD of zonal and meridional winds stresses over 20-, 30-, 40- and 50-year windows from 1950 to 2017, using NCEP/NCAR data sets from 1950–2017. Then, composite analysis, cross and spatial correlation and wavelet coherence analysis were used to investigate the role of ENSO and IOD on the NRB's hydroclimate variability and drought severity over inter-decadal and longer timescales. Field correlations between IOD and El Niño 3.4 amplitudes and NRB surface temperature, GPH, precipitation anomaly, relative humidity, SPI, and sc-PDSI, were used to analyze the ENSO and IOD Teleconnections on NRB hydroclimate and droughts. NRB's hydroclimate and droughts indexes data were computed over 30-year running periods from 1920 to 2017, El Niño 3.4 and IOD amplitude are the SD of El Niño 3.4 and IOD indexes over 30-year windows from 1920 to 2017 using the ERSST data sets.

To better understand hydrologic droughts of NRB, we also investigated the Nile river flow variability and the teleconnection of ENSO and the dipole mode to Nile flow over 1912-2012. The NRB flow are computed over 30-year running periods from 1913 to 2010 for the Blue Nile

station, and from 1913 to 1984 for Dongala station. El Niño 3.4, IOD, SEIO, WTIO amplitudes are computed as the SD of the El Niño 3.4, IOD, SEIO, WTIO indexes over 30-year windows from 1913 to 2017, using the ERSST data sets. We have also analyzed the projected WTIO and IOD using climate projections of 34 global climate models (GCMs) of CMIP5. Future projection of WTIO and IOD were analyzed based on climate projections of 34 global climate models (GCMs) of CMIP5. First, WTIO was estimated as areally weighted SST simulated by each GCM over the Arabian sea (50°E to 70°E and 10°S to 10°N). Then, the multi-model ensemble (MME) of the WTIO computed from the simulations of 34 GCMs was computed over 30-year periods from 1913 to 2100. WTIO estimated from the GCM that best agrees with the observed WTIO will be selected. Furthermore, projections of IOD between 2019 and 2100 were computed as the difference between Western (50°E to 70°E and 10°S to 10°N) and Eastern (90°E to 110°E and 10°S to 0°N) SST of the Indian ocean simulated by the 34 GCMS.

7.3 Results and discussion

As discussed earlier, the NRB has experienced significant climate change impact since 1970, as shown in chapter 6. Furthermore, an analysis of Niño3.4 data shows a statistically significant change point in 1978, with a mean **Niño3.4** of -0.2 °C over 1910-1978 to 0.52 °C over 1978-2017 (Figure 7.1), an overall statistically significant increasing trend of 0.17 °C/decade. This finding shows that droughts of NRB had been affected by both climate warming and stronger El Niño occurring more frequently after 1970s. From the SD (standard deviation) of the Nino 3.4 index estimated over 20-, 30-, 40- and 50-year windows in Figure 7.2(a), it is clear that the amplitude of ENSO variability has increased in NRB over the 1980–2017 period with increasing intensity in ENSO activities, signified by several extreme El Niño events occurring over this period. In Figure 7.2(b), the Indian Ocean dipole (IOD), also known as the Indian “Niño”, defined by a zonal SST

gradient, also exhibited increasing variability similar to ENSO, where the SD of IOD over 1970-2017 was characterized by strong and frequent occurrences of positive events associated with El Niño events. Figure 7.2(c) shows a statistically significant change point in 1993, where the mean IOD of 0.03 °C over 1950-1993 increased to 0.24 °C over 1993-2017, which means an overall statistically significant increasing trend of about 0.1 °C/decade, or IOD had been in a positive phase since 1993. Figures 7.2(a) and 7.2(d) show that higher zonal wind stresses are associated with stronger El Niño, with the zonal wind anomalies abruptly shifted westward when El Niño events typically reach their peak amplitude (see subsequent discussions on U-wind associated with El Niño). On the other hand, as the meridional wind anomalies shifted south, its amplitude in terms of wind speed and discharging effect increased with increasing El Niño amplitude (Figures 7.2(a) and 7.2(e)). A large meridional wind amplitude, which is associated with a prominent anticyclonic circulation in southern NRB, could have contributed to the observed increasing intensity of recent El Niño events. The enhanced zonal and meridional wind stresses attributed to stronger atmospheric heating after 1980s could have also contributed to more severe aridity in NRB, such as statistically significant increasing trends in the warm spell duration (WSD) and maximum daily temperature over NRB at about 3.1 day/decade and 0.35 °C/decade since 1975, respectively (Figure 7.2(f)).

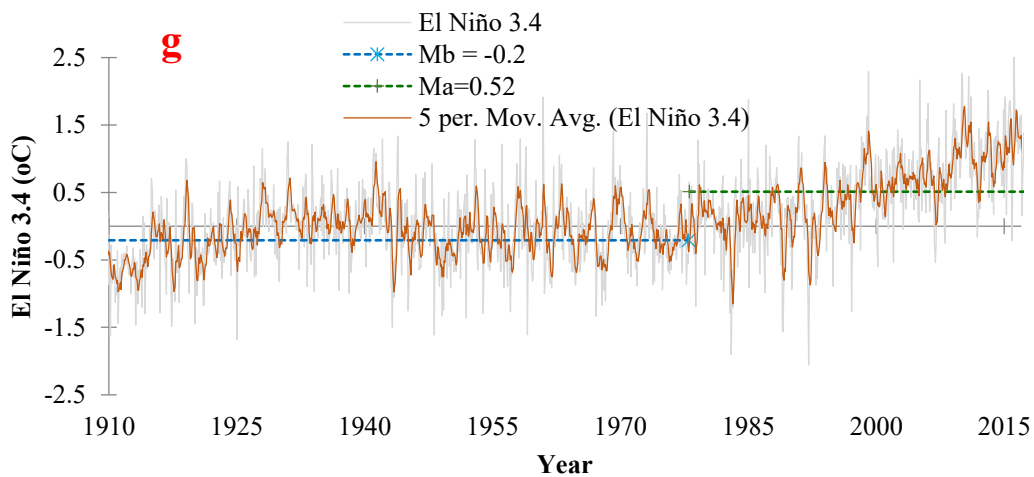


Figure 7.1 El Niño 3.4 index time series, where Mb is the long-term average before the change point, and Ma the long-term average after the change point

Past studies have also teleconnected droughts of NRB (Gissila et al., 2004; Segele et al., 2009) and sub-Saharan Africa (Gizaw and Gan, 2016) to ENSO. Based on IOD's power spectrum and significant coherence with ENSO, our results demonstrate a strong coupling between them, for both exhibited similar change patterns, e.g., positive IOD becomes more intensive as the amplitude of El Niño increases (supplementary Figure D1). A WTC analysis shows that the hydroclimate of NRB is strongly correlated with El Niño (based on Niño3.4) and IOD (supplementary Figures D4 and J1). The wavelet coherence spectrum plot between El Niño and IOD and precipitation (surface temperature) shows an anti-phase (in phase) relationships with statistically significant coherent spatial patterns at 2-4-year band in the 1970s (supplementary Figures D4(a-b) and J1(a-b)). This strong anti-phase relationship between El Niño and IOD and precipitation after 1970s shows that El Niño and IOD had contributed to lower precipitation (drying) over NRB, and their significant in-phase relationship with surface temperature shows that stronger El Niño and IOD after 1970s was related to climate warming (Kim et al., 2014). This is also evident in a strong wavelet coherence (anti-phase) between El Niño and IOD and relative and specific humidity at 1–2-year band in the 1980s and the 1990s (see supplementary Figures D4(d) and J1), and a stronger 4–8 year wavelet coherence after the 2000s. The wavelet coherence between El Niño and IOD and geopotential height (supplementary Figures D4(c) and J1(b)) was also consistently strong at 4–8-year band between 1975 and 2012.

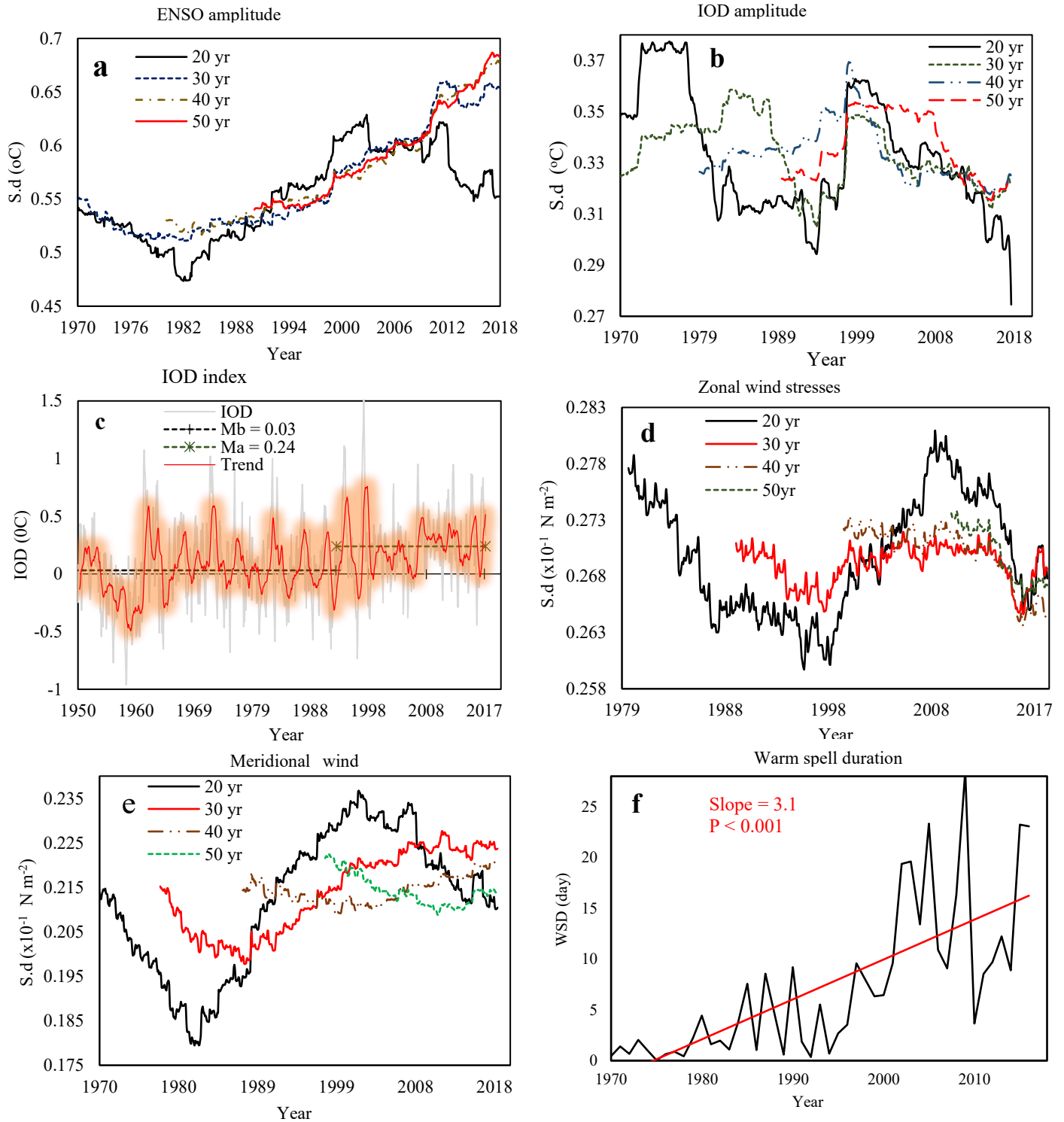


Figure 7.2 Observed ENSO and Indian Ocean dipole (IOD) amplitude, and zonal and meridional winds stresses over the NRB: ENSO and IOD amplitude ($^{\circ}\text{C}$), defined as the standard deviation (s.d.) of the Niño3.4 and IOD index over 20-, 30-, 40- and 50-year windows from 1950 to 2017

(a,b), and IOD characteristics over the NRB (c) using the ERSST data sets. Zonal and meridional wind stresses amplitude (10^{-1} N m^{-2}) are defined as the s.d. of zonal and meridional winds stresses over 20-, 30-, 40- and 50-year windows from 1950 to 2017, using NCEP/NCAR data sets from 1950–2017 (d, e). An increasing meridional wind amplitude (e) associated with a prominent anticyclonic circulation in southern NRB have contributed to the observed increasing intensity of recent El Niño events (a). There is also a statistically significant in-phase, inter-annual relationship between meridional wind stress and El Niño over 1960-2017, and an in-phase, inter-annual relationship between zonal wind stress and El Niño over 1988-2017, while IOD, meridional and zonal wind stresses showed in-phase coherence after 2000s (supplementary Figure D3(a-b)). Warm spell duration (WSD), defined as the annual number of days contributing to events where 6 or more consecutive days experience a daily maximum temperature $\text{TX} > 90\text{th}$ percentile, averaged over the NRB using the HadEX2 observational data set given in Figure 7.2(f) shows a linear increasing trend that is significant at 0.001 significant level (p-value).

A detailed cross correlation (ρ) analysis shows that the hydroclimate of NRB is strongly teleconnected to El Niño and IOD. In addition, the strong negative correlation between IOD and SPI ($\rho = -0.87$) suggest that besides El Niño, IOD has also contributed to lower precipitation and more severe droughts of NRB (supplementary Figure D5(a-f)). The influence of El Niño over NRB's hydroclimate extends across the entire basin, but the degree of influence (ρ) varies over a wide range spatially (supplementary Figure H2). For example, relative humidity is negative correlated with El Niño in Sudan, Uganda and low lands of Ethiopia (supplementary Figure H2(e)), but surface temperature is positively correlated with El Niño in most NRB (supplementary Figure H2(f)), which is expected given recent stronger El Niño episodes have been linked to greenhouse warming (Cai et al., 2015; Kim et al., 2014). To investigate changes in the severity and frequency of meteorological drought of NRB, the Standardized Precipitation Index (SPI) at 1, 3, 6, 12 and

48-month timescales for NRB over 1950-2016 was computed (see supplementary information). The 1-month SPI time series (Figure 7.3(a)) shows statistically significant change point in 1979 with a decreasing trend of 0.15/decade (supplementary Table B1). By defining droughts as $SPI < -1$, recurrent droughts were detected in 1952, 1959, 1965, 1972, 1973, 1978, 1983, 1984, 1987, 1991, 1994, 1999, 2002, and 2011, respectively, with increasing severity after late 1970s. The 48-month SPI (Figure 7.3(b)) also exhibits overall decreasing trends since 1970s, but of higher amplitude than 1-month SPI, in contrast to the increasing trend of the El Niño 3.4 index. The sc-PDSI time series for NRB shows a significant change point in 1983, an overall decreasing trend of 0.58/decade, and hydrologic droughts in 1973, 1987, and recurrent droughts between 2002 and 2011 (Figure 7.3(d)), which means more frequent hydrologic droughts occurring in NRB than the global average since early 2000s (Sheffield et al., 2012). The wavelet coherence between El Niño, SPI and sc-PDSI are statistically significant at 2–4year band. Before 1970s, the wavelet coherence plots show that El Niño and IOD were in phase with both sc-PDSI and SPI, but after 1970s their relationships became predominantly anti-phase. These post 1970s results suggest that stronger El Niño and IOD episodes usually correspond to lower SPI and sc-PDSI, which means El Niño and IOD contributed to more severe droughts in NRB after 1970s (Figure 7.3(c-e) and supplementary Figure D4(e-f)), as is also evident from the strong negative correlation between El Niño and IOD and SPI ($\rho = -0.86$), and sc-PDSI ($\rho = -0.75$) (supplementary Figure D5(d-f)).

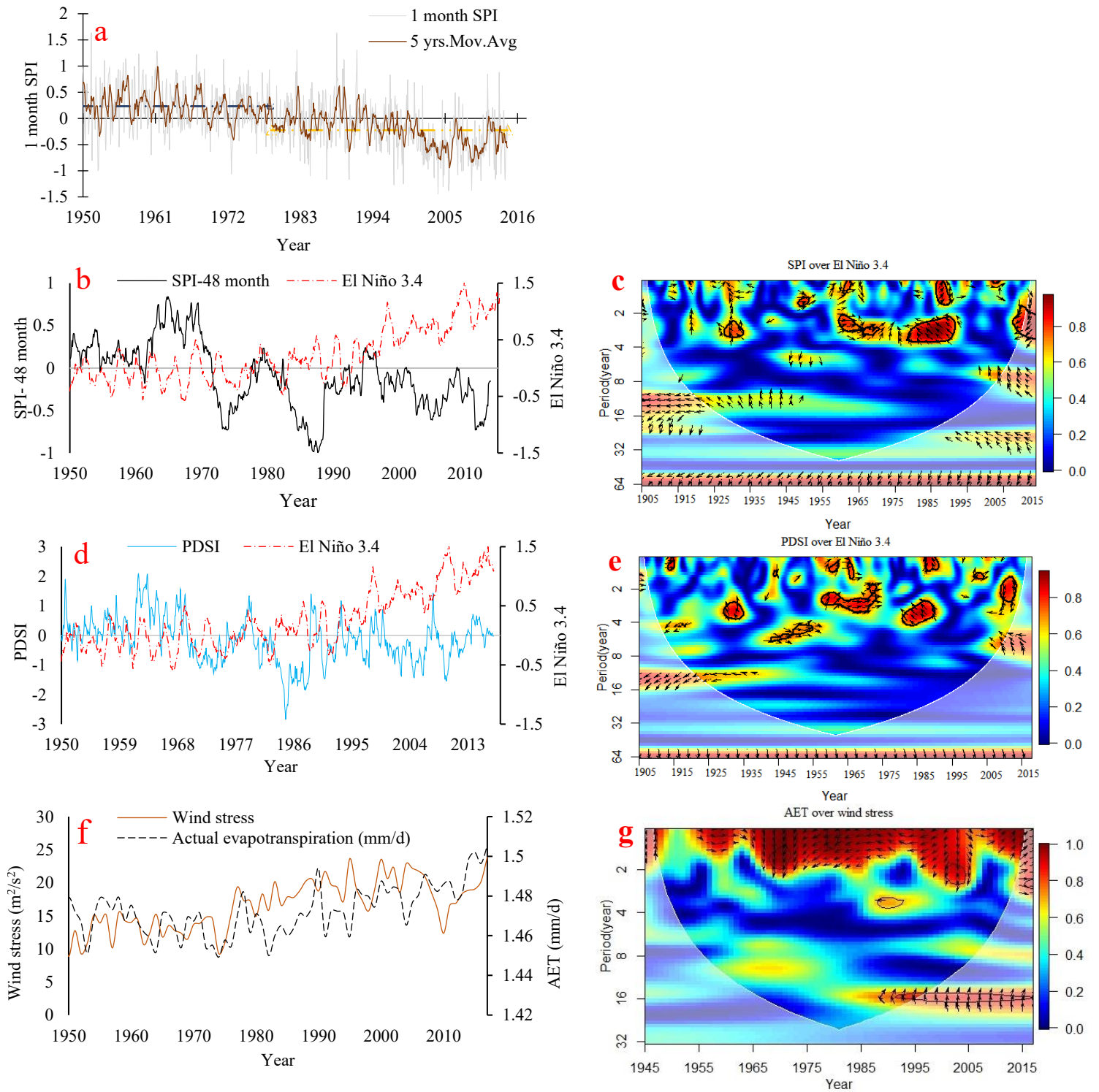


Figure 7.3 The influence of El Niño and La Niña on drought conditions of NRB: (a) 1-month SPI, (b) 48-month SPI vs El Niño 3.4, (c) wavelet coherence between El Niño 3.4 and SPI, (d) self-

calibrated PDSI (sc-PDSI) vs. El Niño 3.4, (e) wavelet coherence between the El Niño 3.4 and sc-PDSI, (f) wind stress vs. actual evapotranspiration, and (g) wavelet coherence between wind stress and actual evapotranspiration. The 1-month SPI values ranged from -1.5 to 1.62 with a standard deviation of 0.514. The sc-PDSI shows a statistically significant change point in 1988, where the long-term average PDSI decreased from 0.125 between 1960 and 1988 to -0.185 between 1988 and 2014 with a statistically significant declining trend of 0.58/decade and a strong correlation with El Niño events. Solid contours in the wavelet coherence plot and the phase difference between El Niño 3.4 and SPI, PDSI enclose periods of statistically significant coherence at 5% level against the red noise process. Right-pointing arrows represent in-phase signals, while left-pointing arrows represent anti-phase signals. After 1970s, the WTC between El Niño, IOD, sc-PDSI and SPI shows significant anti-phase relationships, which demonstrates that more frequent and severe El Niño, IOD and SST gradient over the Arabian Sea (WTIO) in recent years, has led to more severe droughts in NRB. From WTC and strong negative correlations between SPI, sc-PDSI and WTIO, NRB's hydroclimate is shown to be more strongly influenced by WTIO than by IOD.

To further investigate the role of IOD on the hydroclimate of NRB, detrended cross correlation and WTC analysis using the two halves of IOD, i.e. the western pole (WTIO) over the Arabian Sea (50°E - 70°E, 10°S - 10°N) and the southeast Indian Ocean (SEIO) (90°E to 110°E, 10°S to 0°N) shows that SST of the WTIO plays a primary role on NRB's precipitation over interdecadal or perhaps longer timescales. The wavelet coherence plot shows a more prominent anti-phase relationship between NRB's precipitation, SPI and scPDSI and WTIO, than with SEIO, after 1970s (supplementary Fig.D6(a-f)). This dominant anti-phase relationship between WTIO and NRB's precipitation, SPI and scPDSI at interdecadal timescales (> 32-year) show that NRB's hydroclimate is more strongly linked to the SST gradient over the Arabian Sea than to IOD and

SEIO, as evident in the WTC and the significant negative correlation between WTIO and the NRB precipitation variability ($\rho = -0.82$). Apparently, more frequent occurrences of droughts in NRB are related to increased warming in the WTIO (supplementary Figure D7(a)) and other factors, as is also evident from the strong negative correlation between SPI and SST in the western Arabian sea ($\rho = -0.71$ for SPI and -0.8 for PDSI) (supplementary Figure D7(b-c)).

A statistically significant change point was detected in monthly soil moisture content (SMC) and groundwater storage (GWS) in 1979, and after the change point, SMC and GWS data exhibit significant negative trends of 0.84 mm/decade and 1.44 mm/decade, respectively (supplementary Figures F1(c) and F2(c)). These negative trends in SMC and GWS are attributed to significantly lower precipitation and higher AET attributed to more intensive ENSO, stronger and more frequent WTIO events over NRB after 1979. There are strong anti-phase relationships at 16-32 (32-64) year bands between WTIO (SEIO) and SMC (GWS) (supplementary Figure F3(a-d)), with significant negative correlations between NRB's SMC and SEIO ($\rho = -0.92$), and WTIO ($\rho = -0.83$) (supplementary Figure F3(e)), e.g., NRB's SMC decreased under stronger SEIO and WTIO amplitudes. The strong negative correlation between GWS and SEIO ($\rho = -0.95$) and WTIO ($\rho = -0.91$) implies that increased Indian Ocean SST gradient over the Arabian Sea (WTIO) and southeastern Indian Ocean (SEIO) resulted in lower GWS in NRB (supplementary Figure F3(f)). Apparently, WTIO and SEIO explain the variability of NRB's SMC and GWS more than IOD (see supplementary Figures F1 and F2).

From the 1950-2017 reference and actual evapotranspiration (AET) estimated for NRB using a surface energy balance algorithm, the AET of NRB has increased significantly, which is also shown by other studies, that higher AET is related to higher wind speed and wind stress, warming and lower RH (Fischer and Knutti, 2013; Zaroug et al., 2014; Eslamian et al., 2011) As expected, higher AET is found in irrigated land and water bodies in the Ethiopian highlands and in countries

of southern NRB such as Uganda, Egypt, Sudan, Burundi, Congo, Kenya, Rwanda, and Tanzania, where water losses from high AET can be quite substantial (supplementary Figures A1 and A2). The higher AET after 1970s can be partly attributed to the westward propagation of zonal winds and southward propagation of meridional winds associated with stronger El Niño amplitudes, as shown by strong wavelet coherence between zonal and meridional wind stresses and AET at 1-2 year bands (Figure 7.3(f), supplementary Figures D2 and D3). Their recurrent in-phase and anti-phase relationships at 1-2year bands demonstrate the effect of positive (negative) wind stress anomalies when El Niño was active. There is a significant positive correlation between AET and El Niño 3.4 ($\rho = 0.93$), and meridional wind stresses ($\rho = 0.62$). There is also a statistically significant in-phase, inter-annual relationship between meridional wind stress and El Niño over 1960-2017, and an in-phase, inter-annual relationship between zonal wind stress and El Niño over 1988-2017 (supplementary Figure D3(a, b)), while IOD, meridional and zonal wind stresses showed in-phase coherence after 2000s (supplementary Figure D3(c, d)). It seems both increasing meridional wind stress anomalies and stronger El Niño episodes have contributed to the warming and increased aridity in NRB.

The effects of meteorological droughts to agricultural droughts of NRB, based on the Normalized Difference Vegetation Index (NDVI) (supplementary information) shows that moderate meteorological droughts could lead to severe agricultural droughts (supplementary Figure C1) in irrigated areas of Tanzania, Uganda, Rwanda, Burundi, Congo, Ethiopia, and Sudan. The Ethiopian highlands, Ethiopia, Eritrea, Kenya, Tanzania, Congo and Uganda had suffered severe agriculture droughts in 2004, 2005, 2007, 2009, and 2011. Again, results based on NDVI show that NRB has suffered moderate to severe meteorological, agricultural and hydrologic droughts since the 1970s. To further investigate drought conditions of NRB, the time series of sc-PDSI, monthly temperature, temperature anomaly, monthly precipitation, and precipitation anomaly of

each riparian country of the Nile River are analyzed individually (supplementary information). Even though the level of climate warming in the Nile basin varies from one riparian country to another (supplementary Table G1), overall impacts to meteorological, agricultural and hydrological droughts of most riparian countries of NRB have been severe, where regional warming trends have exceeded the mean global warming trend of about 0.15 °C per decade. Detailed drought investigations for each riparian country of the Nile are given in supplementary Figures D4-F1, and supplementary Table G1. Lastly, given the interannual variability of the Nile flow is also projected to increase significantly from the 20th to the 21st century²², it could lead to even more severe droughts in NRB in future.

As discussed in Chapter 6, the composite analysis of NRB's hydroclimate data between 1948 and 2017 also shows significant changes across the entire NRB. For instance, surface temperature has increased at 0.16-0.4 C°/decade over the NRB, with the highest increase in Ethiopia, Uganda, Sudan and Egypt. Because of climate warming, relative humidity has decreased by 1-5%/decade after 1985, with the largest decrease in Ethiopia, Uganda, and Sudan where warming has also been the worst. The surface soil moisture shows high spatial variabilities in NRB but a decreasing trend of 16-45 mm/decade between 1985 and 2017. At an increase trend of 0.2-0.8 m²/sec² between 1985 and 2017, the increase in scalar wind was maximum in Uganda, Sudan, and northwestern regions of Ethiopia, where both meridional and Zonal wind also show similar increase. The aforementioned changes related to warming had resulted in decreased daily precipitation in NRB, lower specific humidity in Sudan, northwestern regions of Ethiopia (in lowland), lower annual surface runoff over Ethiopia, Uganda, and Sudan, and higher potential evapotranspiration over Ethiopia, Uganda, and Sudan. The lower atmosphere stream function of supplementary Figure H1 at 0.8458 sigma level, which depicts the rotational part of the flow (the flow is along the contours), indicates that main waves emanating from northern towards southern parts of NRB, have shifted

further south over the two periods, from 1948-1984 to 1985-2017. This long-term southward shift in the stream function over NRB would have also contributed towards the long-term drying of NRB, as part of the multiple changes due to climate warming, e.g., changes in air temperature, GPH, RH, soil moisture, surface runoff, PET and ENSO.

To better understand hydrologic droughts of NRB, we also investigated the Nile flow variability and the teleconnection of ENSO and the dipole mode to Nile flow over 1912-2012 (supplementary information). Observed annual flow records for 1912-2012 from the Blue Nile station at Khartoum, where the White Nile and Blue Nile merge (Figure 7.4(a)) show a statistically significant change point in 1964, with the mean annual flow decreased from 1645 CBM/s over 1912-1964 to 1478 CBM/s over 1964-2010, a decreasing trend of about 13.7 CBM/decade after 1964. Between 1965 and 1987, the Blue Nile flow decreased so much that the mean annual flow after 1965 was below the long-term mean annual flow by 716 CBM (supplementary Figure E1) partly due to high evaporation losses in water bodies of Sudan. The annual flow of the Dongola station also showed a significant decline in 1900-1982 (Figure 7.4(c)), while the annual flow of the Aswan station in 1900-1987 exhibited high temporal variability, e.g., the August-November wet season over 1900-1950 shows high flow records (supplementary Figure E2(a)), a statistically significant change point in 1965, and a statistically significant negative trend of 114.1 CBM after 1965 (Figure 7.4(e) and supplementary Fig.E3(b)).

Wavelet analysis shows that the Nile River flow exhibited both statistically significant interannual and interdecadal oscillations that appeared and disappeared over 1912–2012, and the wavelet coherence spectrum between El Niño and the Blue Nile flow shows a statistically significant wavelet coherence at 2-4 year band in 1920s, 1930s, and 1960-1970 (Figure 7.4(b)) dominated by off-phase signals between both signals over 1912-2012, except in-phase signals that occurred briefly between 1982 and 1990. While the wavelet coherence plot between the Blue Nile

flow and IOD shows an anti-phase relationship at 32-year band over 1912-2012, and a stronger anti-phase relationship at 2-4- and 4-8-year bands over 2000-2012 (supplementary Figure F4(a-c)). The wavelet coherence between El Niño and IOD and the flow data at the Dongola station of Khartoum-Sudan and the Aswan station of Egypt (downstream) shows anti-phase relationships at inter-annual and inter-decadal time scales with El Niño and IOD, respectively (Figure 7.4(d-f), supplementary Figure F4(b-c)). In comparison, the anti-phase relationship was much stronger between WTIO and SEIO and Nile flow at 32-64-year band (supplementary Figure F5(a-d)). Therefore, the impact of El Niño and both halves of IOD on the Nile River flow extends across the upstream-downstream reaches of Nile River.

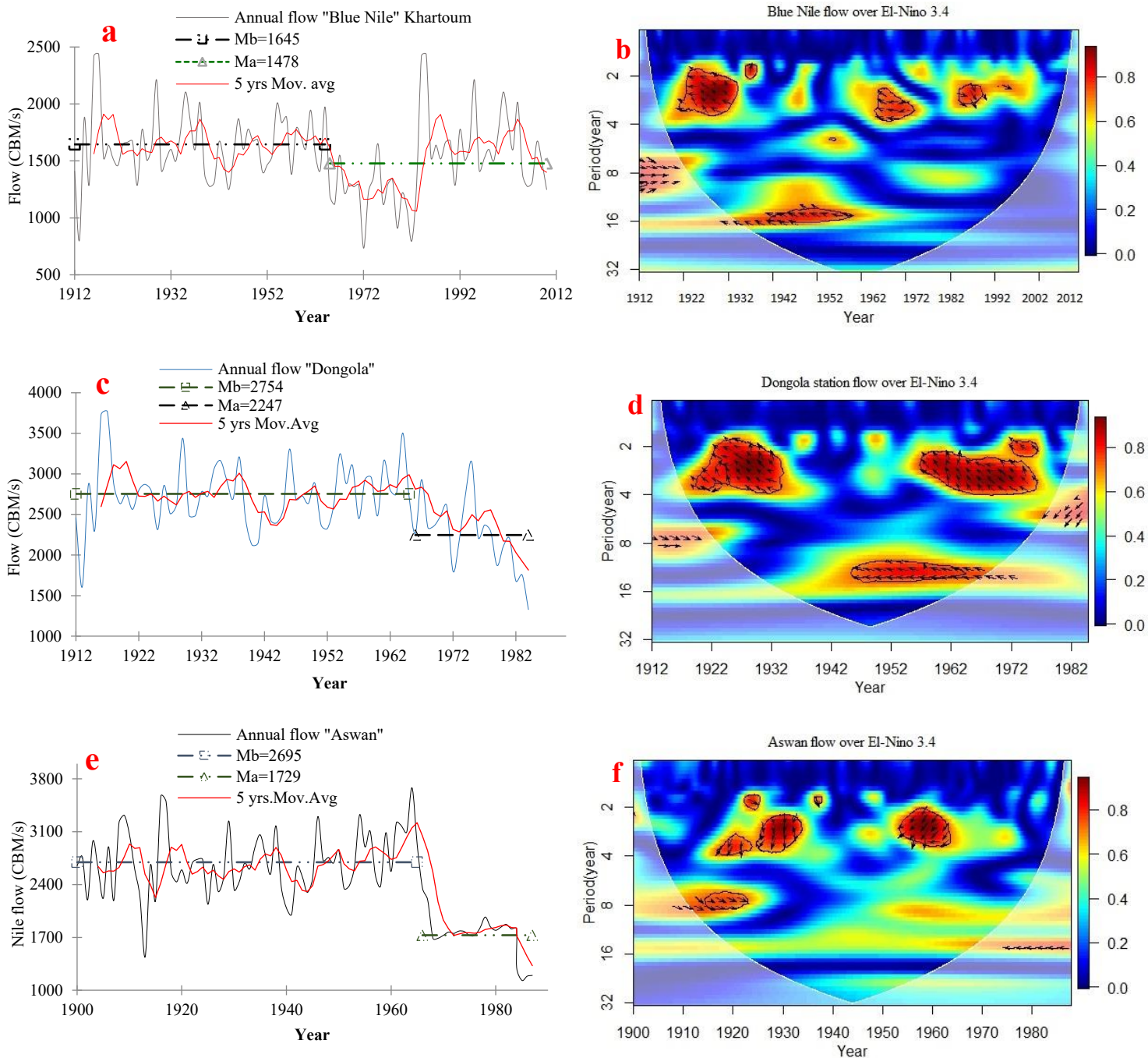


Figure 7.4 Observed annual flows and wavelet coherence with El Niño 3.4: (a) Blue Nile flow, (b) wavelet coherence between El Niño 3.4 and Blue Nile flow, (c) Dongola station flow, (d) wavelet coherence between the El Niño 3.4 and Dongola flow, (e) Aswan station flow, and (f) wavelet coherence between El Niño 3.4 and Aswan station flow. In Figure 7.4, the annual flow of

the Blue Nile river decreased from 1645 CBM/s over 1912-1964 to 1478 CBM/s over 1964-2010, with a decreasing trend of about 13.7 CBM/decade after 1964 due to higher AET losses, warmer WTIO and IOD, and more intensive El Niño events.

Figure 7.5 shows a significant negative correlation between the Nile flow and IOD ($\rho = -0.71$ for the Blue Nile, and -0.57 for the Nile at Dongala station) (Figure 7.5(a)), compared to a less significant negative (positive) correlation between El Niño and the Nile flow at the Blue Nile ($\rho = -0.31$) and Dongala stations ($\rho = 0.25$), respectively (Figure 7.5(b)). Therefore, IOD exerts a stronger influence on the Nile flow than El Niño at inter-annual to inter-decadal time scales. The peak correlation between IOD and the Nile flow occurred a year earlier than that between El Niño and the Blue Nile flow, which agrees with the wavelet coherence between IOD and El Niño (i.e. one lead the other as shown in supplementary Figure D1(a, b)). The increasing intensity in El Niño after 1978 (represented by the change point (yellow color) in Figure 7.5(a)) shows that El Niño occurred more frequently with positive IODs than La Niña events with negative IODs. Our results show a strong teleconnection between the Nile flow and the Indian Ocean SST gradient over the western and the southeastern poles (Figure 7.5(c, d)). There are significant negative correlations between the Nile flow (Dongala station) and WTIO and SEIO ($\rho = -0.72$ and -0.58). However, the negative correlations are stronger between Blue Nile flow and WTIO and SEIO ($\rho = -0.92$ and -0.88), which means that the Nile River flow is strongly linked to WTIO and SEIO, with their warm (cold) phase associated with decreased (increased) Nile flow (shown by arrows in Figure 7.5(c)). These results demonstrate the strong teleconnection between the Nile flow, SST of southern and eastern parts of the Indian Ocean, and El Niño at inter-annual to multi-decadal time scales.

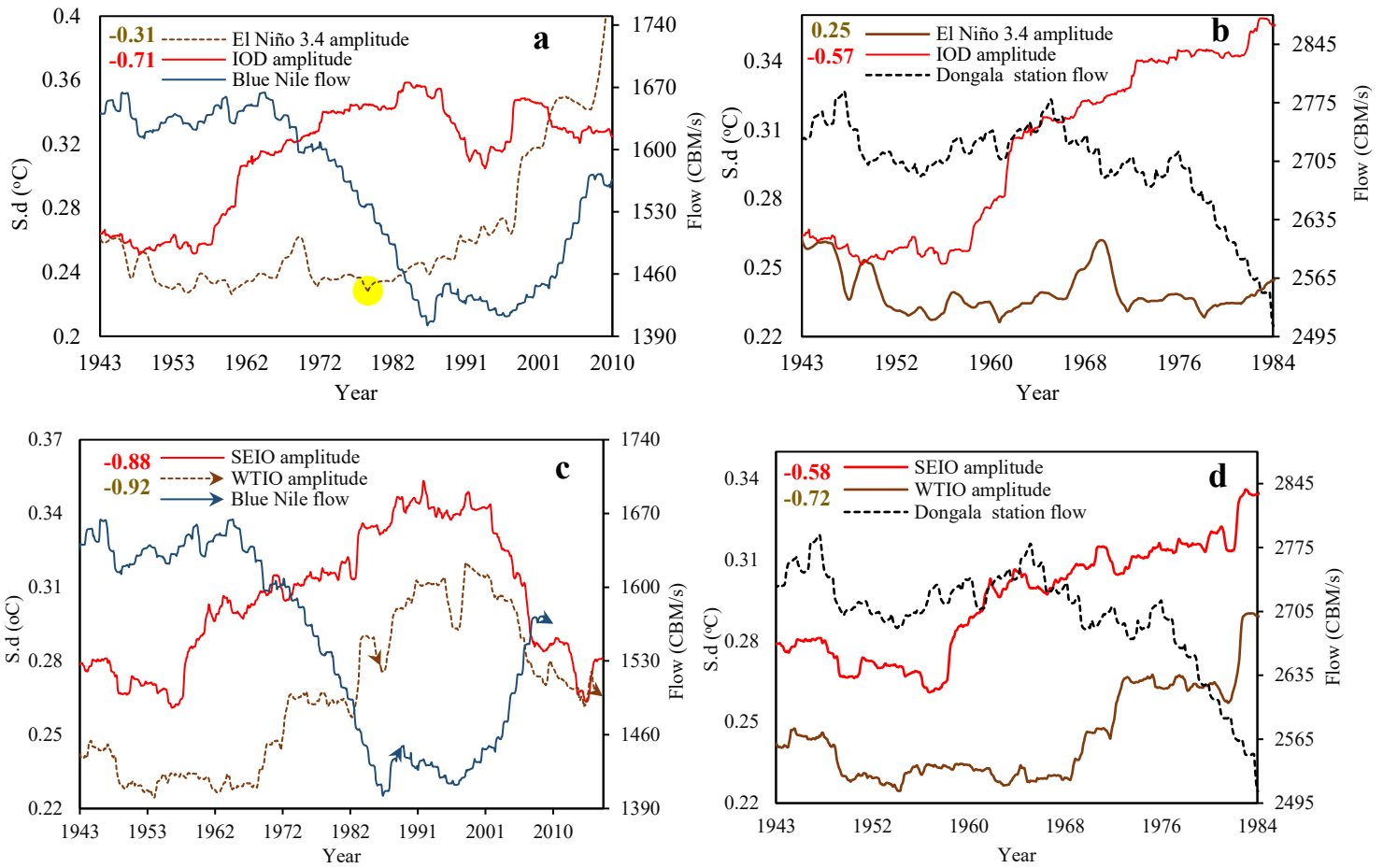


Figure 7.5 Responses of NRB flow variability to El Niño events, IOD amplitude and the IOD two pole amplitudes i.e. western pole amplitude (WTIO) over the Arabian Sea and eastern pole amplitude (SEIO) based on the correlation between NRB flow at Blue Nile and Dongala stations and El Niño 3.4, IOD amplitudes (a, b), SEIO, and WTIO amplitudes (c, d), respectively. The NRB flow are computed over 30-year running periods from 1913 to 2012 for the Blue Nile station, and from 1913 to 1984 for Dongala station. El Niño 3.4, IOD, SEIO, WTIO amplitudes are computed as the s.d. of the El Niño 3.4, IOD, SEIO, WTIO over 30-year windows from 1913 to 2017, using the ERSST data sets. The peak correlation between IOD and the Nile flow occurred one year earlier than that between El Niño and the Blue Nile flow, which agrees with the WTC between IOD and El Niño (i.e. one lead the other as shown in supplementary Figure D1(a, b)). From the WTC and strong negative correlations between Nile flow, SEIO, WTIO and IOD, the

Nile flow is more strongly teleconnected to IOD, SEIO and WTIO than to El Niño at inter-annual and inter-decadal time scales.

To better understand changes to the atmospheric circulation over NRB, we analyzed the responses of stream function fields, geopotential height, and U-wind to climate warming and ENSO. Associated with El Niño (La Niña) episodes, the 750-mb stream function show positive (negative) stream function anomalies which correspond to high (low) geopotential height anomalies. The anomalous stream function pattern during Niño episodes shows anticyclonic flow associated with the ENSO warming (Figure 7.6(a)). The positive northern stream function anomalies induced by El Niño warming is part of the general circulation over the African continent. This intense anticyclonic flow propagates from the northwestern parts towards southern and eastern parts of NRB, controlling the circulation of air mass, heat, and moisture in the NRB. During La Niña episodes, north eastern anticyclone wave originates over the Arabian Peninsula and travelling west over the red sea and part of the Indian ocean towards Egypt, Libya and part of Sudan (Figure 7.6(b)), with negative stream function anomalies only over the BNB, Tanzania, and Uganda. More El Niño events and fewer La Niña events have occurred after 1970s. Figure 7.6(c-f) shows the composite 300-mbar geopotential height (GPH) and wind anomaly patterns associated with El Niño and La Niña episodes, respectively.

The composite-anomaly map of 300-mb GPH during El Niño episodes is dominated by spatially broad positive anomalies (higher than normal), indicating warmer conditions. In particular, the highest positive GPH fields occurred over the Roseires-Ethiopian highlands, the Sudd region in South Sudan, Eritrea, Uganda, and Aswan (Figure 7.6(c)). In contrast, except in the Arabian Peninsula, the composite-anomaly map of 300-mb GPH show predominantly negative anomalies during La Niña episodes (Figure 7.6(d)). The figures show that positive GPH anomalies associated with El Niño episodes (warm phase) are more consistent spatially than negative

anomalies associated with La Niña episodes, partly due to the thermal inertia associated with warm-phase events, i.e. anomalies persist longer during El Niño events. The GPH-ENSO signal in the troposphere demonstrates the teleconnection between El Niño and the climate of NRB. Differences in U-wind patterns between Figures 7.6(e) and 7.6(f) show a more enhanced zonal U-wind flow (positive anomalies) during El Niño episodes, which tends to be the strongest over the Roseires- Ethiopian highlands, the Sudd region in South Sudan, Eritrea, Uganda, and Aswan. In contrast, the U-wind anomaly tends to be negative over these regions during La Niña episodes. These differences between GPH and U-wind anomalies associated with ENSO suggest changes in regional atmospheric circulation will result in drier conditions over the NRB during more persistent and stronger El Niño, than during weaker La Niña episodes.

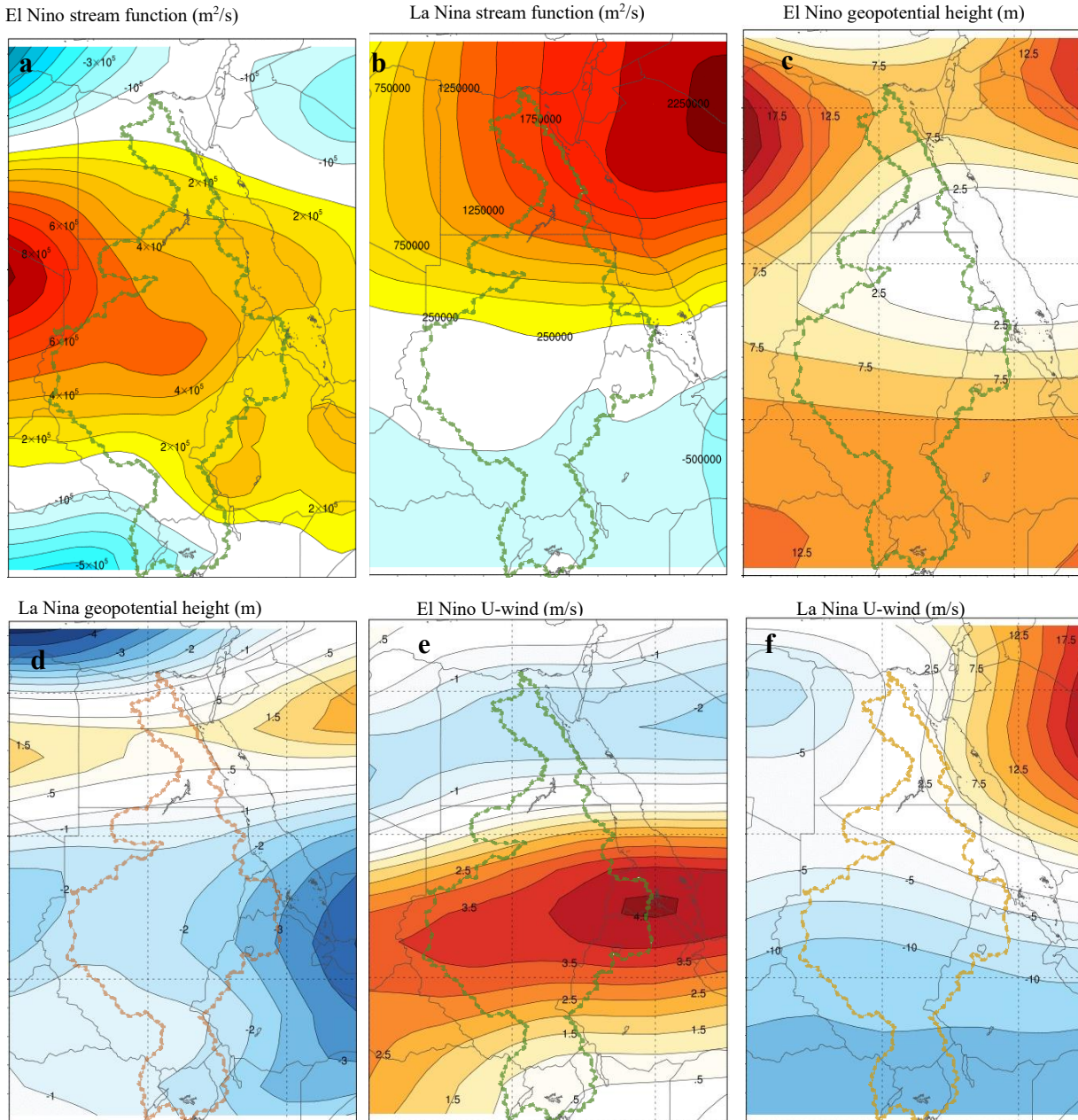


Figure 7.6 The effect of ENSO to the atmospheric circulation over NRB shown by the 750-mb stream function anomaly associated with El Niño (a) and La Niña (b) episodes, 300-mb geopotential height anomaly associated with El Niño (c) and La Niña (d) episodes, zonal and meridional wind anomaly patterns associated with El Niño (e, g) and La Niña (f, h) episodes,

respectively. The signals between ENSO and GPH, stream functions, and meridional/zonal wind in the troposphere demonstrates the teleconnection between El Niño and the atmospheric circulation over of NRB. The warming over the Arabian sea and stronger El Niño, the southward shift of the lower atmospheric stream functions and meridional winds, and the westward shift of zonal winds have together contributed to worsening droughts observed in NRB in recent years.

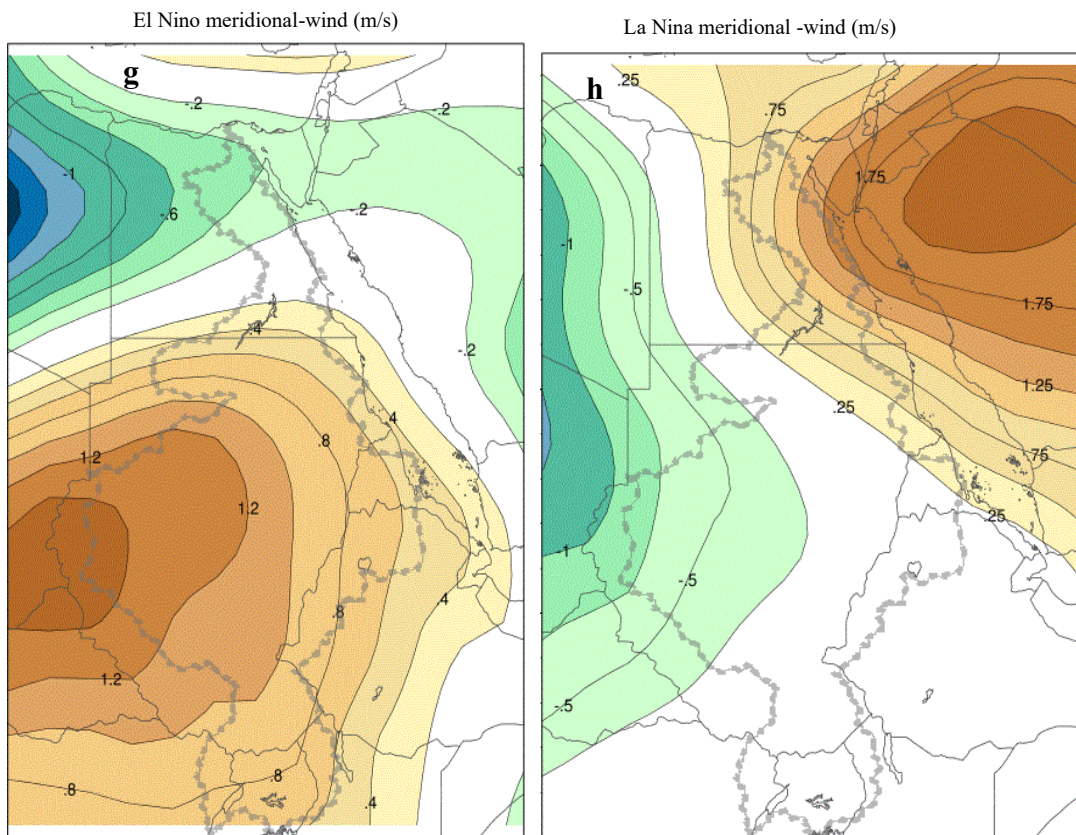


Figure 7.6 (continued)

Based on the analysis of 34 global climate models (GCMs) of CMIP5 (IPCC, 2014), future annual precipitation is projected to decrease at about 16.5 mm/decade over the NRB between 2020 and 2050 under Representative Concentration Pathways RCP 2.6 scenarios. Because of the high spatial variability of precipitation, in countries such as Egypt and Sudan, the annual precipitation could decline by 15.5 mm/decade, while for the White Nile region, the annual precipitation could

increase by 28.9 mm/decade over 2020-2050 (supplementary Figure K3(a)). On the other hand, under RCP4.5 and RCP8.5 scenarios, the annual precipitation of NRB is projected to increase by 5 mm/decade between 2050 and 2100 (supplementary Figure K3(b)). Over 2020-2050, warming in the NRB is projected to be 0.24 °C/decade, 0.36 °C/decade, 0.48 °C/decade based on RCP 2.6, RCP4.5, and RCP8.5, respectively. Under RCP4.5 and RCP8.5, the warming trend is projected at 0.12-0.72 °C/decade between 2050 and 2100, while under RCP 2.6, the warming trend is only projected at 0.1 °C/decade (supplementary Figure K2(a) and supplementary Figure K3(a)). Under RCP 2.6, 4.5, and 8.5 scenarios, the relative humidity trend is projected to decline at 0.87% /decade, 1.04 % /decade, and 1.47% /decade between 2020 and 2050, respectively. However, over 2050-2100, the corresponding declining trend for relative humidity is projected to be more modest, at about 0.23% /decade, 0.34 % /decade, and 0.53 % /decade, respectively (supplementary Figure K3(c)).

Under RCP 2.6, 4.5, and 8.5 scenarios, between 2020 and 2050, the potential evapotranspiration (PET) is projected to increase at 11.4 mm/decade, 18.4 mm/decade and 24.1 mm/decade respectively (supplementary Figure K3(e)), which is consistent with projected rising air temperature and declining relative humidity. As warming continues from 2050 to 2100, PET is projected to increase at about 10 mm/decade, 14.8 mm/decade, and 35.2 mm/decade under RCP 2.6, 4.5, and 8.5, respectively. Corresponding to increasing trends in PET, SMC is projected to decrease at 0.12 kg/m²/decade, 0.72 kg/m²/decade, and 0.96 kg/m²/decade between 2020 and 2050; and by about 0.65 kg/m²/decade, 2.5 kg/m²/decade, and 4.3 kg/m²/decade between 2050 and 2100, under RCP2.6, RCP4.5, and RCP8.5, respectively (supplementary Figure K3(d)). It seems that agricultural drought in the NRB will get worse over the 21st Century. Climate models also project more frequent and stronger El Niño episodes between 2020 and 2100 (Kim et al., 2014; Cai et al., 2014) (supplementary Figure K3(f)), leading to worsening droughts and severe surface drying in

NRB by the end of the 21st century. Furthermore, large parts of Egypt and Sudan are projected to suffer mild to moderate hydrologic droughts over the 21st Century (supplementary Figure K4), and countries such as Kenya, Tanzania, Rwanda, Burundi, Uganda, and Congo are projected to suffer incipient droughts.

Our analysis indicates that IOD, SEIO and WTIO are likely better predictors of the Nile flow than El Niño. Therefore, we have also derived projected WTIO, SEIO and IOD from climate projections of 34 GCMs of CMIP5 over 1900-2100 (see supplementary Figures K5 and K6). The correlation between the multi-model ensemble (MME) of WTIO obtained from GCMs' projections and WTIO estimated from ERSST data range between $\rho = 0.61$ and $\rho = 0.88$ (supplementary Figure K5(a)). The results show that the variability (s.d.) of WTIO has increased since the 1970s in both the observed dataset and the MME of 34 GCMs' simulations for the historical run, which means that the western Indian Ocean (WTIO) has become warmer in recent decades, and it is projected to become much warmer, at a warming trend of 0.01 to 0.023 °C/decade between 2019 and 2100 (supplementary Figure K5(b-d)). The warming over the Western Indian Ocean and the more intensive El Niño in recent years are expected to play a major role modulating the future climatic conditions of NRB, likely resulting in less precipitation, relative humidity, soil moisture and the Nile flow as warming continues in NRB over the 21st Century. Under the projected increase in WTIO over the Arabian sea, future drought conditions of NRB is expected to worsen.

Chapter 8 Conclusion and recommendations

In this thesis, the first five Chapters are devoted to analyzing and characterizing the impact of climate change, human activities and urbanization in arid regions of Africa, while Chapters 6 and 7 are devoted to better understanding of the Nile River basin hydroclimate and possible teleconnection to large-scale climate patterns. The following summaries will be beneficial to planners and governments, water policymakers and engineers involving in water resources management and planning to future land use planning, mitigate potential impact of climate change, urbanization, anthropogenic climate changes and large-scale climate patterns.

1) Urbanization and climate change implications in flood risk management

The effects of urbanization and climate change to the flood risk of arid regions of Africa such as Beheira and Alexandria governorates of Egypt were investigated, and a flood susceptibility model was developed, changes to annual precipitation and temperature, and effects of urbanization to flood risk by using the runoff curve number method to estimate surface runoff time series for the two governorates over 1948-2014. Anomalies in surface runoff were computed to examine the effect of urbanization on the surface runoff time series generated. Finally, a GIS decision support system was developed to delineate flood susceptibility zones in the two governorates of Egypt. Likely related climate change impact, the annual rainfall of the two governorates had declined since 1994 at about 8.96 mm/decade, while rainfall anomalies had declined at about 15.3 mm/decade which is statistically significant. Since 1976, the climate has been warming at about 0.16 °C/decade partly due to effects of rising concentrations of greenhouse gases and partly due to rapid urbanization with a noticeable increase in impervious surfaces in Alexandria and El-Beheira in recent decades. Because of urbanization, the flood risk of both arid regions has increased, despite

of a decline in the annual rainfall, for the annual surface runoff show a significant increasing trend of 12.7 mm/decade after 1970 because of rapid urbanization in both two governorates. With reference to the long-term annual surface runoff, the surface runoff anomalies of both governorates show upward trend of 14.39 mm/decade after 1970.

The flood susceptibility model delineated flood susceptibility zones in the Beheira Governorate to 9.2% (930.1 Km²), 17.9% (1815.2 Km²), 32.3% (3269.7 Km²), 28.3% (2869.2 Km²) and 12.3% (1245.8 Km²) of its area as very high, high moderate, low and very low susceptibility to flooding, respectively. In contrast, for Alexandria Governorate, the flood susceptibility model delineated 15.9% (400.1 Km²), 33.5% (841.9 Km²), 41% (1028.3 Km²), 8.8% (220.6 Km²) and 0.8% (19.7 Km²) of its area as very high, high, moderate, low and very low susceptibility to flooding, respectively. The very high and high susceptible zones were located in the northern, northwestern and northeastern parts of the Beheira governorates, which include Edko, El Mahmoudiyah, Aboul Matamir, Abu Hummus, Rosetta, Shubrakhit, Damanhur, Rahmaniya, Kafr el-Dawwar, and Wadi El Natrun, where for the past decade flooding had occurred every winter, causing heavy damages to roads, agricultural lands and cities. Floods had also occurred in some high to moderate susceptible zones such as El Delengat, Etay El Barud, Hosh Issa, Kom Hamada, Nubariyah, and Badr. For the Alexandria governorates, areas classified as high and very high susceptible zones are Montazah, El-Raml, Sidi Gaber, Bab Sharq, Al Attareen, Moharrem Beik, El-Dekheila, El-Agamy, Borg El Arab, and El-Ameriah areas where many flood events had occurred. From checking historical flood events against flood susceptibility zones of these maps, the results show that they are in good agreement, which demonstrates the accuracy of these maps. Similar surface runoff data developed for Beheira and Alexandria governorates can be replicated for other governorates of Egypt. Such data and flood susceptibility maps developed will be beneficial to planners and governments for choosing suitable locations for future developments to minimize

potential flood damages in Beheira and Alexandria governorates. To develop representative flood susceptibility maps, as many flood contributing factors as possible should be considered unless appropriate data are not available.

2) Multi-criteria Approach to develop flood susceptibility maps in arid regions of Middle East

The spatial distribution of flood susceptibility zones of the Riyadh province and the Riyadh City of Saudi Arabia were mapped using the Analytic Hierarchy Process (AHP) method. According to our findings, very high and high flood susceptibility zones are mainly identified in the northern, northeastern, and northwestern parts of the Riyadh Province typically in areas with slopes $< 5\%$, dense flow accumulation, high annual rainfall, extensive built-up areas, and high runoff depth, where according to historical records, a large number of flood events had occurred in recent years. According to the flood susceptibility map, Riyadh City and its surrounding areas are prone to flooding. In contrast, western parts of Riyadh province are classified in zones of very low to low flood susceptibility. Using historical flood records, the methodology chosen is shown to develop reliable flood susceptibility maps which should be used to assist flood mitigation and in future land use planning in both the province and the city of Riyadh. Further, reliable results obtained for both the Province and the City of Riyadh show that this methodology is useful for planning and flood assessment purposes, and its reliability is independent of the scale of the study site.

The proposed methodology in developing flood susceptibility maps should be more extensively tested in other regions of different climate regimes and basin characteristics. The importance of each contributing factor to floods and the optimal number factors to include in the model should also be further tested against historical flood records of the region. This study shows that key contributing factors in developing flood susceptibility maps are: surface runoff, flow accumulation, soil type, elevation, distance to drainage network, drainage density, land use, slope,

and geology. The optimized weights obtained for the factors are sensitive to the number of factors included in the model. Typically, if less than six factors or if key important factors are not included, it could produce unrepresentative weights dominated by a single weight which increase the possibility of over-rating some contributing factors. It is generally advisable to include more than six factors, from which based on AHP larger weights tend to be for factors related to flow such as surface runoff and flow accumulation, followed by factors related to soil type, elevation and distance to drainage density. Sensitivity analysis is useful to examine the influence of each susceptibility factor in developing mapping flood susceptibility maps.

3) Long-term Impact of rapid urbanization on Urban Climate and Human thermal comfort in Hot-Arid Environment

The long-term impact of rapid urbanization on air temperature, relative humidity, vapor pressure and human thermal comfort in Egypt was analyzed. Three thermal comfort indices; temperature humidity index (THI), effective temperature index (ETI) and relative strain index (RSI) were estimated from climate time series collected between 1950 and 2017. Over this study period, LUC in Cairo was dominated by the growth of new cities, with urban expansion at 75.2 km²/decade, extending into low-lying areas of Cairo and along the direction of roads to lower the cost of development. This trend contributed to shifting most of the urban growth toward New Cairo and Shrouk City after 1990. The significant increase in urban and built-up areas between 1990 and 2017 resulted in rising air temperature after 1995 at 0.19 °C /decade, relative humidity decreasing at 0.55 % /decade, and vapour pressure increasing at 0.24 hPa /decade. These observed changes in the urban climate of Cairo are likely associated with significant LUC, such as growing impervious areas due to rapid urbanization since the 1990s. Heat stress problems and thermal discomfort began to emerge and persisted every July-September after 1994. The THI series computed between 1950 and 2017 showed a statistically significant change point at 1994 and

thereafter a rising trend of 0.33 °C /decade. After 1994, the THI index exceeded the upper limits of the comfort zones because of rapid urbanization. Similarly, the ETI index computed for the 1950-2017 data also show a statistically significant change point at 1994, and thereafter a rising trend of 0.29 °C /decade. The RSI index also show a rising trend of 0.06 /decade.

In conclusion, the rising level of thermal discomfort based on the positive trends of the three indices is primarily attributed to the significant LUC or rapid urbanization in Cairo and the new cities. The relative humidity is negatively correlated with both air temperature and vapor pressure, and negatively correlated with human comfort indices. This shows that as relative humidity decreases, hot distress will increase. Findings from this study demonstrate the significant impact of urban growth on the microclimate, heat stress or human thermal discomfort in Cairo. Findings of this study will benefit urban planners in the urban planning and development of Cairo and other regions of arid environments.

4) Impact of anthropogenic climate change and human activities on environment and ecosystem services in arid regions

The impact of anthropogenic climate change and human activities such as LUC on the environment and ecosystem services in the Jizzan Province, Arabia was analyzed. First, earth observation data of the Landsat satellite was used to derive historical, 1970-2014, land use maps of Jizzan. Next, a Markov-CA model was used to project the dynamics of its LUC pattern over 2014-2100 in response to human activities and their impacts on the study area's climate, environment, and water resources. Pettit's and Mann-Kendall tests were applied to detect change points and to estimate trends of temperature data of 1900-2010 and precipitation data of 1948-2014 and their anomalies, respectively. Change points and trends of CO₂ and several rare gases emitted between 1960 and 2015 was estimated. Climate scenarios (RCP4.5, RCP6.0 and RCP8.5)

of the study area projected by climate models of CMIP5 were used to project future warming in the study area between 2014-2100.

Urbanization and LUC has significant impact the ecosystems, biodiversity and natural habitats of the Jizzan province. In 1970s, human impacts were minimal. However, following the construction of rain-harvesting dams which capture most surface runoff, and with urban expansion at about 53.4 km² yr⁻¹ which extended into coastal regions, areas of forest, shrubland, sparse vegetative cover, bare soil and water bodies declined markedly over 1990–2014. Likely due to climate change impact and urbanization, a statistically significant change point was detected in the monthly temperature data of Jizzan in 1968 and a warming trend of 0.24 oC per decade after 1970. The precipitation data also had a statistically significant change point in 1967, but a negative trend of 12.2 mm/decade. Observed changes in the hydro-climatology of Jizzan are likely associated with significant LUC, such as urbanization and agricultural development (irrigated croplands) at the expense of vegetative cover, forest, shrubland, and sparse vegetative cover since 1970s. A statistically significant change point was detected in CO₂ emissions data in 1985 and statistically significant positive trend of 94,340 Kt/decade. Other anthropogenic greenhouse gases mainly due to industrial processes also have a statistically significant positive trend of 488.5 Kt/decade. On a whole, total greenhouse gas emissions including all anthropogenic sources have been increasing at a statistically significant trend of 78,090 Kt/decade after 1991. Therefore, it is very likely that long-term increasing emission of greenhouse gases, and aforementioned human activities have resulted in warming trends observed in the study area and globally. Future projection of temperature anomaly between 1900-2100 showed a statistically significant future warming trend of 0.19 0C/decade after 1999.

The spatial distribution of the projected annual temperature in 2050 and 2075, also shows that the highest increase in temperature is within urban areas and the mountains regions. The

increase in the warming trend in the mountains areas which were previously occupied by shrubland and forest reflects the impacts of deforestation in the warming trend. The warming trend in mountains regions is estimated at 0.55 -0.83 °C/decade between 2014 and 2050, and at 0.55 °C/decade in south and eastern parts of Jizzan Province. Precipitation is projected to continue declining while LUC such as urbanization and irrigated cropland are projected to continue towards the end of the 21st Century. In conclusion, to reduce the impacts of climate change and LUC, conservation plans for the Jizzan Province are essential to mitigate the significant impact human activities and global warming on the environment and ecosystem services of the study area in the 21st Century.

5) Irrigation Water Management in arid regions of Middle East

This study was designed to estimate average reference and AET over Al-Riyadh, Al-Qassim and Hail Province in the central region of Saudi Arabia during 1950–2013 using soil water balance model on daily, monthly and annual basis. Firstly, the FAO Penman-Monteith method was used to model the spatial distribution of ETo on a grid-by-grid basis using data collected from meteorological stations and GIS techniques. Then, crop coefficients (Kc) were modeled as a function of 16-day time-series MODIS normalized difference vegetation index (NDVI). Next, using Kc maps and ETo as input, daily AET was simulated by the soil water balance (SWB) model and aggregated to monthly and annual AET. ETo is found to be the highest and of the most concern in Al-Qassim Province, Hail Province, and in the northern portion of Al-Riyadh Province. From January to March and from November - December there is a shift of maximum ETo towards southeastern parts of Al-Qassim Province, Hail Province and Al-Riyadh Province except in its northern portion. The annual ETo shows very high values in the entire study area as it ranged from 2127 to 2460 mm/year. From empirical NDVI-Kc relationships developed and applicable at pixel

level, K_c derived from the NDVI- K_c relationships agree well with K_c recommended by FAO over various crop growth stages in the field.

The monthly AET maps for 1950-2013 show a gradual increase in AET during the crop-growing season in January to May but a subsequent decline as the season progresses from June to December. The AET estimated for January to June are arranged in descending order, which are May (3.67-44.7 mm/day), April (5.99-36.8 mm/day), March (2.96-32.7 mm/day), February (0.68-20 mm/day), June (2.42-17.7 mm/day) and January (1-11 mm/day), respectively. Statistical analysis shows that statistically significant change point in daily AET generally occurred in 1990, such that the long-term average daily AET of 1950-1990 at 3.6 mm/day increased to about 5.3 mm/day between 1990 and 2016 with a positive trend of 1.5 mm/decade. The annual AET estimated for irrigated cropland in northern and central regions of Riyadh, Al-Qassim province and Hail province range from 1200 to 2900 mm/year. In these regions, low AET values are found in shrubland, grassland, and other natural vegetation. The annual AET estimated by the SWB model are about 9-11% higher than modeled AET in the study area, where the long-term average daily AET estimated for 1950-2013 range from 2 mm/day to 30 mm/day. The lowest long-term average daily AET is observed from the start of August to the end of September. The measured daily AET for alfalfa crop used to test and validate the SWB model. good agreement between SWB-based daily AET and the measured daily AET for alfalfa. Overall, there was very good agreements between model estimated and observed daily AET for alfalfa, even though the model estimated daily AET are about 4-5% higher than the observed AET for January to April, the period with the best agreement between both datasets. Between the end of April and the middle of June, estimated AET is about 2% lower than the observed AET, and even lower from July to August because of lower atmospheric demand of evaporation loss. Representative AET maps derived from

applying the NDVI-Kc relationships to the SWB model will be useful to achieve the planning and management of sustainable water use in arid regions of Middle East.

6) Multidecadal variability in the Nile River Basin hydroclimate controlled by ENSO and Indian Ocean Dipole

To improve our understanding of the hydrological cycle and variability in hydroclimate variables of the Nile River basin, change point detection, trend analysis, wavelet coherence and detrended cross-correlation function were used to analyze the variability in the Nile River basin hydroclimate at a wide range of time scales and possible linkages to the large-scale climate patterns. First, the spatio-temporal variability, frequency, intensity, change point and trend of monthly precipitation, precipitation anomaly, temperature, temperature anomaly, geopotential height, relative humidity, specific humidity, actual evapotranspiration (AET), and wind stress data were analyzed at the basin level. Next, we also investigated the IOD and El Niño role on NRB's hydroclimate variability over inter-decadal and longer timescales. Our analysis shows that the NRB has experienced significant climate change impact in recent decades, as shown in the detected change point of 1976, and a statistically significant warming trend of 0.19 °C/decade over 1910-2017. A statistically significant change point was detected in 1970 in the monthly precipitation anomaly data with an overall decreasing trend of 16.2 mm/decade. Moreover, a statistically significant change point was detected in wind speed in 1975, with a statistically significant increasing trend of 0.02 m/decade. This is critical as high wind speed tends to replace the saturated air from earth surface with dry air. For the 1948-2017 relative humidity data, there was a statistically significant change point in 1977, and a significant decreasing trend of 0.35% /decade after 1977. Similarly, monthly 1000-mb geopotential height (GPH) data had a statistically significant change point in 1976, with an overall statistically significant increasing trend of 3.1 m/decade, which, as a measure of the atmospheric pressure level, means the lower atmosphere had

become warmer. The monthly specific humidity data of 1948-2016 had a statistically significant change point in 1966, and an overall statistically significant decreasing trend of 0.15 gm/kg per decade. The AET anomaly of the NRB has increased significantly, with a statistically significant change point in 1995 with an upward trend of 1.2 mm/decade. This can be attributed to a higher wind speed and wind stress, warming and lower RH.

Composite analysis of NRB's hydroclimate data between 1948 and 2017 also shows significant changes across the entire NRB. Beside ENSO, our results also show that IOD plays a crucial role on NRB's hydroclimate variability over inter-decadal and longer timescales. The wavelet coherence spectrum plots between AET and El Niño and IOD show in-phase, statistically significant coherent relationship at 2-4 and 8-14-years band after 1970s (Figs 6g, 7g), which peaked at the 14–16-year time scale after 2000s. On the other hand, the wavelet coherence between IOD and AET show that IOD mainly lead AET after 2000s. The higher AET after 1970s can be partly attributed to stronger El Niño amplitudes, as shown by strong wavelet coherence between zonal and meridional wind stresses and AET at 1-2 years bands. Their recurrent in-phase and anti-phase relationships at 1-2 years bands demonstrate the effect of positive (negative) wind stress anomalies when El Niño was active. while IOD, meridional and zonal wind stresses showed in-phase coherence after 2000s. It seems both increasing meridional wind stress anomalies and stronger El Niño episodes have contributed to changes in the heat content of NRB. A detailed cross correlation (ρ) analysis shows that the hydroclimate of NRB is strongly teleconnected to El Niño and IOD, especially to El Niño, with positive or negative correlations between El Niño 3.4, surface temperature (T_s) ($\rho = 0.97$), GPH ($\rho = 0.81$), relative humidity ($\rho = -0.97$) and precipitation ($\rho = -0.7$). The correlation of these climate variables with IOD are generally lower than with El Niño. However, IOD still plays an important role on the hydroclimate variability in the NRB, such as its effect on NRB's surface temperature and precipitation anomalies under neutral ENSO conditions,

The results from this study would help us to better develop mitigation strategies for these riparian countries against the potential impact of climate change.

7) Worsening Drought of Nile Basin by Atmospheric Circulation Shift, Stronger ENSO and Indian Niño

Analysis of hydroclimate data demonstrated following changes that contributed to recent increasing aridity of the Nile river basin. However, besides climate warming, statistical and wavelet transform coherence (WTC) analysis also shows that the influence of stronger ENSO and Indian Ocean dipole (IOD) in NRB has increased after 1980s, particularly the influence of IOD on NRB's hydroclimate over inter-decadal timescales. A shift in zonal winds (westward) and meridional winds (southward) associated with stronger El Niño episodes has contributed to the increased aridity of NRB after 1970s, given stream function, GPH and U-wind anomalies associated with El Niño shows that changes in regional atmospheric circulations during more persistent and stronger El Niño episodes has resulted in drier NRB. The decrease in RH, SMC, and GWS had been the most significant in Uganda, Sudan, and northwestern Ethiopia where the increase in temperature, GPH, AET and wind stresses had also been the highest. After 1970s, WTC between El Niño, IOD, sc-PDSI (self-calibrating Palmer Drought Severity Index) and SPI (Standard Precipitation Index) shows significant anti-phase relationships, which again demonstrates that more frequent and severe El Niño, IOD and SST gradient over the Arabian Sea (WTIO) in recent years has led to more severe droughts in NRB.

Furthermore, from WTC and strong negative correlations between SPI, sc-PDSI and WTIO, NRB's hydroclimate is shown to be more strongly influenced by WTIO than by IOD, and the Nile flow is more strongly teleconnected to IOD and WTIO than El Niño at inter-annual and inter-decadal time scales. Contrary to past findings, results show that IOD and WTIO are better

predictors of the Nile flow than El Niño. In summary, the warming over the Arabian sea and stronger El Niño, attributed to warming, and the southward shift of the lower atmospheric stream functions have contributed to worsening droughts observed in NRB in recent years, where its flow at upstream and downstream stations have decreased from 13.7 to 114.1 CBM/decade, respectively. Climate projections suggest that under the combined impact of warming and stronger WTIO and El Niño episodes, future droughts of the NRB will worsen.

Bibliography

- Abahous, H., Ronchail, J., Sifeddine, A., Kenny, L., & Bouchaou, L. (2017). Trend and change point analyses of annual precipitation in the Souss-Massa Region in Morocco during 1932–2010. *Theoretical and Applied Climatology*, 1-11.
- Abteu, W., & Melesse, A. (2013). Climate change and evapotranspiration. In *Evaporation and Evapotranspiration* (pp. 197-202).
- Abteu, W., Melesse, A. M., & Dessalegne, T. (2009). El Niño southern oscillation link to the Blue Nile River basin hydrology. *Hydrological Processes*, 23(26), 3653-3660.
- Adebayo, Y.R. (1991). Day-time effects of urbanization on relative humidity and vapour pressure in a tropical city. *Theor. Appl. Climatol.* 43, 17–30.
- AghaKouchak, A., (2015). A multivariate approach for persistence-based drought prediction: application to the 2010–2011 East African Drought. *J. Hydrol.* 526, 127–135.
- Agnew, C.T., Chappel, A., (1999). Drought in the Sahel. *Geojournal* 48 (4), 299–311.
- Ahn, K. H. and Merwade, V. (2015). Role of watershed geomorphic characteristics on flooding in Indiana, United States, *Journal of Hydrologic Engineering*, 21, 05015021.
- Alberto, M. C. R., Quilty, J. R., Buresh, R. J., Wassmann, R., Haidar, S., Correa Jr, T. Q., & Sandro, J. M. (2014). Actual evapotranspiration and dual crop coefficients for dry-seeded rice and hybrid maize grown with overhead sprinkler irrigation. *Agricultural Water Management*, 136, 1-12
- Alexakis, D. D., Grillakis, M. G., Koutroulis, A. G., Agapiou, A., Themistocleous, K., Tsanis, I. K., Michaelides, S., Pashiardis, S., Demetriou, C., Aristeidou, K., Retalis, A., Tymvios, F. and Hadjimitsis, D. G. , (2014). GIS and remote sensing techniques for the assessment of land use changes impact on flood hydrology: the case study of Yialias Basin in Cyprus, *Nat. Hazards Earth Syst. Sci.*, 14, 413–426.
- Allen, R. G., Pereira, L. S., Raes, D., & Smith, M. (1998). *Crop evapotranspiration-Guidelines for computing crop water requirements-FAO Irrigation and drainage paper 56*. FAO, Rome, 300(9), D05109.
- Allen, R.G., Pereira, L. S., Raes, D., Smith, M., (1998). *Crop evapotranspiration guidelines for computing crop water requirements*. Irrigation and Drainage Paper, No. 56. FAO, Rome.
- Alley, W. M. (1984). The Palmer drought severity index: limitations and assumptions. *Journal of climate and applied meteorology*, 23(7), 1100-1109.
- Anderson, J., Hardy, E.E., Roach, J.T., and Witmer, R.E. (1976). A land use and land cover classification system for use with remote sensor data. US Geological Survey, Professional Paper 964.

- Anderson, W.B., Zaitchik, B.F., hain, C.R., Anderson, M.C., Yilmaz, M.T., Mecikalski, J., Schultz, L., (2012). Towards an integrated soil moisture drought monitor for East Africa. *Hydrol. Earth Syst. Sci.* 16, 2893–2913.
- Anyamba, A., Tucker, C.J., (2005). Analysis of Sahelian vegetation dynamics using NOAAAVHRR NDVI data from 1981–2003. *J. Arid Environ.* 63 (3), 596–614.
- Araya, Y.H., Cabral, P., (2010). Analysis and modeling of urban land cover change in Setúbal and Sesimbra, Portugal. *Remote Sens* 2:1549–1563.
- Argüeso, D., Evans, J. P., Pitman, A. J., & Di Luca, A. (2015). Effects of city expansion on heat stress under climate change conditions. *PLoS one*, 10(2), e0117066.
- Arsiso, B. K., Tsidu, G. M., Stoffberg, G. H., & Tadesse, T. (2018). Influence of urbanization-driven land use/cover change on climate: The case of Addis Ababa, Ethiopia. *Physics and Chemistry of the Earth, Parts A/B/C*.
- Baker, C., Lawrence, R., Montagne, C., & Patten, D. (2006). Mapping wetlands and riparian areas using Landsat ETM+ imagery and decision-tree-based models. *Wetlands*, 26(2), 465-474.
- Banasik, K., Krajewski, A., Sikorska, A., & Hejduk, L. (2014). Curve Number estimation for a small urban catchment from recorded rainfall-runoff events. *Archives of Environmental Protection*, 40(3), 75-86.
- Baranowski, P., Krzyszczak, J., Slawinski, C., Hoffmann, H., Kozyra, J., Nieróbca, A., Siwek, K. and Gluza, A., (2015). Multifractal analysis of meteorological time series to assess climate impacts. *Climate Research*, 65, pp.39-52.
- Bastiaanssen, W.G.M., (1995). Regionalization of surface flux densities and moisture indicators in composite terrain, a remote sensing approach under clear skies in Mediterranean climates, Report 109, Agricultural Department, Wageningen, The Netherlands.
- Bathrellos, G. D., Karymbalis, E., Skilodimou, H. D., Gaki-Papanastassiou, K., & Baltas, E. A. (2016). Urban flood hazard assessment in the basin of Athens Metropolitan city, Greece. *Environmental Earth Sciences*, 75(4), 319.
- Batjes, N. H., (2002a). Revised soil parameter estimates for the soil types of the world, *Soil Use Manage.*, 18, 232– 235.
- Batjes, N. H., (2002b). Soil parameter estimates for the soil types of the world for use in global and regional modeling (Version 2.1; July 2002), ISRIC Report 2002/02c, Int. Food Policy Res. Inst. and Int. Soil Ref. and Inf. Cent., Wageningen, Netherlands. (Available on-line at <http://www.isric.org>.)
- Bausch, W. C., (1995). Remote sensing of crop coefficients for improving the irrigation scheduling of corn. *Agric. Water Manage.* 27(1), 55-68.
- Belihu, M., Abate, B., Tekleab, S., & Bewket, W. (2017). Hydro-meteorological trends in the Gidabo catchment of the Rift Valley Lakes Basin of Ethiopia. *Physics and Chemistry of the Earth, Parts A/B/C*.

- Bian, G. D., Du, J. K., Song, M. M., Xu, Y. P., Xie, S. P., Zheng, W. L., & Xu, C. Y. (2017). A procedure for quantifying runoff response to spatial and temporal changes of impervious surface in Qinhuai River basin of southeastern China. *CATENA*, 157, 268-278.
- Biftu, G. F., and T.Y. Gan, 2004, A semi-distributed, physics-based hydrologic model using remotely sensed and Digital Terrain Elevation Data for semi-arid catchments, *Int. J. Remote Sensing*, 25(20), 4351-4379.
- Biquand, S., Biquand-Guyot, V., Boug, A., & Gautier, J. P. (1992). The distribution of *Papio hamadryas* in Saudi Arabia: Ecological correlates and human influence. *International Journal of Primatology*, 13(3), 223-243.
- Birhanu, D., Kim, H., Jang, C., & Park, S. (2016). Flood Risk and Vulnerability of Addis Ababa City Due to Climate Change and Urbanization. *Procedia Engineering*, 154, 696-702.
- Birsan, M., Molnar, P., Burlando, P., Pfaundler, M., (2005). Streamflow trends in Switzerland. *J. Hydrol.* 314, 312–329.
- Bitew, M.M., Gebremichael, M., Hirpa, F.A., Gebrewubet, Y.M., Seleshi, Y., Girma, Y., (2010). On the local-scale spatial variability of daily summer rainfall in the humid and complex terrain of the Blue Nile: observational evidence. *Hydrol. Process.* 23, 3670–3674.
- Bo, X. I. A. O., Qing-Hai, W. A. N. G., Jun, F. A. N., Feng-Peng, H. A. N., & Quan-Hou, D. A. I. (2011). Application of the SCS-CN model to runoff estimation in a small watershed with high spatial heterogeneity. *Pedosphere*, 21(6), 738-749.
- Bodner, G., Loiskandl, W., Kaul, H.-P., (2007). Cover crop evapotranspiration under semi-arid conditions using FAO dual crop coefficient method with water stress compensation. *Agric. Water Manage.* 93, 85–98,
- Boegh, E., Sogaard, H., Hanan, N., Kabat, P., Lesch, L., (1999). A remote sensing study of the NDVI–Ts relationship and the transpiration from sparse vegetation in the Sahel based on high-resolution satellite data. *Remote sensing of Environment*, 69(3), 224-240.
- Borbias, E. E., Seemann, S., Li, Z., Li, J., Kern, A., Menzel, W.P. (2016). MODIS Atmosphere L2 Atmosphere Profile Product. NASA MODIS Adaptive Processing System, Goddard Space Flight Center, USA.
- Bounoua, L., Zhang, P., Mostovoy, G., Thome, K., Masek, J., Imhoff, M., Shepherd, M., Quattrochi, D., Santanello, J., Silva, J., Wolfe, R., Toure, A.M. (2015). Impact of urbanization on US surface climate. *Environ. Res. Lett.* 10084010.
- Briffa, K.E., Jones, P.D., Hulme, M. (1994). Summer moisture variability across Europe, 1892–1991: An analysis based on the Palmer Drought Severity Index. *Int. J. Climatol.* 14,475–506
- Bronstert, A., (2003). Floods and climate change: interactions and impacts, *Risk Anal.*, 23, 545–557.

- Buishand, T. A. (1982). Some methods for testing the homogeneity of rainfall records. *Journal of hydrology*, 58(1-2), 11-27.
- Buishand, T. A., De Martino, G., Spreeuw, J. N., & Brandsma, T. (2013). Homogeneity of precipitation series in the Netherlands and their trends in the past century. *International journal of climatology*, 33(4), 815-833.
- Cai, W., Borlace, S., Lengaigne, M., Van Rensch, P., Collins, M., Vecchi, G., Timmermann, A., Santoso, A., McPhaden, M.J., Wu, L. and England, M.H. (2014). Increasing frequency of extreme El Niño events due to greenhouse warming. *Nat. Clim. Change* 4(2), 111
- Cai, W., Wang, G., Santoso, A., McPhaden, M.J., Wu, L., Jin, F.F., Timmermann, A., Collins, M., Vecchi, G., Lengaigne, M. and England, M.H. (2015). Increased frequency of extreme La Niña events under greenhouse warming. *Nat. Clim. Change* 5, 132-137.
- Camberlin, P., (2009). Nile basin climates. In: Dumont, H.J. (Ed.), *The Nile: Origin, Environments, Limnology and Human Use, Monographiae Biologicae*, vol. 89. Springer, Dordrecht, pp. 307–333.
- Campos, I., Balbontín, C., González-Piqueras, J., González-Dugo, M. P., Neale, C. M., & Calera, A. (2016b). Combining a water balance model with evapotranspiration measurements to estimate total available soil water in irrigated and rainfed vineyards. *Agricultural Water Management*, 165, 141-152.
- Campos, I., González-Piqueras, J., Carrara, A., Villodre, J., & Calera, A. (2016a). Estimation of total available water in the soil layer by integrating actual evapotranspiration data in a remote sensing-driven soil water balance. *Journal of Hydrology*, 534, 427-439.
- Campos, I., Neale, C. M., Suyker, A. E., Arkebauer, T. J., & Gonçalves, I. Z. (2017). Reflectance-based crop coefficients REDUX: For operational evapotranspiration estimates in the age of high producing hybrid varieties. *Agricultural water management*, 187, 140-153.
- Cao, Q., Yu, D., Georgescu, M., Wu, J., & Wang, W. (2018). Impacts of future urban expansion on summer climate and heat-related human health in eastern China. *Environment international*, 112, 134-146.
- Chakraborty, A., Sachdeva, K., & Joshi, P. K. (2016). Mapping long-term land use and land cover change in the central Himalayan region using a tree-based ensemble classification approach. *Applied Geography*, 74, 136-150.
- Changnon SA, Huff FA (1986) The urban-related nocturnal rainfall anomaly at St. Louis. *J Clim Appl Meteorol* 25:1985–1995.
- Chen, J., Theller, L., Gitau, M. W., Engel, B. A., & Harbor, J. M. (2017). Urbanization impacts on surface runoff of the contiguous United States. *Journal of environmental management*, 187, 470-481.
- Chen, S. T., Kuo, C. C., & Yu, P. S. (2009). Historical trends and variability of meteorological droughts in Taiwan/Tendances historiques et variabilité des sécheresses météorologiques à Taiwan. *Hydrological sciences journal*, 54(3), 430-441.

- Chen, Y. R., Yeh, C. H. and Yu, B. (2011). Integrated application of the analytic hierarchy process and the geographic information system for flood risk assessment and flood plain management in Taiwan, *Natural hazards*, 59, 1261–1276.
- Chen, Y., Liu, R., Barrett, D., Gao, L., Zhou, M., Renzullo, L., & Emelyanova, I. (2015). A spatial assessment framework for evaluating flood risk under extreme climates. *Science of the Total Environment*, 538, 512-523.
- Cherqui, F., Belmeziti, A., Granger, D., Sourdril, A., & Le Gauffre, P. (2015). Assessing urban potential flooding risk and identifying effective risk-reduction measures. *Science of The Total Environment*, 514, 418-425.
- Cheung, W.H., Senay, G.B. and Singh, A., (2008). Trends and spatial distribution of annual and seasonal rainfall in Ethiopia. *International Journal of Climatology: A Journal of the Royal Meteorological Society*, 28(13), pp.1723-1734.
- Choudhury, B. J., Ahmed, N. U., Idso, S. B., Reginato, R. J., & Daughtry, C. S. (1994). Relations between evaporation coefficients and vegetation indices studied by model simulations. *Remote sensing of environment*, 50(1), 1-17.
- Chowdhury, S., Al-Zahrani, M., (2015). Characterizing water resources and trends of sector wise water consumptions in Saudi Arabia. *Journal of King Saud University-Engineering Sciences*, 27(1), 68-82.
- Christensen, J. H. and Christensen, O. B. (2003). Climate modelling: severe summertime flooding in Europe, *Nature*, 421, 805–806.
- Clarke, K. C., & Gaydos, L. J. (1998). Loose coupling a cellular automaton model and GIS: long-term urban growth prediction for San Francisco and Washington/Baltimore. *International journal of geographical information science*, 12(7), 699-714.
- Coêlho, M., & Gonçalves, F. (2010). Statistical analysis aiming at predicting respiratory tract disease hospital admissions from environmental variables in the city of São Paulo. *Journal of environmental and public health*, *J. Environ. Public Health*: 11 Article ID 209270, DOI:10.1155/2010/209270
- Conway, D. (2005). From headwater tributaries to international river: observing and adapting to climate variability and change in the Nile Basin. *Global Environ. Change* 15, 99–114.
- Cruz-Blanco, M., Lorite, I. J., & Santos, C. (2014). An innovative remote sensing-based reference evapotranspiration method to support irrigation water management under semi-arid conditions. *Agricultural water management*, 131, 135-145.
- Dahri, N., Habib A., (2017). Monte Carlo simulation-aided analytical hierarchy process (AHP) for flood susceptibility mapping in Gabes Basin (southeastern Tunisia). *Environmental Earth Sciences* 76.7: 302.
- Dai, A. (2013). Increasing drought under global warming in observations and models. *Nature Climate Change*, 3(1), 52.

- Dai, A., (2011). Characteristics and trends in various forms of the Palmer Drought Severity Index (PDSI) during 1900-2008. *J. Geophys. Res.*, 116
- Dale, V. H., Erosion, R. A., & Kline, K. L. (2011). The land use–climate change–energy nexus. *Landscape ecology*, 26(6), 755-773.
- Dastane, N., (1974). Effective Rainfall. FAO Irrigation and Drainage Paper No. 25. Rome, Italy: Food and Agriculture Organization of the United Nations.
- Dawood, M. (2017). Spatio-statistical analysis of temperature fluctuation using Mann–Kendall and Sen’s slope approach. *Climate Dynamics*, 48(3-4), 783-797.
- Department of Statistics and Information, (2008). Statistical yearbook. Editions 38-44. Ministry of Economy and Planning, Kingdom of Saudi Arabia.
- Dobrica, V., Demetrescu, C., Mares, I. and Mares, C., (2018). Long-term evolution of the Lower Danube discharge and corresponding climate variations: solar signature imprint. *Theoretical and Applied Climatology*, 133(3-4), pp.985-996.
- Doorenbos, J., Pruitt, W. O., (1977). Crop water requirements, FAO Irrigation and Drainage Paper No. 24 (revised), Food and Agriculture Organization, Rome, Italy.
- Dou, X., Song, J., Wang, L., Tang, B., Xu, S., Kong, F., & Jiang, X. (2018). Flood risk assessment and mapping based on a modified multi-parameter flood hazard index model in the Guanzhong Urban Area, China. *Stochastic Environmental Research and Risk Assessment*, 32(4), 1131-1146.
- Douglas, E. M., Jacobs, J. M., Sumner, D. M., Ray, R. L., (2009). A comparison of models for estimating potential evapotranspiration for Florida land cover types. *Journal of Hydrology*, 373(3), 366-376.
- Drerup, P., Brueck, H., & Scherer, H. W. (2017). Evapotranspiration of winter wheat estimated with the FAO 56 approach and NDVI measurements in a temperate humid climate of NW Europe. *Agricultural Water Management*, 192, 180-188.
- Duchemin, B., Hadria, R., Er-Raki, S., Boulet, G., Maisongrande, P., Chehbouni, A., Escadafal, R., Ezzahar, J., Hoedjes, J., Karrou, H., Khabba, S., Mougenot, B., Olioso, A., Rodriguez, J.-C., Simonneaux, V., (2006). Monitoring wheat phenology and irrigation in Central Morocco: on the use of relationship between evapotranspiration, crops coefficients, leaf area index and remotely sensed vegetation indices. *Agric. Water Manage.* 79, 1–27.
- Eastman, J.R., Fulk, M., (1993). Long sequence time series evaluation using standardized principle components. *Photogramm. Eng. Rem. Sens.* 59, 991–996.
- Edwards, D. C., and T. B. McKee, (1997). Characteristics of 20th century drought in the United States at multiple time scales. Colorado State University Dept. of Atmospheric Science Climatology Rep. 97-2/Atmospheric Science Paper 634, 174 pp.
- Eiste, E., Diriba, K., Sorteberg, A., (2012). Recent drought and precipitation tendencies in Ethiopia. *Theor. Appl. Climatol.* 112 (3–4), 535–551.

- Elkhrachy, I. (2015). Flash Flood Hazard Mapping Using Satellite Images and GIS Tools: A case study of Najran City, Kingdom of Saudi Arabia (KSA). *The Egyptian Journal of Remote Sensing and Space Science*, 18(2), 261-278.
- Eludoyin, O. M., Adelekan, I. O., Webster, R., & Eludoyin, A. O. (2014). Air temperature, relative humidity, climate regionalization and thermal comfort of Nigeria. *International Journal of Climatology*, 34(6), 2000-2018.
- EM-DA. (2018). The OFDA/CRED - International Disaster Database <http://www.emdat.be> - Université catholique de Louvain Brussels - Belgium
- Emmanuel, R. (2005). Thermal comfort implications of urbanization in a warm-humid city: the Colombo Metropolitan Region (CMR), Sri Lanka. *Building and environment*, 40(12), 1591-1601.
- Er-Raki, S., Chehbouni, A., Duchemin, B., (2010). Combining satellite remote sensing data with the FAO-56 dual approach for water use mapping in irrigated wheat fields of a semi-arid region. *Remote Sensing*, 2(1), 375-387.
- Er-Raki, S., Chehbouni, A., Guemouria, N., Duchemin, B., Ezzahar, J., & Hadria, R., (2007). Combining FAO-56 model and ground-based remote sensing to estimate water consumptions of wheat crops in a semi-arid region. *Agric. Water Manage.* 87(1), 41-54.
- Er-Raki, S., Rodriguez, J. C., Garatuza-Payan, J., Watts, C. J., & Chehbouni, A. (2013). Determination of crop evapotranspiration of table grapes in a semi-arid region of Northwest Mexico using multi-spectral vegetation index. *Agricultural water management*, 122, 12-19.
- Eslamian, S., Khordadi, M. J., & Abedi-Koupai, J. (2011). Effects of variations in climatic parameters on evapotranspiration in the arid and semi-arid regions. *Global and Planetary Change*, 78(3), 188-194.
- Fang, Z., Lin, Z., Mak, C. M., Niu, J., & Tse, K. T. (2018). Investigation into sensitivities of factors in outdoor thermal comfort indices. *Building and Environment*, 128, 129-142.
- FAO, 1974. FAO-UNESCO Soil Map of the World, 1:5.000.000. UNESCO, Paris.
- Fernández, D. S., & Lutz, M. A. (2010). Urban flood hazard zoning in Tucumán Province, Argentina, using GIS and multicriteria decision analysis. *Engineering Geology*, 111(1), 90-98.
- Fischer, E. M. & Knutti, R. (2013). Robust projections of combined humidity and temperature extremes. *Nat. Clim. Change* 3, 126–130
- Folland, C. K., Palmer, T. N., & Parker, D. E. (1986). Sahel rainfall and worldwide sea temperatures, 1901–85. *Nature*, 320(6063), 602.
- Frias, M. D., Zorita, E., Fernández, J., & Rodriguez-Puebla, C. (2006). Testing statistical downscaling methods in simulated climates. *Geophysical Research Letters*, 33(19).
- Fu, P., & Weng, Q. (2016). A time series analysis of urbanization induced land use and land cover change and its impact on land surface temperature with Landsat imagery. *Remote Sensing of Environment*, 175, 205-214.

- Fu, P., Rich, P.M., (1999) Design and implementation of the Solar Analyst: an ArcView extension for modeling solar radiation at landscape scales. In Proceedings of the Nineteenth Annual ESRI User Conference (pp. 1-31). Chicago
- Fu, Q., Li, B., Hou, Y., Bi, X., & Zhang, X. (2017). Effects of land use and climate change on ecosystem services in Central Asia's arid regions: A case study in Altay Prefecture, China. *Science of The Total Environment*, 607, 633-646.
- Gebremedhin, K., Shetty, A., Nandagiri, L., (2016). Analysis of variability and trends in rainfall over northern Ethiopia. *Arab J Geosci*. 9 (451)
- Gebremicael, T.G., Mohamed, Y.A., Betrie, G.D., van der Zaag, P., Teferi, E., (2013). Trend analysis of runoff and sediment fluxes in the upper Blue Nile basin: a combined analysis of statistical tests, physically based models and landuse maps. *J. Hydrol.* 482, 57–68.
- Ghaffarianhoseini, A., Berardi, U., Ghaffarianhoseini, A. (2015). Thermal performance characteristics of unshaded courtyards in hot and humid climates. *Building and Environment*, 87, 154-168.
- Giacinto, G., & Roli, F. (2001). Design of effective neural network ensembles for image classification purposes. *Image and Vision Computing*, 19(9), 699-707.
- Giannini, A., Saravanan, R., Chang, P. (2003). Oceanic forcing of Sahel rainfall on interannual to interdecadal time scales. *Science* 302, 1027–1030.
- Gissila, T., Black, E., Grimes, D.I.F. and Slingo, J.M. (2004). Seasonal forecasting of the Ethiopian summer rains. *Int J Climatol* 24:1345–1358
- Gizaw, M. S., & Gan, T. Y. (2017). Impact of climate change and El Niño episodes on droughts in sub-Saharan Africa. *Climate Dynamics*, 49(1-2), 665-682.
- Gizaw, M., and Gan, T. Y. (2015) Possible Impact of climate change on future extreme precipitation of the Oldman, Bow and Red Deer River Basins of Alberta, *Int. Journal Climatology*, DOI:10.1002/joc.4338.
- Global Soil Data Task Group, (2000). Global Gridded Surfaces of Selected Soil Characteristics, Oak Ridge Natl. Lab., Distributed Active Archive Cent., Oak Ridge, Tenn. (Available at <http://daacsti.ornl.gov/SOILS/guides/igbp-surfaces.html>.)
- Gocic, M., & Trajkovic, S. (2013). Analysis of changes in meteorological variables using Mann-Kendall and Sen's slope estimator statistical tests in Serbia. *Global and Planetary Change*, 100, 172-182.
- Goldschmidt Jr, A. (2008). A brief history of Egypt. Infobase Publishing.
- Gong, D. Y., Drange, H., & Gao, Y. Q. (2007). Reconstruction of Northern Hemisphere 500 hPa geopotential heights back to the late 19th century. *Theoretical and Applied Climatology*, 90(1-2), 83-102.
- González-Dugo, M. P., Mateos, L., (2008). Spectral vegetation indices for benchmarking water productivity of irrigated cotton and sugarbeet crops. *Agric. Water Manage.* 95(1), 48-58.

- González-Dugo, M. P., S. Escuin, F. Cano, V. Cifuentes, F. L. M. Padilla, J. L. Tirado, N. Oyonarte, P. Fernández, L., Mateos., (2013). Monitoring evapotranspiration of irrigated crops using crop coefficients derived from time series of satellite images. II. Application on basin scale." *Agric. Water Manage.* 125: 92-104.
- Gornall, J., Betts, R., Burke, E., Clark, R., Camp, J., Willett, K., Wiltshire, A., (2010). Implications of climate change for agricultural productivity in the early twenty-first century. *Phil. Trans. R. Soc. B : Biol. Sci.* 365, 2973–2989.
- Grimmond, S. U. E. (2007). Urbanization and global environmental change: local effects of urban warming. *The Geographical Journal*, 173(1), 83-88.
- Gu, C., Hu, L., Zhang, X., Wang, X., & Guo, J. (2011). Climate change and urbanization in the Yangtze River Delta. *Habitat International*, 35(4), 544-552.
- Guan, D., Li, H., Inohae, T., Su, W., Nagaie, T., & Hokao, K. (2011). Modeling urban land use change by the integration of cellular automaton and Markov model. *Ecological Modelling*, 222(20), 3761-3772.
- Guan, M., Sillanpää, N., & Koivusalo, H. (2016). Storm runoff response to rainfall pattern, magnitude and urbanization in a developing urban catchment. *Hydrological Processes*, 30(4), 543-557.
- Guha-Sapir, D., Below, R., & Hoyois, P. (2014). EM-DAT: International disaster database. Univ. Cathol. Louvain, Brussels: Belgium. [www. em-dat. net](http://www.em-dat.net). Accessed, 20 Oct. 2016.
- Guo, Y., Li, J., & Li, Y. (2014). Seasonal forecasting of North China summer rainfall using a statistical downscaling model. *Journal of Applied Meteorology and Climatology*, 53(7), 1739-1749.
- Hajian, S. and Movahed, M.S., (2010). Multifractal detrended cross-correlation analysis of sunspot numbers and river flow fluctuations. *Physica A: Statistical Mechanics and its Applications*, 389(21), pp.4942-4957.
- Han, M., & Liu, B. (2015). Ensemble of extreme learning machine for remote sensing image classification. *Neurocomputing*, 149, 65-70.
- Han, Y., & Jia, H. (2017). Simulating the spatial dynamics of urban growth with an integrated modeling approach: A case study of Foshan, China. *Ecological Modelling*, 353, 107-116.
- Hill, C., Verjee, F., & Barrett, C. (2010). *Flash Flood Early Warning System Reference Guide*. University Corporation for Atmospheric Research, ISBN, 978-0.
- Hoell A, Shukla S, Barlow M, Cannon F, Kelley C, Funk C. (2015). The forcing of monthly precipitation variability over Southwest Asia during the Boreal Cold Season. *J. Clim.* 28(18): 7038–7056.
- Hong, H., Tsangaratos, P., Ilija, I., Liu, J., Zhu, A. X., & Chen, W. (2018). Application of fuzzy weight of evidence and data mining techniques in construction of flood susceptibility map of Poyang County, China. *Science of The Total Environment*, 625, 575-588.
- Hong, Haoyuan, Mahdi Panahi, Ataollah Shirzadi, Tianwu Ma, Junzhi Liu, A-Xing Zhu, Wei Chen, Ioannis Kougias, and Nerantzis Kazakis. (2017). Flood susceptibility assessment in Hengfeng area coupling

- adaptive neuro-fuzzy inference system with genetic algorithm and differential evolution. *Science of The Total Environment*. In press
- Hossain, M.A., T.Y., Gan, A.B.M., Baki, 2013, Assessing morphological changes of the Ganges River using satellite images, *Quaternary international*, 304, 142-155, DOI: 10.1016/j.quaint.2013.03.028
- Hsu, Tai-Wen, Dong-Sin Shih, Chi-Yu Li, Yuan-Jyh Lan, and Yu-Chen Lin. (2017). "A Study on Coastal Flooding and Risk Assessment under Climate Change in the Mid-Western Coast of Taiwan." *Water* 9, no. 6: 390.
- Hu, S., Cheng, X., Zhou, D., & Zhang, H. (2017). GIS-based flood risk assessment in suburban areas: a case study of the Fangshan District, Beijing. *Natural Hazards*, 87(3), 1525-1543.
- Huishi, D., Eerdun, H., Yi, Y., & Jing, A. (2012). Land Coverage Changes in the Hulun Buir Grassland of China Based on the Cellular Automata-Markov Model. *International Proceedings of Chemical, Biological & Environmental Engineering*, 69-74.
- Hulme, M. (1992). A 1951–80 global land precipitation climatology for the evaluation of general circulation models. *Climate Dynamics*, 7(2), 57-72.
- Hwang, R. L., Lin, T. P., & Matzarakis, A. (2011). Seasonal effects of urban street shading on long-term outdoor thermal comfort. *Building and Environment*, 46(4), 863-870.
- Imteaz, M. A., Mahmood, W., Sagar, K. A., & Yilmaz, A. (2017). Climate change fingerprints in lower Euphrates basin: climate and flow data trend analysis. *International Journal of Water*, 11(3), 279-293.
- IPCC. *Climate Change*. (2014). Synthesis Report. Contribution of Working Groups I, II and III to the Fifth Assessment Report of the Intergovernmental Panel on Climate Change [Core Writing Team, R.K. Pachauri and L.A. Meyer (eds.)]. IPCC, Geneva, Switzerland, 151 pp (2014).
- Irmak, S., Odhiambo, L., Specht, J., Djaman, K., (2013). Hourly and daily single and basal evapotranspiration crop coefficients as a function of growing degree days after emergence, leaf area index, fractional green canopy cover, and plant phenology for soybean. *Trans. ASABE* 56, 1785–1803.
- Islam, M., & Sado, K. (2000). Flood hazard assessment in Bangladesh using NOAA AVHRR data with geographical information system. *Hydrological Processes*, 14(3), 605-620.
- Itoh, Y., Takemura, K., Kawabata, D., Tanaka, Y., & Nakaseko, K. (2001). Quaternary tectonic warping and strata formation in the southern Osaka Basin inferred from reflection seismic interpretation and borehole sequences. *Journal of Asian Earth Sciences*, 20(1), 45-58.
- Jacinto, R., Grosso, N., Reis, E., Dias, L., & Garrett, P. (2014). Continental Portuguese Territory Flood Susceptibility Index-Contribution for a Vulnerability Index. *Natural Hazards and Earth System Sciences Discussions*, 2(12), 7521-7552.
- Janssen, R., & Van Herwijnen, M. (1994). *Multi-objective decision support for environmental management*. Kluwer Academic Publishers, Dordrecht, p 232

- Jarušková, D. (1996). Change-point detection in meteorological measurement. *Monthly Weather Review*, 124(7), 1535-1543.
- Jensen, J.R. (2005). *Introductory Digital Image Processing: A Remote Sensing Perspective*. Prentice Hall, Toronto.
- Jensen, J.R., Cowen, D.C., (1999). Remote sensing of urban suburban infrastructure and socio-economic attributes. *Photogramm. Eng. Rem. Sens.* 65, 611–622.
- Jevrejeva, S.; Moore, J.C.; Grinsted, A. (2003). Influence of the Arctic Oscillation and El Niño-Southern Oscillation (ENSO) on ice conditions in the Baltic Sea: The wavelet approach. *J. Geophys. Res.*, 108, 1–11.
- Jiang, R. G., Gan, T. Y., Xie, J., and Ni, W., (2014). Spatiotemporal variability of Alberta's seasonal precipitation, their teleconnection with large-scale climate anomalies and sea surface temperature, *Int. J. Climatology*, RMS, 34(9), 2899-2917. DOI: 10.1002/joc.3883.
- Jiang, R., Gan, T. Y., Xie, J., Ni, W., and Kuo, C. C. (2015), Historical and Potential Changes of Precipitation and Temperature of Alberta subjected to Climate Change Impact: 1900-2100, *Journal of Theoretical and Applied Climatology*, DOI 10.1007/s00704-015-1664-y.
- Jiménez-Bello, M. A., Ruiz, L. A., Hermosilla, T., Recio, J., & Intrigliolo, D. S. (2012). Use of remote sensing and geographic information tools for irrigation management of citrus trees. *Options Méditerranéennes B*, 67, 65-75.
- Johansson, E., Yahia, M. W., Arroyo, I., & Bengs, C. (2018). Outdoor thermal comfort in public space in warm-humid Guayaquil, Ecuador. *International journal of biometeorology*, 62(3), 387-399.
- Ju, C. Y., Jia, Y. G., Shan, H. X., Tang, C. W. and Ma, W. J. (2012). GIS-based coastal area suitability assessment of geo-environmental factors in Laoshan district, Qingdao, *Natural Hazards and Earth System Science*, 12, 143–150.
- Justice, C.O., Townshend, J.R.G., (2002). Special issue on the Moderate Resolution Imaging Spectroradiometer (MODIS): A new generation of land surface monitoring. *Remote Sens. Environ.* 83 (1), 1–2.
- Kalma, J. D., McVicar, T. R., McCabe, M. F., (2008). Estimating land surface evaporation: Review of methods using remotely sensed surface temperature data. *Surv. Geophys.* 29, 421–469.
- Kalnay E, Kanamitsu M, Kistler R, Collins W, Deaven D, Gandin L, Iredell M, Saha S, White G, Woollen J, Zhu Y, Leetmaa A, Reynolds R, Chelliah M, Ebisuzaki W, Higgins W, Janowiak J, Mo KC, Ropelewski C, Wang J, Jenne R, Joseph D. (1996). The NCEP/NCAR 40-year reanalysis project. *Bull. Am. Meteorol. Soc.* 77(3): 437–471.
- Kang, S., Zhang, F., & Liang, Y. (1999). Effects of Soil Water and the Atmospheric CO₂ Concentration Increase on Evapotranspiration, Photosynthesis, Growth of Wheat, Maize and Cotton. *Acta Agronomica Sinica*, 25, 55-63.

- Kazakis, N., Kougiyas, I., & Patsialis, T. (2015). Assessment of flood hazard areas at a regional scale using an index-based approach and Analytical Hierarchy Process: Application in Rhodope–Evros region, Greece. *Science of the Total Environment*, 538, 555-563
- Kendall, M.G., (1975). *Rank Correlation Methods*, second ed. (New York: Hafner).
- Kerschgens, M.J., Drauschke, R.L. (1986). on the energy budget of a wintry mid-latitude city atmosphere. *Contrib Atmos Phys* 59:115–125.
- Keshtkar, H., & Voigt, W. (2016). A spatiotemporal analysis of landscape change using an integrated Markov chain and cellular automata models. *Modeling Earth Systems and Environment*, 2(1), 10.
- Kim, S.T., Cai, W., Jin, F.F., Santoso, A., Wu, L., Guilyardi, E. and An, S. I. (2014). Response of El Niño sea surface temperature variability to greenhouse warming. *Nat. Clim. Change* 4, 786_790.
- Kolios, S., & Stylios, C. D. (2013). Identification of land cover/land use changes in the greater area of the Preveza peninsula in Greece using Landsat satellite data. *Applied Geography*, 40, 150-160.
- Kourgialas, N. N., & Karatzas, G. P. (2011). Flood management and a GIS modelling method to assess flood-hazard areas—a case study. *Hydrological Sciences Journal—Journal des Sciences Hydrologiques*, 56(2), 212-225.
- Kullberg, E. G., DeJonge, K. C., & Chávez, J. L. (2017). Evaluation of thermal remote sensing indices to estimate crop evapotranspiration coefficients. *Agricultural Water Management*, 179, 64-73.
- Kumar, P. K., Gopinath, G., & Seralathan, P. (2007). Application of remote sensing and GIS for the demarcation of groundwater potential zones of a river basin in Kerala, southwest coast of India. *International Journal of Remote Sensing*, 28(24), 5583-5601.
- Kurnik, B., Barbosa, P., Vogt, J., (2011). Testing two different precipitation datasets to compute the standardized precipitation index over the Horn of Africa. *Int. J. Remote Sens.* 32 (21), 5947–5964
- Kurukulasuriya, Mendelsohn, (2008). A Ricardian analysis of the impact of climate change on African cropland. *African Journal of Agricultural and Resource Economics* 2 (1), 1–23.
- La Riche, W. (1996). *Alexandria: the sunken city*. Weidenfeld & Nicolson.
- Lee, D.O. (1991). Urban rural humidity differences in London. *Int J Climatol* 11:577–582
- Lee, S., & Pradhan, B. (2006). Probabilistic landslide hazards and risk mapping on Penang Island, Malaysia. *Journal of Earth System Science*, 115(6), 661-672
- Lehner, B., Verdin, K., & Jarvis, A. (2006). *HydroSHEDS Technical Documentation* (Washington, DC: World Wildlife Fund US) available at <http://hydrosheds.cr.usgs.gov>
- Leng, G., Tang, Q., & Rayburg, S. (2015). Climate change impacts on meteorological, agricultural and hydrological droughts in China. *Global and Planetary Change*, 126, 23-34
- Li, J., Y., Chen, D., Gan, T.Y., and Lau, G.N.C. (2018). Elevated increases in human-perceived temperature under climate warming, *Nature Climate Change*, Nature Publishing Group, doi.org/10.1038/s41558-017-0036-2

- Li, Q., Li, W., Si, P., Xiaorong, G., Dong, W., Jones, P., ... & Cao, L. (2010). Assessment of surface air warming in northeast China, with emphasis on the impacts of urbanization. *Theoretical and Applied Climatology*, 99(3-4), 469.
- Liang, J., Zhong, M., Zeng, G., Chen, G., Hua, S., Li, X., Yuan, Y., Wu, H. and Gao, X., (2017). Risk management for optimal land use planning integrating ecosystem services values: A case study in Changsha, Middle China. *Science of The Total Environment*, 579, pp.1675-1682.
- Lim, K. J., Engel, B. A., Muthukrishnan, S., & Harbor, J. (2006). Effects of initial abstraction and urbanization on estimated runoff using CN technology. *JAWRA Journal of the American Water Resources Association*, 42(3), 629-643.
- Liu, W., You, H., Dou, J. (2009). Urban–rural humidity and temperature differences in the Beijing area. *Theor. Appl. Climatol.* 96, 201–207.
- Liu, Z., Wang, L., Yu, X., Wang, S., Deng, C., Xu, J., Chen, Z. and Bai, L., (2017). Multi-scale response of runoff to climate fluctuation in the headwater region of the Kaidu River in Xinjiang of China. *Atmospheric Science Letters*, 18(5), pp.230-236.
- Loewenberg, S., (2011). Humanitarian response inadequate in Horn of Africa crisis. *The Lancet* 378 (9791), 555–558.
- Long, H., Tang, G., Li, X., & Heilig, G. K. (2007). Socio-economic driving forces of land-use change in Kunshan, the Yangtze River Delta economic area of China. *Journal of Environmental Management*, 83(3), 351-364.
- Longley P., M. Batty (1996). *Spatial Analysis: Modeling in a GIS Environment*, Geo-Information International, Cambridge, UK, pp. 1–15
- Longley, Paul A., Michael F. Goodchild, and David J. Maguire, eds. (2005). *Geographic Information Systems and Science*. England: John Wiley & Sons, Ltd.
- Lu, D., Mausel, P., Brondízio, E., & Moran, E. (2004). Change detection techniques. *International Journal of Remote Sensing*, 25(12), 2365-2407.
- Ma, Z., Kang, S., Zhang, L., Tong, L., & Su, X. (2008). Analysis of impacts of climate variability and human activity on streamflow for a river basin in arid region of northwest China. *Journal of Hydrology*, 352(3), 239-249.
- Madugundu, R., Al-Gaadi, K. A., Tola, E., Hassaballa, A. A., & Kayad, A. G. (2018). Utilization of Landsat-8 data for the estimation of carrot and maize crop water footprint under the arid climate of Saudi Arabia. *PloS one*, 13(2), e0192830.
- Mahé, G., & Paturel, J. E. (2009). 1896–2006 Sahelian annual rainfall variability and runoff increase of Sahelian Rivers. *Comptes Rendus Geoscience*, 341(7), 538-546.
- Mahgoub, F., (2014). *Current Status of Agriculture and Future Challenges in Sudan*. Nordiska Afrikainstitutet.

- Mahmoud, A. H. A. (2011). Analysis of the microclimatic and human comfort conditions in an urban park in hot and arid regions. *Building and environment*, 46(12), 2641-2656.
- Mahmoud, S. H. and Alazba, A. A. (2015). The potential of in situ rainwater harvesting in arid regions: developing a methodology to identify suitable areas using GIS-based decision support system, *Arabian Journal of Geosciences*, 8, 5167–5179.
- Mahmoud, S. H. and Tang, X. (2015). Monitoring prospective sites for rainwater harvesting and stormwater management in the United Kingdom using a GIS-based decision support system, *Environmental Earth Sciences*, 73, 8621–8638.
- Mahmoud, S. H., & Alazba, A. A. (2016). A coupled remote sensing and the Surface Energy Balance based algorithms to estimate actual evapotranspiration over the western and southern regions of Saudi Arabia. *Journal of Asian Earth Sciences*, 124, 269-283.
- Mahmoud, S. H., & Gan, T. Y. (2018a). Impact of anthropogenic climate change and human activities on environment and ecosystem services in arid regions. *Science of The Total Environment*, 633, 1329-1344.
- Mahmoud, S. H., & Gan, T. Y. (2018b). Urbanization and climate change implications in flood risk management: Developing an efficient decision support system for flood susceptibility mapping. *Science of The Total Environment*, 636, 152-167.
- Mahmoud, S. H., (2014). Delineation of potential sites for groundwater recharge using a GIS-based decision support system. *Environmental earth sciences*, 72(9), 3429-3442.
- Mahmoud, S.H. and Gan, T.Y., (2018a). Long-term impact of rapid urbanization on urban climate and human thermal comfort in hot-arid environment. *Building and Environment*, 142, pp.83-100.
- Mahmoud, S.H., (2014). Investigation of rainfall–runoff modeling for Egypt by using remote sensing and GIS integration. *Catena*, 120, pp.111-121.
- Mann, H.B., (1945). Nonparametric tests against trend. *Econometrica* 13, 245–259.
- Maraun, D.; Kurths, J. (2004). Cross wavelet analysis: Significance testing and pitfalls. *Nonlinear Process. Geophys.* 11, 505–514.
- Marshall, E., & Randhir, T. O. (2008). Spatial modeling of land cover change and watershed response using Markovian cellular automata and simulation. *Water Resources Research*, 44(4).
- Martínez, M. D., Serra, C., Burgueño, A., & Lana, X. (2010). Time trends of daily maximum and minimum temperatures in Catalonia (ne Spain) for the period 1975–2004. *International Journal of Climatology*, 30(2), 267-290.
- Martins, S., Bernardo, N., Ogashawara, I., & Alcantara, E. (2016). Support Vector Machine algorithm optimal parameterization for change detection mapping in Funil Hydroelectric Reservoir (Rio de Janeiro State, Brazil). *Modeling Earth Systems and Environment*, 2(3), 138

- Mateos, L., González-Dugo, M. P., Testi, L., Villalobos, F. J., (2013). Monitoring evapotranspiration of irrigated crops using crop coefficients derived from time series of satellite images. I. Method validation. *Agric. Water Manage.* 125, 81-91.
- Matzarakis, A. (2001). Assessing climate for tourism purposes: Existing methods and tools for the thermal complex. In *Proceedings of the first international workshop on climate, tourism and recreation*, ed. by A. Matzarakis and CR de Freitas. International Society of Biometeorology, Commission on Climate Tourism and Recreation (pp. 101-112).
- McKee TB, Doesken NJ, Kleist J. (1993). The relationship of drought frequency and duration to time scales. In *Proceedings of the 8th Conference on Applied Climatology*. AMS: Boston, MA; 179–184.
- McVicar, T. R., Van Niel, T. G., Li, L., Hutchinson, M. F., Mu, X., Liu, Z., (2007). Spatially distributing monthly reference evapotranspiration and pan evaporation considering topographic influences. *Journal of hydrology*, 338(3), 196-220.
- Melesse, A. M., & Abtew, W. (Eds.). (2016). *Landscape Dynamics, Soils and Hydrological Processes in Varied Climates*. Springer International Publishing.
- Méndez, M., & Magaña, V. (2010). Regional aspects of prolonged meteorological droughts over Mexico and Central America. *Journal of Climate*, 23(5), 1175-1188.
- Mengistu, D., Bewket, W., & Lal, R. (2014). Recent spatiotemporal temperature and rainfall variability and trends over the Upper Blue Nile River Basin, Ethiopia. *International Journal of Climatology*, 34(7), 2278-2292.
- Minaei, M., & Irannezhad, M. (2018). Spatio-temporal trend analysis of precipitation, temperature, and river discharge in the northeast of Iran in recent decades. *Theoretical and Applied Climatology*, 131(1-2), 167-179.
- Moghaddam, D. D., Rezaei, M., Pourghasemi, H. R., Pourtaghie, Z. S., & Pradhan, B. (2015). Groundwater spring potential mapping using bivariate statistical model and GIS in the Taleghan Watershed, Iran. *Arabian Journal of Geosciences*, 8(2), 913-929.
- Mohammed, A., Li, J., Elaru, J., Elbashier, M.M., Keesstra, S., Artemi, C., Martin, K., Reuben, M. and Teffera, Z., (2018). Assessing drought vulnerability and adaptation among farmers in Gadaref region, Eastern Sudan. *Land Use Policy*, 70, 402-413.
- Mojaddadi, H., Pradhan, B., Nampak, H., Ahmad, N., & Ghazali, A. H. B. (2017). Ensemble machine-learning-based geospatial approach for flood risk assessment using multi-sensor remote-sensing data and GIS. *Geomatics, Natural Hazards and Risk*, 8(2), 1080-1102.
- Monteith, J.L., (1965) Evaporation and environment. In *Symp. Soc. Exp. Biol* (Vol. 19, No. 205-23, p. 4).
- Morris, K.I., Chan, A., Morris, K.J.K., Ooi, M.C., Oozeer, M.Y., Abakr, Y.A., Nadzir, M.S.M., Mohammed, I.Y. and Al-Qrimli, H.F. (2017). Impact of urbanization level on the interactions of urban area, the urban climate, and human thermal comfort. *Applied geography* 79: 50-72.

- Mueller, B., & Seneviratne, S. I. (2012). Hot days induced by precipitation deficits at the global scale. *Proceedings of the national academy of sciences*, 109(31), 12398-12403
- Muhire, I. and Ahmed, F., (2015). Spatio-temporal trend analysis of precipitation data over Rwanda. *South African Geographical Journal*, 97(1), pp.50-68.
- Mukherjee, S., Singh, C. K., Shashtri, S., Avtar, R., & Singh, S. K. (2010). Monitoring change in land use and land cover in Rupnagar district of Punjab, India using Landsat and IRS LISS III satellite data. *Ecological Questions*,13(1), 73.
- Mushore, T. D., Odindi, J., Mutanga, O., & Dube, T. (2017). Prediction of future urban surface temperatures using medium resolution satellite data in Harare metropolitan city, Zimbabwe. *Building And Environment*, 122397-410.
- Mutiibwa, D., & Irmak, S. (2013). AVHRR-NDVI-based crop coefficients for analyzing long-term trends in evapotranspiration in relation to changing climate in the US High Plains. *Water Resources Research*, 49(1), 231-244.
- Mwale, D., Gan, T. Y., Devito, K., and Silins, 2009, *Precipitation Variability & Its Relationship to Hydrologic Variability and Physical Features in Alberta*, *Hydrol. Proc.*, 23(21), 3040-3056. DOI: 10.1002/hyp.7415.
- Mwangi, E., Wetterhall, F., Dutra, E., Di Giuseppe, F., Pappenberger, F., (2014). Forecasting droughts in East Africa. *Hydrol. Earth Syst. Sci.* 18 (2), 611–620. [http:// dx.doi.org/10.5194/hess-18-611-2014](http://dx.doi.org/10.5194/hess-18-611-2014).
- Myint, S. W., & Wang, L. (2006). Multicriteria decision approach for land use land cover change using Markov chain analysis and a cellular automata approach. *Canadian Journal of Remote Sensing*, 32(6), 390-404.
- Myint, S.W., Wentz, E.A., Brazel, A.J., Quattrochi, D.A. (2013). The impact of distinct anthropogenic and vegetation features on urban warming. *Landsc. Ecol.* 28, 959–978.
- Narasimhan, B., & Srinivasan, R. (2005). Development and evaluation of Soil Moisture Deficit Index (SMDI) and Evapotranspiration Deficit Index (ETDI) for agricultural drought monitoring. *Agricultural and Forest Meteorology*, 133(1-4), 69-88.
- Nashwan, M.S. and Shahid, S., (2019). Spatial distribution of unidirectional trends in climate and weather extremes in Nile river basin. *Theoretical and applied climatology*, 137(1-2), pp.1181-1199.
- Nasta, P., Palladino, M., Ursino, N., Saracino, A., Sommella, A. and Romano, N., (2017). Assessing long-term impact of land-use change on hydrological ecosystem functions in a Mediterranean upland agro-forestry catchment. *Science of the Total Environment*, 605, pp.1070-1082.
- Naumann, G., Dutra, E., Pappenberger, F., Wetterhall, F., Vogt, J.V., (2014). Comparison of drought indicators derived from multiple data sets over Africa. *Hydrol. Earth Syst. Sci.* 18, 1625–1640.
- Neale, C. M. U., Bausch, W. C., and Heermann, D. F., (1989). Development of reflectance-based crop coefficients for corn, *Trans. Am. Soc. Agric. Eng.* 32:1891-1899.

- Negri, A. J., Burkardt, N., Golden, J. H., Halverson, J. B., Huffman, G. J., Larsen, M. C., McGinley, J. A., Updike, R. G., Verdin, J. P. and Wieczorek, G. F. (2005). The hurricane flood- landslide continuum, *Bull. Am. Meteorol. Soc.*, 86, 1241–1247.
- Nicholson, S. E. (2014). A detailed look at the recent drought situation in the Greater Horn of Africa. *Journal of Arid Environments*, 103, 71-79.
- Nouh, M.A. (2006). Wadi flow in the Arabian Gulf states. *Hydrol Process* 20:2393-2413
- Nyarko, B.K. (2002). Application of a rational model in GIS for flood risk assessment in Accra, Ghana. *J Spat Hydrol* 2(1):1–14
- Nyeko-Ogiramoi, P., Willems, P., Ngirane-Katashaya, G., (2013). Trend and variability in observed hydrometeorological extremes in the Lake Victoria basin. *Hydrol.* 489, 56–73.
- Ogden, F.L., Raj Pradhan, N., Downer, C.W. and Zahner, J.A., (2011). Relative importance of impervious area, drainage density, width function, and subsurface storm drainage on flood runoff from an urbanized catchment. *Water Resources Research*, 47(12).
- Ol'dekop, E.M., (1911). On evaporation from the surface of river basins. *Tr Meteorol Observ, Iur'evskogo Univ Tartu* 4
- Olivera-Guerra, L., Merlin, O., Er-Raki, S., Khabba, S., & Escorihuela, M. J. (2018). Estimating the water budget components of irrigated crops: Combining the FAO-56 dual crop coefficient with surface temperature and vegetation index data. *Agricultural Water Management*, 208, 120-131.
- Omoto, Y., K. Hamotani & Um. H. (1994). Recent Changes in Trends of Humidity of Japanese Cities. *J. Japan Soc. Hydrol. & Water Resour.*7(2), 106-113.
- Ongoma, V., Chen, H., Gao, C. and Sagero, P.O., (2018). Variability of temperature properties over Kenya based on observed and reanalyzed datasets. *Theoretical and Applied Climatology*, 133(3-4), pp.1175-1190.
- Onyutha, C., & Willems, P. (2017). Influence of spatial and temporal scales on statistical analyses of rainfall variability in the River Nile basin. *Dynamics of Atmospheres and Oceans*, 77, 26-42.
- Onyutha, C., (2016a). Variability of seasonal and annual rainfall in the River Nile riparian countries and possible linkages to ocean–atmosphere interactions. *Hydrol. Res.* 47, 171–184.
- Onyutha, C., (2016b). Statistical analyses of potential evapotranspiration changes over the period 1930–2012 in the Nile River riparian countries. *Agric. For. Meteorol.* 226–227C, 80–95.
- Onyutha, C., Tabari, H., Taye, M. T., Nyandwaro, G. N., & Willems, P. (2016). Analysis of rainfall trends in the Nile River Basin. *Journal of hydro-environment research*, 13, 36-51
- Onyutha, C., Willems, P., (2015). Spatial and temporal variability of rainfall in the Nile Basin. *Hydrol. Earth Syst. Sci.* 19, 2227–2246.
- Ostro, B., Rauch, S., & Green, S. (2011). Quantifying the health impacts of future changes in temperature in California. *Environmental research*, 111(8), 1258-1264.

- Ouma, Y. O., & Tateishi, R. (2014). Urban flood vulnerability and risk mapping using integrated multi-parametric AHP and GIS: Methodological overview and case study assessment. *Water*, 6(6), 1515-1545.
- Panda, S. S., Hoogenboom, G., & Paz, J. (2009). Distinguishing blueberry bushes from mixed vegetation land use using high resolution satellite imagery and geospatial techniques. *Computers and Electronics in Agriculture*, 67(1), 51-58.
- Parka, J., Baik, J., & Choi, M. (2017). Satellite-based crop coefficient and evapotranspiration using surface soil moisture and vegetation indices in Northeast Asia. *Catena*, 156, 305-314.
- Parmesan, C., & Yohe, G. (2003). A globally coherent fingerprint of climate change impacts across natural systems. *Nature*, 421(6918), 37.
- Partal, T., & Kahya, E. (2006). Trend analysis in Turkish precipitation data. *Hydrological processes*, 20(9), 2011-2026.
- Pastor J., Bonde J., Johnston C. and Naiman R.J. (1993). Markovian analysis of the spatially dependent dynamics of beaver ponds. *Lectures on Mathematics in the Life Sciences* 23: 5-27.
- Patra, S., Mishra, P., & Mahapatra, S. C. (2012). Delineation of groundwater potential zone for sustainable development: A case study from Ganga Alluvial Plain covering Hooghly district of India using remote sensing, geographic information system and analytic hierarchy process. *Journal of Cleaner Production*, 172, 2485-2502.
- Perrings, C., Duraiappah, A., Larigauderie, A., & Mooney, H. (2011). The biodiversity and ecosystem services science-policy interface. *Science*, 331(6021), 1139-1140.
- Petrosillo, I., Semeraro, T., Zaccarelli, N., Aretano, R., & Zurlini, G. (2013). The possible combined effects of land-use changes and climate conditions on the spatial-temporal patterns of primary production in a natural protected area. *Ecological Indicators*, 29, 367-375.
- Pettit, A.N. (1979) A non-parametric approach to the change point problem. *Appl Stat* 28: 126-135
- Phillips, J., McIntyre, B., (2000). ENSO and interannual rainfall variability in Uganda: implications for agricultural management. *Int. J. Climatol.* 20, 171–182.
- Pielke, R. A. (2005). Land use and climate change. *Science*, 310(5754), 1625-1626.
- Pielke, R.A., Adegoke, J., BELTRÁN-PRZEKURAT, A., Hiemstra, C.A., Lin, J., Nair, U.S., Niyogi, D. and Nobis, T.E., (2007). An overview of regional land-use and land-cover impacts on rainfall. *Tellus B*, 59(3), pp.587-601.
- Pike, J.G., (1964). The estimation of annual runoff from meteorological data in a tropical climate. *J Hydrol* 2:116–123
- Pilgrim, D. H., Chapman, T. G., & Doran, D. G. (1988). Problems of rainfall-runoff modelling in arid and semiarid regions. *Hydrological Sciences Journal*, 33(4), 379-400.

- Pontius, G.R., Malanson, J., (2005). Comparison of the structure and accuracy of two land change models. *Int. J. Geogr. Inf. Sci.* 19, 243–265.
- Power, A. G. (2010). Ecosystem services and agriculture: tradeoffs and synergies. *Philosophical transactions of the royal society B: biological sciences*, 365(1554), 2959-2971.
- Pradhan, B. (2009). Flood Susceptible mapping and risk area delineation using logistic regression, GIS and remote sensing. *J. Spatial Hydrol.*, 9: 1-18.
- Prestele, R., Arneith, A., Bondeau, A., de Noblet-Ducoudré, N., Pugh, T.A., Sitch, S., Stehfest, E. and Verburg, P.H., (2017). Current challenges of implementing anthropogenic land-use and land-cover change in models contributing to climate change assessments. *Earth System Dynamics*, 8(2), p.369.
- Ragab, R., & Prudhomme, C. (2002). Sw—soil and Water: climate change and water resources management in arid and semi-arid regions: prospective and challenges for the 21st century. *Biosystems engineering*, 81(1), 3-34.
- Ramanathan, V., Crutzen, P.J., Kiehl, J.T., Rosenfeld, D., (2001). Aerosols, climate, and the hydrological cycle. *Science* 294, 2119–2124.
- Ray, S.S., Dadhwal, V.K., (2001). Estimation of crop evapotranspiration of irrigation command area using remote sensing and GIS. *Agric. Water Manage.* 49, 239–249.
- Reeves, M. C., Manning, M. E., DiBenedetto, J. P., Palmquist, K. A., Lauenroth, W. K., Bradford, J. B., & Schlaepfer, D. R. (2018). Effects of climate change on rangeland vegetation in the Northern Rockies. In *Climate Change and Rocky Mountain Ecosystems* (pp. 97-114). Springer, Cham.
- Ren, G., Zhou, Y., Chu, Z., Zhou, J., Zhang, A., Guo, J., & Liu, X. (2008). Urbanization effects on observed surface air temperature trends in North China. *Journal of Climate*, 21(6), 1333-1348.
- Rhee, J., Im, J., & Carbone, G. J. (2010). Monitoring agricultural drought for arid and humid regions using multi-sensor remote sensing data. *Remote Sensing of Environment*, 114(12), 2875-2887.
- Ridd, M., & Liu, J. (1998). A comparison of four algorithms for change detection in an urban environment. *Remote Sensing of Environment*, 63, 95-100.
- Robitu, M., Musy, M., Inard, C., & Groleau, D. (2006). Modeling the influence of vegetation and water pond on urban microclimate. *Solar Energy*, 80(4), 435-447.
- Rojas, O., Vrieling, A., & Rembold, F. (2011). Assessing drought probability for agricultural areas in Africa with coarse resolution remote sensing imagery. *Remote Sensing of Environment*, 115(2), 343-352.
- Rozenstein, O., Haymann, N., Kaplan, G., & Tanny, J. (2018). Estimating cotton water consumption using a time series of Sentinel-2 imagery. *Agricultural Water Management*, 207, 44-52.
- Ruiz-Arias JA, Tovar-Pescador J, Pozo-Vázquez D, Alsamamra H (2009) A comparative analysis of DEM-based models to estimate the solar radiation in mountainous terrain. *International Journal of Geographical Information Science*, 23(8), 1049-1076.
- Saaty, T.L. (1977). A scaling method for priorities in hierarchical structures. *J Math Psychol* 15:57–68

- Saaty, T.L. (1980). *The analytic hierarchy process*. McGraw-Hill, New York
- Saaty, T.L. (1990). How to make a decision: the analytic hierarchy process. *Eur J Oper Res* 48:9–26
- Saaty, T.L. (2008). Decision making with analytic hierarchy process. *Int J Serv Sci* 1(1):16.
- Saharia, M., P.-E. Kirstetter, H. Vergara, J. J. Gourley, Y. Hong, and M. Giroud, (2017). Mapping flash flood severity in the United States. *J. Hydrometeor.*, 18,397-411.
- Samanta, S., Koloa, C., Kumar Pal, D., & Palsamanta, B. (2016). Flood Risk Analysis in Lower Part of Markham River Based on Multi-Criteria Decision Approach (MCDA). *Hydrology*, 3(3), 29.
- Sánchez, N., Martínez-Fernández, J., Calera, A., Torres, E., Pérez-Gutiérrez, C., (2010). Combining remote sensing and in situ soil moisture data for the application and validation of a distributed water balance model (HIDROMORE). *Agric. Water Manage.* 98(1), 69-78.
- Satterthwaite, D. (2008). Climate change and urbanization: Effects and implications for urban governance. In United Nations Expert Group meeting on population distribution, urbanization, internal migration and development (pp. 21-23).
- Saxton, K. E. Rowls, W. J., (2006). Soil water characteristic estimates by texture and organic matter for hydrologic solutions, *Soil Sci. Soc. Am. J.*, 70, 1569–1578.
- Schleusener, F., Kempe, S., Dirks, H., Rausch, R., & Göbel, PDP (2013) Die Erdfälle von Layla und Al-Kharj–Einblicke in die Karst-Hydrogeologie des oberen Jura von Saudi Arabien. *Grundwasser*, 18(4), 271-276.
- Schreiber, P., (1904). On the relationship between precipitation and the runoff of rivers in Central Europe. *Meteoro Z* 21:441–452
- Searchinger, T., Heimlich, R., Houghton, R.A., Dong, F., Elobeid, A., Fabiosa, J., Tokgoz, S., Hayes, D. and Yu, T.H. (2008). Use of US croplands for biofuels increases greenhouse gases through emissions from land-use change. *Science*, 319(5867), pp.1238-1240.
- Segele ZT, Lamb PJ, Leslie, L.M. (2009). Seasonal-to-inter annual variability of Ethiopia/Horn of Africa monsoon. Part I: associations of wavelet-filtered large-scale atmospheric circulation and global sea surface temperature. *J Clim* 22:3396–3421.
- Seleshi Y., Camberlin, P. (2006). Recent changes in dry spell and extreme rainfall events in Ethiopia. *Theoret Appl Climatol* 83:181–191
- Seleshi, Y., Zanke, U., (2004). Recent changes in rainfall and rainy days in Ethiopia. *Int. J. Climatol.* 24 (8), 973–983.
- Sen, P.K. (1968). Estimates of the regression coefficient based on Kendall's tau. *J. Am. Stat. Assoc.* 63, 1379–1389.
- Şen, Z. (2004). *Hydrograph Methods, Arid Regions*, Saudi Geological Survey (SGS), Technical Report

- Senay, G. B., Schauer, M., Friedrichs, M., Velpuri, N. M., & Singh, R. K. (2017). Satellite-based water use dynamics using historical Landsat data (1984–2014) in the southwestern United States. *Remote Sensing of Environment*, 202, 98-112.
- Serdeczny, O., Adams, S., Baarsch, F., Coumou, D., Robinson, A., Hare, W., Schaeffer, M., Perrette, M., Reinhardt, J. (2016). Climate change impacts in Sub-Saharan Africa: from physical changes to their social repercussions. *Reg. Environ. Change* 17(6), 1585-1600
- Seyoum, W.M., (2018). Characterizing water storage trends and regional climate influence using GRACE observation and satellite altimetry data in the Upper Blue Nile River Basin. *Journal of Hydrology*, 566, pp.274-284.
- Shaharuddin, A., Noorazuan, M. H., & Takeuchi, W. (2014). The effects of urban heat islands on human comfort: A case of Klang Valley Malaysia. *Global Journal on Advances Pure and Applied Sciences*, 2, 1-8.
- Shalaby, A., & Tateishi, R. (2007). Remote sensing and GIS for mapping and monitoring land cover and land-use changes in the Northwestern coastal zone of Egypt. *Applied Geography*, 27(1), 28-41.
- Shanahan, T.M., Overpeck, J.T., Anchukaitis, K.J., Beck, J.W., Cole, J.E., Dettman, D.L., Peck, J.A., Scholz, C.A., King, J.W., (2009). Atlantic forcing of persistent drought in West Africa. *Science* 324, 377–380.
- Sheffield J, Goteti G, Wood EF. (2006). Development of a 50-year high-resolution global dataset of meteorological forcings for land surface modeling. *J. Clim.* 19(13): 3088–3111.
- Sheffield, J., Wood, E. F., & Roderick, M. L. (2016). Little change in global drought over the past 60 years. *Nature*, 491(7424), 435 (2012).
- Shehata, M., & Mizunaga, H. (2018). Flash Flood Risk Assessment for Kyushu Island, Japan. *Environmental Earth Sciences*, 77(3), 76.
- Shi, P. J., Yuan, Y., Zheng, J., Wang, J. A., Ge, Y., & Qiu, G. Y. (2007). The effect of land use/cover change on surface runoff in Shenzhen region, China. *Catena*, 69(1), 31-35.
- Shojaei, P., Gheysari, M., Myers, B., Eslamian, S., Shafieiyoun, E., & Esmaeili, H. (2017). Effect of different land cover/use types on canopy layer air temperature in an urban area with a dry climate. *Building and Environment*, 125, 451-463.
- Shukla, S., McNally, A., Husak, G., Funk, C., (2014). A seasonal agricultural drought forecast system for food-insecure regions of East Africa. *Hydrol. Earth Syst. Sci.* 18 (10), 3907–3921.
- Siam, M. S., & Eltahir, E. A., (2017). Climate change enhances interannual variability of the Nile river flow. *Nat. Clim. Change*, 7, 350-354.
- Siam, M. S., Demory, M. E., & Eltahir, E. A. (2013). Hydrological cycles over the Congo and Upper Blue Nile Basins: Evaluation of general circulation model simulations and reanalysis products. *Journal of Climate*, 26(22), 8881-8894.

- Sigdel, M., & Ikeda, M. (2010). Spatial and temporal analysis of drought in Nepal using standardized precipitation index and its relationship with climate indices. *Journal of Hydrology and Meteorology*, 7(1), 59-74.
- Silva, J. S., da Silva, R. M., & Santos, C. A. (2018). Spatiotemporal impact of land use/land cover changes on urban heat islands: A case study of Paço do Lumiar, Brazil. *Building And Environment*, doi: 10.1016/j.buildenv.2018.03.041
- Singh, L. K., Jha, M. K., & Chowdary, V. M. (2017). Multi-criteria analysis and GIS modeling for identifying prospective water harvesting and artificial recharge sites for sustainable water supply. *Journal of Cleaner Production*, 142, 1436-1456.
- Singh, S. K., Mustak, S., Srivastava, P. K., Szabó, S., & Islam, T. (2015). Predicting spatial and decadal LULC changes through cellular automata Markov chain models using Earth observation datasets and geo-information. *Environmental Processes*, 2(1), 61-78.
- Sinha, R., Bapalu, G. V., Singh, L. K., & Rath, B. (2008). Flood risk analysis in the Kosi river basin, north Bihar using multi-parametric approach of analytical hierarchy process (AHP). *Journal of the Indian Society of Remote Sensing*, 36(4), 335-349.
- Sirami, C., Caplat, P., Popy, S., Clamens, A., Arletta, R., Jiguet, F., Brotons, L. and Martin, J.L., (2017). Impacts of global change on species distributions: obstacles and solutions to integrate climate and land use. *Global Ecology and Biogeography*, 26(4), pp.385-394.
- Sneyers, R. (1992). On the use of statistical analysis for the objective determination of climate change. *Meteorologische Zeitschrift*:(1992), 1(5), 247-256.
- Srivastava, P. K., Han, D., Rico-Ramirez, M. A., Bray, M., & Islam, T. (2012). Selection of classification techniques for land use/land cover change investigation. *Advances in Space Research*, 50(9), 1250-1265.
- Srivastava, P.K., & Bhattacharya, A.K. (2006). Groundwater assessment through an integrated approach using remote sensing, GIS and resistivity techniques: a case study from a hard rock terrain. *Int J Remote Sens* 27(20):4599–4620.
- Stampoulis, D., Andreadis, K.M., Granger, S.L., Fisher, J.B., Turk, F.J., Behrangi, A., Ines, A.V., Das, N.N., (2016). Assessing hydro-ecological vulnerability using microwave radiometric measurements from WindSat. *Remote Sens. Environ.* 184, 58–72.
- Streutker, D. R. (2003). Satellite-measured growth of the urban heat island of Houston, Texas. *Remote Sensing of Environment*, 85(3), 282-289.
- Swenson, S., & Wahr, J. (2006). Estimating large-scale precipitation minus evapotranspiration from GRACE satellite gravity measurements. *Journal of Hydrometeorology*, 7(2), 252-270.
- Tabari, H., Taye, M.T., Willems, P., (2015). Statistical assessment of precipitation trends in the Upper Blue Nile River basin. *Stoch. Environ. Res. Risk Assess.* 29, 1751–1761.

- Tang, Z., Yi, S., Wang, C., & Xiao, Y. (2018). Incorporating probabilistic approach into local multi-criteria decision analysis for flood susceptibility assessment. *Stochastic Environmental Research and Risk Assessment*, 32(3), 701-714.
- Taye, M.T., Willems, P., (2012). Temporal variability of hydroclimatic extremes in the Blue Nile basin. *Water Resour. Res.* 48, W03513.
- Tehrany, M. S., Pradhan, B., & Jebur, M. N. (2013). Spatial prediction of flood susceptible areas using rule based decision tree (DT) and a novel ensemble bivariate and multivariate statistical models in GIS. *Journal of Hydrology*, 504, 69-79.
- Tehrany, M. S., Pradhan, B., Mansor, S., & Ahmad, N. (2015). Flood susceptibility assessment using GIS-based support vector machine model with different kernel types. *Catena*, 125, 91-101
- Tempel, P., Batjes N. H., van Engelen V. W. P., (1996). IGBP-DIS soil data set for pedo transfer function development, Working Paper and Preprint 96/05, Int. Soil Ref. and Inf. Cent. (ISRIC), Wageningen, Netherlands.
- Termeh, S. V. R., Kornejady, A., Pourghasemi, H. R., & Keesstra, S. (2018). Flood susceptibility mapping using novel ensembles of adaptive neuro fuzzy inference system and metaheuristic algorithms. *Science of the Total Environment*, 615, 438-451.
- Tesemma, Z.K., Mohamed, Y.A. and Steenhuis, T.S., (2010). Trends in rainfall and runoff in the Blue Nile Basin: 1964–2003. *Hydrological processes*, 24(25), pp.3747-3758.
- Theil, H., (1950). A rank-invariant method of linear and polynomial analysis, part 3. *Nederlandse Akademie van Wetenschappen. Proceedings* 53, 1397–1412.
- Thom, E.C., (1959) The discomfort index. *Weatherwise*, 12: 57-60.
- Thouless, C. (1991). Conservation in Saudi Arabia. *Oryx* 25: 222-228.
- Thouless, CR. and Al Bassri, K. (1991). Taxonomic status of the Farasan Island gazelle. *Journal of Zoology* 223: 151-159.
- Thouless, CR., Grainger, JG., Shobrak, M., & Habibi, K. (1991) Conservation status of gazelles in Saudi Arabia. *Biological Conservation*, 58(1), 85-98.
- Tierney, J.E., Smerdon, J.E., Anchukaitis, K.J. and Seager, R., (2013). Multidecadal variability in East African hydroclimate controlled by the Indian Ocean. *Nature*, 493(7432), pp.389-392.
- Tong, S. T., Sun, Y., Ranatunga, T., He, J., & Yang, Y. J. (2012). Predicting plausible impacts of sets of climate and land use change scenarios on water resources. *Applied Geography*, 32(2), 477-489.
- Tong, S., Wong, N., Tan, C., Wong, H., Ignatius, M., Tan, E., & Jusuf, S. (2018). Study on correlation between air temperature and urban morphology parameters in built environment in northern China. *Building And Environment*, 127239-249. doi: 10.1016/j.buildenv.2017.11.013

- Toureiro, C., Serralheiro, R., Shahidian, S., & Sousa, A. (2017). Irrigation management with remote sensing: Evaluating irrigation requirement for maize under Mediterranean climate condition. *Agricultural Water Management*, 184, 211-220.
- Townshend, J.R.G. (1981). *Terrain analysis and remote sensing*. George Allen and Unwin, London, UK.
- Trail, T. A., V. Raghavan, S^o Masumoto, and G. Yonezawa. (2017). Application of Multi-parametric AHP for Flood Hazard Zonation in Coastal Lowland Area of Central Vietnam. *International Journal of Geoinformatics* 13, no. 1.
- Trenberth, K. E., Dai, A., Van Der Schrier, G., Jones, P. D., Barichivich, J., Briffa, K. R., & Sheffield, J. (2014). Global warming and changes in drought. *Nature Climate Change*, 4(1), 17.
- Um, H. H., Ha, K. J., & Lee, S. S. (2007). Evaluation of the urban effect of long-term relative humidity and the separation of temperature and water vapor effects. *International Journal of Climatology*, 27(11), 1531-1542.
- Unkasevic, M., Jovanovic, O., Popovic, T. (2001). Urban–suburban/rural vapour pressure and relative humidity differences at fixed hours over the area of Belgrade city. *Theor. Appl. Climatol.* 68, 67–73.
- Ustuner, M., Balik Sanli, F., & Dixon, B. (2015). Application of support vector machines for land use classification using high-resolution rapid eye images: a sensitivity analysis. *Eur. J. Remote Sens*, 48, 403-422.
- Verburg, P. H., Neumann, K., & Nol, L. (2011). Challenges in using land use and land cover data for global change studies. *Global Change Biology*, 17(2), 974-989.
- Wang, H., Li, X., Long, H., Gai, Y., & Wei, D. (2009). Monitoring the effects of land use and cover changes on net primary production: A case study in China's Yongding River basin. *Forest ecology and management*, 258(12), 2654-2665.
- Wang, J., Sammis, T. W., Meier, C. A., Simmons, L. J., Miller, D. R., & Samani, Z. (2005). 7. 13 A Modified SEBAL Model for Spatially Estimating Pecan Consumptive Water Use for Las Cruces, New Mexico.
- Wang, X. L., Wen, Q. H., & Wu, Y. (2007). Penalized maximal t test for detecting undocumented mean change in climate data series. *Journal of Applied Meteorology and Climatology*, 46(6), 916-931.
- Weng, Q. (2001). A remote sensing- GIS evaluation of urban expansion and its impact on surface temperature in the Zhujiang Delta, China. *International journal of remote sensing*, 22(10), 1999-2014.
- Williams, A., Funk, C., (2011). A westward extension of the warm pool leads to a westward extension of the Walker circulation drying eastern Africa. *Climate Dynamics*, 1–19.
- Williams, F., & Boren, S. A. (2008). The role of electronic medical record in care delivery in developing countries. *International Journal of Information Management*, 28(6), 503-507.

- Wilson, C. O., & Weng, Q. (2011). Simulating the impacts of future land use and climate changes on surface water quality in the Des Plaines River watershed, Chicago Metropolitan Statistical Area, Illinois. *Science of the Total Environment*, 409(20), 4387-4405.
- Winney, B.J., Hammond, R.L., Macasero, W., Flores, B., Boug, A., Biquand, V., Sylvain Biquand & Bruford, M.W. (2004). Crossing the Red Sea: phylogeography of the hamadryas baboon, *Papio hamadryas*. *Molecular Ecology*, 13(9), 2819-2827.
- Winstanley, D. (1973). Recent rainfall trends in Africa, the Middle East and India. *Nature*, 243(5408), 464-465.
- Woldeamlak, B., Conway, D., (2007). A note on the temporal and spatial variability of rainfall in the drought-prone Amhara region of Ethiopia. *Int. J. Climatol.* 27, 1467–1477.
- Woldesenbet, T.A., Elagib, N.A., Ribbe, L. and Heinrich, J., (2017). Hydrological responses to land use/cover changes in the source region of the Upper Blue Nile Basin, Ethiopia. *Science of The Total Environment*, 575, pp.724-741.
- Wolkoff, P., & Kjærgaard, S. K. (2007). The dichotomy of relative humidity on indoor air quality. *Environment international*, 33(6), 850-857.
- Woo, Chi. (2003). Cramer's V. <http://planetmath.org/encyclopedia/CramersV.html>. (Accessed June 25, 2017).
- Worku, G., Teferi, E., Bantider, A., & Dile, Y. T. (2018). Observed changes in extremes of daily rainfall and temperature in Jemma Sub-Basin, Upper Blue Nile Basin, Ethiopia. *Theoretical and Applied Climatology*, 1-16.
- Wypych, A. (2010). Twentieth century variability of surface humidity as the climate change indicator in Kraków (Southern Poland). *Theoretical and applied climatology*, 101(3-4), 475-482.
- Xiao, Y., Yi, S., & Tang, Z. (2017). Integrated flood hazard assessment based on spatial ordered weighted averaging method considering spatial heterogeneity of risk preference. *The Science of the total environment*, 599, 1034.
- Xiong, Y., Huang, S., Chen, F., Ye, H., Wang, C., & Zhu, C. (2012). The impacts of rapid urbanization on the thermal environment: A remote sensing study of Guangzhou, South China. *Remote sensing*, 4(7), 2033-2056.
- Xoplaki, E., González-Rouco, J. F., Luterbacher, J. U., & Wanner, H. (2004). Wet season Mediterranean precipitation variability: influence of large-scale dynamics and trends. *Climate dynamics*, 23(1), 63-78.
- Xu, Q., Dong, Y. X., & Yang, R. (2018). Urbanization impact on carbon emissions in the Pearl River Delta region: Kuznets curve relationships. *Journal of Cleaner Production*.
- Yagoub, M. M., & Al Bizreh, A. A. (2014). Prediction of land cover change using Markov and cellular automata models: case of Al-Ain, UAE, 1992-2030. *Journal of the Indian Society of Remote Sensing*, 42(3), 665-671.

- Yahia, M. W., Johansson, E., Thorsson, S., Lindberg, F., & Rasmussen, M. I. (2018). Effect of urban design on microclimate and thermal comfort outdoors in warm-humid Dar es Salaam, Tanzania. *International journal of biometeorology*, 62(3), 373-385.
- Yan, Z., Li, Z., & Jones, P. (2010). Effects of site change and urbanization in the Beijing temperature series 1977–2006. *International Journal of Climatology*, 30(8), 1226-1234.
- Yang, X., Zheng, X. Q., & Chen, R. (2014). A land use change model: Integrating landscape pattern indexes and Markov-CA. *Ecological Modelling*, 283, 1-7.
- Yue, S., Pilon, P., & Cavadias, G. (2002). Power of the Mann–Kendall and Spearman's rho tests for detecting monotonic trends in hydrological series. *Journal of hydrology*, 259(1), 254-271.
- Yue, S., Pilon, P., & Cavadias, G. (2002). Power of the Mann–Kendall and Spearman's rho tests for detecting monotonic trends in hydrological series. *Journal of hydrology*, 259(1-4), 254-271.
- Yue, S., Pilon, P., & Cavadias, G. (2002). Power of the Mann–Kendall and Spearman's rho tests for detecting monotonic trends in hydrological series. *Journal of hydrology*, 259(1), 254-271.
- Zaroug, M., Eltahir, E. A. B., and Giorgi, F. (2014). Droughts and floods over the upper catchment of the Blue Nile and their connections to the timing of El Niño and La Niña events, *Hydrology and Earth System Sciences* 18(3), DOI: 10.5194/hess-18-1239.
- Zehra, S., Afsar, S. (2016). Flood Hazard Mapping of Lower Indus Basin Using Multi-Criteria Analysis. *Journal of Geoscience and Environment Protection*.4: 54- 62.
- Zeng R, Cai X. (2016). Climatic and terrestrial storage control on evapotranspiration temporal variability: Analysis of river basins around the world. *Geophys. Res. Lett.* 43(1): 185–195.
- Zeng, N. (2003). Drought in the Sahel. *Science* 302, 999–1000.
- Zhai, P., Zhang, X., Wan, H. and Pan, X., (2005). Trends in total precipitation and frequency of daily precipitation extremes over China. *Journal of climate*, 18(7), pp.1096-1108.
- Zhan, X., & Huang, M. L. (2004). ArcCN-Runoff: an ArcGIS tool for generating curve number and runoff maps. *Environmental Modelling & Software*, 19(10), 875-879.
- Zhang, H., Ma, W. C., & Wang, X. R. (2008a). Rapid urbanization and implications for flood risk management in hinterland of the Pearl River Delta, China: The Foshan study. *Sensors*, 8(4), 2223-2239.
- Zhang, J., Zhengjun, L., & Xiaoxia, S. (2009). Changing landscape in the Three Gorges Reservoir Area of Yangtze River from 1977 to 2005: Land use/land cover, vegetation cover changes estimated using multi-source satellite data. *International Journal of Applied Earth Observation and Geoinformation*, 11(6), 403-412.
- Zhang, Q., Xu, C. Y., Zhang, Z., Chen, Y. D., Liu, C. L., & Lin, H. (2008b). Spatial and temporal variability of precipitation maxima during 1960–2005 in the Yangtze River basin and possible association with large-scale circulation. *Journal of Hydrology*, 353(3), 215-227.

- Zhang, W., Zhu, Y., & Jiang, J. (2016). Effect of the Urbanization of Wetlands on Microclimate: A Case Study of Xixi Wetland, Hangzhou, China. *Sustainability*, 8(9), 885.
- Zhang, X., Vincent, L. A., Hogg, W. D., & Niitsoo, A. (2000). Temperature and precipitation trends in Canada during the 20th century. *Atmosphere-ocean*, 38(3), 395-429.
- Zhang, Z., Xu, C.Y., El-Tahir, M.E.H., Cao, J. and Singh, V.P., (2012). Spatial and temporal variation of precipitation in Sudan and their possible causes during 1948–2005. *Stochastic environmental research and risk assessment*, 26(3), pp.429-441.
- Zhao, G., Pang, B., Xu, Z., Yue, J., & Tu, T. (2018). Mapping flood susceptibility in mountainous areas on a national scale in China. *Science of The Total Environment*, 615, 1133-1142.
- Zhao, Y., Colin, C., Liu, Z., Paterne, M., Siani, G., & Xie, X. (2012). Reconstructing precipitation changes in northeastern Africa during the Quaternary by clay mineralogical and geochemical investigations of Nile deep-sea fan sediments. *Quaternary Science Reviews*, 57, 58-70.
- Zomer, R., Trabucco, A., van Straaten, O., & Bossio, D. (2006). Carbon, land and water: A global analysis of the hydrologic dimensions of climate change mitigation through afforestation/reforestation (Vol. 101). IWMI.
- Zou, Q., Zhou, J., Zhou, C., Song, L., & Guo, J. (2013). Comprehensive flood risk assessment based on set pair analysis-variable fuzzy sets model and fuzzy AHP. *Stochastic Environmental Research and Risk Assessment*, 27(2), 525-546.

Appendices

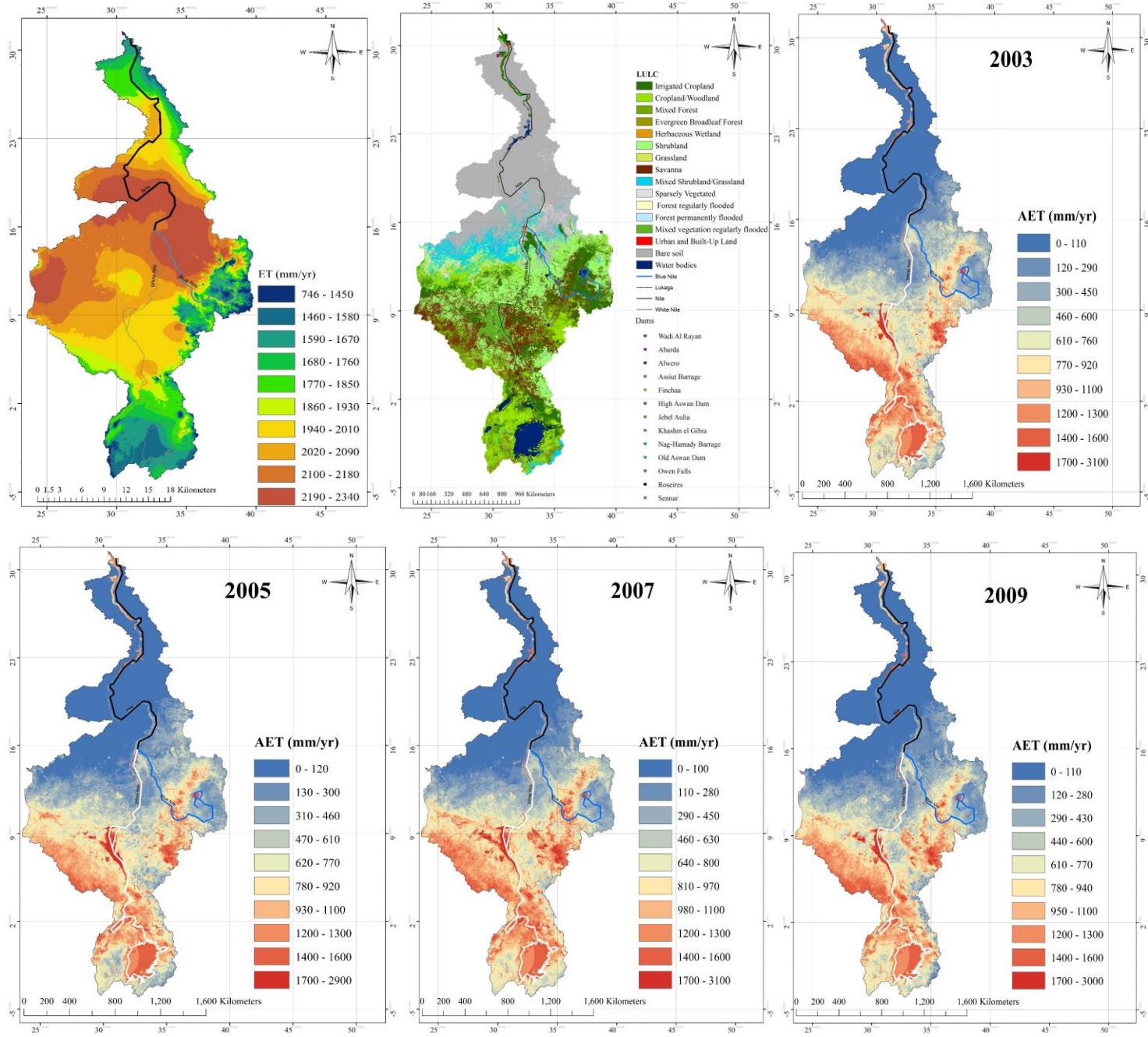
This section covers the supplementary discussions for Chapter 7

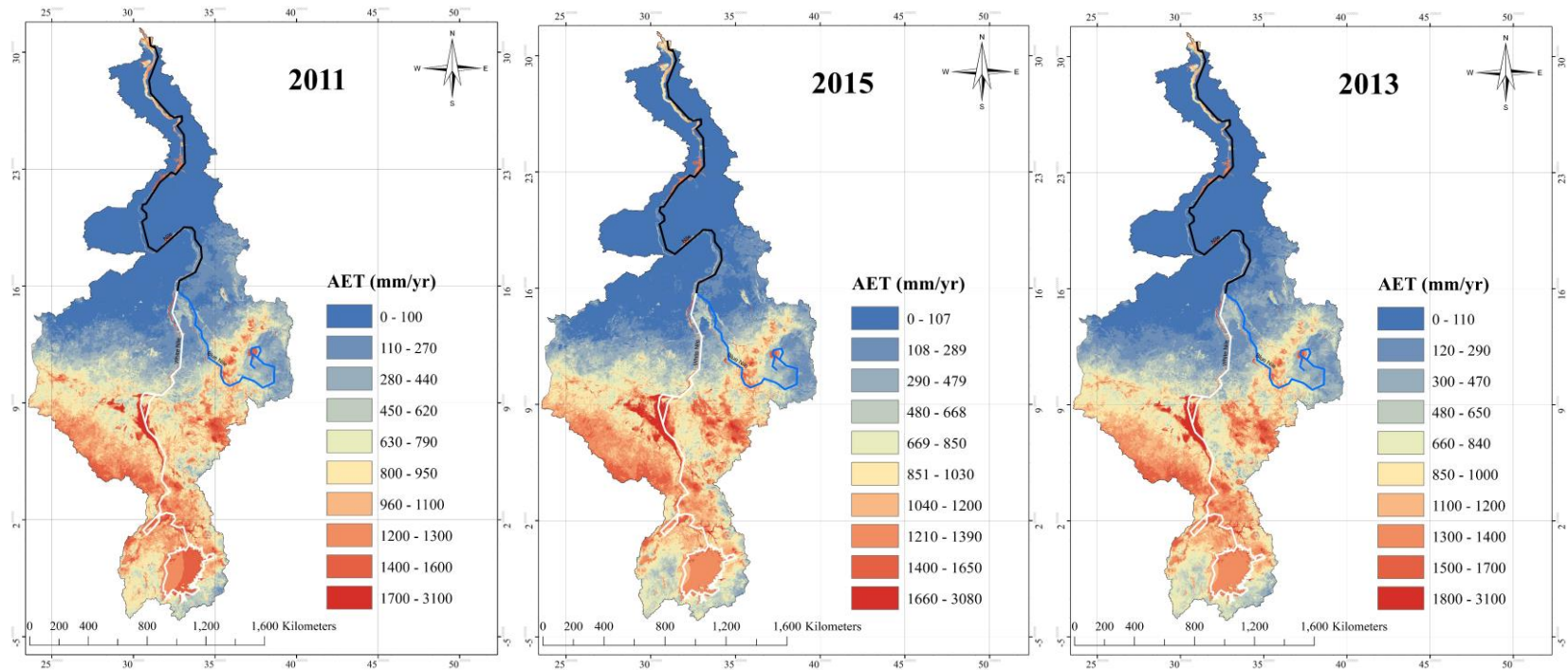
Appendix A: Spatiotemporal variability of reference and actual evapotranspiration

Reference evapotranspiration was calculated for the NRB based on penman Montieth formula; the highest monthly evapotranspiration rates were observed within the months of June to October. The average annual ETo ranged from 746 to 2340 mm/yr, with the lowest annual ETo values observed in Rwanda and Burundi with mean annual Eto ranges from 746-1100 mm/yr, and 1150-1450 mm/yr respectively. While the highest values of annual ETo rates were observed mainly over Sudan and some parts of Egypt with Sudan portions of the NRB almost dominated the areas with high very high reference Eto with an annual value range from 2020-2340 mm/yr-very high evapotranspiration rate from the surface water where most the Nile water is lost due to evapotranspiration. Temperature also plays a very important role in increasing evapotranspiration as mentioned earlier, as Sudan and Egypt also occupied the highest mean monthly temperature among the riparian countries. Therefore, conservation measurement should be taken to reduce these losses (supplementary Figure A1(a)). In the other hand Eritrea “1810 mm/yr”, Kenya “1740 mm/yr”, Ethiopia “1620 mm/yr”, Uganda “1500 mm/yr”, Tanzania “1400 mm/yr”, Congo ‘Zaire’ have reference annual Eto of 1150 mm/yr.

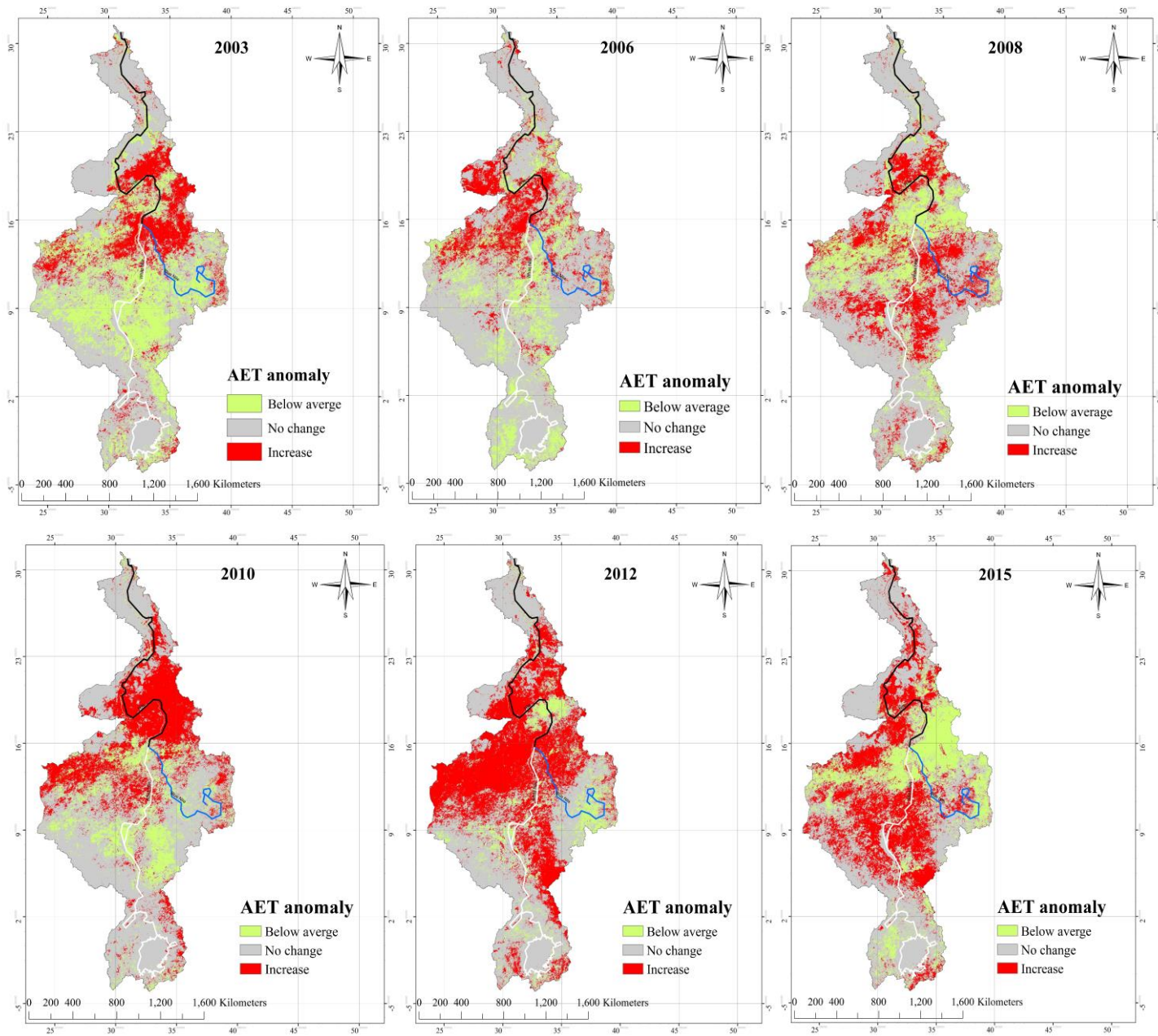
To measure the influence of increasing trend in relative humidity and wind speed we calculated reference and actual evapotranspiration in the NRB based on the methodology adopted in supplementary information. Actual evapotranspiration follows the rainy seasonal pattern. From the land cover map (supplementary Figure A1(b)), it's clear that very high AET is observed in irrigated land and from water bodies in these regions with the highest AET rates being in the

Ethiopian highlands and the southern portion of the NRB in countries such as Uganda, Egypt, Sudan, Burundi, Congo, Kenya, Rwanda, and Tanzania, which lead to very high losses due to increased rate of AET. Supplementary Figure A1 also shows spatiotemporal distribution of annual AET from 2003 to 2015. The magnitude of AET also increased, to determine the change rate AET anomaly was calculated between 2003 and 2015. In 2003, results showed significant increase in AET values in the White Nile region in Sudan, Eritrea and Ethiopia, with the highest rate of increase observed over the White Nile in Sudan, this can be attributed to the increase in temperature anomalies, decrease in relative humidity decreased, and the increase in zonal wind, which caused more water to evaporate. This finding is in agreement with previous studies, which attributed the increase in ET rate to the increases in wind speed and decreases in relative humidity (Eslamian et al., 2011). In 2005, AET increased by 50% in Sudan, and the Aswan high dam in Egypt compared to its value in 2003, this led to a significant amount of water losses. Very high spots also observed in the Roseires Dam and the Ethiopian highlands (supplementary Fig A2). By 2008, increasing trend in AET anomalies continued and affected a larger area in Sudan including Sudd region – a vast swamp in South Sudan-, Ethiopia, Eritrea and Uganda. This trend became more dominant and clearer in 2010 in the White Nile Basin, which witnessed significant increase in AET anomalies (supplementary Figure A2). However, AET anomaly in 2012 showed significant increase in the entire NRB in countries such as Egypt, Sudan, Ethiopia, Eritrea and Congo. This increasing trend reached its peak in 2012 and continued to increase in 2015, leading to more drought in these regions.





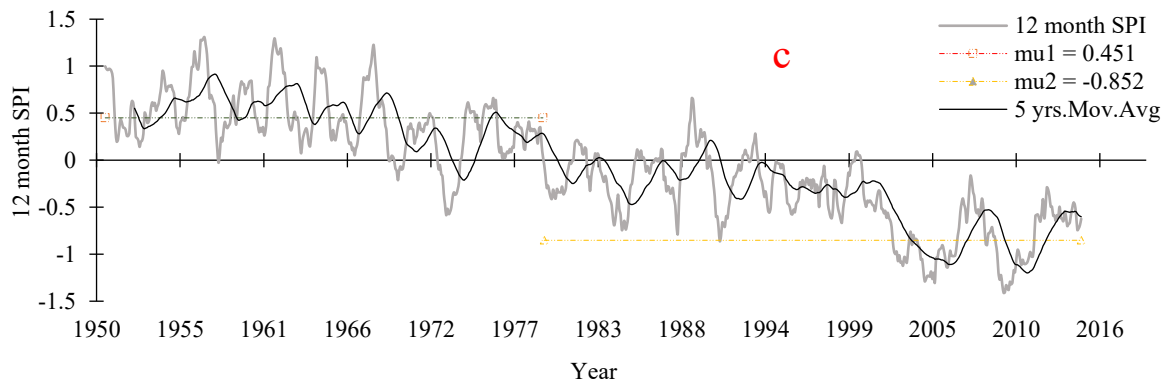
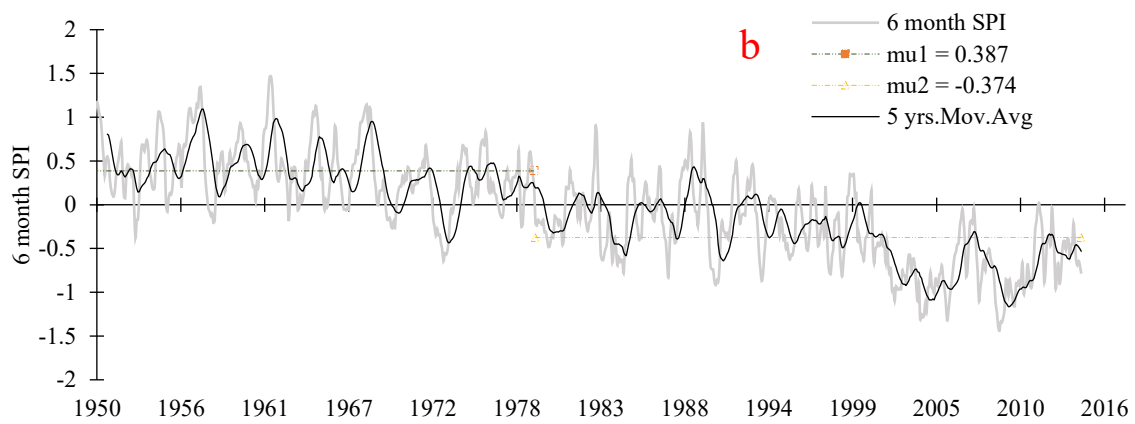
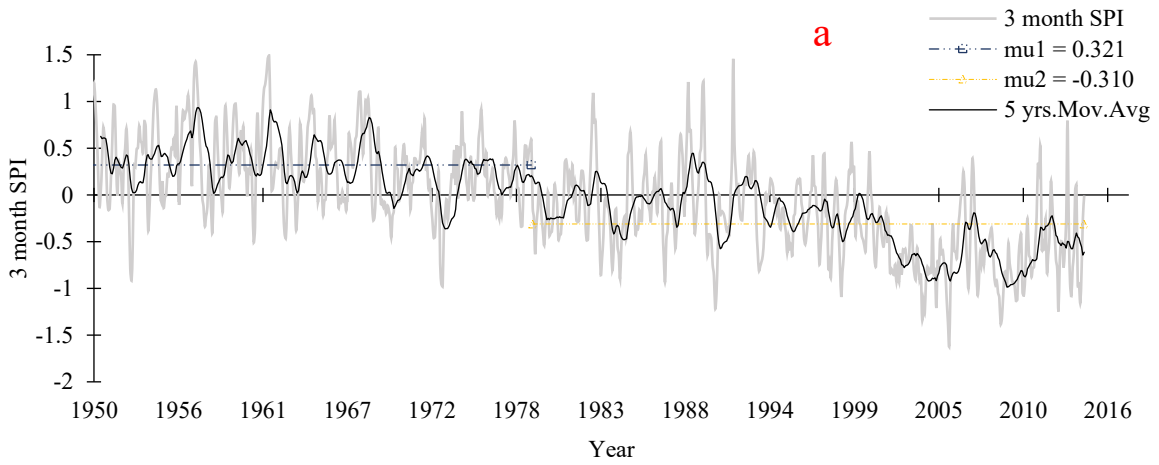
Supplementary Figure A1. Spatial distribution of annual reference evapotranspiration (a), land cover (b), and actual evapotranspiration (2003-2015)



Supplementary Figure A2: Actual evapotranspiration anomalies -calculated from the long-term average actual evapotranspiration between 2003 and 2015

Appendix B: NRB's metrological drought under climate warming

Implications of the decrease in precipitation anomaly by 16.2 mm/decade, increase in warming trend after 1976, and decreasing trend in relative humidity with increased AET caused severe effects on the agricultural sector and reduced availability of water. For instance, rainfed agriculture in Ethiopia and Sudan, where most of the farmers depend on the rainy season to irrigate their crops, reduced precipitation and increased warming made the life of those farmers worse and led to the documented historical drought in the region in 1978, 1983, 1984, 1987, 1991, 1994, 1999, 2002, 2004, 2005 which were captured in 1-month SPI trend analysis. The 3-months SPI (supplementary Fig B1 (a)) ranged from -1.616 to 1.44 with standard deviation of 0.554. At the 3-month SPI statistics showed significant change point at 1979 where average SPI decreased from 0.321 between 1950-1979 to -0.31 between 1979-2016 with significant downward trend in SPI value with 0.2/decade (supplementary Table B1). These periods also identified more clearly by increasing the timestep. It's also logical to capture sign of severe droughts at shorter timestep as the variability between monthly precipitation is very high and some are very dry. This result also reflects the accuracy of SPI in reconstructing historical occurrences of drought. At the 6-month time scale, the highest value was 1.466 and the lowest observed value was -1.439 with standard deviation of 0.56, the 6 and 12-month SPI showed similar trend with significant change point in 1979 (supplementary Fig B1(b,c)), but the amplitude is higher, where the decline trend in SPI was 0.23/decade and 0.27/decade respectively which amplify the existence of extreme climate change in the NRB and dry conditions during ENSO events.



Supplementary Figure B1: Metrological drought trend-SPI: 3-month (a), 6-month (b), 12-month (c)

Supplementary Table B1: Change point and trend analysis of metrological drought in the NRB

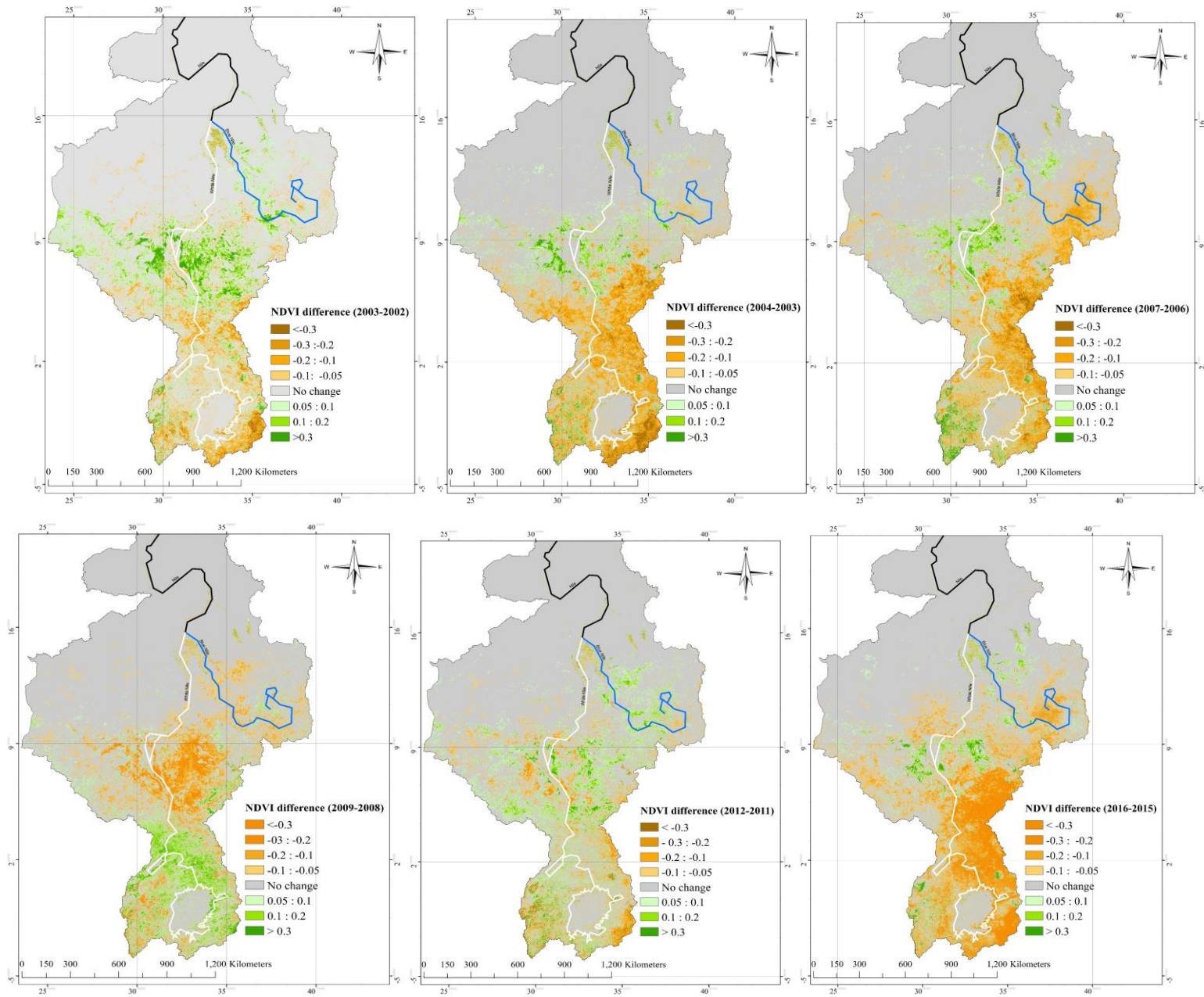
Nile river basin	Years	Pettitt test				Mann–Kendall test					
		K	t	P	trend	Tau	Sen's slope	P	trend	Mb	Ma
1-month SPI	1950-2016	79564	1979	< 0.0001	Ha	0.362	-0.015	< 0.0001	-	0.223	-0.225
3-month SPI	1950-2016	101530	1979	< 0.0001	Ha	0.464	-0.02	< 0.0001	-	0.321	-0.31
6-month SPI	1950-2016	117354	1979	< 0.0001	Ha	0.548	-0.023	< 0.0001	-	0.387	-0.381
12-month SPI	1950-2016	132794	1979	< 0.0001	Ha	0.638	-0.027	< 0.0001	-	0.451	-0.852

Appendix C: NRB's agricultural drought assessment

Agriculture drought might occur in two situations if water availability/ precipitation decreased which lead to decreased soil moisture or increased warming trend which increase evaporation rate. Supplementary Fig C1 shows results of the change detection for the period 2002-2016. Results showed a large variation of droughts in various regions in the NRB. Difference between NDVI values in 2002-2003 revealed decrease in NDVI values up to 0.3 which indicate large decrease in vegetation cover, regions that dominated the highest decrease in vegetation cover were Tanzania, Uganda, Rwanda, Burundi, Congo, Ethiopia, and Sudan. By investigating the type of land cover that witnessed decrease in NDVI values, agriculture fields were the most affected, reflecting agricultural drought. It's also noted that the same countries witnessed an increase in AET during the same period. The difference between 2004-2003 also showed continuous drought in more areas than the observed drought in 2003, the entire regions of Ethiopia, Eritrea, Kenya, Tanzania, Congo and Uganda faced severe agriculture droughts in 2004. These results agree with the observed trend in SPI between 2003 and 2004, it seems like what might be moderate metrological drought can have severe consequences in agricultural drought.

Between 2006 and 2007, agricultural land decreased dramatically in Ethiopian highlands, Eritrea, Uganda, Rwanda, Burundi, Congo and Sudan-which also depend on rainfed agriculture in the White Nile region. Between 2008 and 2009, there was a little improvement in Uganda as NDVI values increased by 0.1. However, extensive drought spread all over the agricultural land due to altered precipitation pattern and warming trend as captured by the SPI trend analysis in 2008 and 2009. This indicate that irrigated crops in arid regions are so sensitive to shortage of moisture due to the high rate of evapotranspiration. In 2012, the NRB showed sings of vegetation recovery and

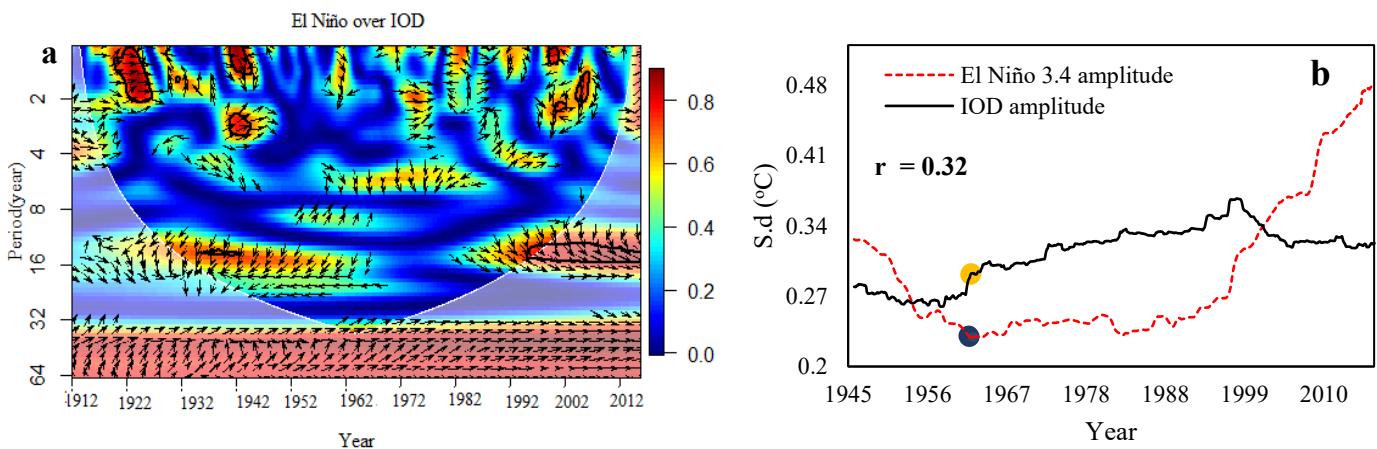
an increase in agricultural areas (supplementary Fig C1), this year also showed an increase in annual precipitation compared to 2011. In 2016, agricultural drought continued with more severe drought in Ethiopian highlands, Kenya, Eritrea, Uganda, Rwanda, Burundi, Congo and Sudan. We can conclude that increasing warming trend along with altered precipitation patterns, leads to severe agriculture drought in the NRB.



Supplementary Figure C1: Agricultural drought change detection 2002-2016

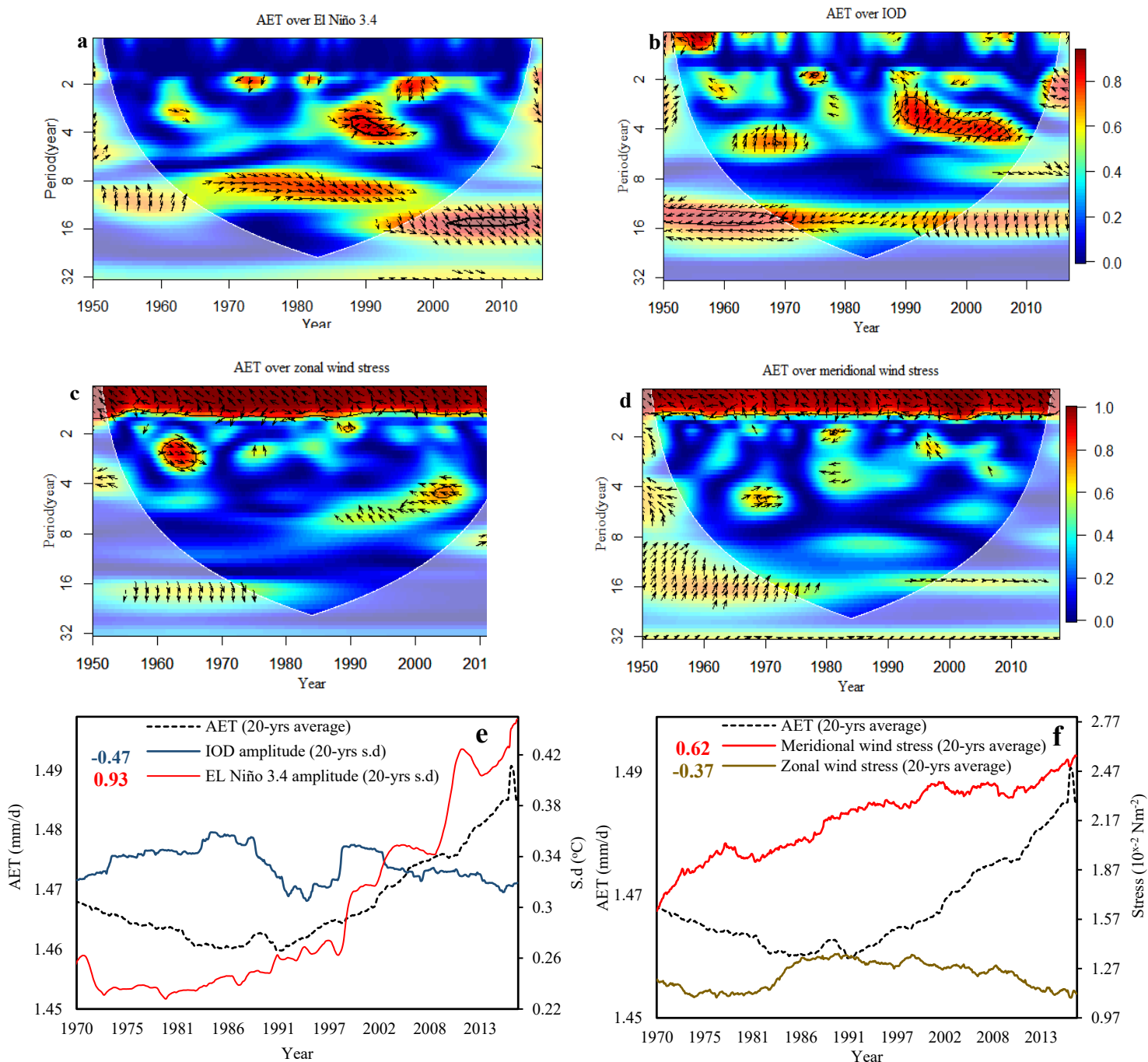
Appendix D: Influence of Indian Ocean dipole (IOD) and ENSO on NRB's hydroclimate

Beside ENSO, our results also show that IOD plays a crucial role on NRB's hydroclimate variability and drought severity over inter-decadal and longer timescales. Based on IOD's power spectrum and significant coherence with ENSO at 1-2, 2-4, 4-8, 14-16, and 32-64 year time scales, our results demonstrate a strong coupling between IOD and ENSO, for both exhibited similar change patterns, e.g., positive IOD becomes more intensive as the amplitude of El Niño increases (supplementary Fig D1 (a)). In 1-2- and 2-4-year bands, ENSO and IOD are almost in phase, but are out of phase by about a year in other periodicities. This ENSO–IOD teleconnection has strengthened since the 1970s partly because of the recent enhancement of the Walker circulation (Cai et al., 2015), resulting in significant positive correlation between El Niño and IOD amplitudes ($r = 0.32$) (supplementary Fig D1 (b)).

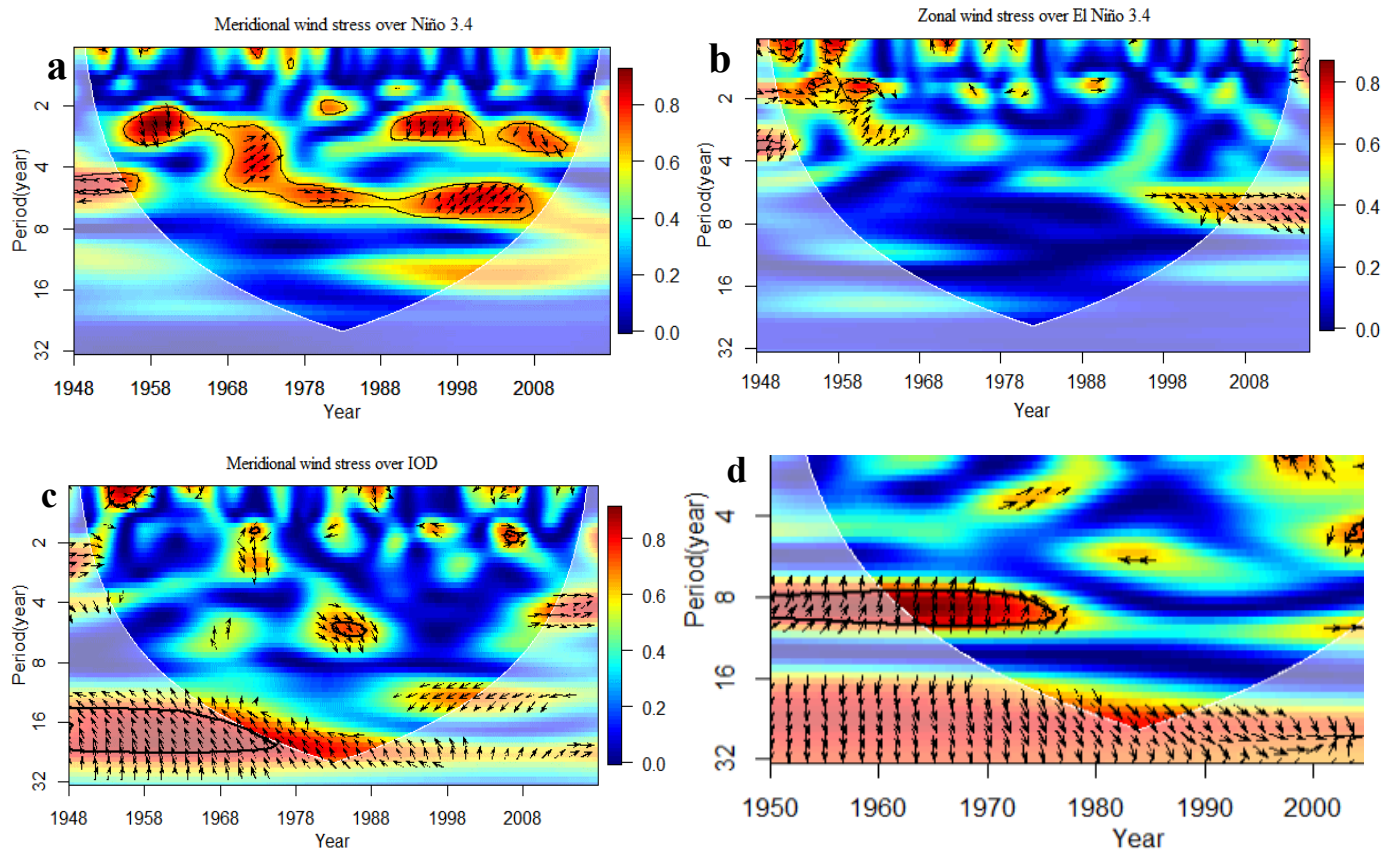


Supplementary Figure D1. IOD-ENSO relationship over the NRB basin: (a) wavelet coherence between El Niño 3.4 and IOD index, and (b) correlation between El Niño 3.4 and IOD amplitudes. El Niño 3.4 and IOD amplitude computed as the SD of El Niño 3.4 and IOD over 30-year window from 1913 to 2017. In b, there is a significant positive correlation between El Niño and IOD amplitudes ($r = 0.32$). This positive correlation indicates that positive IOD occur simultaneously with El Niño. In b, IOD seems to have an independent mode of variability from El Niño. For instance, a strong positive IOD event (shown by a yellow mark in b) occurred in 1961 under a neutral ENSO conditions (blue colour in b).

The wavelet coherence spectrum plots between AET and El Niño and IOD show in-phase, statistically significant coherent relationship at 2-4 and 8-14-years band after 1970s (supplementary Fig D2 (a, b)), which peaked at the 14–16-year time scale after 2000s. On the other hand, the wavelet coherence between IOD and AET show that IOD mainly lead AET after 2000s. The higher AET after 1970s can be partly attributed to the westward propagation of zonal winds and southward propagation of meridional winds associated with stronger El Niño amplitudes, as shown by strong wavelet coherence between zonal and meridional wind stresses and AET at 1-2 years bands (supplementary Fig D2 (c, d)). Their recurrent in-phase and anti-phase relationships at 1-2 years bands demonstrate the effect of positive (negative) wind stress anomalies when El Niño was active. There is a significant positive correlation between AET and El Niño 3.4 ($r = 0.93$) and meridional wind stresses ($r = 0.62$) in contrast to negative correlation between AET and IOD ($r = -0.47$) and zonal wind stresses ($r = -0.37$) (supplementary Fig D2 (e, f)), which shows that El Niño and meridional wind affect the AET of NRB. A statistically significant in-phase relationship between meridional wind stress and El Niño at 2-4 and 4-8 year band was detected over 1960-2017, and in-phase relationship between zonal wind stress and El Niño at the 4-8-year band 1988 and 2017 (supplementary Fig D3(a, b)), while IOD, meridional and zonal wind stresses showed in-phase coherence after 2000s (supplementary Fig D3 (c, d)). It seems both increasing meridional wind stress anomalies and stronger El Niño episodes have contributed to changes in the heat content of NRB.



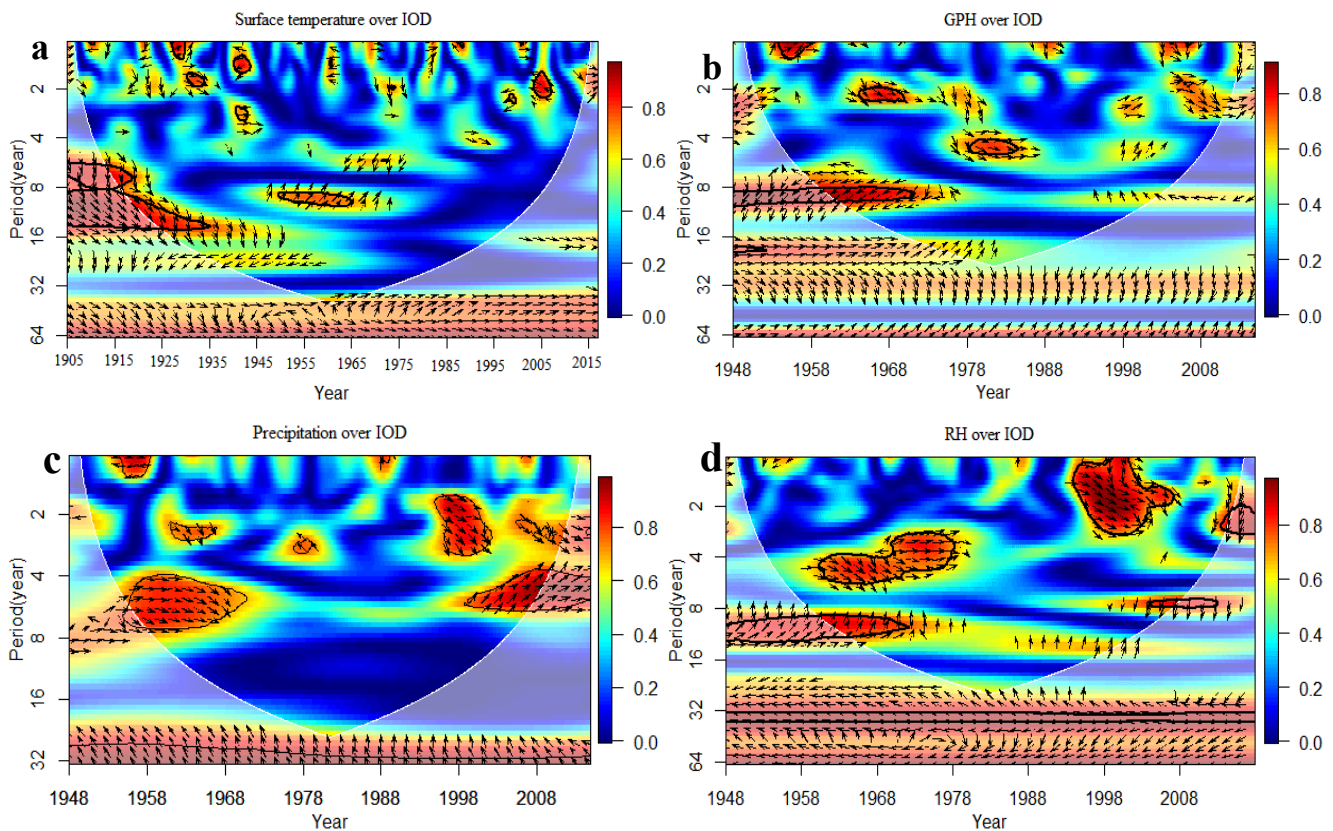
Supplementary Figure D2. Wavelet coherence between NRB actual evapotranspiration (AET) and El Niño 3.4 (a), AET and IOD (b), AET and zonal and meridional wind stresses (c, d). Field correlations between NRB AET and El Niño 3.4 and IOD amplitudes (e), and wind stresses (f). AET, meridional and zonal wind stresses computed over 20-year running periods from 1950 to 2017, El Niño 3.4 and IOD amplitude are the SD of El Niño 3.4 and IOD indexes over 20-year windows from 1950 to 2017 using the ERSST data sets. The numbers in the top right are the cross-correlation coefficient at the 5% level.

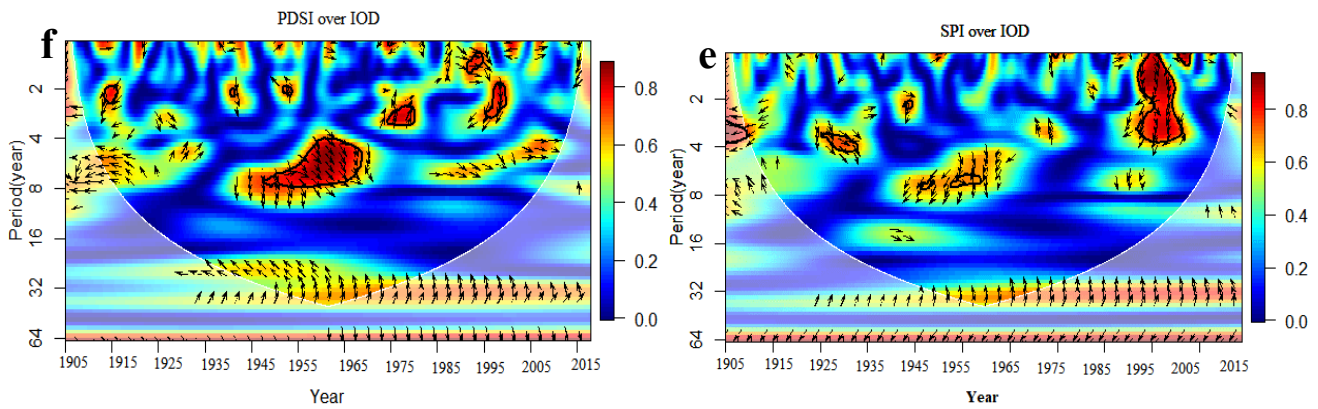


Supplementary Figure D3. Wavelet coherence between El Niño 3.4, IOD and wind stresses: Wavelet coherence between El Niño 3.4 Niño and meridional and zonal wind stresses (a, b), IOD and meridional and zonal wind stresses (c, d).

The wavelet coherence plot between IOD and surface temperature (T_s) shows statistically significant, interannual (1-4yr) in-phase and anti-phase relationships over 1905 and 2018, revealing the interannual response of T_s and GPH to the variability of IOD in the last 100 years. At inter-decadal time scale, IOD and T_s show only significant, in-phase coherence at 8–16, 16-32, 32-64-year bands over 1975-2018 (supplementary Fig D4(a)). On the other hand, IOD and GPH were continuously in phase with significant coherent spatial pattern at 2-4- and 4-8-years band after 1970s (supplementary Figure D4 (b)). The wavelet coherence spectrum plot between precipitation and IOD shows in phase relationship with significant coherent spatial pattern at 2-4-

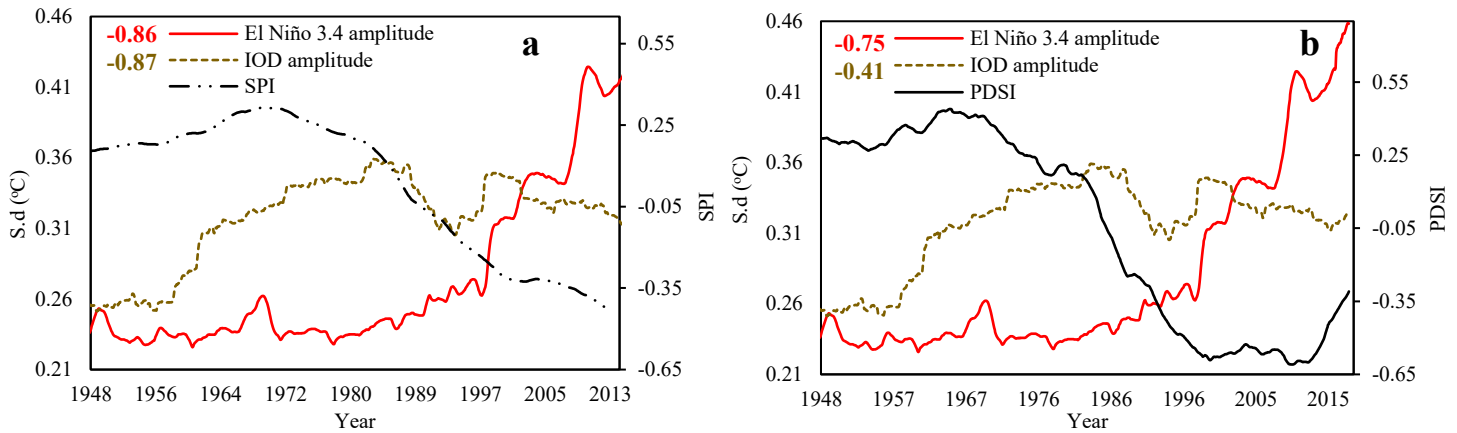
and 4-8-year band after 1990, and an anti-phase relationship at 32-year band between 1948 and 2018 (supplementary Fig D4(c)). This strong anti-phase relationship shows that IOD primarily influenced NRB's precipitation at inter-decadal timescales. There is a strong in-phase relationship between IOD and relative humidity at 2-4 yr band over 1998-2008, and at 4-8 and 8-16-year bands over 1960-1980, and an anti-phase relationship in the 32-64 -year band (supplementary Fig D4 (d)). The wavelet coherence between IOD and SPI and sc-PDSI are statistically significant at 2–4, 4-8, and 32-64-year bands, respectively. Before 1970s, IOD was in-phase with both sc-PDSI and SPI, but after 1970s their relationships became predominantly anti-phase, which means that stronger positive IOD episodes after 1970s has led to lower SPI and sc-PDSI, resulting in more severe droughts in NRB after 1970s (supplementary Fig D4 (e-f)).





Supplementary Figure D4. Wavelet coherence between IOD and (a) surface temperature, (b) GPH, (c) precipitation, (d) relative humidity, (e) SPI, and (f) PDSI.

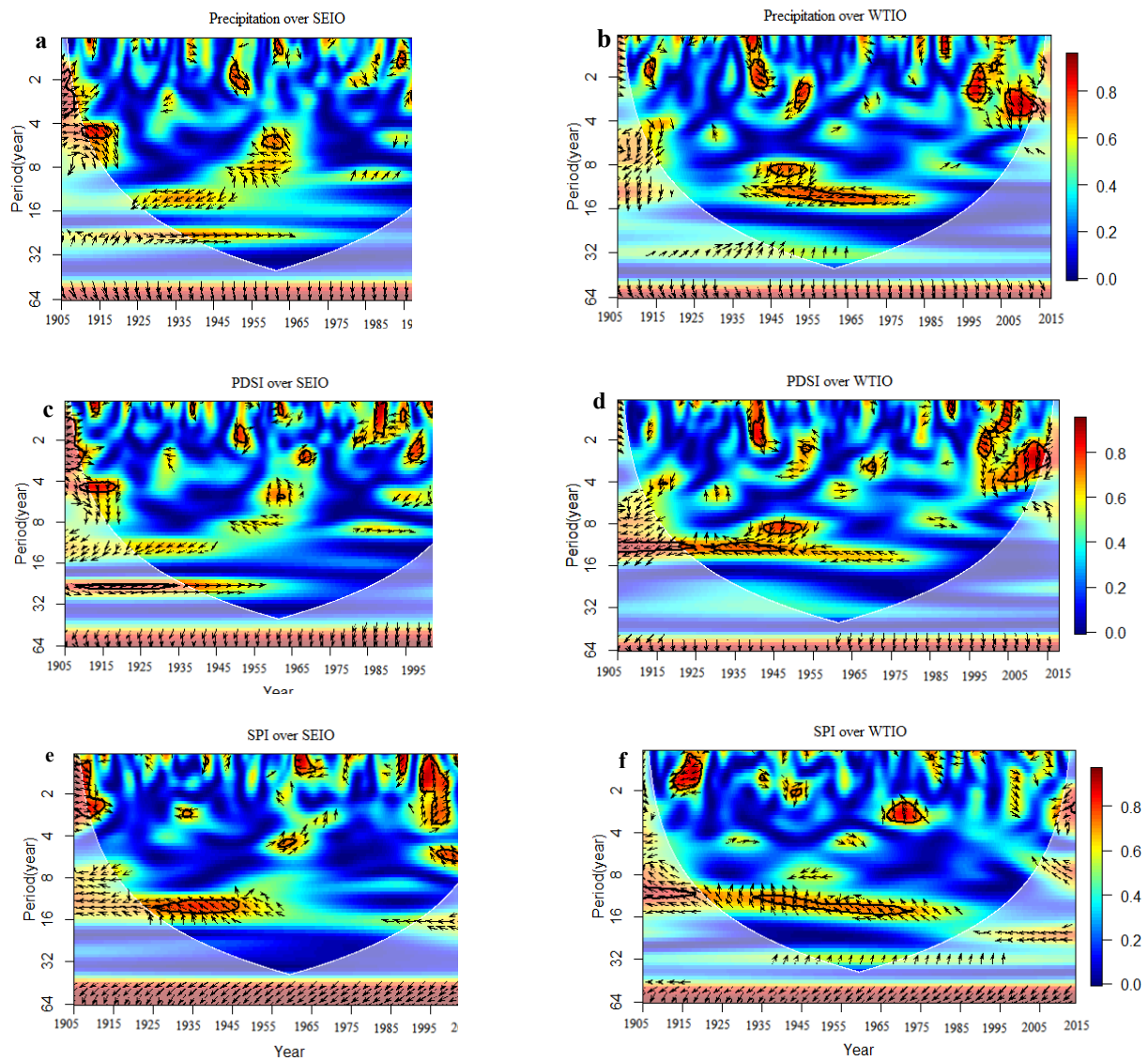
Supplementary Figure D5 shows strong negative correlation between IOD and SPI ($\rho = -0.87$) which suggest that besides El Niño, IOD has also impacted the metrological drought of NRB similar to the mechanism that teleconnects East African precipitation to ENSO and IOD.



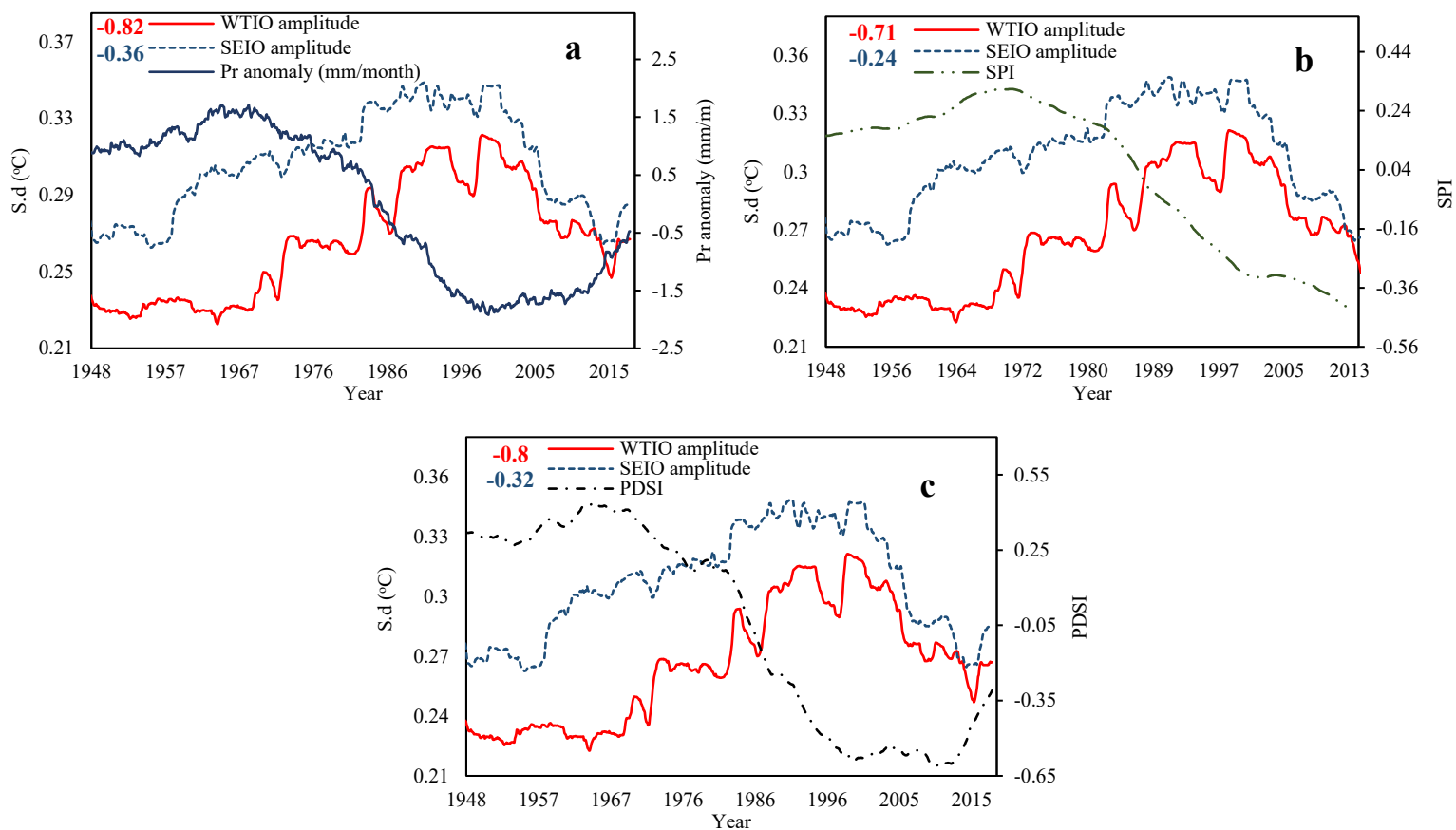
Supplementary Figure D5. ENSO and IOD Teleconnections on NRB SPI (a) and PDSI (b). El Niño 3.4 and IOD amplitude are the SD of El Niño 3.4 and IOD indexes over 30-year windows from 1920 to 2017 using the ERSST data sets. The numbers in the top right are the cross-correlation coefficient between hydrologic variables and IOD amplitude (brown colour) and El Niño 3.4 amplitude (red colour) at the 5% level.

To further investigate the role of IOD on the hydroclimate of NRB, cross correlation and wavelet coherence analysis using the two halves of IOD, i.e. the western pole (WTIO) over the Arabian Sea

(50°E - 70°E, 10°S - 10°N) and the southeast Indian Ocean (SEIO) (90°E to 110°E, 10°S to 0°N) suggest that the western part of the Indian Ocean SSTs plays a primary role on NRB's precipitation over inter-decadal or perhaps longer timescales. The wavelet coherence plot shows a more prominent anti-phase relationship between WTIO and NRB's precipitation anomalies at 2-4, 4-8, and 8-16-year bands after 1970s than the relationship between SEIO and NRB's precipitation (supplementary Figure D6(a-b)). A stronger anti-phase relationship was also detected between WTIO and SPI and scPDSI throughout most of the period between 1905 and 2018, except between 1950 and 1965 (supplementary Figure D6 (d-f)). This dominant anti-phase relationship between WTIO and NRB's precipitation at interdecadal timescale (> 32 -year) show that NRB's hydroclimate is more strongly linked to the SST gradient over the Arabian Sea than by IOD and SEIO, such that WTIO exerted a significant negative influence on the NRB precipitation variability ($\rho = -0.82$). The result implies that the more frequent occurrences of droughts in NRB are related to increased warming in the western Indian Ocean (supplementary Figure D7(a)), as is also evident from the strong negative correlation between SPI and SST in the western Arabian sea ($\rho = -0.71$ for SPI and -0.8 for PDSI) (supplementary Fig D7(b-c)). Apparently, the variability in WTIO has contributed to severe droughts in NRB.



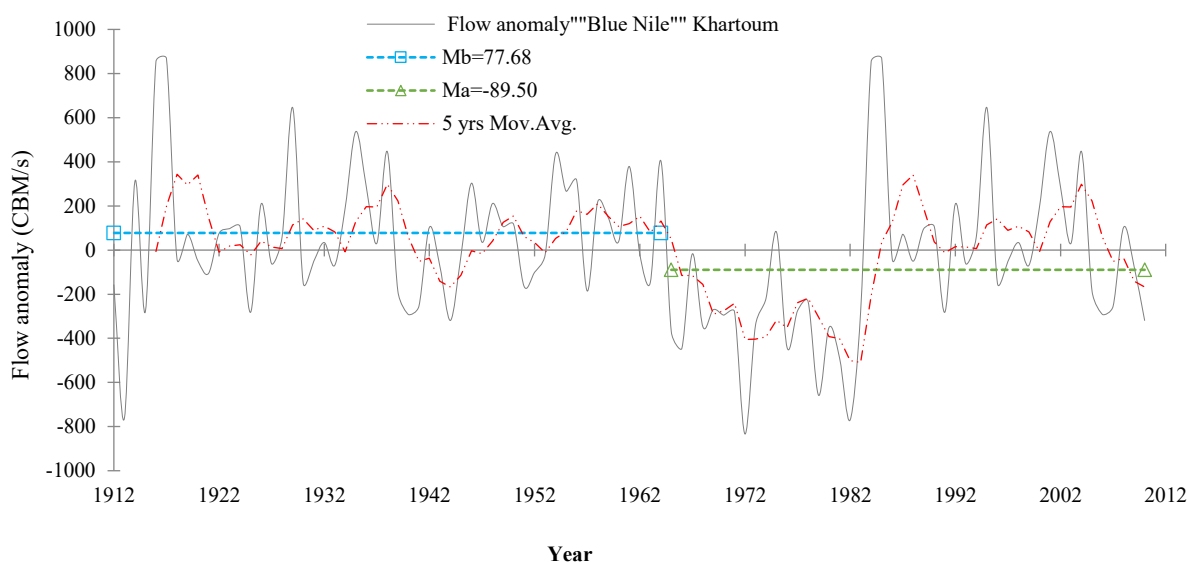
Supplementary Figure D6. Impact of SEIO and WTIO on NRB precipitation and drought. Wavelet coherence between SEIO and WTIO and precipitation (a, b), Wavelet coherence between SEIO and WTIO and PDSI (c, d), Wavelet coherence between SEIO and WTIO and SPI (e, f).



Supplementary Figure D7. WTIO and SEIO Teleconnections on NRB precipitation and droughts. Field correlation between SEIO and WTIO and NRB precipitation (a), correlation between SEIO and WTIO and NRB SPI (b), and (c) correlation between SEIO and WTIO and NRB PDSI. There is a strong negative correlation between WTIO and NRB precipitation ($r = -0.82$), this result indicates that increasing frequency of extreme dry events in the NRB are attributed to increased warming in the western parts of the Indian Ocean. This is also evident from the strong negative correlation between SPI and SST amplitudes in the western Arabian sea. The variability in WTIO seems to be one of the main causes of severe droughts. In other word, the WTIO variations play a significant role in NRB droughts.

Appendix E: Flow variability and response of hydrological droughts to climate change

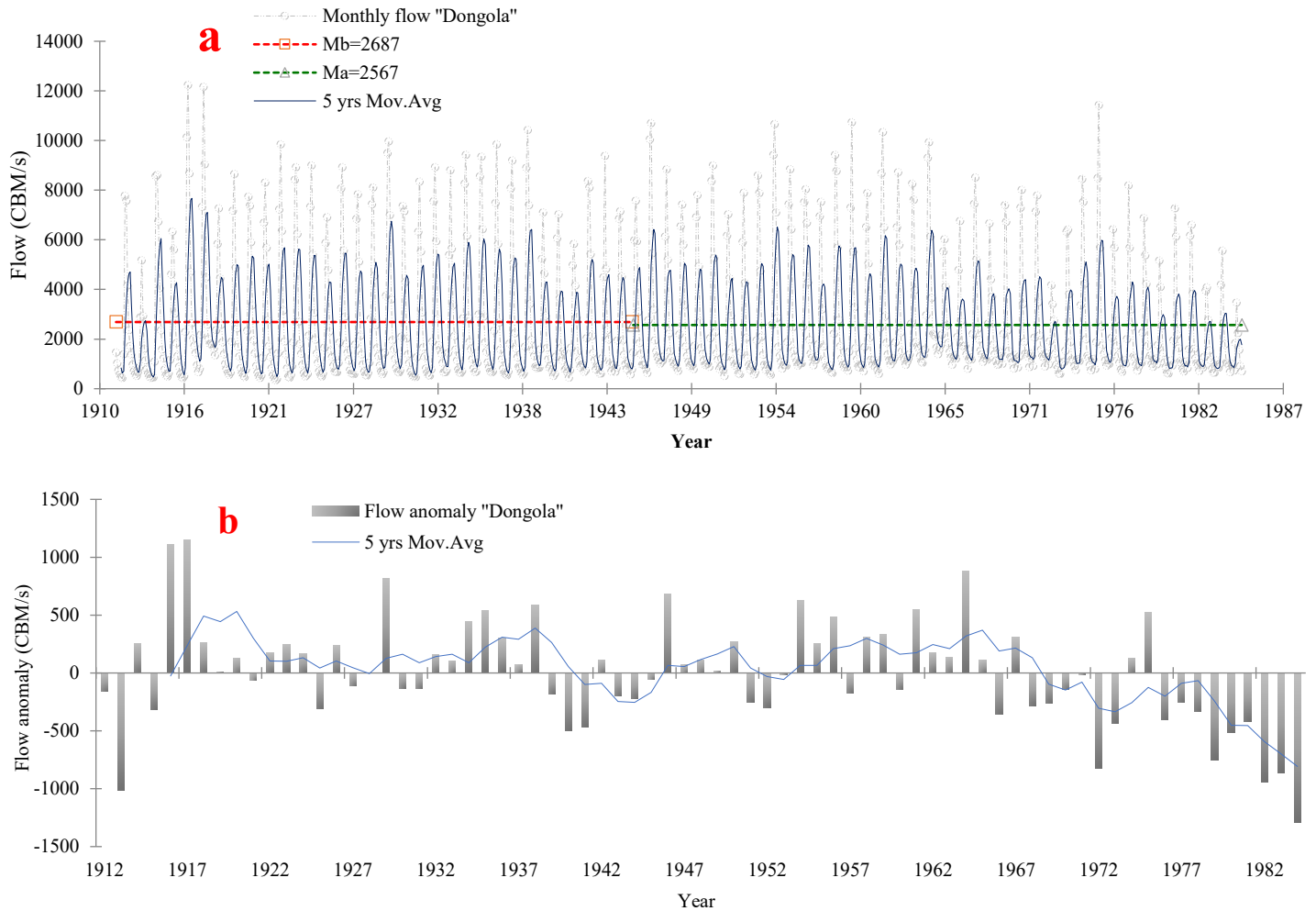
Supplementary Fig E1 illustrates the departure in flow anomaly from the long-term average observed flow in Blue Nile. Generally, there is a decline in observed flow in Blue Nile, since 1964 average flow is below normal. Average observed flow anomaly declined from 77.78 CBM/s between 1912-1964 to -89.5 CBM/s between 1964-2010. This is a statistically significant decline at the rate of 13.7 CBM/decade according to MK test. Nonparametric test also revealed statistically significant change point at 1964 as illustrated in supplementary Fig E1.



Supplementary Figure E1. Time series analysis of flow anomaly at Blue Nile station Khartoum

The observed monthly flow records at Dongola showed high variability. Statistical analysis of the observed monthly flow data showed a statistically significant decline after 1945 (supplementary Fig E2(a)). There is a significant decline in flow anomaly at Dongola with a higher decline rate than the observed trend in Blue Nile station (supplementary Fig E2(b)) with a statistically significant change point in flow anomaly at 1965, just one year after the observed change in Blue Nile station. Hence, long term flow anomaly declined from 132 CBM/s between 1910-1965 to -375 CBM/s between 1965-1984. This is a statistically significant decline trend at the rate of 77.4

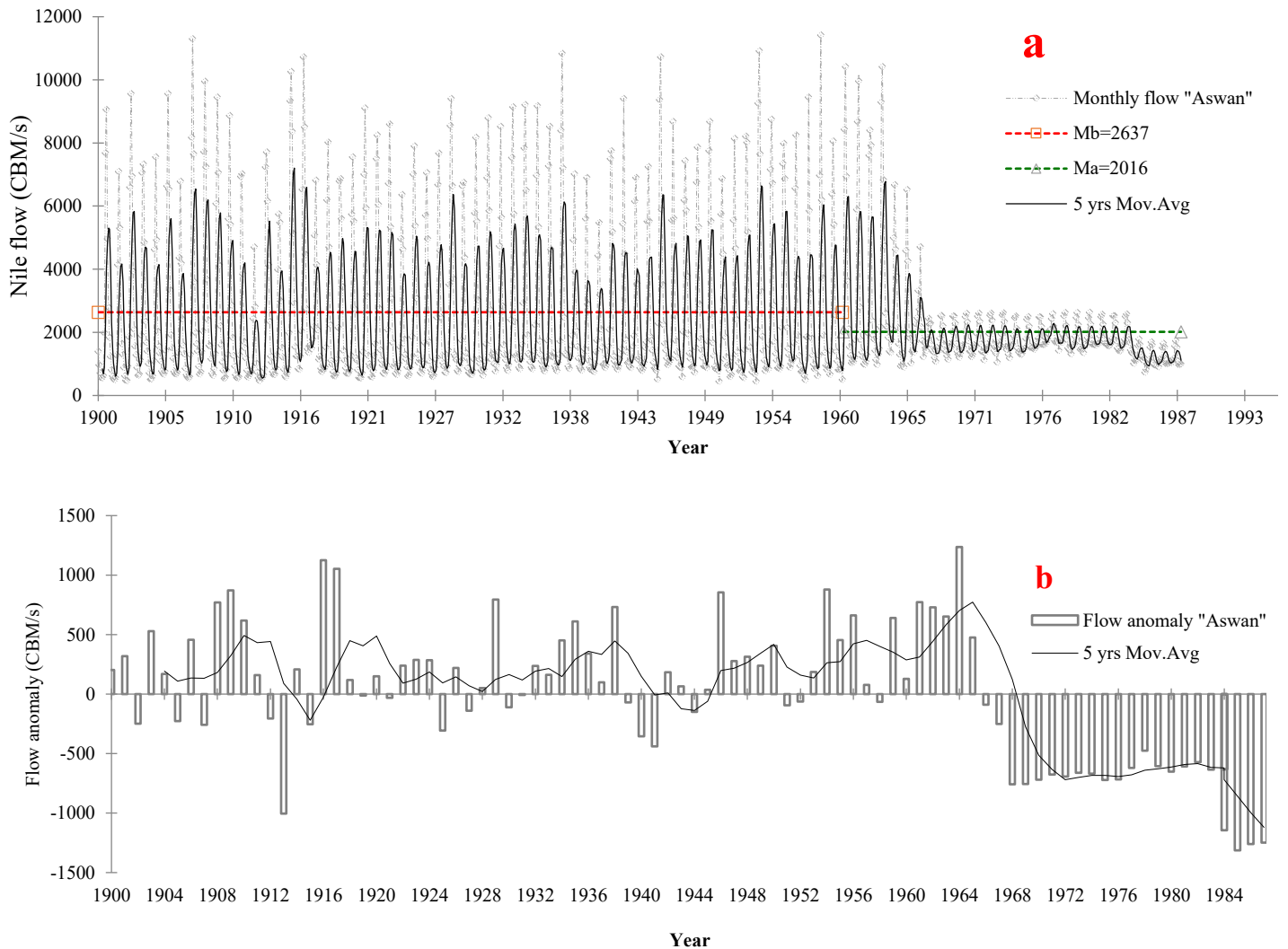
CBM/decade. If compared with the trend in flow anomaly at Blue Nile station, this trend is more significant, and might be attributed to increased actual evapotranspiration in Blue Nile regions in Sudan in addition to warming trend and decreased precipitation. This agrees with reported information in the literature, where increase in warming trend and actual evapotranspiration can cause reduced river flow.



Supplementary Figure E2. Time series analysis of monthly flow (a), and flow anomaly (b) at Dongola station-Sudan

Furthermore, Pettit's change point test showed a statistically significant change point in the monthly Nile River flow at Aswan in 1965, where mean monthly flow declined from 2637 CBM/s between 1900-1965 to 2016 CBM/s between 1965 and 1987 (supplementary Fig E3 (a)). This is a statistically significant

decline in monthly flow records at Aswan station, with a decline trend of 39.6 CBM/decade since 1965 (supplementary Table E1). Supplementary Fig E3(b) shows the observed flow anomaly at Aswan station, as expected the decline trend is greater and more significant. Where climate change and change in hydroclimate variables led to a significant change in the observed flow. According to Non-parametric tests, there is a statistically significant change point in observed flow at 1965, where long term average flow anomaly dropped from 249 CBM/s between 1910-1965 to -716 CBM/s between 1965-1984. This is a statistically significant decline trend of 114.1 CBM/decade. This indicate the severe implications of climate change in the observed flow in the Nile river basin, leading to severe droughts in most of the riparian of the Nile.

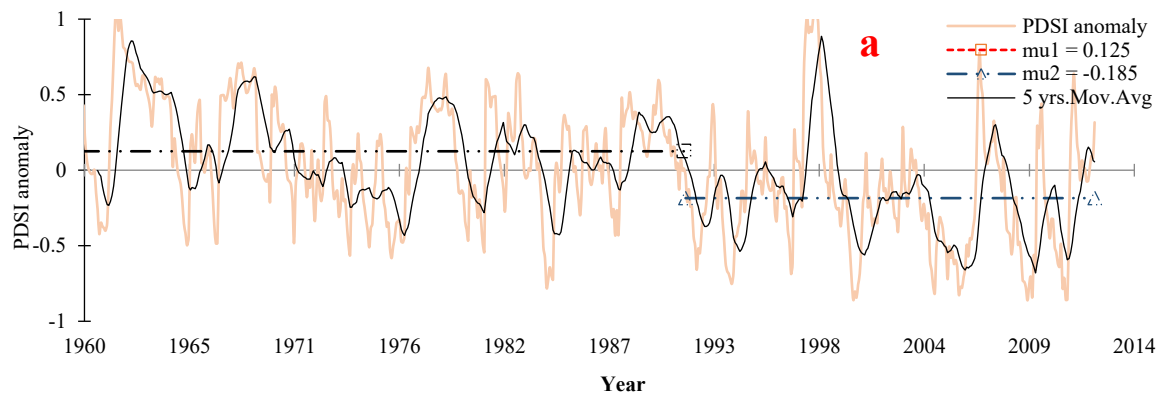


Supplementary Figure E3. Time series analysis of monthly flow (a), and flow anomaly (b) at Aswan Dam station-Egypt

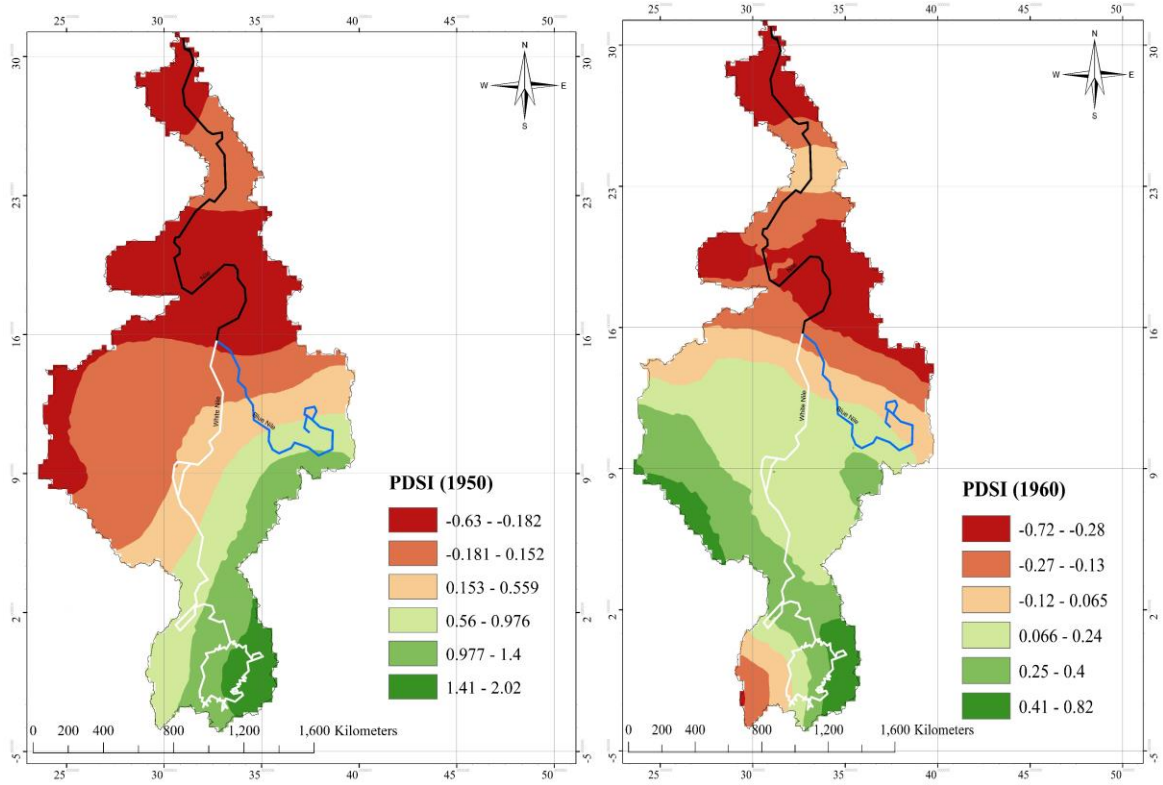
Supplementary Table E1: Nile river flow trend change detection and trend analysis

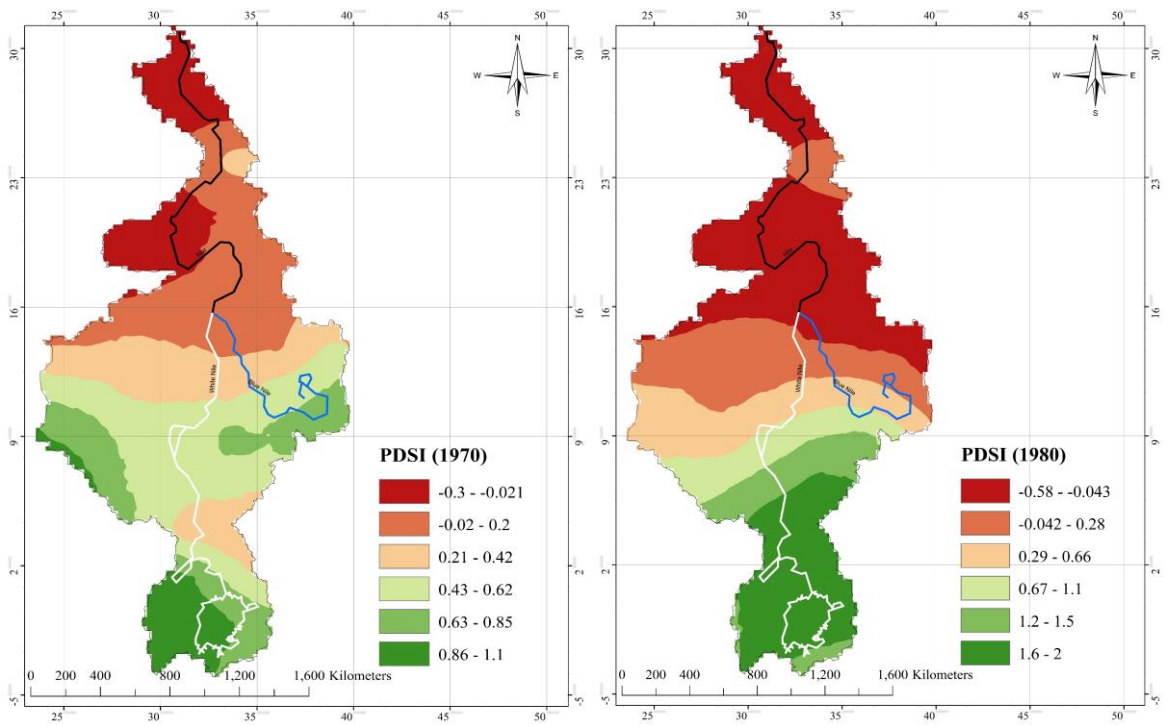
Nile river basin	Pettitt test					Mann–Kendall test					
	Years	K	t	P	trend	Tau	Sen's slope	P	trend	Mb	Ma
Monthly flow “Aswan dam”	1900-1987	40862	1965	0.001	Ha	0.134	3.966	<0.0001	-	2637	2016
Annual flow “Aswan dam”	1900-1987	1446	1965	<0.0001	Ha	0.2063	11.41	0.027	-	2754	2247
Flow anomaly “Aswan dam”	1900-1987	1446	1965	<0.0001	Ha	0.2063	11.41	0.027	-	249.7	-716.5
Monthly flow “Dongola” Sudan	1910-1984	15669	1945	0.02	Ha	0.010	2.008	0.05	-	2687	2567
Annual flow “Dongola” Sudan	1910-1984	658	1965	0.001	Ha	0.278	7.74	0.008	-	2754	2247
Flow anomaly “Dongola” Sudan	1910-1984	658	1965	0.001	Ha	0.241	7.74	0.003	-	132.05	-375.3
Monthly flow “Blue Nile” Sudan	1912-2010	17702	N	0.6	Ha	0.04	0.61	0.044	-	1575	
Annual flow “Blue Nile” Sudan	1912-2010	854	1964	0.015	Ha	0.08	1.37	0.15	-	1645	1478
Flow anomaly “Blue Nile” Sudan	1912-2010	854	1964	0.015	Ha	0.054	1.37	0.14	-	77.68	-89.5

Hydrological drought investigation based on self-calibrated PDSI for the NRB showed significant change point at 1983 with increasing trend in hydrological droughts, significant change in hydrological drought was observed after 1983 with decreasing trend in PDSI of 0.58/decade causing severe hydrological droughts in 1973, 1987, 2002, 2003, 2004, 2005, 2006, 2008, 2009, 2010, and 2011 (supplementary Fig E4 (a)). Using ArcGIS 10.1, the self-calibrated PDSI was analyzed for the period between 1950-2020 (supplementary Fig E4 (b, c)). The spatiotemporal distribution of PDSI shows similar pattern in all the NRB with incipient drought to moderate drought all over the entire basin with increase in areas occupied by moderate drought with time. To further investigate the hydrological drought in the NRB, we created time series of the self-calibrated PDSI, monthly temperature timeseries, temperature anomaly and monthly precipitation timeseries and temperature anomaly for each riparian of the Nile individually, to capture the trend and change points in PDSI compared to the change points and trends in monthly and anomaly of temperature and precipitation.

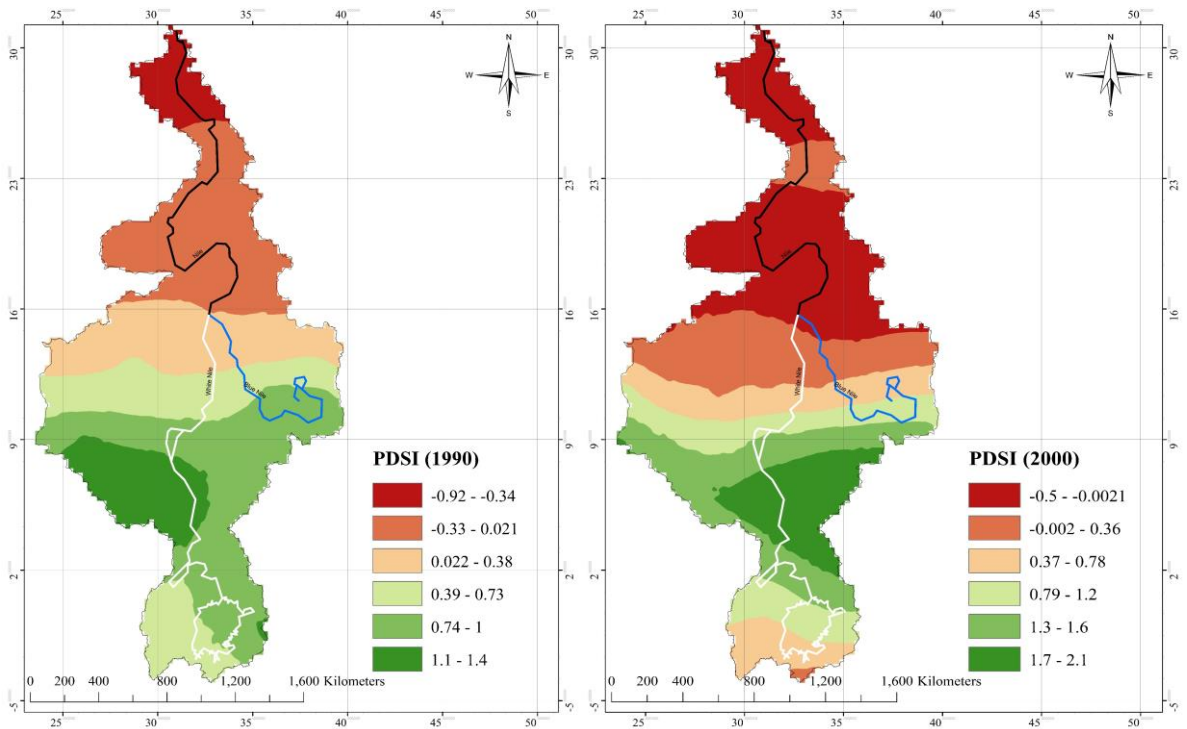


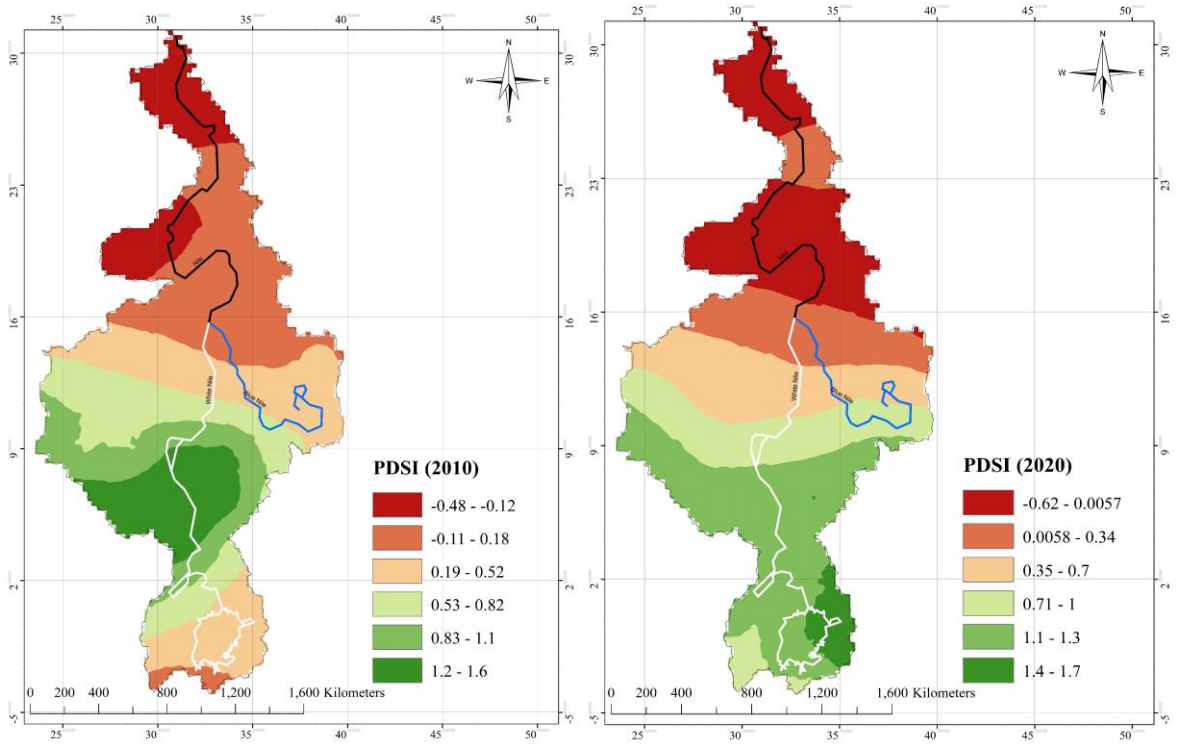
Supplementary Figure E4 (a) Palmer drought severity index anomaly 1960-2015





Supplementary Figure E4 (b) Palmer drought severity index 1950-1980

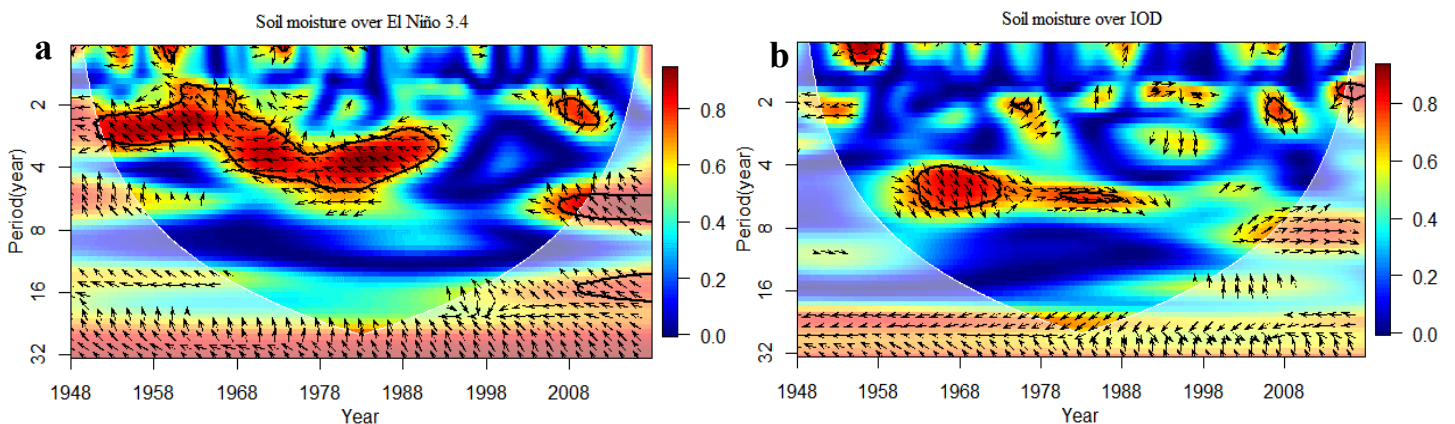


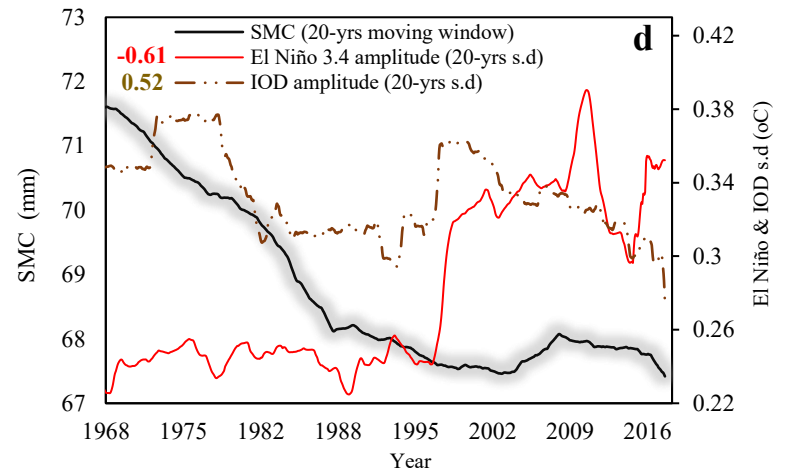
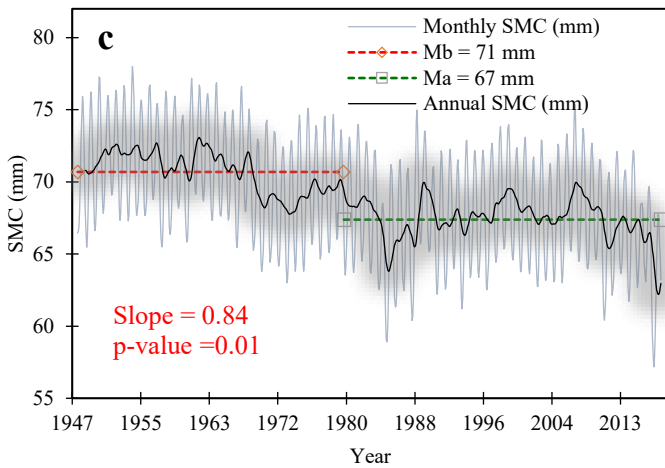


Supplementary Figure E4 (c) Palmer drought severity index 1990-2020

Appendix F: Response of NRB's streamflow, soil moisture content and groundwater storage to El Niño 3.4 and IOD

The wavelet coherence between El Niño 3.4, the soil moisture content (SMC) and groundwater storage (GWS) of NRB shows an anti-phase relationship with statistically significant coherence at 1-2, 2-4-year bands over 1960-1998, 2-4-year band over 2000-2017, and an interdecadal, 16-32-year band (supplementary Fig F1(a), Fig F2(a)). The wavelet coherence between IOD and SMC and GWS shows in-phase, interannual relationships over 1948-2017, but anti-phase relationships at larger timescales (supplementary Fig F1(b), Fig F2(b)). A statistically significant change point of 1979 was detected in SMC and GWS which show significant negative trends of 0.84 mm/decade and 1.44 mm/decade over 1979-2017, respectively (supplementary Fig F1(c), Fig F2(c)). These negative trends in SMC and GWS are attributed to significantly lower amount of precipitation and higher AET associated with intensive ENSO and WTIO activities over NRB in the same period, as shown by the significant negative (positive) correlation between El Niño 3.4 (IOD) amplitude and SMC ($\rho = -0.61$ for Niño 3.4 and 0.52 for IOD) (supplementary Fig F1(d)). Similarly, GWS is negatively correlated with El Niño 3.4 ($\rho = -0.72$), but positively correlated to IOD ($\rho = 0.43$).

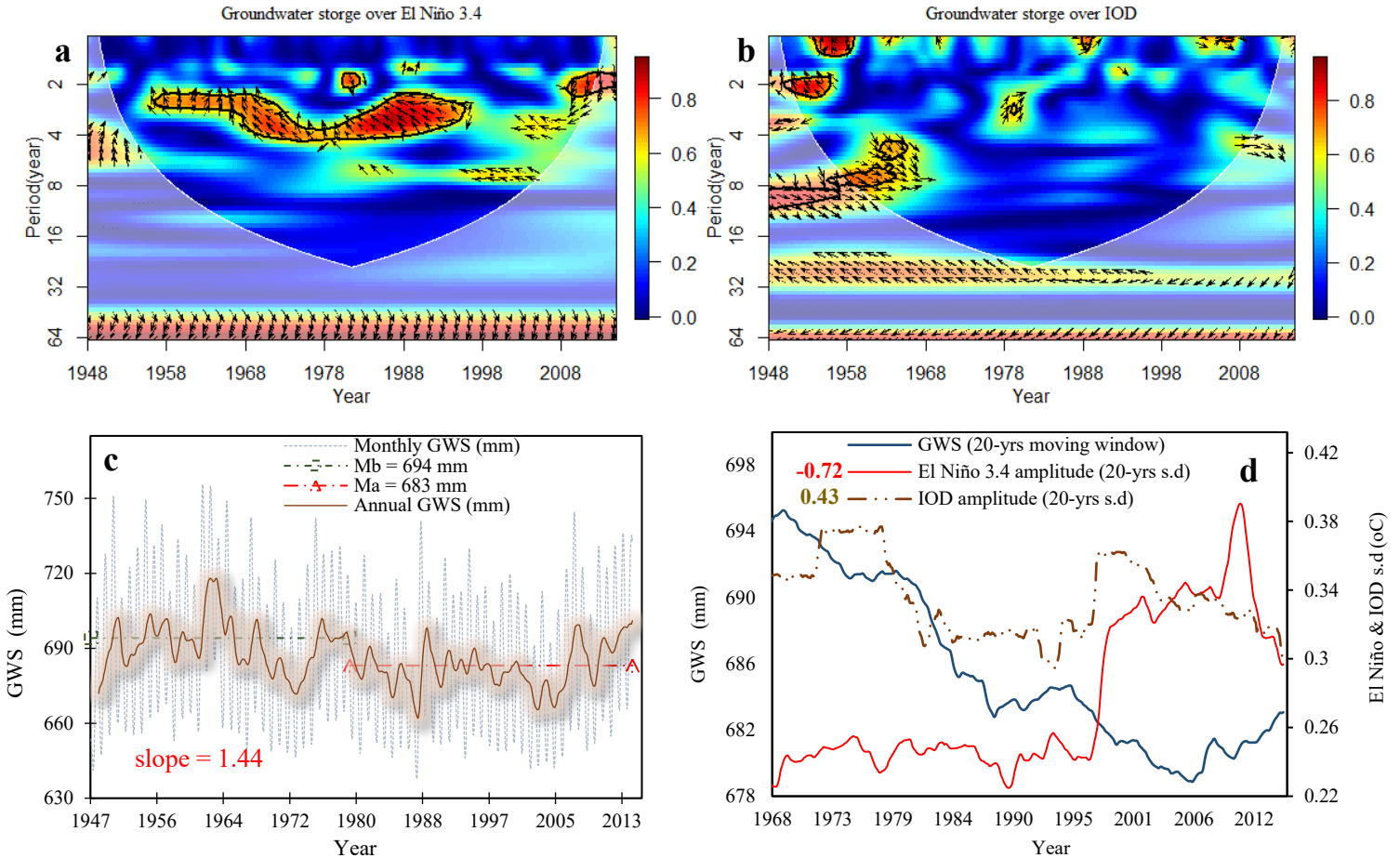




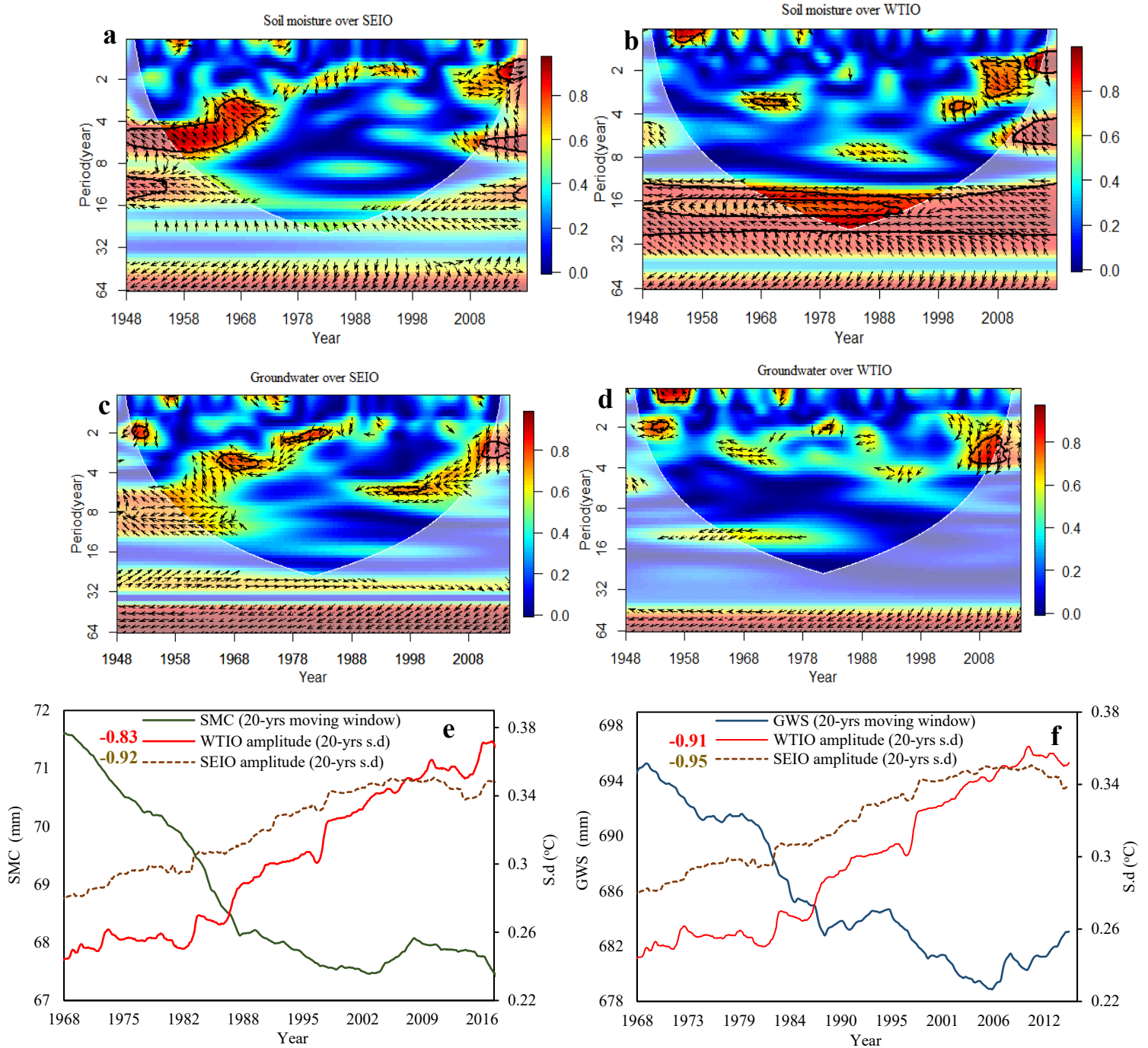
Supplementary Figure F1. Influence of El Niño 3.4 and IOD on NRB soil moisture content (SMC). Wavelet coherence between SMC and El Niño 3.4 (a), IOD and SMC (b), SMC time series, where Mb is the long-term average before change point, and Ma the long-term average after change point (c). SMC are computed over 20-years moving periods and then correlated with El Niño 3.4 and IOD amplitudes (d), using ERA-Interim, FLDAS and GLADS soil moisture datasets. The correlation coefficients (at 0.05 significant level) in the top right. The slope is the linear trend estimated and the p-value is the trend significance based on the Mann–Kendall test.

In contrast to the in-phase relationship between IOD and SMC and GWS over 1948-2017, there are stronger anti-phase relationships at 16-32 and 32-64 year bands between WTIO (SEIO) and soil moisture (GWS) (supplementary Fig F3(a-d)), with significant negative correlation between NRB’s SMC and SEIO ($\rho = -0.92$) and WTIO ($\rho = -0.83$) (supplementary Fig F3(e), which means that NRB’s SMC decreased under increased SEIO and WTIO amplitudes. The strong negative correlation between GWS and SEIO ($\rho = -0.95$) and WTIO ($\rho = -0.91$) implies that increased Indian Ocean SST gradient over the Arabian Sea and southeastern Indian Ocean resulted in lower groundwater storage in NRB (supplementary Fig F3(f)). It seems that the Arabian Sea (western pole) and the eastern Indian Ocean SST (southeastern pole) explains more of the variability of

NRB's SMC and GWS than IOD, for both SMC and GWS of NRB were positively correlated with IOD amplitude (see supplementary Fig F1 and F2)



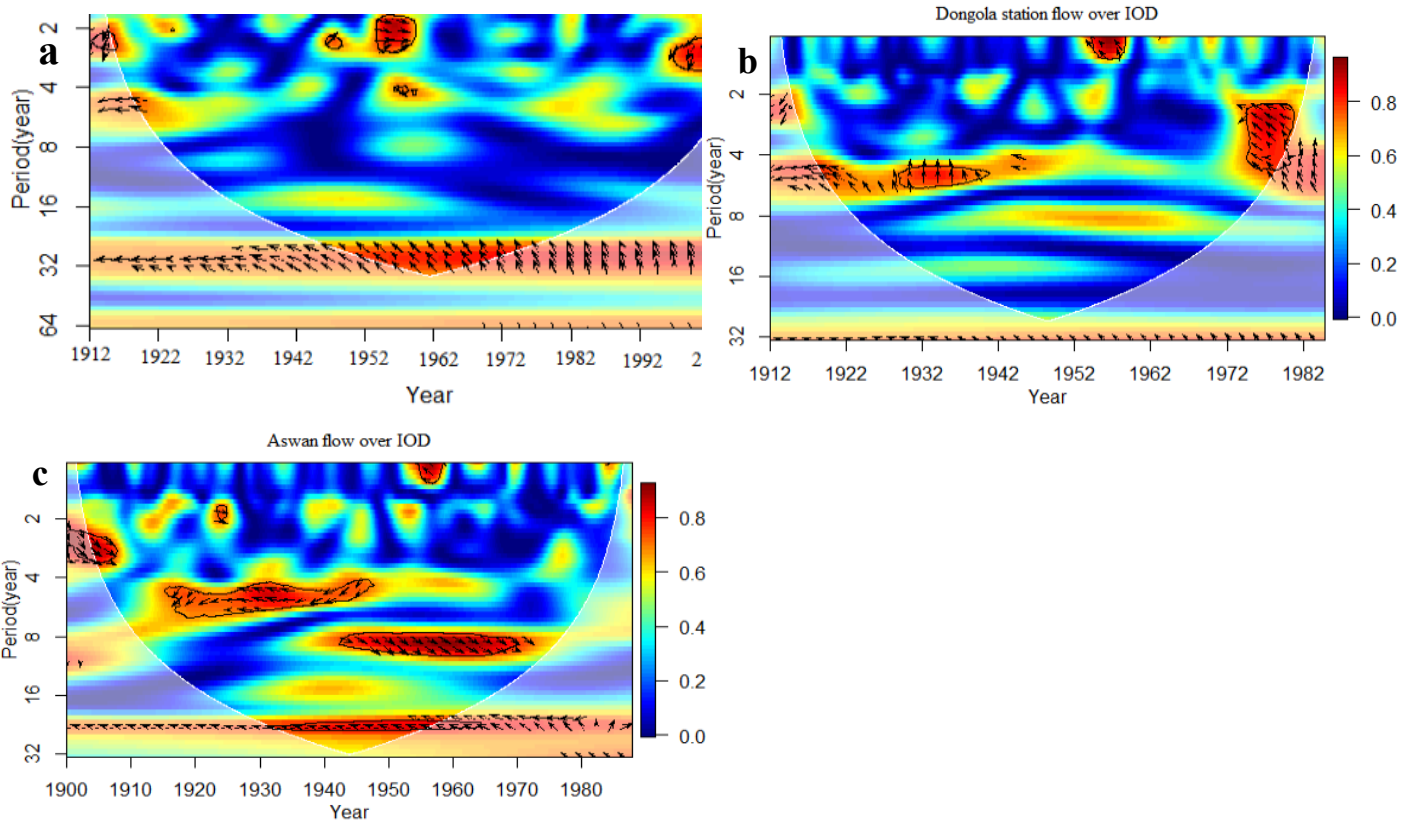
Supplementary Figure F2. Same as in supplementary Figure 37 but for groundwater storage (GWS). GWS are area averaged daily groundwater storage from GLADS-CLSM025 between 1948-2014 and the Gravity Recovery and Climate Experiment (GRACE) between 2003 and 2017. A negative trend of 1.44 mm/decade in monthly GWS was observed after 1979 (c). This trend could be attributed to a significantly lower amount of precipitation, higher AET and lower SMC after 1979. In d, a statistically significant negative correlation can be seen between El Niño 3.4 amplitude and GWS ($\rho = -0.72$), however a moderate positive correlation with IOD amplitude was detected ($\rho = 0.43$).



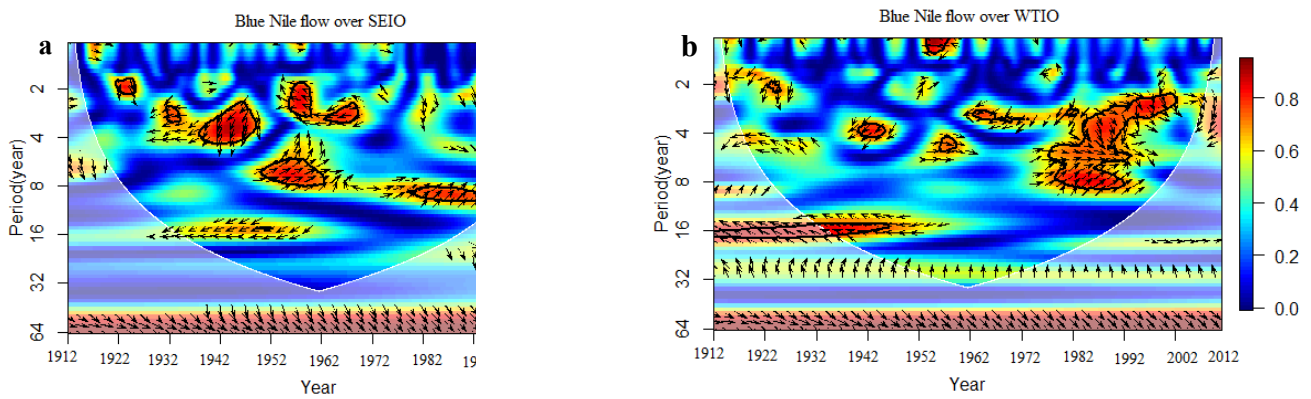
Supplementary Figure F3: Influence of WTIO and SEIO on NRB soil moisture content and groundwater storage. Wavelet coherence between SMC and SEIO and WTIO (a, b), Wavelet coherence between GWS and SEIO and WTIO (c, d). SMC and GWS were computed same as in supplementary Figure 20 and then correlated with WTIO and SEIO amplitudes. There is significant negative correlation between NRB SMC with SEIO and WTIO amplitudes ($\rho = -0.83$ for WTIO and -0.92 for SEIO). This strong negative

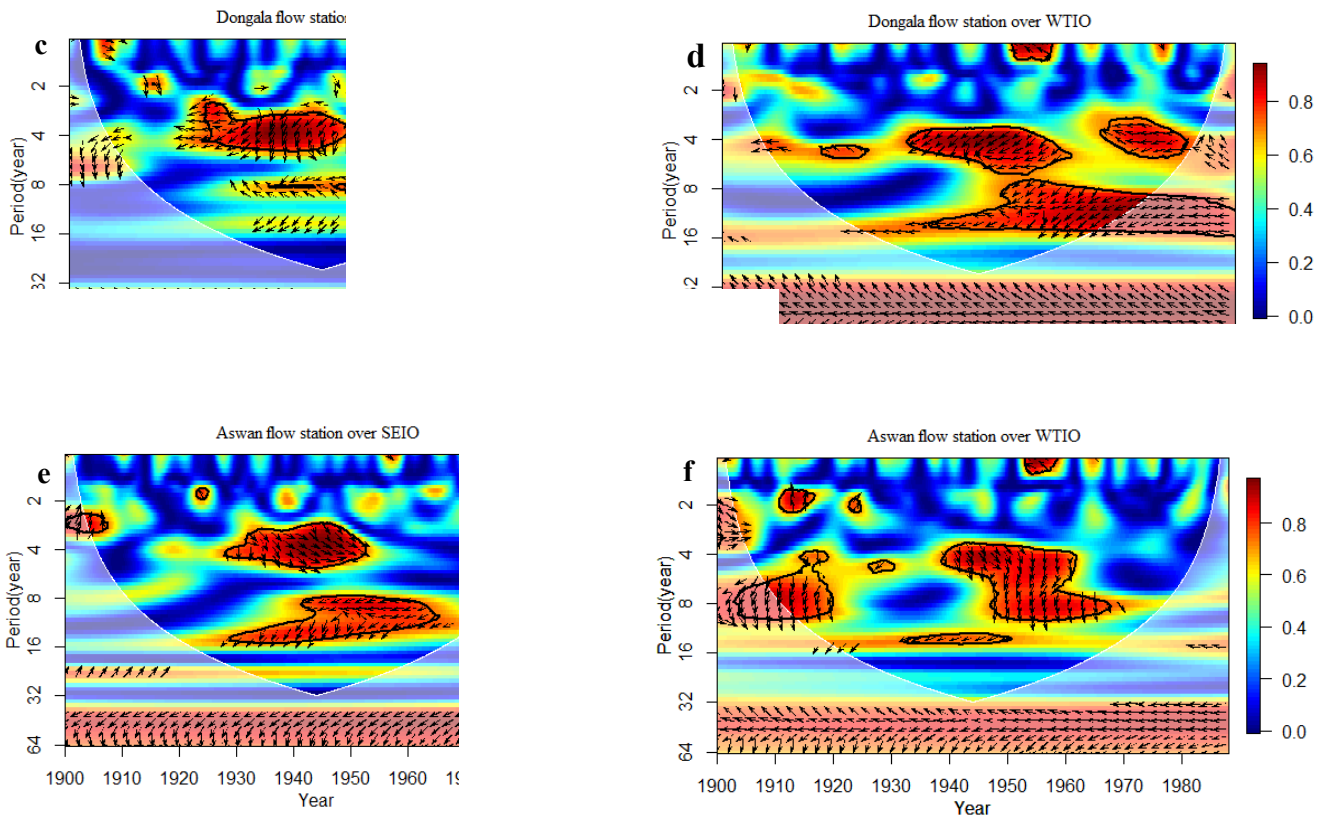
correlation indicates that the reduction in the NRB SMC is strongly linked to increased SEIO and WTIO amplitudes. In fact, the strong negative correlation between GWS and SEIO and WTIO ($\rho = -0.91$ for WTIO and -0.95 for SEIO) implies that the large deviations in the Indian ocean SST gradient over the Arabian Sea and southeastern parts of the Indian Ocean are the main controllers of the NRB groundwater storage. This result suggests that the Arabian Sea (western pole) and the eastern Indian Ocean SST (southeastern pole) amplitudes *are more important than* the difference between the two poles (IOD). This is due to the fact that IOD is not sufficient to explain SMC and GWS variability in the NRB as both were positively correlated with IOD amplitude (see supplementary Fig F1 and F2).

The wavelet coherence between the Blue Nile streamflow and IOD shows a strong anti-phase relationship at 32-year band over 1905-2012 and a stronger anti-phase relationship at 2-4- and 4-8-year bands over 2000-2012 (supplementary Fig F4(a)). The Nile flow at Dongala station and IOD also exhibited significant anti-phase relationship after 1970s at 2-4 and 4-8 year bands (supplementary Fig F4(b)) while the Nile river flow at the Aswan station (downstream) showed anti-phase relationships with IOD at 20-25 year band over 1930-1984 (supplementary Fig F4(c)). The wavelet coherence between WTIO and SEIO and Blue Nile flow show a significant, anti-phase relationship at 2-4 year band over 1960-1980, in phase relationship at 4-8 year band over 1982-2000, and both WTIO and SEIO lead Blue Nile streamflow at 32-64 year bands over 1912-2012 (supplementary Fig F5(a, b)). The anti-phase relationship was much stronger between WTIO and Blue Nile flow after 2000s. Nile flow at Dongala station also exhibited anti-phase relationship at 4-8- and 8-16-year band between 1940 and 1984. A dominant anti-phase relationship at 32-64-year band was observed between Nile flow at Dongala and Aswan with both indexes (supplementary Fig F5(c, d)).



Supplementary Figure F4. Wavelet coherence between observed monthly flows and IOD: (a) wavelet coherence between IOD and Blue Nile flow, (b) wavelet coherence between IOD and Dongola flow, and (c) wavelet coherence between IOD and Aswan flow.

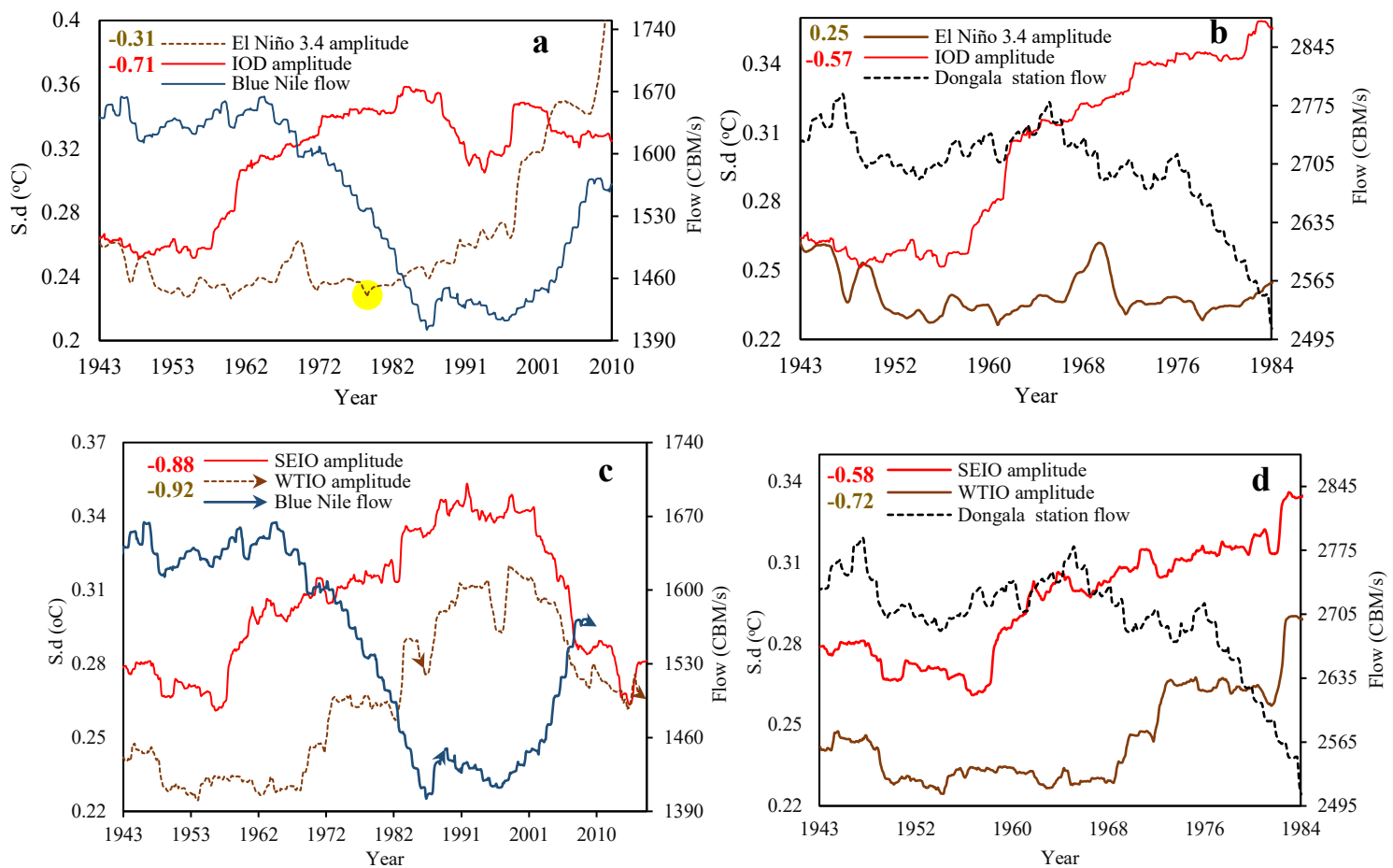




Supplementary Figure F5. Wavelet coherence between observed monthly Nile flows and SEIO and WTIO. Wavelet coherence between SEIO and WTIO and Blue Nile flow (a, b), wavelet coherence between SEIO and WTIO and Dongola flow (c, d), and wavelet coherence between SEIO and WTIO and Aswan station flow (e, f).

Supplementary Figure F6 shows a significant negative correlation between the Nile streamflow and IOD ($\rho = -0.71$ for Blue Nile flow and -0.57 for Nile flow at Dongala station) (supplementary Fig F6(a)), compared to a less significant negative (positive) correlation between El Niño and the Nile streamflow at Blue Nile ($\rho = -0.31$) and Dongala stations ($\rho = 0.25$), respectively (supplementary Fig F6(b)), which demonstrate the influence of IOD on the Nile streamflow at inter-annual to inter-decadal time scales. The peak correlation between IOD and the Nile streamflow occurred a year earlier than that between El Niño and the Blue Nile streamflow, which agrees with the wavelet coherence between El Niño and IOD (i.e. one lead the other shown in supplementary Figure D1(a, b). The increasing intensity in El Niño after 1978

(represented by the change point (yellow color) in supplementary Fig F6(a) shows that El Niño occurred more frequently with positive IODs than La Niña events with negative IODs. Our results show a strong teleconnection between the Nile streamflow and the Indian Ocean SST gradient over the western and the southeastern poles (supplementary Fig F6(c, d)). There are significant negative correlations between the Nile flow (Dongala station) and the southern Indian Ocean SST gradient over the Arabian Sea (WTIO) and the southeastern Indian Ocean (SEIO) ($\rho = -0.72$ and -0.58). However, the negative correlations are stronger between Blue Nile flow and WTIO and SEIO ($\rho = -0.92$ and -0.88), which means that the Nile River streamflow is strongly linked to WTIO and SEIO, with their warm (cold) phase associated with decreased (increased) Nile streamflow (shown by arrows in Fig. F6(c)). These results demonstrate the teleconnection between the Nile streamflow, SST of southern and eastern parts of the Indian Ocean, and El Niño at inter-annual to multi-decadal time scale. These results indicate that the intensity of the Indian Ocean Dipole and western pole are a better predictor of the Nile river flow than El Niño.



Supplementary Figure F6. Response of NRB flow variability to El Niño 3.4, IOD amplitude and the IOD two pole amplitudes i.e. western pole amplitude (WTIO) over the Arabian Sea and eastern pole amplitude (SEIO) over south of Indonesia: Correlation between NRB flow at Blue Nile and Dongala stations with El Niño 3.4 and IOD amplitudes (a, b), and SEIO and WTIO amplitudes (c, d), respectively. The NRB flow are computed over 30-year running periods from 1913 to 2010 for the Blue Nile station, and from 1913 to 1984 for Dongala station. El Niño 3.4, IOD, SEIO, WTIO amplitudes are computed as the SD of the El Niño 3.4, IOD, SEIO, WTIO indexes over 30-year windows from 1913 to 2017, using the ERSST data sets.

Appendix G: Countries ‘drought classification system based on drought severity indexes

sc-PDSI, monthly temperature, temperature anomaly, monthly precipitation and precipitation anomaly and composite analysis of the NRB’s hydroclimate data were analyzed for each riparian country of NRB, to relate climate warming to trend and change points in hydrologic droughts of these countries.

- **Ethiopia**

Pettit’s test showed that there is a change point in monthly precipitation in 1968 and change point in precipitation anomaly in 1977. Monthly and anomaly of temperature have the same change point in 1994. Analysis of long-term precipitation and temperature data between 1960-2015 in Ethiopia revealed statistically significant warming trend of 0.23 °C per decade (Supplementary Fig G1(b)) and both monthly precipitation and precipitation anomaly showed statistically significant decreasing trend. With precipitation anomaly (supplementary Fig G1(c)) decreasing at much higher rate 18.01 mm/decade (supplementary Table G1). This result agrees with the main trend in the NRB and does not agree with result of Mengistu et al (2014), where they reported a warming trend of 0.1 and 0.15 °C per decade in Ethiopia, between 1981-2010, and according to their study, precipitation showed statistically non-significant increasing trends of 35 mm per decade at the annual timescale. This is not true, as they used short time period 1981-2010 to conduct trend analysis and just 4 years before their data there is a change point and decline trend in precipitation and increase in warming that they did not include in their study. So, what they reported is a sub-trend for short time that we also captured for the same period but represent the overall trend over Ethiopia. There is also a statistically significant change point in PDSI in 1983 (supplementary Fig G1(a)), MK trend analysis revealed statistically significant decreasing trend in PDSI with 0.58/decade. This illustrate the change of the climate of Ethiopia and recurrent of drought events. Based on PDSI drought classification (supplementary Table G2), Ethiopia witnessed severe hydrological droughts in 1973, 1987, 2002, 2003, 2004, 2005, 2006, 2008, 2009, 2010, and 2011. While there was moderate hydrological drought during the following years 1965,

1969, 1971, 1972, 1975, 1984, 1985, 1986, 1988, 1990, 1991, 1992, 1994, 1995, 1997 and 2012. This is in good agreement with the observed agricultural drought trend in Ethiopia as 2011 there a huge decrease in irrigated land and significant increase in actual evapotranspiration due to very high warming trend. This is also in agreement with the trend observed from SPI trend analysis.

Supplementary Table G1. Change points and trend analysis of PDSI, temperature and precipitation in each riparian country

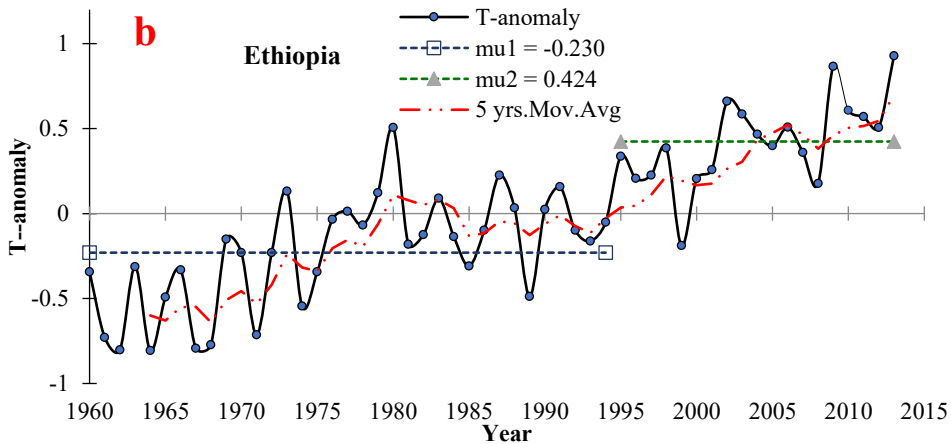
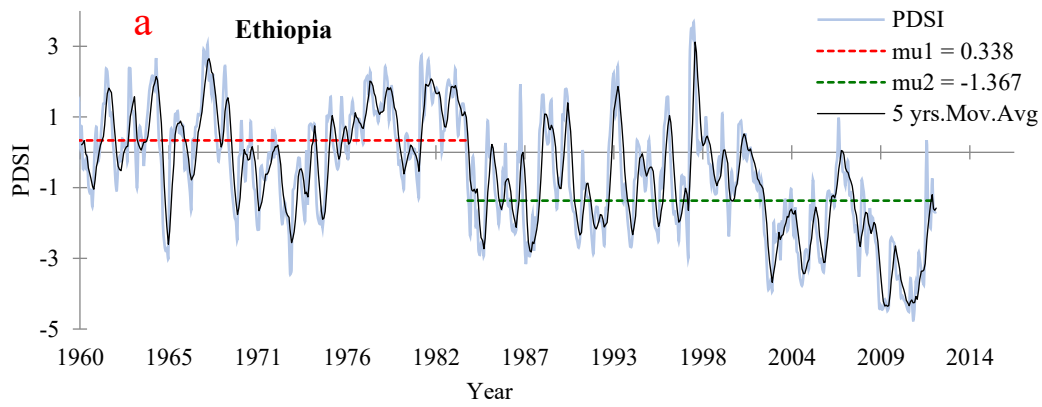
Ethiopia subbasin	Years	Pettitt test				Mann–Kendall test					
		K	t	P	trend	Tau	Sen's slope	P	trend	Mb	Ma
PDSI time series	1960-2013	60763	1983	< 0.0001	Ha	0.35	-0.058	< 0.0001	-	0.338	-1.36
Temperature time series	1960-2014	29866	1994	< 0.0001	Ha	0.44	0.023	< 0.0001	+	20.934	21.6
Temperature anomaly	1960-2015	601	1994	< 0.0001	Ha	0.653	0.028	< 0.0001	+	-0.23	0.424
Precipitation time series	1960-2015	3794	1968	0.007	Ha	0.01	-0.014	0.021	-	89.156	80.94
Precipitation anomaly	1960-2015	200	1977	0.02	Ha	0.073	-1.801	0.04	-	40.15	-30.2
Uganda subbasin											
PDSI time series	1960-2013	50079	1979	< 0.0001	Ha	0.321	-0.058	< 0.0001	-	0.379	-1.314
Temperature time series	1960-2014	55944	1994	< 0.0001	Ha	0.485	0.033	< 0.0001	+	22.255	23.42
Temperature anomaly	1960-2013	645	1994	< 0.0001	Ha	0.694	0.033	0.03	+	-0.41	0.756
Precipitation time series	1960-2015	6800	N	0.687	Ho	0.03	-0.113	0.279	-	104.704	
Precipitation anomaly	1960-2013	197	1978	0.025	Ha	0.073	-0.864	0.003	-	29.69	-37.9
Kenya subbasin											
PDSI time series	1960-2013	45349	1991	< 0.0001	Ha	0.28	-0.056	< 0.0001	-	0.126	-1.424
Temperature time series	1960-2014	42974	1994	< 0.0001	Ha	0.444	0.026	< 0.0001	+	21.258	22.16
Temperature anomaly	1960-2014	634	1994	< 0.0001	Ha	0.611	0.028	0.002	+	-0.317	0.584
Precipitation time series	1960-2015	6032	N	0.419	Ho	0.023	-0.017	0.401	-	94.764	
Precipitation anomaly	1960-2014	171	1968	0.0.3	Ha	0.11	-1.801	0.05	-	110.07	-52.4
Tanzania subbasin											
PDSI time series	1960-2013	50493	1991	< 0.0001	Ha	0.263	-0.045	< 0.0001	-	0.148	-1.314
Temperature time series	1960-2014	33073	1986	< 0.0001	Ha	0.433	0.021	< 0.0001	+	22.295	22.96
Temperature anomaly	1960-2014	659	1986	< 0.0001	Ha	0.639	0.022	< 0.0001	+	-0.325	0.325
Precipitation time series	1960-2015	7144	N	0.872	Ho	0.064	-0.103	0.019	-	85.492	

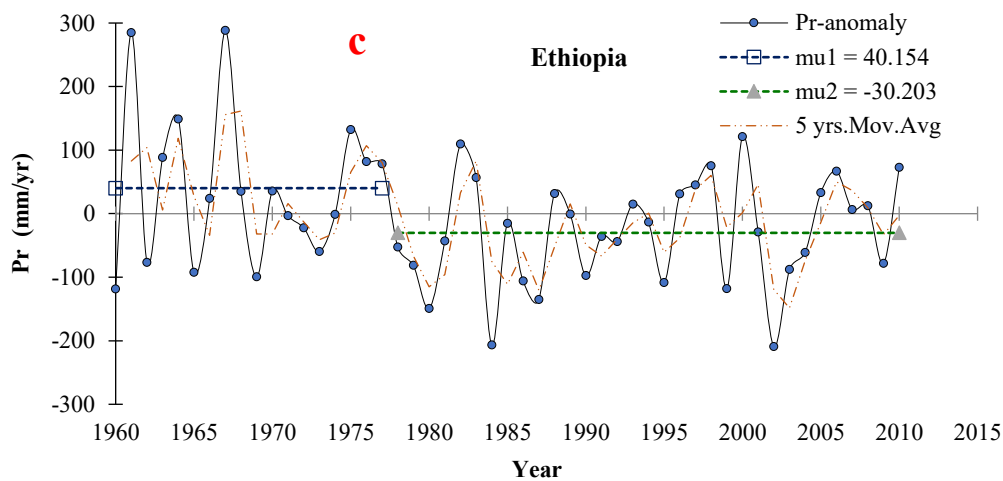
Precipitation anomaly	1960-2015	236	1991	0.049	Ha	0.215	-2.418	0.028	-	-0.318	-80.58
Sudan subbasin											
PDSI time series	1960-2013	35944	1968	<0.0001	Ha	0.124	-0.017	<0.0001	-	0.171	-1.49
Temperature time series	1960-2014	23117	1979	<0.0001	Ha	0.439	0.039	<0.0001	+	27.198	28.33
Temperature anomaly	1960-2014	603	1978	<0.0001	Ha	0.677	0.039	<0.0001	+	-0.735	0.399
Precipitation time series	1960-2015	4754	N	0.129	Ho	0.013	-0.01	0.647	-	30.154	
Precipitation anomaly	1960-2015	241	1968	0.01	Ha	0.124	-0.757	0.11	-	42.77	-13.03
Congo 'Zaire' subbasin											
PDSI time series	1960-2013	15801	1963	0.001	Ha	0.04	-0.003	0.104	-	2.406	0.003
Temperature time series	1960-2014	16342	1985	0.005	Ha	0.197	0.007	<0.0001	+	24.429	24.78
Temperature anomaly	1960-2014	501	1982	<0.0001	Ha	0.318	0.007	0.001	+	-0.194	0.144
Precipitation time series	1960-2015	5165	N	0.248	Ho	0.040	-0.141	0.147	-	131.425	
Precipitation anomaly	1960-2015	42.3	1970	0.049	Ha	0.163	-1.905	0.01	-	77.43	-20.93
Burundi subbasin											
PDSI time series	1960-2013	18044	1990	<0.0001	Ha	0.054	-0.004	0.049	-	0.122	-0.404
Temperature time series	1960-2014	54455	1994	<0.0001	Ha	0.39	0.02	<0.0001	+	20.129	20.9
Temperature anomaly	1960-2014	656	1989	<0.0001	Ha	0.564	0.021	0.02	+	-0.31	0.388
Precipitation time series	1960-2015	5518	N	0.278	Ho	0.009	-0.072	0.013	-	102.6	
Precipitation anomaly	1960-2014	280	1989	0.04	Ha	0.389	-1.917	0.008	-	27.53	-46.48
Rwanda subbasin											
PDSI time series	1960-2013	18435	1969	<0.0001	Ha	0.023	-0.04	0.039	-	0.836	-0.227
Temperature time series	1960-2014	65428	1994	<0.0001	Ha	0.399	0.021	<0.0001	+	18.729	19.59
Temperature anomaly	1960-2014	663	1990	<0.0001	Ha	0.543	0.022	<0.0001	+	-0.326	0.44
Precipitation time series	1960-2015	5192	N	0.198	Ho	0.021	-0.013	0.440	-	99.614	
Precipitation anomaly	1960-2015	254	1983	0.123	Ha	0.126	-1.558	0.10	-	34.56	-35.56
Eritrea subbasin											
PDSI time series	1960-2013	54130	2001	<0.0001	Ha	0.207	-0.048	<0.0001	-	0.201	-2.72
Temperature time series	1960-2014	24322	1979	<0.0001	Ha	0.431	0.03	<0.0001	+	23.656	24.57
Temperature anomaly	1960-2013	579	1987	<0.0001	Ha	0.649	0.03	<0.0001	+	-0.573	0.311
Precipitation time series	1960-2015	6498	N	0.593	Ho	0.028	-0.004	0.305	-	28.05	
Precipitation anomaly	1960-2015	263	1988	0.10	Ha	0.175	-1.505	0.06	-	27.34	-37.02

*Mb, mean value before the change point, Ma mean after the change point 't'

Supplementary Table G2: PDSI drought severity categories

PDSI	Category
3.00–3.99	Very wet
2.00–2.99	Moderately wet
1.00–1.99	Slightly wet
0.50–0.99	Incipient wet spell
-0.49 to 0.49	Near normal
-0.5 to -0.99	Incipient drought
-1 to -1.99	Mild drought
-2 to -2.99	Moderate drought
-3 to -3.99	Severe drought



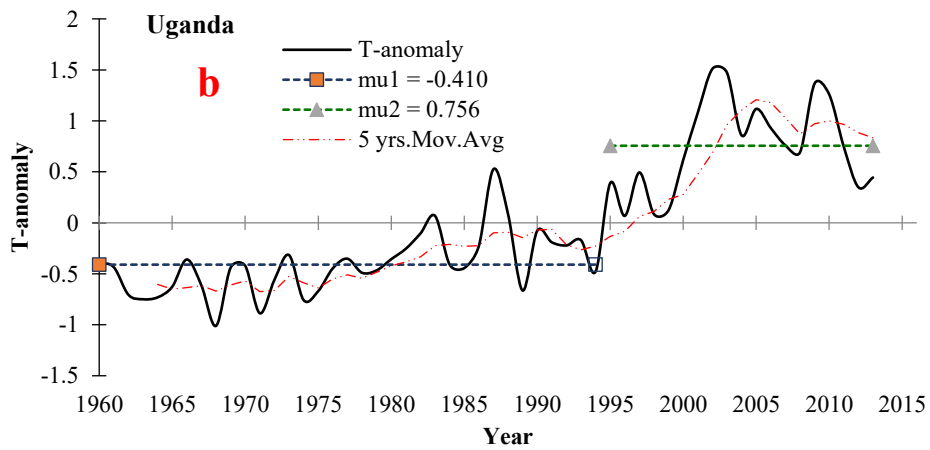
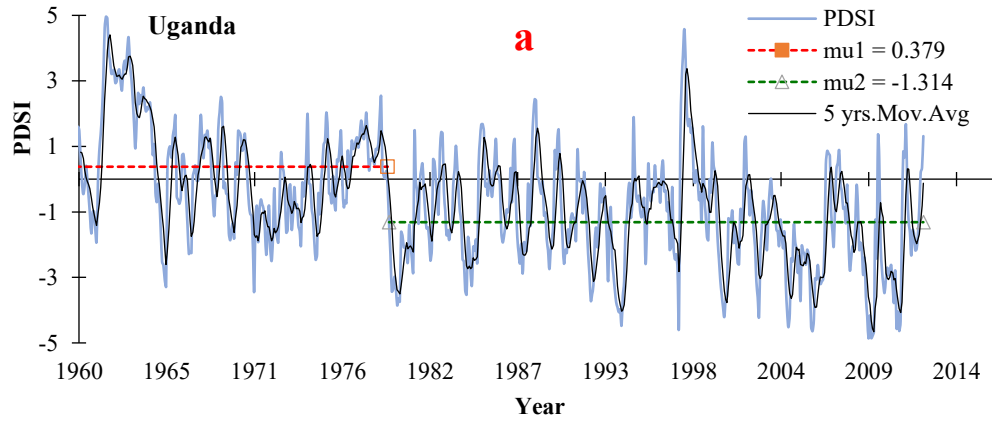


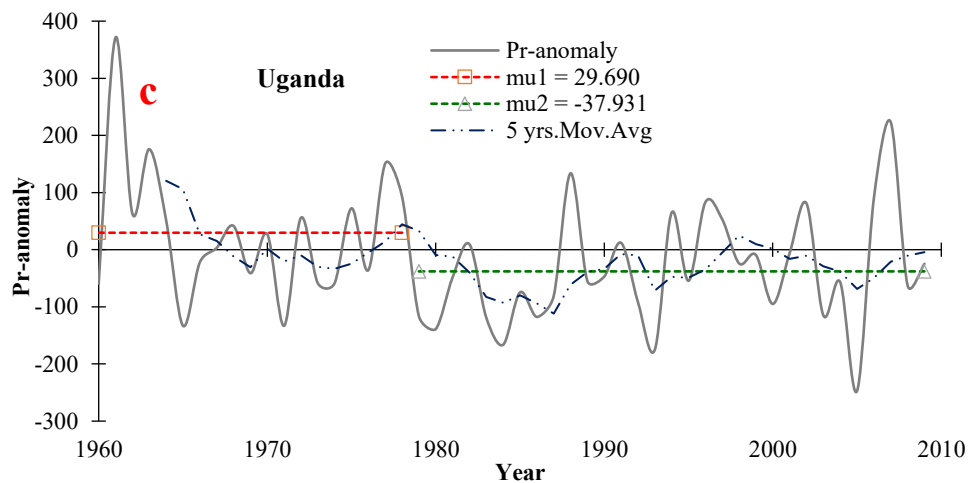
Supplementary Figure G1: Long term hydrological drought, PDSI trend (a), temperature anomaly (b), precipitation anomaly (c) over Ethiopia ‘Blue Nile’

- **Uganda**

There is no change point in monthly precipitation, but precipitation anomaly showed a statistically significant change point in 1978 (supplementary Fig G2(c)). Monthly and anomaly of temperature have the same change point in 1994 similar with Ethiopia. Analysis of long-term precipitation and temperature data between 1960-2015 in Uganda revealed statistically significant warming trend of 0.33 °C per decade (supplementary Fig G2(b)) much higher warming rate than Ethiopia. While, precipitation anomaly showed statistically significant decreasing trend with 8.3 mm/decade (supplementary Table G1). There is also a statistically significant change point in PDSI in 1979 (supplementary Fig G2(a)), MK trend analysis revealed statistically significant decreasing trend in PDSI at the same rate as Ethiopia. This illustrate that warming trend in Uganda have more effect on hydrological drought than the decline in precipitation. Based on PDSI drought classification (supplementary Table G2), Uganda suffered from severe hydrological droughts in 1965, 1971, 1972, 1979, 1980, 1984, 1992, 1993, 1994, 1997, 2000, 2002, 2004, 2005, 2006, 2009, 2010, 2011 and moderate hydrological drought during the following years 1967, 1974, 1975, 1981, 1982, 1985, 1987, 1988, 1989, 1990, 1995, 2001, 2003, 2007, 2008, and 2012. Uganda faced more

hydrological drought than Ethiopia due to the very high warming rate, for instance out of the 55 years of PDSI data Uganda is marked with severe drought and moderate drought in 35 years. This is in good agreement with the observed agricultural drought trend in Uganda in 2002, 2004, 2005, 2006, 2009, 2010, 2011 and increased AET anomaly at the same years, which signify the effect of increased warming.

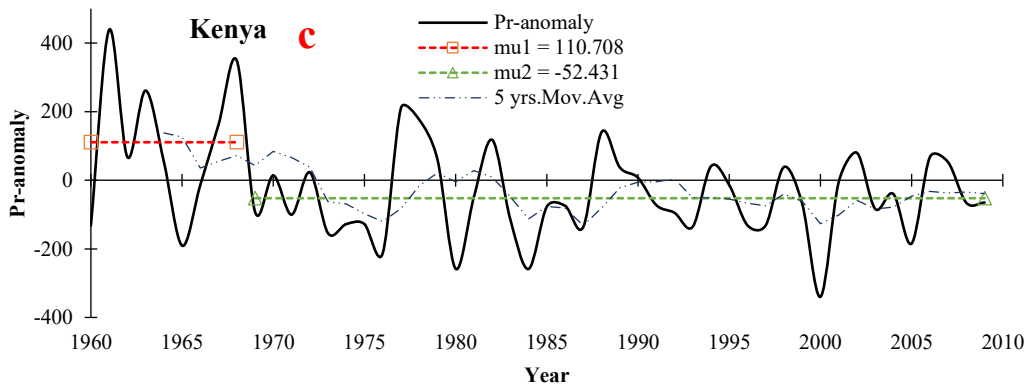
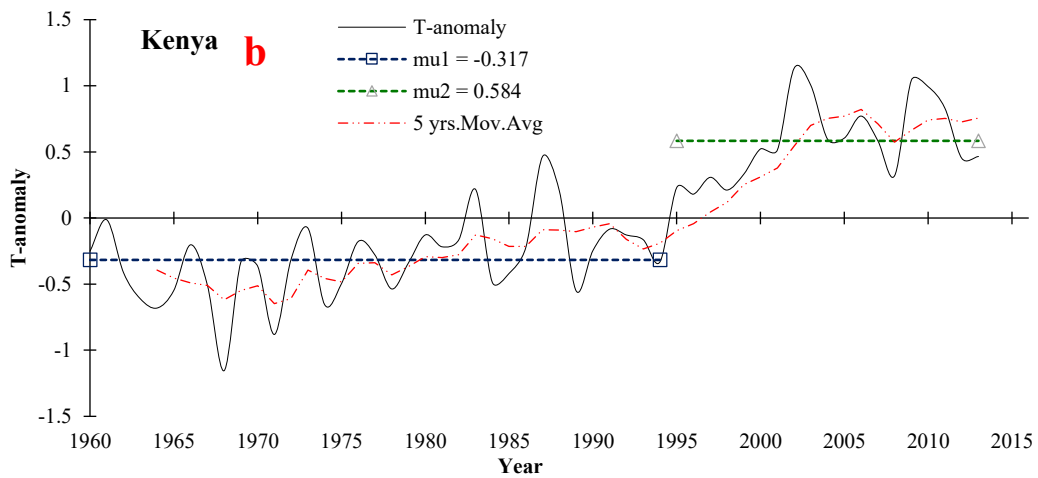
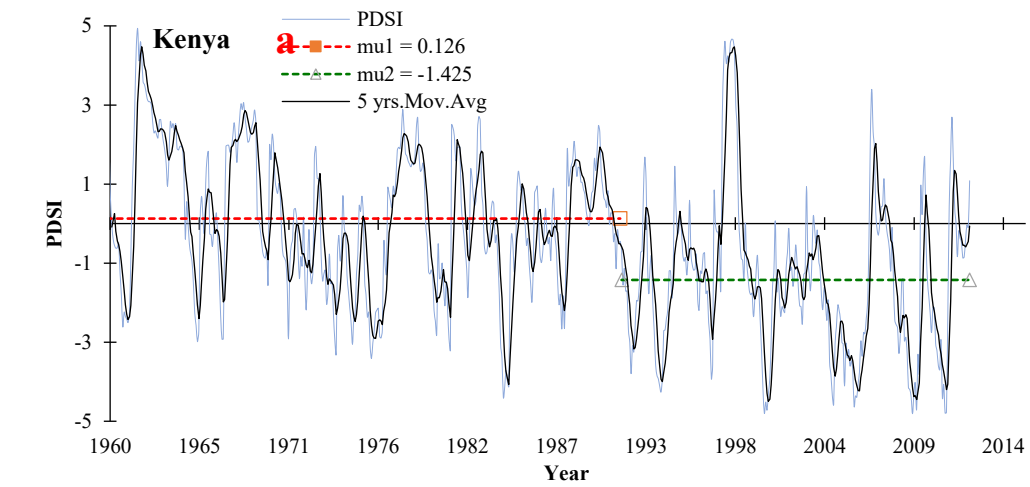




Supplementary Figure G2: Long term hydrological drought, PDSI trend (a), temperature anomaly (b), precipitation anomaly (c) over Uganda 1960-2016 F

- **Kenya**

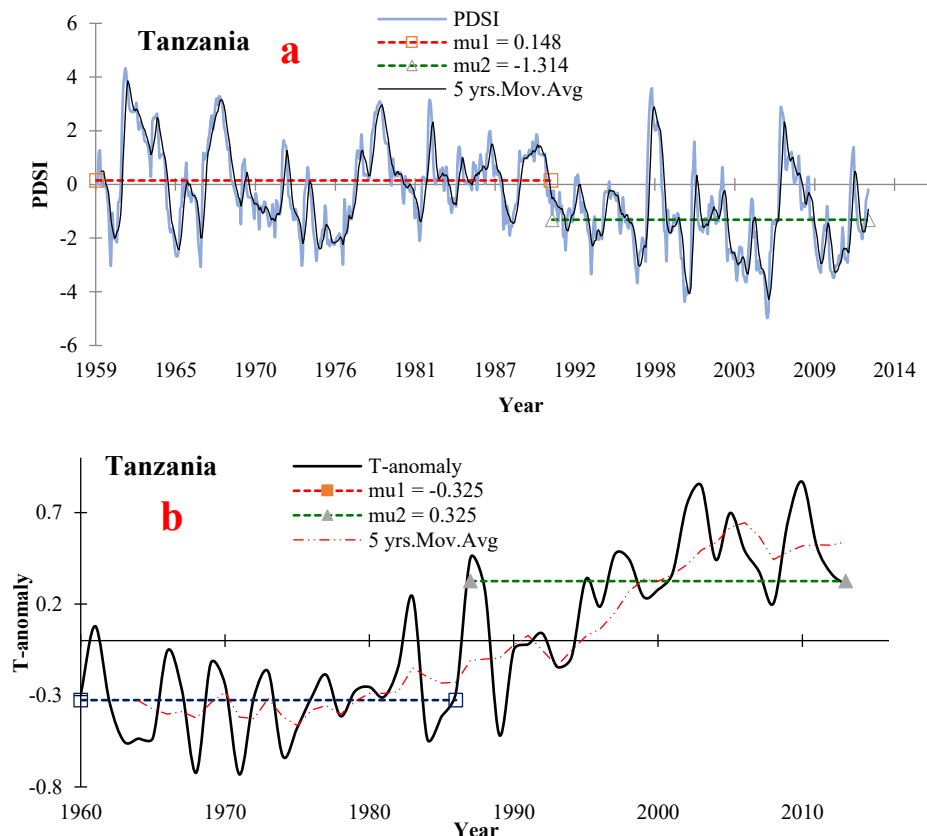
Precipitation anomaly showed a change point in 1968 (supplementary Fig G3(c)). Monthly and anomaly of temperature have the same change point in 1994 similar with Ethiopia and Uganda. There is a statistically significant warming trend of 0.28 °C per decade (supplementary Fig G3(b)) slightly higher than Ethiopia but lower than Uganda. Precipitation anomaly showed statistically significant decreasing trend with 18.01 mm/decade (supplementary Table G1), this is an interesting point as Kenya shares borders with Ethiopia. There is also a statistically significant change point in PDSI in 1991 (supplementary Fig G3(a)), MK trend analysis revealed statistically significant decreasing trend in PDSI at 0.56/decade. Based on PDSI drought classification (supplementary Table G2), Kenya suffered from severe hydrological droughts in 1965, 1974, 1975, 1976, 1981, 1984, 1992, 1993, 1994, 1997, 2000, 2004, 2005, 2006, 2008, 2009, 2010, 2011 and moderate hydrological drought during the following years 1961, 1967, 1971, 1972, 1973, 1980, 1986, 1987, 1988, 1996, 1999, 2001, 2002, 2003. Severe and moderate drought in 32 years. This is in good agreement with the observed agricultural drought trend in Kenya in 2002, 2004, 2005, 2006, 2009, 2010, 2011 and increased AET anomaly at the same years.

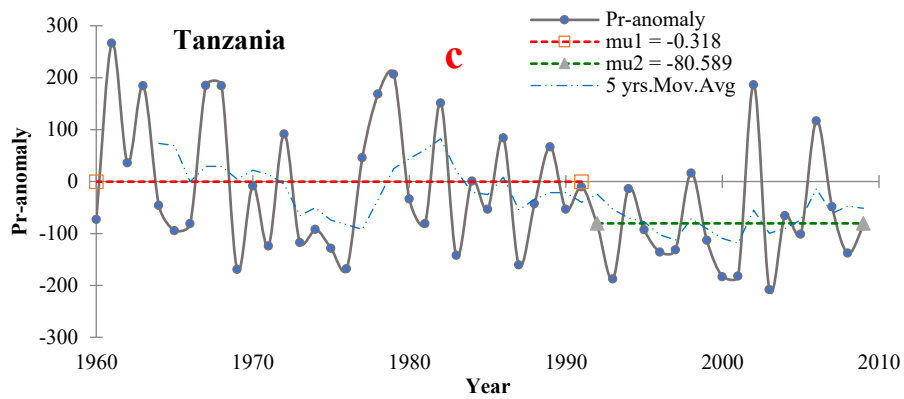


Supplementary Figure G3: Long term hydrological drought, PDSI trend (a), temperature anomaly (b), precipitation anomaly (c) over Kenya 1960-2016

- **Tanzania**

Precipitation anomaly (supplementary Fig G4(c)) showed a change that there is a statistically change point in 1991. Monthly and anomaly of temperature have the same change point in 1986 with warming trend of 0.22 °C per (supplementary Fig G4(b)) slightly lower than Ethiopia. Precipitation anomaly showed significant decreasing trend with 24.18 mm/decade. There is also a statistically significant change point in PDSI in 1991 (supplementary Fig G4(a)), trend analysis revealed significant decreasing trend in PDSI at 0.45/decade. Based on PDSI drought classification, Tanzania suffered from severe hydrological droughts in 1961, 1967, 1974, 1993, 1997, 2000, 2003, 2004, 2005, 2006, 2009, 2010 and moderate hydrological drought during the following years 1960, 1965, 1967, 1975, 1976, 1982, 1992, 1994, 1996, 2011, 2012. This is in good agreement with the observed agricultural drought trend in Tanzania in 2002, 2004, 2005, 2006, 2009, 2010, 2011 and increased AET anomaly at the same years.

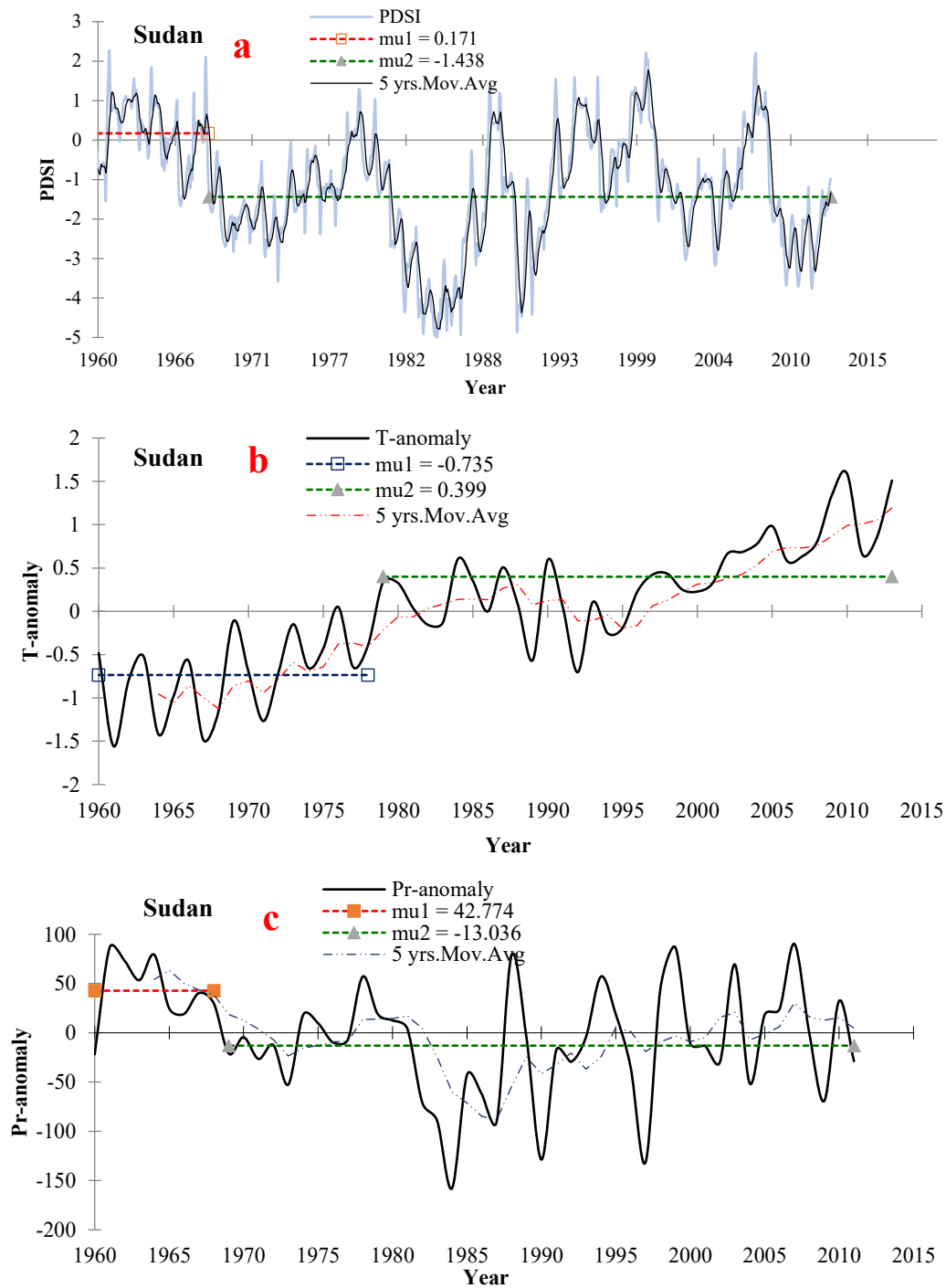




Supplementary Figure G4: Long term hydrological drought, PDSI trend (a), temperature anomaly (b), precipitation anomaly (c) over Tanzania 1960-2016

- **Sudan**

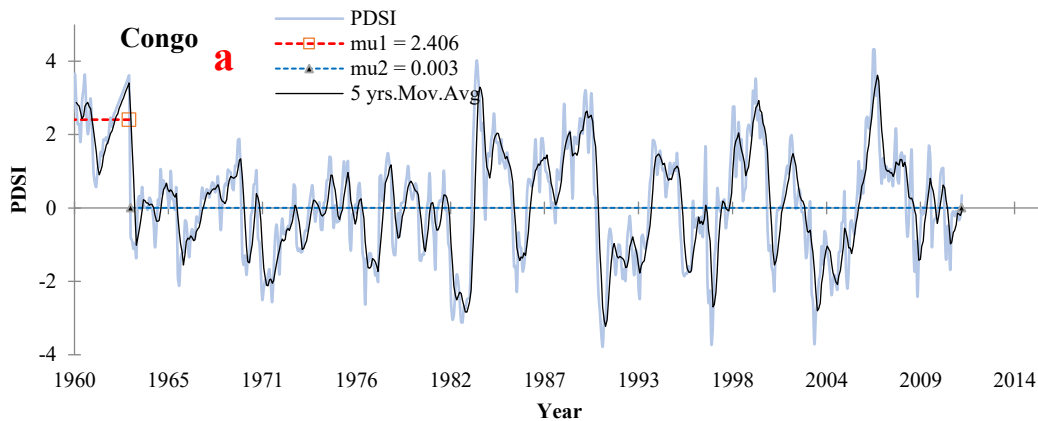
Precipitation anomaly showed a change point in 1968 (supplementary Fig G5(c)). Monthly and anomaly of temperature have two change points 1979 for monthly temperature timeseries and 1978 for temperature anomaly. There is a statistically significant warming trend of 0.39 °C per decade (supplementary Fig G5(b)), the highest warming rate in the entire NRB. Precipitation anomaly showed statistically significant decreasing trend of 7.57 mm/decade, there is also a statistically significant change point in PDSI in 1968 (supplementary Fig G5(a)) in the same year of the change point in precipitation anomaly, trend analysis showed statistically significant decreasing trend in PDSI at 0.17/decade. According to PDSI drought classification, Sudan witnessed severe hydrological droughts in 1973, 1982, 1983, 1984, 1985, 1986, 1987, 1990, 1991, 2002, 2004, 2009, 2010, 2011 and moderate hydrological drought during the following years 1960, 1969, 1970, 1971, 1972, 1974, 1975, 1976, 1977, 1981, 1988, 2000, 2008, 2012. This is in good agreement with the observed agricultural drought trend in Sudan in 2002, 2004, 2005, 2006, 2009, 2010, 2011 and increased AET anomaly at the same years.

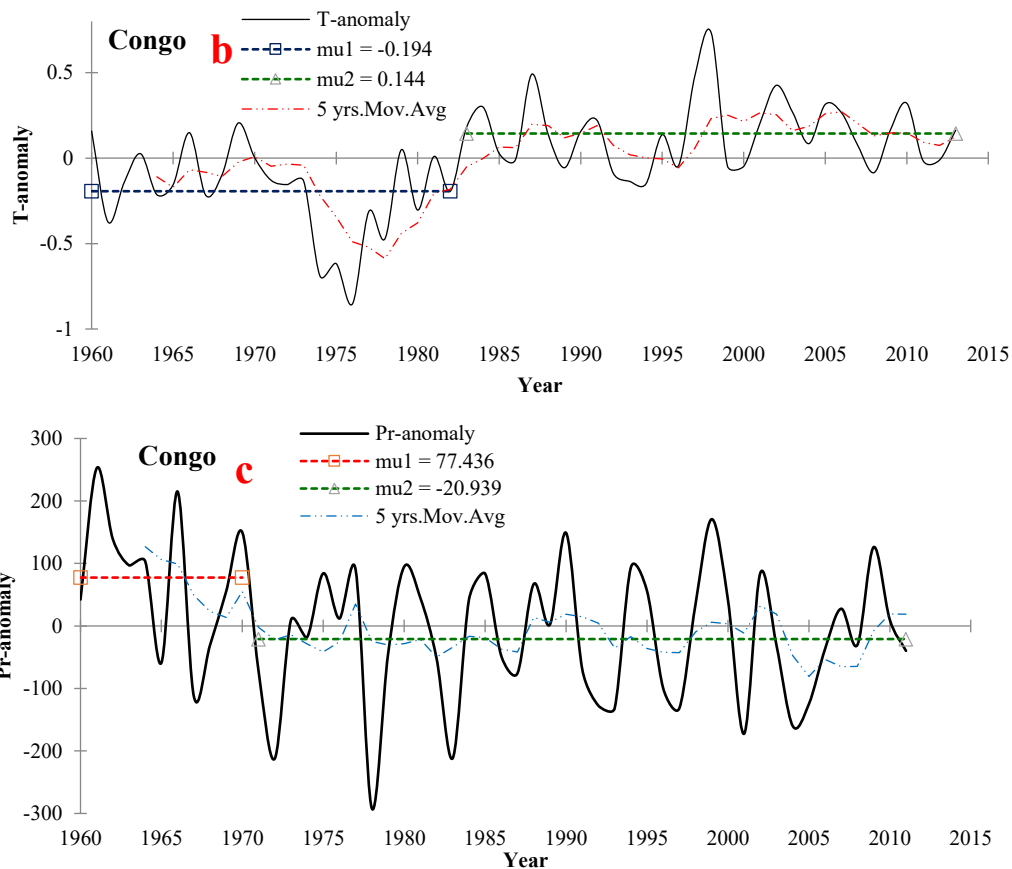


Supplementary Figure G5: Long term hydrological drought, PDSI trend (a), temperature anomaly (b), precipitation anomaly (c) over Sudan ‘White Nile’1960-2016

- **Congo**

Precipitation anomaly showed a change point in 1970 (supplementary Fig G6(c)). Monthly and anomaly of temperature have two different change points in 1985 for monthly temperature timeseries and 1982 for the anomaly. Increasing warming trend of 0.07 °C per decade (supplementary Fig G6(b)), the lowest warming rate in the NRB. Precipitation anomaly showed statistically significant decreasing trend with 19.05 mm/decade , there is also a statistically significant change point in PDSI in 1963 (supplementary Fig G6(a)), despite the very high decline trend in precipitation anomaly, the decreasing trend in PDSI is only 0.03/decade and at a lower confidence level “90”. Based on PDSI drought classification, Congo faced severe hydrological droughts in 1982, 1990, 1991, 1997, 2003 and moderate hydrological drought during the following years 1966, 1971, 1977, 1983, 1986, 1993,2001,2004, 2009. This is in good agreement with the observed agricultural drought trend in Congo in 2003, 2004, 2009 and increased AET anomaly at the same years.



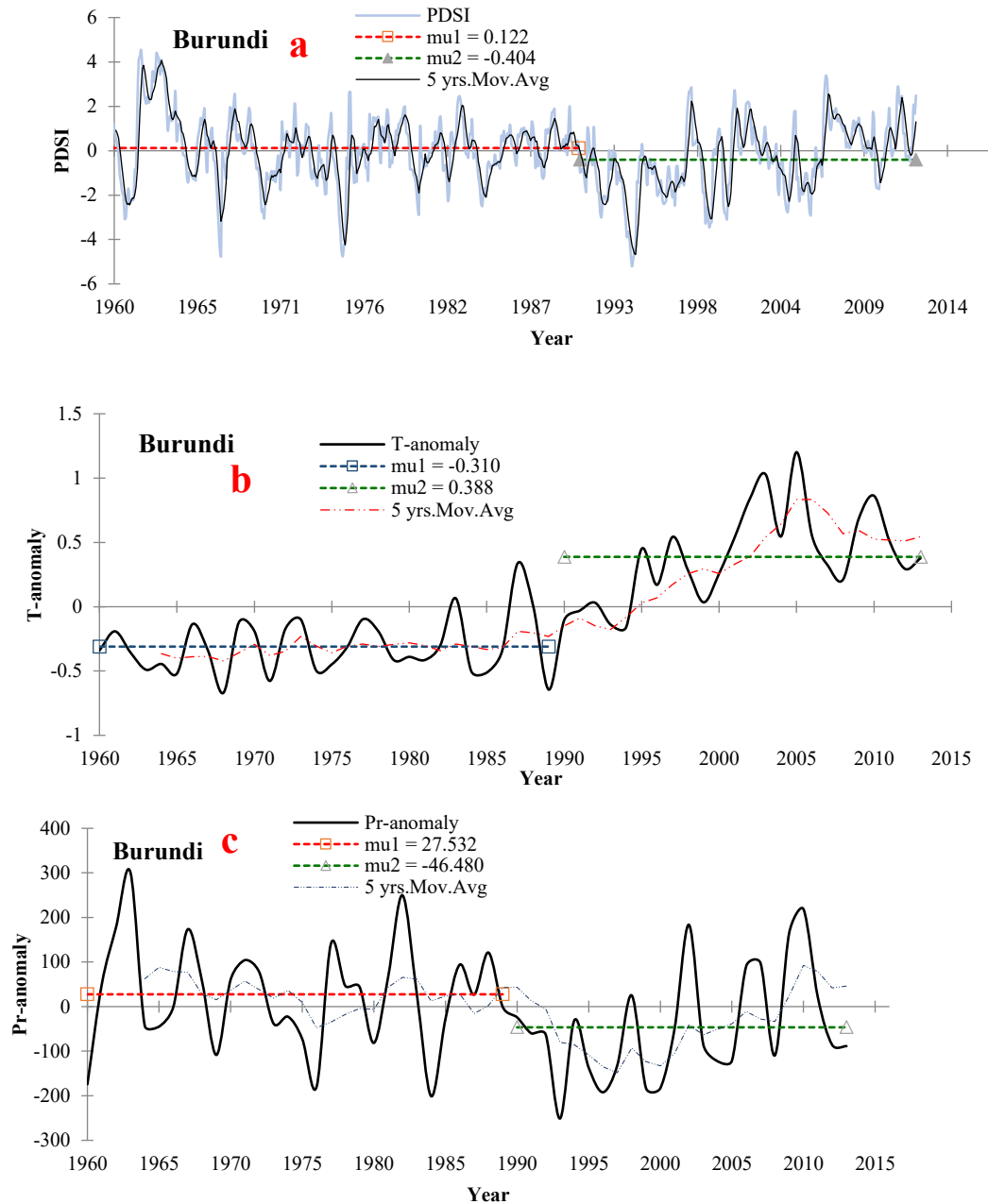


Supplementary Figure G6: Long term hydrological drought, PDSI trend (a), temperature anomaly (b), precipitation anomaly (c) anomaly over Congo

- **Burundi**

precipitation anomaly showed a change point in 1989 (supplementary Fig G7(c)). Monthly and anomaly of temperature has two change points, the monthly temperature has a change point in 1994 while temperature anomaly has change point in 1989 (supplementary Fig G7(b)). There is a statistically significant warming trend of 0.21 °C per decade and precipitation anomaly showed statistically significant decreasing trend with 19.017 mm/decade (supplementary Table G1). There is also a statistically significant change point in PDSI in 1991 (supplementary Fig G7(a)), trend analysis also revealed significant decreasing trend in PDSI at 0.49/decade. Based on PDSI drought classification, Burundi witnessed severe hydrological droughts in 1960, 1967, 1970, 1975, 1992,

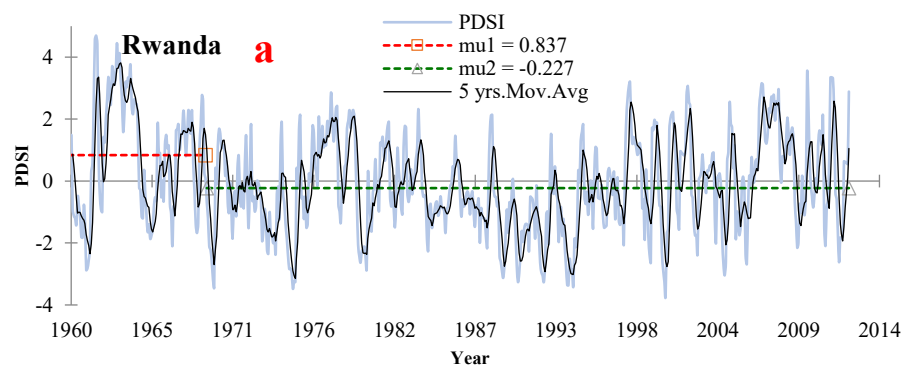
1993, 1994, 1999, 2000 and moderate hydrological drought during the following years 1961, 1969, 1974, 1980, 1984, 1996, 1997, 1998, 2002, 2003, 2004, 2005, 2006. This is in good agreement with the observed agricultural drought trend in Burundi in 2002, 2004, 2005, 2006 and increased AET anomaly at the same years.

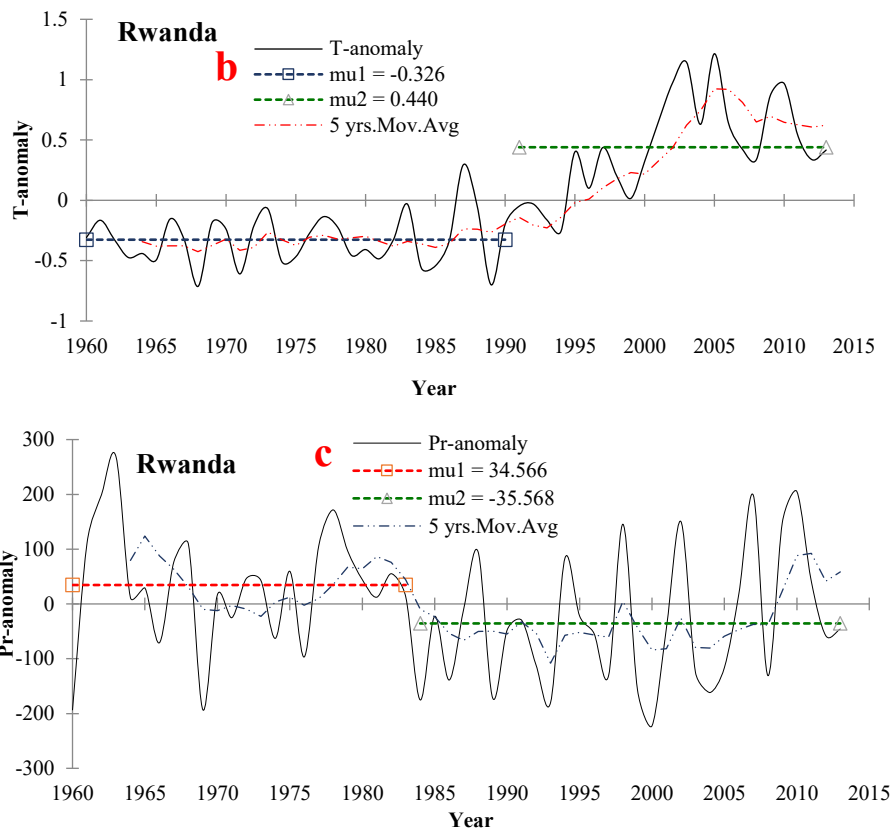


Supplementary Figure G7: Long term hydrological drought, PDSI trend (a), temperature anomaly (b), precipitation anomaly (c) over Burundi 1960-2016

- **Rwanda**

Precipitation anomaly showed a change point in 1983 (supplementary Fig G8(c)). Monthly temperature timeseries has a change point in 1994 while temperature anomaly has a change point in 1990. There is a statistically significant warming trend of 0.22 °C per decade (supplementary Fig G8(b)). Precipitation anomaly showed statistically significant decreasing trend with 15.58 mm/decade (supplementary Table G1), there is also a statistically significant change point in PDSI in 1969 (supplementary Fig G8(a)). Trend analysis also revealed statistically significant decreasing trend in PDSI at 0.4/decade. Based on PDSI drought classification, Rwanda suffered from severe hydrological droughts in 1969, 1975, 1989, 1990, 1992, 1993, 1994, 2000, 2004 and moderate hydrological drought during the following years 1961, 1967, 1973, 1974, 1979, 1980,1984, 1987,1988,1991, 1997, 1999, 2002, 2005, 2006, 2009, 2011, 2012. Rwanda is dominated by moderate hydrological drought. This is in good agreement with the observed agricultural drought trend in Rwanda in 2002, 2004, 2005, 2006, 2009, 2010, 2011 and increased AET anomaly at the same years.



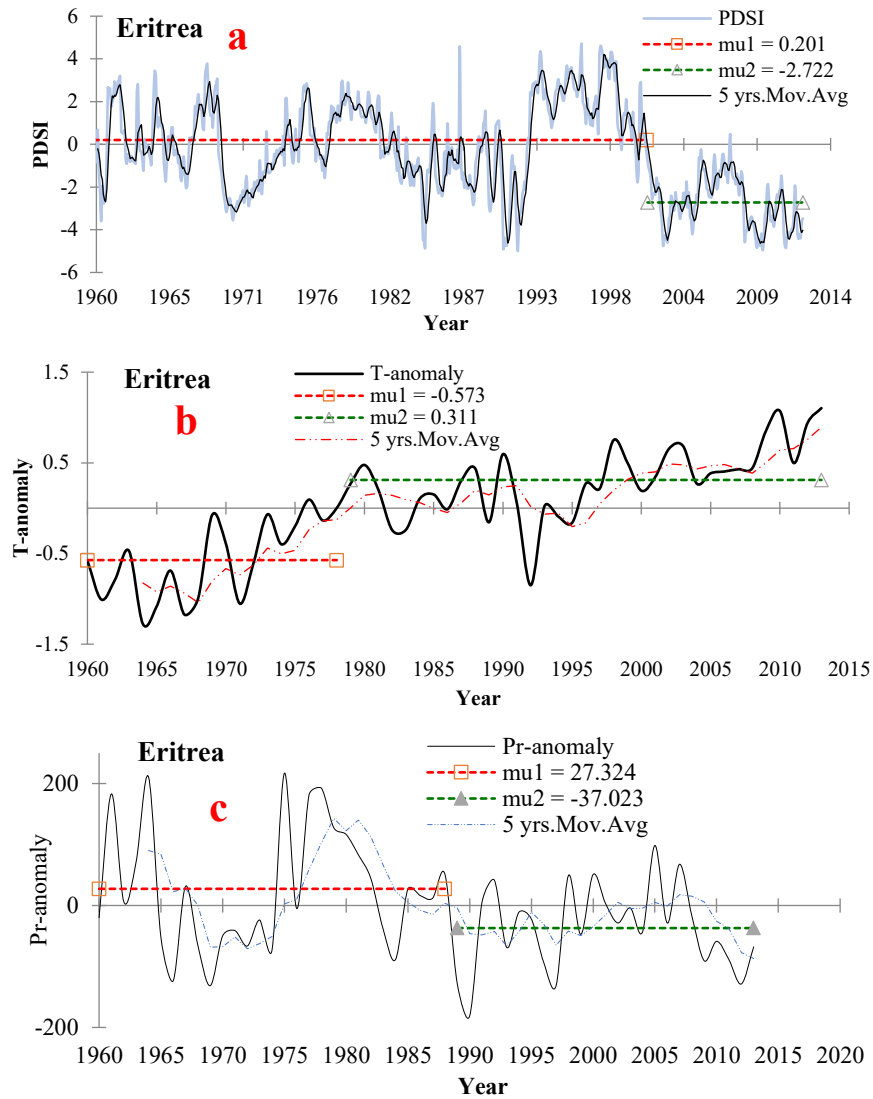


Supplementary Figure G8: Long term hydrological drought, PDSI trend (a), temperature anomaly (b), precipitation anomaly (c) over Rwanda

- **Eritrea**

Precipitation anomaly showed a change point in 1988 (supplementary Fig G9(c)). Monthly temperature timeseries has a change point in 1979 while temperature anomaly has a change point in 1987 (supplementary Fig G9(b)). There is a statistically significant warming trend of 0.3 °C per decade. Precipitation anomaly showed statistically significant decreasing trend with 15.05 mm/decade (supplementary Table G1), there is also a statistically significant change point in PDSI in 2001 (supplementary Fig G9(a)). Trend analysis also revealed statistically significant decreasing trend in PDSI at 0.48/decade. Based on PDSI drought classification, Eritrea suffered from severe hydrological droughts in 1960, 1969, 1970, 1984, 1989, 1990, 1991, 2001, 2002, 2003, 2004, 2008,

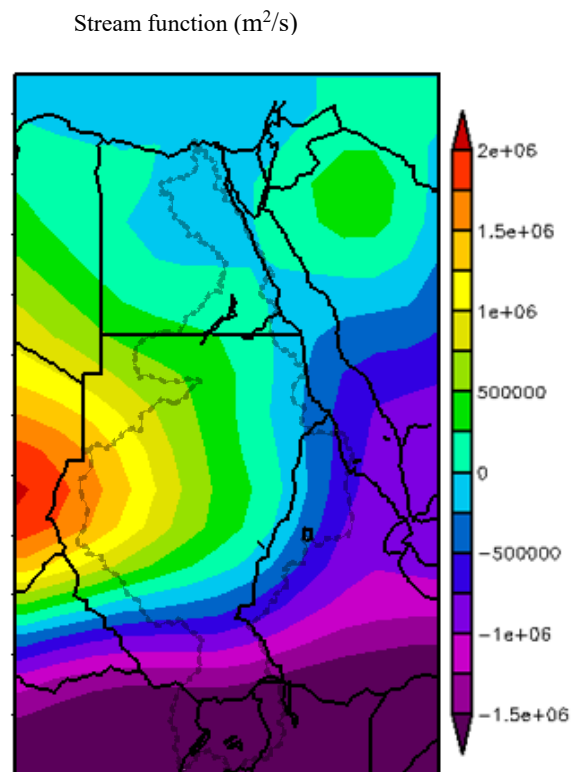
2009, 2010, 2011, and 2012 and moderate hydrological drought during the following years 1966, 1967, 1971, 1972, 1983, 1985, 1986, 1987, 1988, 2005, and 2006. This is in good agreement with the observed agricultural drought trend in Eritrea in 2002, 2004, 2005, 2006, 2009, 2010, 2011 and increased AET anomaly at the same years.



Supplementary Figure G9: Long term hydrological drought, PDSI trend (a), temperature anomaly (b), precipitation anomaly (c) over Eritrea 1960-2016

Appendix H: Changes to driving variables and atmospheric circulation

The lower atmosphere stream function of supplementary Fig H1 at 0.8458 sigma level, which depicts the rotational part of the flow (the flow is along the contours), indicates that main waves emanating from northern towards southern parts of NRB, have shifted further south over the two periods, from 1948-1984 to 1985-2017. This long-term southward shift in the stream function over NRB would have also contributed towards the long-term drying of NRB, as part of the multiple changes due to climate warming, e.g., changes in air temperature, GPH, RH, soil moisture, surface runoff, PET and ENSO.

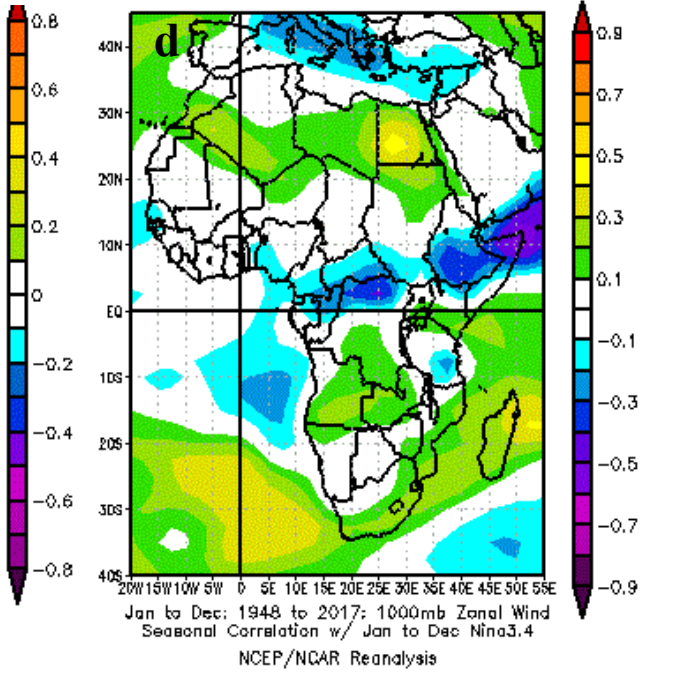
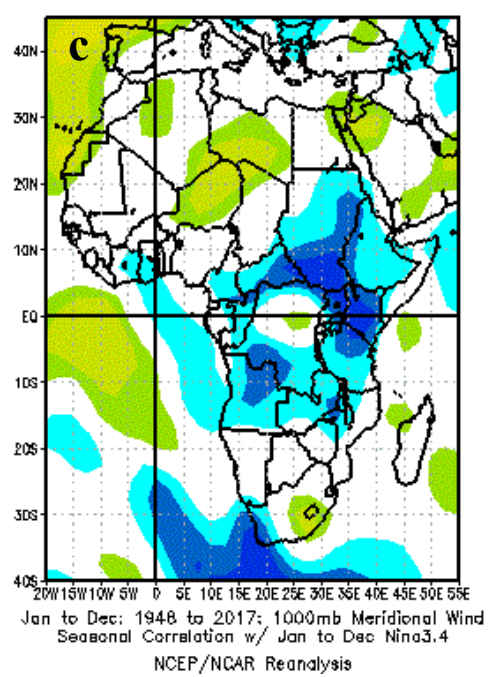
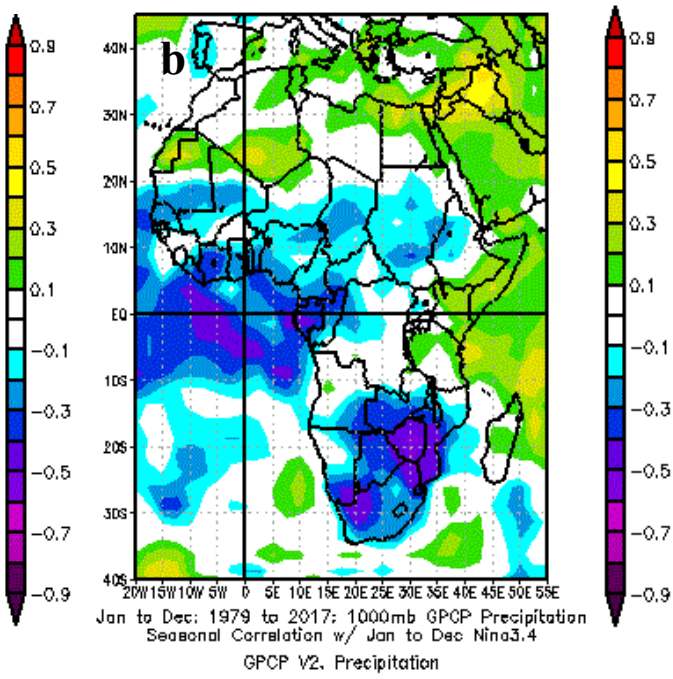
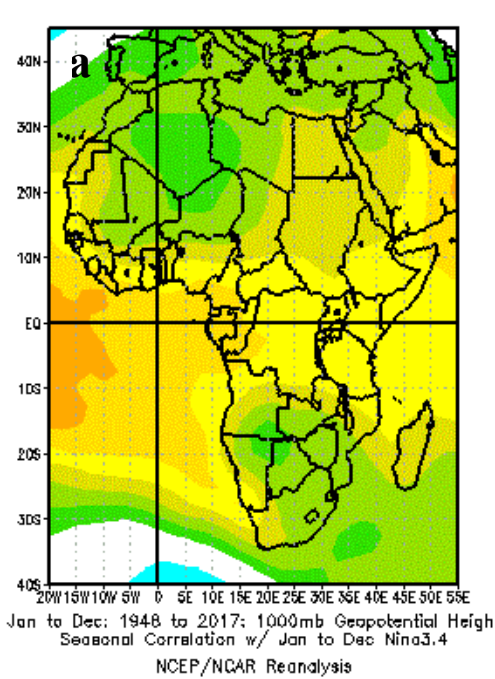


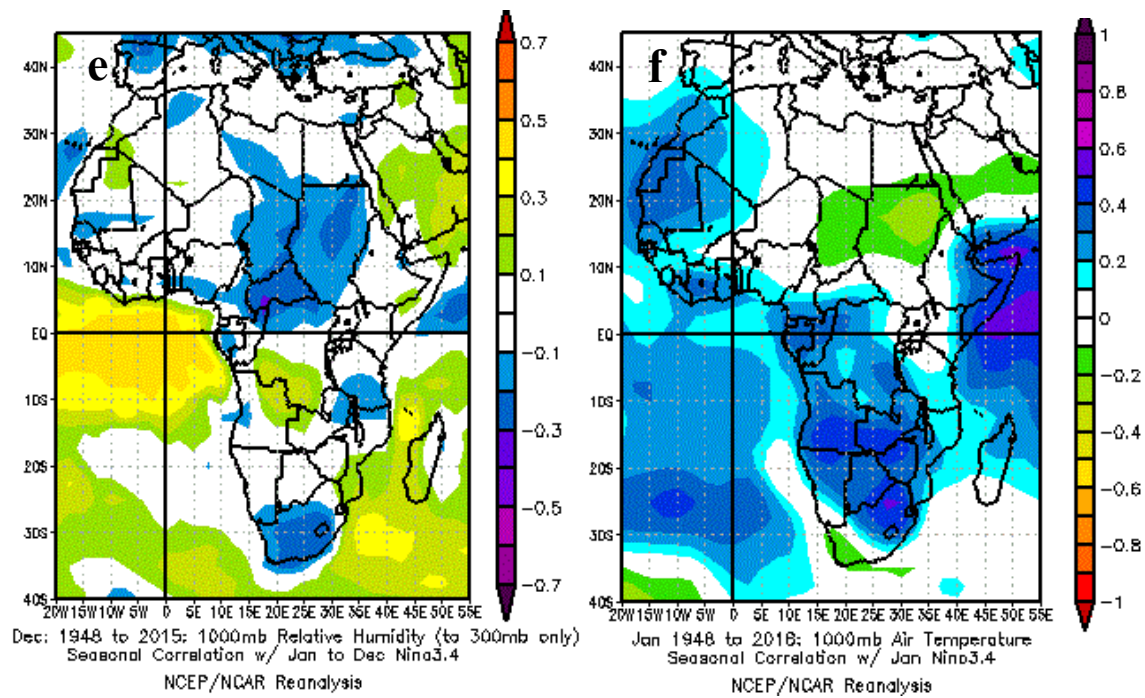
Supplementary Figure H1: Composite maps 300-mb stream function derived from data of 1985-2017 minus data of 1948-1984. Between the two periods, 1948-1984 and 1985-2017, the 300-mb stream function had shifted southward during these two periods.

Spatial correlation between El Nino 3.4 and geopotential height, precipitation, meridional wind, zonal wind, relative humidity, and surface temperature are presented in supplementary

Figure H2. There was a strong spatial correlation between El Nino 3.4 and geopotential height in the entire NRB with correlation coefficient ranging from 0.3-0.7 (supplementary Fig H2(a)). Negative weak to strong correlation was seen between precipitation and El Nino 3.4 in Uganda, this negative correlation can explain the increase in precipitation over Uganda. However, positive correlations indicate a decrease in precipitation as can be seen in the composite mean map of precipitation. For instance, precipitation composite mean map shows a decrease in the low land of Ethiopia and a slightly higher precipitation in its high land and therefore a weak correlation coefficient was seen in Ethiopia between El Nino 3.4 and precipitation (supplementary Fig H2(b)).

Results also shows no correlations between El Nino 3.4 and precipitation over Egypt and northwestern regions of Sudan. Similarly, meridional, and zonal wind fluctuations associated with El Nino 3.4 occur mainly in Ethiopia, Sudan, Egypt and Uganda: However, meridional wind and zonal wind showed weak to strong negative correlations with El Nino 3.4 over Uganda, Ethiopia, and Sudan (decline in meridional and zonal wind). In addition to a positive weak correlation over Egypt (increase in meridional and zonal wind) (supplementary Fig H2(c, d)). Relative humidity also shows a negative correlation with El Nino 3.4 in Sudan, Uganda and lowlands of Ethiopia (supplementary Fig H2(e)). Moreover, surface temperature shows a strong positive correlation with El Nino 3.4 in most of the NRB. This imply that El Nino 3.4 drive the increase in surface air temperature in the Sudan, Ethiopia and Uganda (supplementary Fig H2(f)). These results agree well with the findings of the trend analysis and wavelet coherence between El Nino 3.4 and surface temperature.





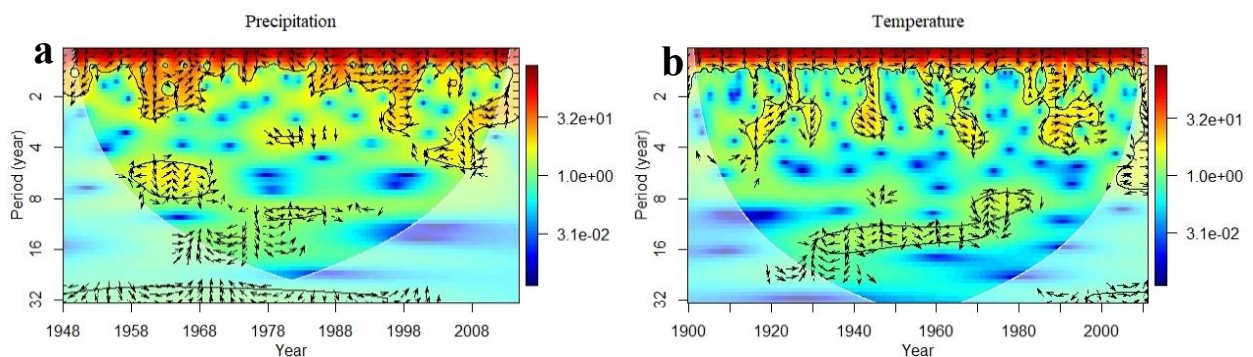
Supplementary Figure H2: Correlation of El Niño 3.4 index with (a) geopotential height, (b) precipitation, (c) meridional wind, (d) zonal wind, (e) relative humidity, and (f) surface temperature between 1948:2017 ($p < 5\%$) in the Nile River basin. Statistically, there is almost certainly a significant connection in the map ($p_{\text{field}} < 0.1\%$). The fraction of the map with $p < 5.00\%$ is 85.13%. With an estimated decorrelation scale of 24.5° and $(45.^\circ)^2$ with data there are about 2 degrees of freedom in the map. This gives a field significance of $0.0\% < p_{\text{field}} < 0.1\%$. The correlation coefficient between El Niño and GPH over NRB ranges from 0.3 to 0.7 (supplementary Fig 37a) but between precipitation and El Niño, the correlation varies from weak negative to strong positive in Uganda. Meridional and zonal wind in Ethiopia, Sudan, Egypt and Uganda are correlated with El Niño but the relation ranges from weak to strong negative correlations (supplementary Fig H2(c, d)). Relative humidity is negative correlated with El Niño in Sudan, Uganda and low lands of Ethiopia (supplementary Fig H2(e)), while surface temperature is positively correlated with El Niño in most NRB (supplementary Fig H2(f)), which is expected given recent stronger El Niño episodes have been linked to greenhouse warming.

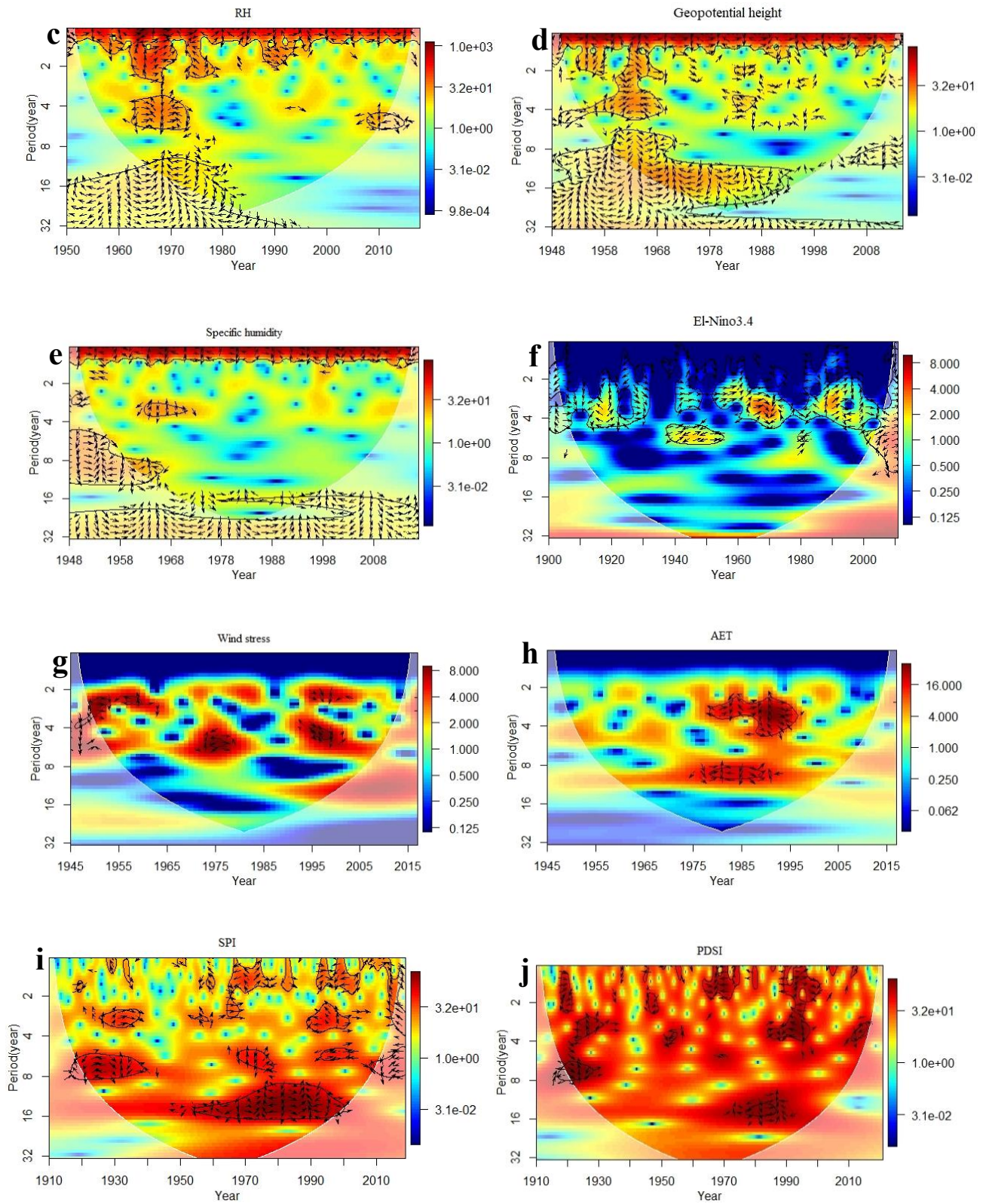
Appendix I: Wavelet power spectrum of drought drivers

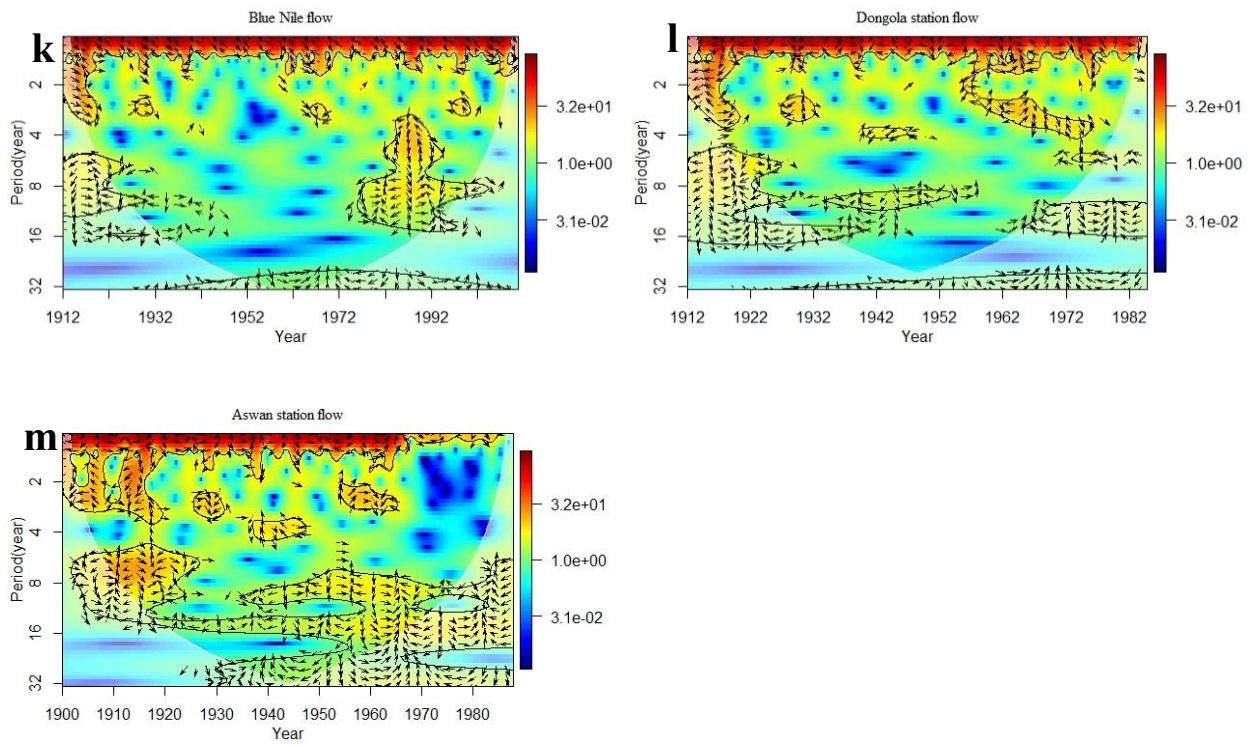
Supplementary Figure I1 shows the wavelet power spectra of precipitation, temperature, relative humidity, geopotential height, specific humidity, wind stress, actual evapotranspiration, El Nino, SPI, self-calibrated PDSI, Blue Nile flow, Dongola station flow, and Aswan station flow of the NRB. The solid contours show statistically significant power at the 95% significance level against red noise, and the white sag line is the cone of influence, outside of which results may be affected by edge effects of zero paddings. All the variables showed similar oscillation patterns in the NRB. For instance, the power spectrum plot of precipitation reveals three distinct bands at 1–2-yr, 4–8-yr, and 2–4 yr periodicities from 1948 to 1958, 1958 to 1970 and the 1970 to 2010, respectively (supplementary Figure I1(a)). The power spectrum plot of surface temperature shows a dominate band of 1–2 yr (1910 to 2010), a band of 2–4 yr (1910 to 1930, 1940 to 1945 and 1980 to 2000), and a band of 8–16 yr in 1920–1990 (supplementary Figure I1(b)). Similarly, the power spectrum plot of relative humidity shows a dominate band of 1–2 yr in 1950 to 2010, a dominate band of 16–32 yr in 1950 to 1995, and a band of 4 to 8 yr in 1960 to 1980 (Supplementary Figure I1(c)). For geopotential height and specific humidity (supplementary Figure I1(d, e)), two dominate bands of 1–2 yr and 16–32 yr were found in 1948 to 2010 and 1948–2008, respectively. In addition to a much smaller band of 4–8 yr in 1948 to 1970. Moreover, the power spectrum plot of El Niño 3.4 reveals a distinct band of 2–4-yr from 1948 to 2010, however the power spectrum is stronger after 1960. Wind stress and actual evapotranspiration wavelet spectra show a strong 2–4 yr band between in 1950s and between 1995 to 2008, another 4–8 band was found in some years after the 1970s (supplementary Figure I1(g, f)).

Continuous wavelet transform was conducted to identify the relative power of drought indices “SPI and self-calibrated PDSI” in different period scales. Similar wavelet power spectra were found for both indexes. Four distinct bands at 1–2-yr, 2–4-yr, 4–8 yr, and 8–16 yr periodicities

were found in PSI and self-calibrated PDSI. The 1–2-yr and 2-4 yr bands show a significant variability in the drought indexes between the years 1920 to 1940, 1950 to 1970, 1980 to 2010. However, strong power existed for the 4 -8 yr band between 1920 to 1940, 1970 to 1980 and 1990s. This agrees with major drought observed in the NRB. On the other hand, the highest concentration of the power spectrum was noticed for the periods 16 to 32 yr between 1955 to 2012. Overall, periodicity of 8-16 and 16-32 yr bands were the most significant periods in both indexes after 1970 (supplementary Figure I1(i, j)). Wavelet spectra are useful for summarizing a river's temporal variability, therefore the power spectrum plot of Blue Nile flow, Dongola station flow and Aswan station flow were computed. Blue Nile flow power spectrum plot reveals three distinct bands at 1–2-yr, 8–16-yr, and 4-16 yr periodicities from 1912 to 2012, 1912 to 1932 and the 1975 to 2012, respectively. Where, the 1–2-yr band is the dominant feature in Blue Nile flow (supplementary Figure I1 (k)). Similar pattern was observed in the Dongola and Aswan stations flow. Overall, the Nile River flow showed a combination of significant interannual and decadal oscillations that appeared and disappeared over 1912–2012.







Supplementary Figure II: wavelet power spectra of (a) precipitation, (b) temperature, (c) relative humidity, (d) geopotential height, (e) specific humidity, (f) wind stress, (g) actual evapotranspiration, (h) El Nino, (i) SPI, (j) self-calibrated PDSI, (k) Blue Nile flow, (l) Dongola station flow, and (m) Aswan station flow of the NRB.

Appendix J: Wavelet coherence between driving variables and El-Nino 3.4

To evaluate the possible impacts of El Nino 3.4 on climate variables and droughts in the NRB, wavelet coherence, was used to detect the relationship between climate variables, drought indexes (SPI, self-calibrated PDSI) and El Nino 3.4. The wavelet coherence plots (WTC) between El Nino 3.4 and precipitation, temperature, relative humidity, geopotential height, specific humidity, SPI, self-calibrated PDSI, Blue Nile flow, Dongola station flow, and Aswan station flow of the NRB are shown in supplementary Fig J1. The arrows show the phase difference: right-pointing arrows indicates that the two-time series are in phase signals, while left-pointing arrows represents anti-phase signals and mean that one time series leads (lags) the other by 90° .

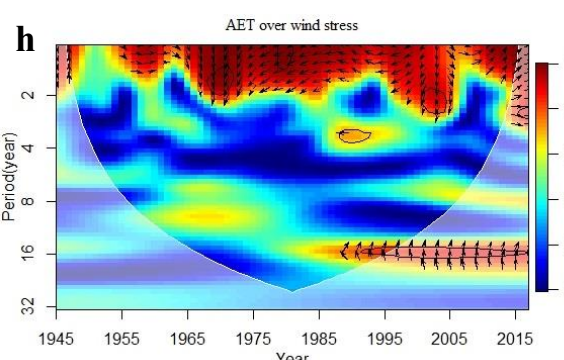
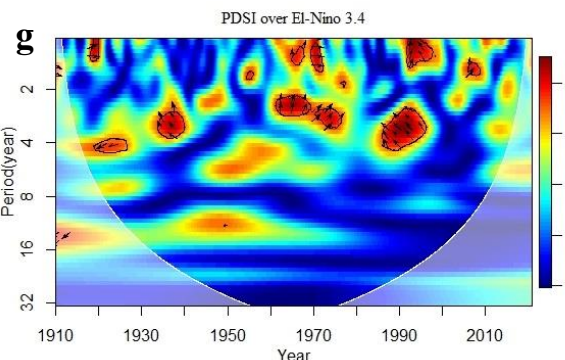
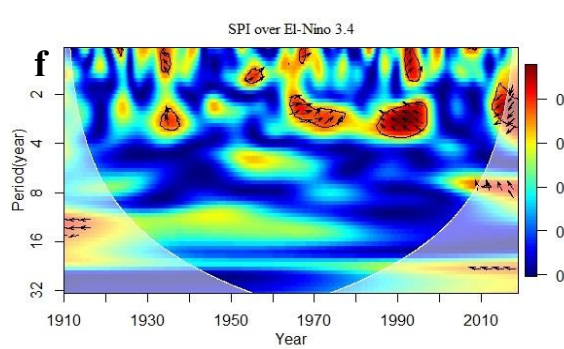
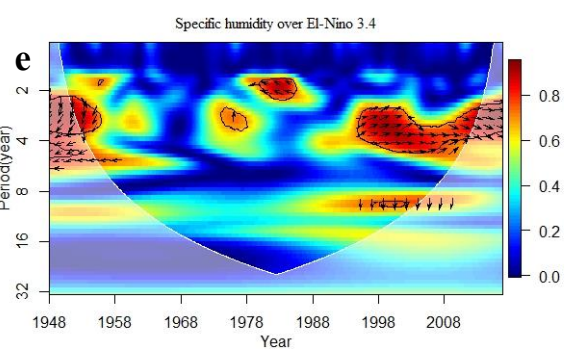
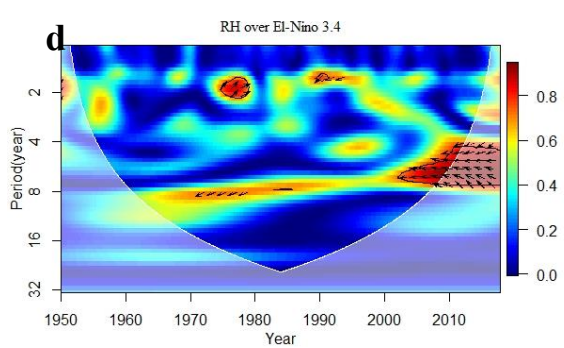
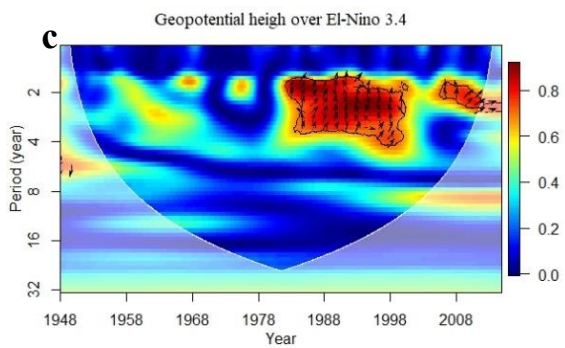
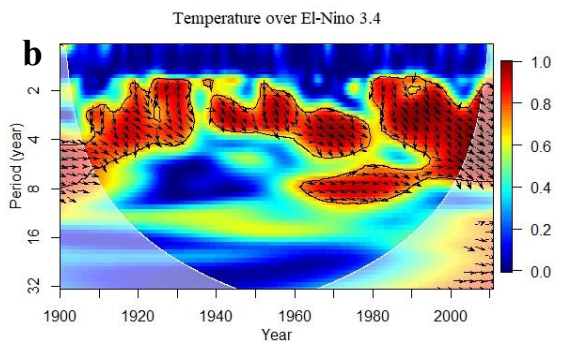
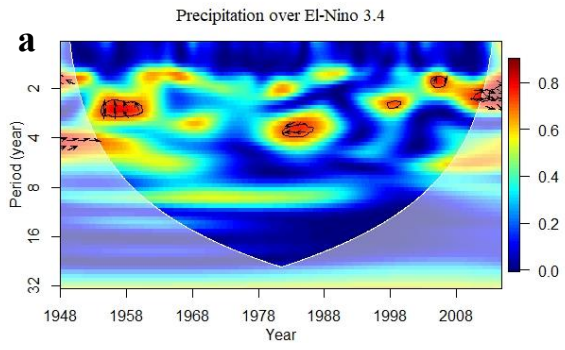
The influence of El Nino 3.4 on precipitation can be seen in wavelet coherence plot (supplementary Figure J1(a)). Precipitation exhibits coherent spatial patterns with respect to El Niño, as the wavelet coherence spectra revealed a statistically significant coherency at 2-4 yr band in 1960s and 1970s and indicates anti-phase relationships between precipitation and El Nino 3.4 after 1970s. The coherence spectrum plots between El Nino 3.4 and surface temperature show statistically significant power at 2–4-yr bands in 1920 to 1940, 1950 to 1970, and 1975 to 2012 over NRB (supplementary Figure J1(b)). After 1970s, there was a consistently strong coherence at 4–8-yr bands between El Nino 3.4 and surface temperature. This observed strong in-phase relationship between El Nino 3.4 and surface temperature after 1970 indicates that El Nino 3.4 leads the warming trend in the NRB. Similarly, the power of the wavelet coherence between El Nino 3.4 and geopotential height (supplementary Figure J1(c)) was consistently strong at 4–8-yr band between 1975 and 2012, which is expected because of the close relationship between geopotential height and air temperature. In addition, there was a strong 1–2-yr wavelet coherence in the 1980s and the 1990s between El Nino 3.4 and relative humidity (anti-phase) (supplementary Figure J1(d)), and a stronger 4–8-yr wavelet coherence after the 2000s. Moreover, the wavelet

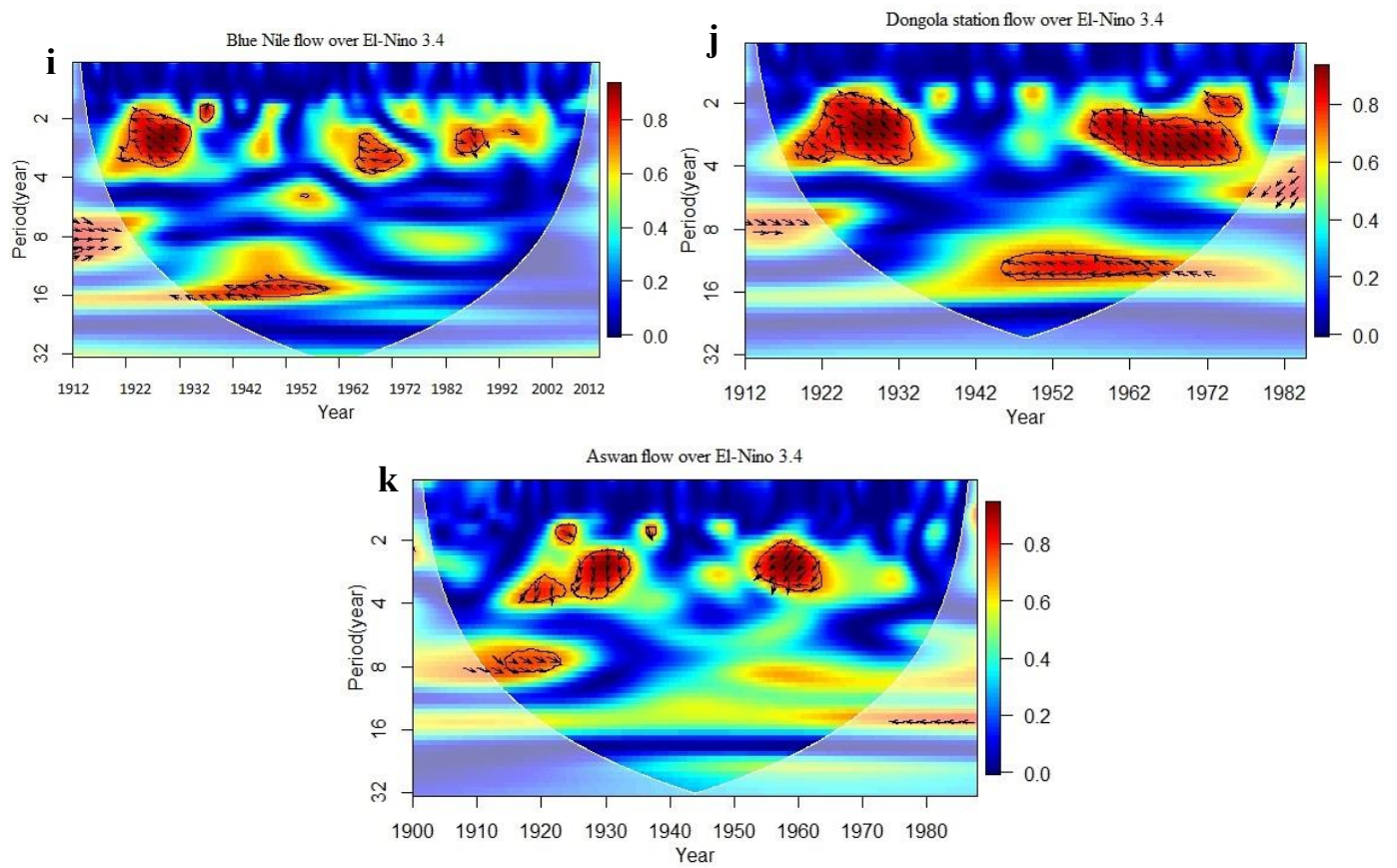
coherence plot between specific humidity and El Nino 3.4 shows a high 2–4-yr wavelet coherence from 1948 to 1958, 1970s and from 1990 to 2012, and a strong 8-16 yr wavelet coherence after the 1990s (supplementary Figure J1(e)).

El Nino 3.4 had significant coherency with SPI after 1970s compared to drought conditions in the earlier years. Wavelet coherence between El Nino 3.4 revealed strong correlation and phase relationship between the two series. As it shows a statistically significant coherency at 2–4-yr bands in 1952, 1959, 1965, 1972, 1973, 1978, 1983, 1984, 1987, 1991, 1994, 1999, 2002, and 2011 (supplementary Figure J1(f)). Before 1970s, wavelet coherence indicates that El Nino 3.4 and SPI were in phase relationships, however after 1970s there was a significant common power dominantly present anti-phase relationships between SPI and El Nino 3.4. These results suggest that a higher El Nino 3.4 index usually corresponds to a lower SPI value (more severe drought) and explains the more frequent droughts in the NRB after 1970. Similarly, the cross-power spectra between El Nino 3.4 and self-calibrated PDSI showed a significant common power at 2- 4-yr band during 1970–2015 (supplementary Figure J1(g)). In addition, there was a significant clear anti-phase relationship between the self-calibrated PDSI and El Nino 3.4 in 1987, 2002, 2003, 2004, 2005, 2006, 2008, 2009, 2010, and 2011. Overall, the wavelet analysis detected the correlations between climate variables, droughts, and El Niño 3.4 in the NRB. These statistically significant positive correlations directly indicate that the El Niño 3.4 events have strong impacts on inducing droughts in the NRB. Wavelet coherence spectrum plots between wind stress and actual evapotranspiration show statistically significant power at 1–2-yr band between 1945 and 2015, and 16-32 yr band between 1985 and 2015 (supplementary Figure J1(h)). However, between 1945 and 1970 wind stress and actual evapotranspiration were in phase, and after 1975 the 1–2-yr band was dominated by anti-phase relationship. On the other hand, the entire 16-32 yr band coherence represent the anti-phase relationship between wind stress and actual evapotranspiration. These

results indicate that the increase in wind stress after 1970s drives the increase in actual evapotranspiration in the NRB.

Wavelet coherence spectrum between El Nino 3.4 and the Blue Nile flow (supplementary Figure J1(i)), discloses a statistically significant wavelet coherence at 2-4 yr bands in 1920s, 1930s, and 1960 to 1970. The anti-phase signals between El Nino 3.4 and the Blue Nile flow clearly dominate the entire period between 1912 and 2012 except for a small in phase signals between 1982 and 1990. In addition to a strong 16-20 yr anti-phase bands between 1930 and 1965, implying that El Nino 3.4 has large influence on the Blue Nile flow. Similar El Nino 3.4 effects on Dongola flow station at Khartoum-Sudan can be seen in supplementary Figure J1(j). However, the wavelet coherence between El Nino 3.4 and Dongola flow reveals higher coherence at both short and relatively longer periods, as shown by more extensive statistically significant wavelet coherence between El Nino 3.4 and Dongola flow. Wavelet coherence analysis further show that the Nile River flow at Aswan station-Egypt (downstream) are strongly correlated with El Nino 3.4 (supplementary Figure J1(k)). These results indicate that the Nile River flow exhibits coherent spatial patterns with respect to El Niño downstream and upstream. In other words, the decrease in the flow of the Nile River is associated with the frequent occurrence of El Nino in recent years, increase in AET, warming trend, and decrease in precipitation.

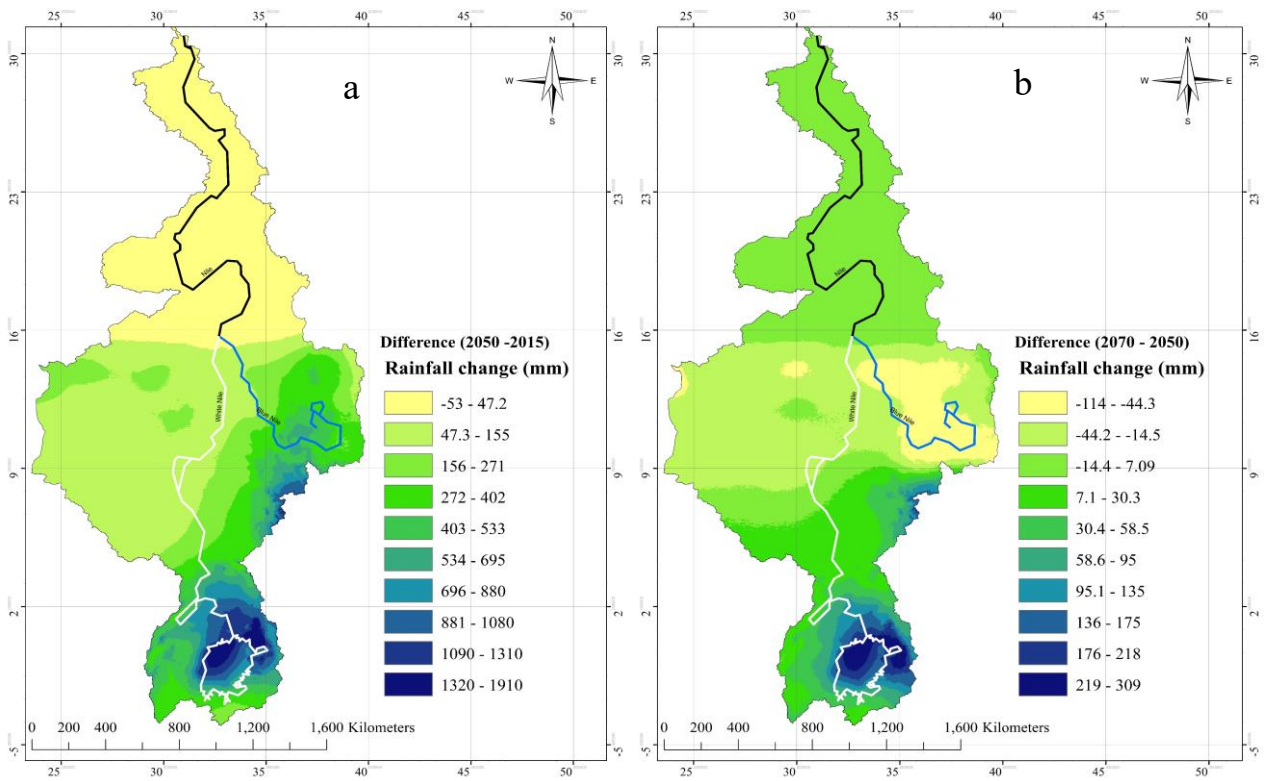




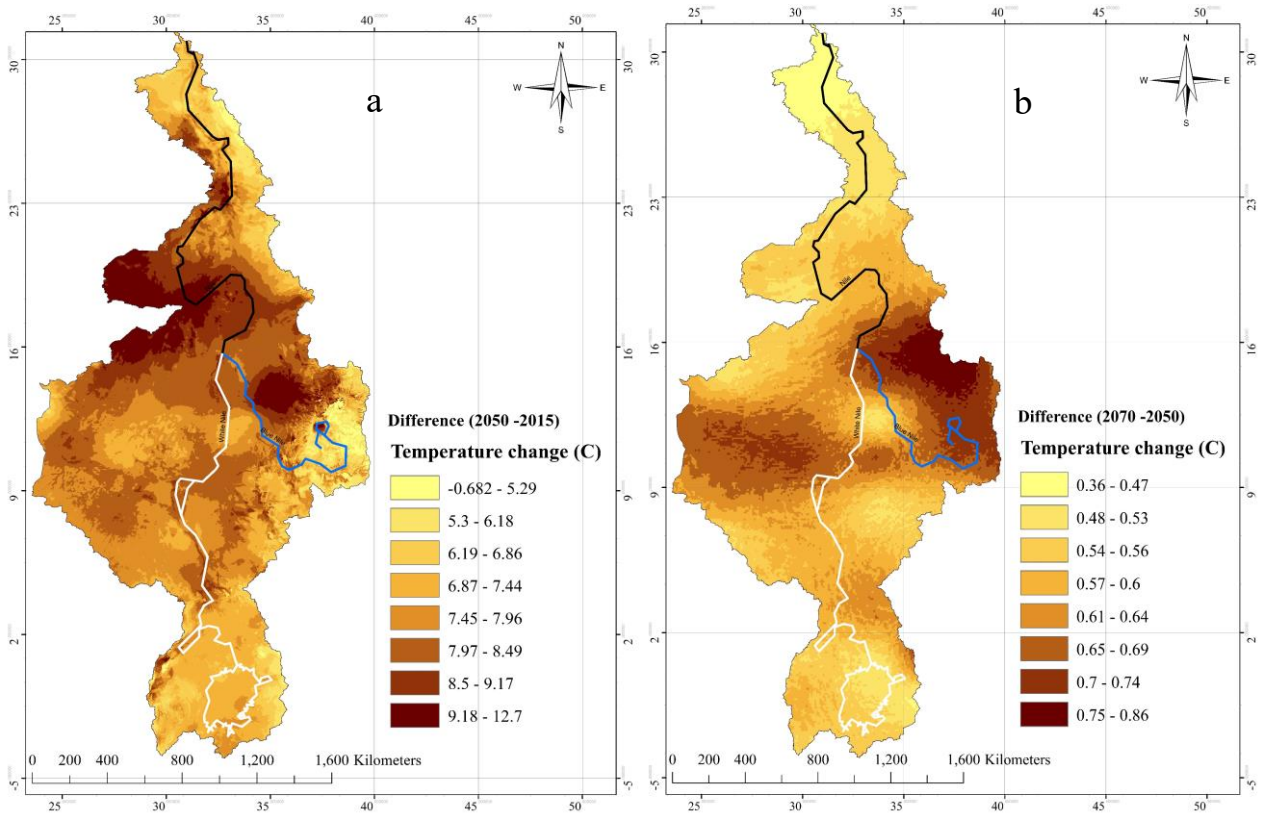
Supplementary Figure J1: Wavelet coherence between El Nino 3.4 and (a) precipitation, (b) temperature, (c) relative humidity, (d) geopotential height, (e) specific humidity, (f) SPI, (g) self-calibrated PDSI, (h) AET and wind stress, (i) Blue Nile flow, (j) Dongola station flow, and (k) Aswan station flow

Appendix K: Projected climatic changes in the NRB

Supplementary Figure K1(a) illustrate the future change in annual precipitation in the NRB. Between 2015-2050, the projection shows decrease of annual precipitation by with 1.55 mm/yr over Egypt and Sudan, except for the White Nile region which will witness an increase in annual precipitation with 2.89 mm/yr. Annual precipitation in Eritrea and Ethiopia is projected to increase by 9.6 mm/yr. Kenya, Tanzania, Rwanda, Burundi, Uganda, and Congo are projected to have the highest increase in annual precipitation with 31.3 mm/yr over the same period. By 2070, annual precipitation is expected to decrease by 2.25 mm/yr between 2050 and 2070 in Eritrea and Ethiopia. Decline trend in precipitation in Sudan and Egypt is projected to 0.84 mm/yr, similar trend to historical trend between 1960-2015, where precipitation decline trend was 7.57 mm/decade “0.76 mm/yr”. Increasing trend over Kenya, Tanzania, Rwanda, Burundi, Uganda, and Congo will continue but at a lower rate 5.7 mm/yr between 2050 and 2070 (supplementary Figure K1(b)). Future projection of warming trend over the NRB. Between 2015-2050 (supplementary Figure K2(a)), showed warming trend over Sudan and Egypt will increase and the projected increase in mean temperature in this period is 6.82 °C, while between 2050-2070 this warming trend will continue but at a lower rate than the previous period as the difference between mean temperature in 2050 and 2070 is 0.79 °C (supplementary Figure K2(b)). The increases of mean temperature in Ethiopia and Eritrea between 2015– 2050 and 2050–2070, is about 6.08 °C, and 0.56-0.58 °C, respectively. While in Kenya, Tanzania, Rwanda, Burundi, Uganda, and Congo increase in mean temperature is 5.5 °C between 2015-2050 and 0.48 °C between 2050-2070.



Supplementary Figure K1. Future change of annual Precipitation (a) 2050, (b) 2070

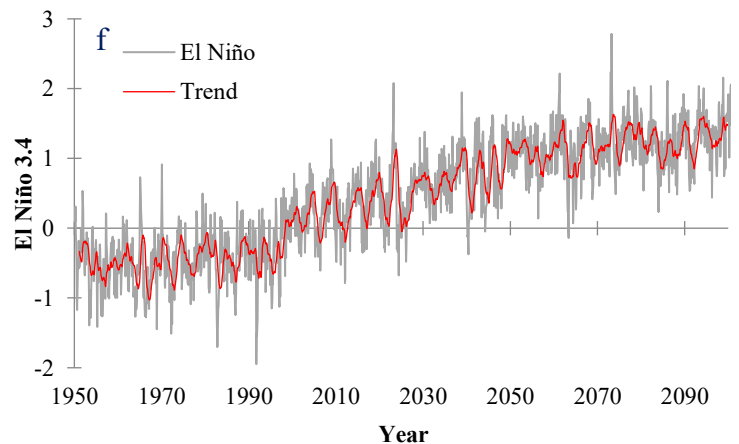
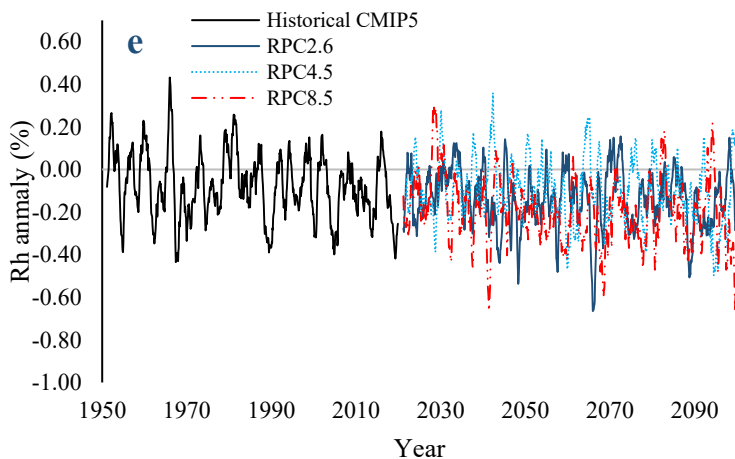
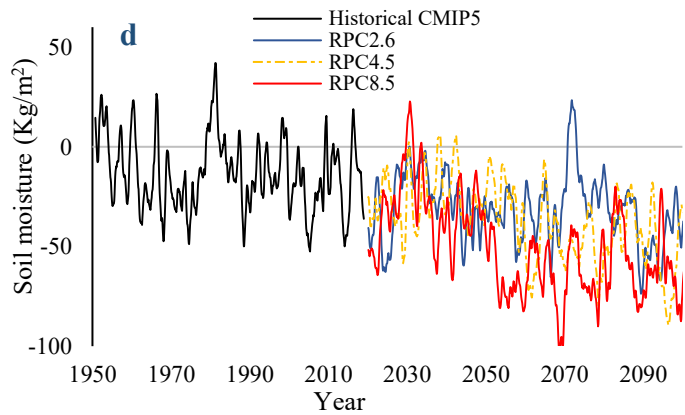
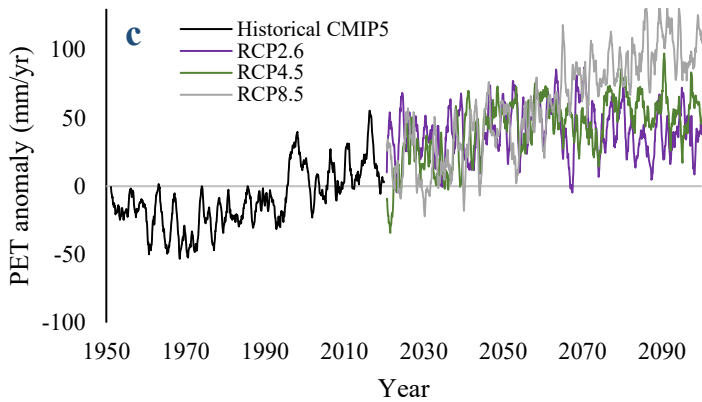
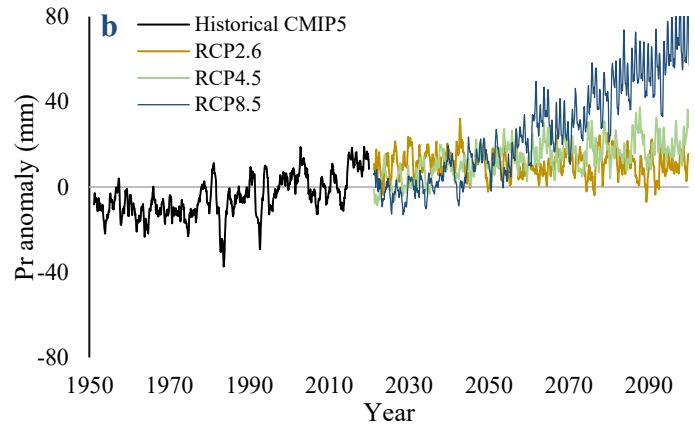
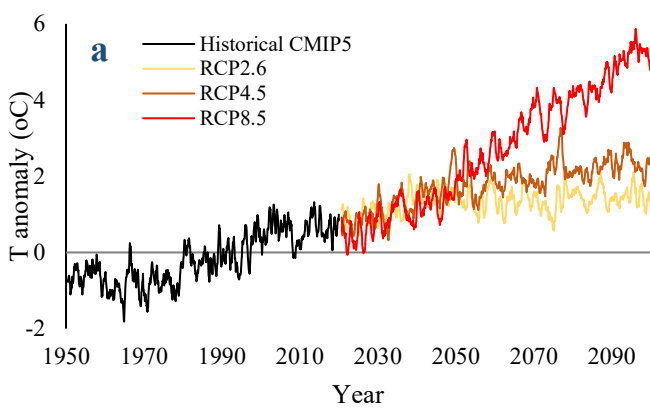


Supplementary Figure K2. Future projection of warming trend (a) 2050 and (b) 2070

Based on the analysis of three climate changes scenarios (RCP 2.6, 4.5, and 8.5) of 34 global climate models of CMIP5, future annual precipitation is projected to decrease at about 16.5 mm/decade over the NRB between 2020 and 2050. The spatial distribution of this trend shows that in countries such as Egypt and Sudan annual precipitation will decline by 15.5 mm/decade, but for the White Nile region, the annual precipitation could increase at 28.9 mm/decade between 2020-2050 (supplementary Figure K3(a)). In the other hand, under the lower scenarios (RCP4.5 and RCP2.6), annual precipitation in the NRB will increase by 5 mm/decade between 2050 and 2100 (supplementary Figure K3(b)). Over 2020-2050, warming in the NRB is projected to be 0.24 °C/decade, 0.48 °C/decade, 0.36 °C/decade based on RCP 2.6, RCP4.5, and RCP8.5 respectively. For both RCP4.5 and RCP8.5 scenarios, warming will continue but at 0.12-0.72 °C/decade between 2050 and 2100, while under a lower scenario (RCP 2.6) warming trend is just 0.1 °C/decade. (supplementary Figures K2(a) and K3(a)). Under the three climate changes scenarios (RCP 2.6, 4.5, and 8.5), relative humidity trend will continue to decline but at 1.04 % /decade, 1.47% /decade, and 0.87/decade between 2020 and 2050, respectively. However, over 2050-2100, the decline trend in relative humidity is about 0.34 % / decade, 0.53 % /decade, and 0.23% /decade (supplementary Figure K3(e)).

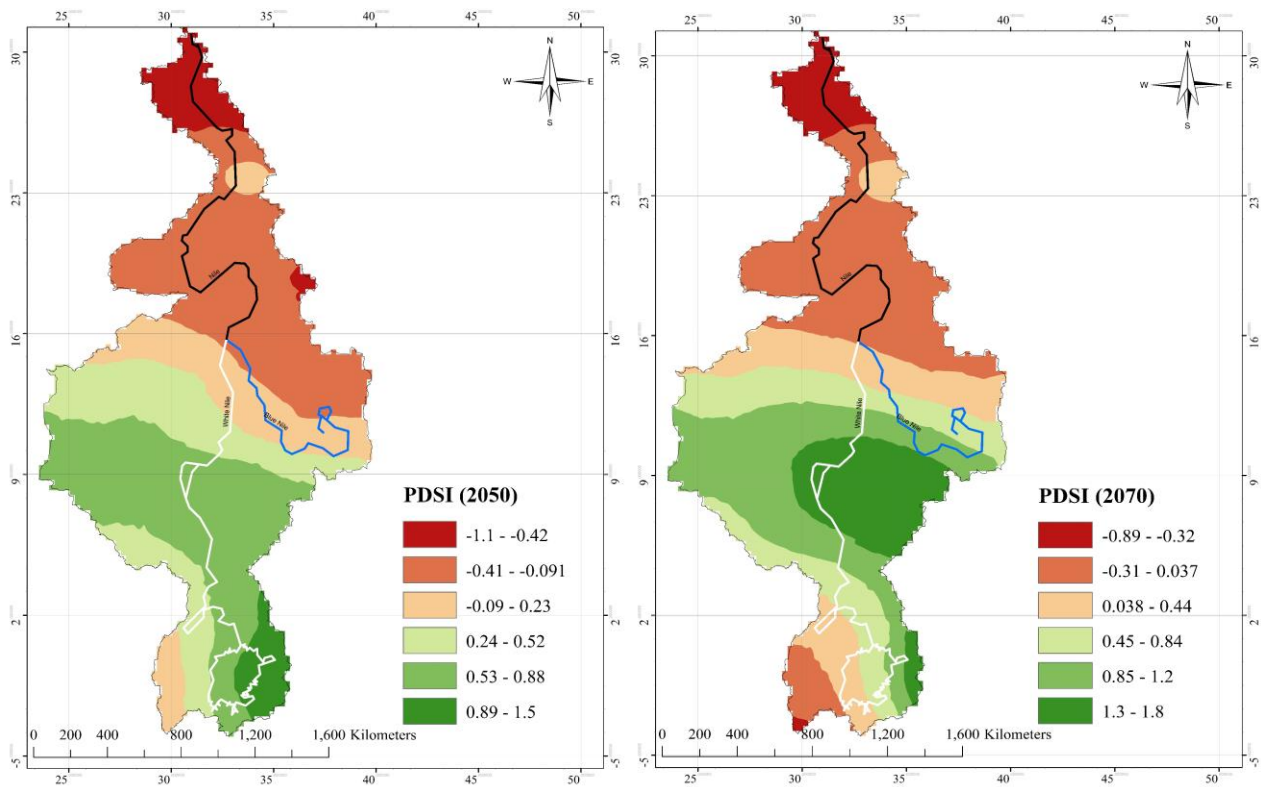
Under RCP 2.6, 4.5, and 8.5 scenarios, between 2020 and 2050, the potential evapotranspiration (PET) is projected to increase at 11.4 mm/decade, 18.4 mm/decade and 24.1 mm/decade respectively (supplementary Figure K3(c)), which is consistent with projected rising air temperature and declining relative humidity. As warming continues from 2050 to 2100, PET is projected to increase at about 10 mm/decade, 14.8 mm/decade, and 35.2 mm/decade under RCP 2.6, 4.5, and 8.5, respectively. Corresponding to increasing trends in PET, the soil moisture content (SWC) is projected to decrease at 0.12 kg/m²/decade, 0.72 kg/m²/decade, and 0.96 kg/m²/decade between 2020 and 2050; and by about 0.65 kg/m²/decade, 2.5 kg/m²/decade, and

4.3 kg/m²/decade between 2050 and 2100, under RCP2.6, RCP4.5, and RCP8.5, respectively (supplementary Figure K3(d)). It seems that agricultural drought in the NRB will get worse over the 21st Century. Climate models also project more frequent and stronger El Niño episodes between 2020 and 2100 (supplementary Fig K3(f)), leading to worsening droughts and severe surface drying in NRB by the end of the 21st century.



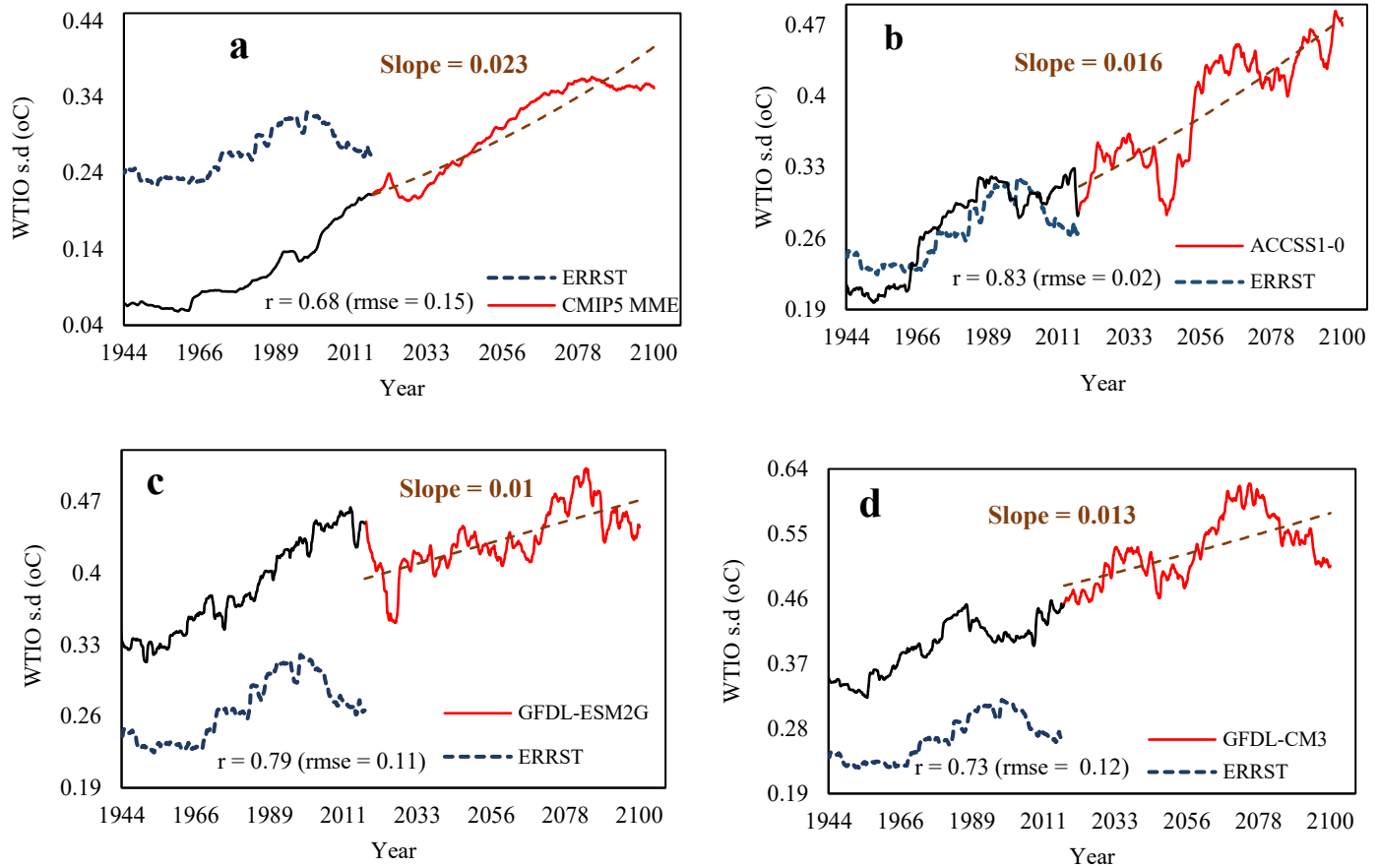
Supplementary Figure K3. Historical CMIP5 and future projection of warming trend (a), precipitation (b), potential evapotranspiration (c), soil moisture content (d), relative humidity under three climate change scenarios (e), and projected change in El Niño 3.4 index (f)

Furthermore, large parts of Egypt and Sudan are projected to suffer mild to moderate hydrologic droughts over the 21st Century (supplementary Figure K4), and countries such as Kenya, Tanzania, Rwanda, Burundi, Uganda, and Congo are projected to suffer incipient droughts. Future projection of hydrological drought in the NRB responded to the increased rate of warming and projected increase in precipitation. Major areas of Egypt and Sudan is projected to have mild to moderate drought, this can be explained by the very high increase in projected mean temperature. While the situation is different in White Nile region in Sudan which is projected to be Slightly wet to incipient wet spell which agrees with the increased precipitation in the portion of Sudan, which will have an increase in annual precipitation of 2.89 mm/yr between 2015-2050. Ethiopia is expected to have incipient wet spell while Eritrea climate is near normal according to PDSI classification. Kenya, Tanzania, Rwanda, Burundi, Uganda, and Congo climate are projected to be near normal to slightly wet which also explain the increase of precipitation at these countries at the same projection period (supplementary Figure K4). Between 2050 and 2070 as the increase in mean temperature is lower than the previous period and precipitation increase is also lower, the entire region is covered by incipient drought (mainly Egypt and Sudan-except the White Nile region) and slightly wet to moderately wet in Kenya, Tanzania, Rwanda, Burundi, Uganda, and Congo and Ethiopia. This reflects the effect of warming rate in future drought conditions (supplementary Figure K4).



Supplementary Figure K4. Future projection of drought severity ‘PDSI’ 2050,2070

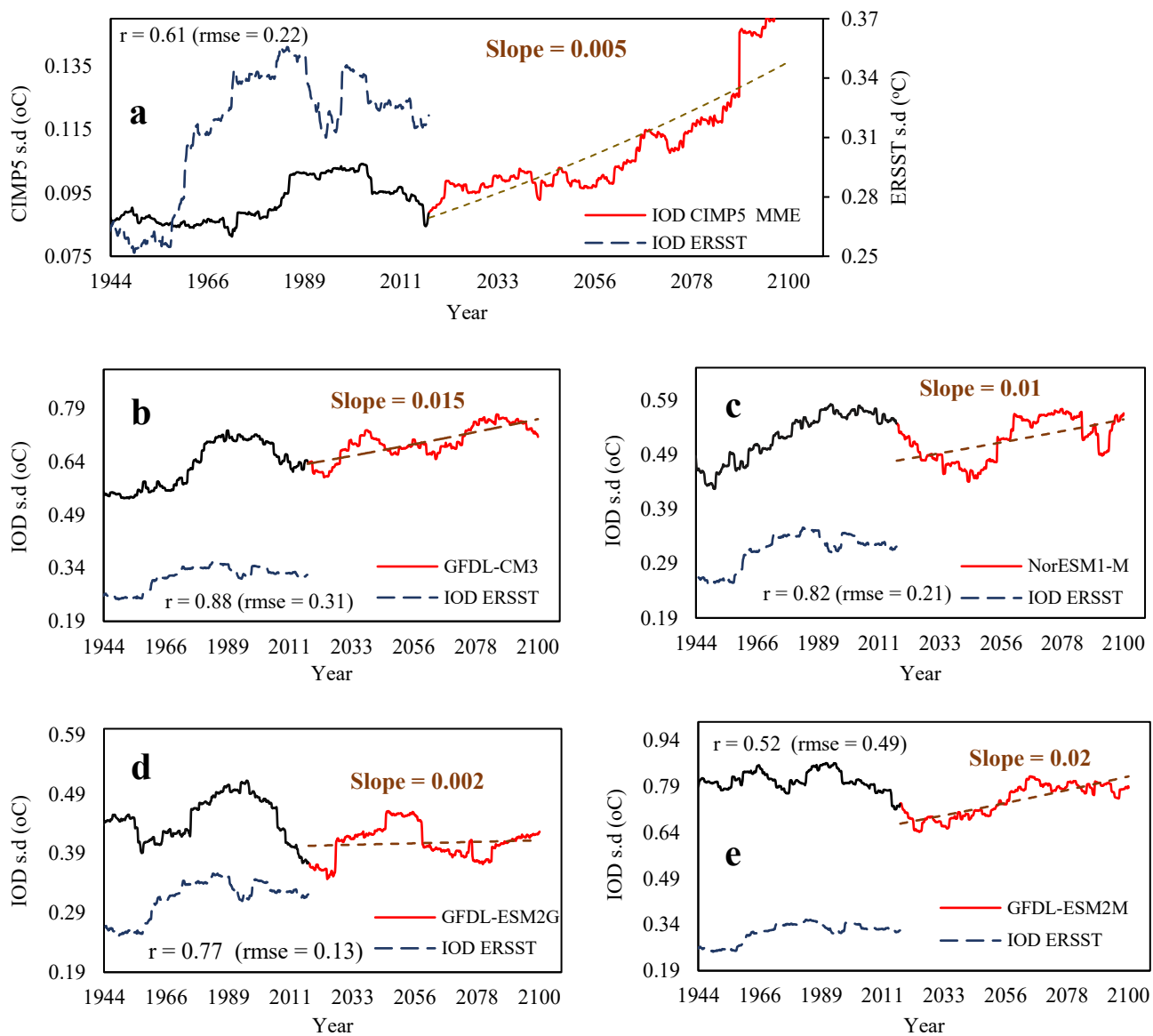
Supplementary Figures K5 and K6 show the analyzed and projected WTIO and IOD using climate projections of 34 global climate models (GCMs) of CMIP5. First, WTIO was estimated as areally weighted SST simulated by each GCM over the Arabian sea (50°E to 70°E and 10°S to 10°N). Then, the multi-model ensemble (MME) of the WTIO computed from the simulations of 34 GCMs was computed over 30-year periods from 1913 to 2100. WTIO estimated from the GCM that best agrees with the observed WTIO were selected. Furthermore, projections of IOD between 2019 and 2100 were computed as the difference between Western (50°E to 70°E and 10°S to 10°N) and Eastern (90°E to 110°E and 10°S to 0°N) SST of the Indian ocean simulated by the 34 GCMS.



Supplementary Figure K5. Time variation of simulated WTIO amplitude. **a**, the multi-model ensemble (MME) of the WTIO amplitude from 34 climate models computed over 30-year running periods from 1913 to 2100. The WTIO from the MME was calculated as area weighted average of the Indian Ocean SST over the Arabian sea (50°E to 70°E and 10°S to 10°N) in each model simulations. The 30-year running WTIO amplitudes from ERSST over the period 1913–2017 are also shown (blue). Pearson correlation coefficients between the best models and observations (ERSST data), are displayed. The slope is the linear trend estimated at the 5% level based on the Mann–Kendall test.

The correlation between the MME of WTIO obtained from GCMs and WTIO estimated from ERSST data range between $\rho = 0.61$ and $\rho = 0.88$ (supplementary Figure K5(a)). The variability (s.d.) of WTIO in the Arabian sea has increased since the 1970s in both the observed dataset and the MME of 34 GCMs' simulations for the historical run, which means that the western Indian

Ocean has become warmer, and projected to be much warmer, at a warming trend of 0.01 to 0.023 °C/decade between 2019 and 2100 (supplementary Figure K5(b–d)). The warming over the Western Indian Ocean and the more intensive El Niño in recent years are expected to play a major role modulating the future climatic conditions of NRB, likely resulting in less precipitation, relative humidity, soil moisture and the Nile streamflow as warming continues in NRB over the 21st Century. Under the projected increase in WTIO over the Arabian sea, future drought conditions of NRB is expected to worsen. There is significant correlation between the IOD calculated from the MME and ERSST observations ($\rho = 0.61$) (supplementary Figure K6(a-d)). Supplementary Figure K5(d) shows projected increasing trends of 0.01 to 0.02 °C/decade in IOD over 2019-2100, which will double the observed increasing trend in IOD between 1993 and 2018. As future positive IOD events are projected by GCMs to be more extreme in the future because of global warming, NRB could suffer from more severe droughts more frequently in the future.



Supplementary Figure K6. Time variation of simulated IOD amplitude. **a**, the multi-model ensemble (MME) of the IOD. The MME IOD was computed as the difference between West (50°E to 70°E and 10°S to 10°N) and Eastern (90°E to 110°E and 10°S to 0°N) SST of the Indian ocean from 34 climate models. The 30-year running IOD amplitudes from ERSST over the period 1913–2017 are also shown (blue lines).